FIGURES

FIGURES (Continued)

FIGURES (Continued)

FIGURES (Continued)

FIGURES (Continued)

FIGURES (Continued)

FIGURES (Continued)

FIGURES (Continued)

FIGURES (Continued)

FIGURES (Continued)

FIGURES (Continued)

FIGURES (Continued)

FIGURES (Continued)

FIGURES (Continued)

FIGURES (Continued)

FIGURES (Continued)

FIGURES (Continued)

INTENTIONALLY LEFT BLANK

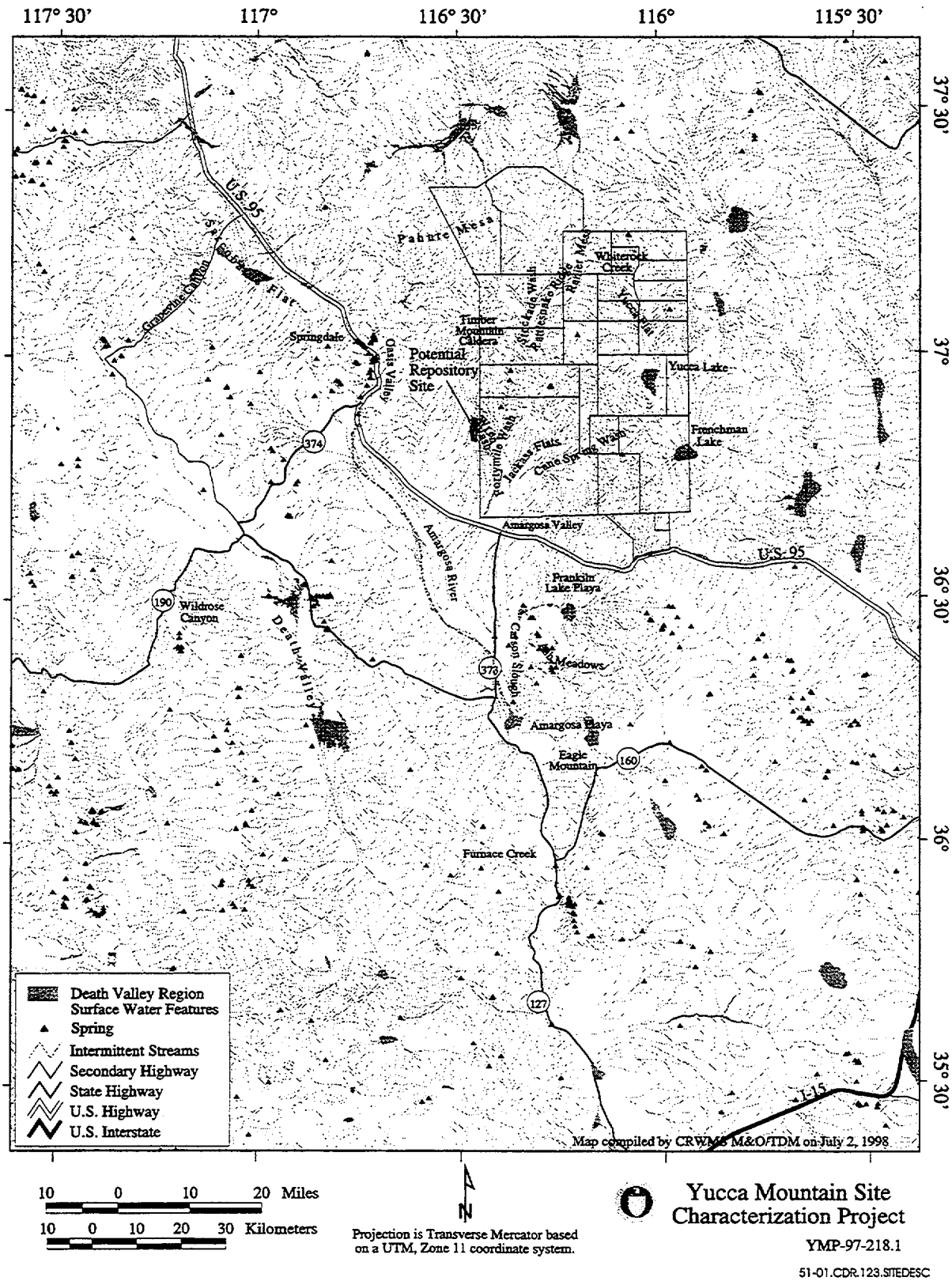

Figure 5.1-1. Surface Water Features in the Yucca Mountain Area

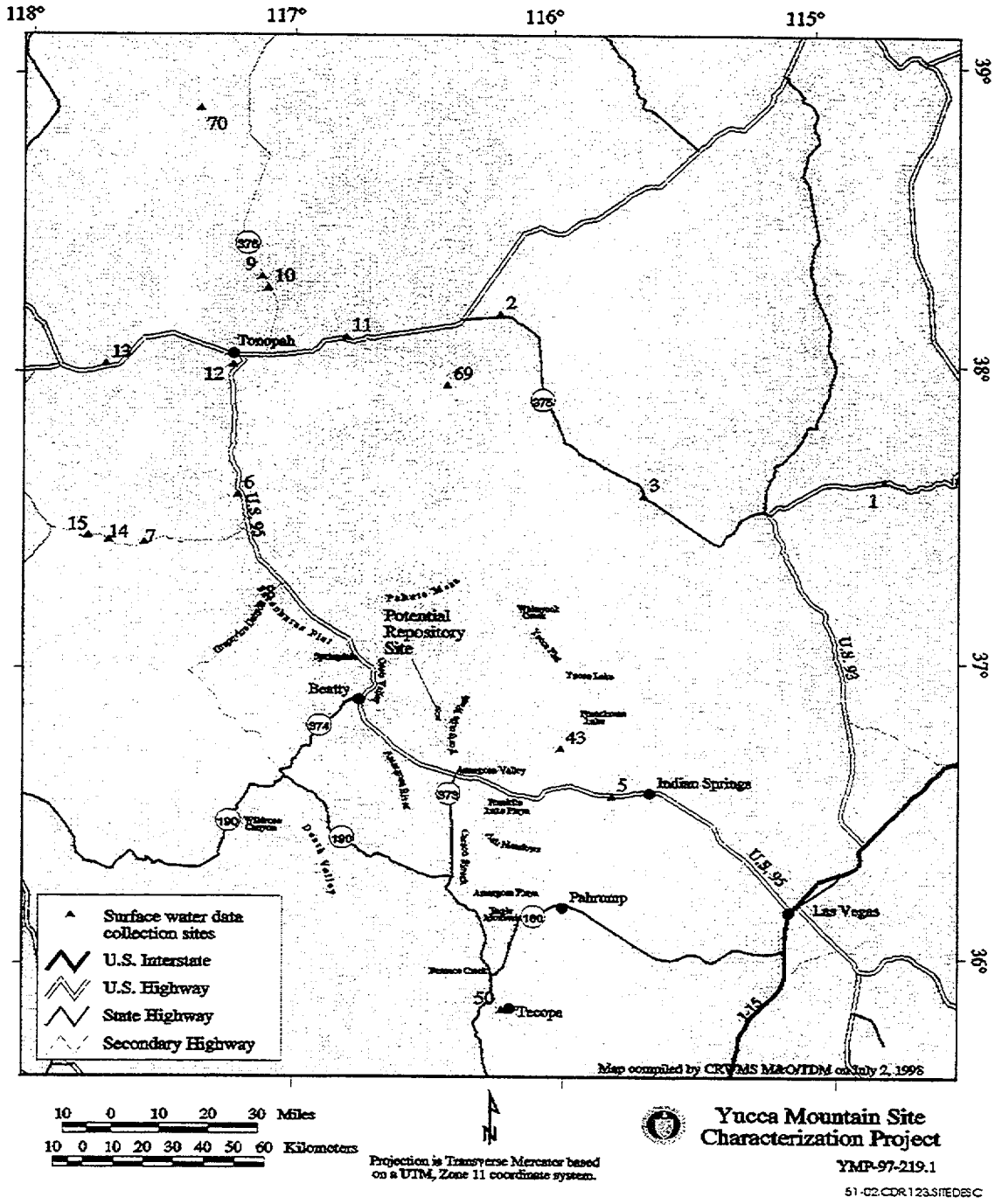

NOTE: See Tables 5.1-1, 5.1-2, and 5.1-6 for listing of data collection sites.

Figure 5.1-2. Surface Water Data Collection Sites in the Yucca Mountain Region

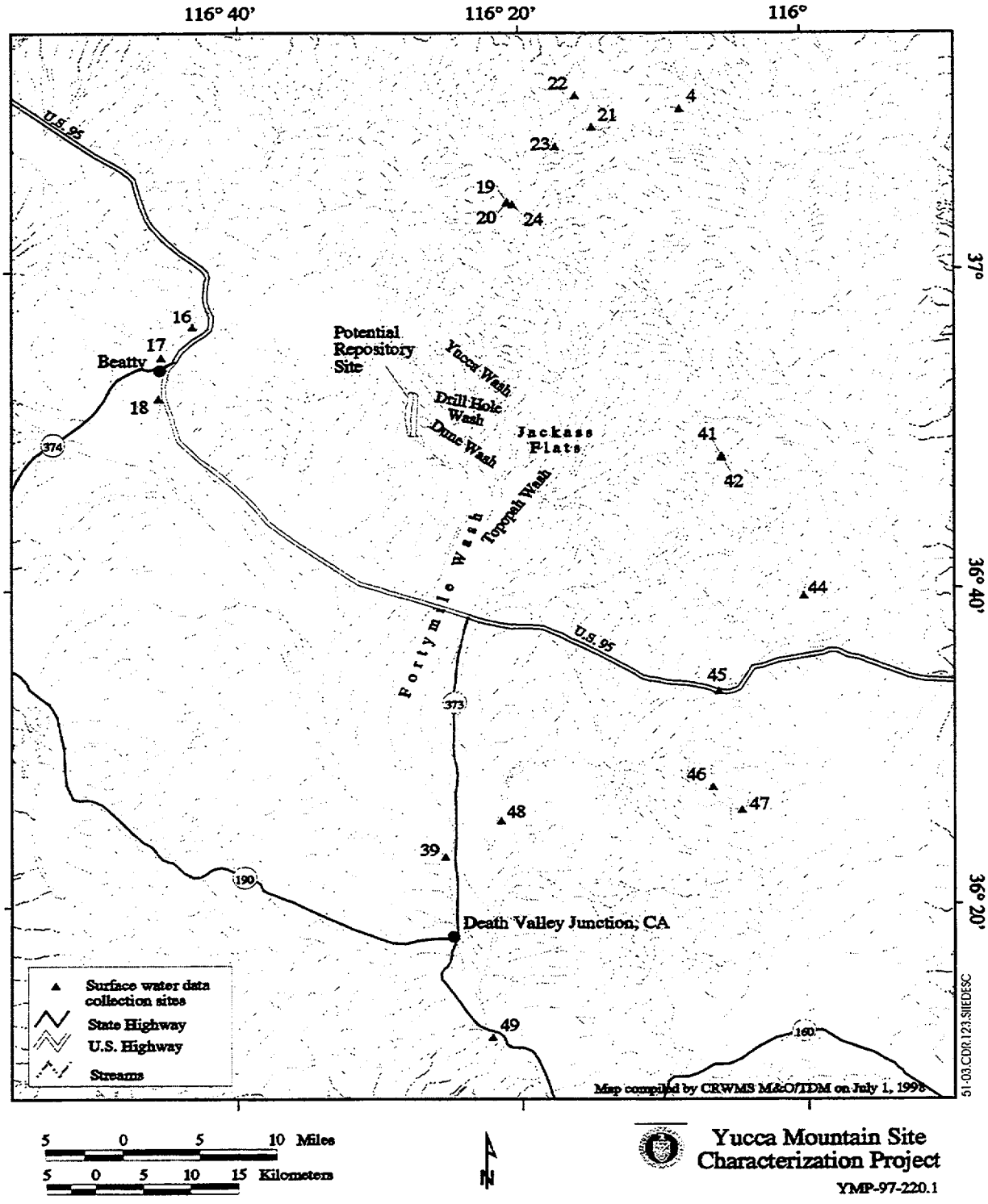

NOTE: See Tables 5.1-1, 5.1-2, and 5.1-6 for listing of data collection sites.

Figure 5.1-3. Surface Water Data Collection Sites Near Yucca Mountain

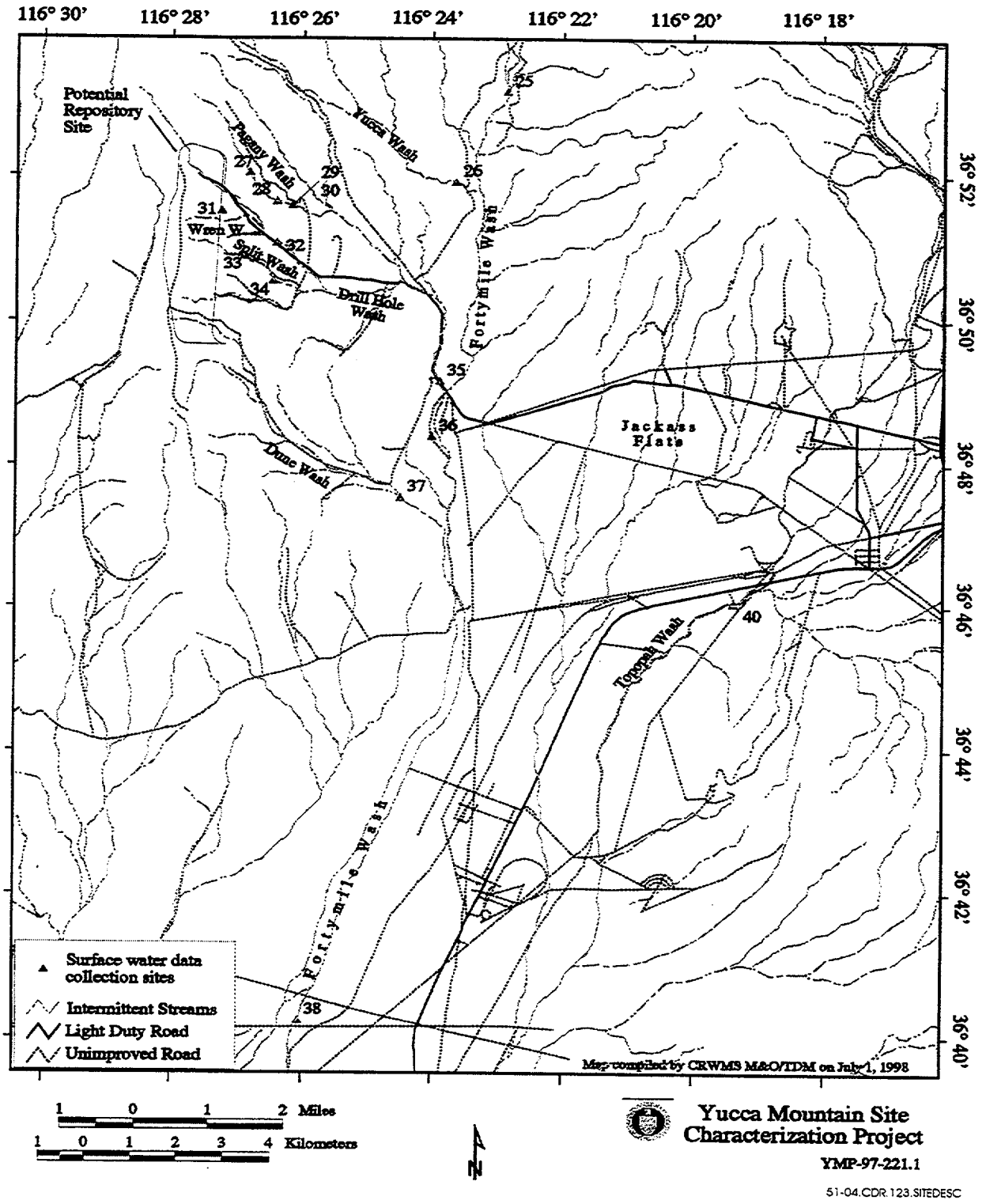

NOTE: See Tables 5.1-1, 5.1-2, and 5.1-6 for listing of data collection sites.

Figure 5.1-4. Surface Water Data Collection Sites At and Near Yucca Mountain

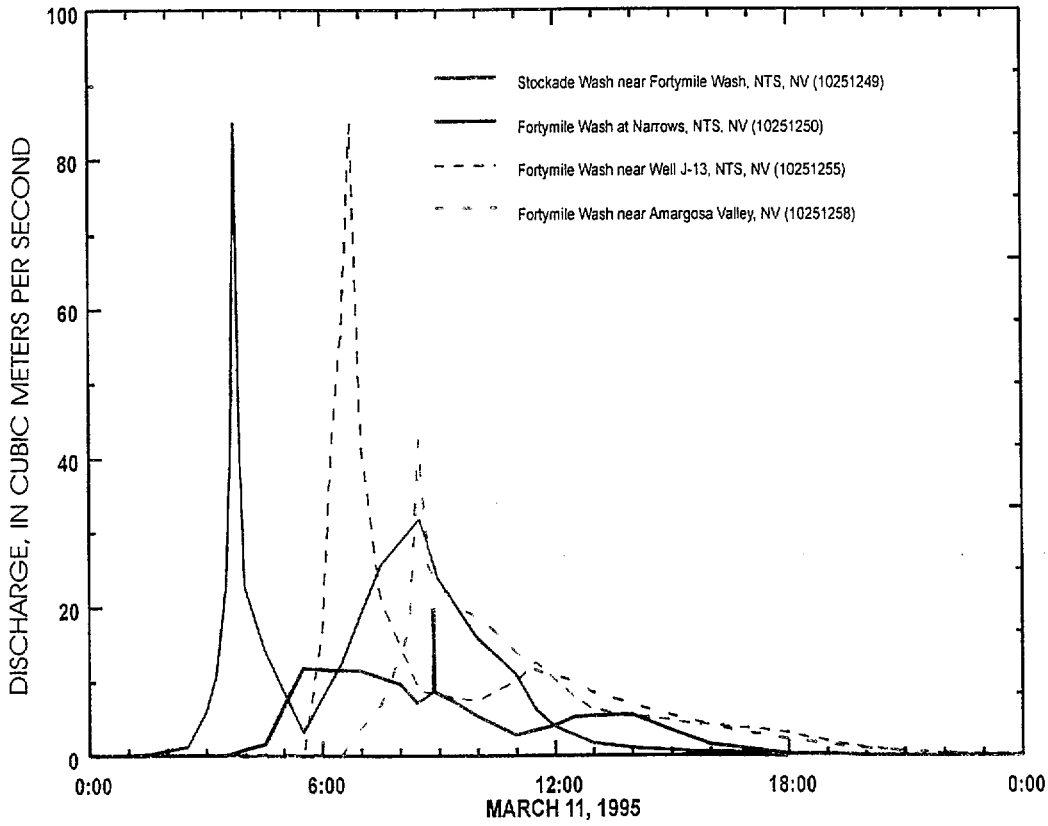

Figure 5.1-5. Hydrographs of Fortymile Wash Sites During March 11, 1995

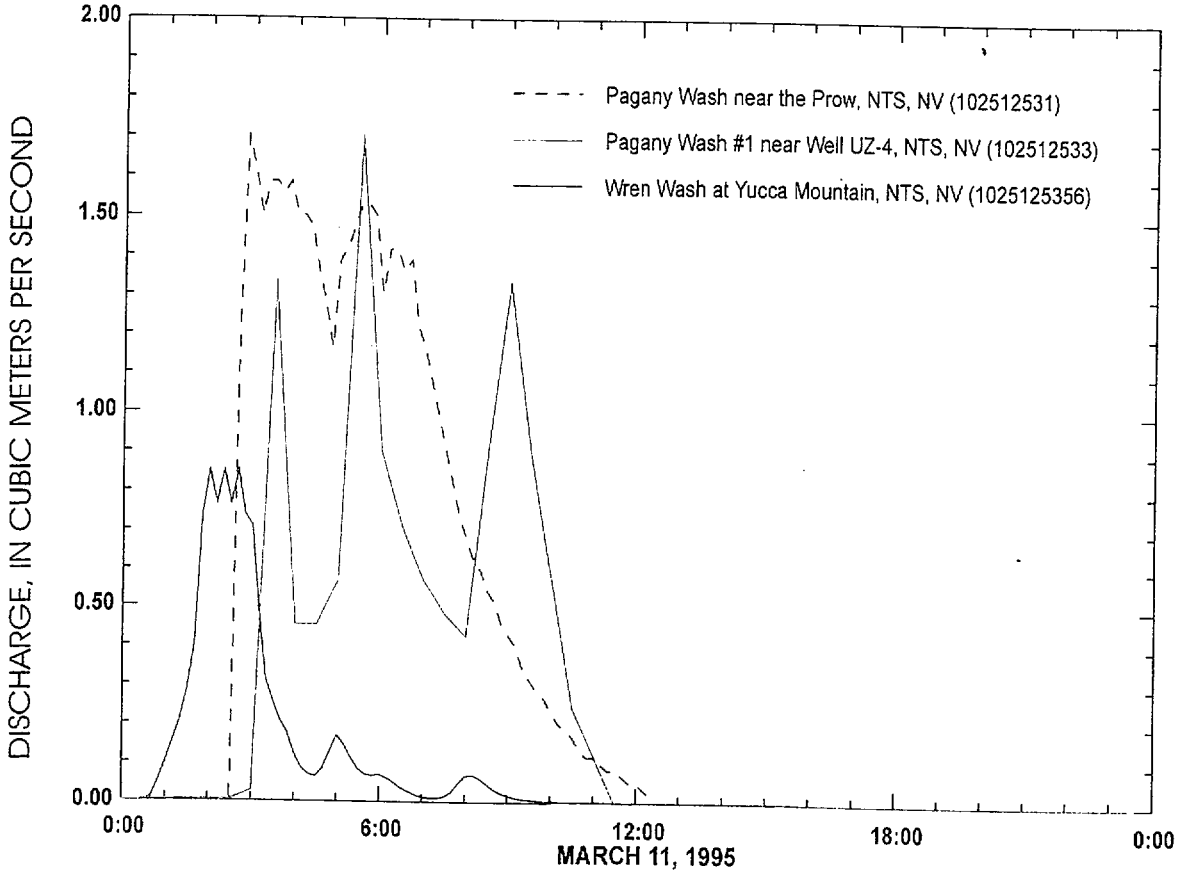

Figure 5.1-6. Hydrographs of Yucca Mountain Sites for March 11, 1995

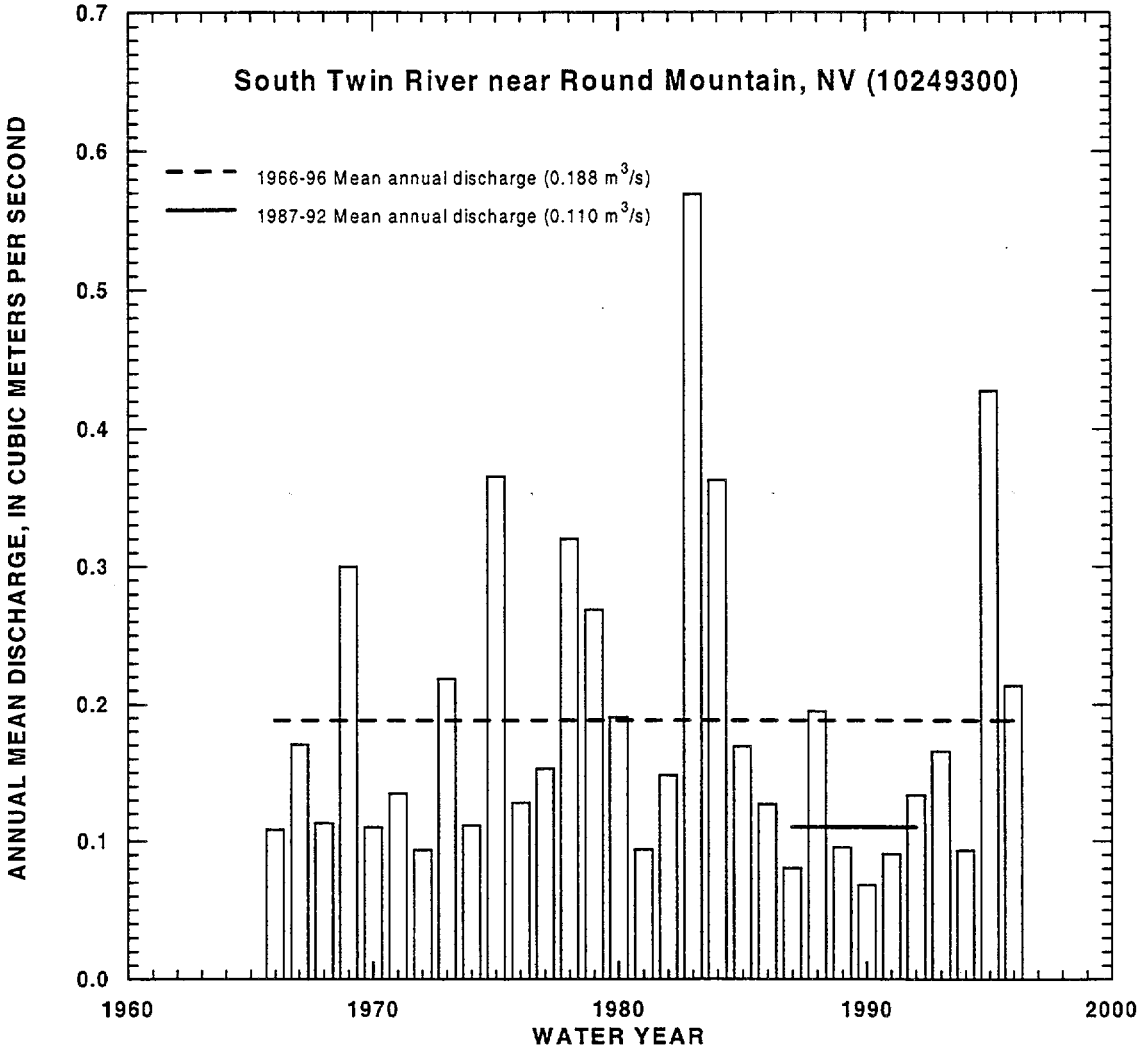

Figure 5.1-7. Annual Mean Discharges and Comparison of 1966-96 and 1987-92 Mean Annual Discharge for South Twin River Near Round Mountain, Nevada

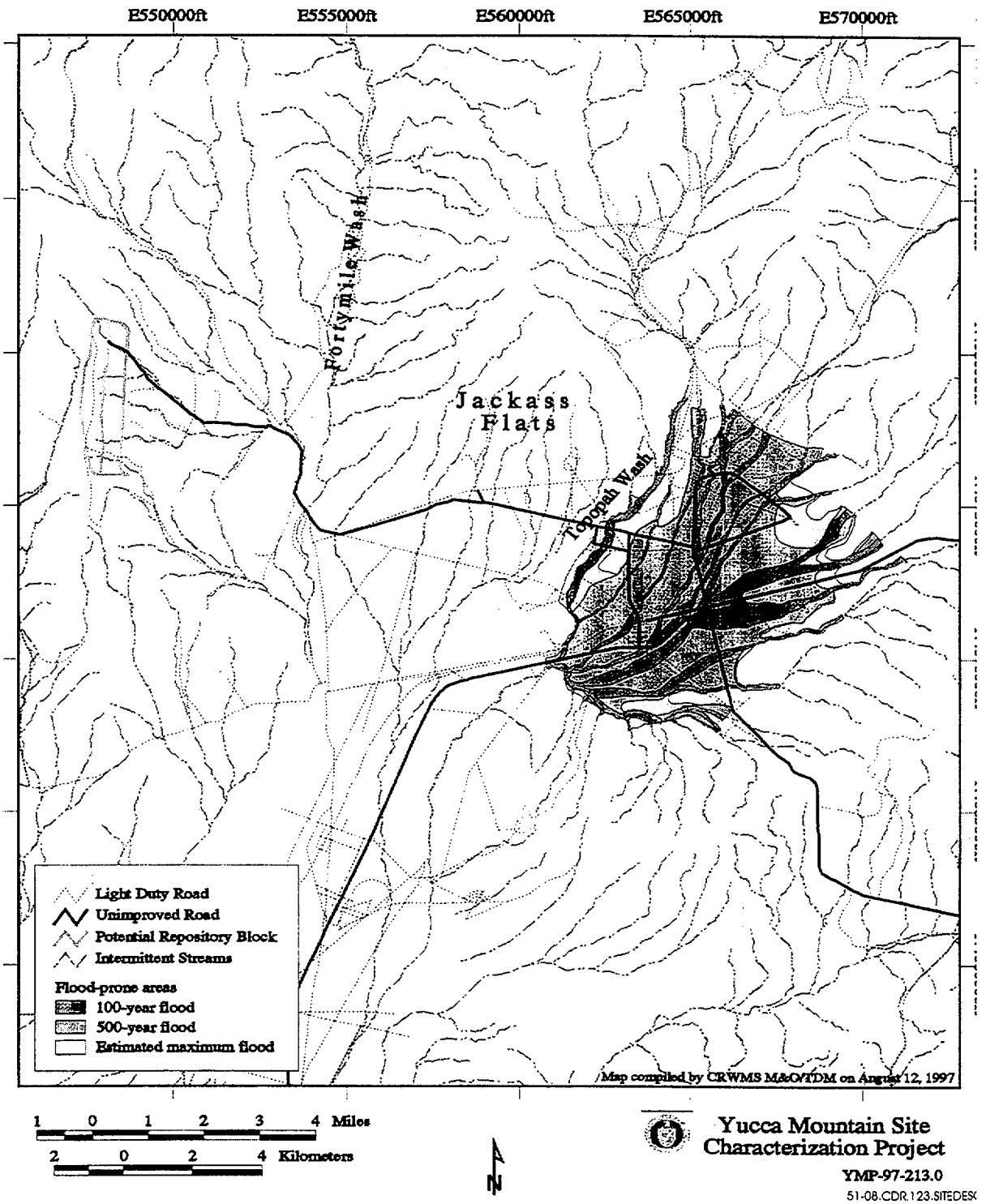

Figure 5.1-8. Approximate Flood-Prone Areas for Topopah Wash and Tributaries in the Yucca Mountain Area (modified from Christensen and Spahr 1980, Plate 1)

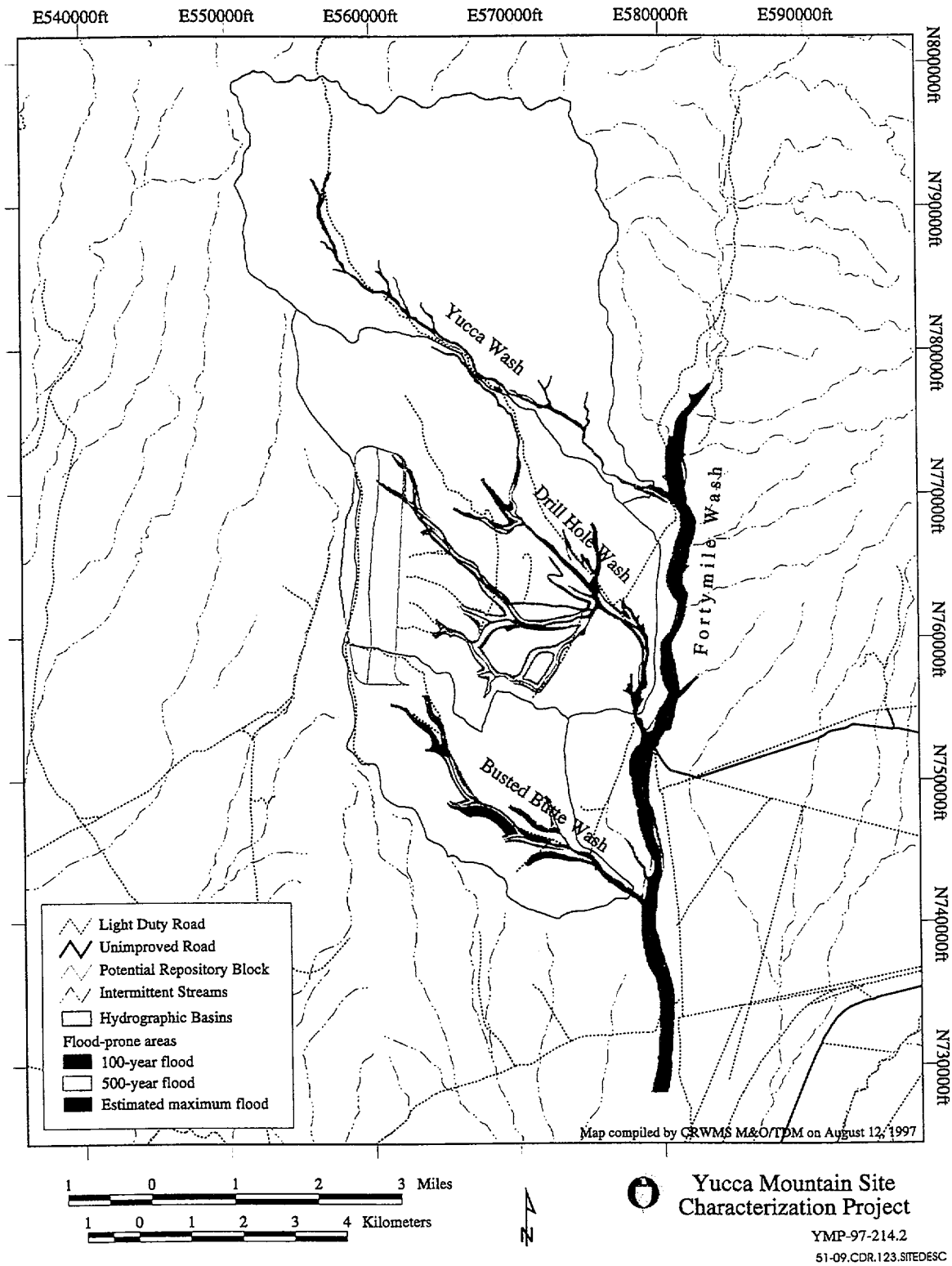

Figure 5.1-9. Approximate Flood-Prone Areas for Fortymile Wash and its Principal Southwestern Tributaries in the Yucca Mountain Area (modified from Squires and Young 1984, Plate 1)

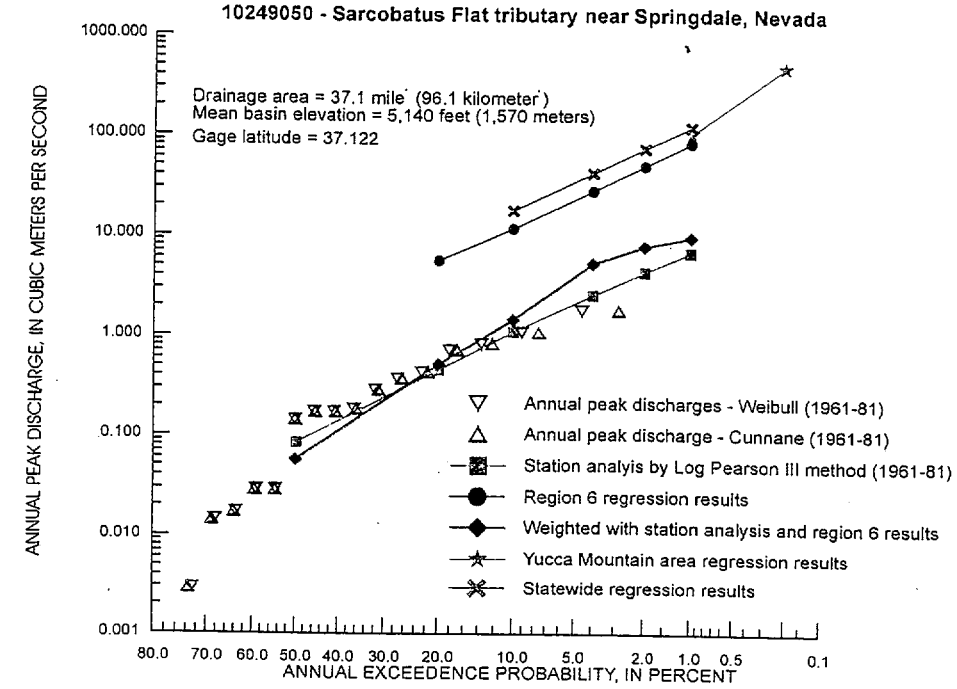

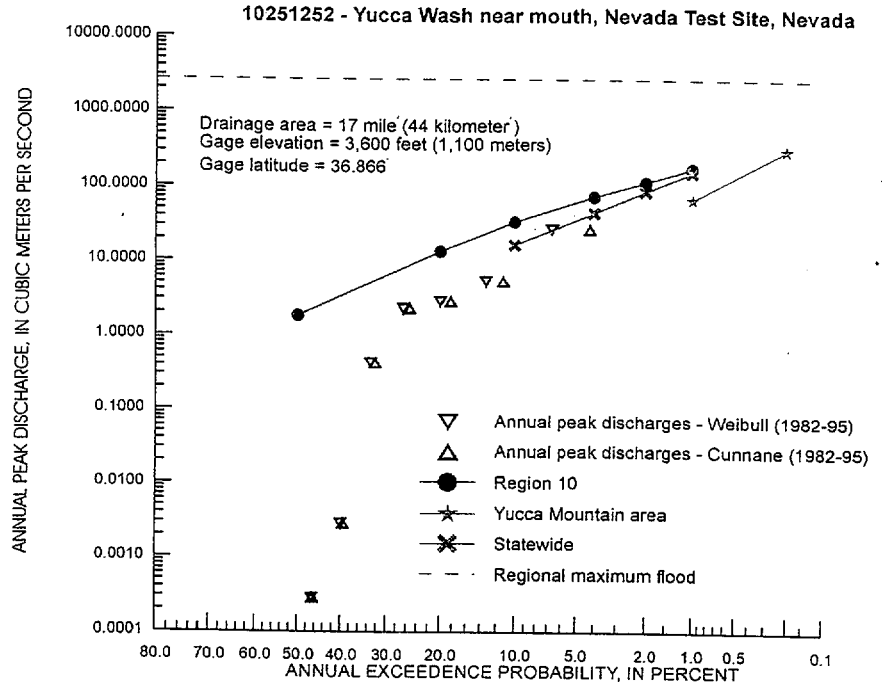

Figure 5.1-10. Systematic Annual Peak Discharges From Gage Record and Flood Frequency Regression Results for Sarcobatus Flat Tributary and Yucca Wash

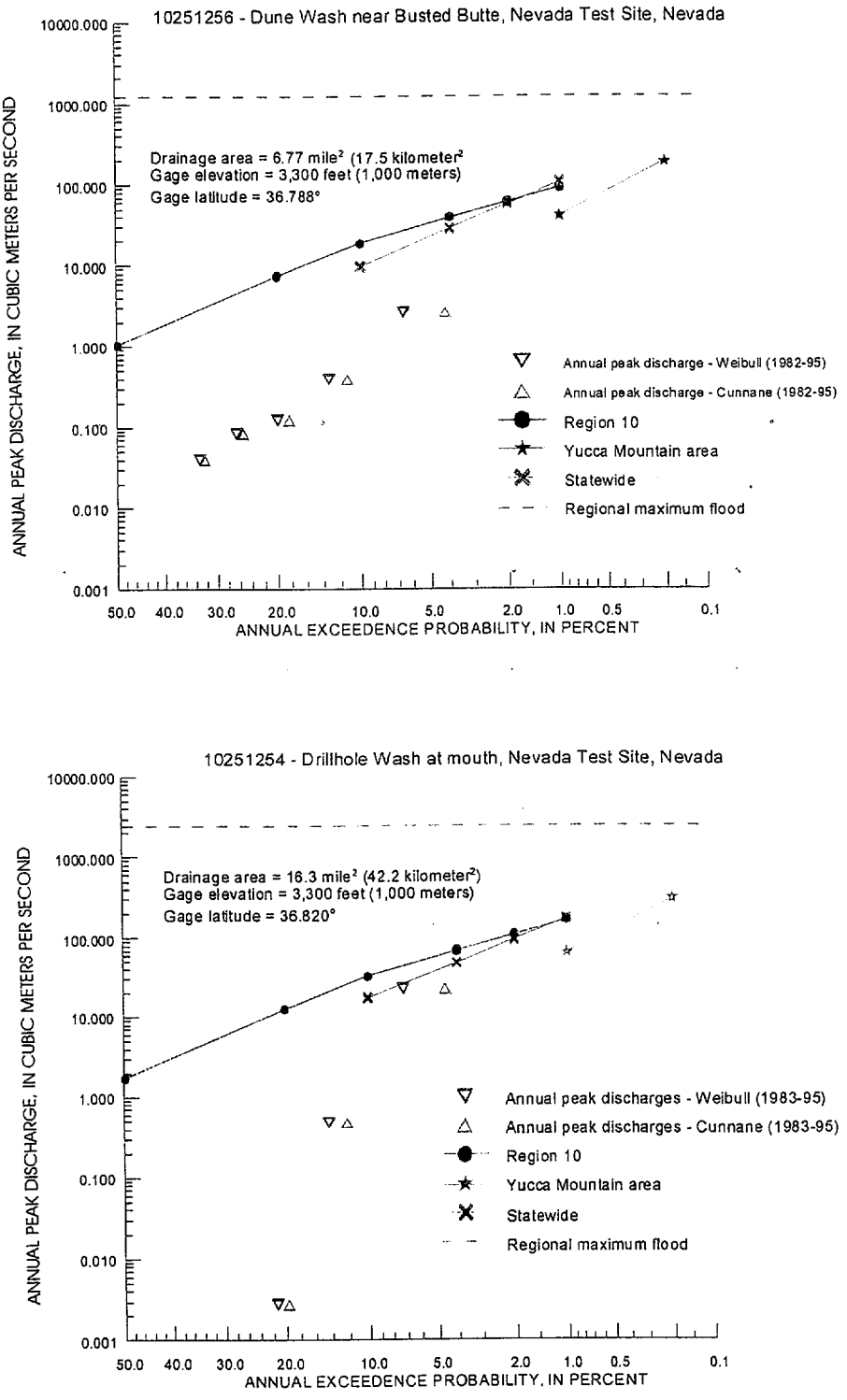

Figure 5.1-11. Systematic Annual Peak Discharges From Gage Record and Flood Frequency Regression Results for Dune and Drill Hole Wash

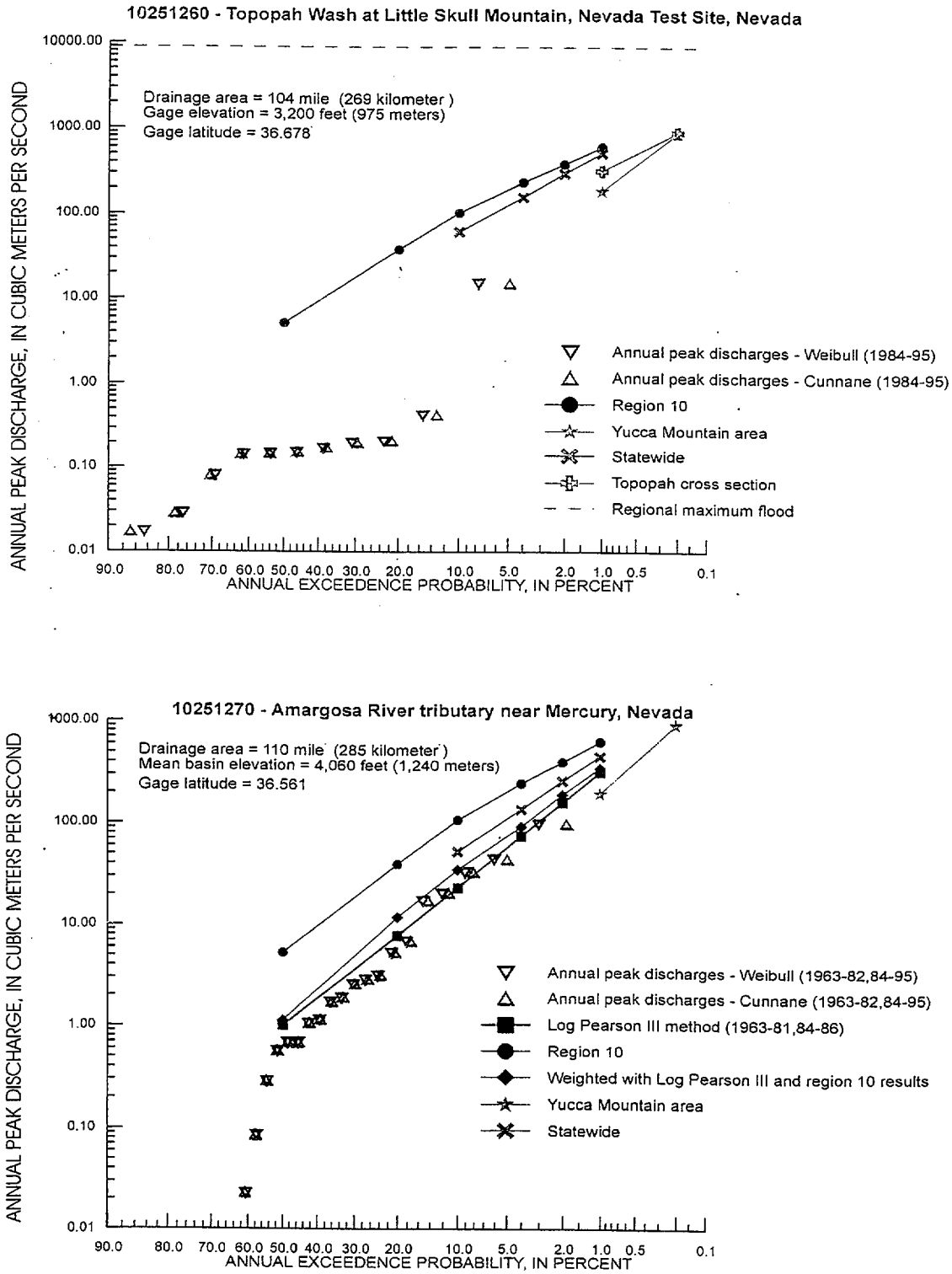

Figure 5.1-12. Systematic Annual Peak Discharges from Gage Record and Flood Frequency Regression Results for Topopah Wash and Amargosa River Tributary

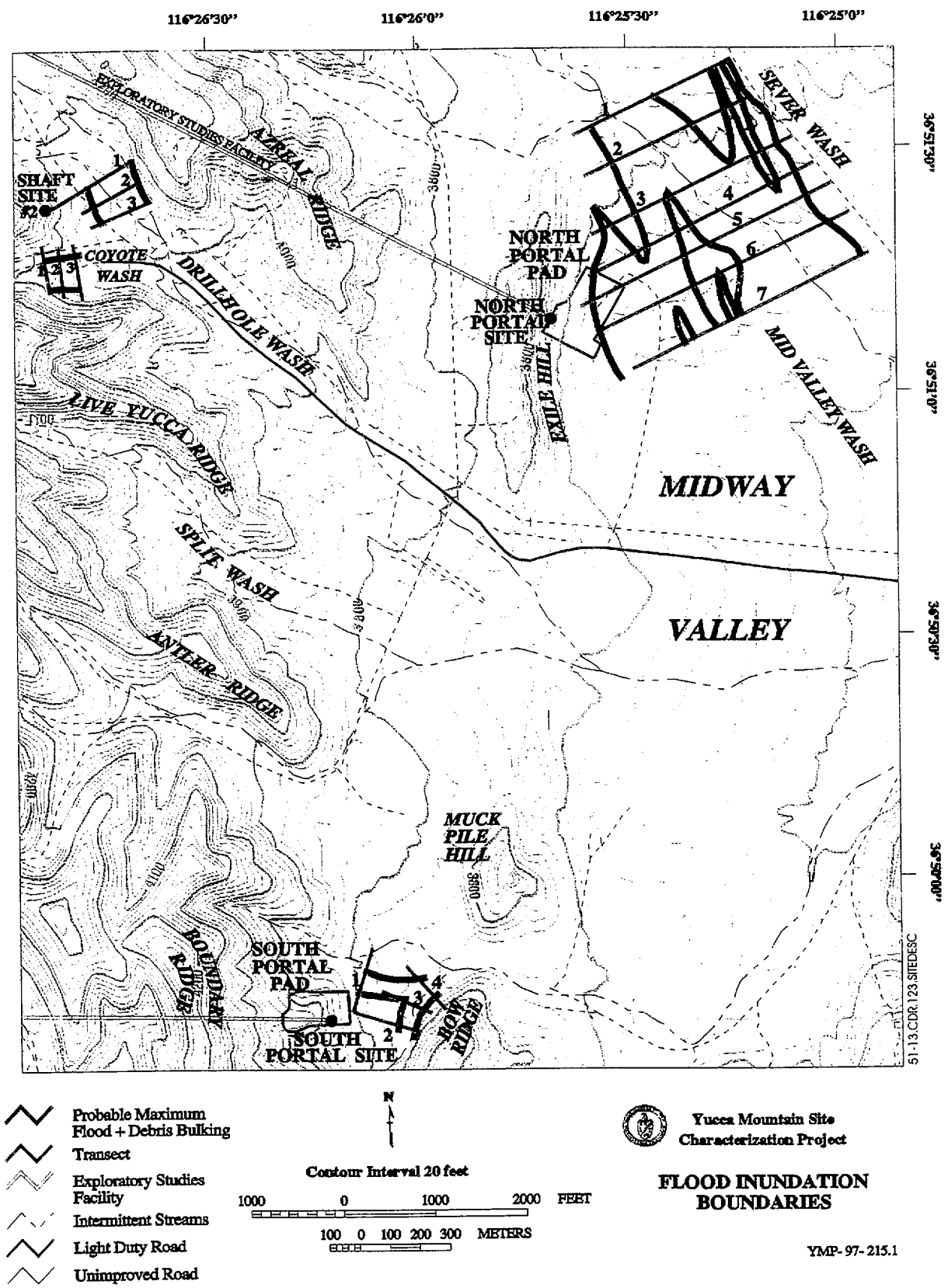

Figure 5.1-13. Approximate Probable Maximum Flood and Debris Bulking Inundation Areas in the Yucca Mountain Area (modified from Blanton 1992)

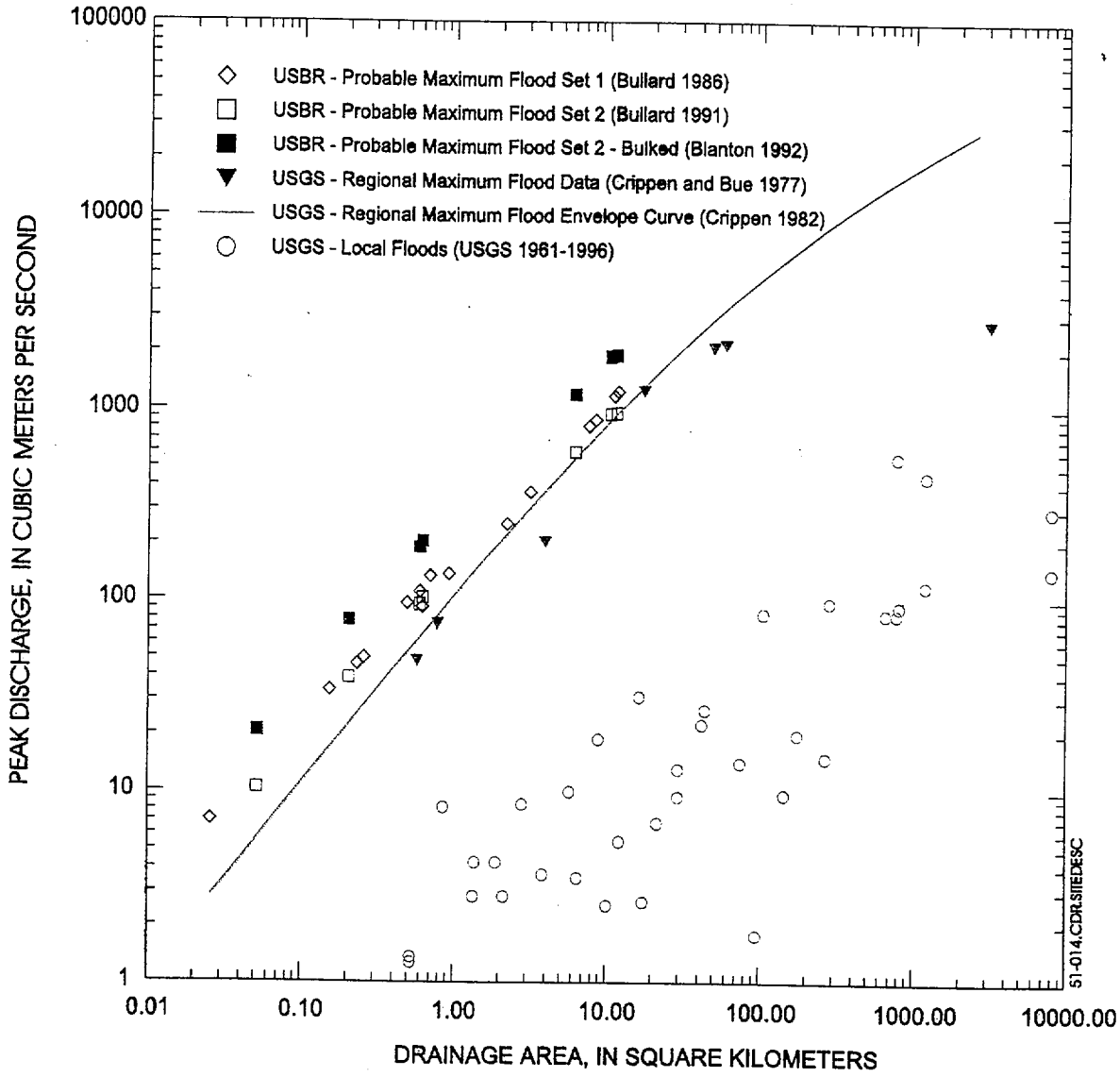

Figure 5.1-14. U.S. Bureau of Reclamation Computed Probable Maximum Flood Peak Discharges, U.S. Geological Survey Measured Local and Regional Maximum Peak Discharges, and U.S. Geological Survey Region 16 Maximum Flood Envelope Curve for the Yucca Mountain Area

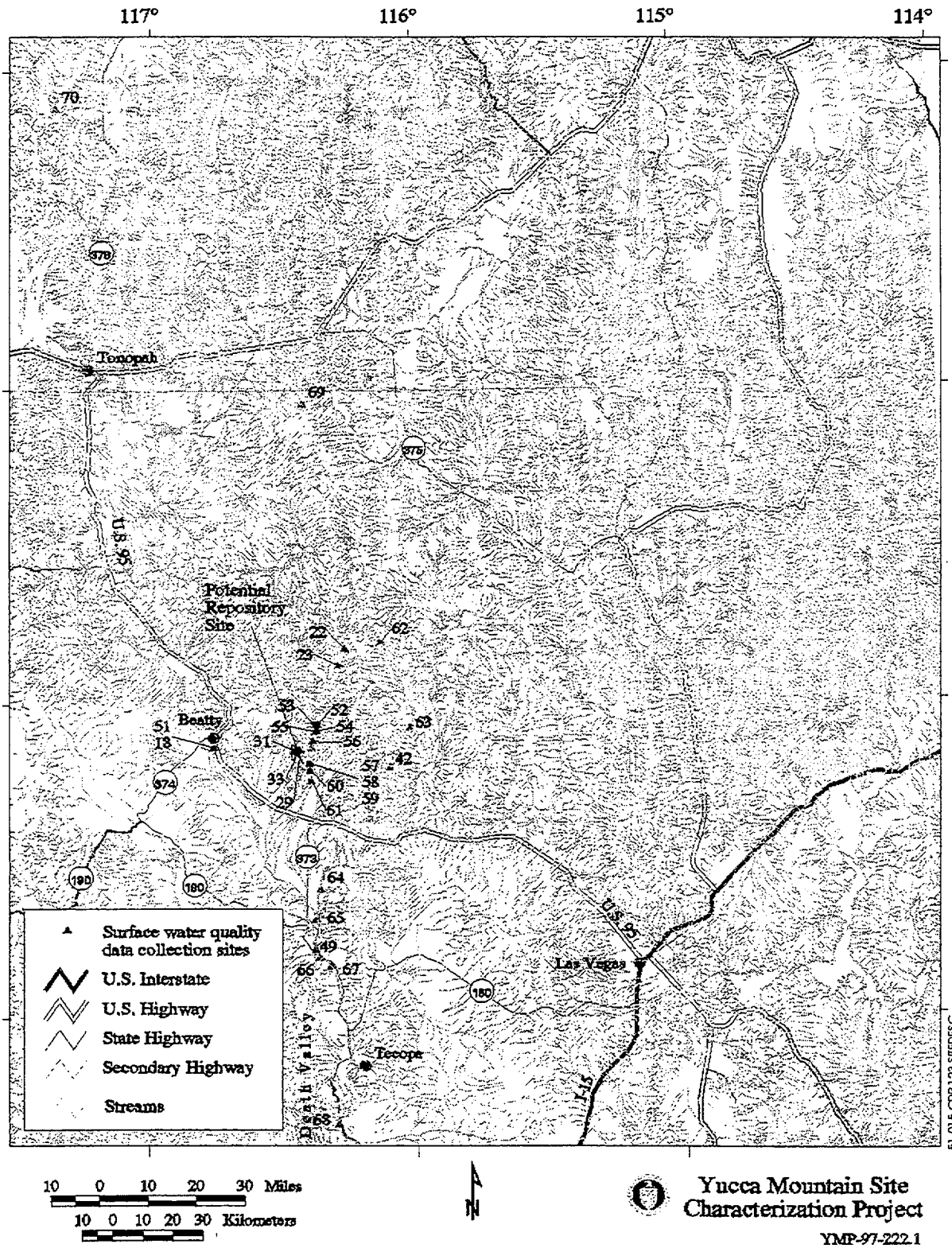

NOTE: See Tables 5.1-1, 5.1-2, and 5.1-6 for listing of data collection sites.

Figure 5.1-15. Surface Water Quality Data Collection Sites At and Near Yucca Mountain

INTENTIONALLY LEFT BLANK

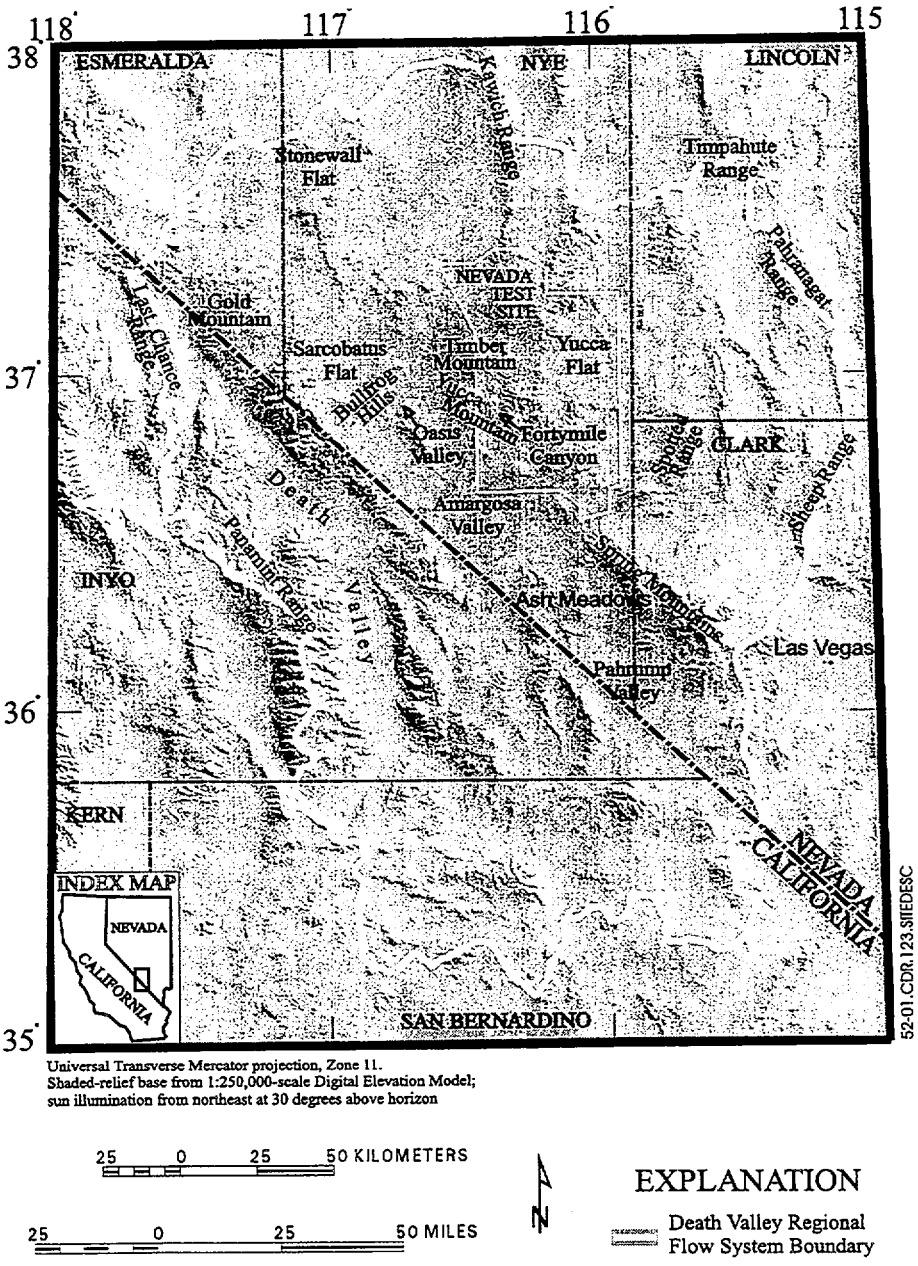

Figure 5.2-1. Geographic Features of the Death Valley Region

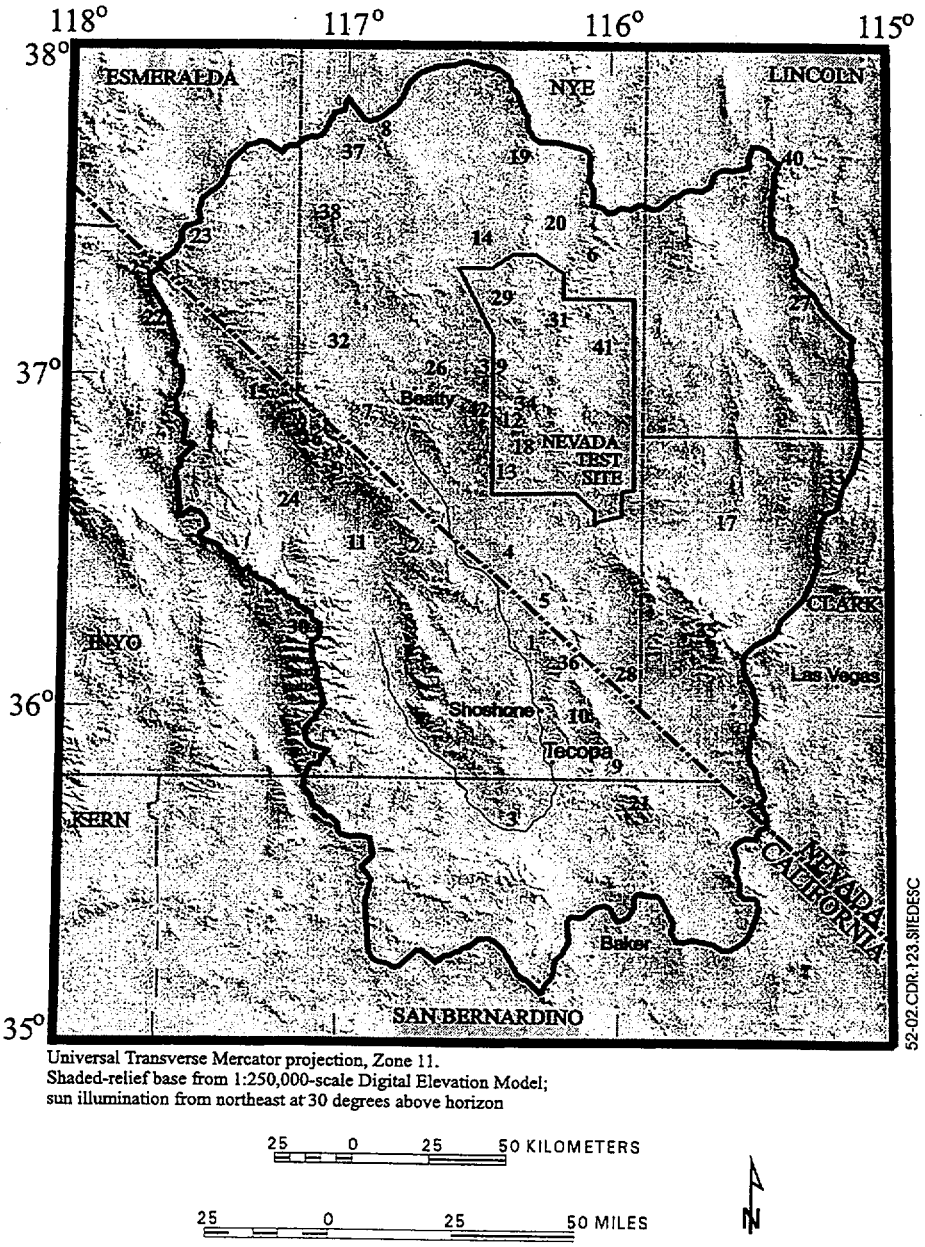

Universal Transverse Mercator projection, Zone 11.
Shaded-relief base from 1:250,000-scale Digital Elevation Model;
sun illumination from northeast at 30 degrees above horizon

25 0 25 50 KILOMETERS

25 0 25 50 MILES

N

LOCATION KEY

1. Alkali Flat
2. Amargosa Range
3. Amargosa River
4. Amargosa Valley
5. Ash Meadows
6. Belted Range
7. Bullfrog Hills
8. Cactus Range
9. California Valley
10. Chicago Valley
11. Death Valley
12. Fortymile Canyon
13. Fortymile Wash
14. Gold Flat
15. Grapevine Canyon
16. Grapevine Mountains
17. Indian Springs
18. Jackass Flats
19. Kawich Range
20. Kawich Valley
21. Kingston Range
22. Last Chance Range
23. Magruder Mountain
24. Mesquite Flat
25. Montezuma Range
26. Oasis Valley
27. Pahranagat Range
28. Pahrump Valley
29. Pahute Mesa
30. Panamint Range
31. Rainier Mesa
32. Sarcobatus Flat
33. Sheep Range
34. Shoshone Mountain
35. Spring Mountains
36. Stewart Valley
37. Stonewall Flat
38. Stonewall Mountain
39. Timber Mountain
40. Timpahute Range
41. Yucca Flat
42. Yucca Mountain

Figure 5.2-2. Prominent Topographic Features of the Death Valley Region

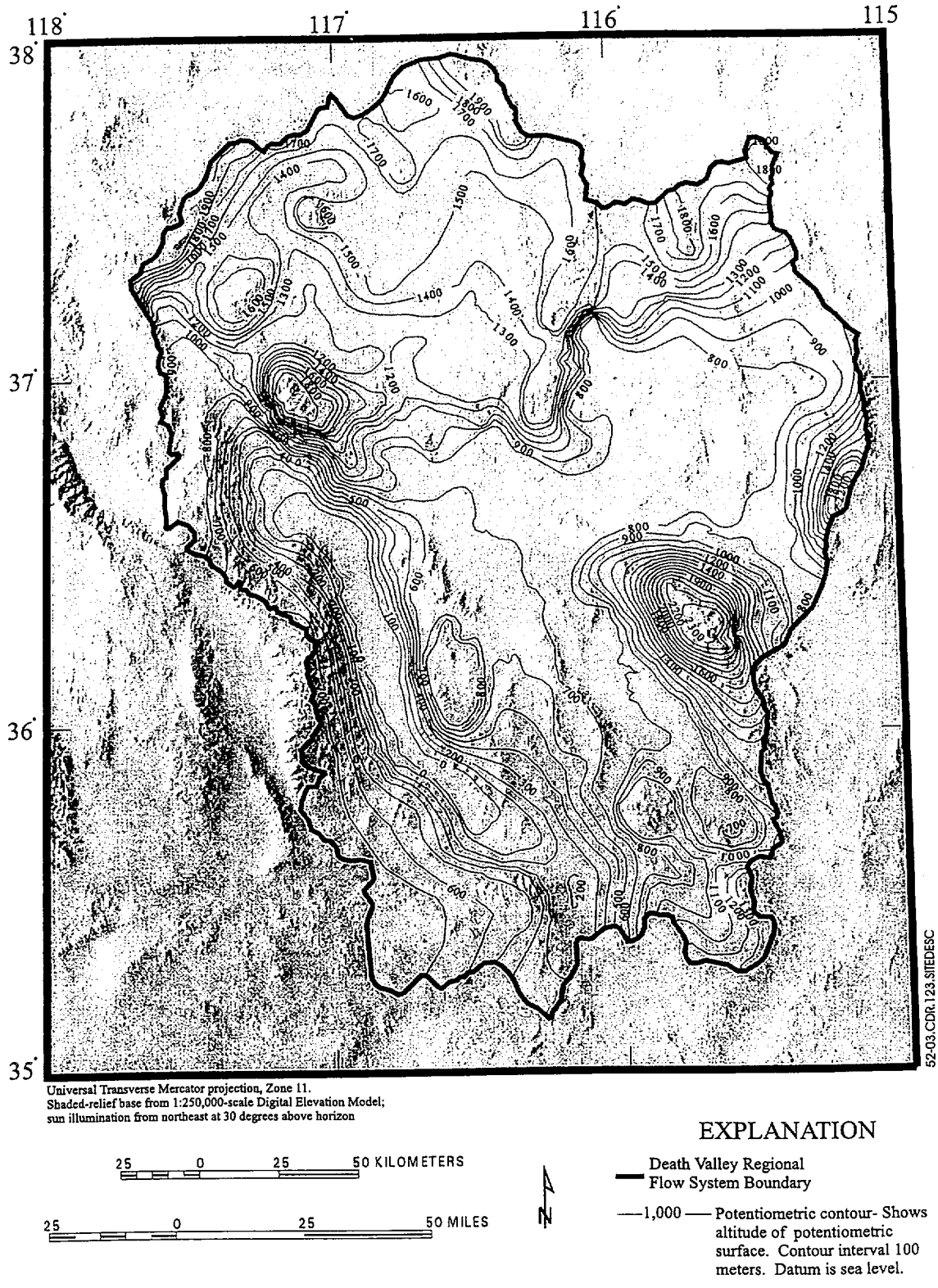

Figure 5.2-3. Estimated Potentiometric Surface of the Death Valley Region

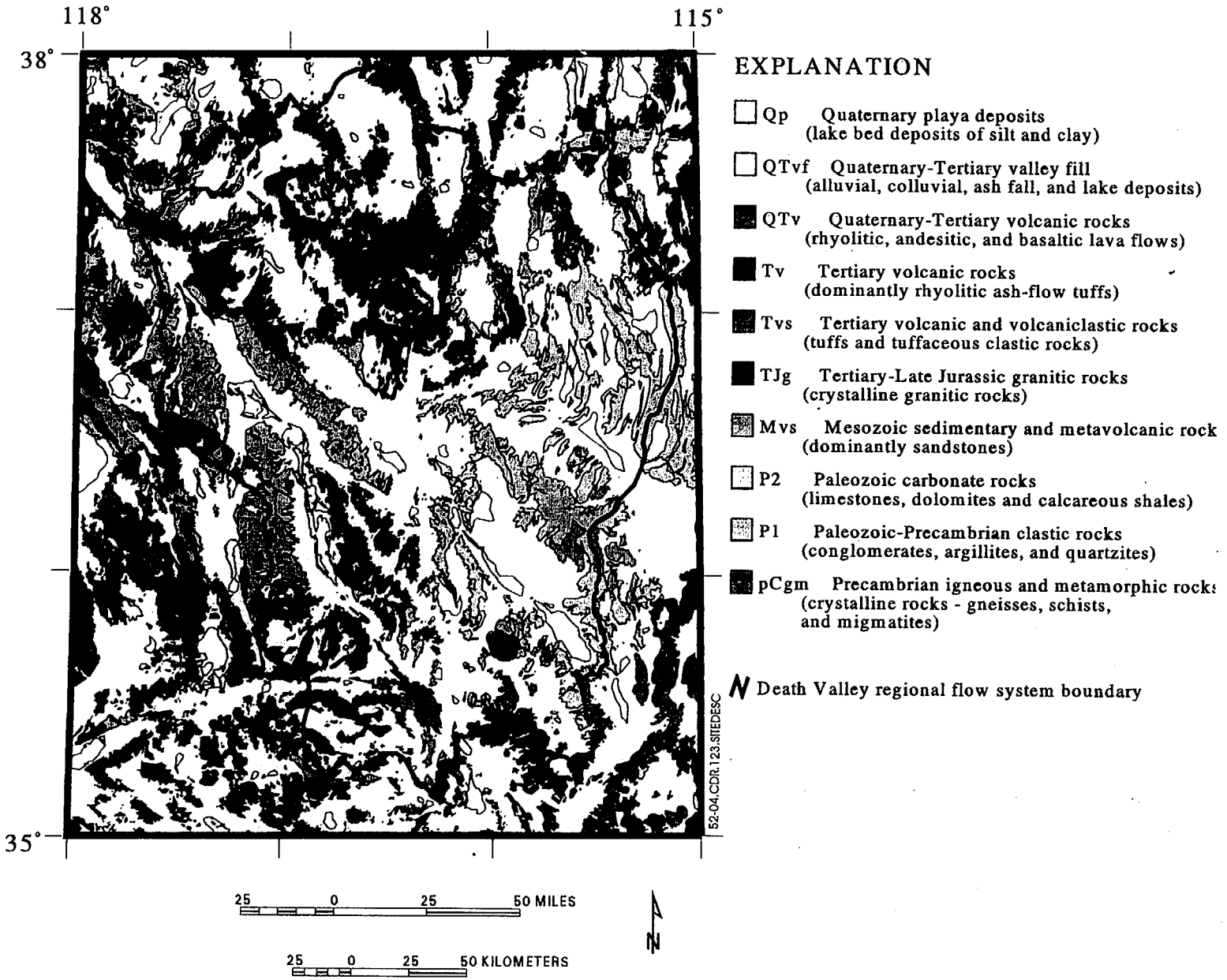

Figure 5.2-4. Hydrogeologic Units in the Death Valley Region

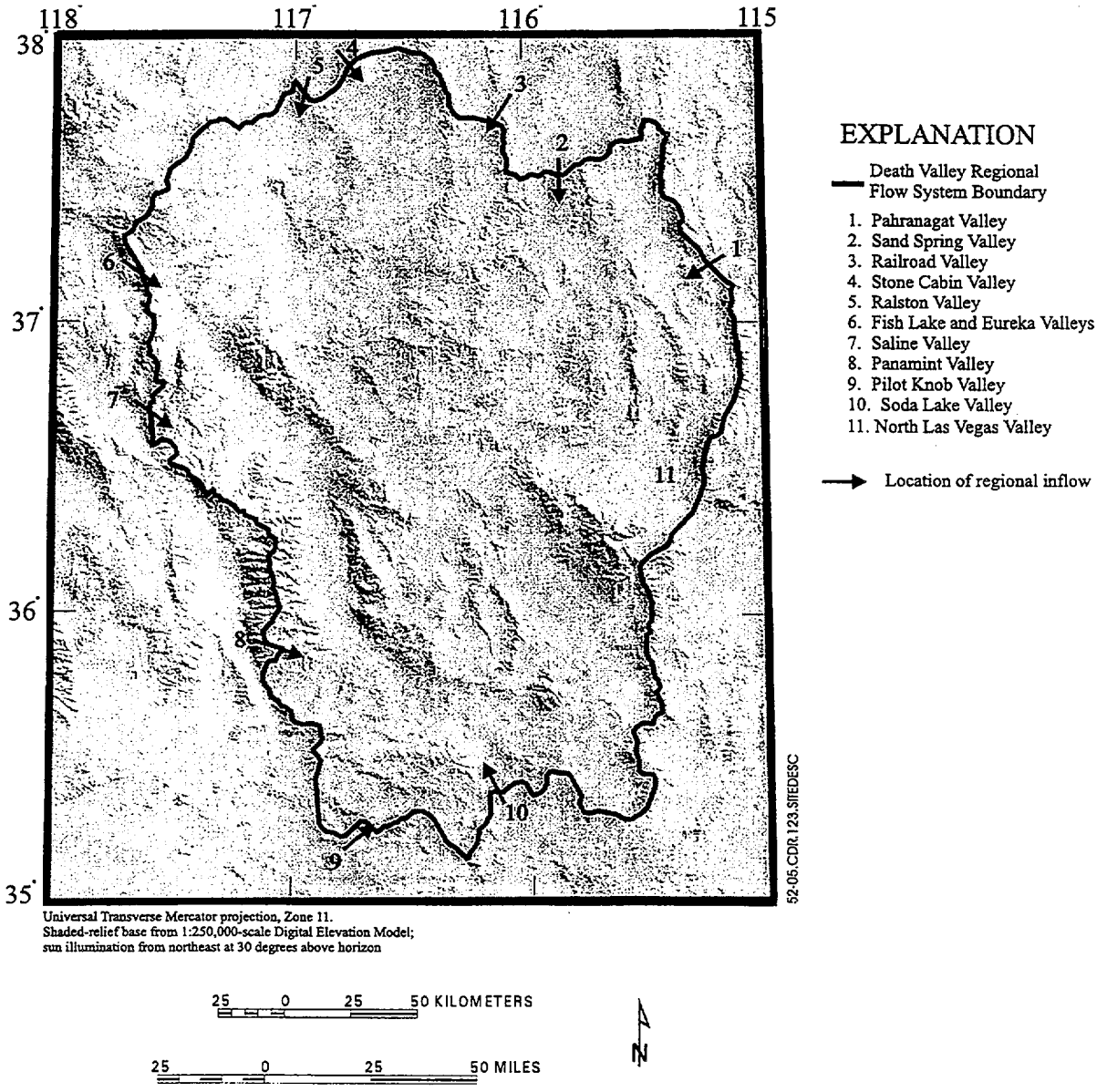

Figure 5.2-5. Locations of Regional Inflows Across Flow System Boundaries

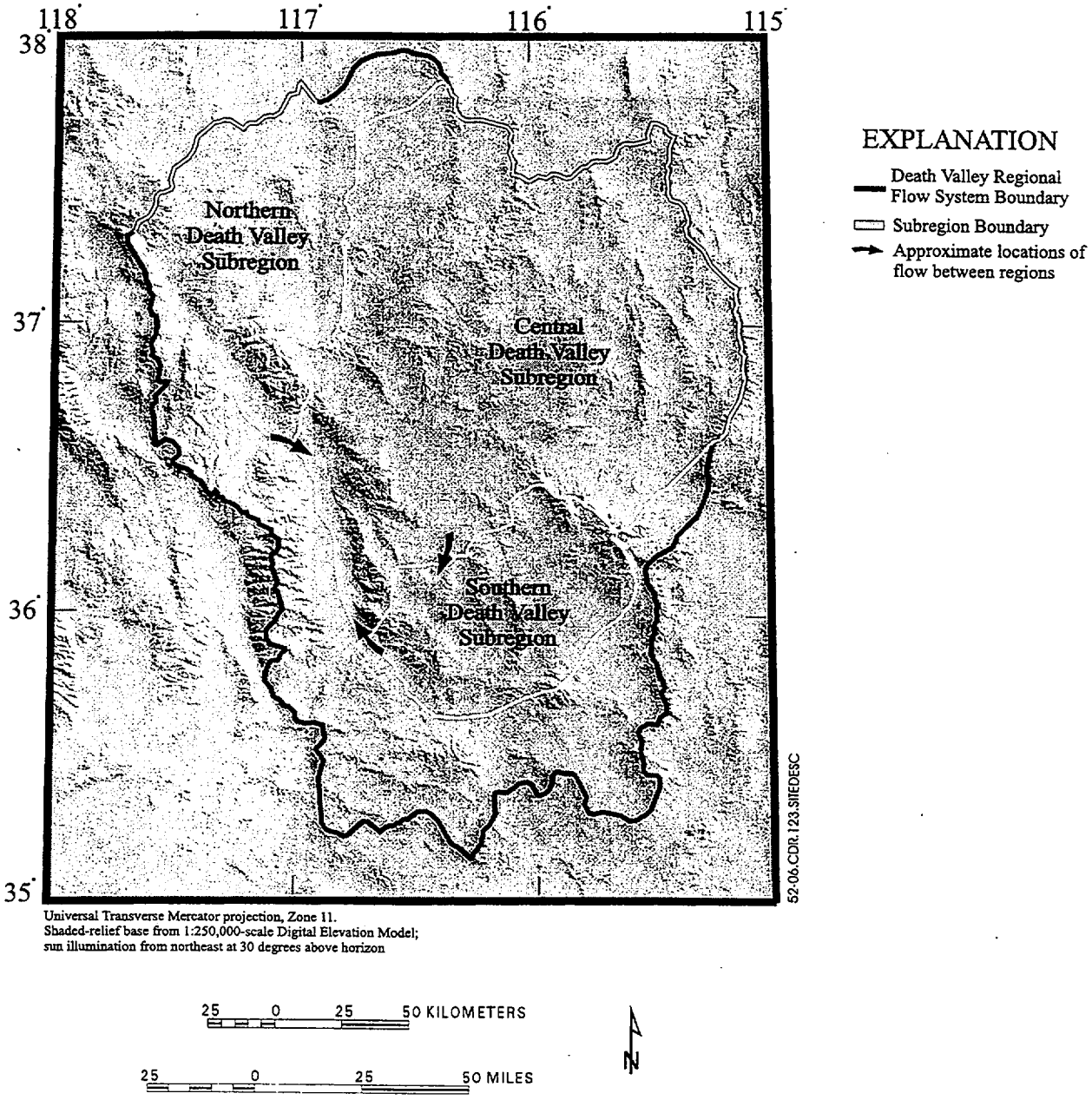

Figure 5.2-6. Three Subregions of the Death Valley Regional Groundwater Flow System

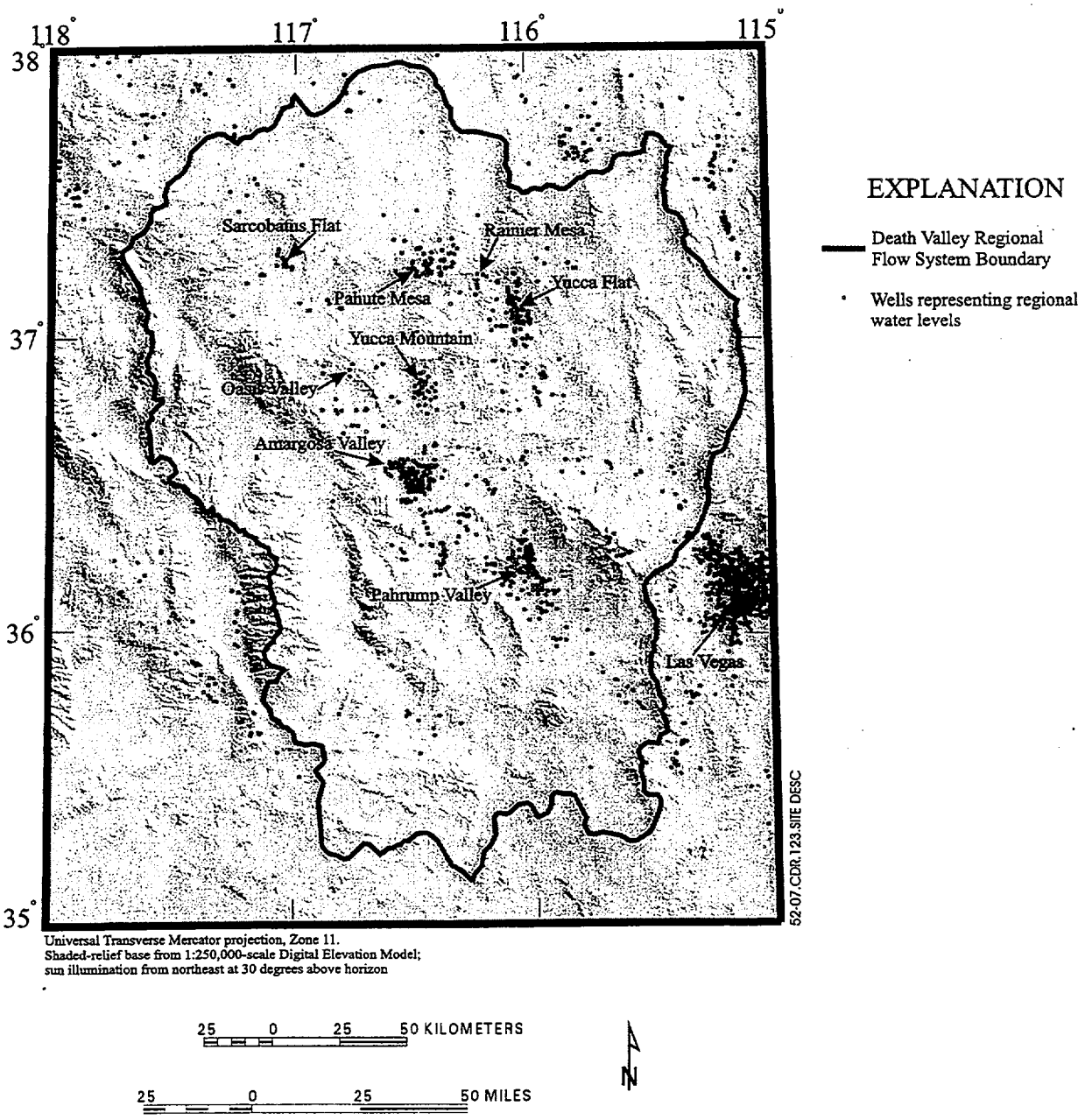

Figure 5.2-7. Locations of Water-Level Data in the Death Valley Region

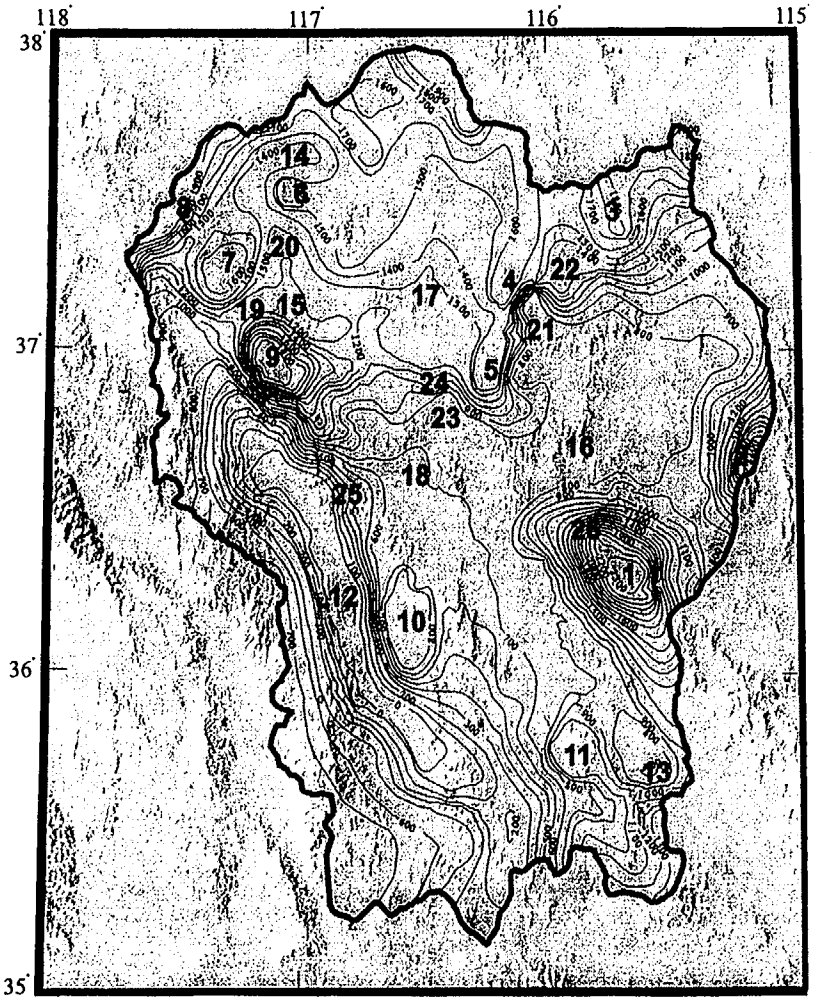

EXPLANATION

Death Valley Regional Flow System Boundary

—1,000— Potentiometric contour- Shows altitude of potentiometric surface. Contour interval 100 meters. Datum is sea level.

Potentiometric surface mounds
1 Spring Mountains
2 Sheep Range
3 Groom Range
4 Ranier Mesa
5 Shoshone Mountain
6 Stonewall Mountain
7 Gold Mountain
8 Magruder Mountain
9 Grapevine Mountains
10 Black Mountains
11 Kingston Peak

Potentiometric surface sinks
12 Death Valley
13 Mesquite Lake
14 Stonewall Flats
15 Sarcobatus Flats

Potentiometric surface troughs
16 Area north of Spring Mountains
17 Western Pahute Mesa
18 Amargosa Valley
19 Grapevine Canyon
20 Stonewall Pass
21 Yucca Flat
22 Emigrant Valley
23 Fortymile Canyon

Large Hydraulic Gradients

Local Area
24 Area north of Yucca Mountain

Regional Area
25 Area northeast and east of Death Valley
26 Western margins of the Spring Mountains

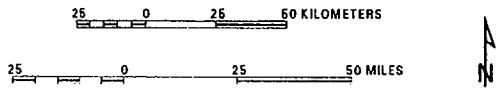

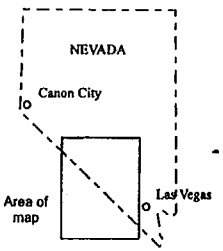

52-08.CDR.123.SITEDESC

Figure 5.2-8. Estimated Potentiometric Surface of the Death Valley Region and Areas of Major Potentiometric Features

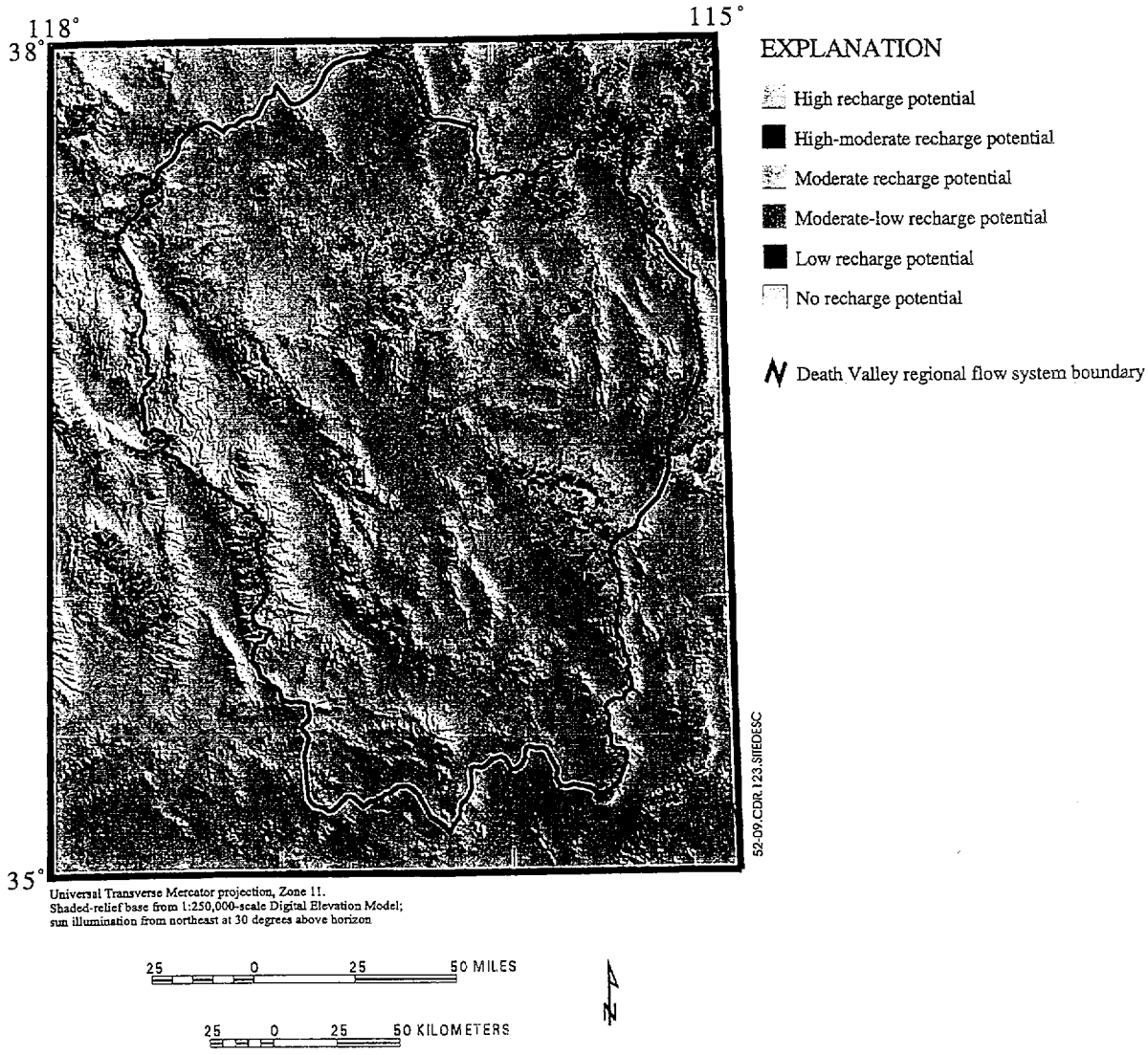

Figure 5.2-9. Refined Potential Recharge Areas for the Death Valley Region

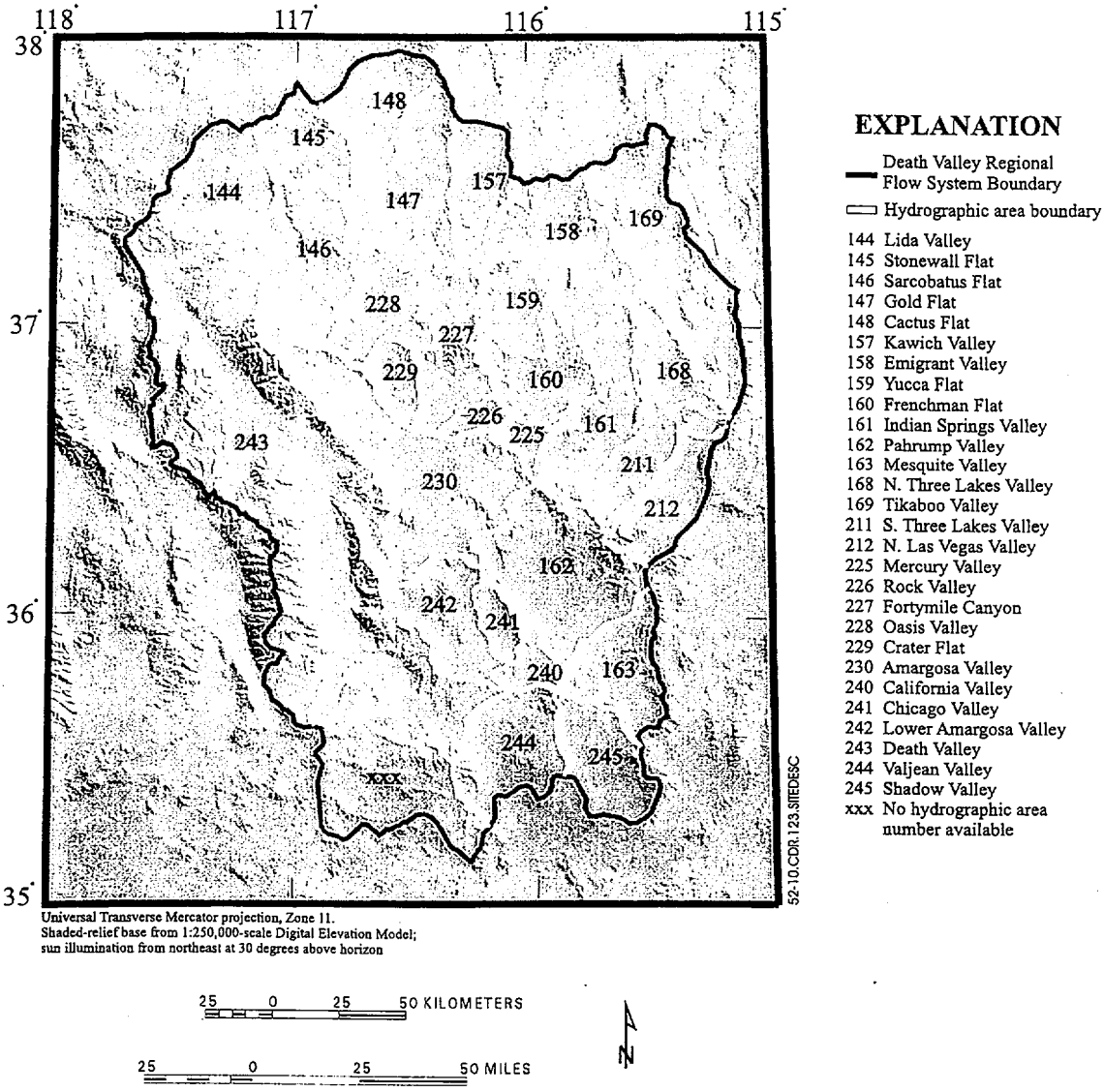

Figure 5.2-10. Hydrographic Areas of the Death Valley Region

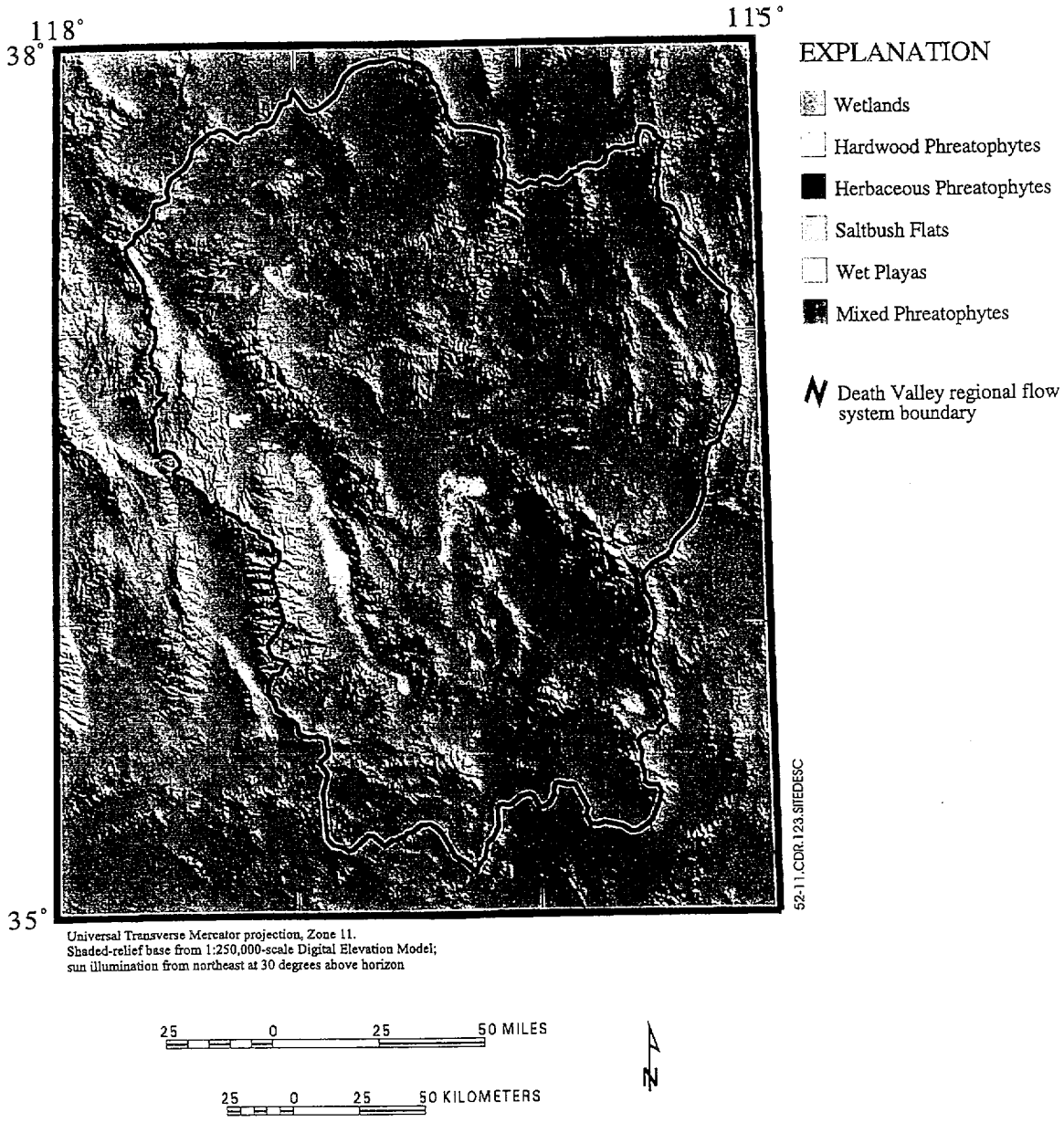

Figure 5.2-11. Final Evapotranspiration Areas in the Death Valley Region

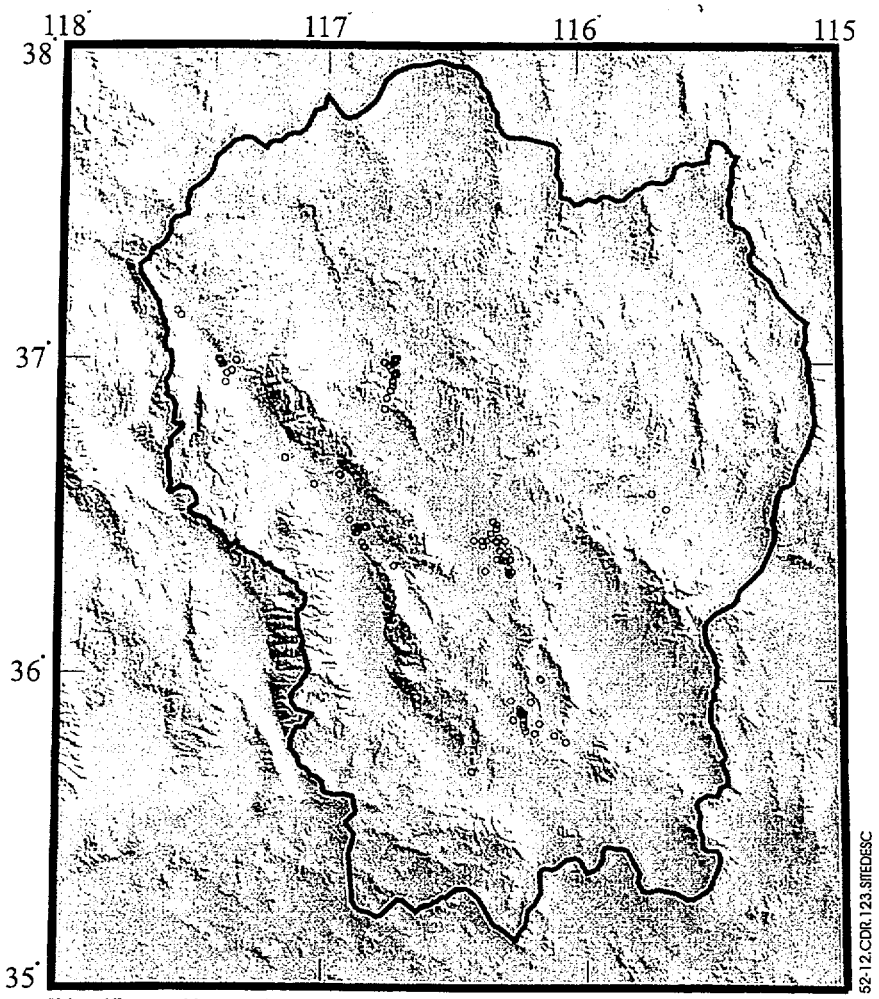

Figure 5.2-12. Locations of Regional Springs

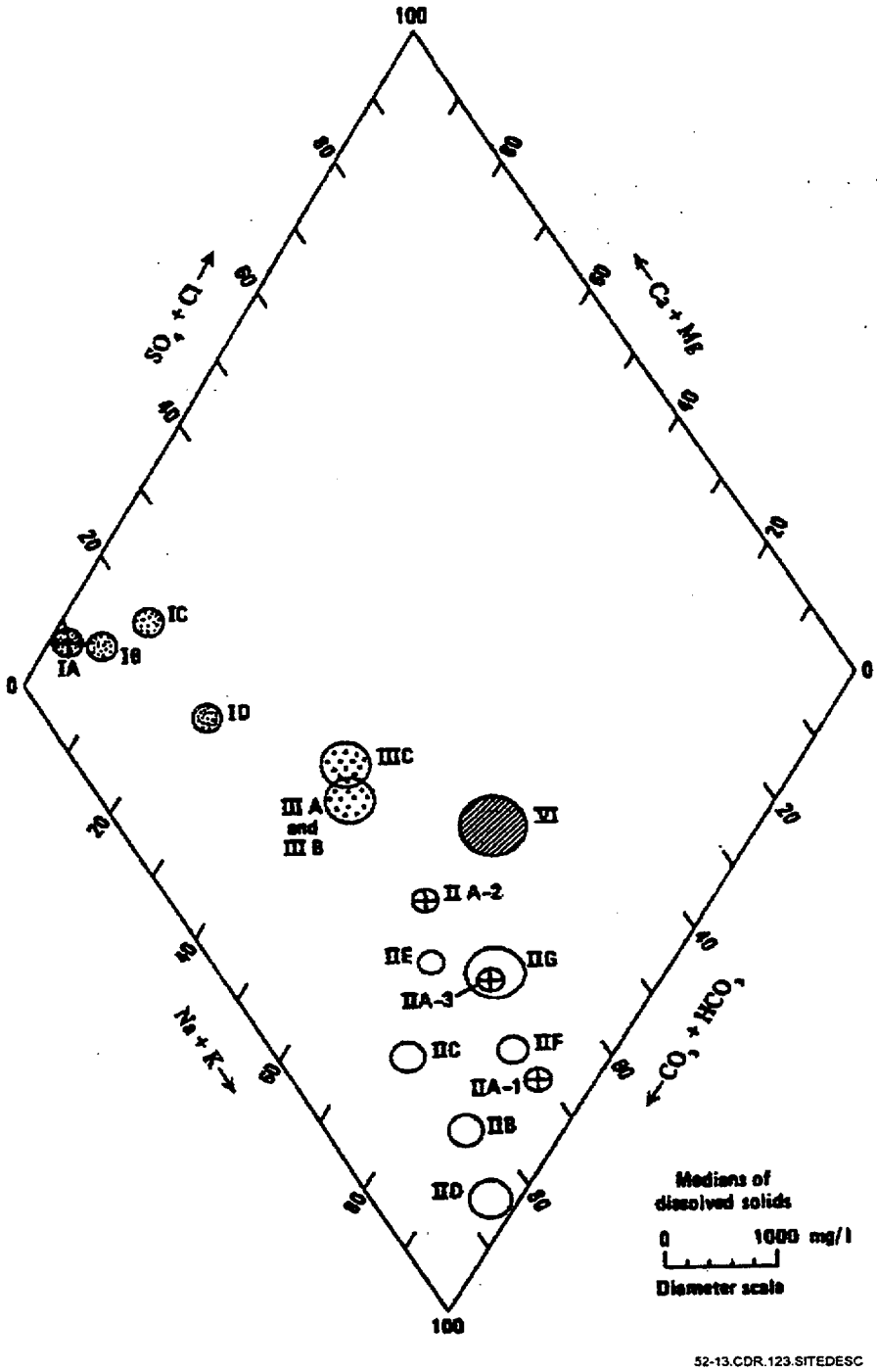

NOTE: Roman numeral I waters characterize the regional carbonate aquifer; roman numeral II waters characterize waters from the tuff aquifer (or waters in tuff-derived alluvial aquifers). Type III and VI waters are believed to derived through a mixture of types I and II either by mixing of waters or by flow through a mixed source. Circles with crosses represent perched waters.

Figure 5.2-13. Piper Diagram Showing Types of Chemical Compositions Found at and Near the Nevada Test Site (From Winograd and Thordarson 1975)

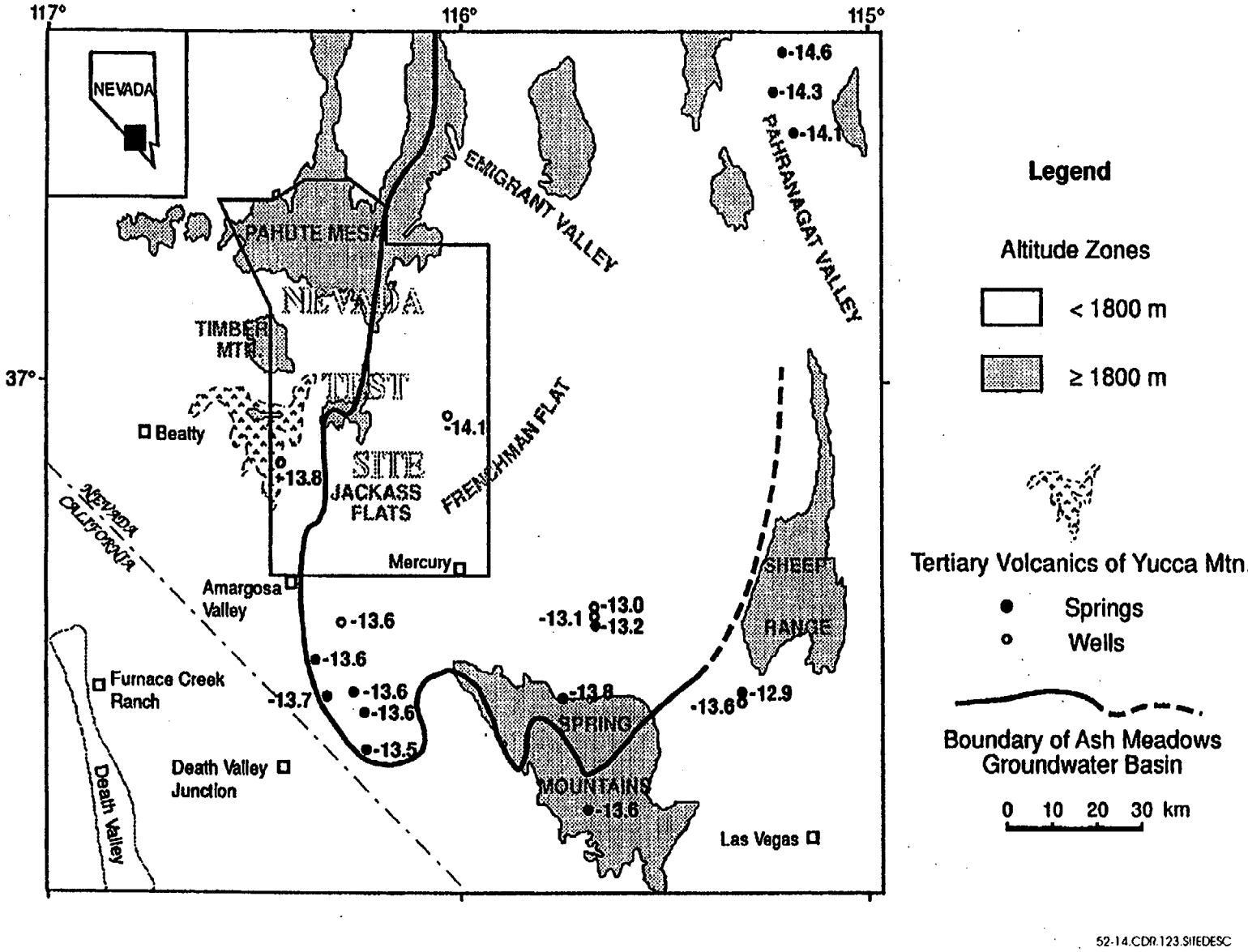

Figure 5.2-14. Map Showing Delta Oxygen-18 Values for Groundwater in the Carbonate Aquifer

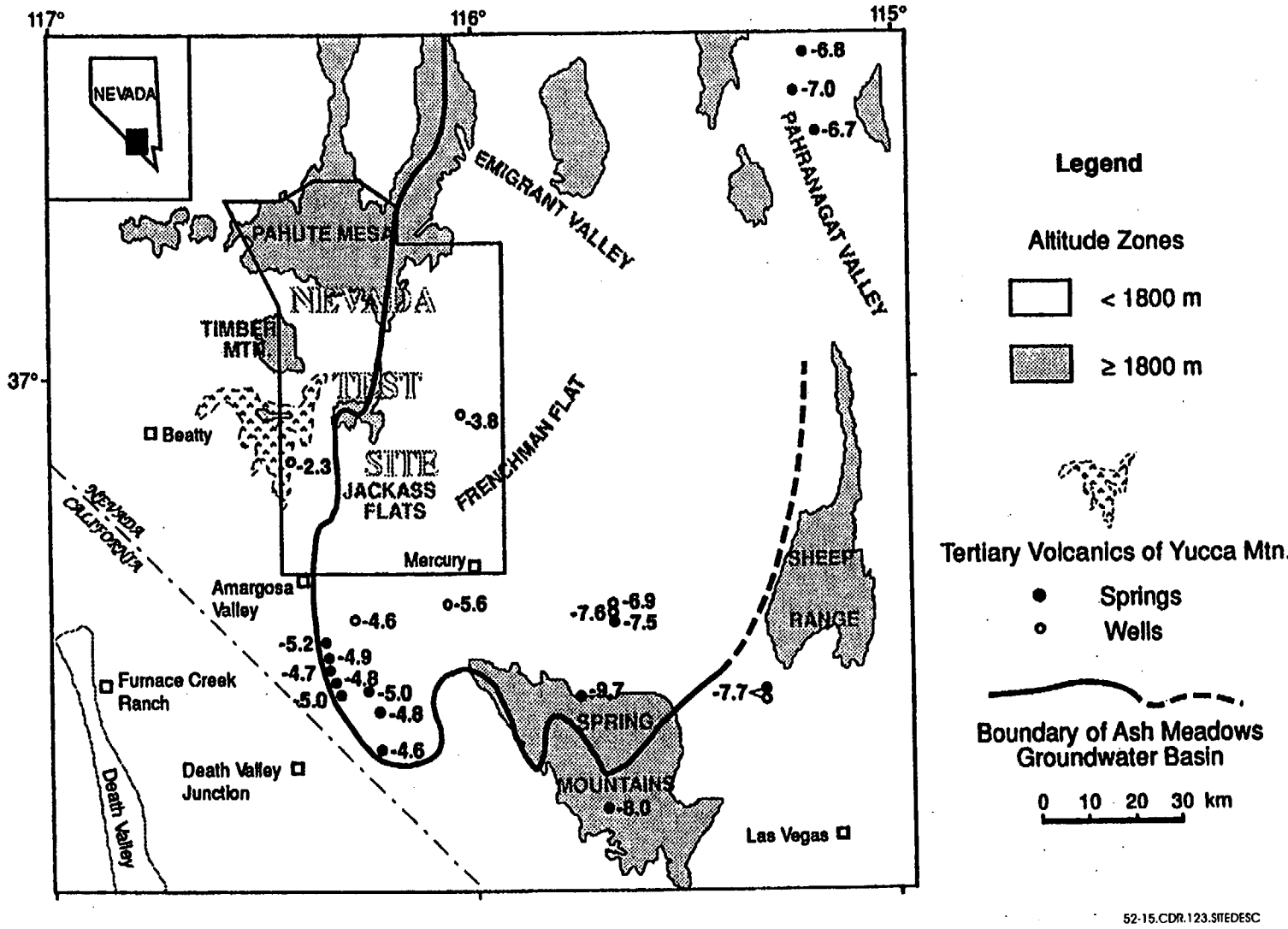

Figure 5.2-15. Map Showing Delta Carbon-13 Values for Groundwater in the Carbonate Aquifer

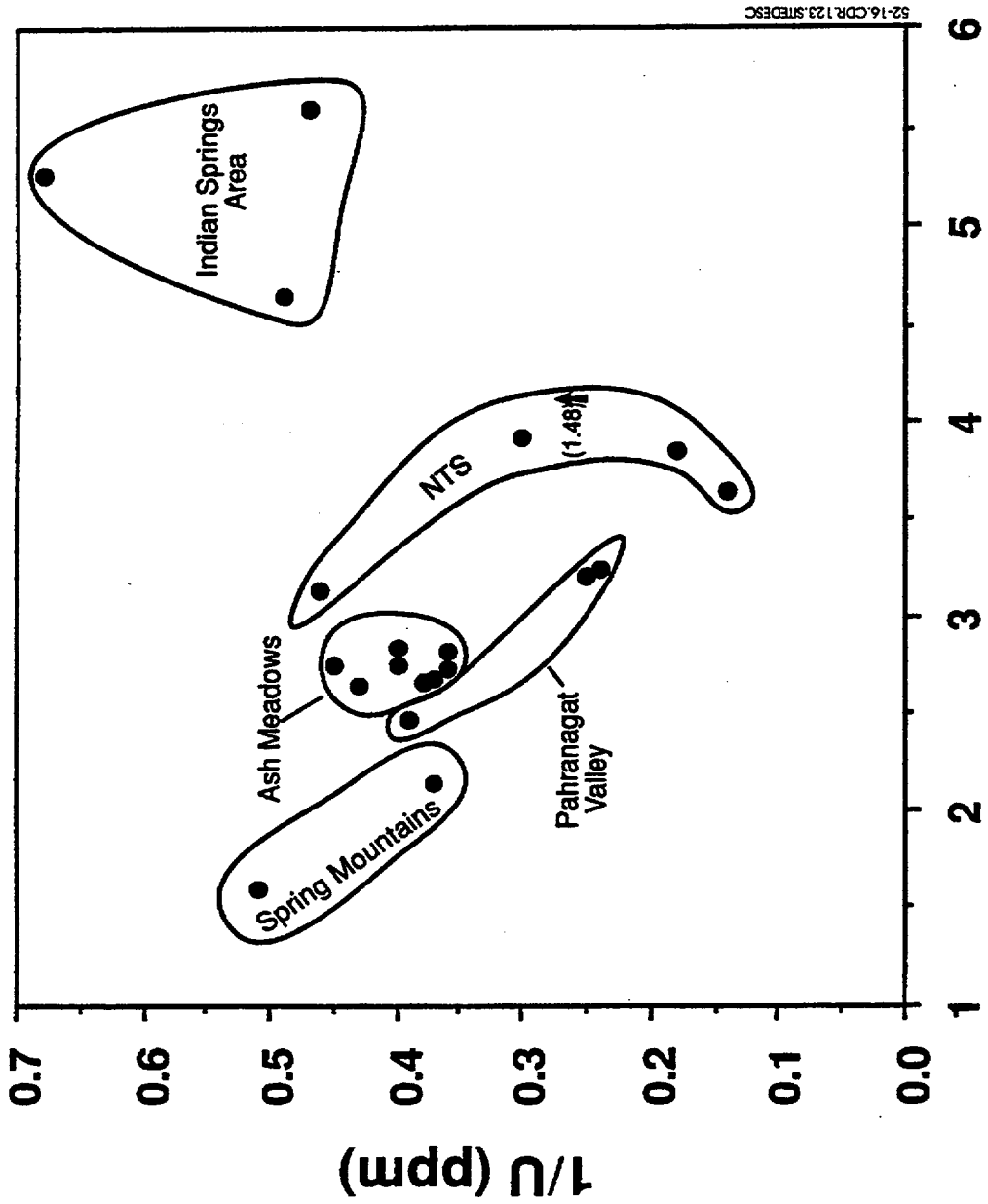

Figure 5.2-16. Plot Showing the Relationship Between Uranium Concentration and Isotopic Composition in Water from the Carbonate Aquifer

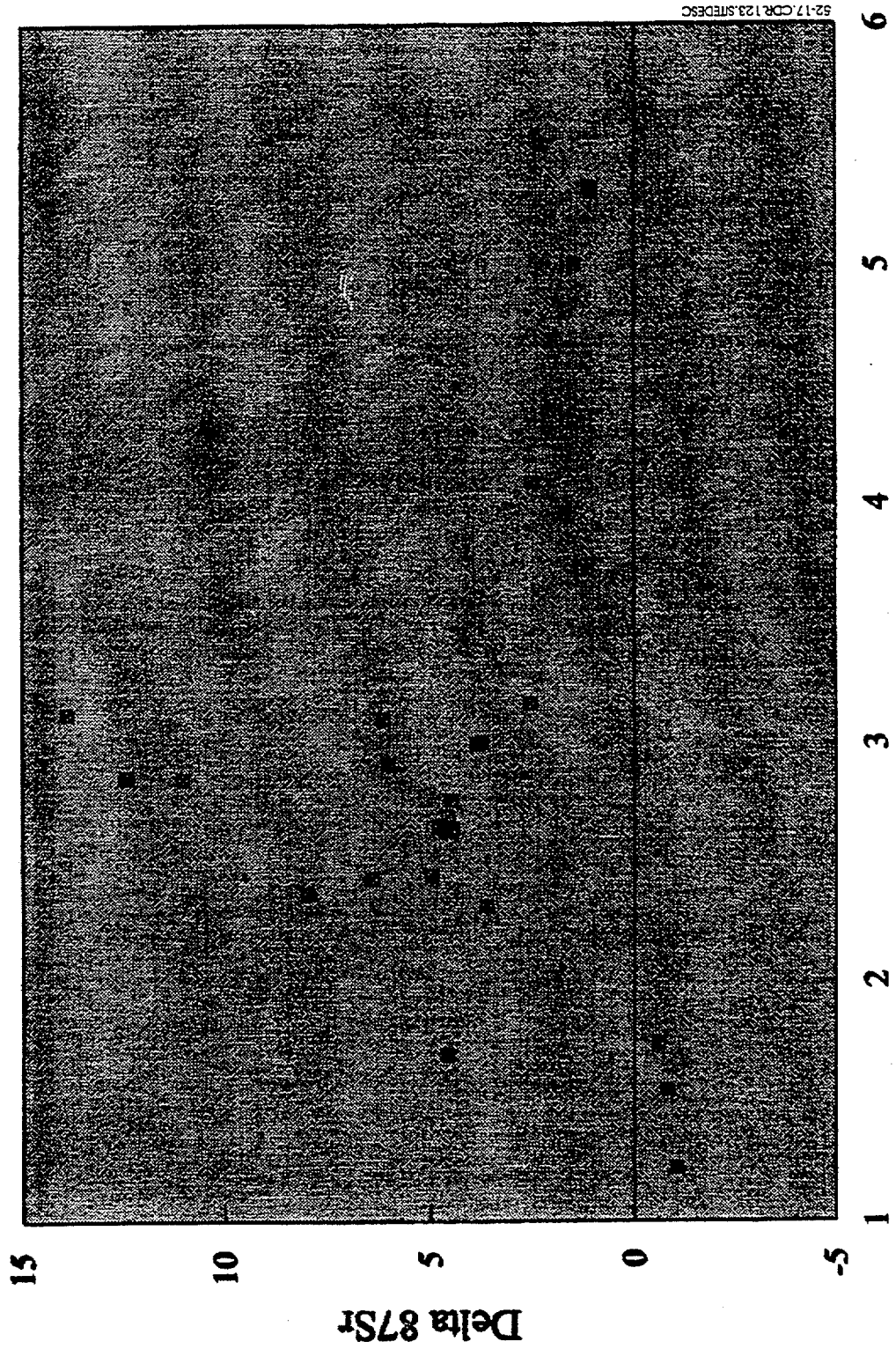

Figure 5.2-17. Plot Showing the Relationship Between the Isotopic Compositions of Strontium and Uranium in Water from the Carbonate Aquifer

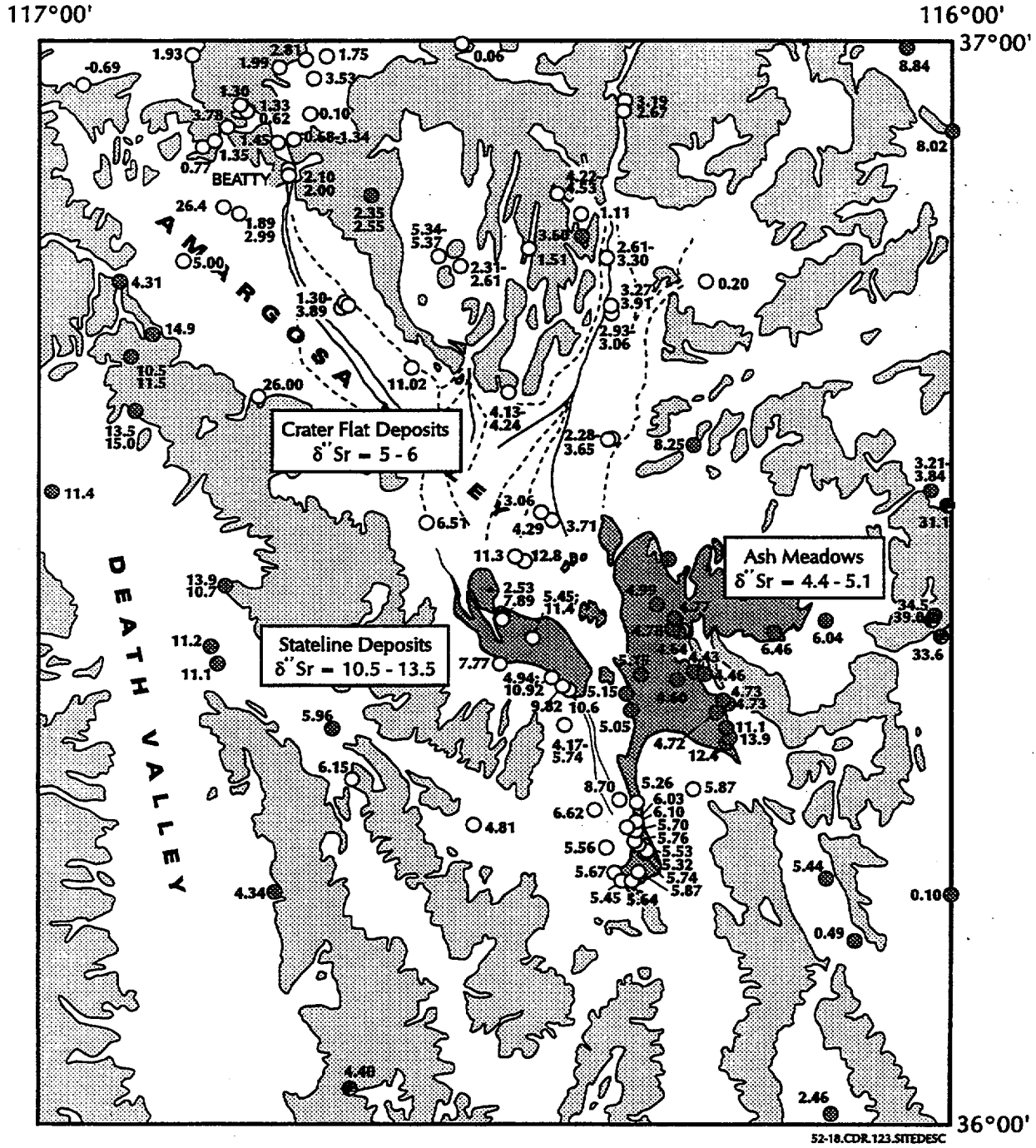

NOTE: Bedrock ranges are shown in shaded patterns, and alluvial-filled valleys are shown unpatterned. Solid and dashes lines within alluvial valleys represent active channels and alluvial fan boundaries. Dark circles represent sample sites classified as Paleozoic aquifer, open circles represent sample sites from volcanic or alluvium aquifers, and circles with hatch marks represent sites classified as Precambrian aquifer. Values in ‰ relative to sea-water = 0.70920.

Figure 5.2-18. Location of Wells and Springs Analyzed for Delta Strontium-87 from Waters

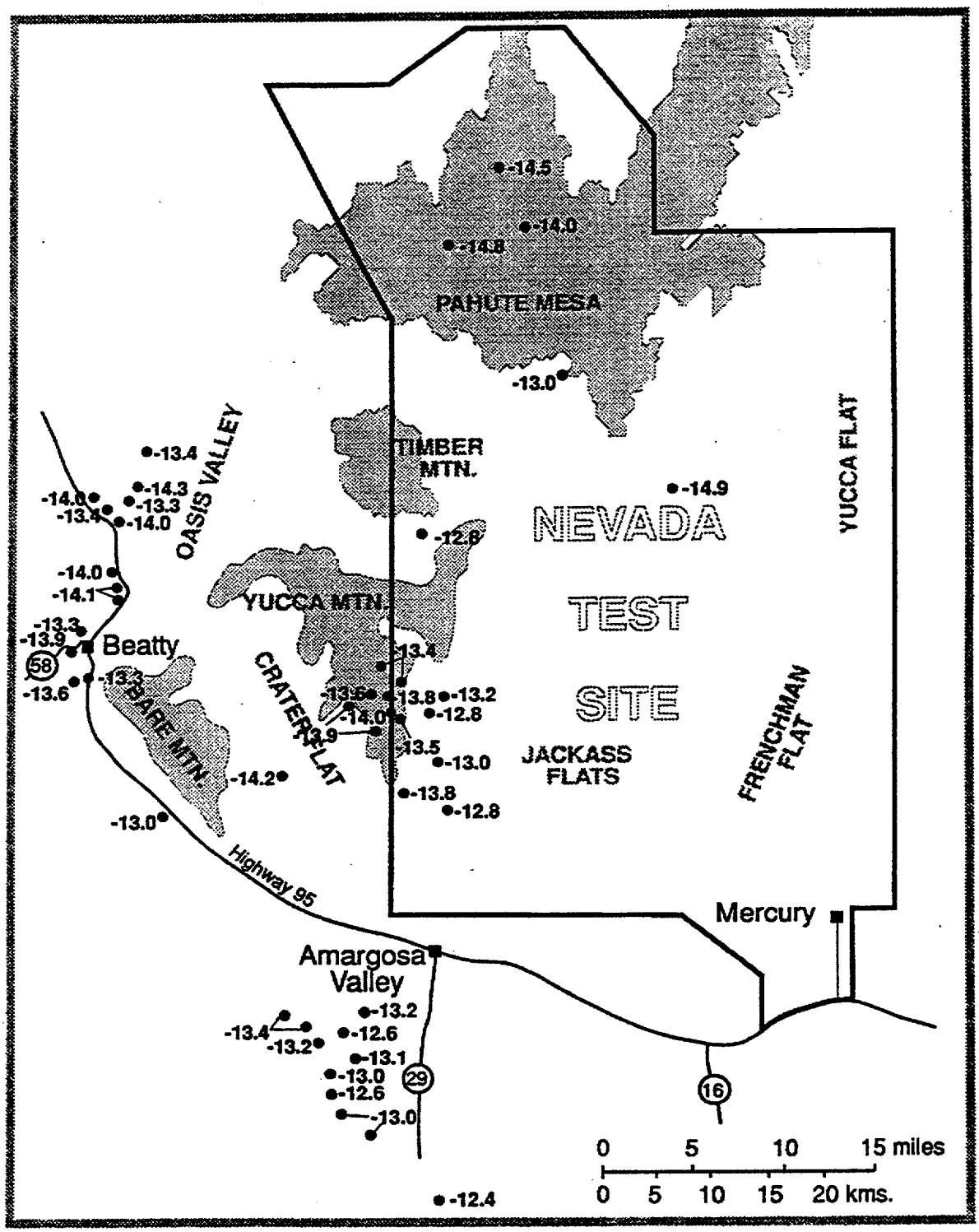

Figure 5.2-19. Map Showing Delta Oxygen-18 Values for Groundwater in the Valley-Fill Aquifer

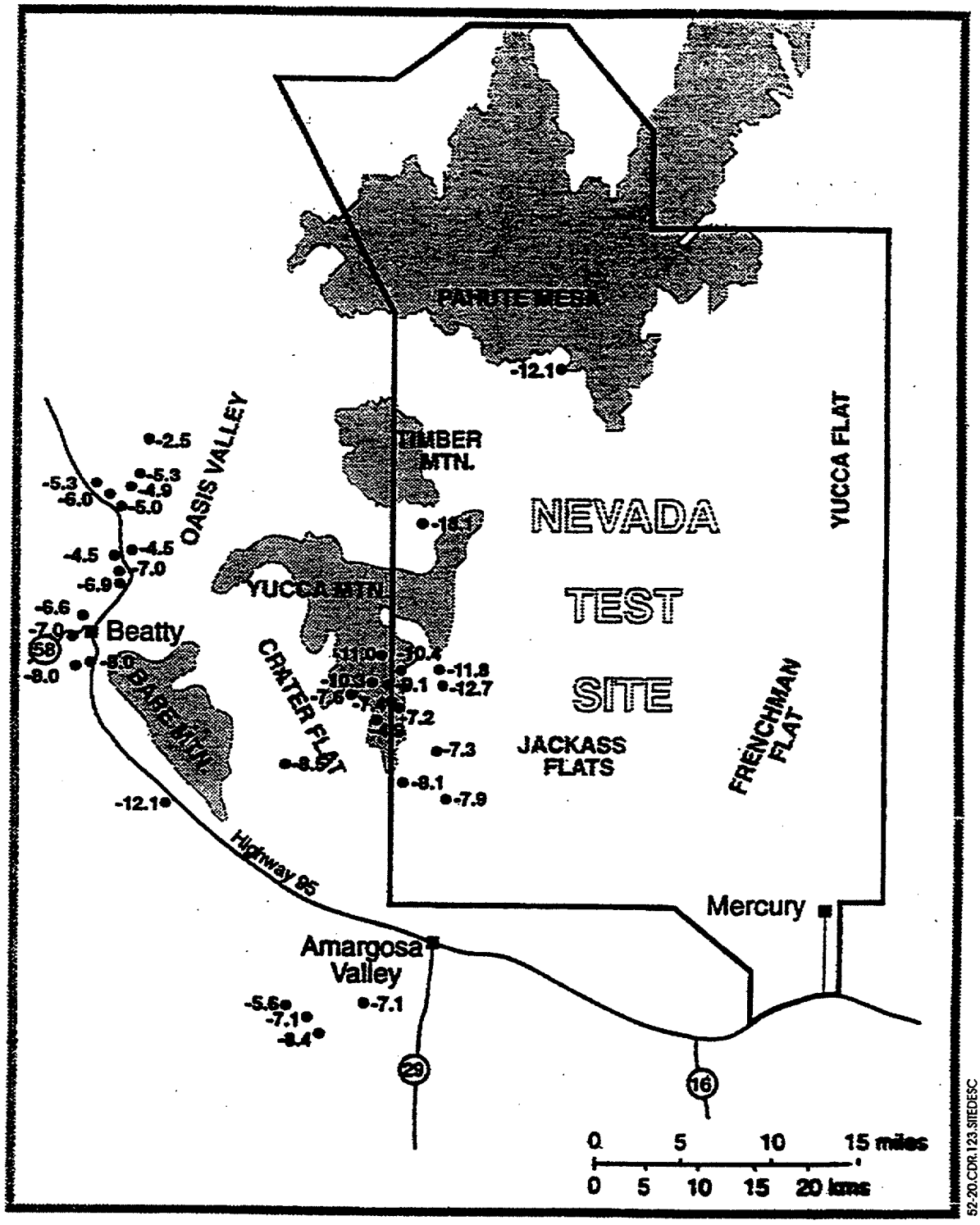

Figure 5.2-20. Map Showing Delta Carbon-13 Values for Groundwater in the Valley-Fill Aquifer

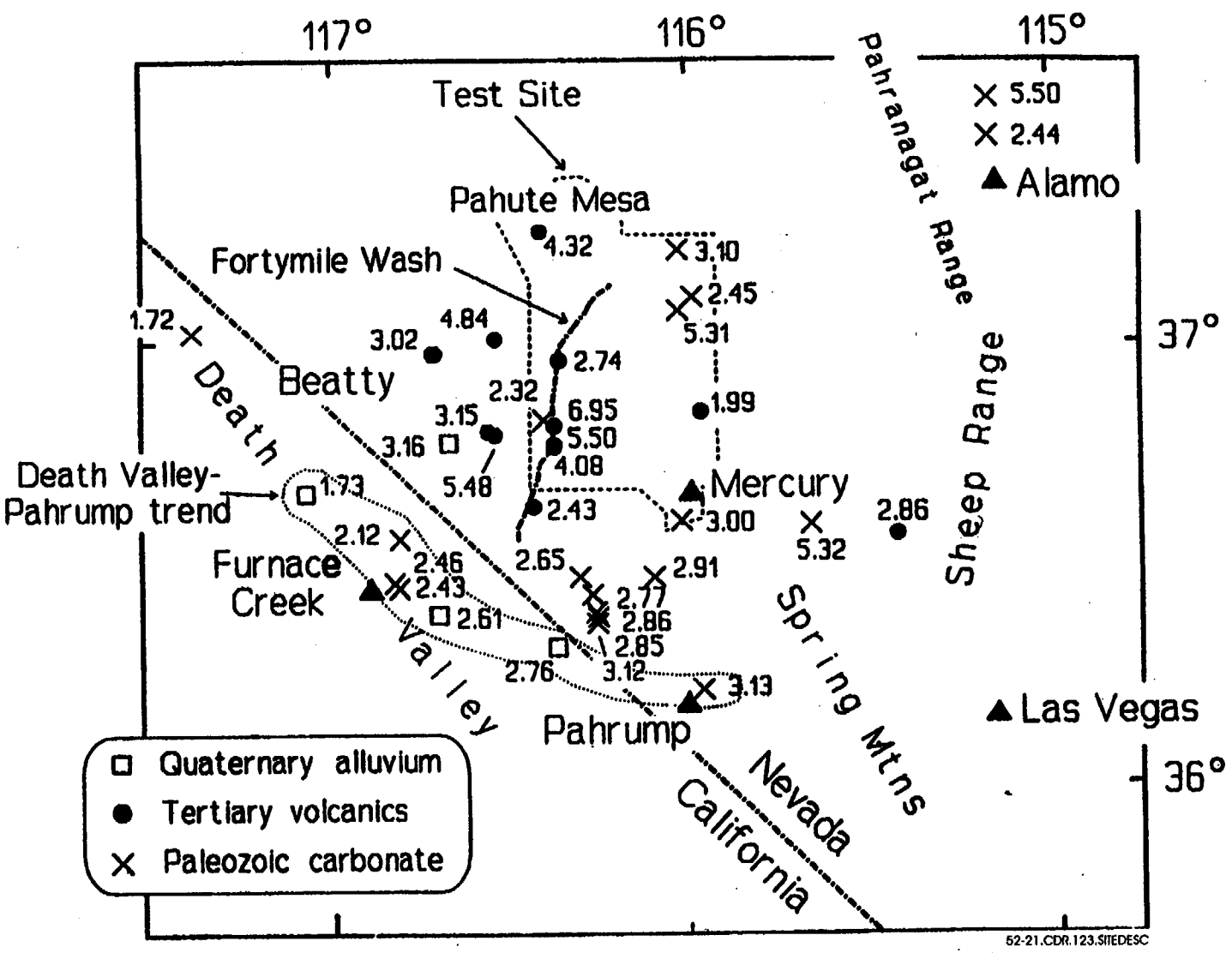

Figure 5.2-21. Map Showing $^{234}U/^{238}U$ Values for Groundwater in Southern Nevada and Adjacent California

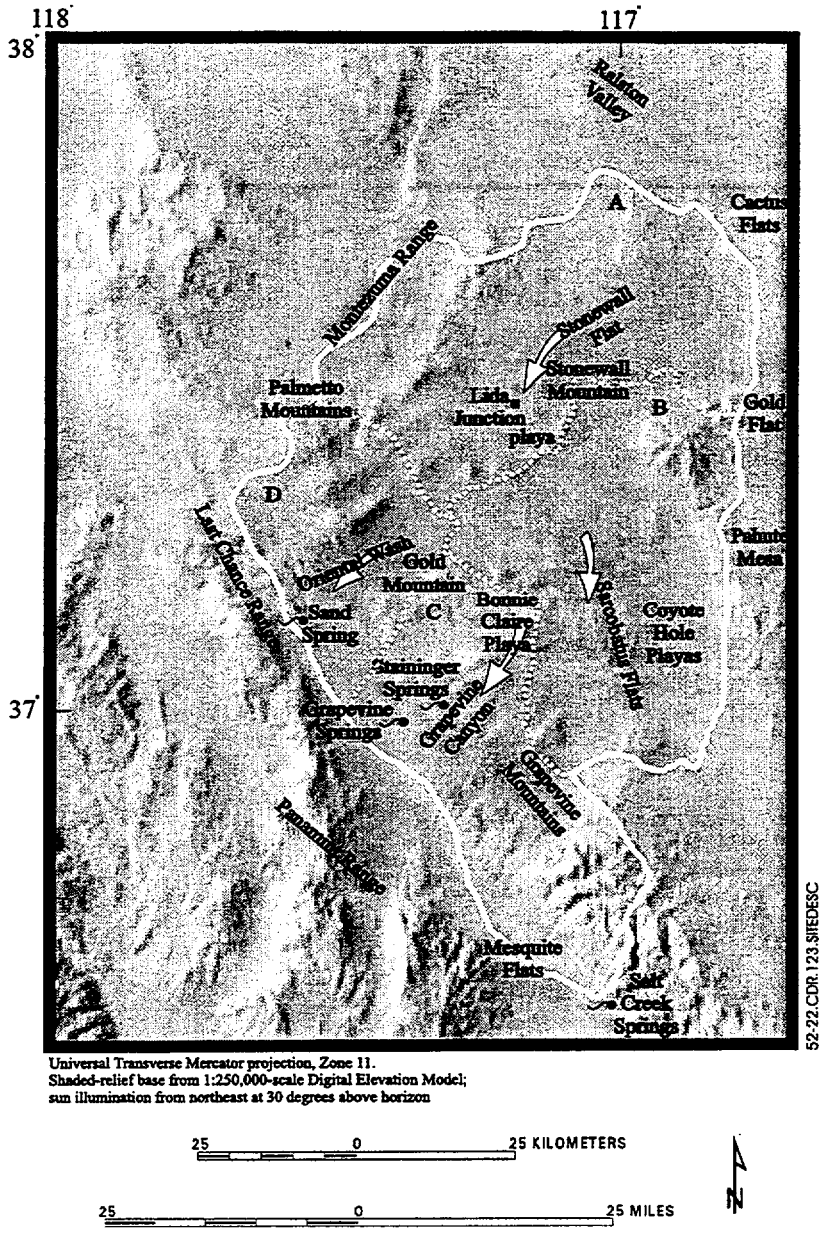

Figure 5.2-22. The Northern Death Valley Subregion

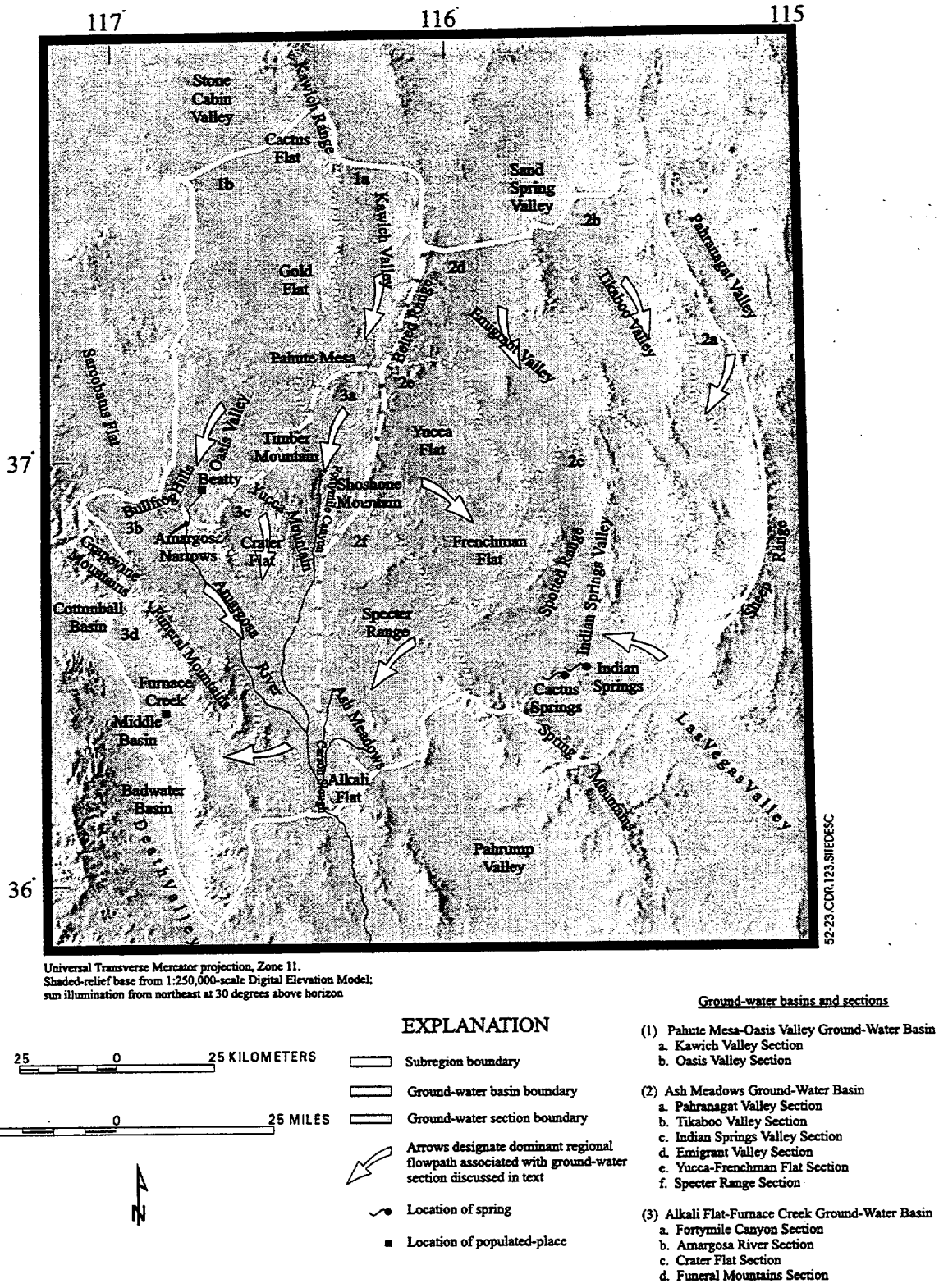

Universal Transverse Mercator projection, Zone 11.
Shaded-relief base from 1:250,000-scale Digital Elevation Model;
sun illumination from northeast at 30 degrees above horizon

25 0 25 KILOMETERS

25 0 25 MILES

N

EXPLANATION

- Subregion boundary
- Ground-water basin boundary
- Ground-water section boundary
- Arrows designate dominant regional flowpath associated with ground-water section discussed in text
- Location of spring
- Location of populated-place

Ground-water basins and sections

(1) Pahute Mesa-Oasis Valley Ground-Water Basin
  a. Kawich Valley Section
  b. Oasis Valley Section

(2) Ash Meadows Ground-Water Basin
  a. Pahranagat Valley Section
  b. Tikaboo Valley Section
  c. Indian Springs Valley Section
  d. Emigrant Valley Section
  e. Yucca-Frenchman Flat Section
  f. Specter Range Section

(3) Alkali Flat-Furnace Creek Ground-Water Basin
  a. Fortymile Canyon Section
  b. Amargosa River Section
  c. Crater Flat Section
  d. Funeral Mountains Section

Figure 5.2-23. The Central Death Valley Subregion

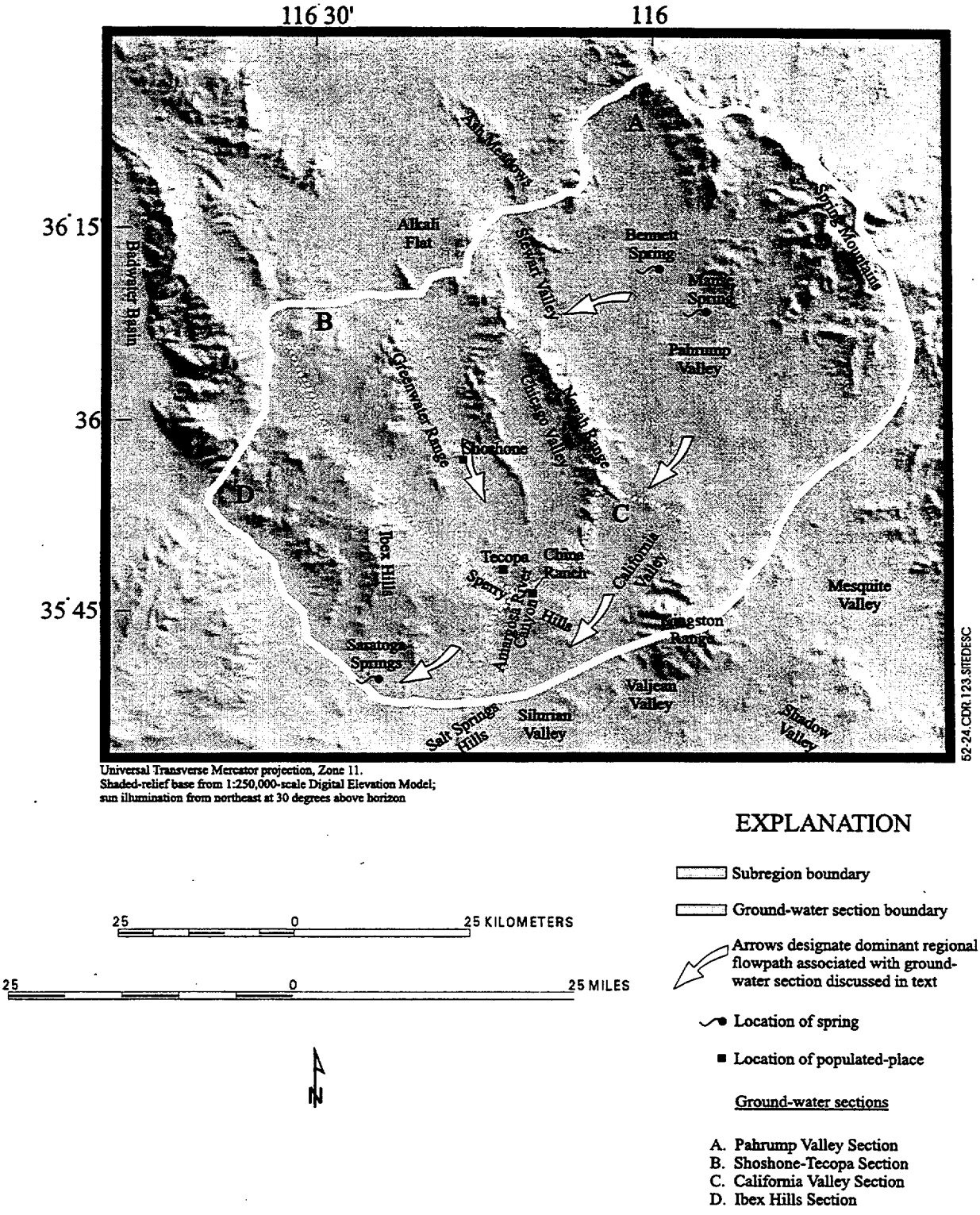

Figure 5.2-24. The Southern Death Valley Subregion

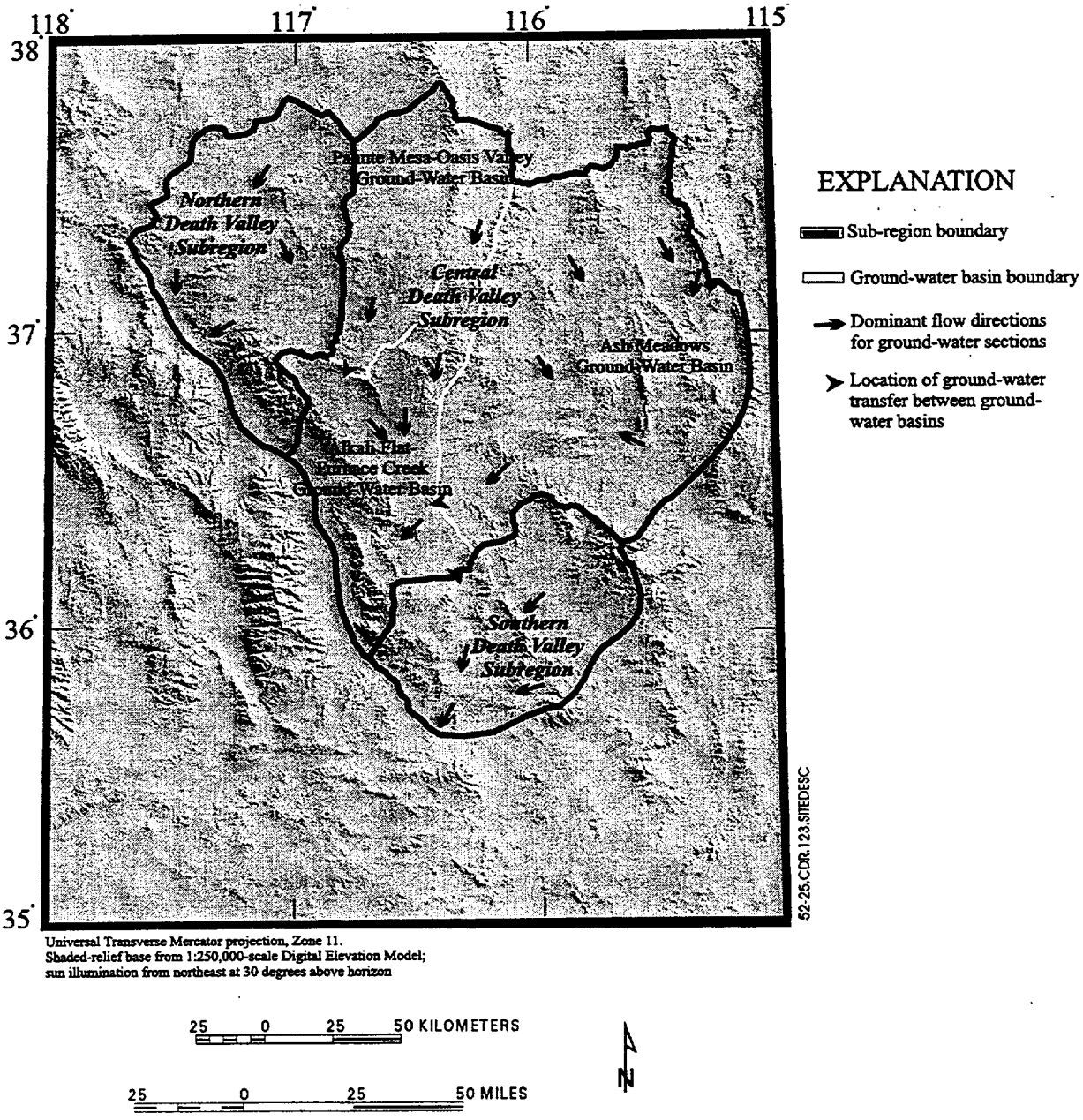

Figure 5.2-25. Subregions, Groundwater Basins, and Associated Flow Paths of the Death Valley Regional Groundwater Flow System

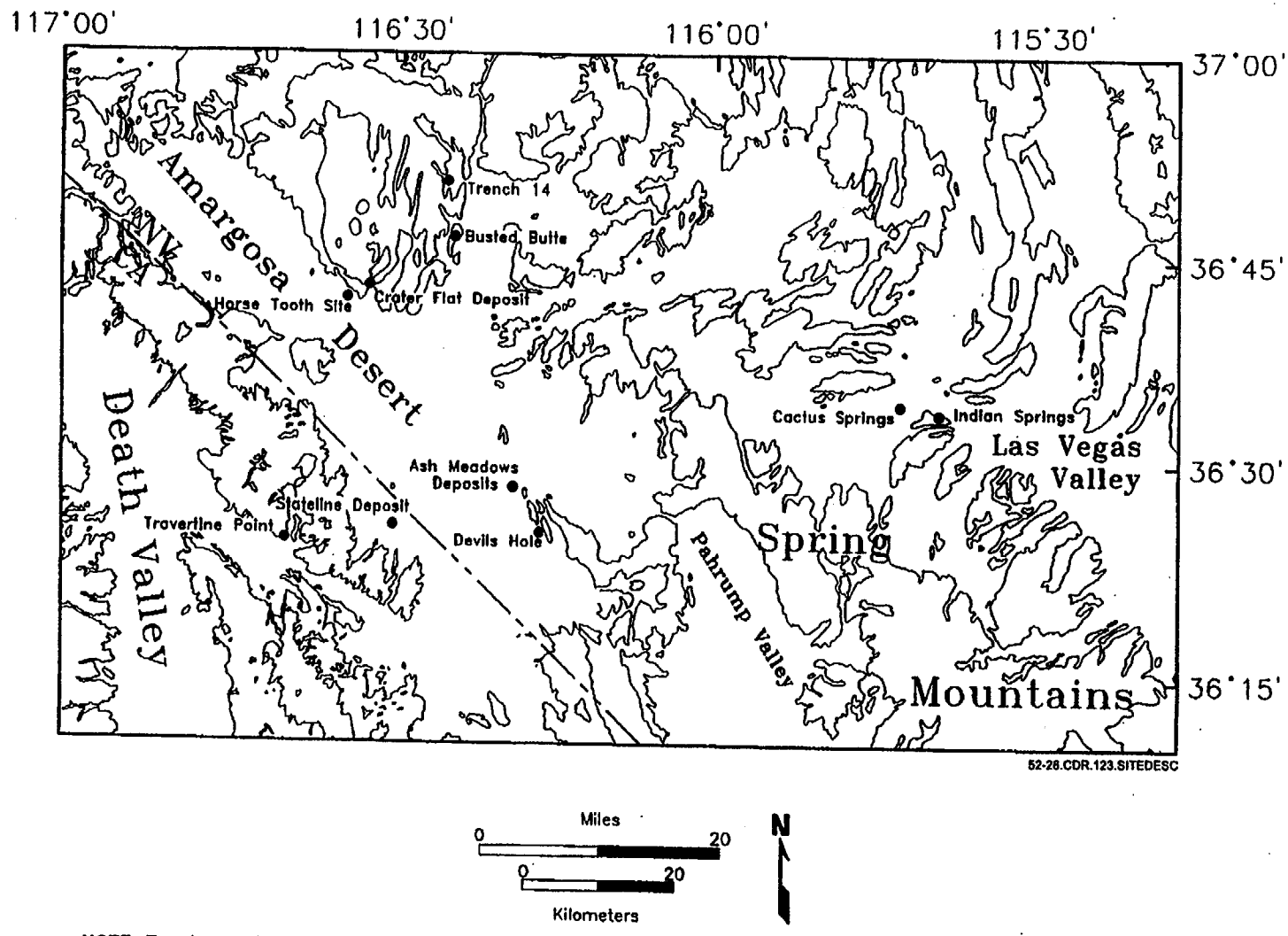

NOTE: Trench 14 and Busted Butte, which have been intensively studied, are not former discharge sites.

Figure 5.2-26. Locations of Sites of Former Discharge from the Regional Groundwater System and Other Study Sites

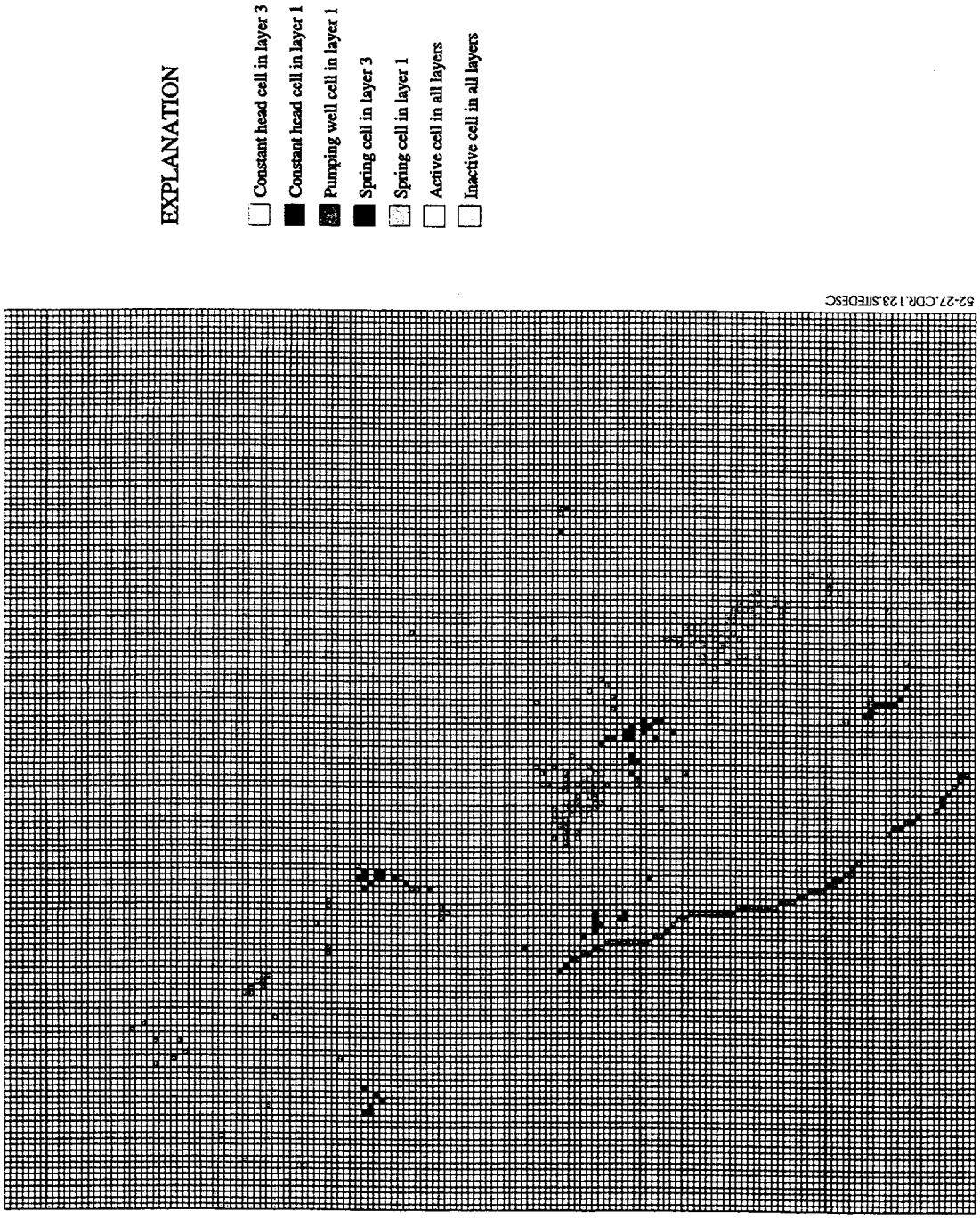

Figure 5.2-27. Map Showing Regional Model Boundary Conditions: Constant Heads, Springs, Wells

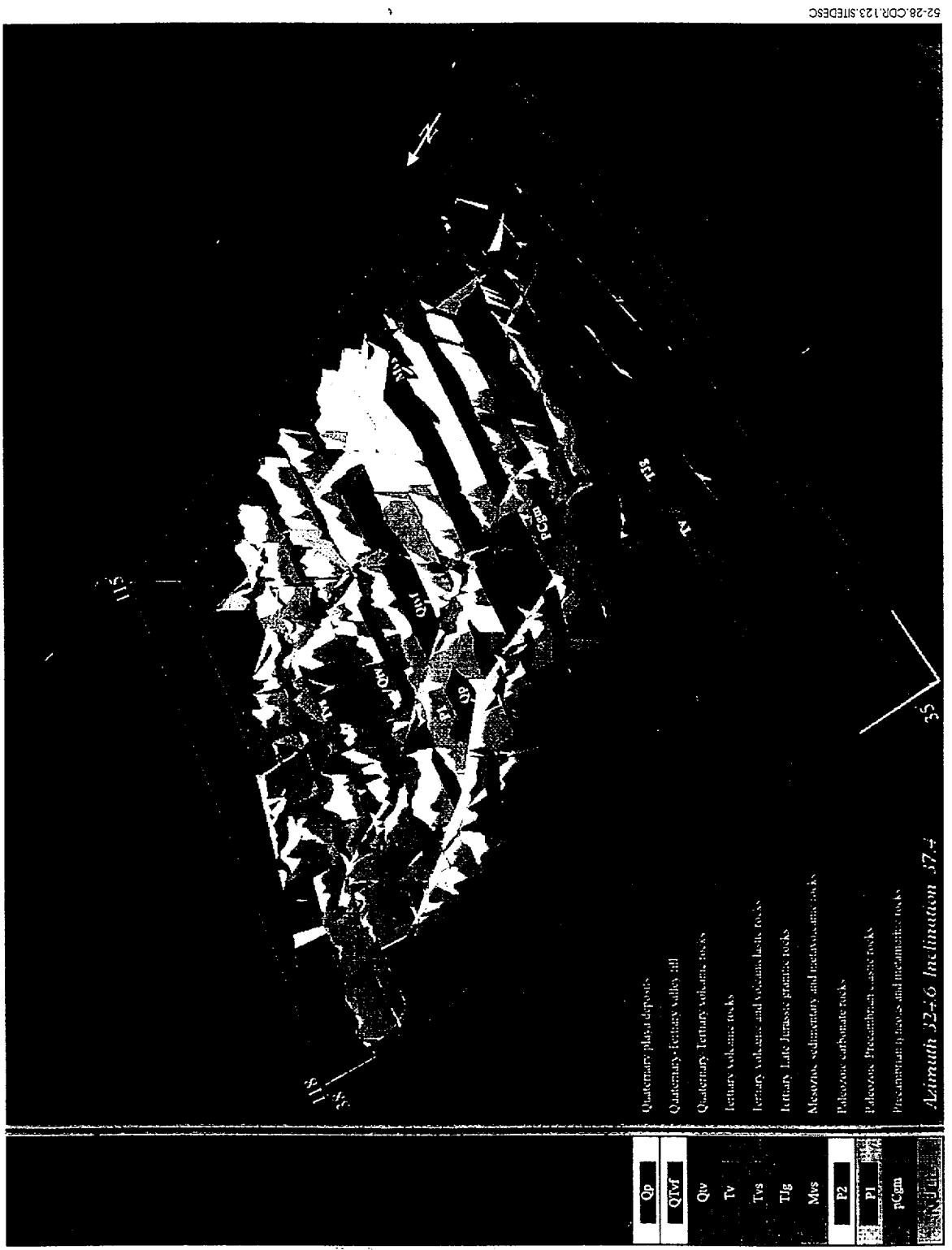

Figure 5.2-28. Fence Diagram of Regional Hydrogeologic Units

Figure 5.2-29. Hydraulic Head Residuals (Observed Minus Simulated) for Model Layer 1

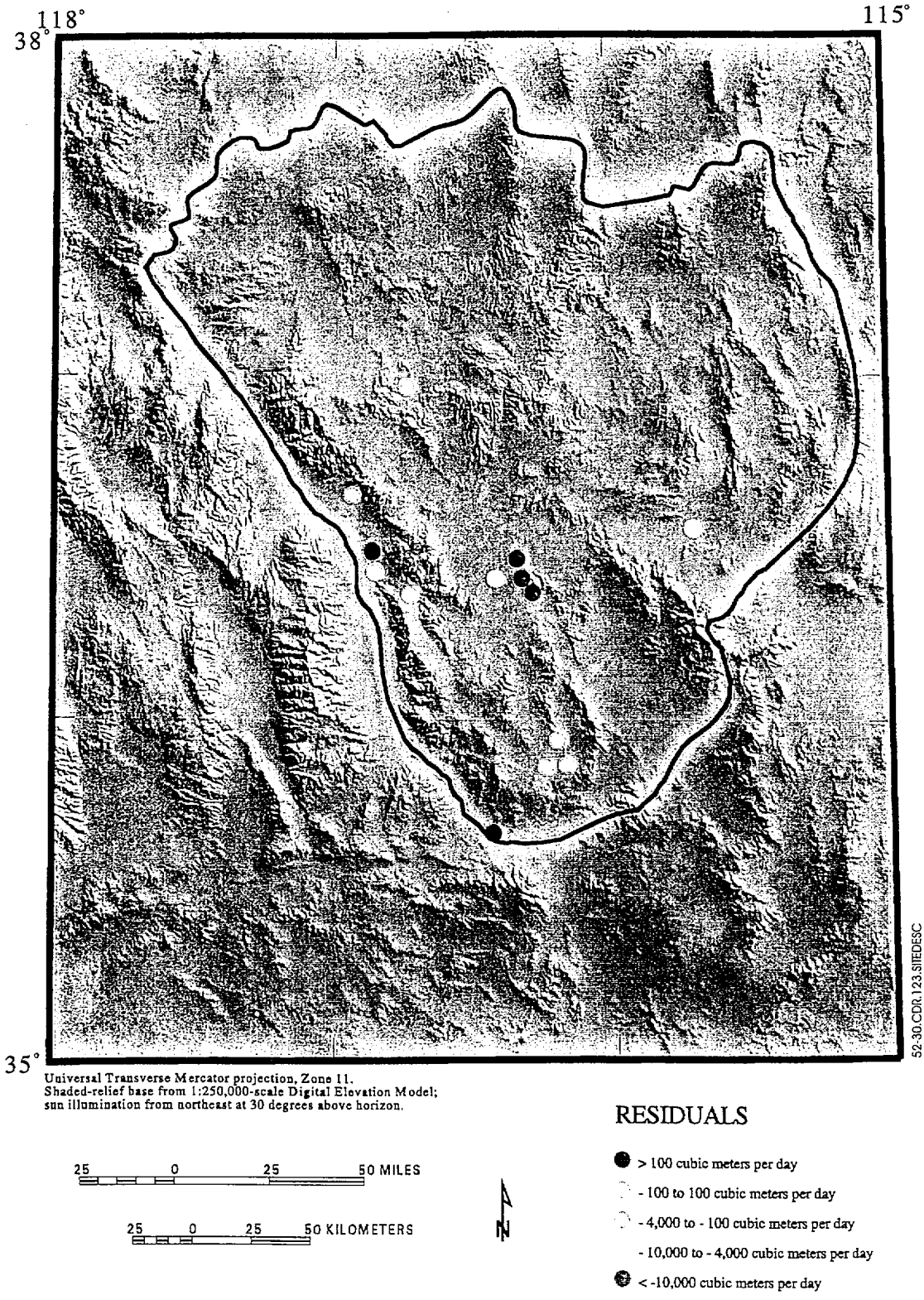

Figure 5.2-30. Spring Flow Residuals

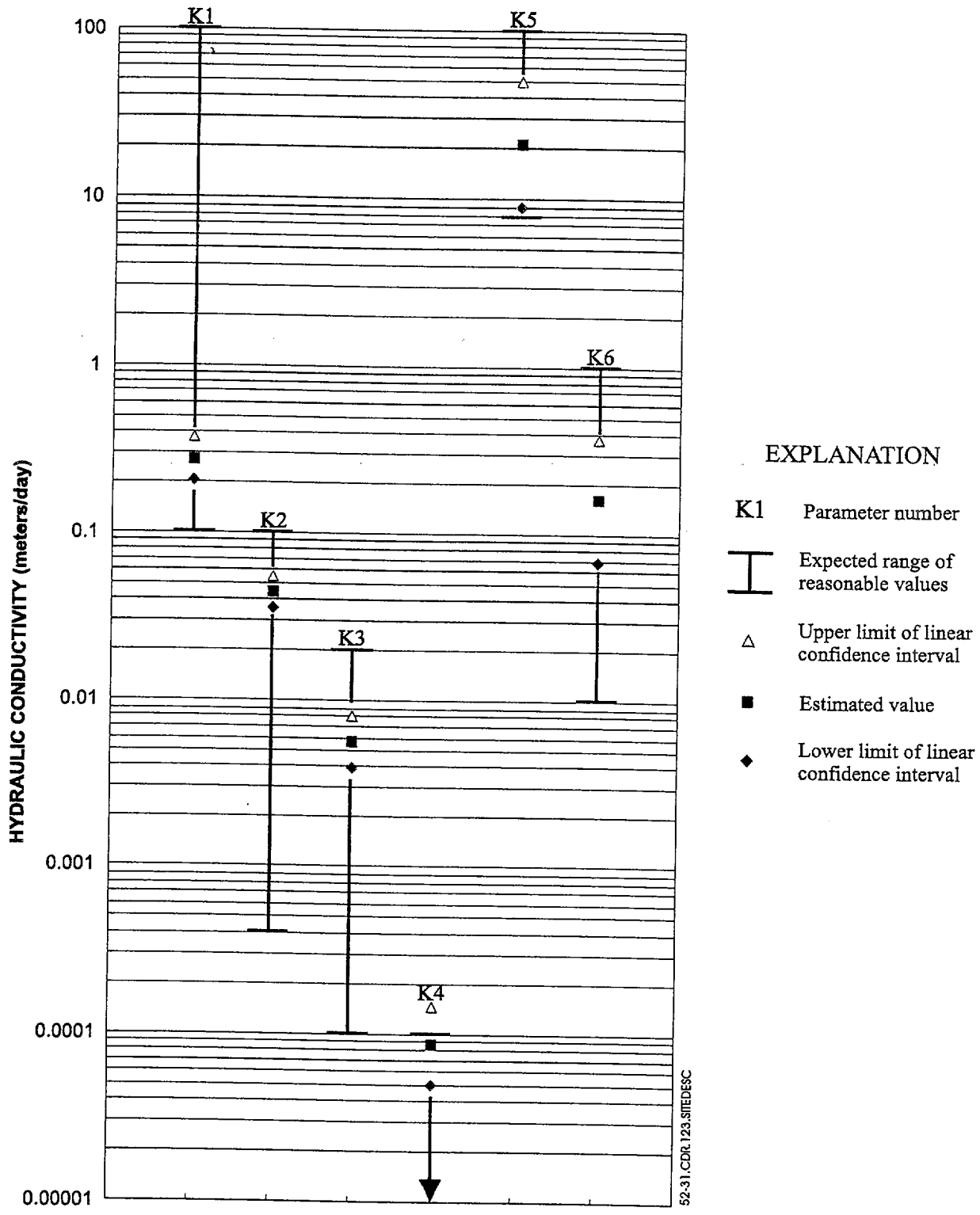

Figure 5.2-31. Estimated Hydraulic Conductivity Parameters, Their 95-Percent Linear Confidence Intervals, and the Range of Reasonable Values

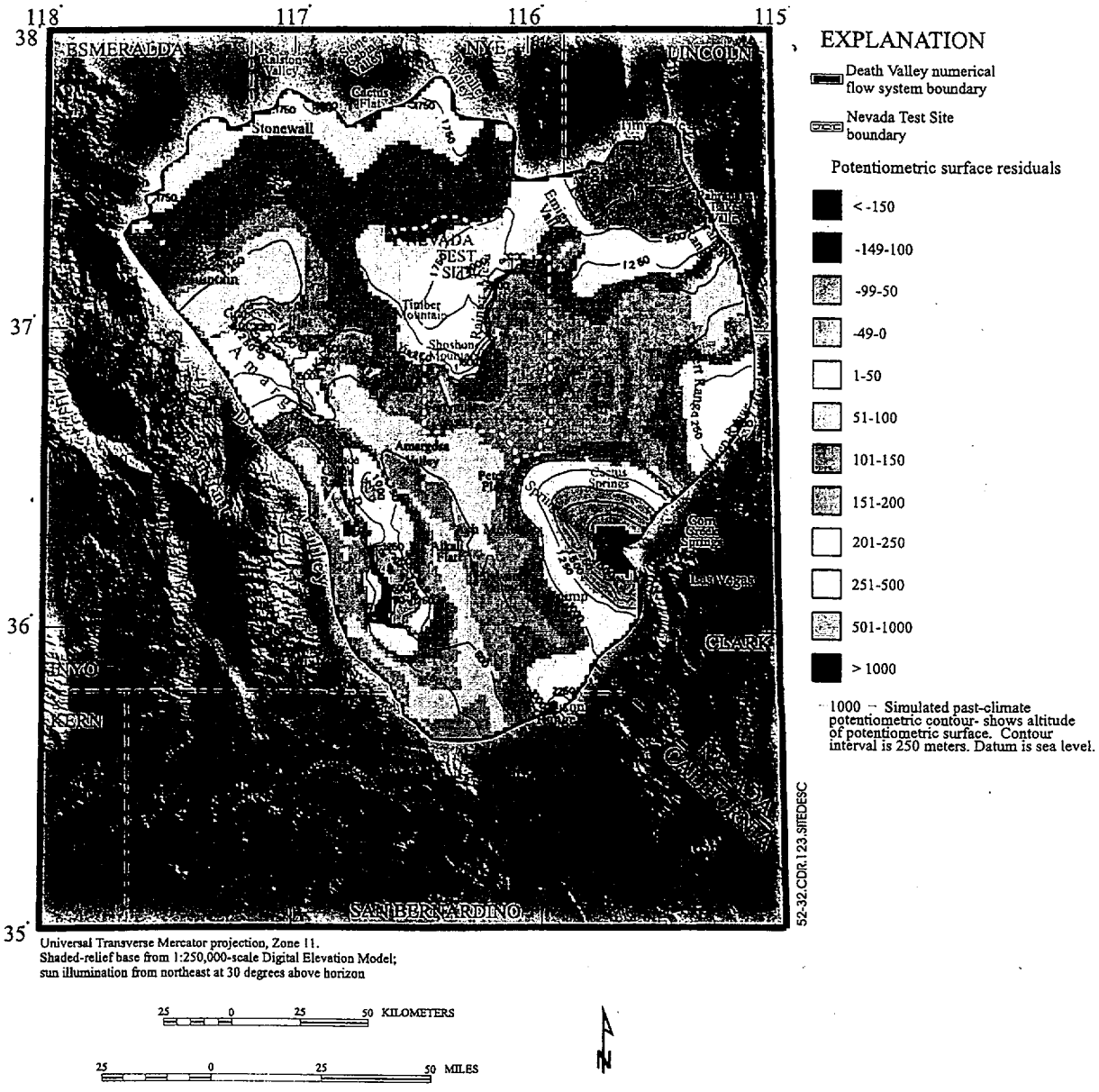

Figure 5.2-32. Simulated Past-Climate Potentiometric Surface for Model Layer 1 and the Difference Between the Past and Present-Day Model Layer 1 Potentiometric Surface

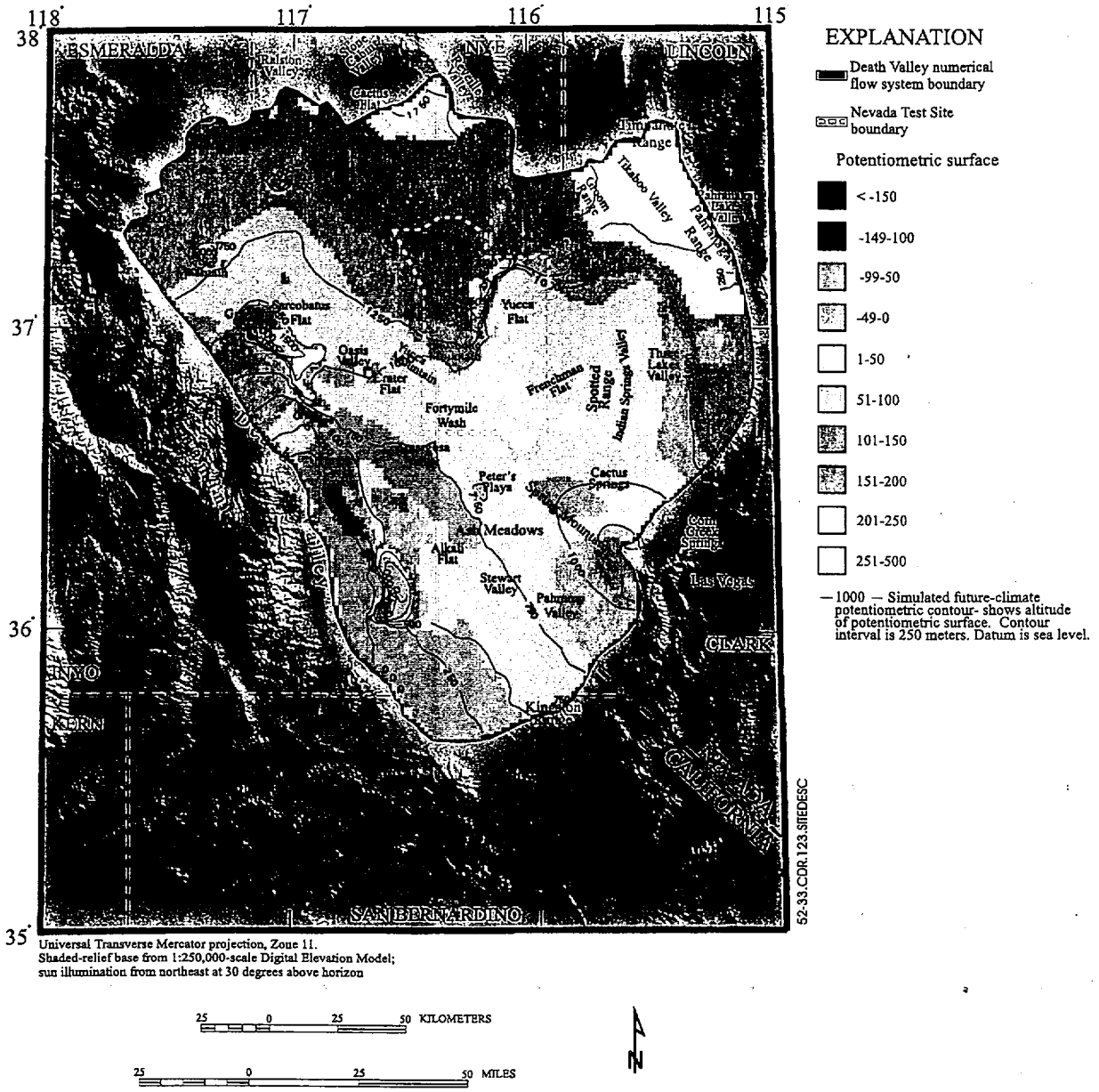

Figure 5.2-33. Simulated Future-Climate Potentiometric Surface for Model Layer 1 and the Difference Between the Future and Present-Day Model Layer 1 Potentiometric Surface

INTENTIONALLY LEFT BLANK

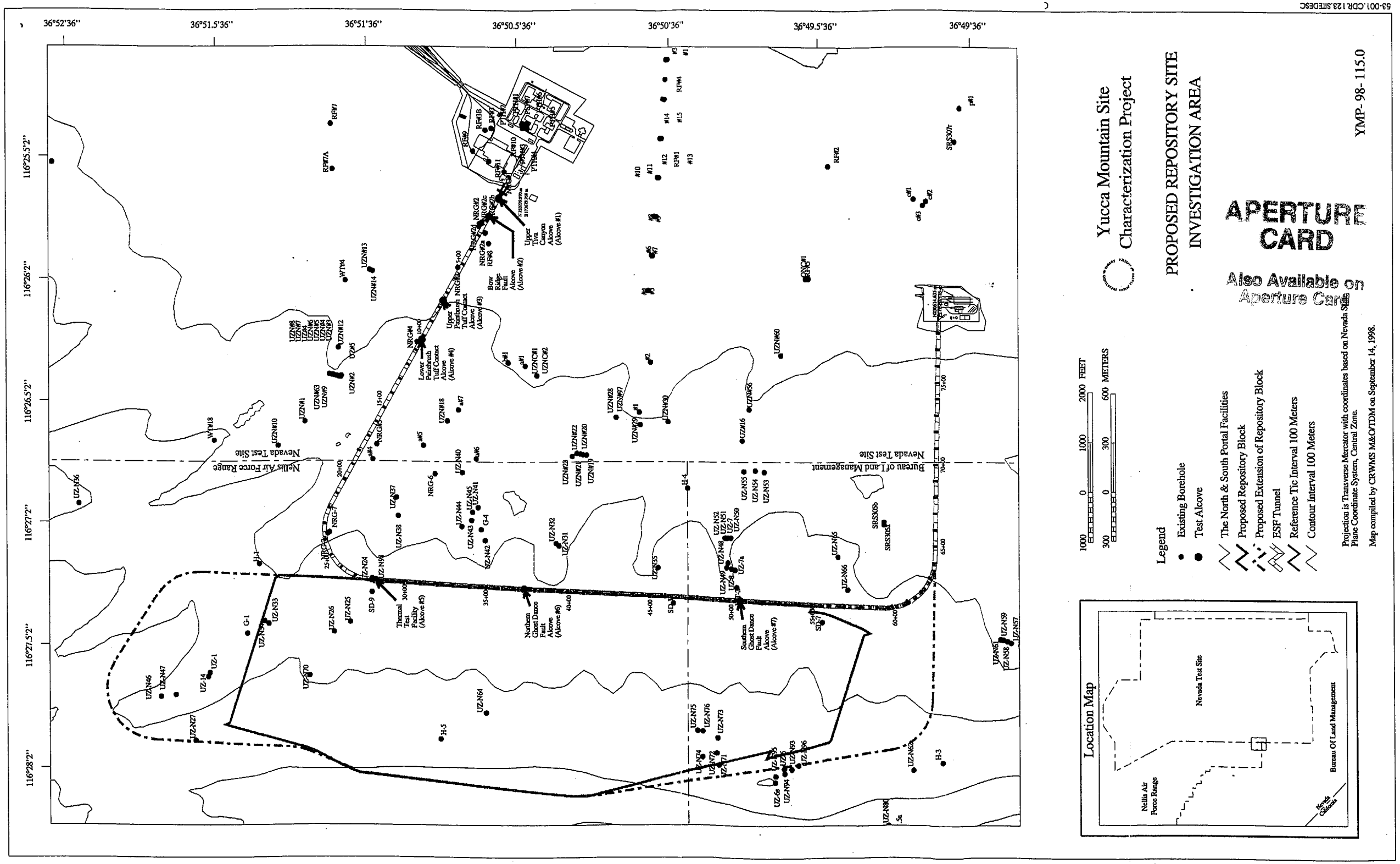

Figure 5.3-1 Topographic Map of the Site Area Showing Exploratory Tunnel and Boreholes and the Design and Extended Boundaries of the Proposed Repository

' LEFT BLANK

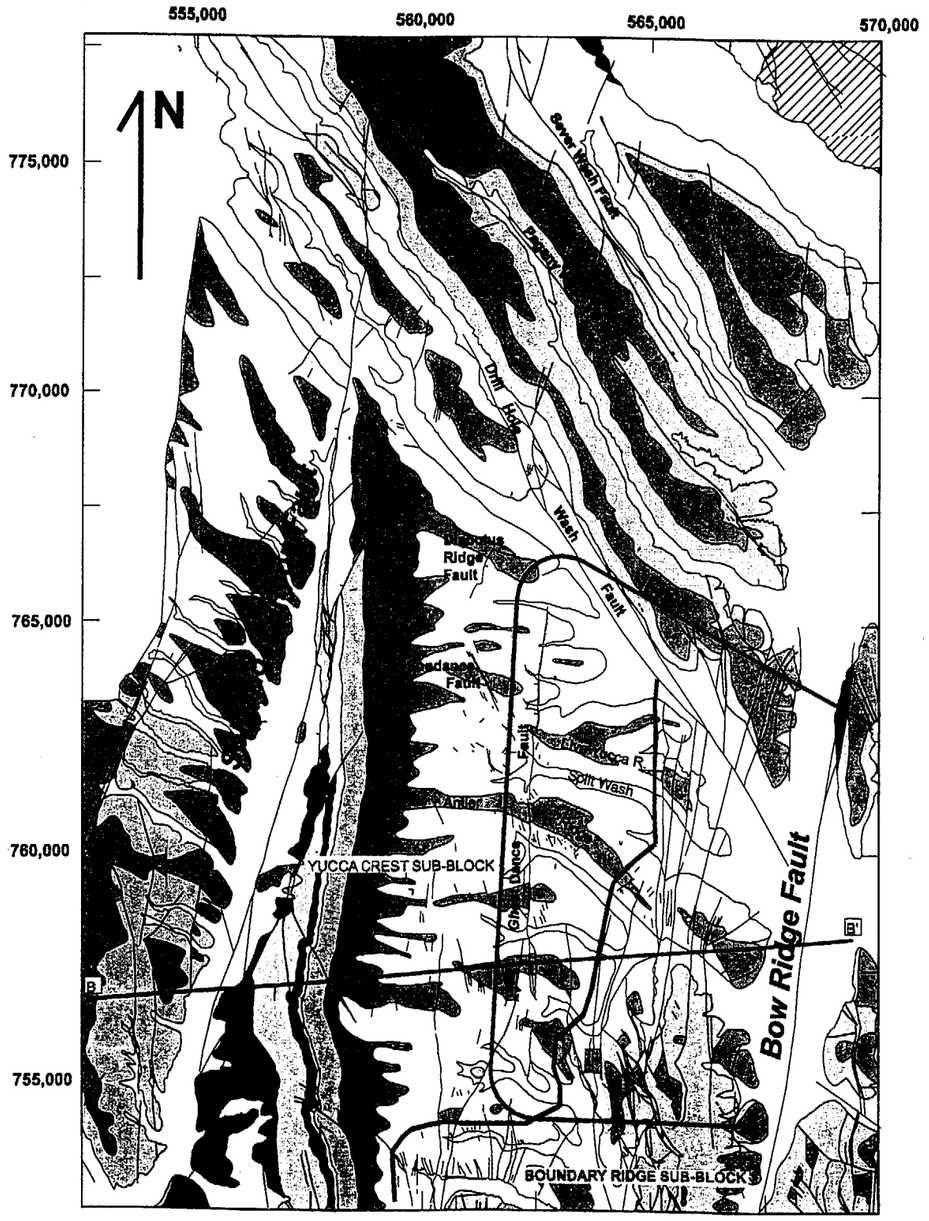

NOTE: Solid black lines are faults, whether exposed or concealed beneath surficial deposits. Line B-B' is the location of the cross section in Figure 5.3-3

Bedrock Geologic Map of the Central Block Area, Yucca Mountain, Nevada

Explanation

Quaternary
- Alluvium & Colluvium

Tertiary
- Rainier Mesa Tuff
- Comb Peak Rhyolite

Tiva Canyon Tuff
- Crystal - rich member
- Crystal - poor member

Pah Canyon, Yucca Mountain Tuffs - undivided

Topopah Spring Tuff
- Crystal - rich member
- Crystal - poor member

Tiva Canyon & Topopah Spring Tuff (lenses in fault zone)

0 1 km

63-02.COR.123.SITEDESC

Figure 5.3-2. Simplified Geologic Map of the Central Block (after Day et al. 1998)

' LEFT BLANK

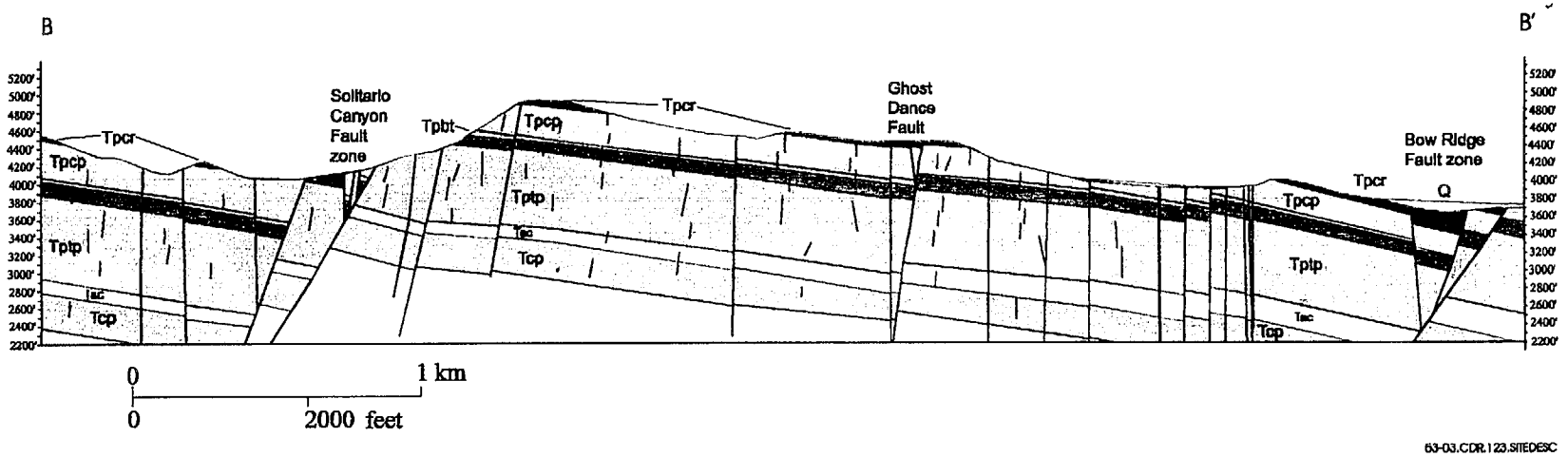

NOTE: The Line of Section, B-B' is from west to east and is shown on Figure 5.3-2. Q, unconsolidated Quaternary deposits; Tpcr and Tpcp, welded members of the Tiva Canyon Tuff; Tpbt, bedded and nonwelded tuffs of the Middle Paintbrush Group; Tptr and Tptp, welded members of the Topopah Spring Tuff; Tac, Calico Hills Formation; Tcp, Prow Pass Tuff; unlabeled, deeper units of the Crater Flat Group. The water table is near the bottom of the cross-section, at an approximate altitude of 2,400 feet.

Figure 5.3-3. Simplified Geologic Cross-Section Through the Site Area

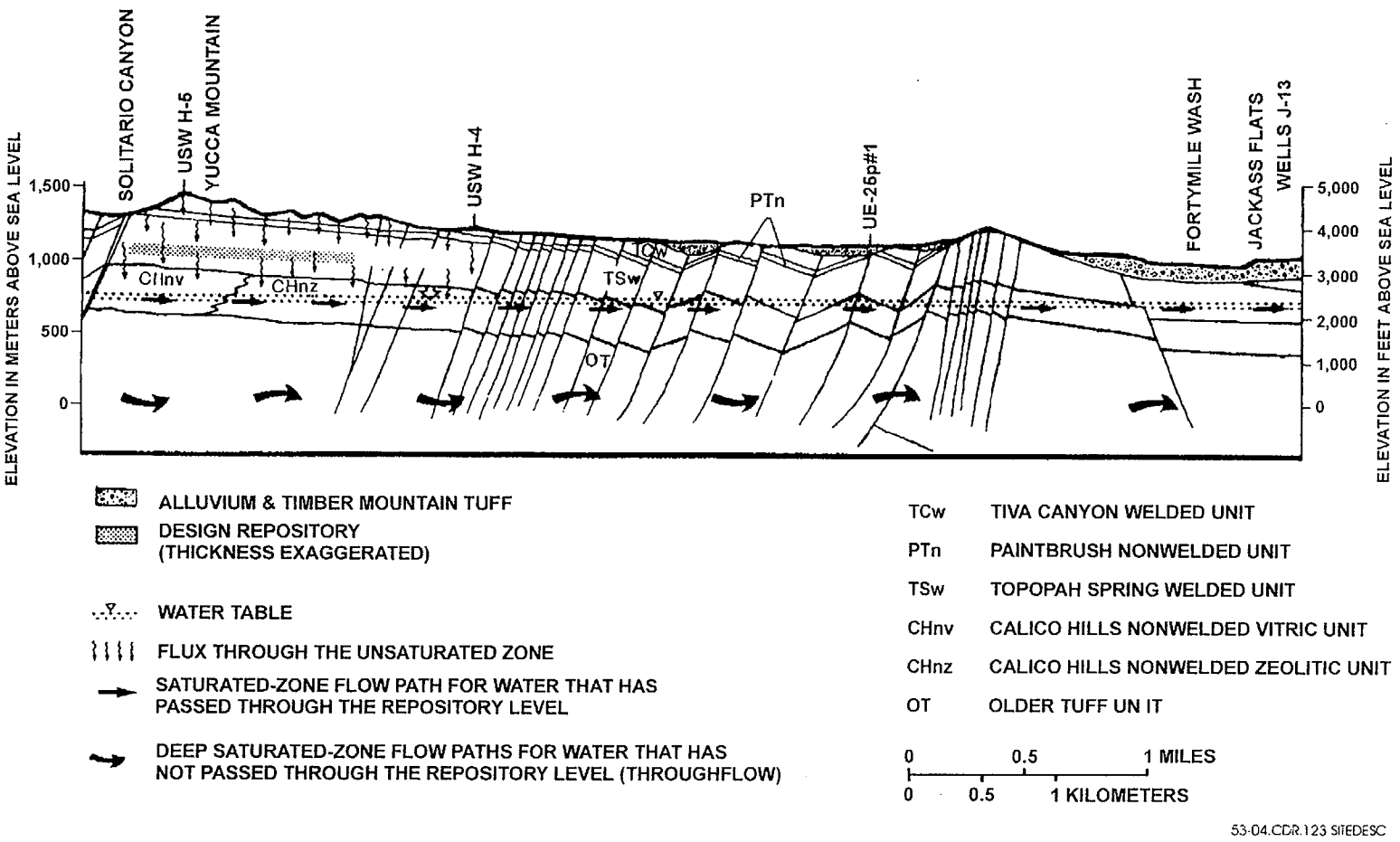

NOTE: Part, perhaps most, of the indicated lateral flow below the water table is diverted southward before reaching the Fortymile Wash area (adapted from DOE 1988, Figure 3-46)

Figure 5.3-4. Conceptual Hydrogeologic Cross-Section from Northwest to Southeast Across the Site Area to Jackass Flats

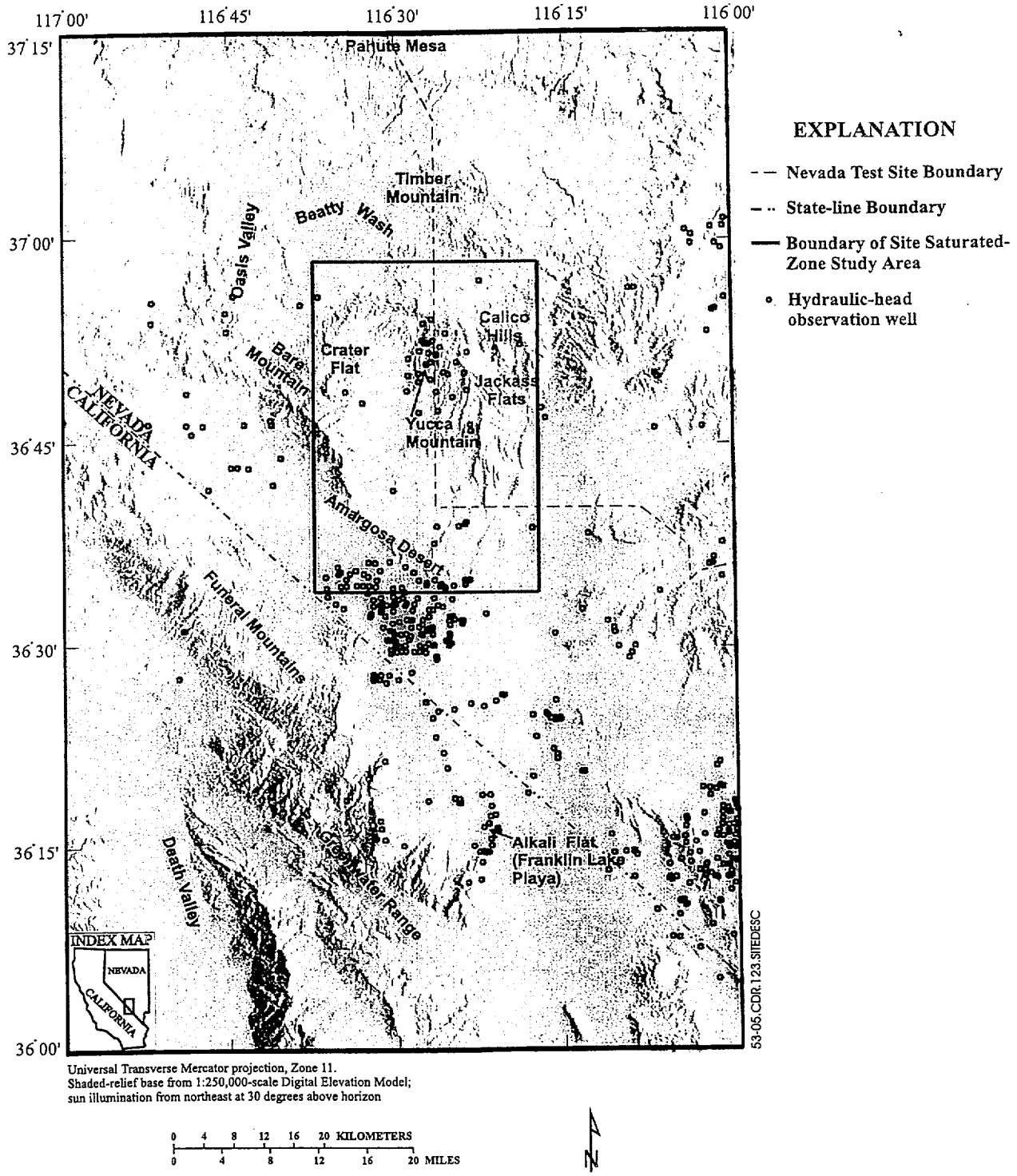

NOTE: adapted from Czarnecki, Faunt et al. 1997

Figure 5.3-5. Location of the Site Saturated Zone Study Area Within the Region, Showing Associated Geographic Features and Hydraulic-Head Observation Wells

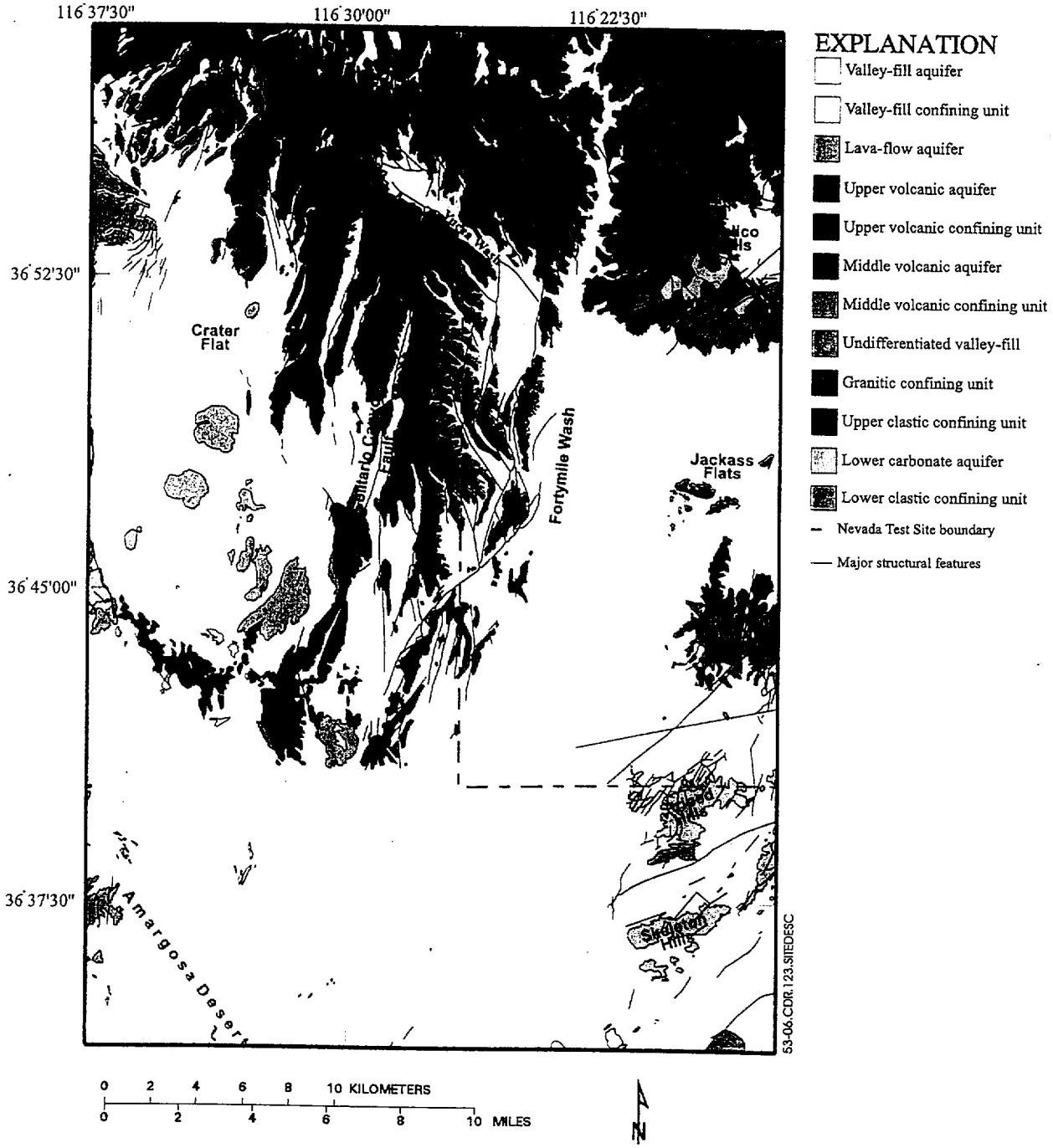

NOTE: See text and Table 5.3-1 for definitions of hydrogeologic units and their geologic equivalents. Limestone aquifer, lower volcanic aquifer, and lower volcanic confining unit do not appear at the land surface (after Czarnecki, Faunt et al. 1997).

Figure 5.3-6. Generalized Hydrogeologic Map of Site Saturated Zone Study Area With Major Structural Features

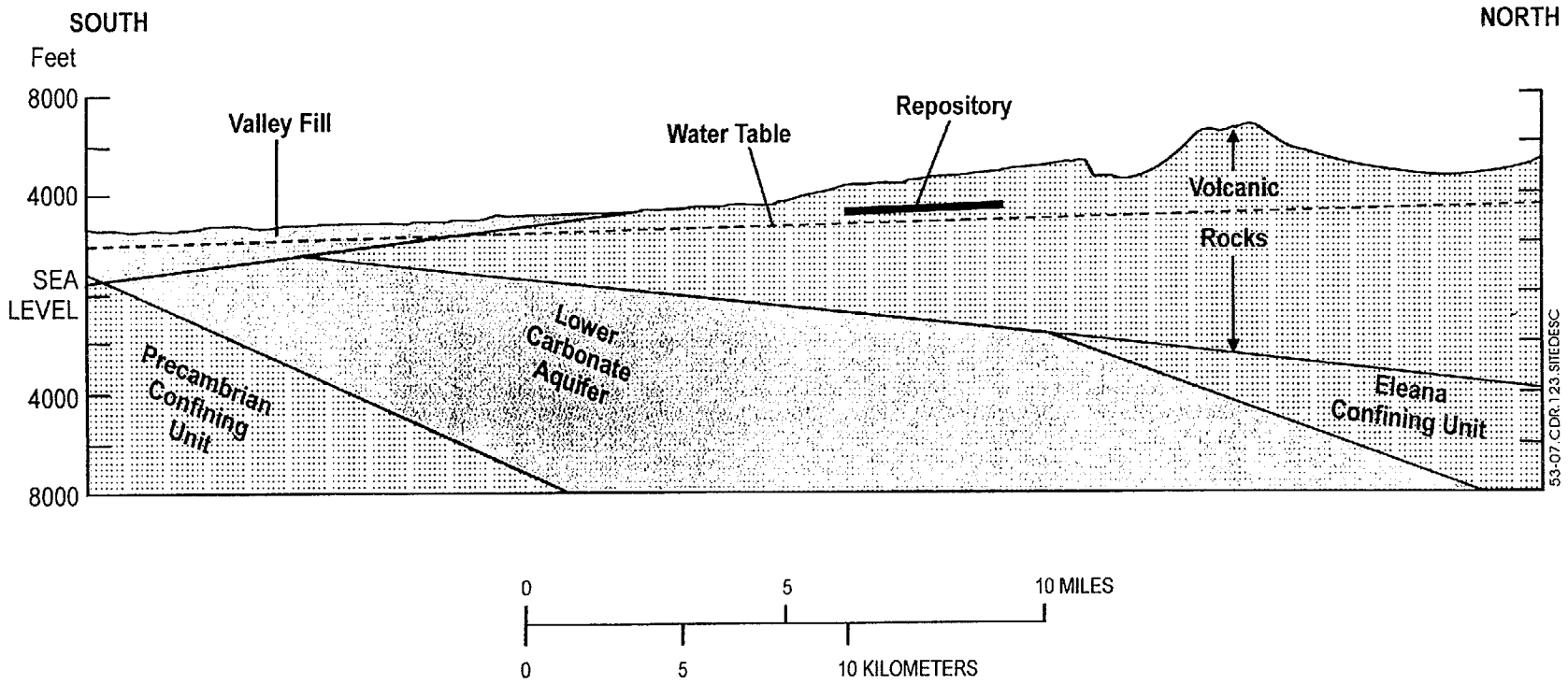

Figure 5.3-7. Cross-Section from Northern Yucca Mountain to Northern Amargosa Desert, Showing Generalized Geology and the Water Table (adapted from Robinson, G.D. 1985, Figure 9)

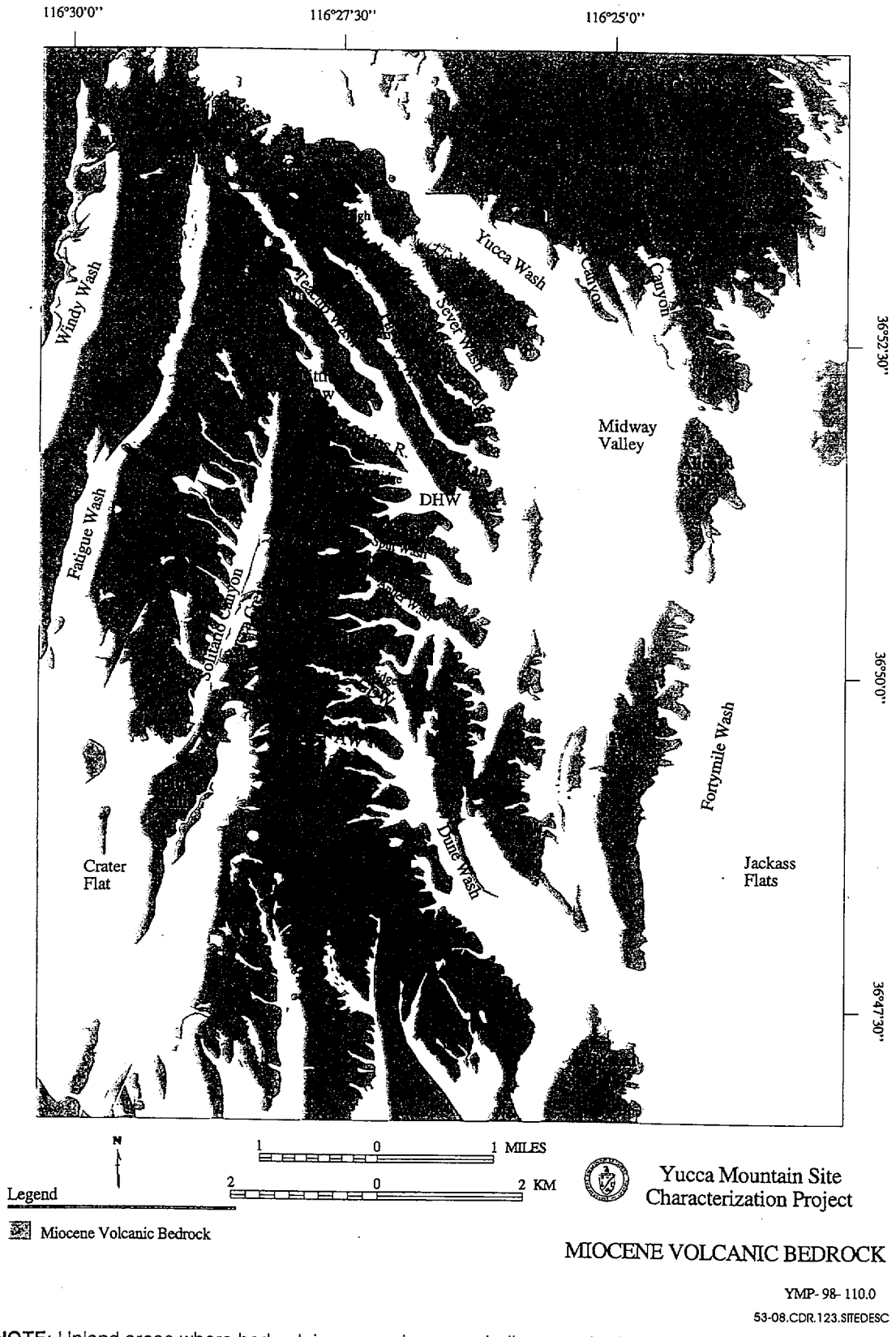

NOTE: Upland areas where bedrock is exposed or very shallow are shaded.

Figure 5.3-8. Index Map Showing the Names of Principle Geographic Features in the Site Area

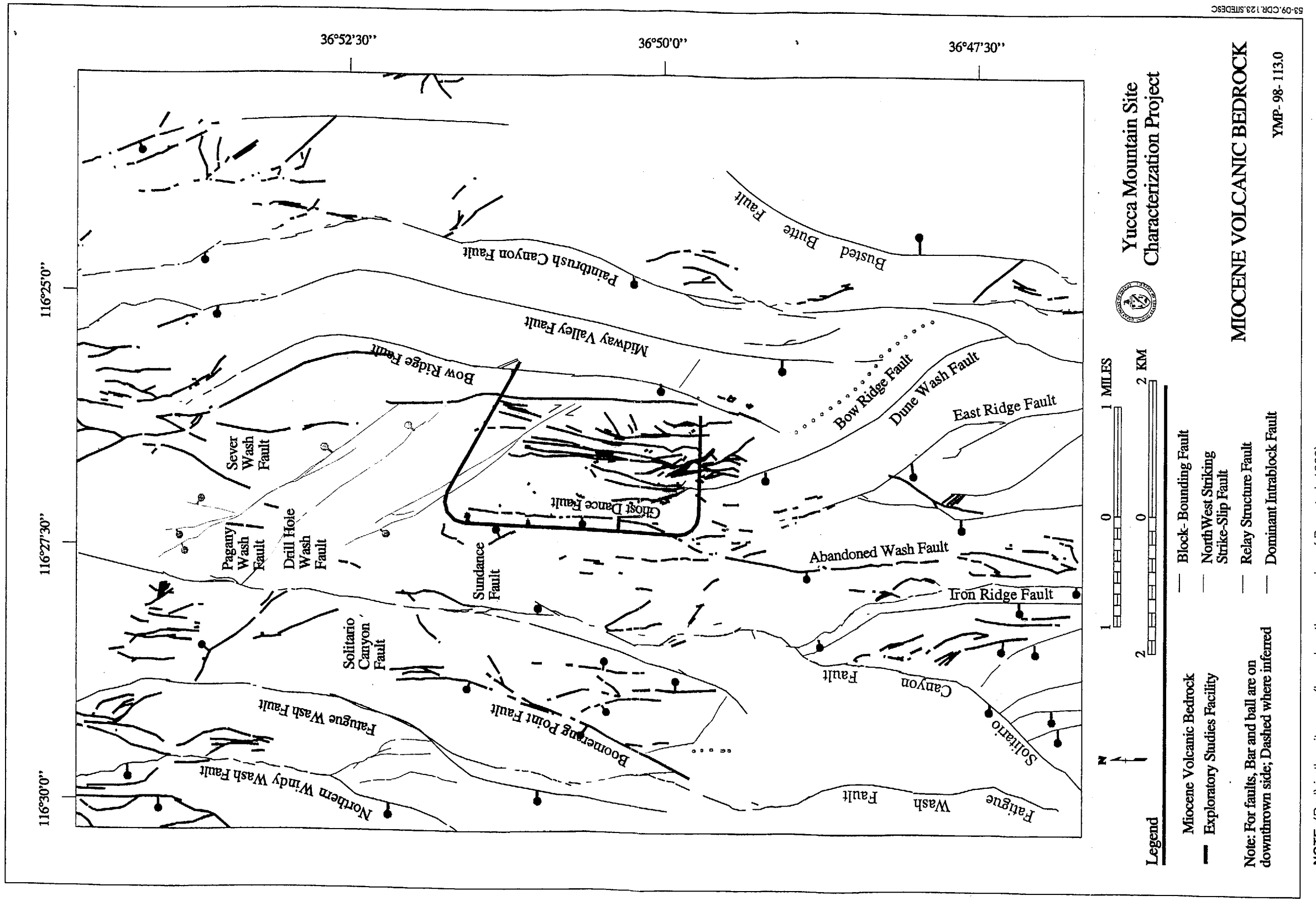

NOTE: (Red) in the site area (based on the mapping of Day et al. 1998)

Figure 5.3-9. Map Showing Block-Bounding Faults (black) and Important Intra-Block Faults

INTENTIONALLY LEFT BLANK

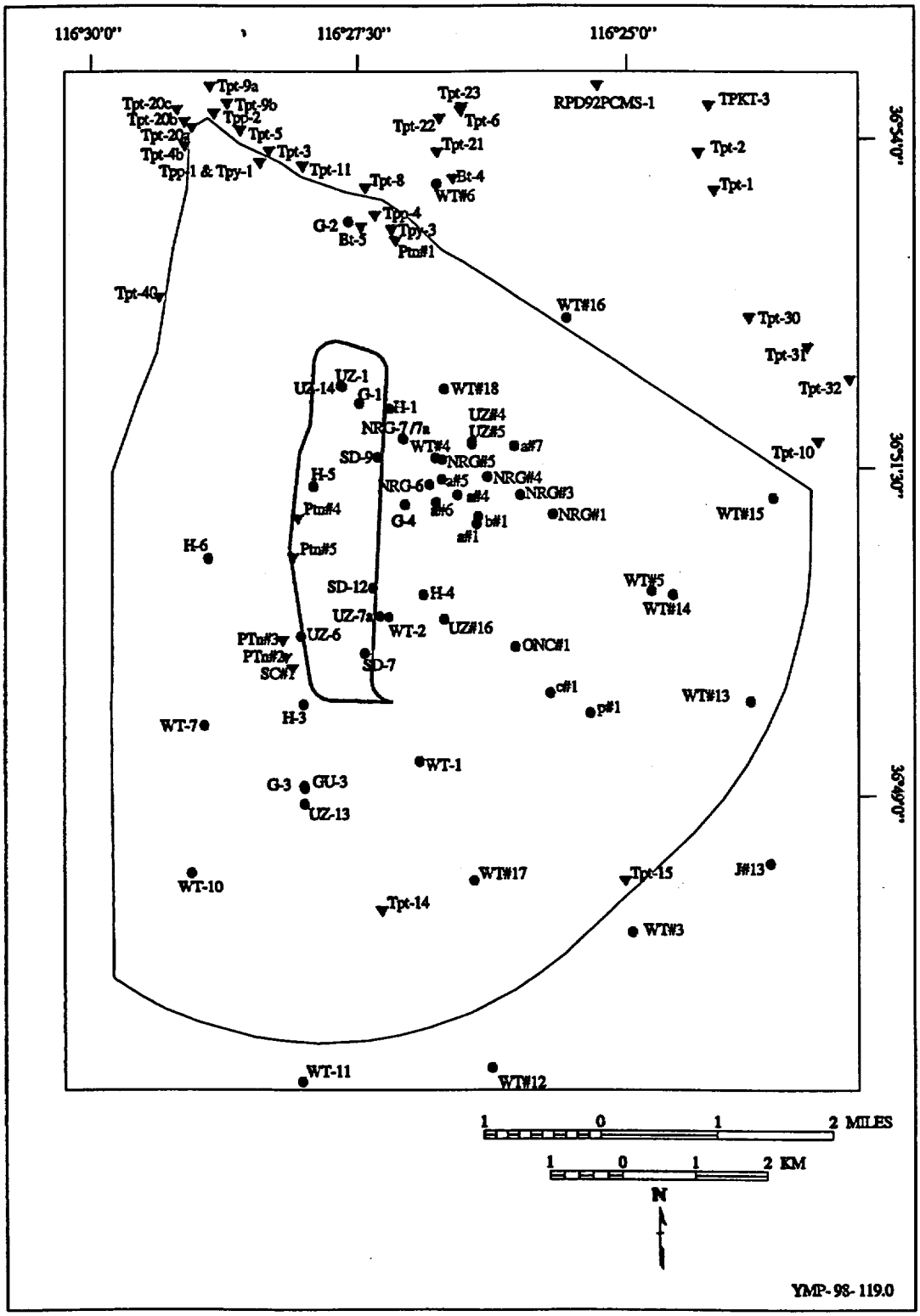

NOTE: Most boreholes on the Nevada Test Site have the prefix UE-25; boreholes west of the Nevada Test Site boundary have the prefix USW.

Figure 5.3-10. Locations of Deep Boreholes Used for Unsaturated Zone and Saturated Zone Hydrologic Investigations at the Yucca Mountain Site

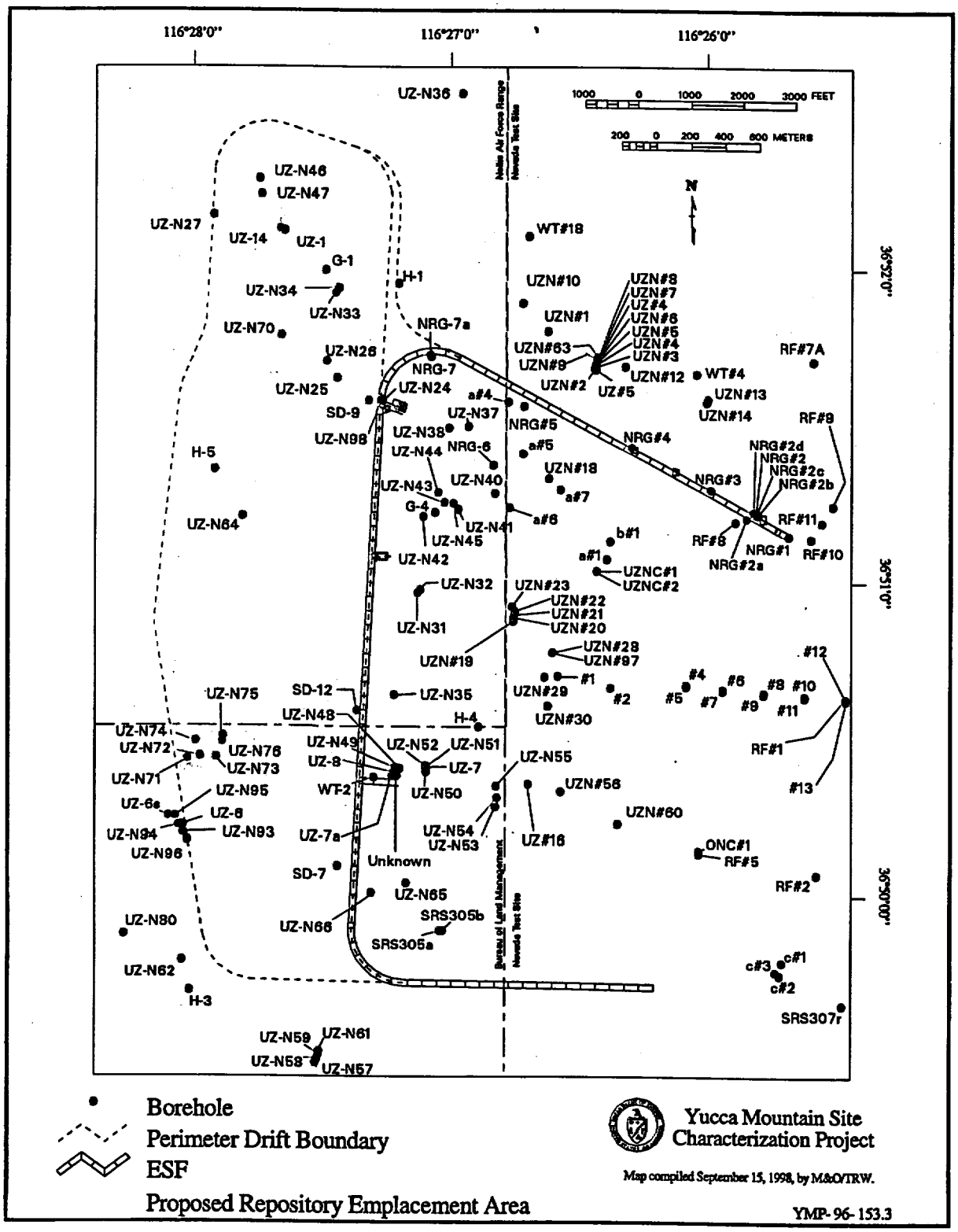

Figure 5.3-11. Map Showing Repository Area Boreholes and the Exploratory Studies Facility

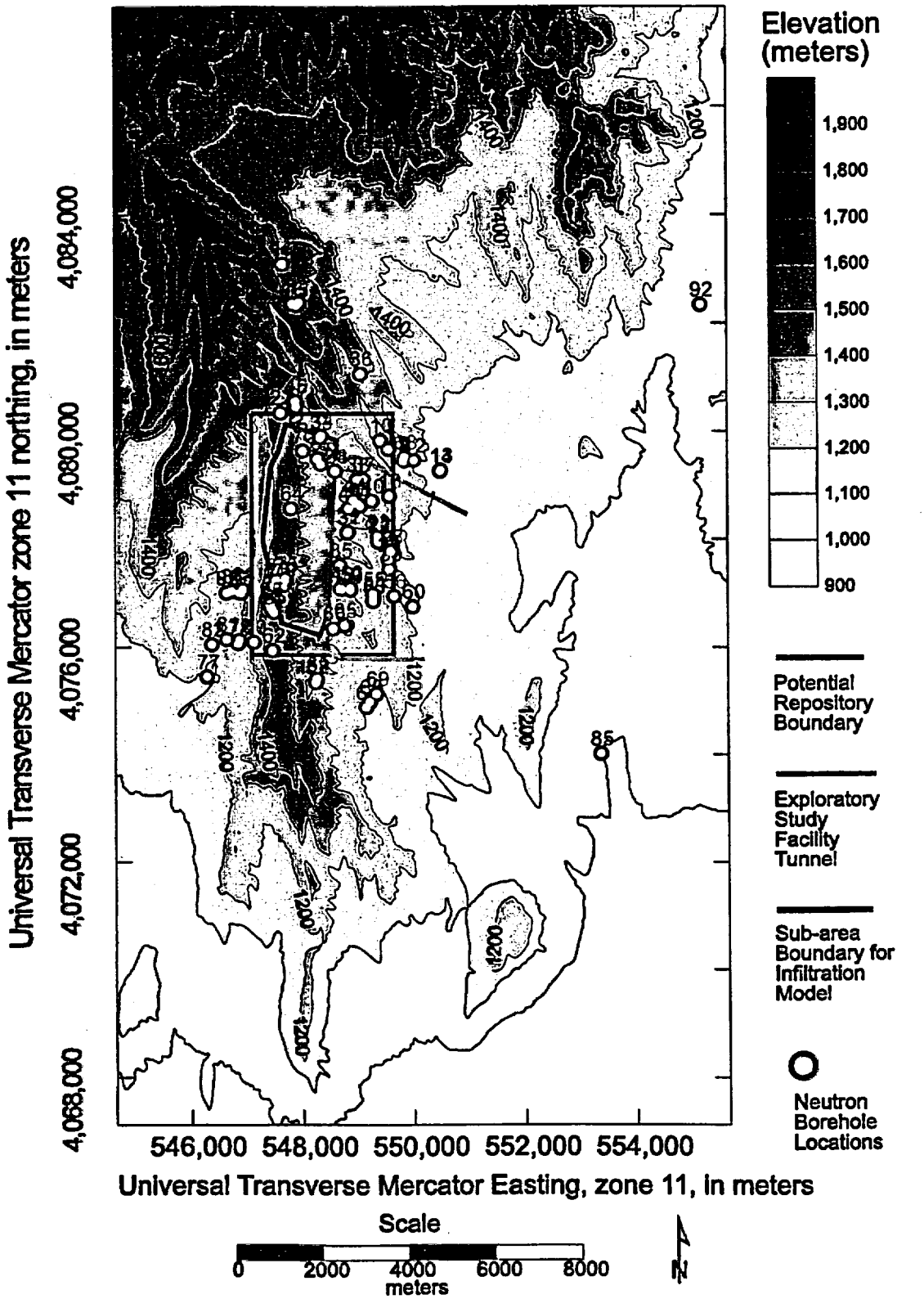

53-12.CDR.123.SITEDESC

Figure 5.3-12. Location of Neutron Boreholes Within the Yucca Mountain Site Area

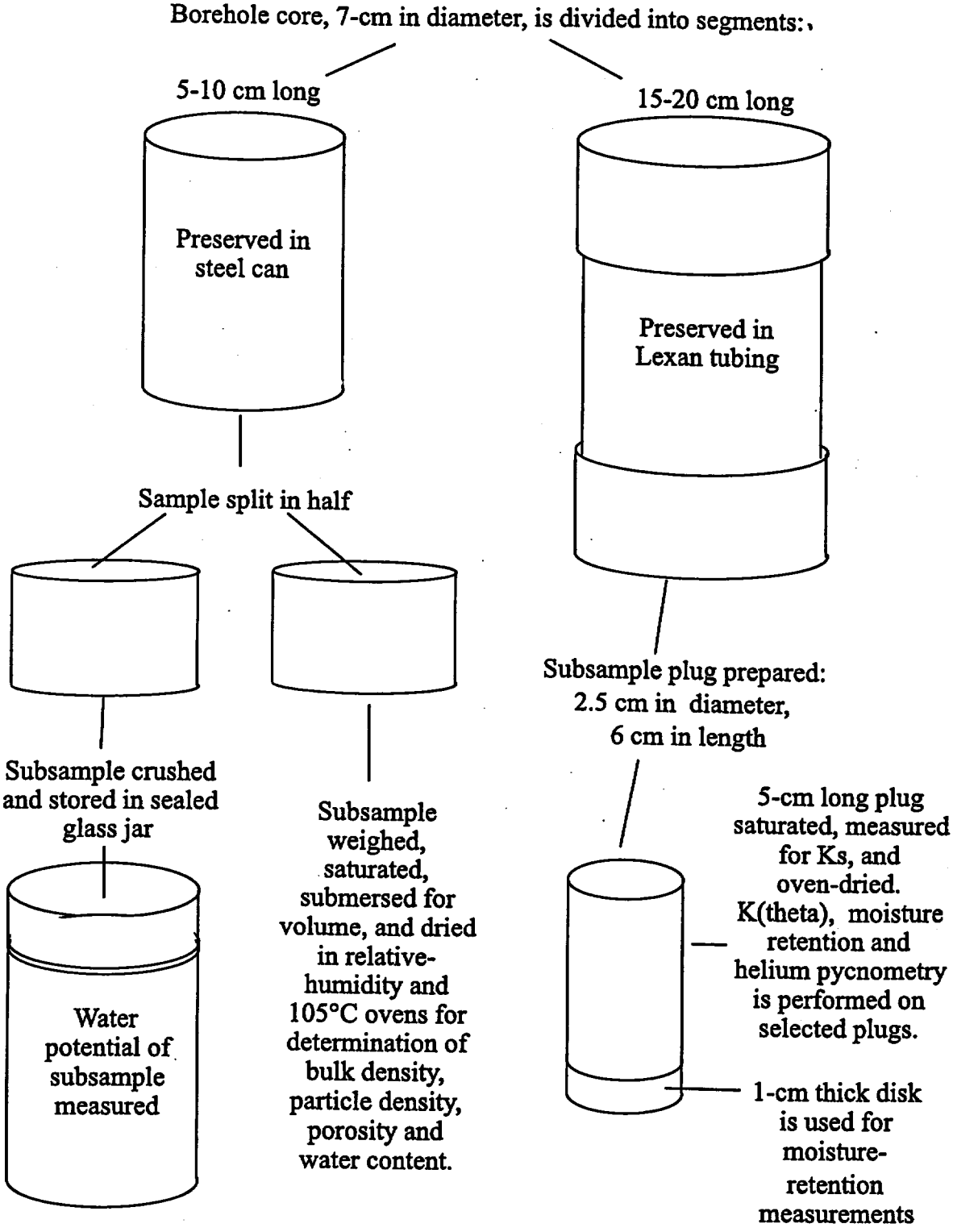

Figure 5.3-13. Diagram of the Steps Used to Process Core Samples in Preparation for Hydrologic-Property Measurements

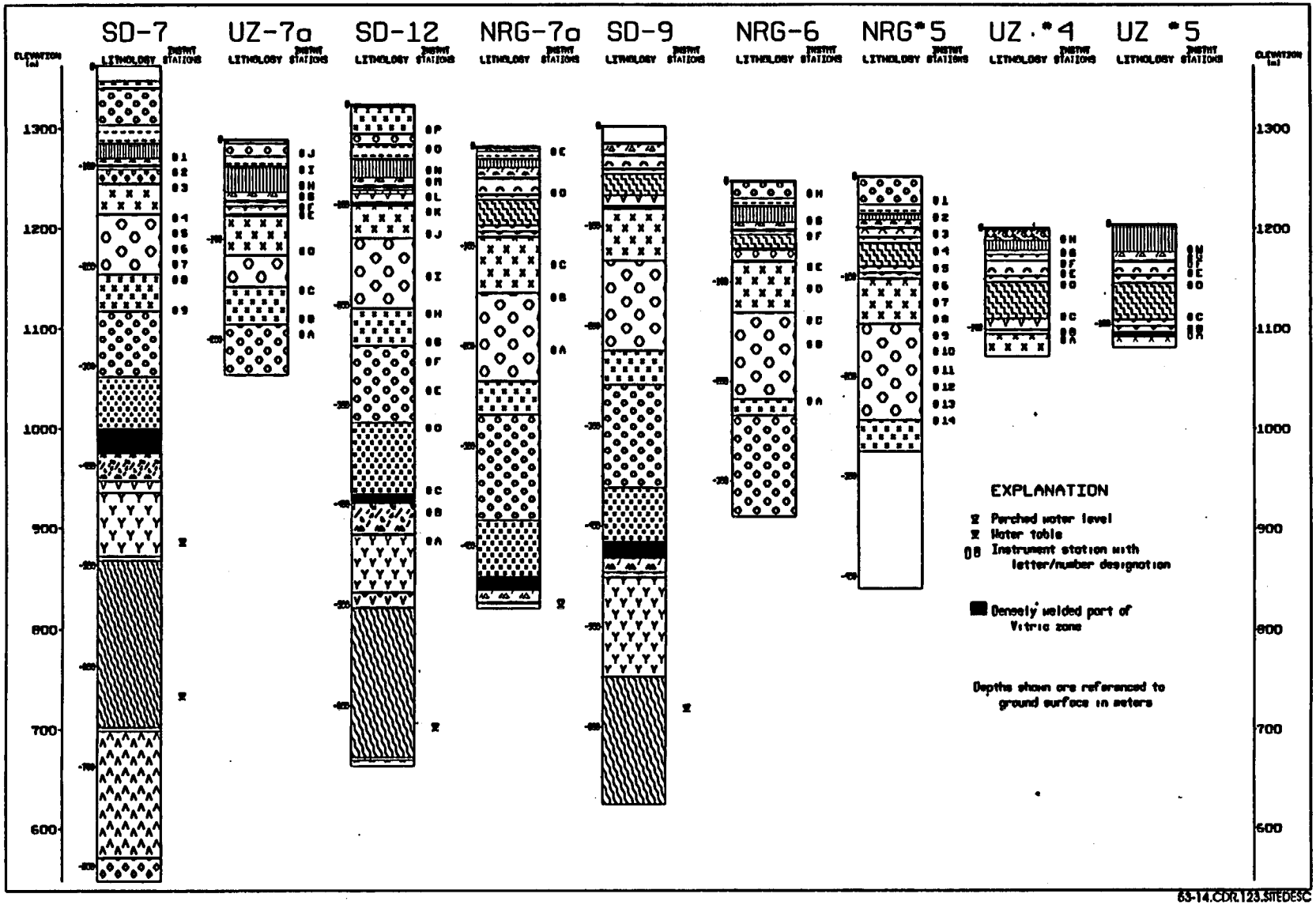

Figure 5.3-14. Location of Instrument Stations and Lithostratigraphy for Instrumented Boreholes

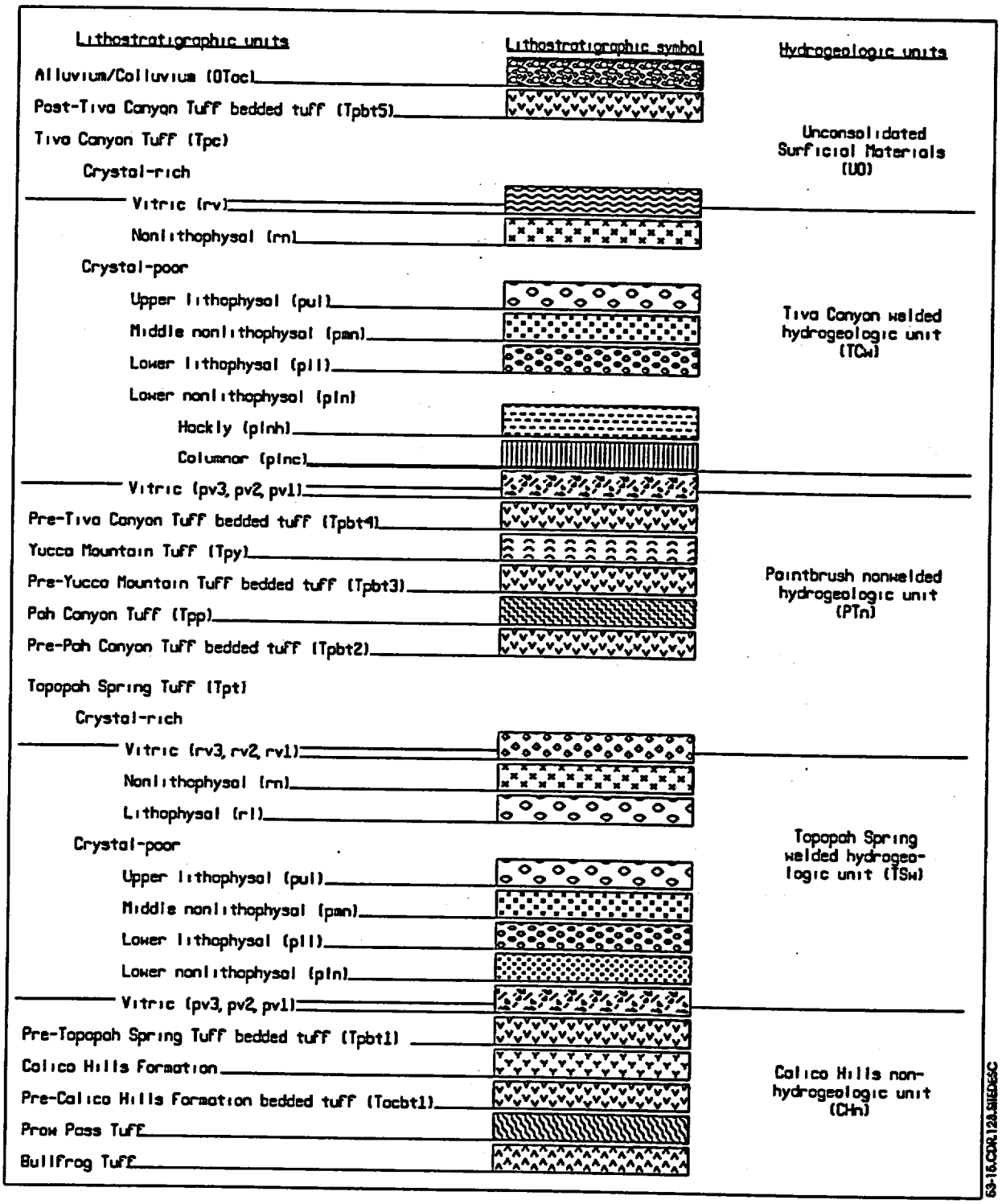

Figure 5.3-15. Lithostratigraphic and Hydrogeologic Units in the Yucca Mountain Area

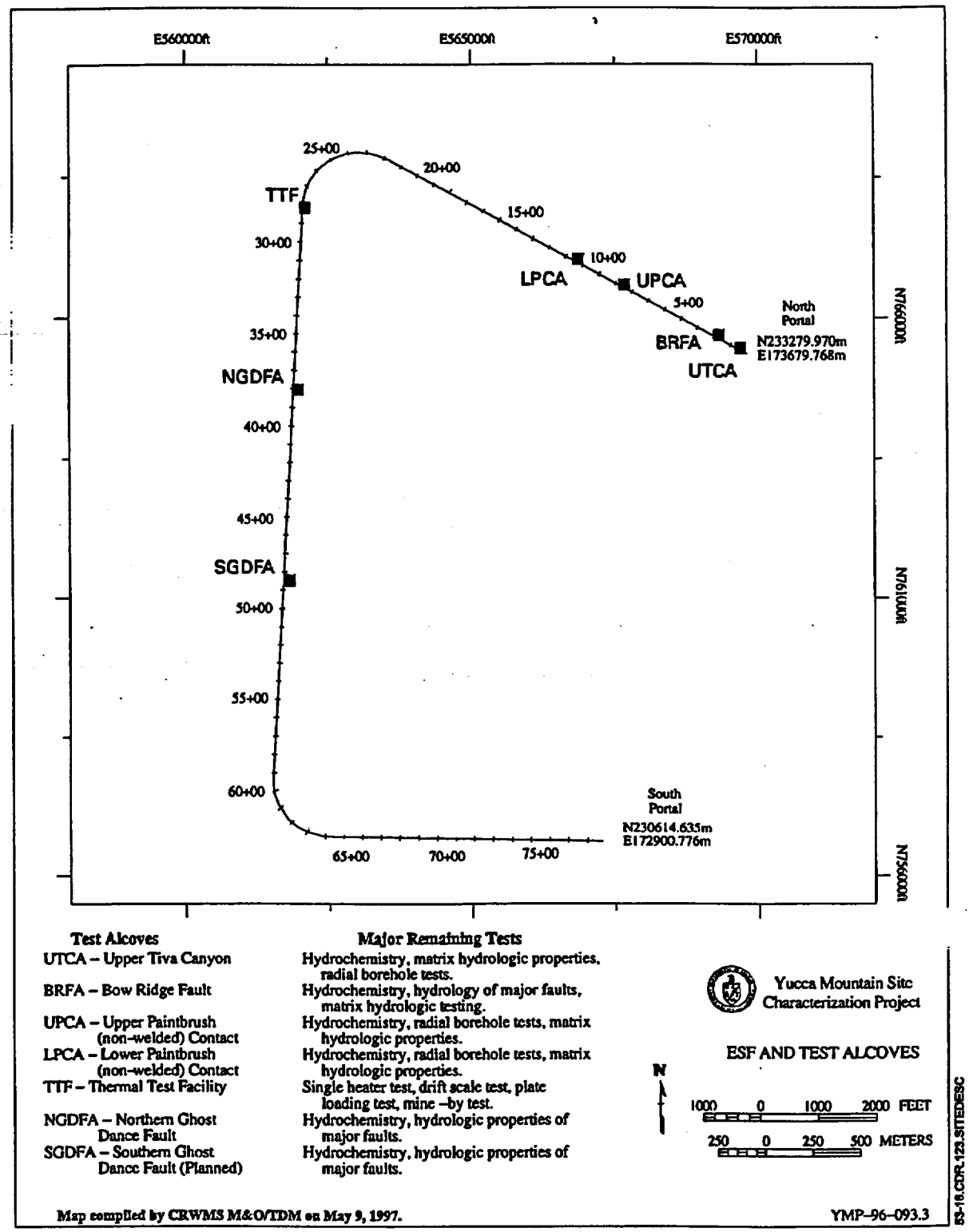

Figure 5.3-16. Map of Exploratory Studies Facility Showing Locations of Test Alcoves and Tests Planned for Each Alcove

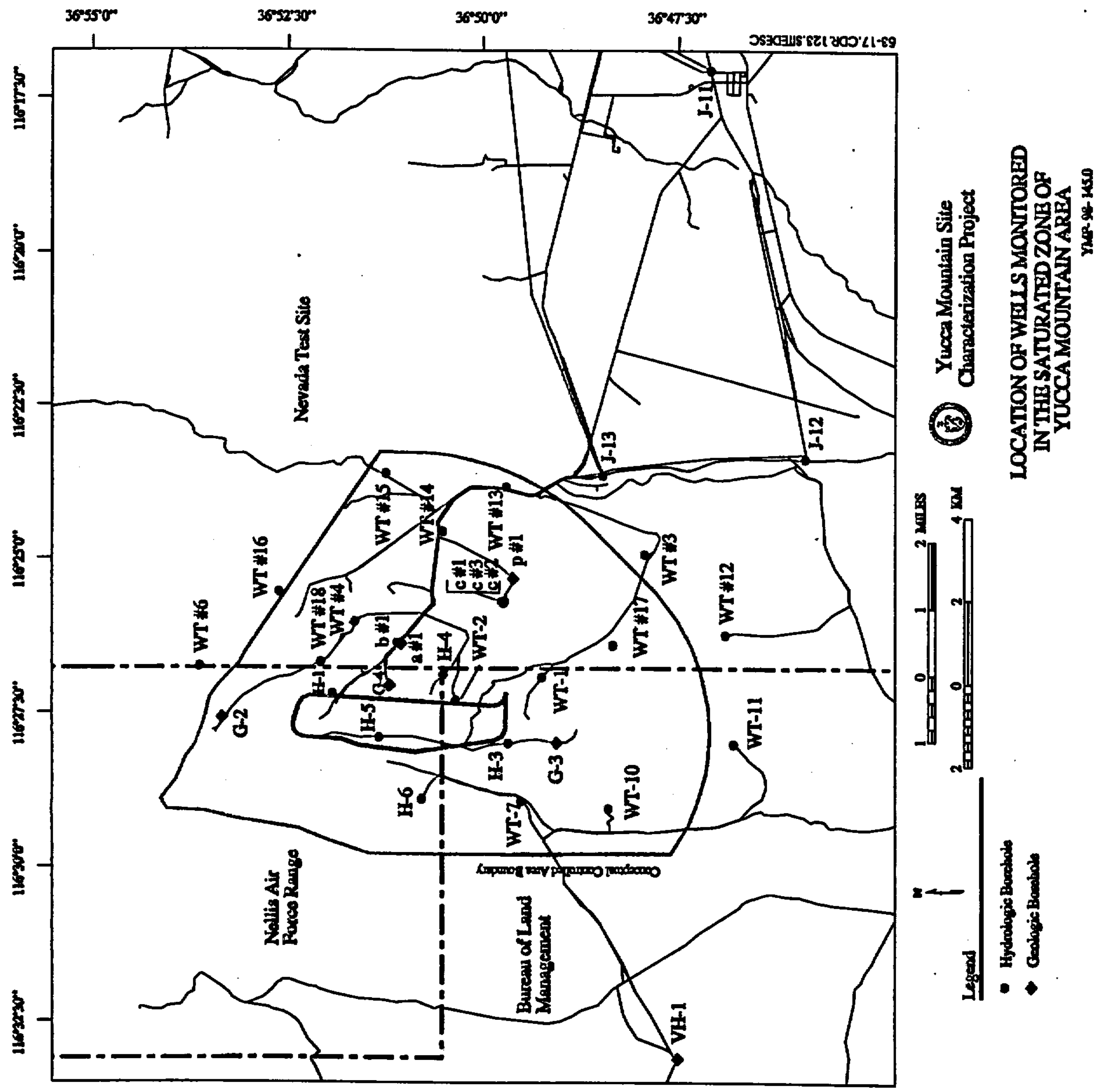

Figure 5.3-17. Location of Wells Monitored in the Saturated Zone in the Yucca Mountain Area

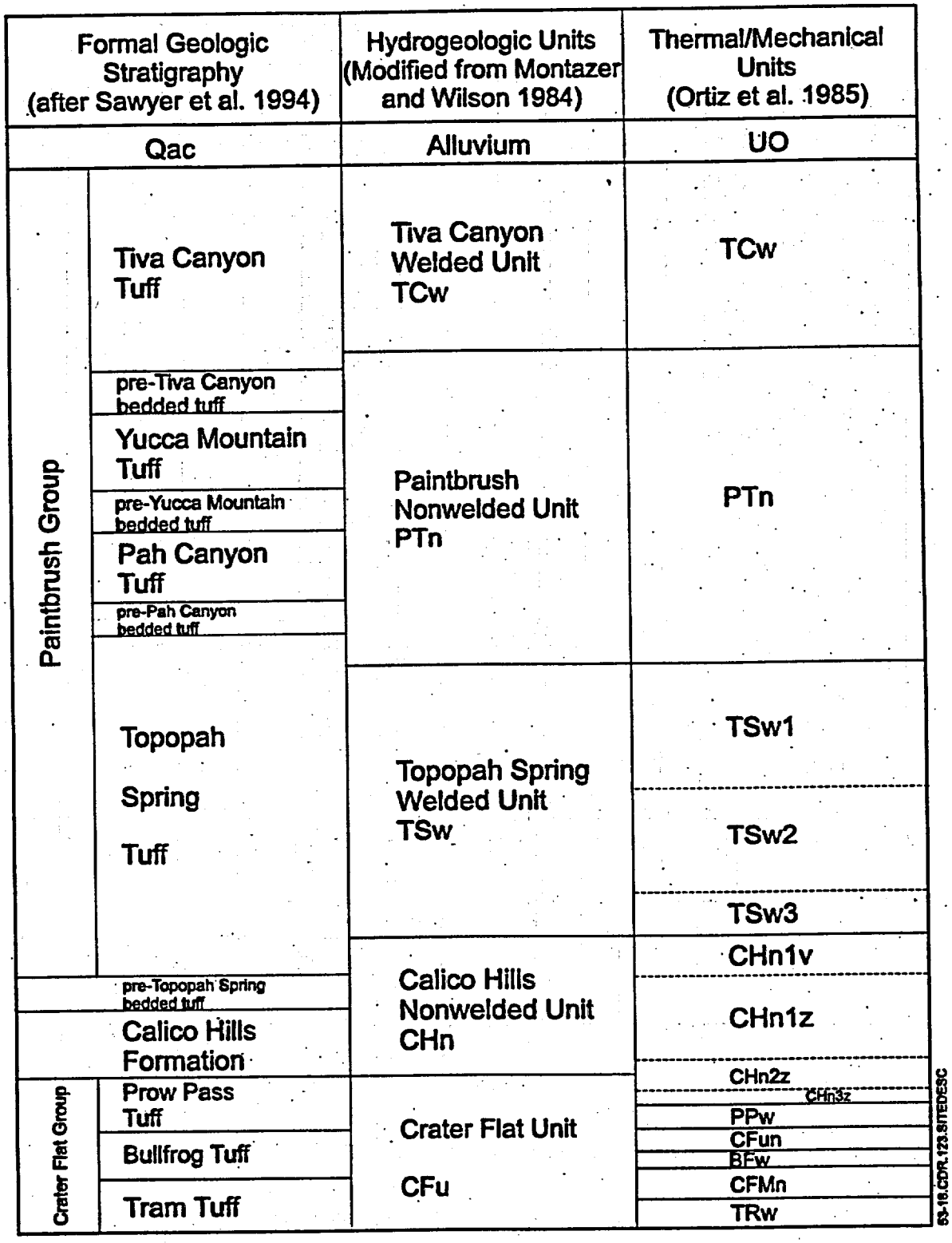

*From Sawyer et al. 1994

Figure 5.3-18. Comparison of Lithostratigraphic, Hydrogeologic, and Thermomechanical Units at Yucca Mountain

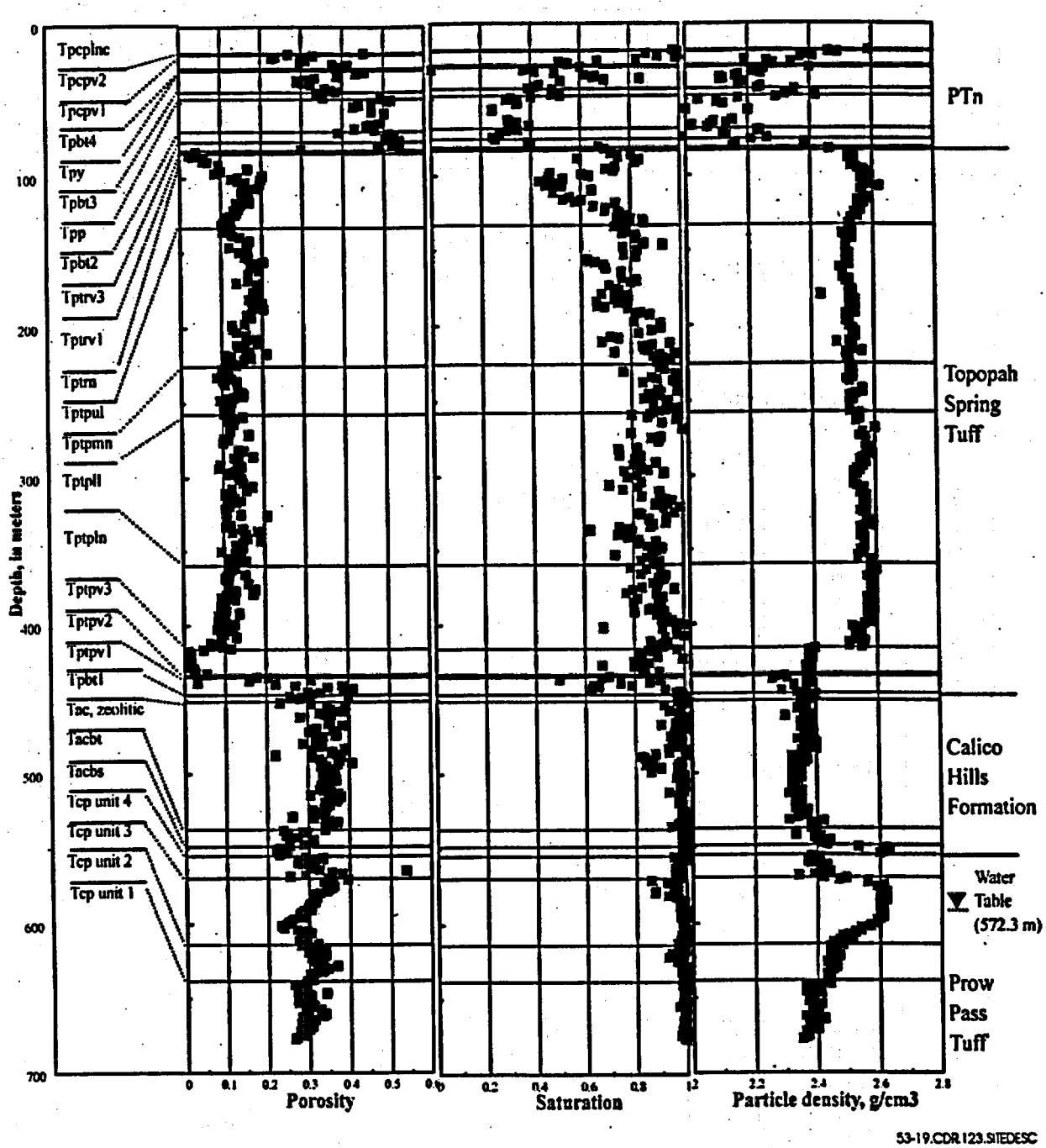

NOTE: Lithostratigraphic-Unit Assignments are from Engstrom and Rautman 1996, and Moyer and Geslin 1995.

Figure 5.3-19. Porosity, Saturation, and Particle Density with Depth for Borehole SD-9

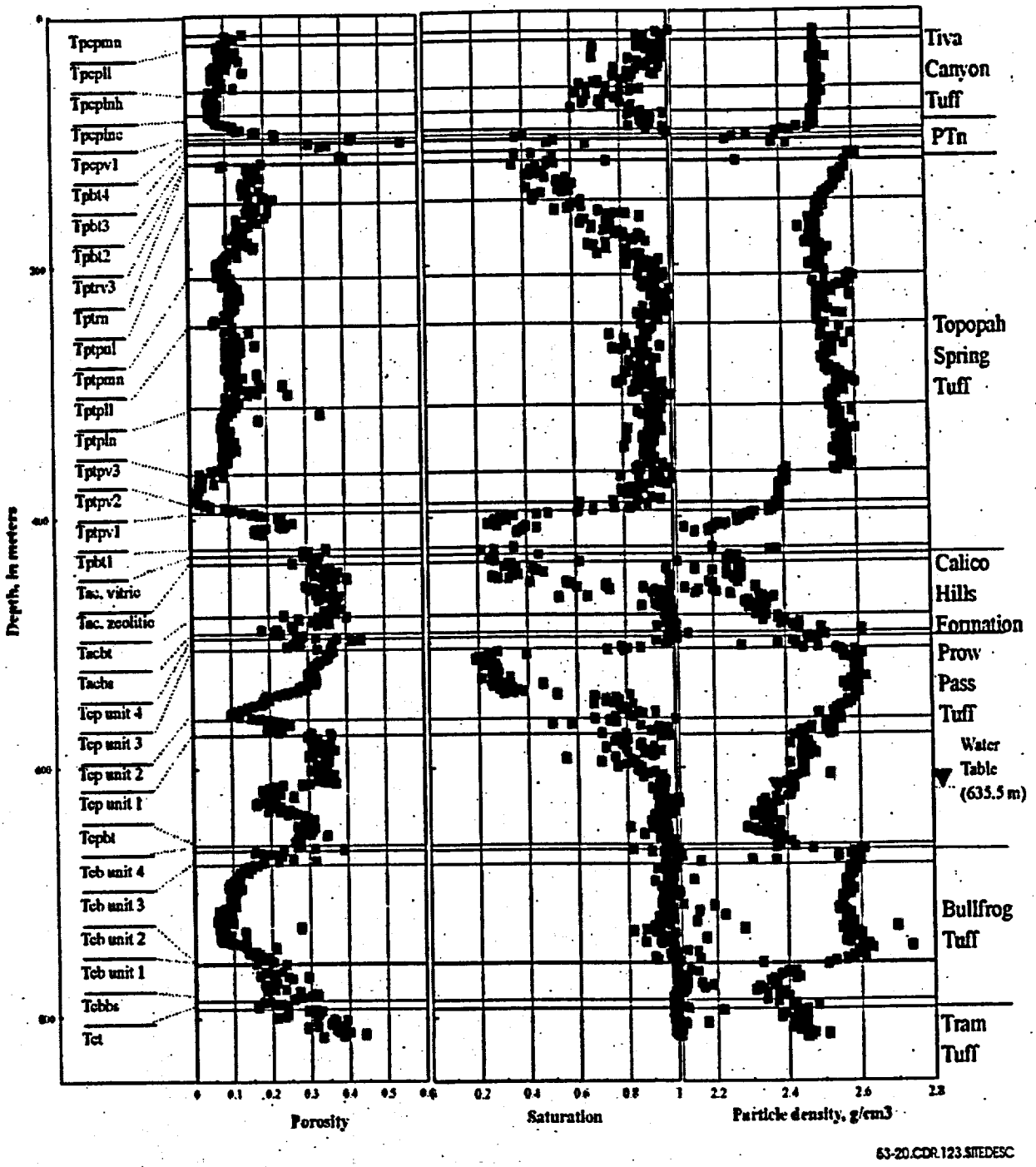

NOTE: Lithostratigraphic-Unit Assignments are from Rautman and Engstrom 1996a

Figure 5.3-20. Porosity, Saturation, and Particle Density with Depth for Borehole SD-7

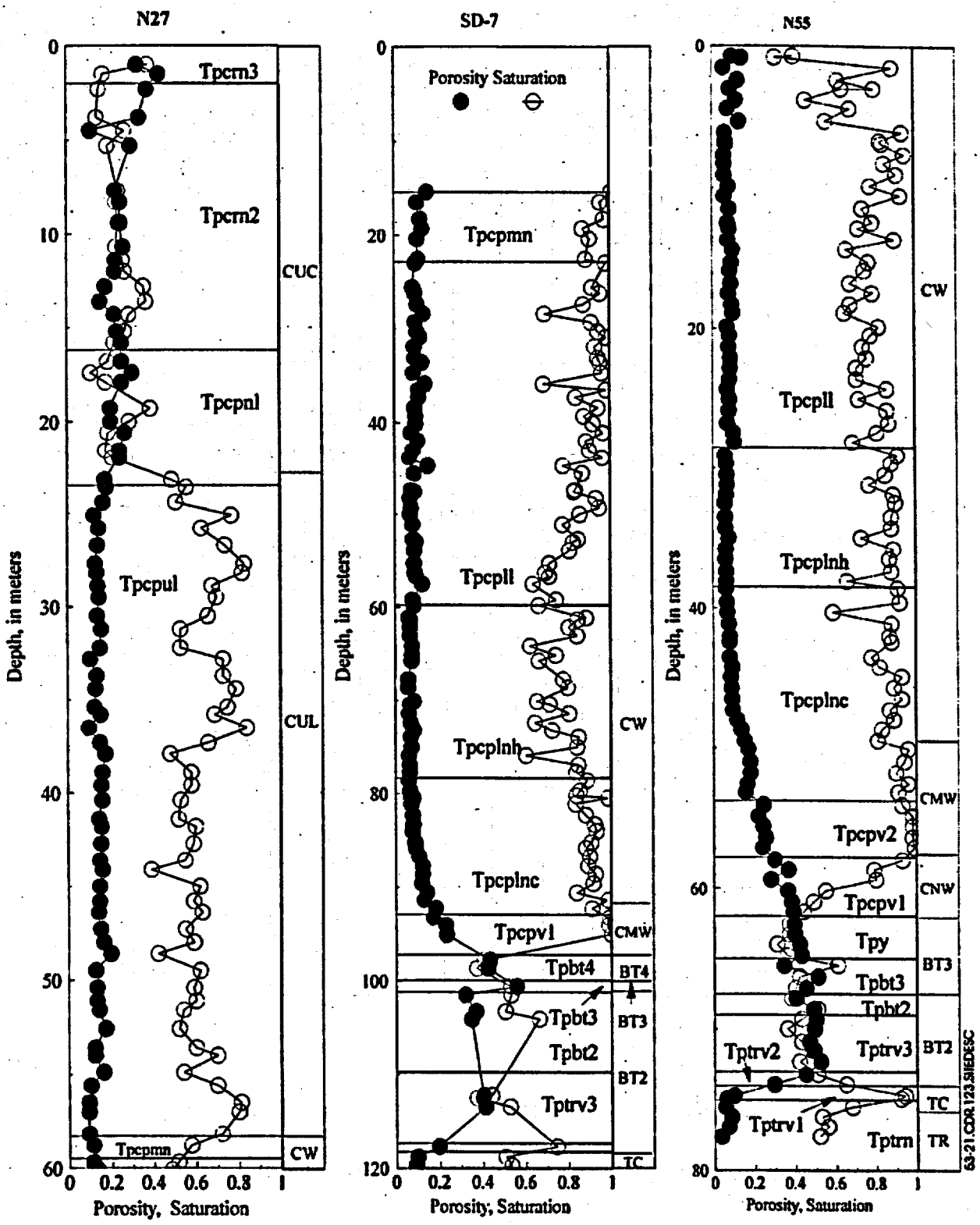

NOTE: Lithostratigraphic-Unit Assignments are from Rautman and Engstrom 1996a, and Moyer et al. 1996.

Figure 5.3-21. Porosity and Saturation with Depth for Boreholes N27, SD-7 and N55 Indicating Properties of the Tiva Canyon Tuff and PTn

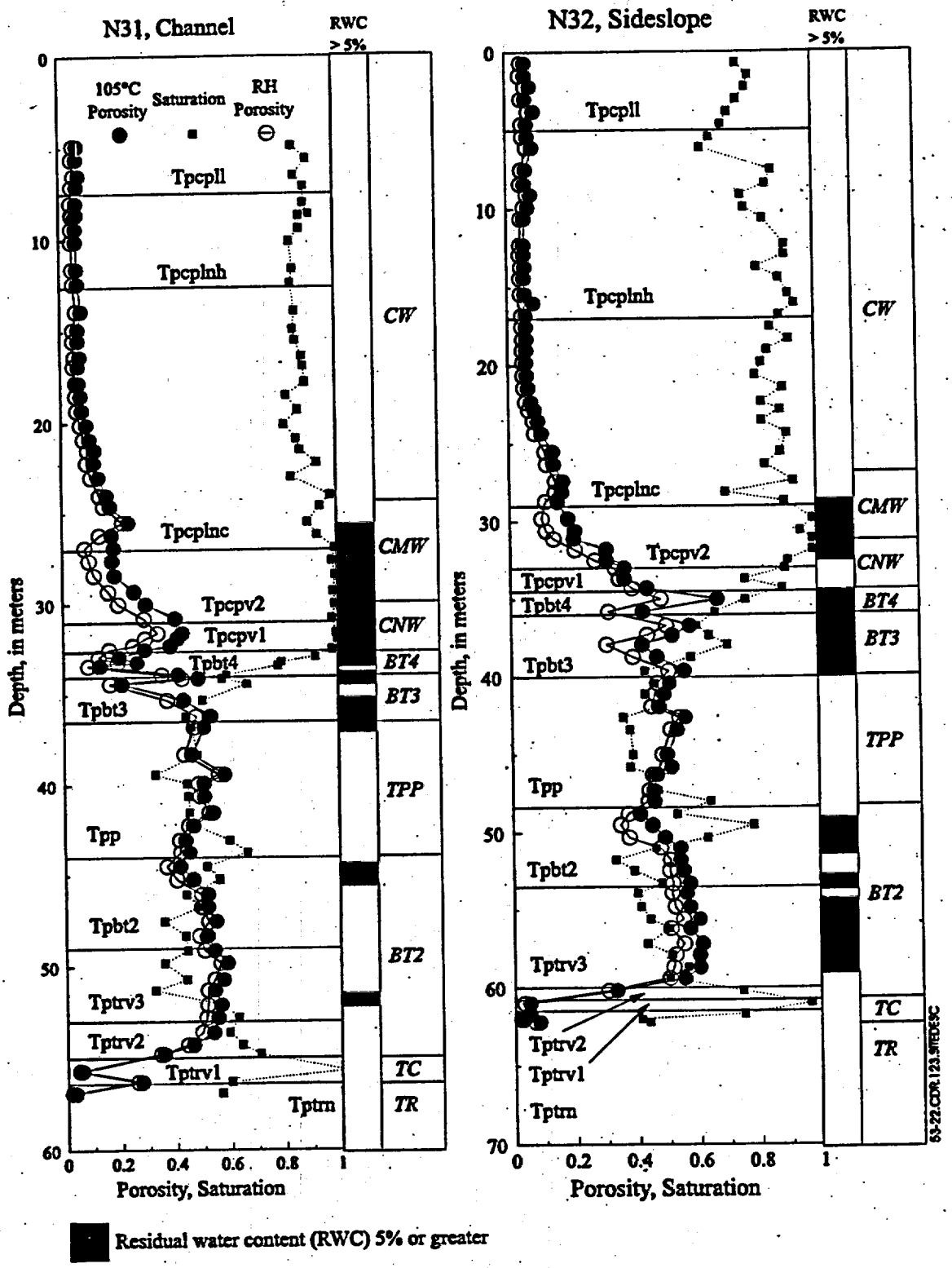

NOTE: Lithostratigraphic-Unit Assignments are from Moyer et al. 1996.

Figure 5.3-22. Porosity Calculated from Relative Humidity and 105°C Oven Drying, Saturation, and 5 Percent and Greater Residual Water Content of Samples for Boreholes N31 and N32

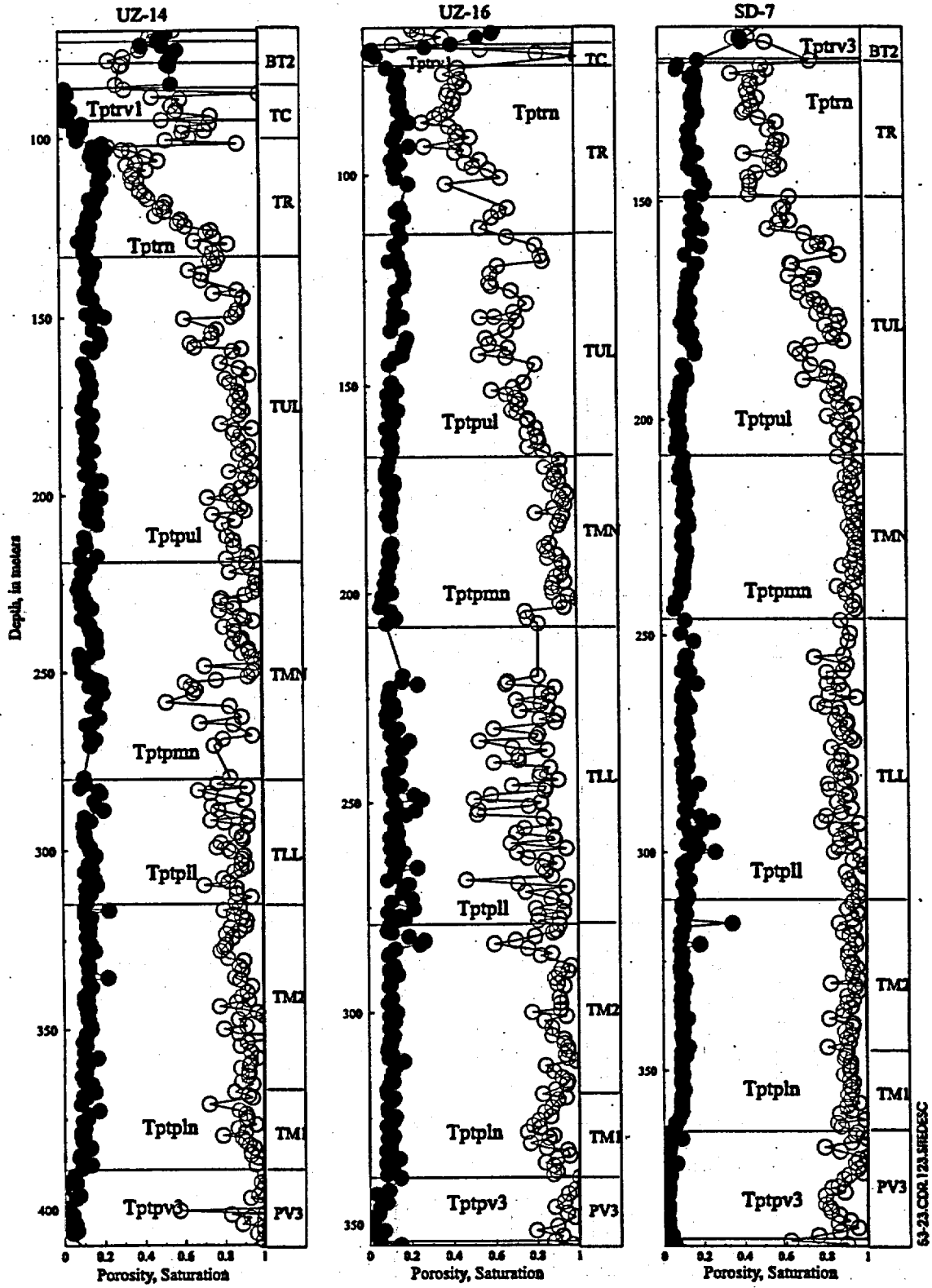

NOTE: Lithostratigraphic-Unit Assignments are from Rautman and Engstrom 1996a, and Moyer et al. 1996.

Figure 5.3-23. Porosity and Saturation with Depth for Boreholes UZ-14, UZ-16, and SD-7 Indicating Properties of the Topopah Spring Tuff

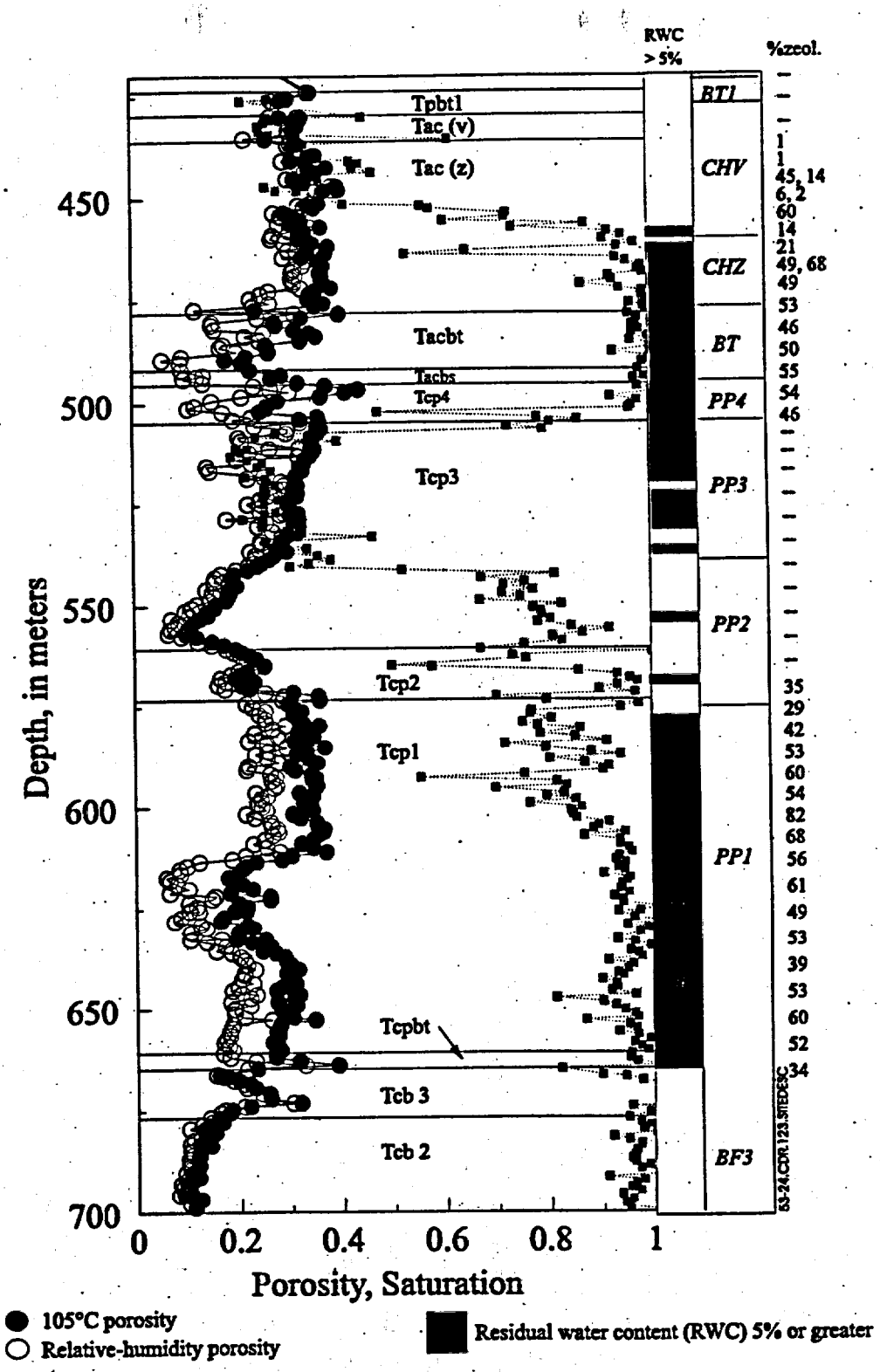

NOTE: Lithostratigraphic-Unit Assignments are from Rautman and Engstrom 1996a.

Figure 5.3-24. Porosity Calculated from Relative Humidity and 105°C Oven Drying, Saturation, and 5 Percent and Greater Residual Water Content of Samples of Rocks below the Basal Vitrophyre of the Topopah Spring Tuff in Borehole SD-7

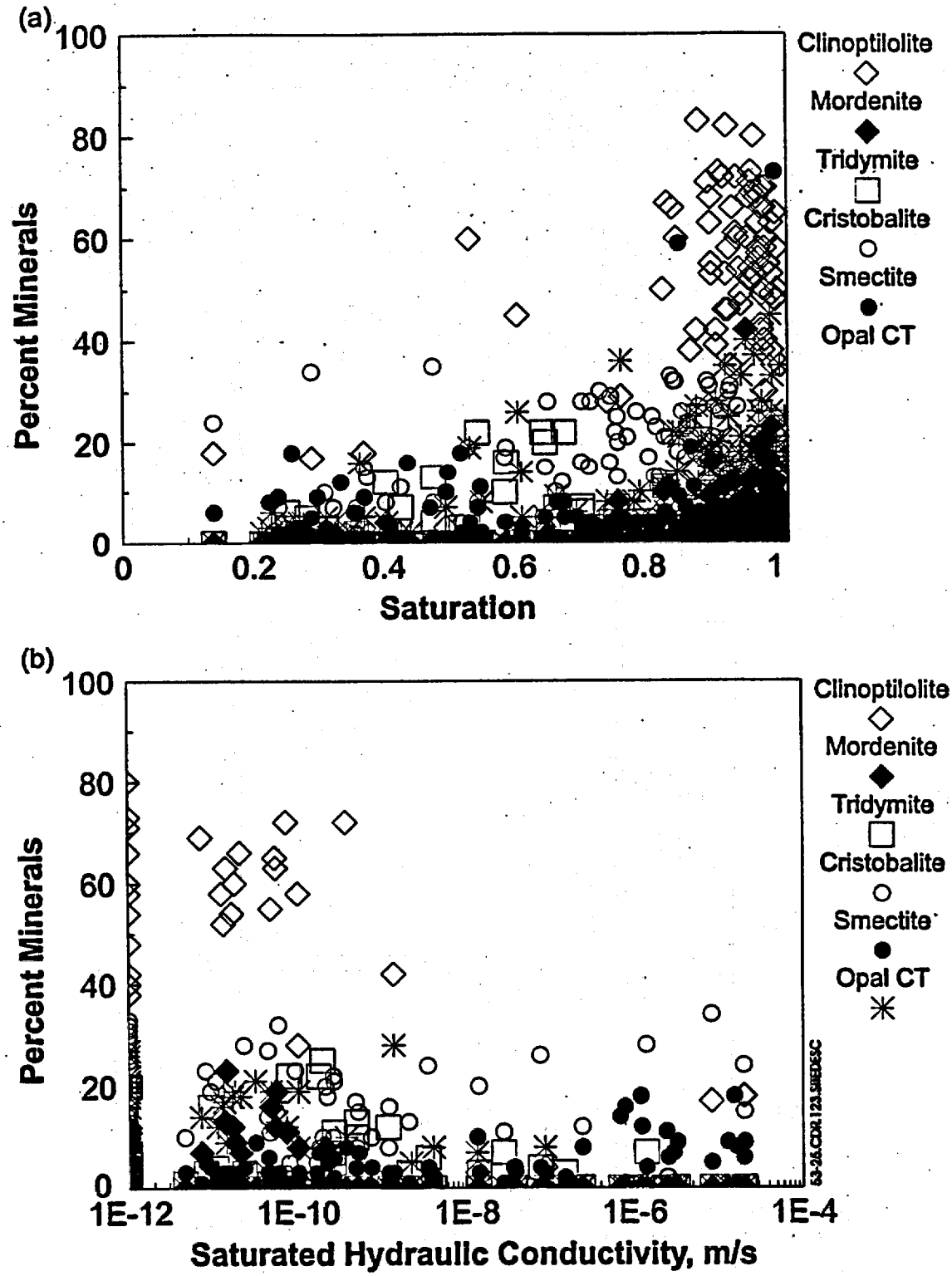

Figure 5.3-25. Relation Between Mineral Content for Six Minerals and (a) Degree of Saturation and (b) Saturated Hydraulic Conductivity

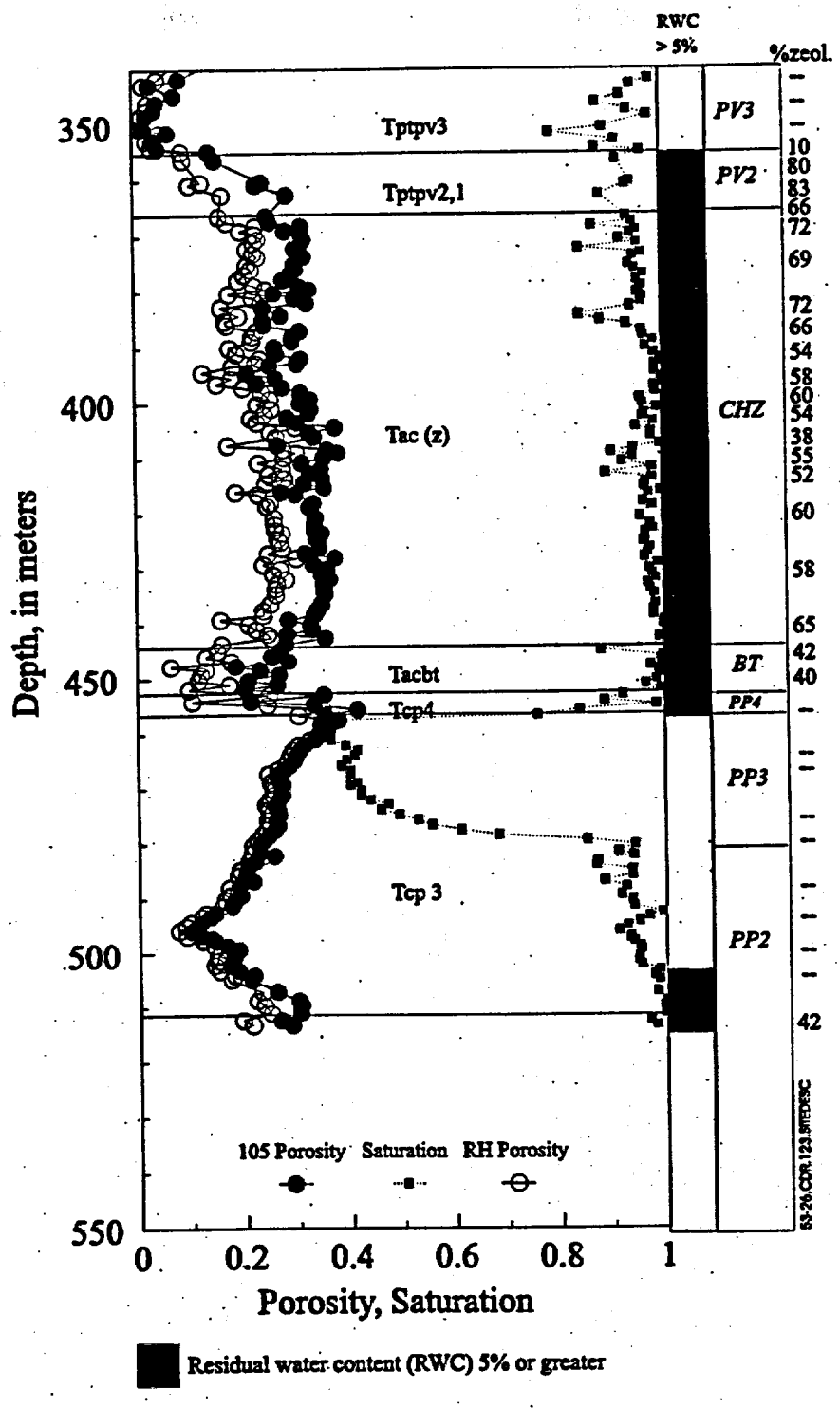

NOTE: Lithostratigraphic-Unit Assignments are from Moyer et al. 1996.

Figure 5.3-26. Porosity Calculated from Relative Humidity and 105°C Oven Drying, Saturation, and 5 Percent and Greater Residual Water Content of Samples of Rocks below the Basal Vitrophyre of the Topopah Spring Tuff in Borehole UZ-16

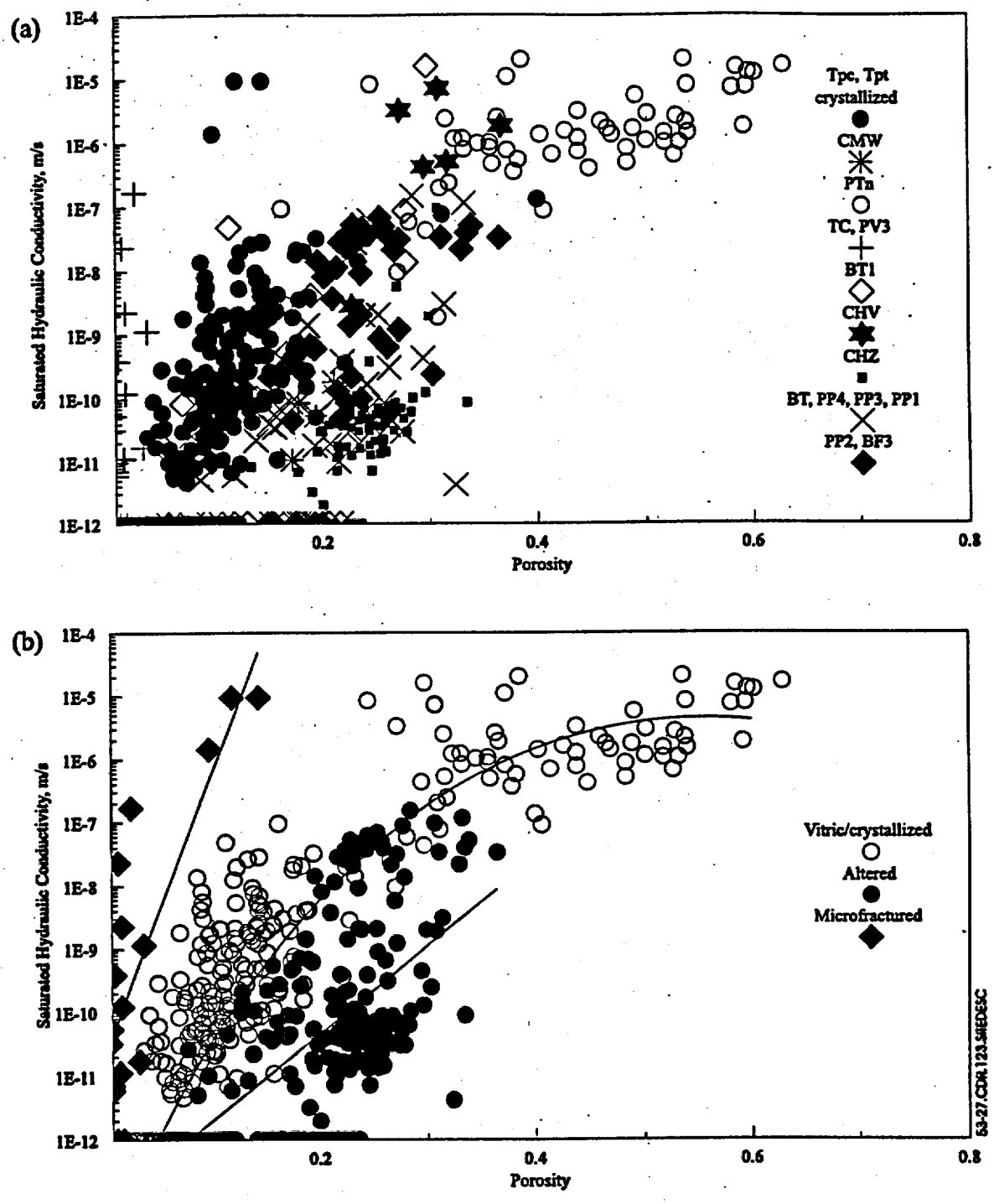

NOTE: Values of 1 x 10^{-12} M/S are samples that had conductivities too low to measure.

Figure 5.3-27. Relationship Between Porosity and Saturated Hydraulic Conductivity for Samples Grouped by (a) Various Hydrogeologic Units and (b) Vitric/Crystallized, Altered and Microfractured Units

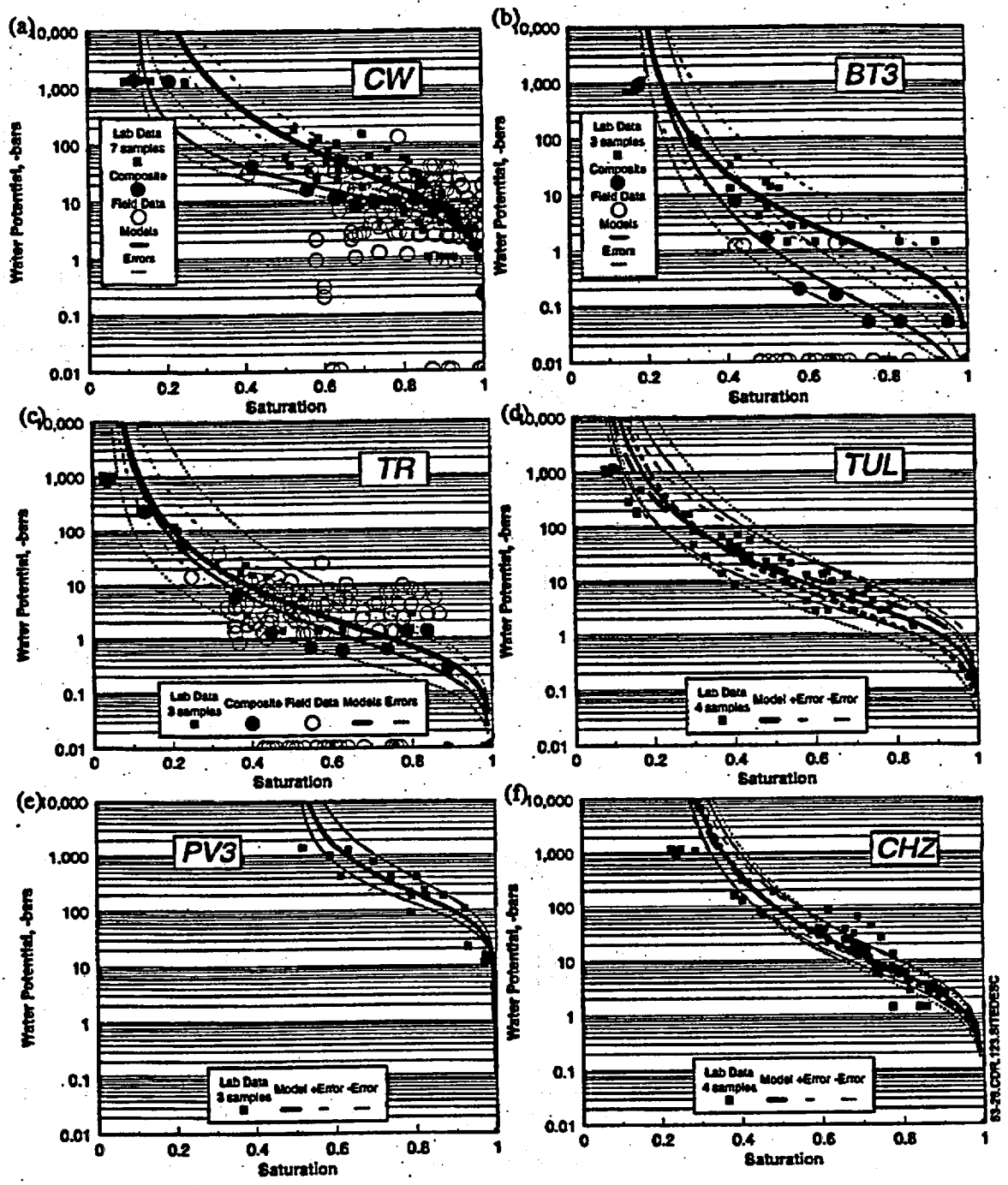

NOTE: Data sets all units include laboratory measurements of core whereas data sets for units CW, BT3 and TR also include field measurements

Figure 5.3-28. Moisture Retention Curves for Core Samples from Hydrogeologic Units (a) CW, (b) BT3, (c) TR, (d) TUL, (e) PV3, and f) CHz

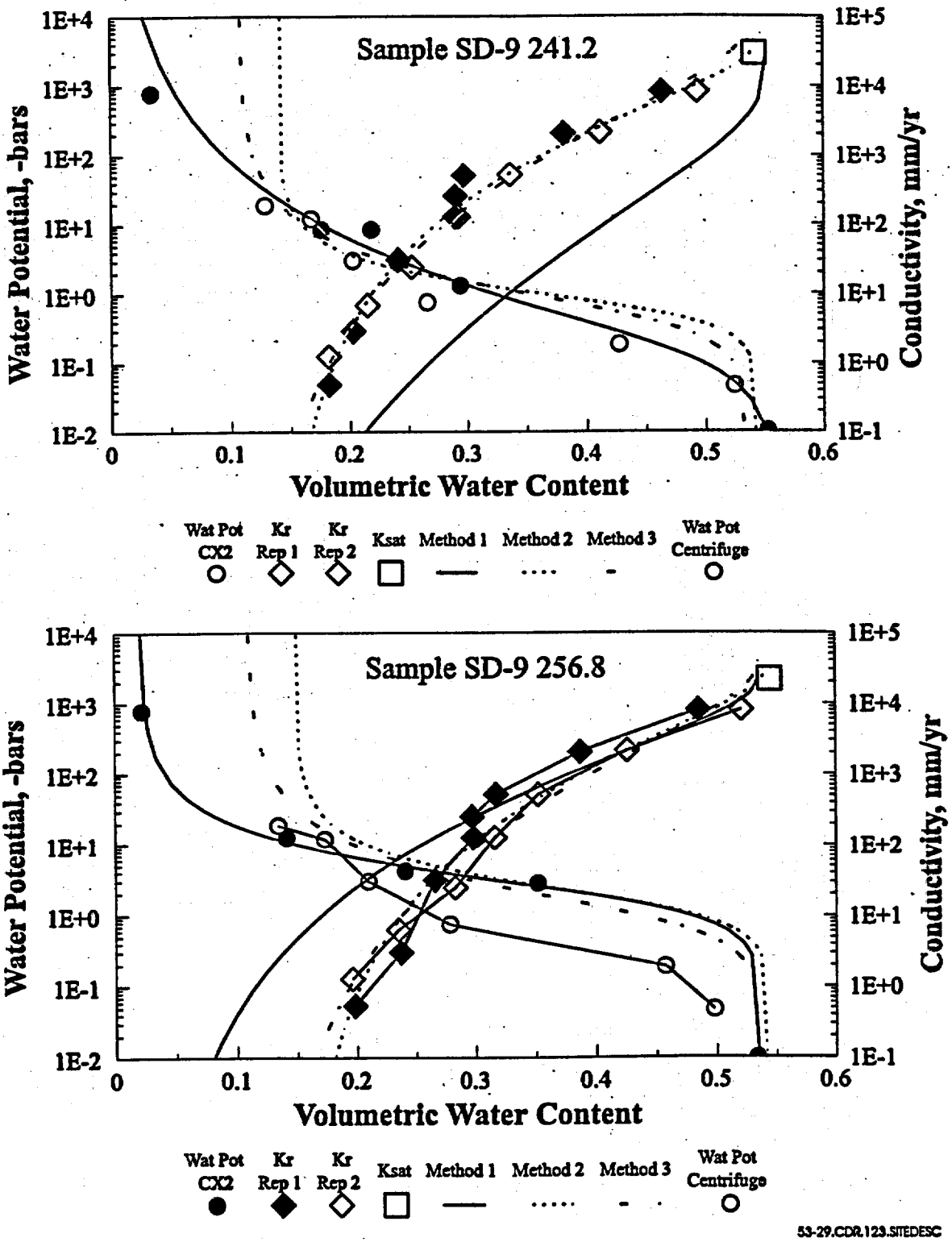

Figure 5.3-29. Unsaturated Hydraulic Conductivity, Moisture Retention Measurements, and Modeled Estimates for Two Samples from Tpbt2

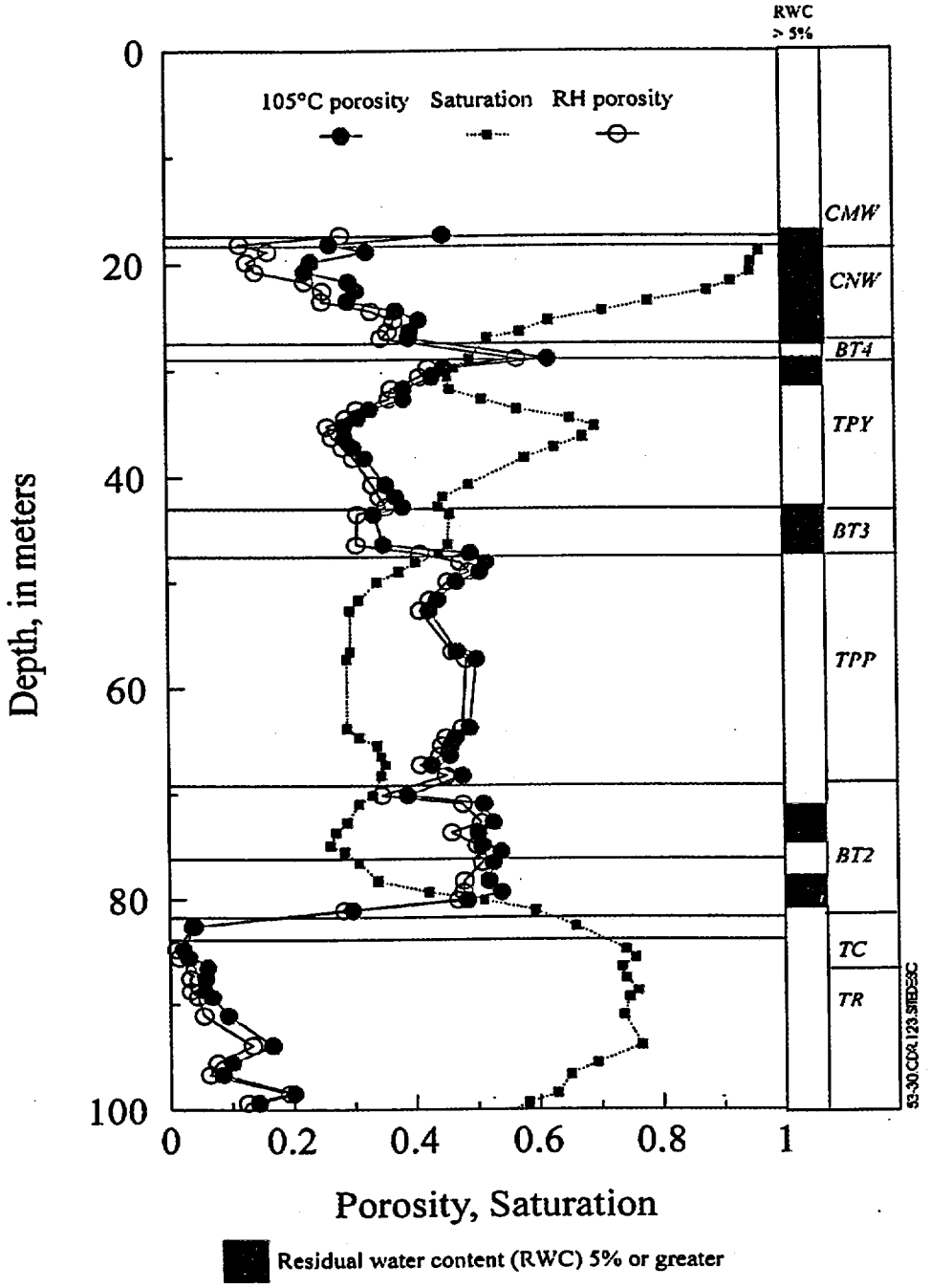

NOTE: Lithostratigraphic-Unit Assignments are from Engstrom and Rautman 1996

Figure 5.3-30. Porosity Calculated from Relative Humidity and 105°C Drying, Saturation, and 5 Percent and Greater Residual Water Content of Samples from Borehole SD-9

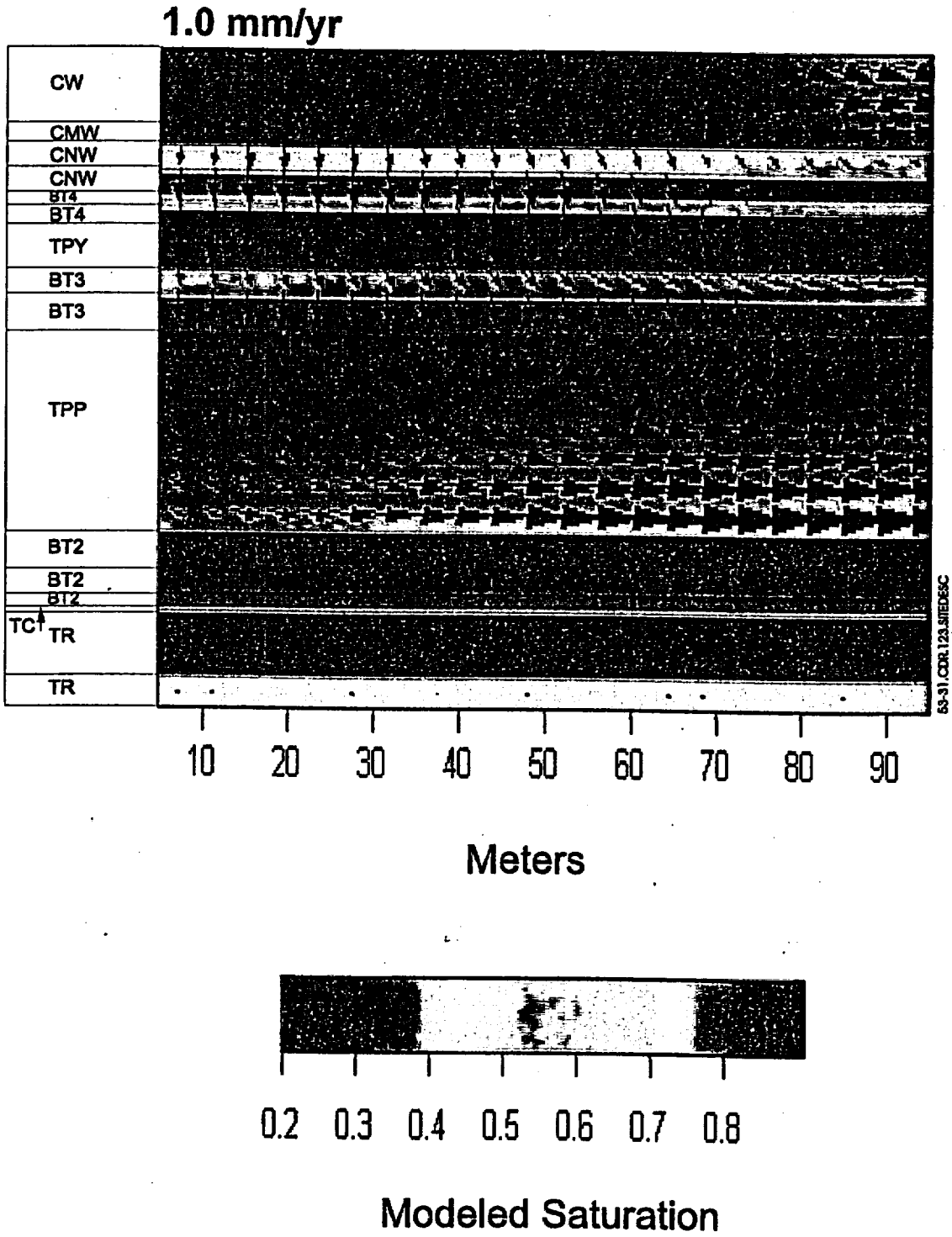

Figure 5.3-31. Simulated Saturation and Flow Direction for Model Layers with Properties of the PTn

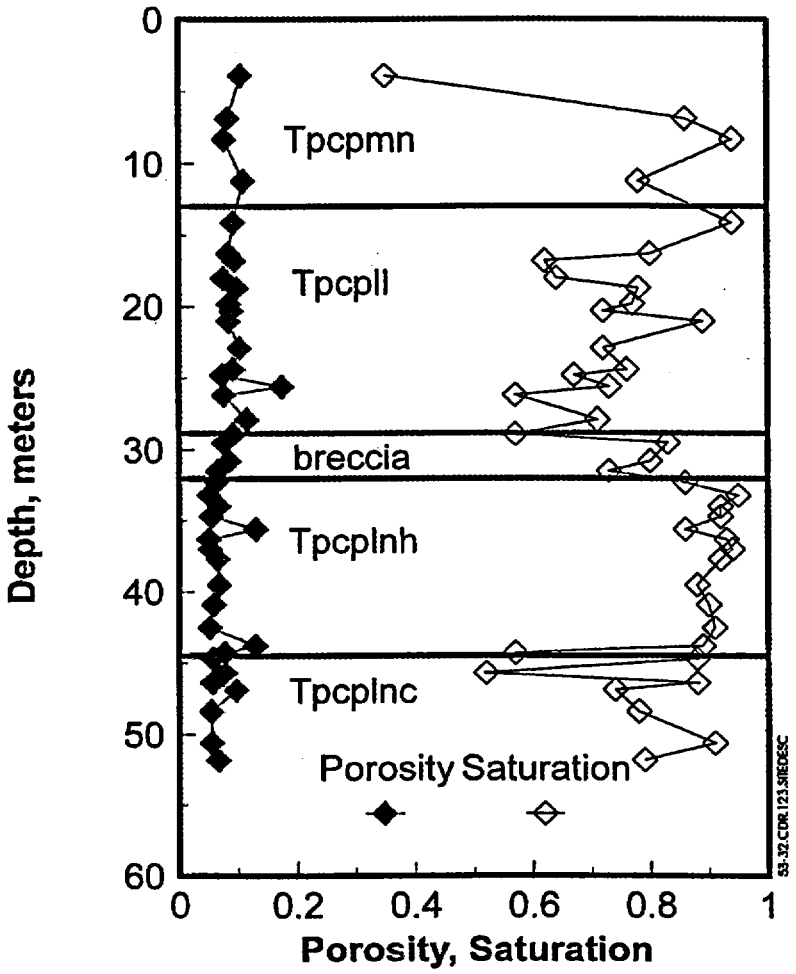

NOTE: Lithostratigraphic-Unit Assignments are from Moyer et al. 1996.

Figure 5.3-32. Porosity and Saturation for Borehole N35, Which Penetrates the Brecciated Zone of the Ghost Dance Fault

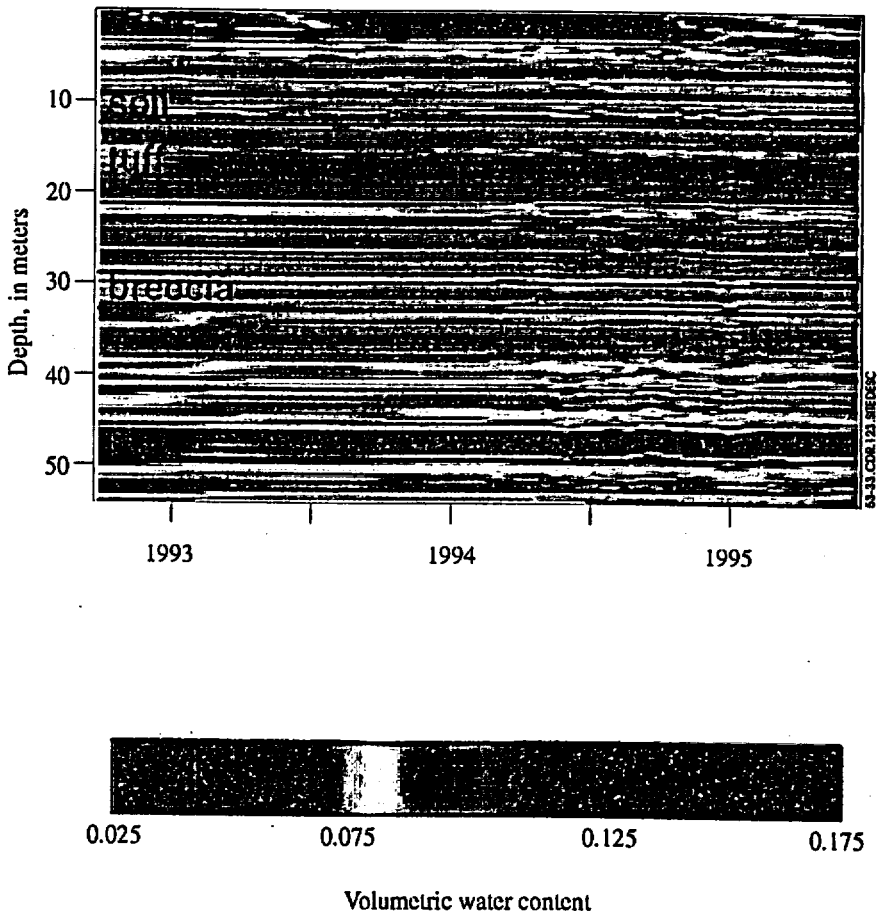

Figure 5.3-33. Volumetric-Water-Content Changes with Time and Depth for Borehole N35 Located Within the Ghost Dance Fault Zone

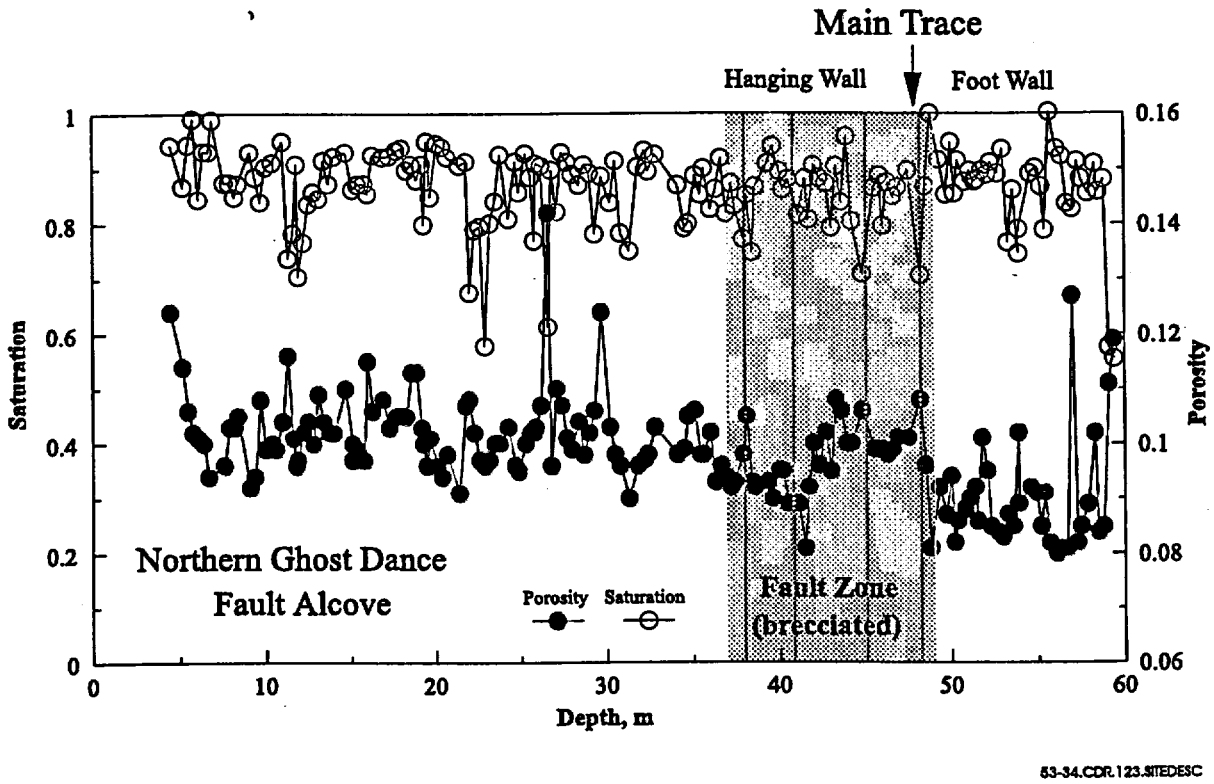

Figure 5.3-34. Porosity and Saturation for Borehole ESF-NAD-GTB#1A in the Exploratory Studies Facility Northern Ghost Dance Fault Alcove

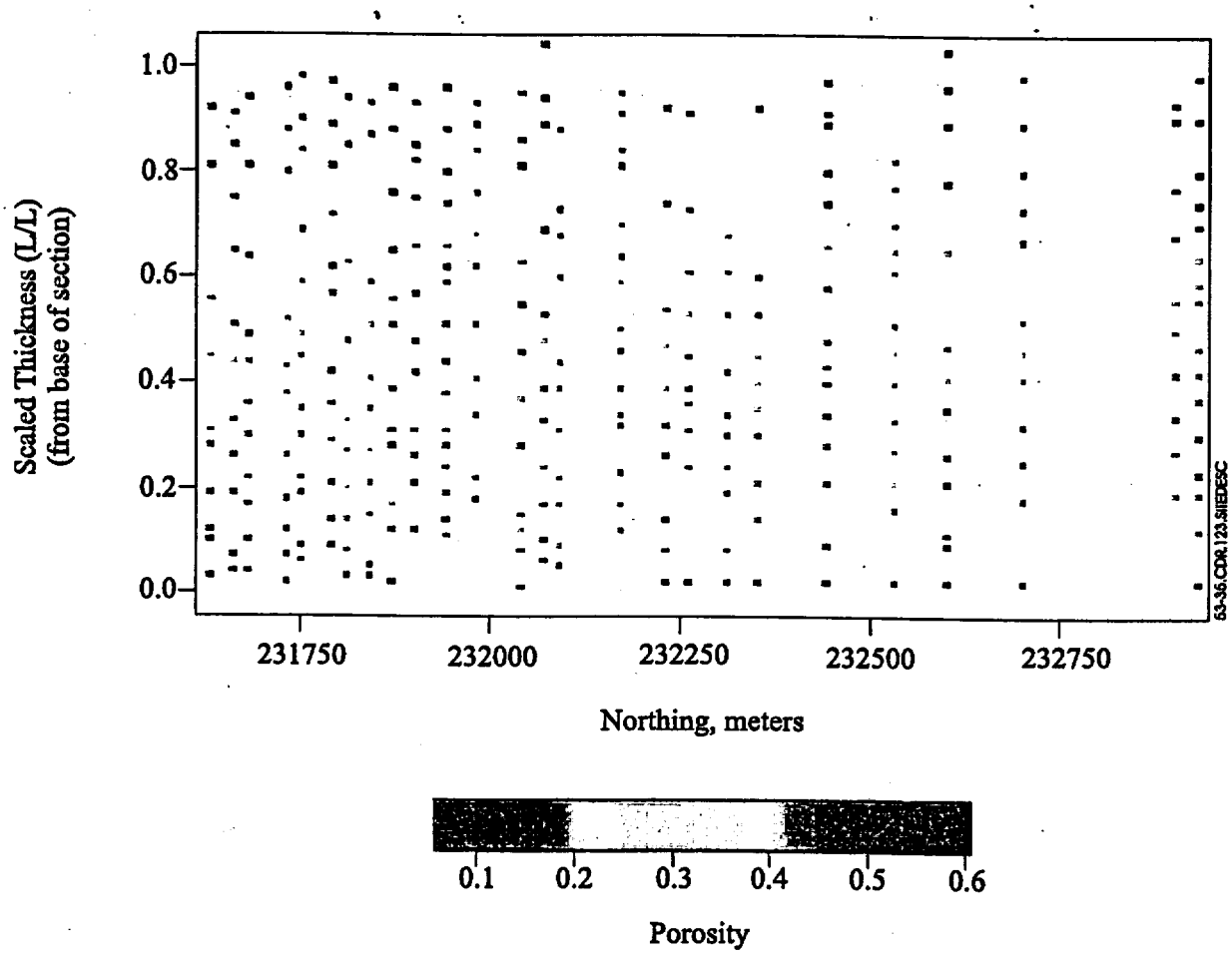

Figure 5.3-35. Porosity of Samples Collected from 26 Vertical Transects along the Solitario Canyon Exposure of the Base of the Tiva Canyon Tuff

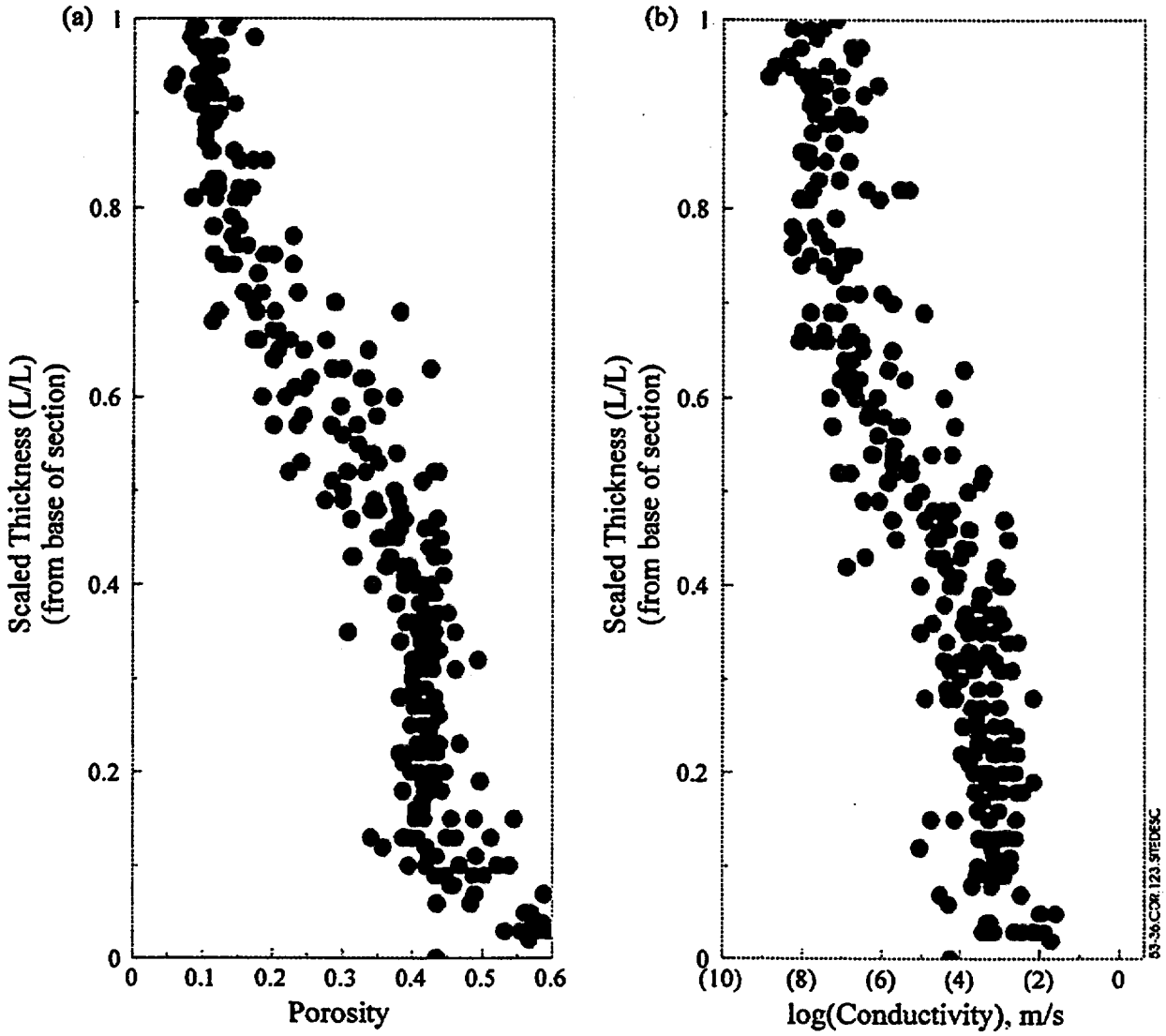

Figure 5.3-36. Porosity and Log of Saturated Hydraulic Conductivity of All Samples from 26 Vertical Transects of the Base of the Tiva Canyon Tuff

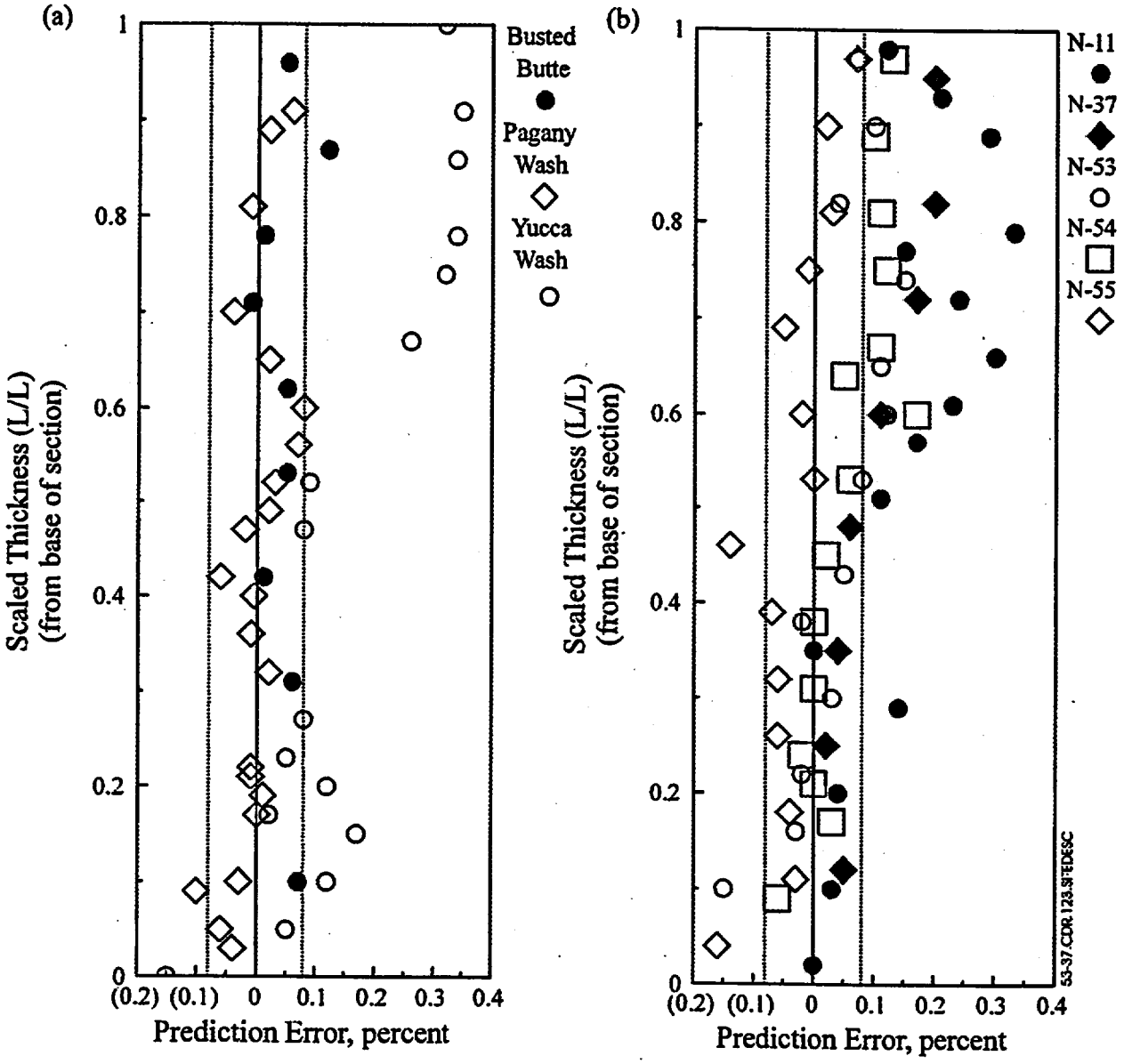

NOTE: Dashed vertical lines give approximate 95 percent confidence levels for fitted model.

Figure 5.3-37. Validation of Vertical Trend Model Developed in Solitario Canyon with Measured Values of Porosity for (a) Outcrop Sampling Transects and (b) Boreholes

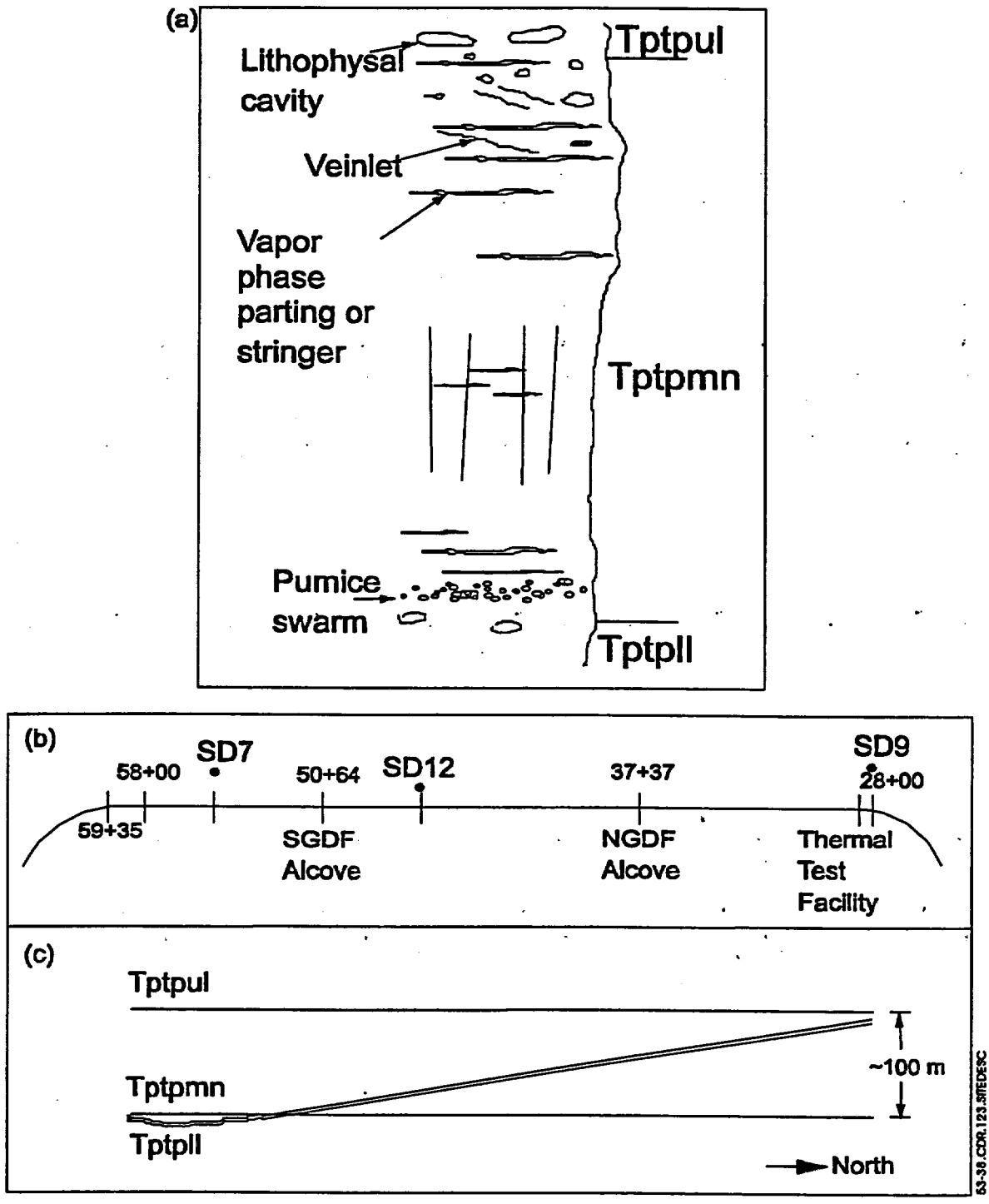

Figure 5.3-38. Schematic Diagram of (a) Vertical Section of Unit Tptpmn, (b) Plan View of the Exploratory Studies Facility Main Drift, and (c) Cross-Section of Unit Tptpmn Showing Route of the Exploratory Studies Facility Main Drift

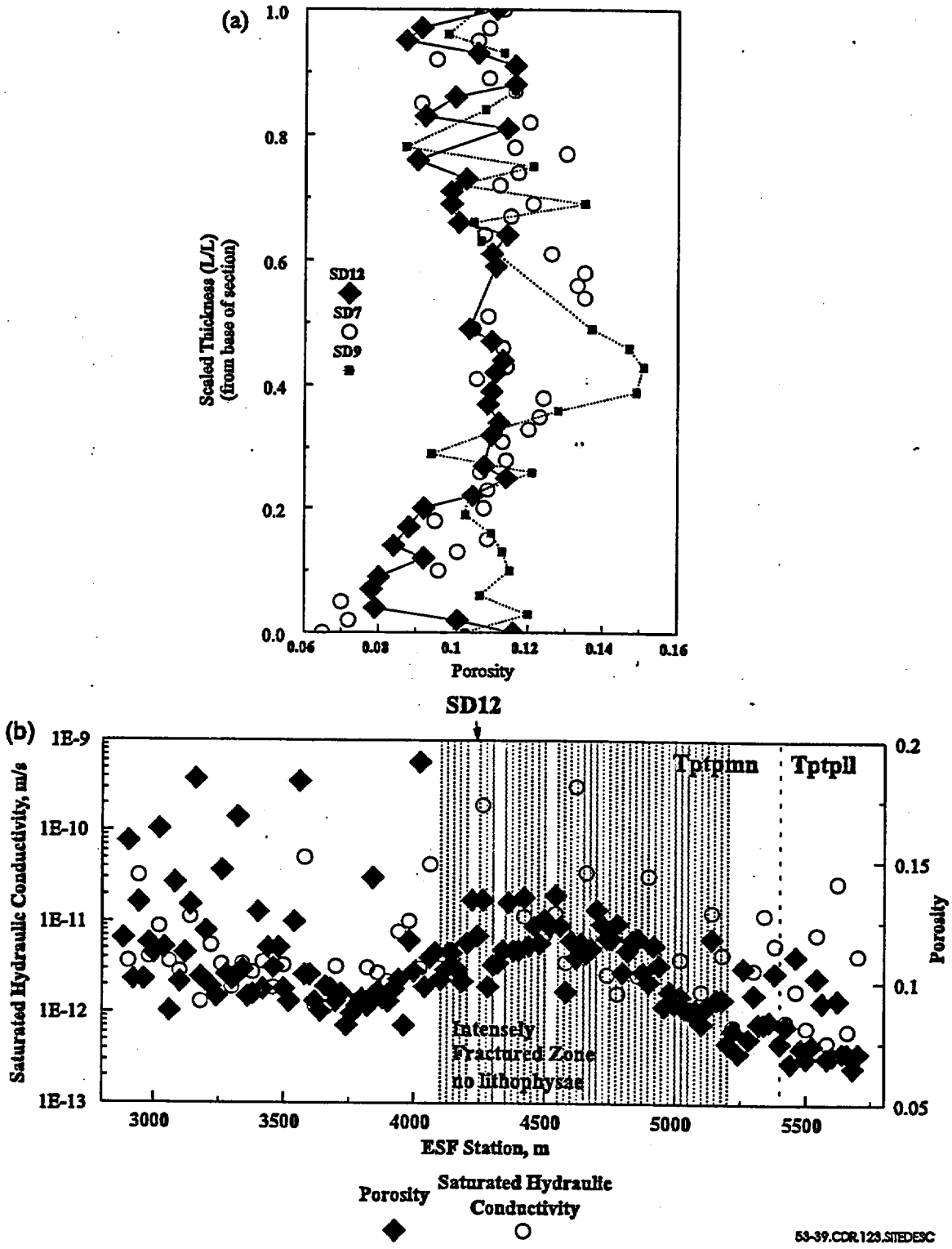

Figure 5.3-39. (a) Porosity Calculated from Relative-Humidity Drying of Samples from Three Surface-Based Boreholes, and (b) Porosity and Saturated Hydraulic Conductivity Measured Along the Systematic-Sampling Transect in the Exploratory Studies Facility Main Drift

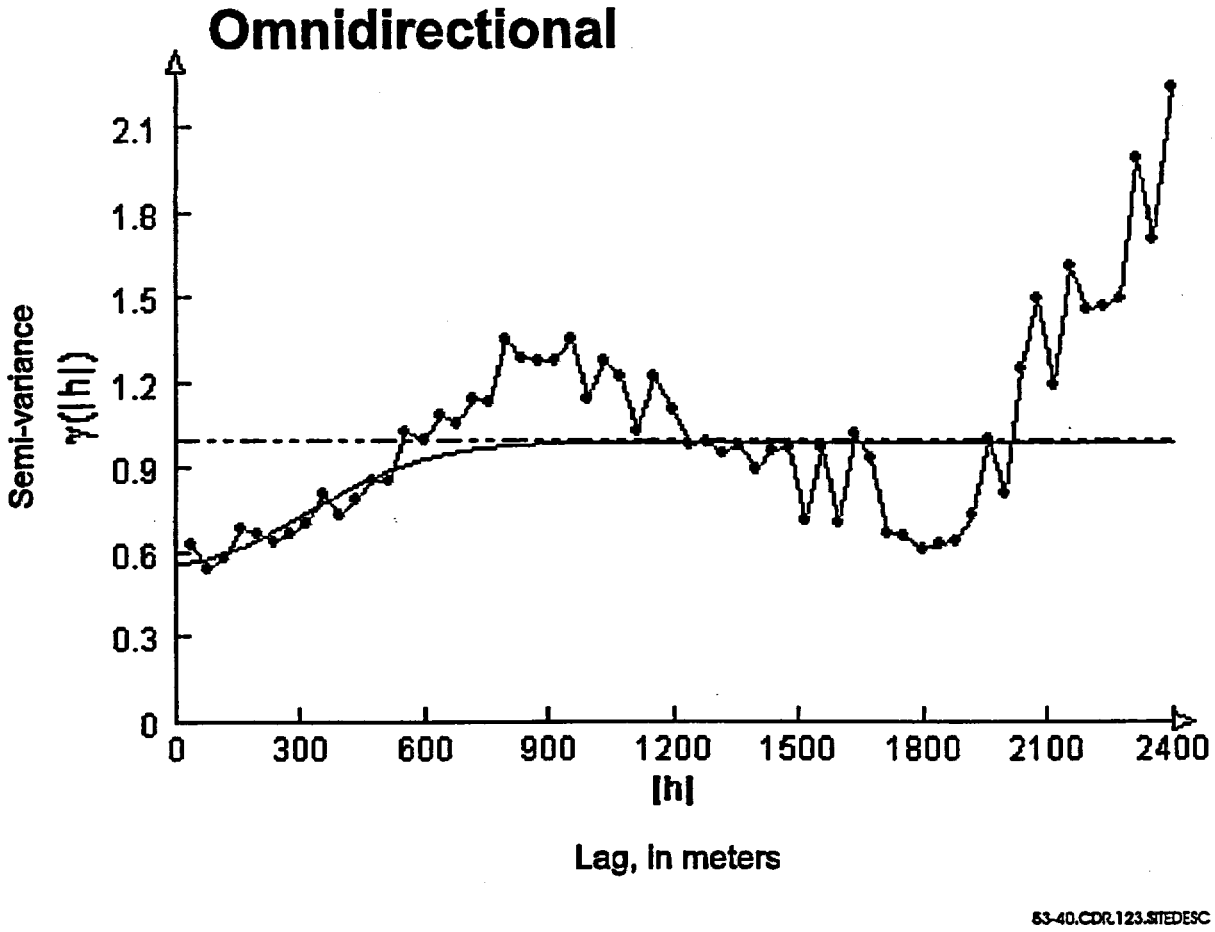

Figure 5.3-40. Semivariogram of Porosity Determined Along Systematic-Sampling Transect of the Tptpmn in the Exploratory Studies Facility Main Drift

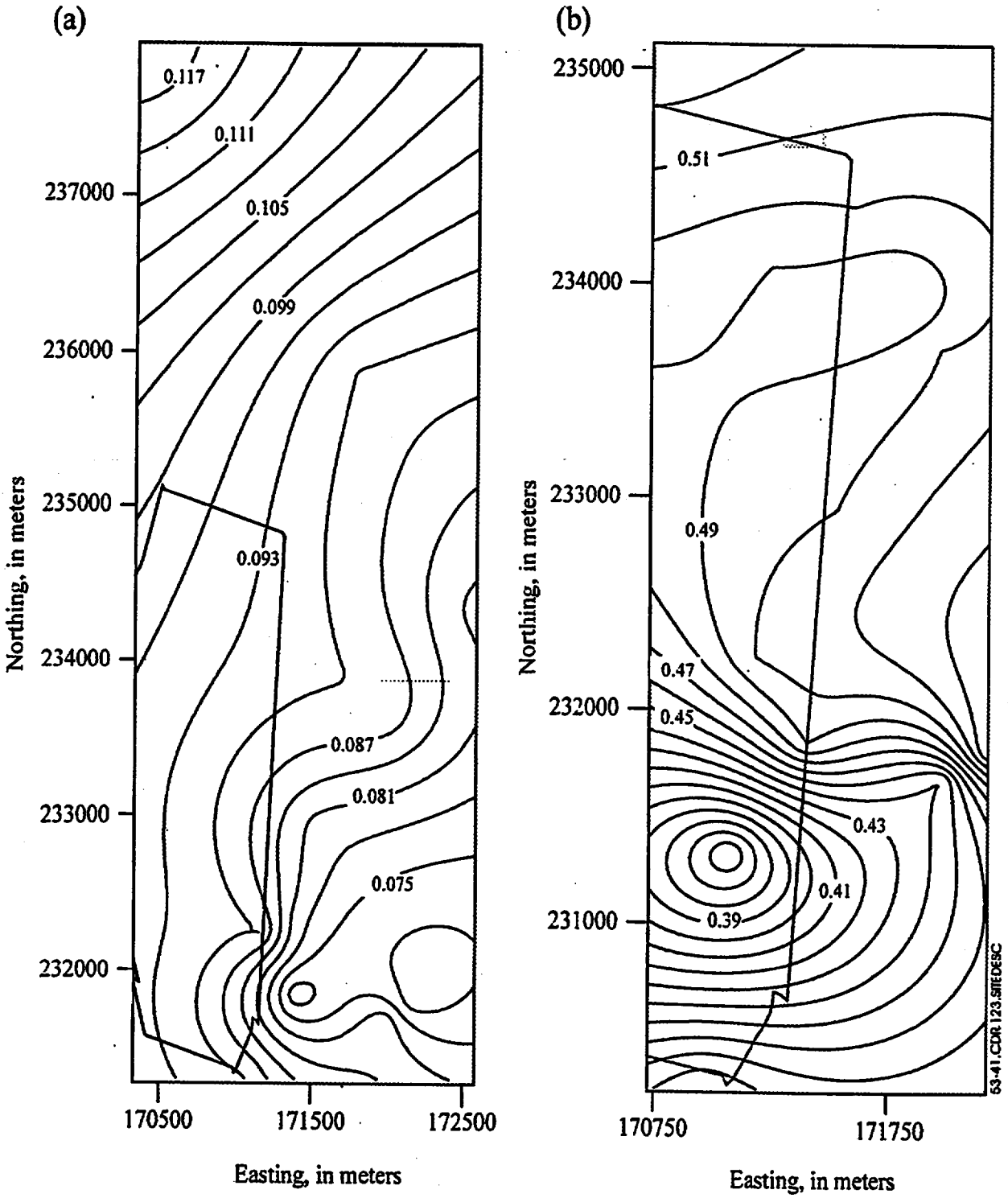

NOTE: Outline of Potential repository location is indicated.

Figure 5.3-41. Contour Plots of the Spatial Distribution of Porosity for Hydrogeologic Units (a) CW, Using 15 Boreholes, and (b) BT2, Using 13 Boreholes

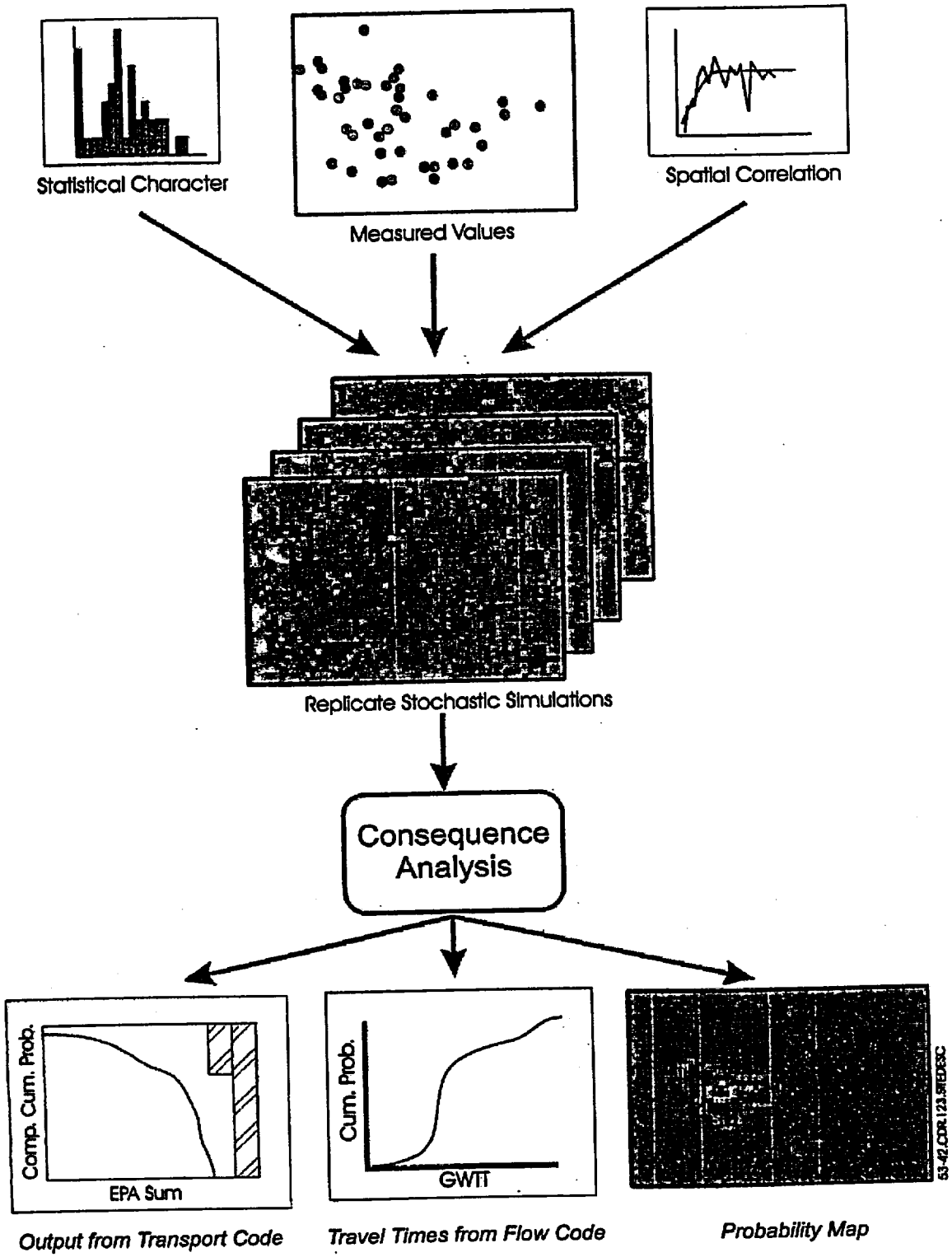

Figure 5.3-42. Conceptual Representation of a Monte Carlo Process Incorporating Geostatistical Simulation Techniques as the Basis for Assessing the Impact of Geologic Uncertainty on a Performance Measure Relevant to Licensing of a Geologic Repository

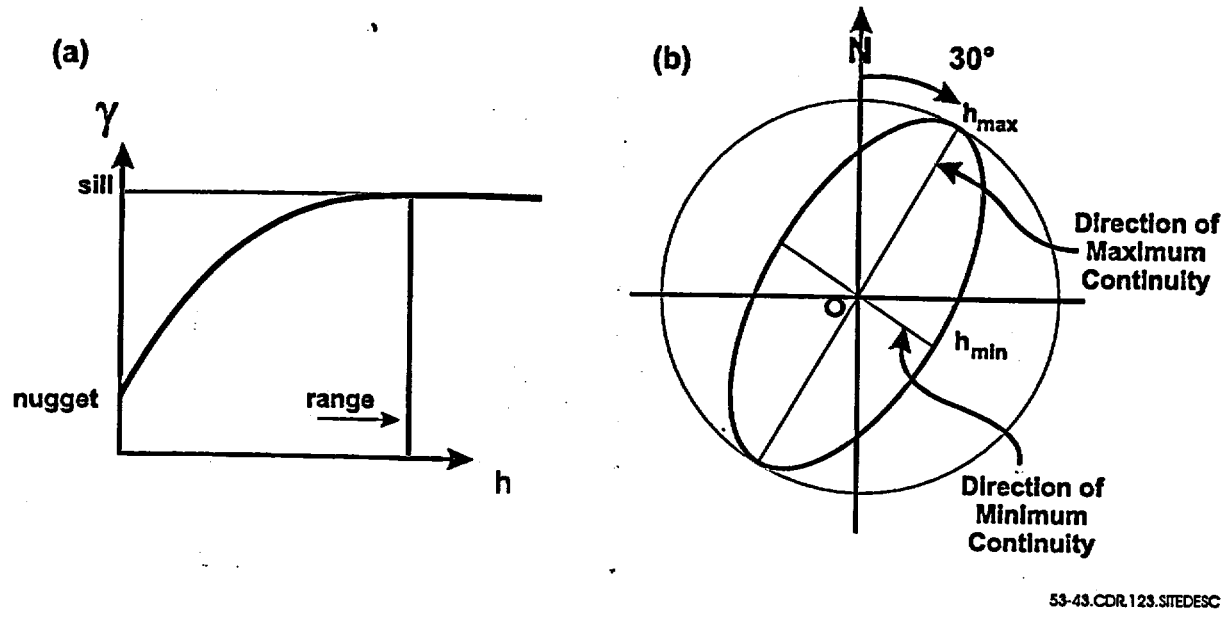

Figure 5.3-43. Schematic Diagram of (a) Components of a Simple Spherical Variogram and (b) Rotation and Stretching Necessary to Describe Anisotropy Using a Correlation Ellipse in Two Dimensions

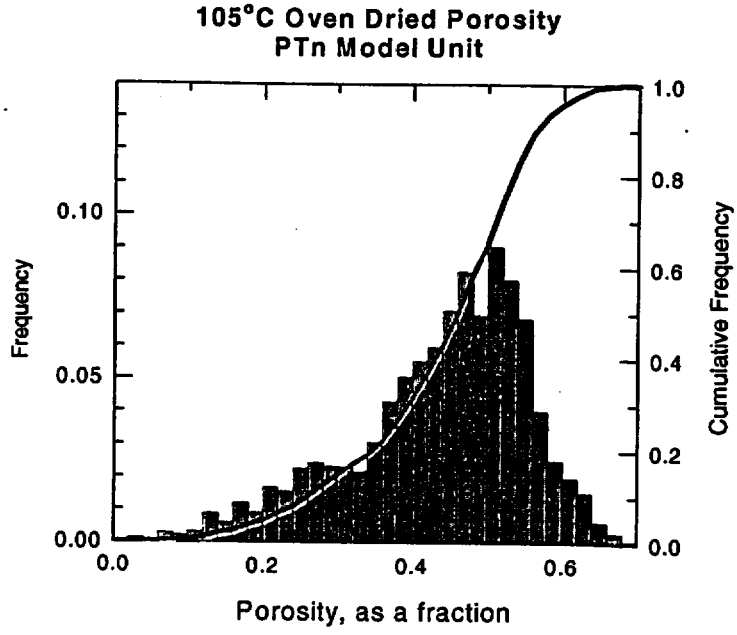

Figure 5.3-44. Histograms and Cumulative Distribution Functions of Total Porosity Values for Samples from the PTn Model Unit of Rautman and McKenna (1997)

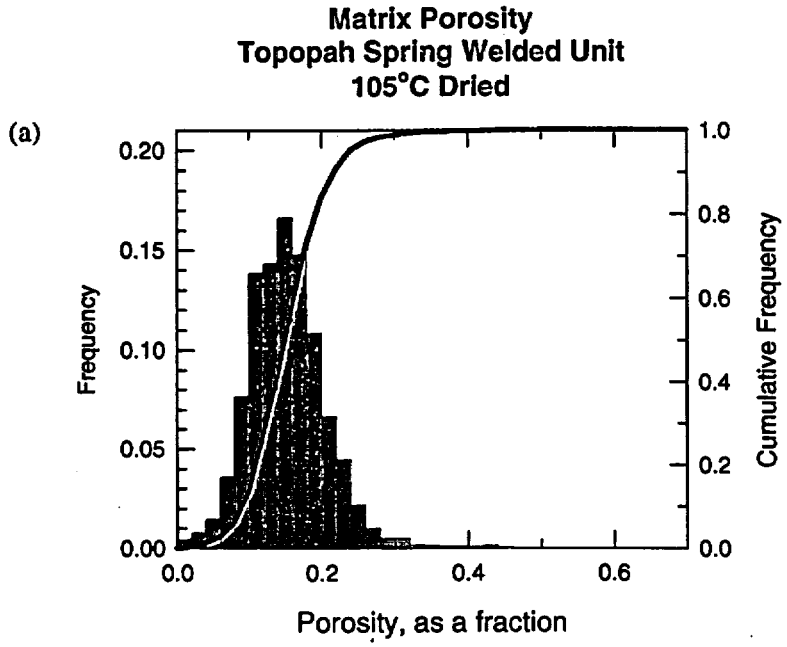

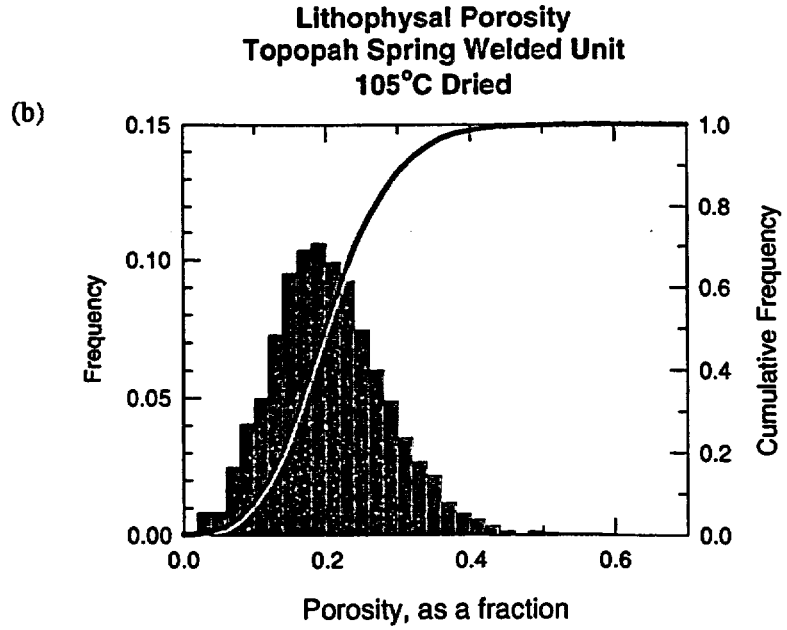

53-45.DOC.123.SITEDESC

Figure 5.3-45. Histograms and Cumulative Distribution Functions of Porosity for (a) Matrix and (b) Lithophysal Porosity Values from the TSw Model Unit of Rautman and McKenna (1997)

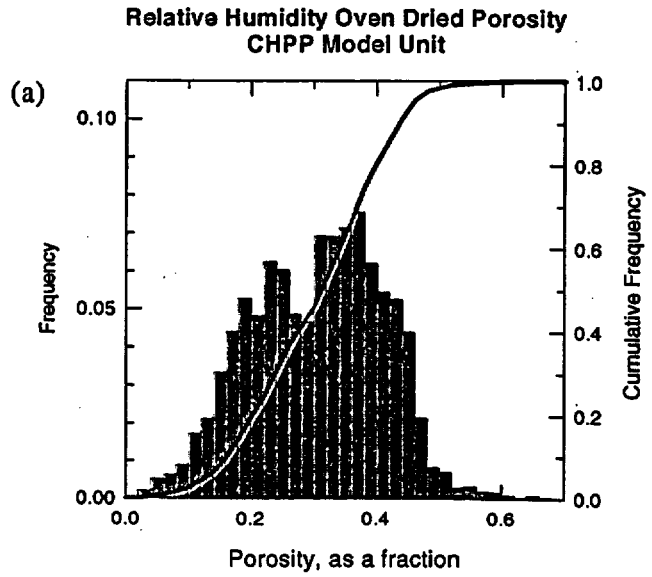

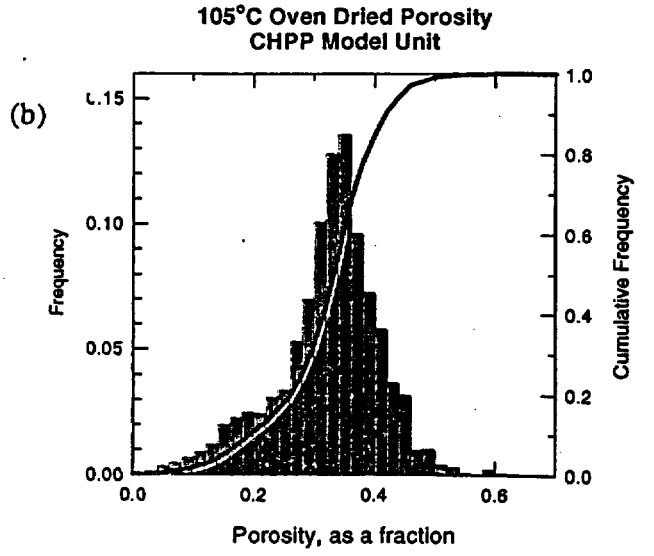

53-46.DOC.123.SITEDESC

Figure 5.3-46. Histograms and Cumulative Distribution Functions of Total Porosity for Samples from the Calico Hills-Prow Pass Model Unit of Rautman and McKenna (1997)

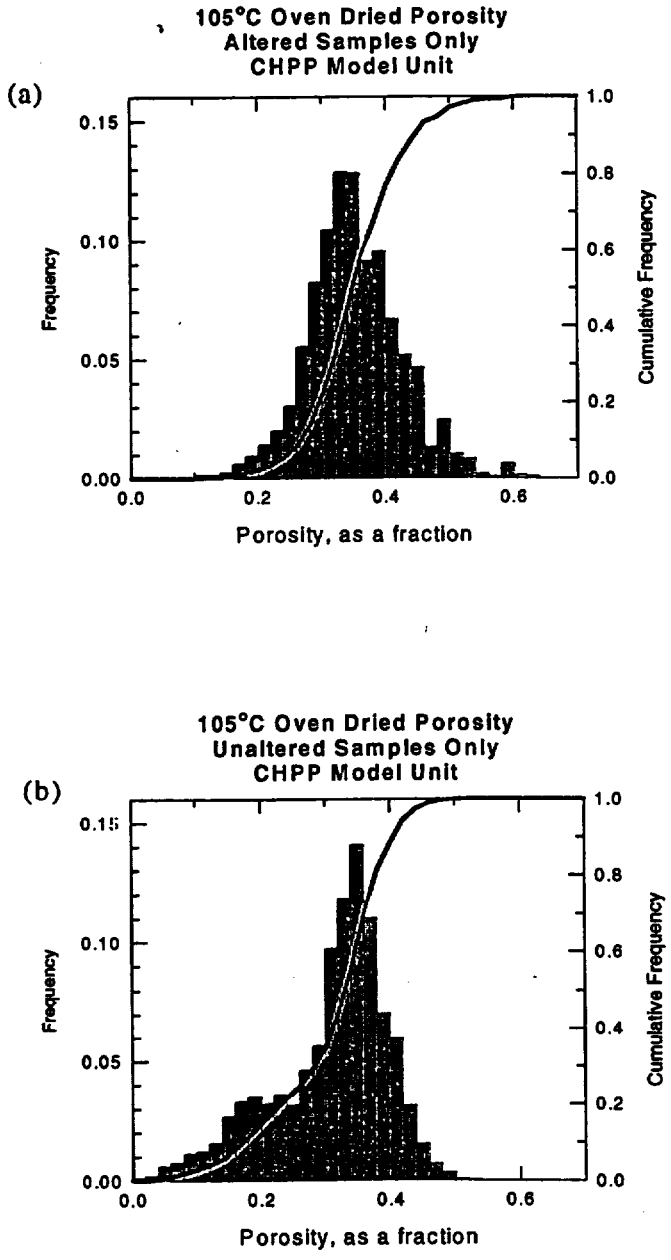

Figure 5.3-47. Histograms and Cumulative Distribution Functions of Porosity for 105°C-Dried Samples of (a) Altered and (b) Unaltered Rocks from the Calico Hills-Prow Pass Model Unit of Rautman and McKenna (1997)

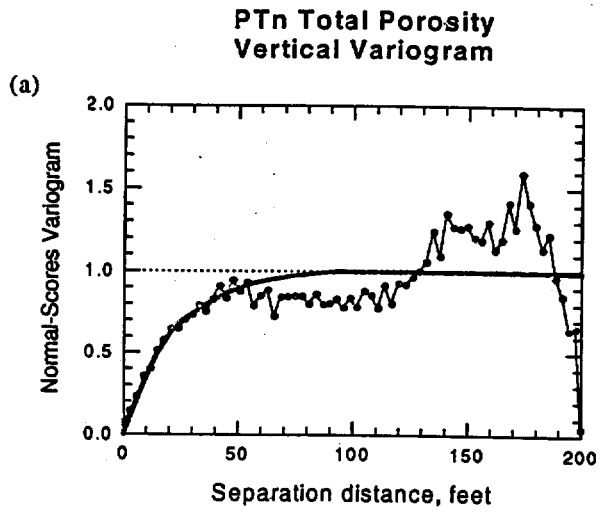

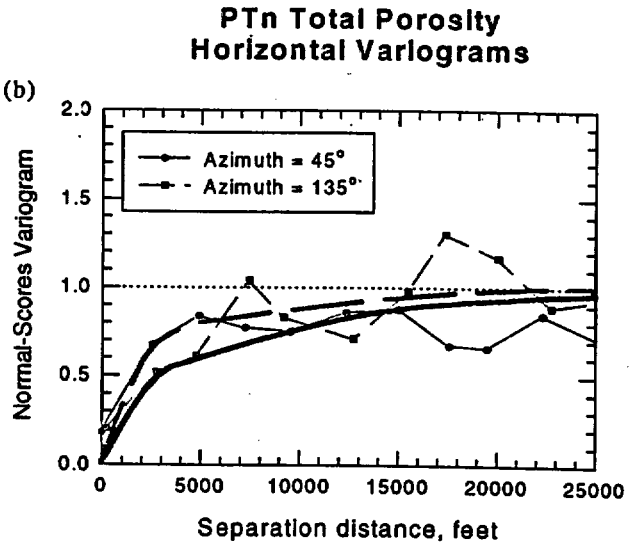

53-48.DOC.123.SITEDESC

NOTE: Curves with symbols represent measured data; heavy curves of corresponding line type represent fitted models; dotted line is the a priori variance of the data; number of pairs: (a) 200-500; (b) 300-1900).

Figure 5.3-48. Variograms of Total Porosity Normal-Score Values from the PTn Model Unit (a) Vertical; (b) Horizontal

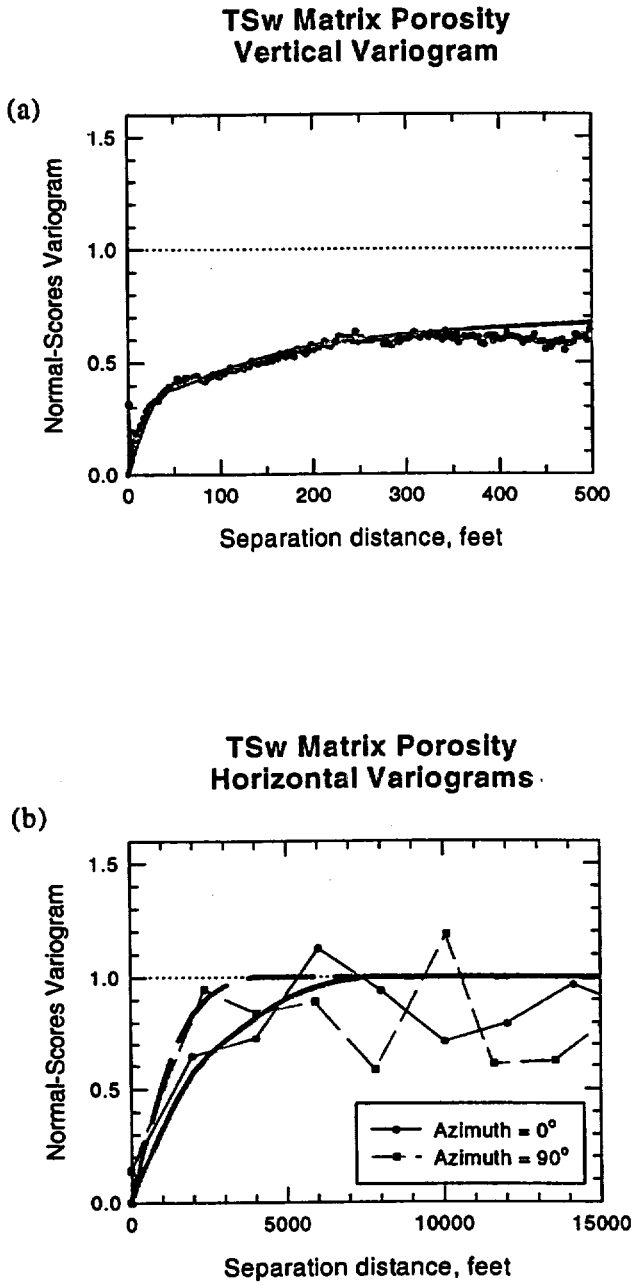

53-49.DOC.123.SITEDESC

NOTE: Curves with symbols represent measured data, heavy curves of corresponding line type represent fitted models; dotted line is the a priori variance of the data; number of pairs: (a) 1400-4000; (b) 1000-17,000).

Figure 5.3-49. Variograms of Matrix Total Porosity Normal-Score Values from the TSw Model Unit (a) Vertical; (b) Horizontal

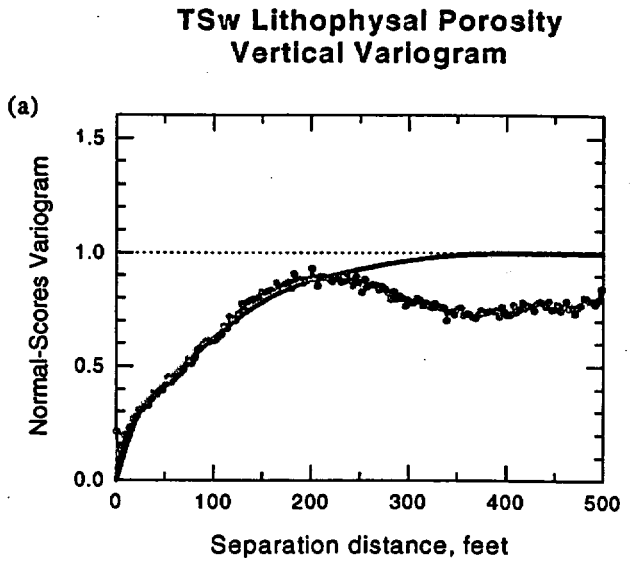

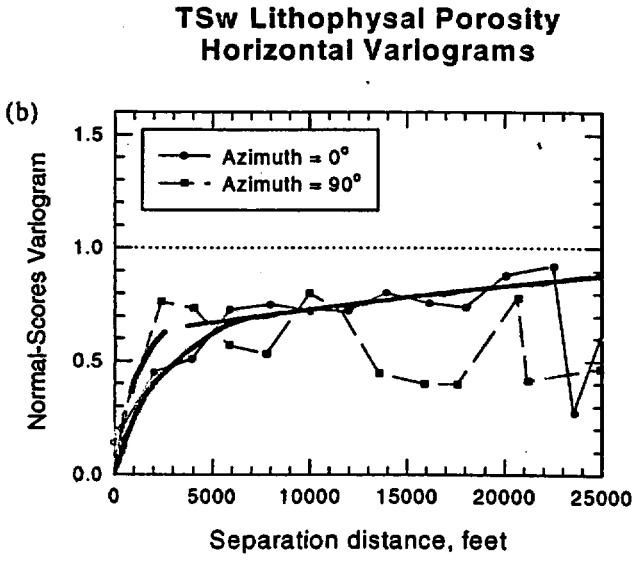

53-50.DOC.123.SITEDESC

NOTE: Curves with symbols represent measured data, heavy curves of corresponding line type represent fitted models; dotted line is the a priori variance of the data; number of pairs: (a) 2000-4000; (b) 599-18,000).

Figure 5.3-50. Variograms of Lithophysal Porosity Normal-Score Values from the TSw Model Unit (a) Vertical; (b) Horizontal

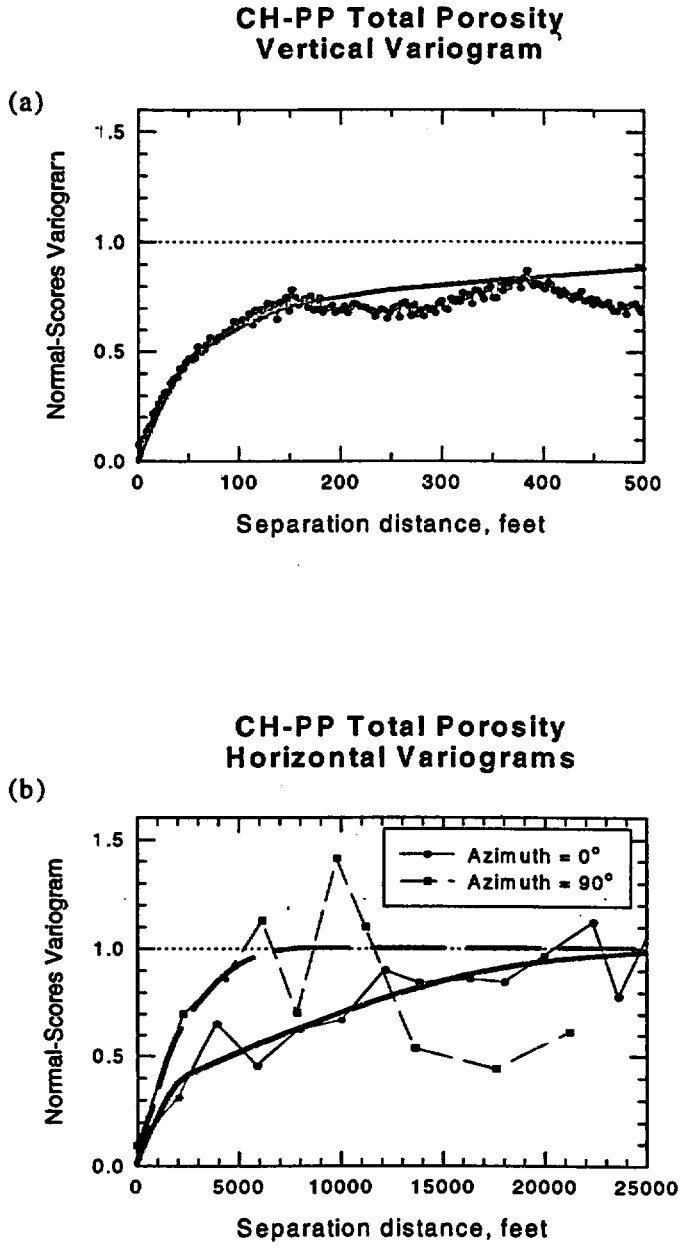

NOTE: Curves with symbols represent measured data, heavy curves of same line type represent fitted models; dotted line is the a priori variance of the data; number of pairs: (a) 1000-3000; (b) 700-11,000).

Figure 5.3-51. Variograms of Matrix Total Porosity Normal-Score Values from the CH-PP Model Unit (a) Vertical; (b) Horizontal

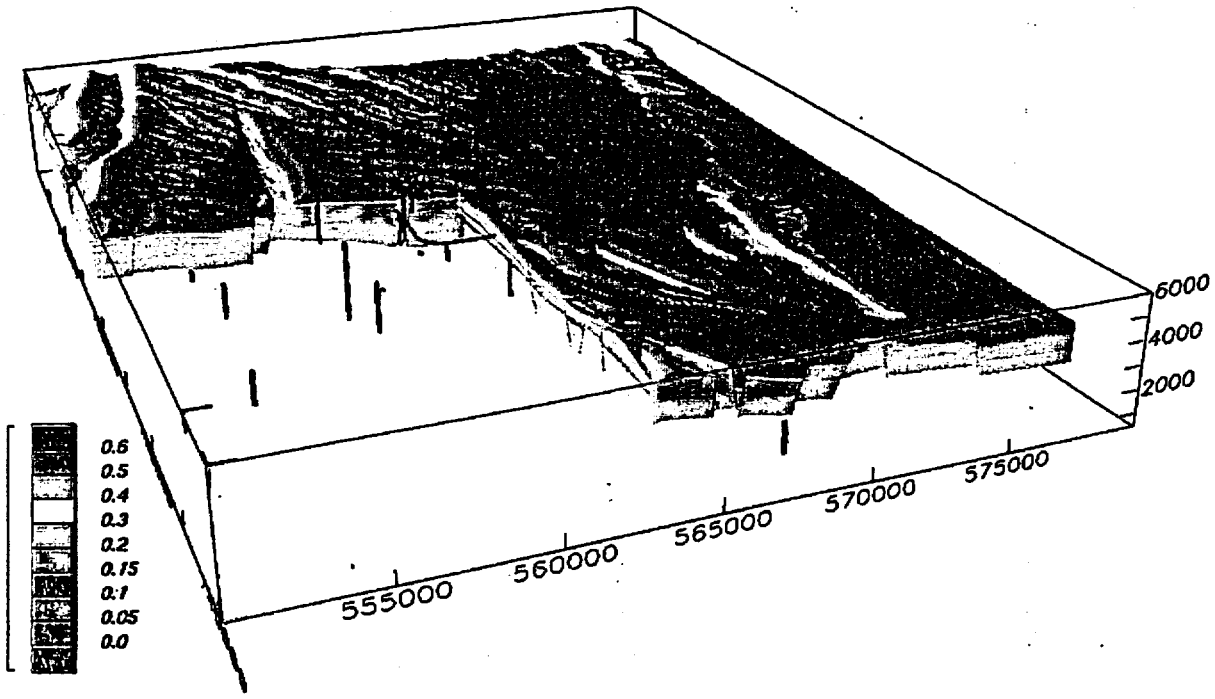

NOTE: Red objects are drill holes and Exploratory Studies Facility drifts; welded portions of the Tiva Canyon Tuff shown in grey (not modeled); coordinates are Nevada State Plane Coordinate System in feet.

Figure 5.3-52. Cut-Away Perspective Diagram Showing Distribution and Spatial Variability of Total Porosity at Yucca Mountain

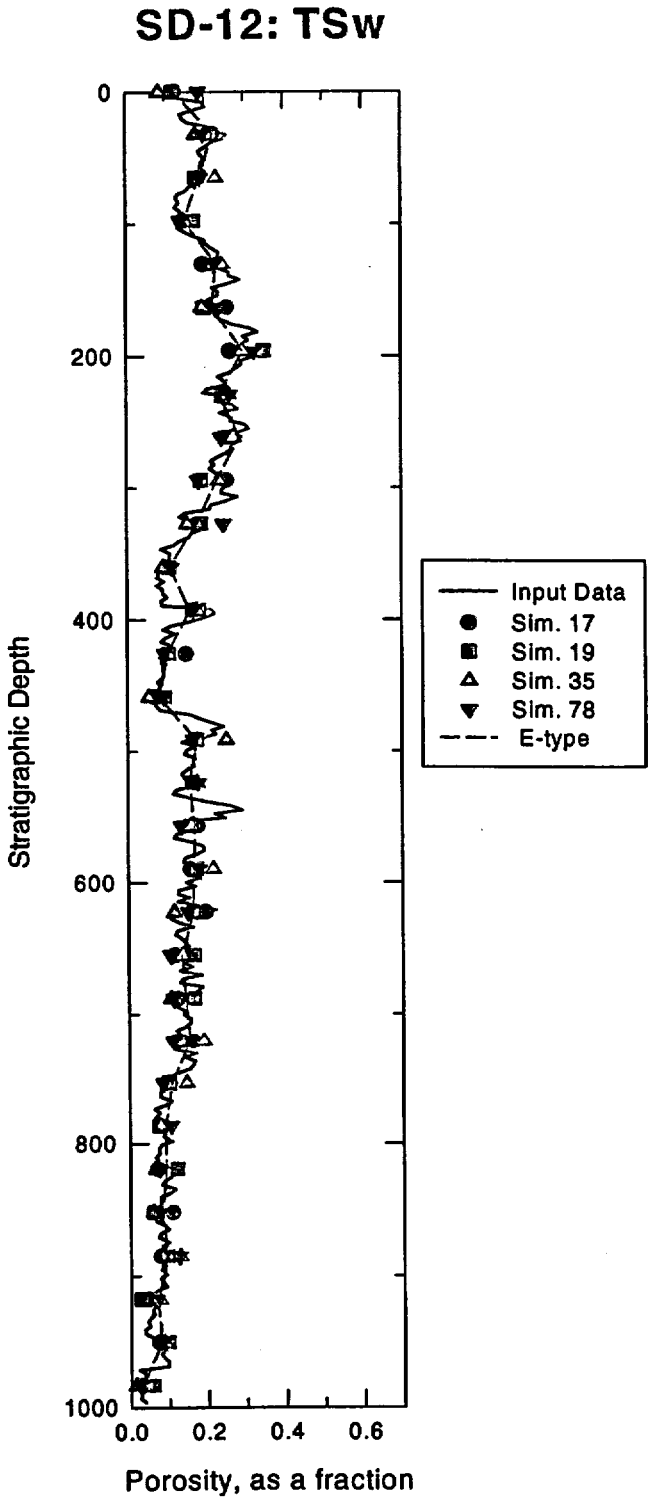

Figure 5.3-53. Statistical Validation of Simulated Total (Lithophysal) Porosity Models for the TSw Model Unit of Rautman and McKenna (1997): Reproduction of Measured Porosity Data at Borehole SD-12

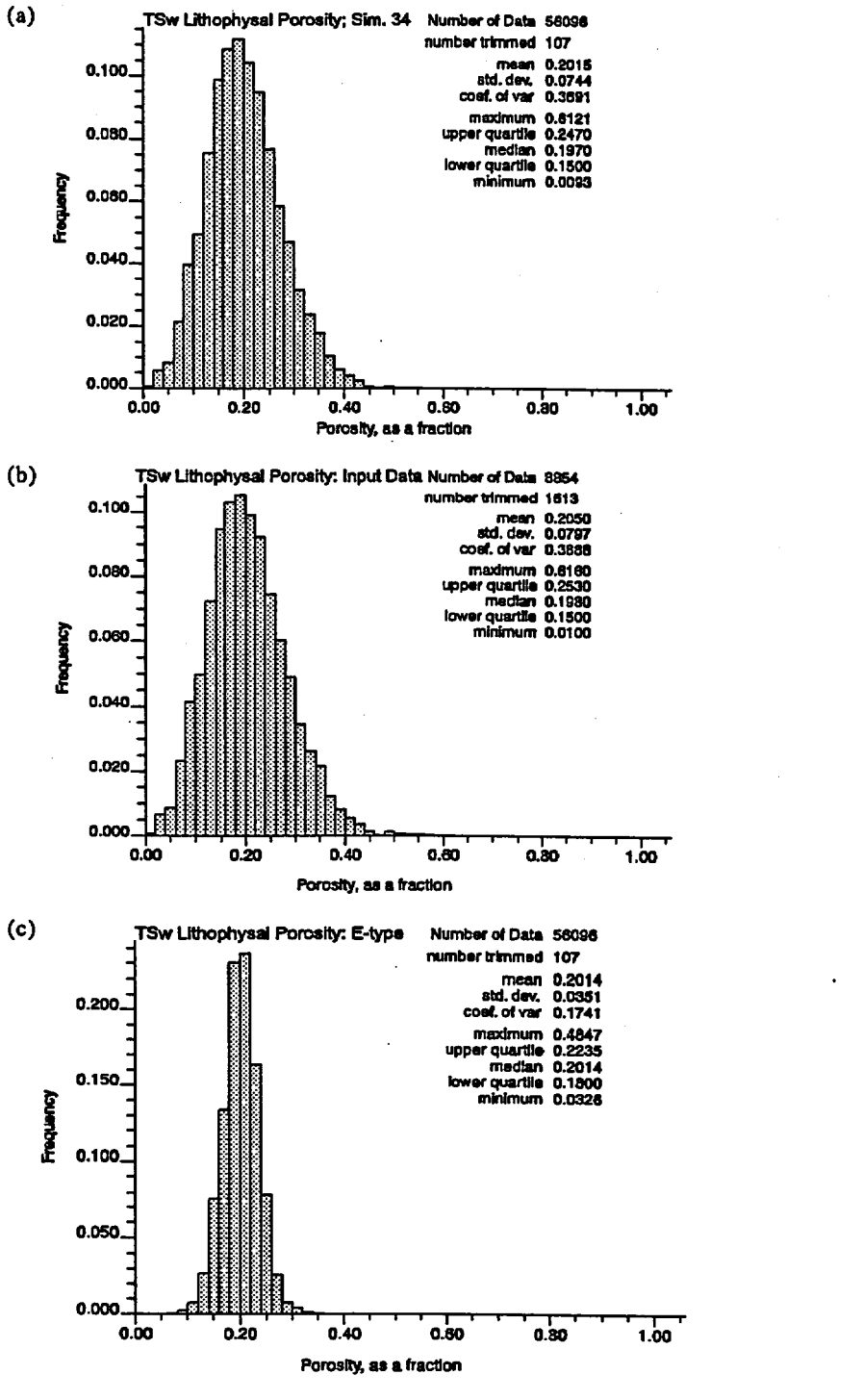

Figure 5.3-54. Statistical Validation of Simulated Total (Lithophysal) Porosity Models for the TSw Model Unit of Rautman and McKenna (1997): Reproduction of Overall Statistical Character

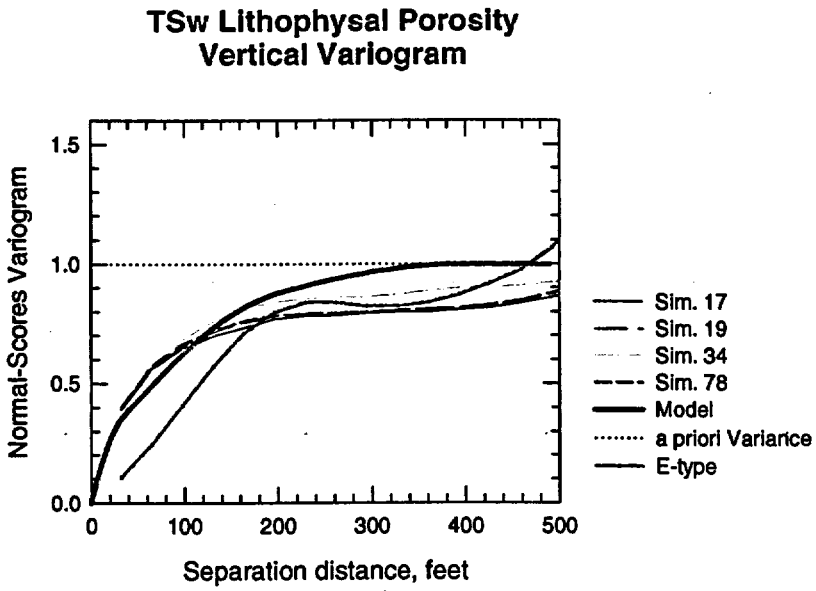

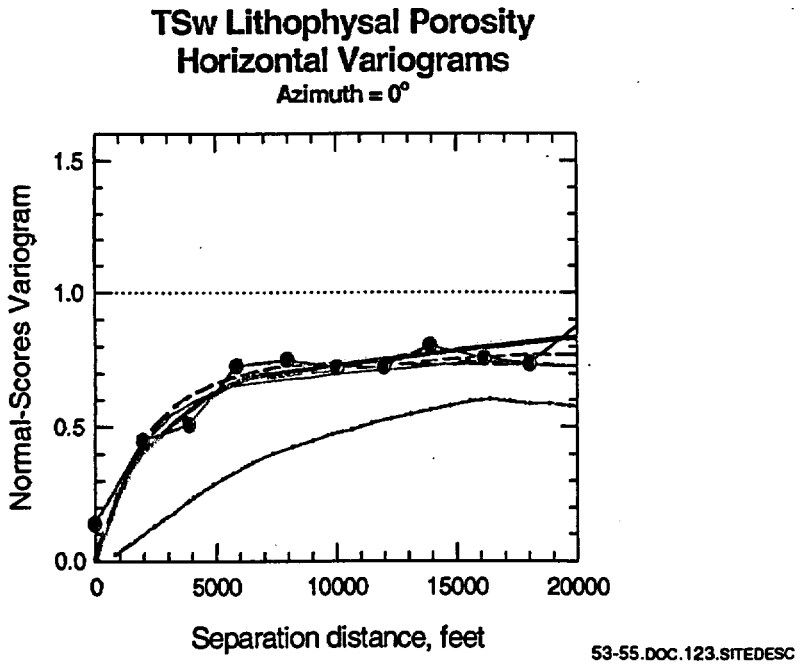

Figure 5.3-55. Statistical Validation of Simulated Total (Lithophysal) Porosity Models for the TSw Model Unit of Rautman and McKenna (1997): Reproduction of Spatial Continuity Patterns for (a) Horizontal and (b) Vertical Variograms

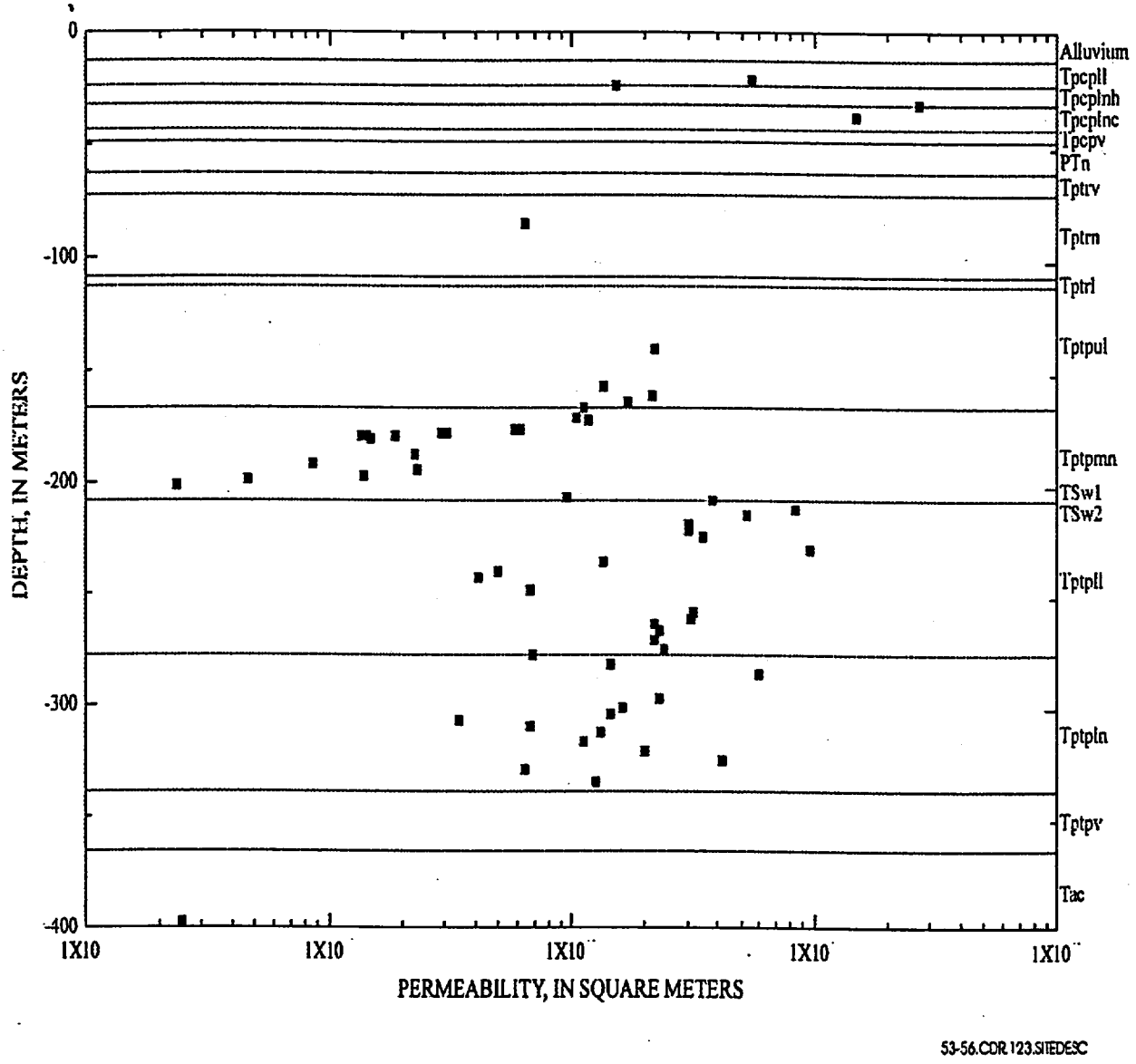

Figure 5.3-56. Relation of Air-Injection Permeability Values to Depth and Lithostratigraphic Units Penetrated in Borehole UZ-16

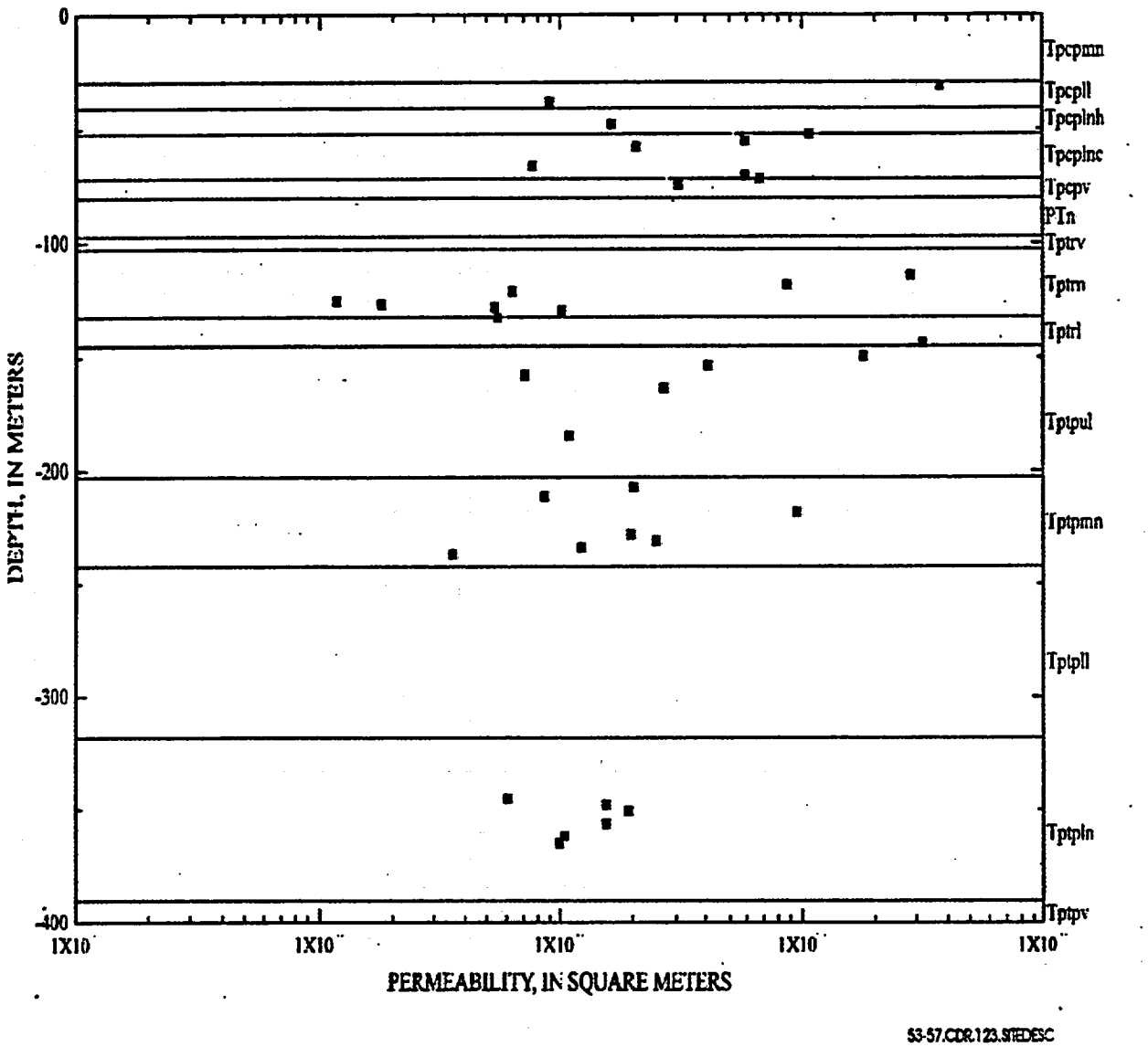

Figure 5.3-57. Relation of Air-Injection Permeability Values to Depth and Lithostratigraphic Units Penetrated in Borehole SD-12

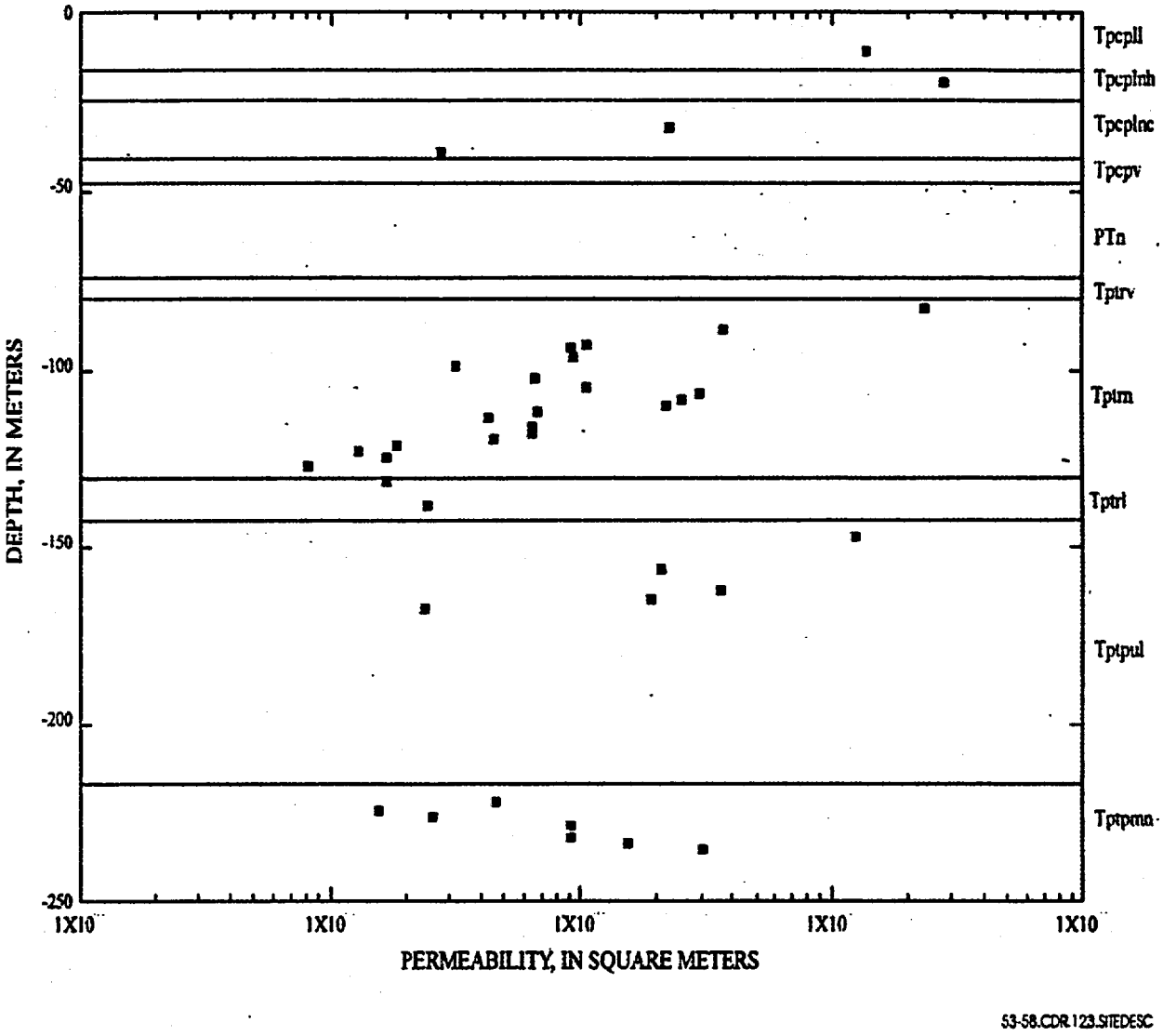

Figure 5.3-58. Relation of Air-Injection Permeability Values to Depth and Lithostratigraphic Units Penetrated in Borehole NRG-6

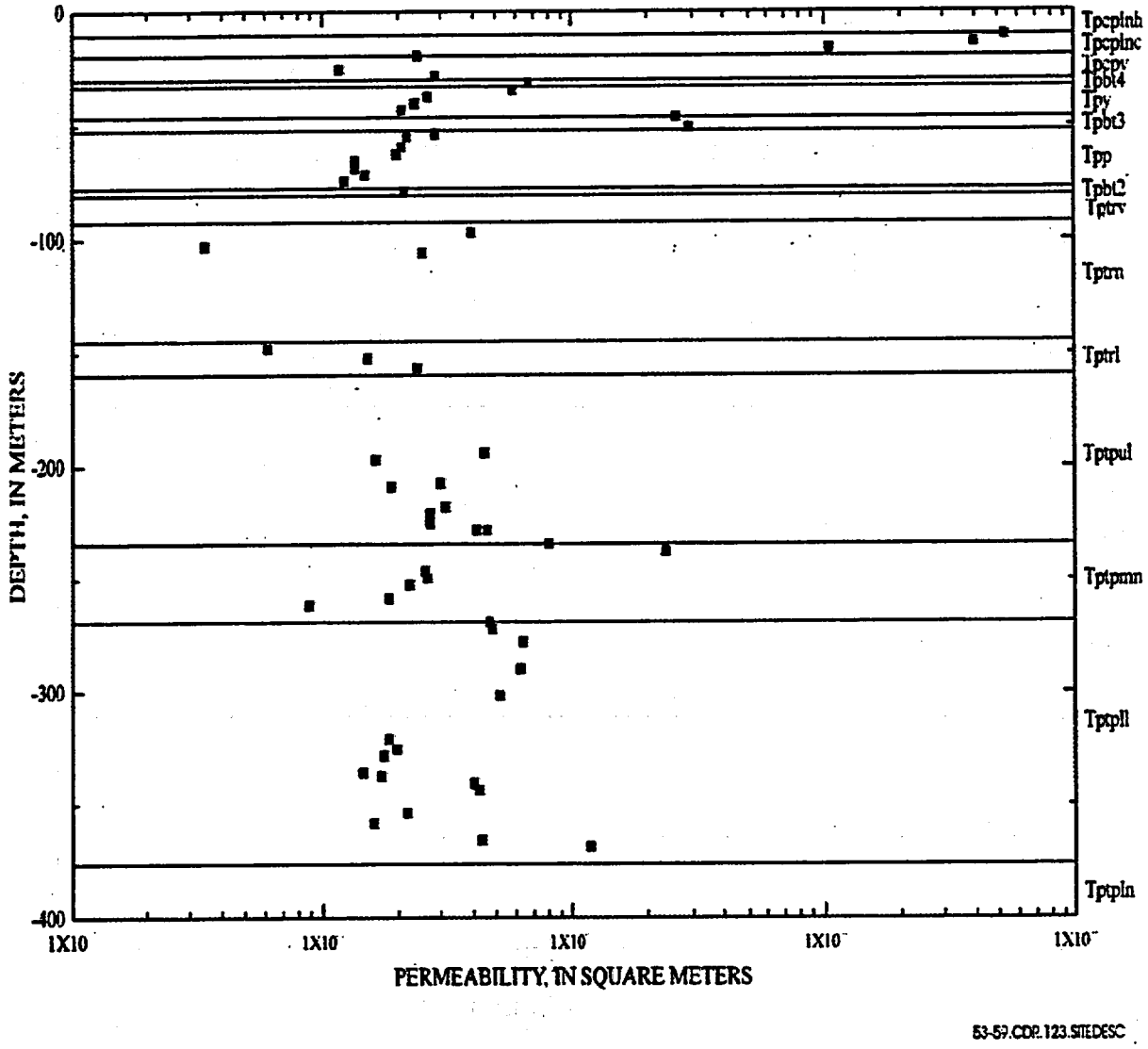

Figure 5.3-59. Relation of Air-Injection Permeability Values to Depth and Lithostratigraphic Units Penetrated in Borehole NRG-7a

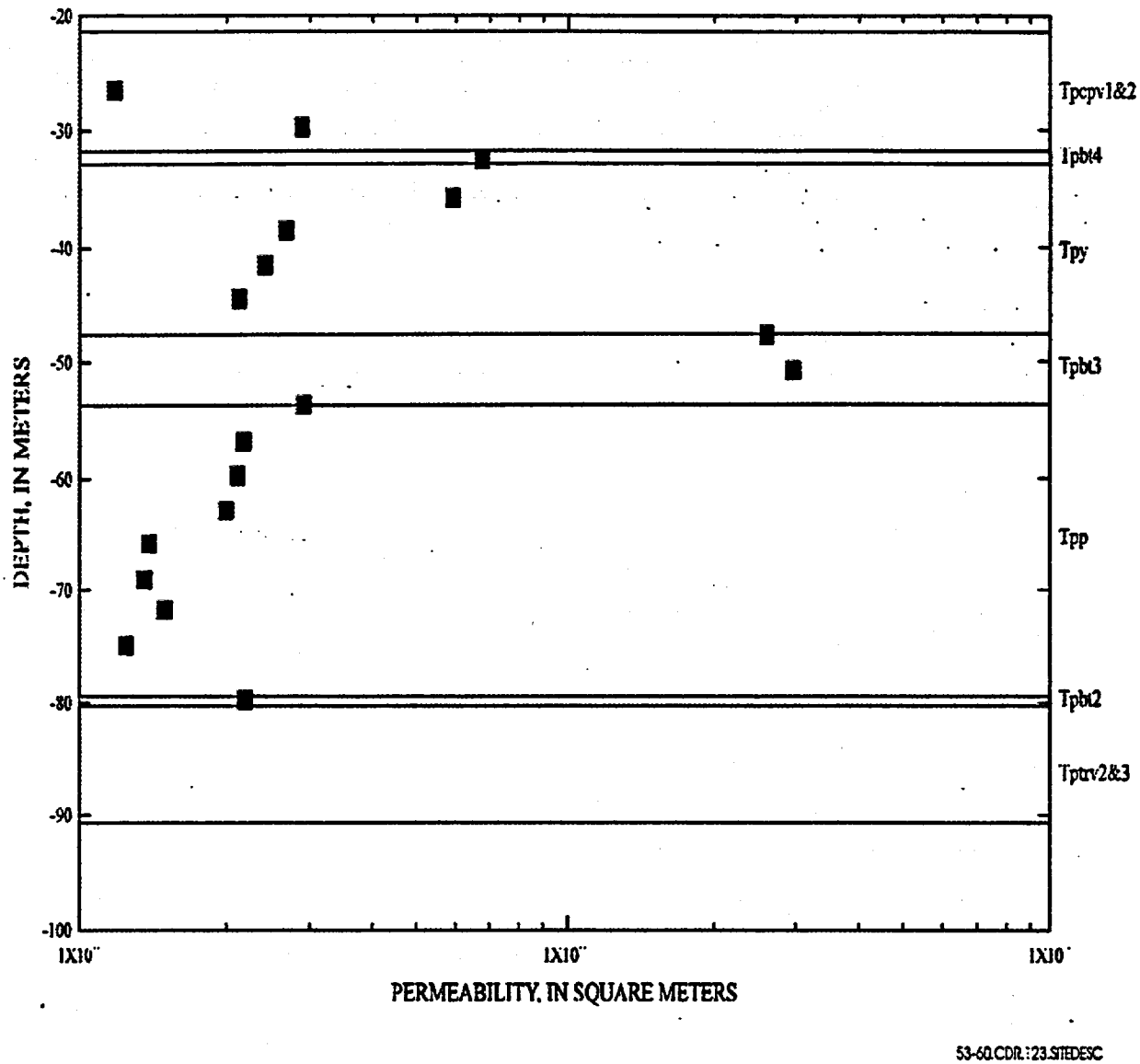

Figure 5.3-60. Air-Injection Permeability Values in the Paintbrush Nonwelded Hydrogeologic Unit with Depth in Borehole NRG-7a

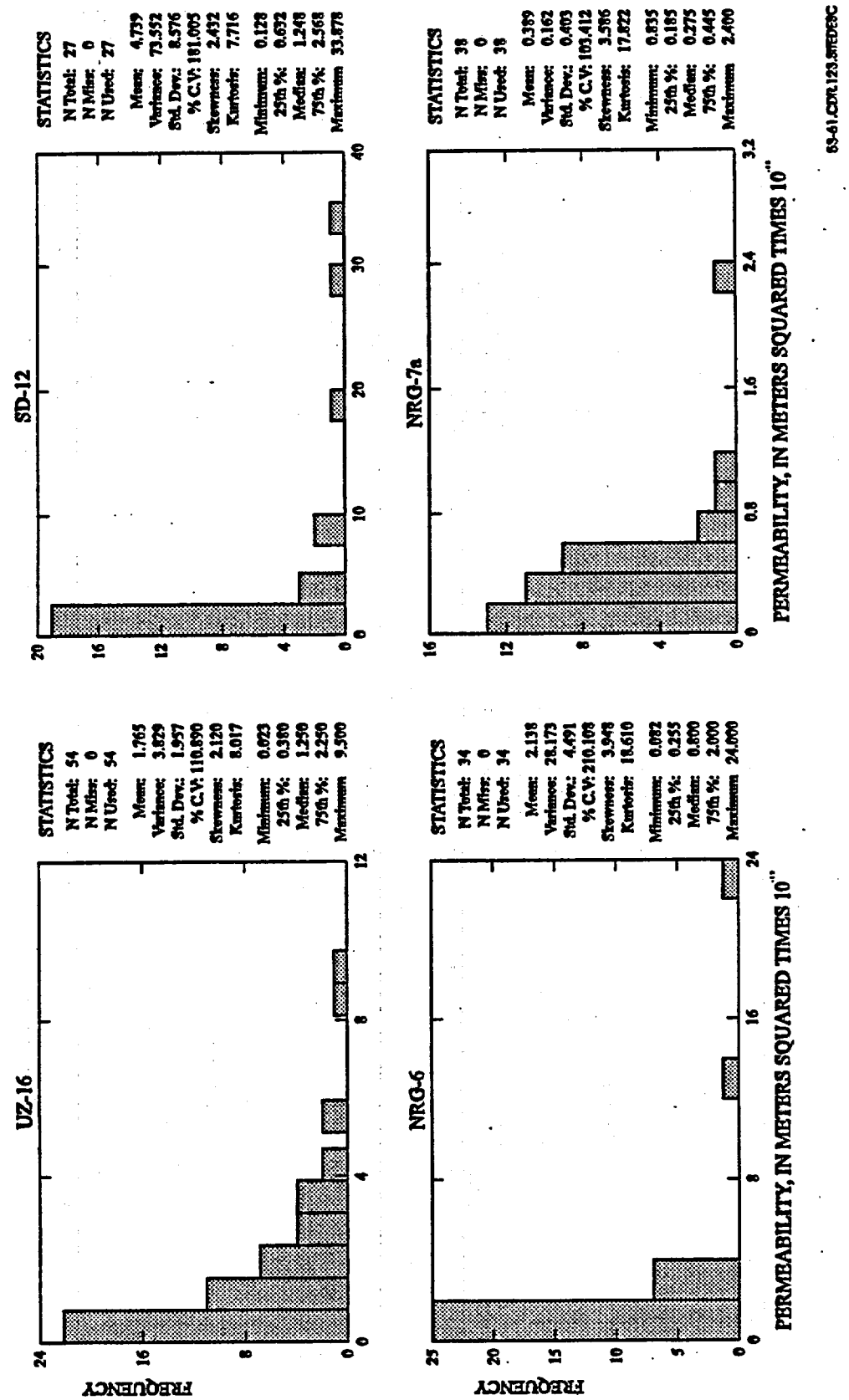

Figure 5.3-61. Histograms of Air-injection Permeability Values and Basic Statistics by Borehole for the Topopah Spring Tuff

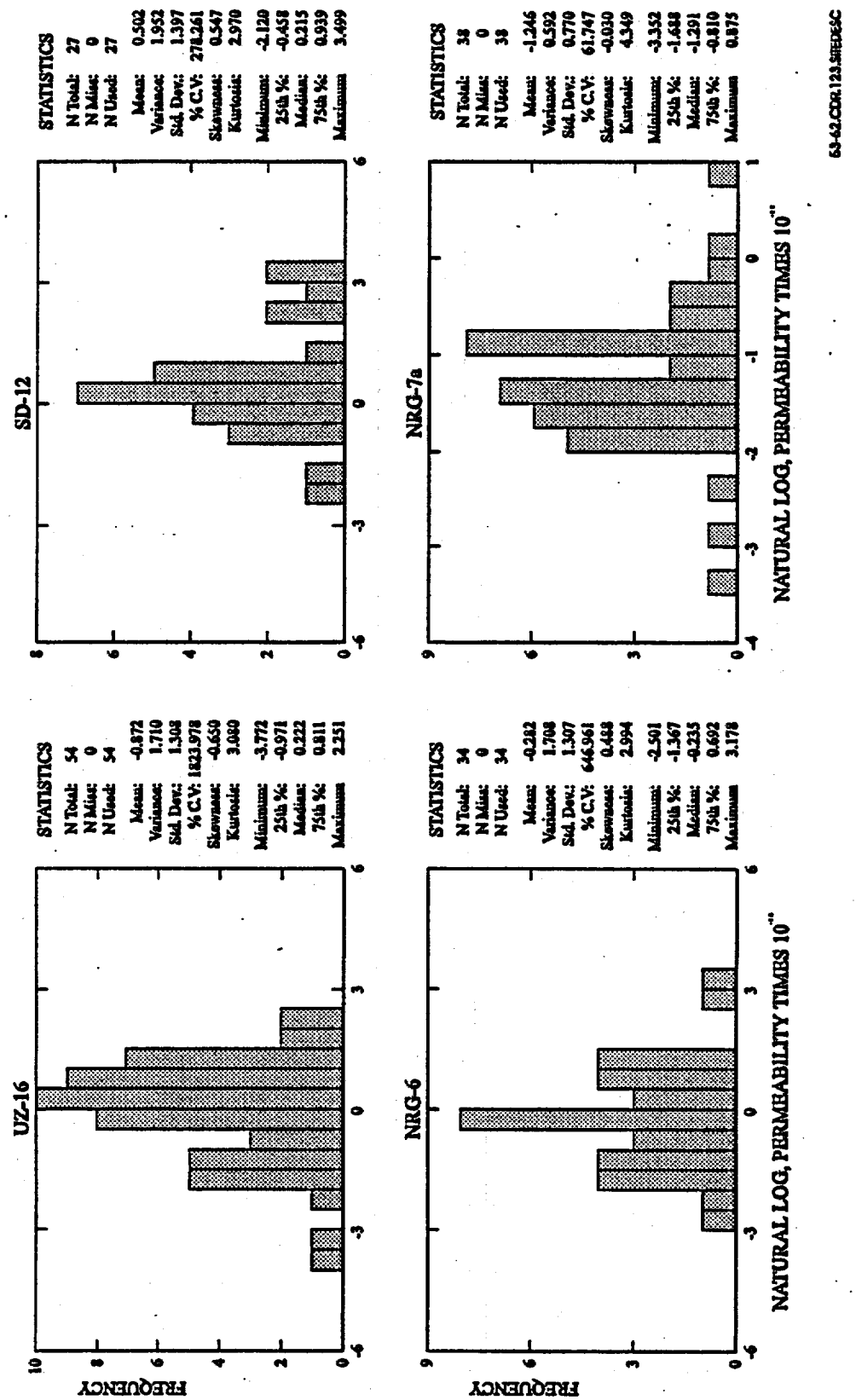

Figure 5.3-62. Histograms of Natural Log Air-Injection Permeability Values and Basic Statistics by Borehole for the Topopah Spring Tuf

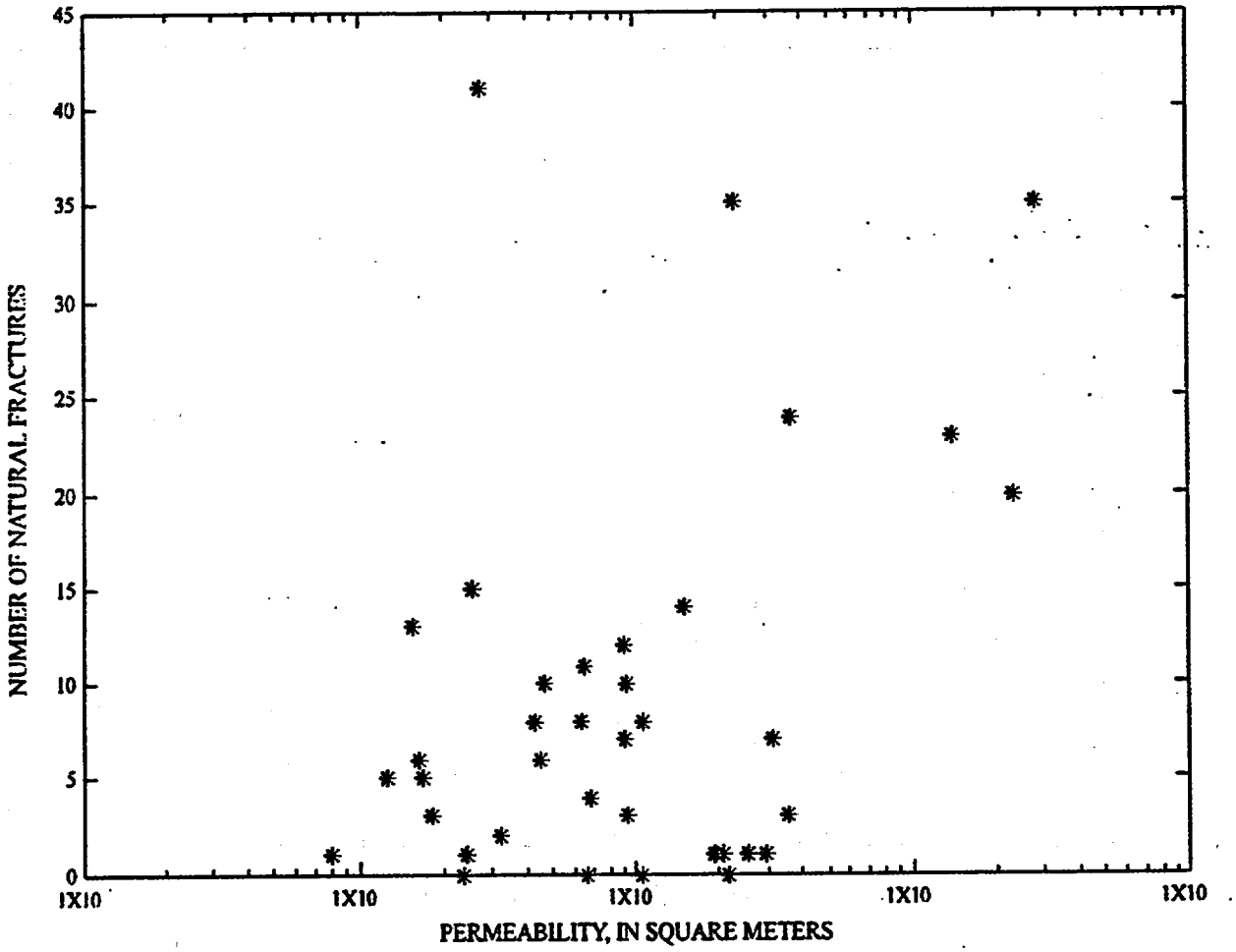

NOTE: Map shows sites where marine cores were taken. The individual records were normalized and averaged to produce the "stack" record which was subsequently smoothed with a 9-point gaussian filter ("smoothed stack") to make the commonly used SPECMAP oxygen isotope curve for correlation and timing of Quaternary climate changes.

Figure 5.3-63. Relation Between Air-Injection Permeability Values and Number of Natural Fractures per Test Interval, Borehole NRG-6

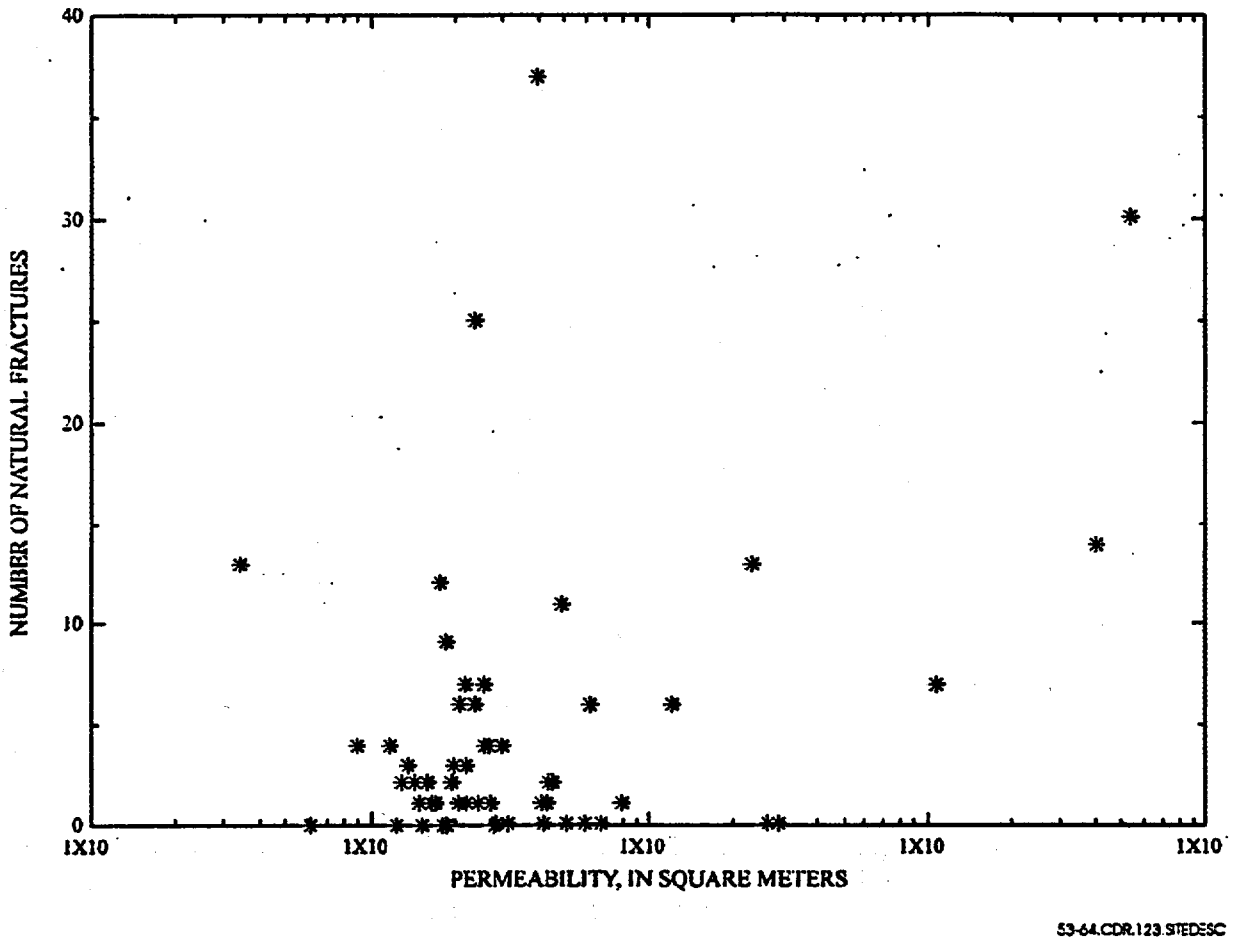

Figure 5.3-64. Relation Between Air-Injection Permeability Values and Number of Natural Fractures per Test Interval, Borehole NRG-7a

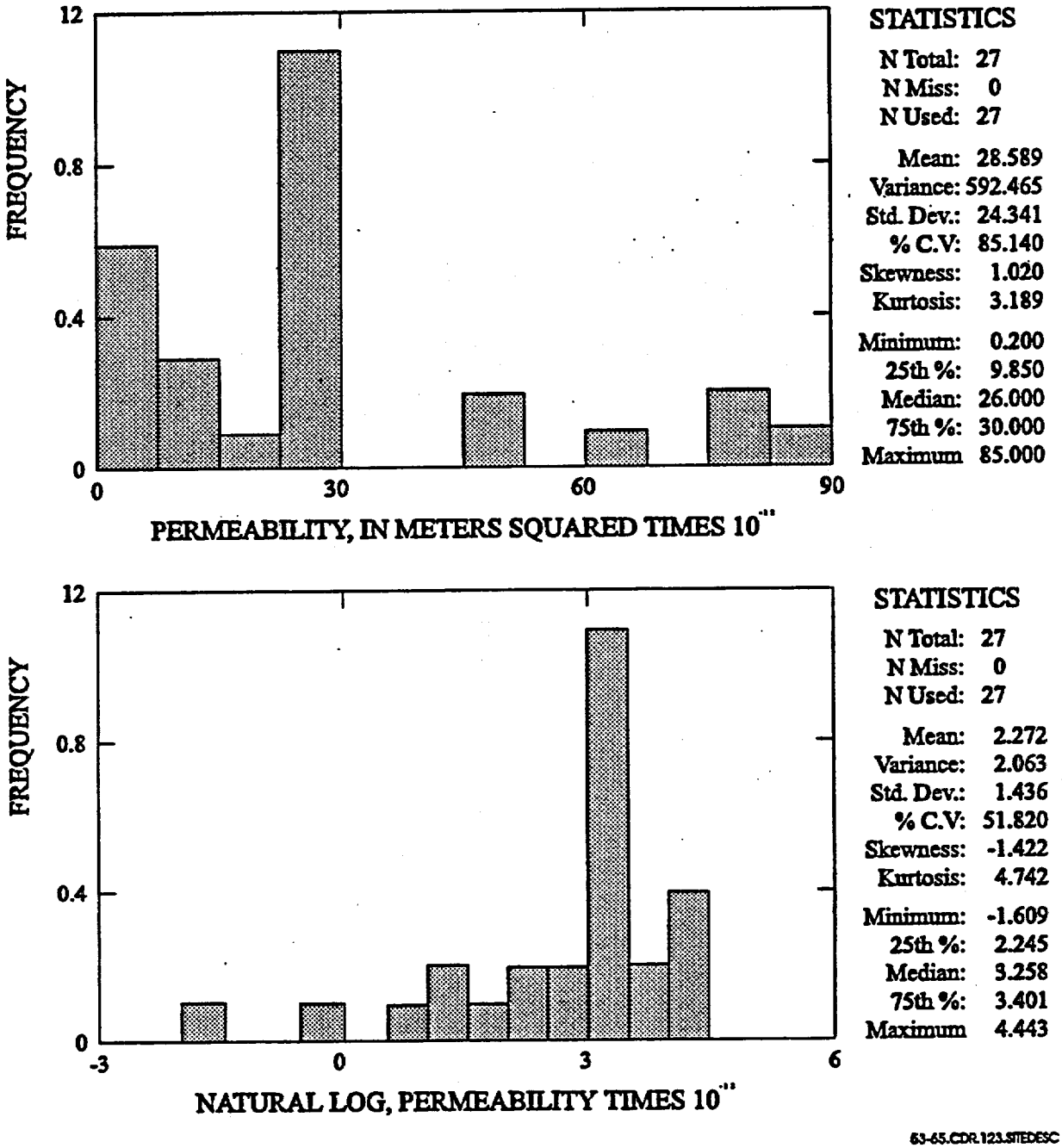

Figure 5.3-65. Composite Histograms and Statistics for Air-Permeability Values from the Upper Tiva Canyon Alcove Radial Boreholes RBT#1, RBT#2, and RBT#3

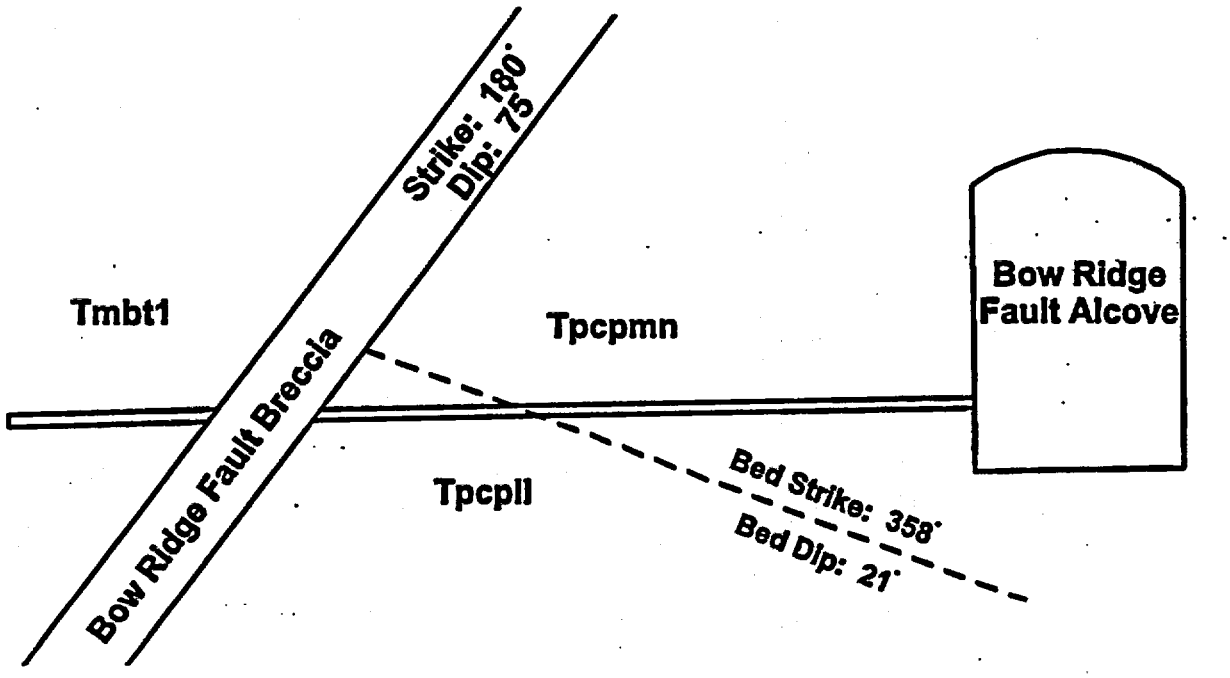

Figure 5.3-66. Cross-Section of the Bow Ridge Fault, the Bow Ridge Fault Alcove, and Borehole HPF#1

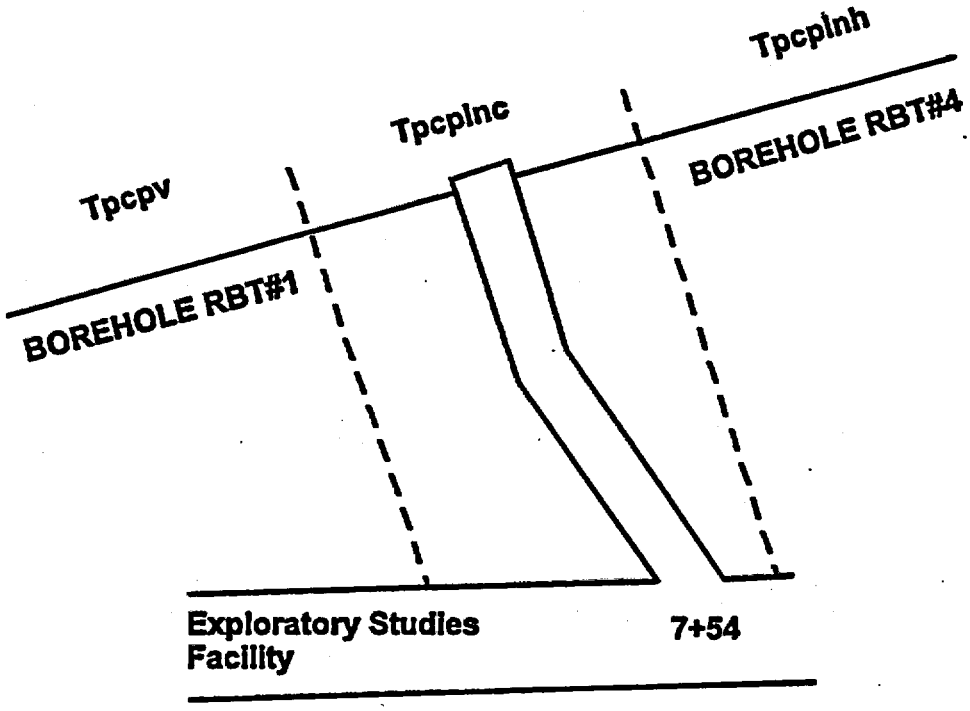

Figure 5.3-67. Plan-View Schematic Diagram of the Upper Paintbrush Contact Alcove and Boreholes RBT#1 and RBT#4

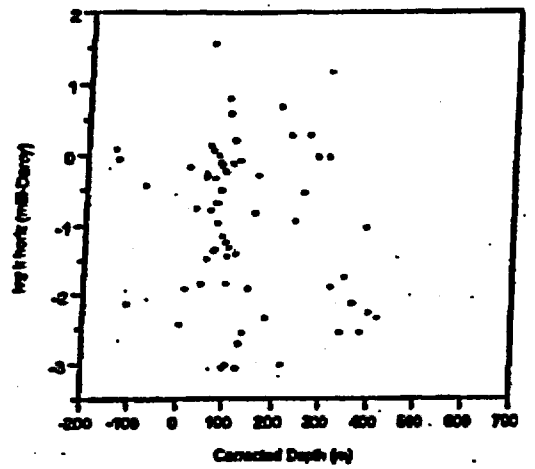

Horizontal permeability versus depth.

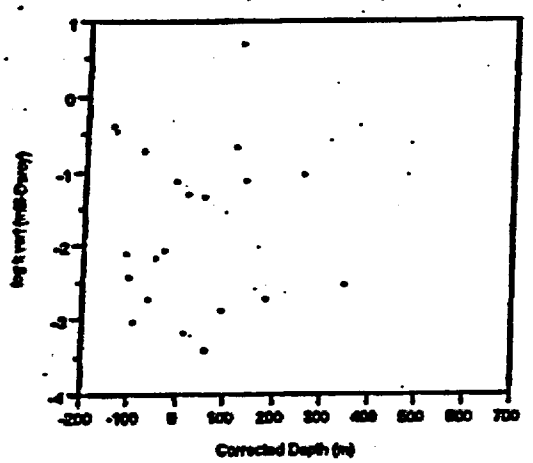

Vertical permeability versus depth.

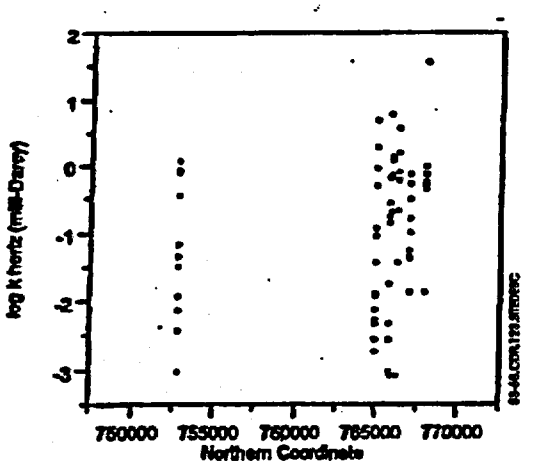

Lateral distribution of horizontal permeability.

Figure 5.3-68. Distribution of Permeability in the Topopah Spring Tuff

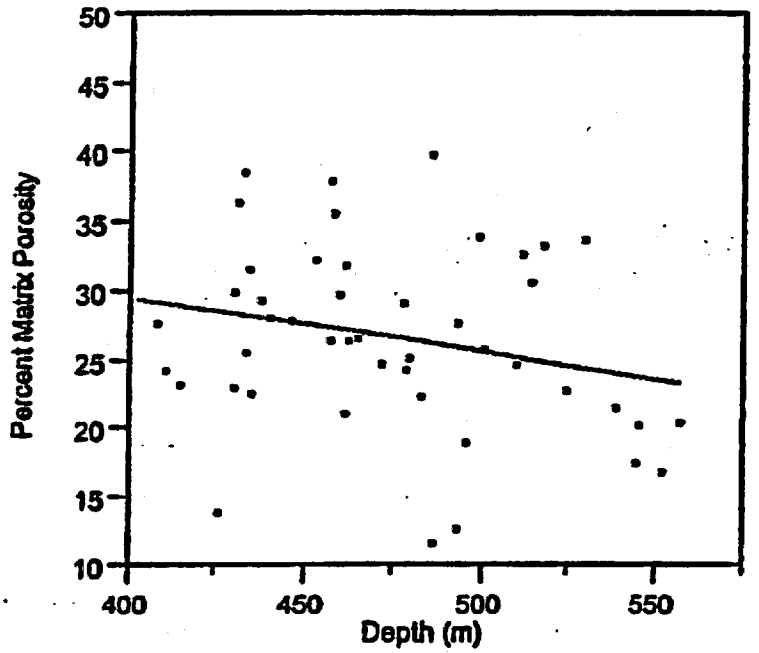

Matrix porosity versus depth

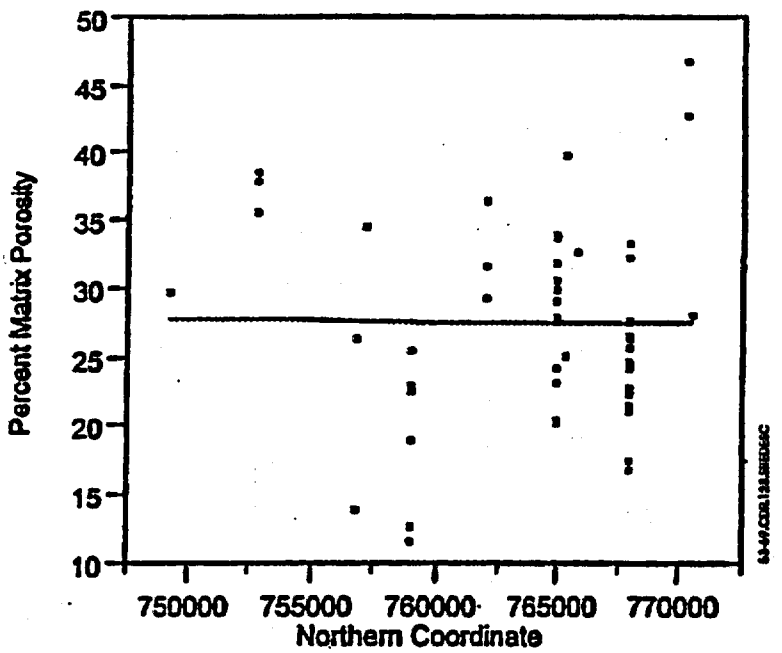

Lateral distribution of matrix porosity

Figure 5.3-69. Distribution of Matrix Porosity in the Calico Hills Formation

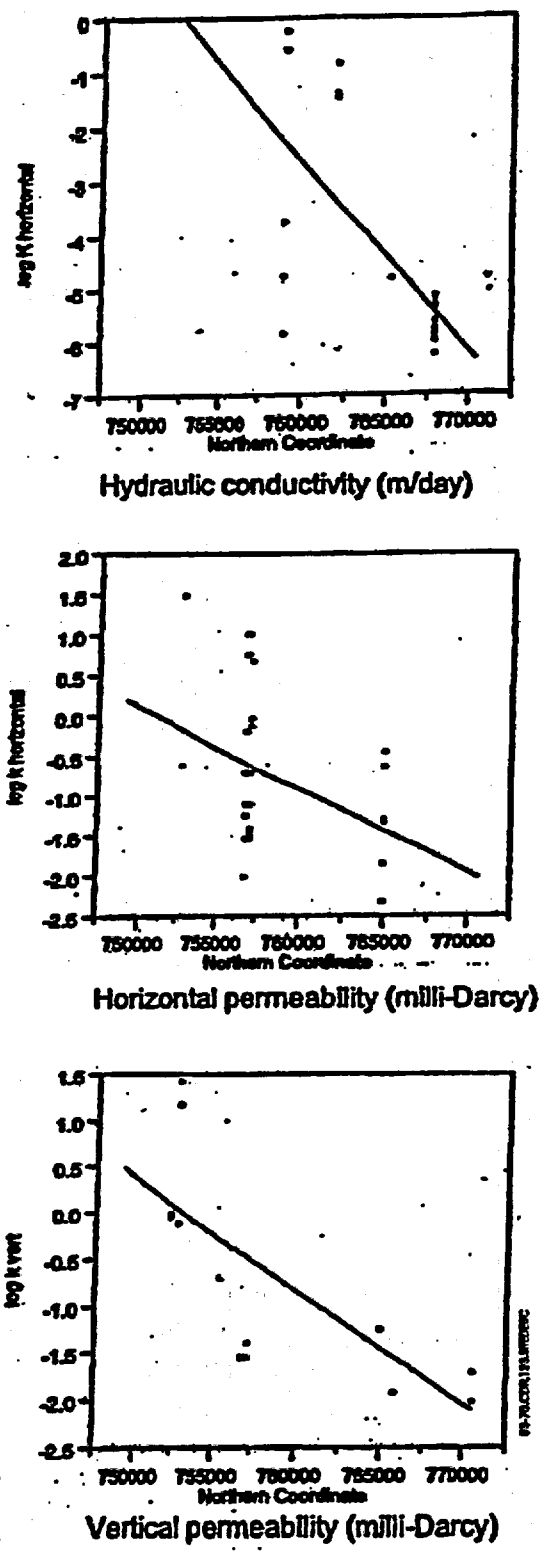

Figure 5.3-70. Distribution of Hydraulic Conductivity and Permeability Values in the Calico Hills Formation

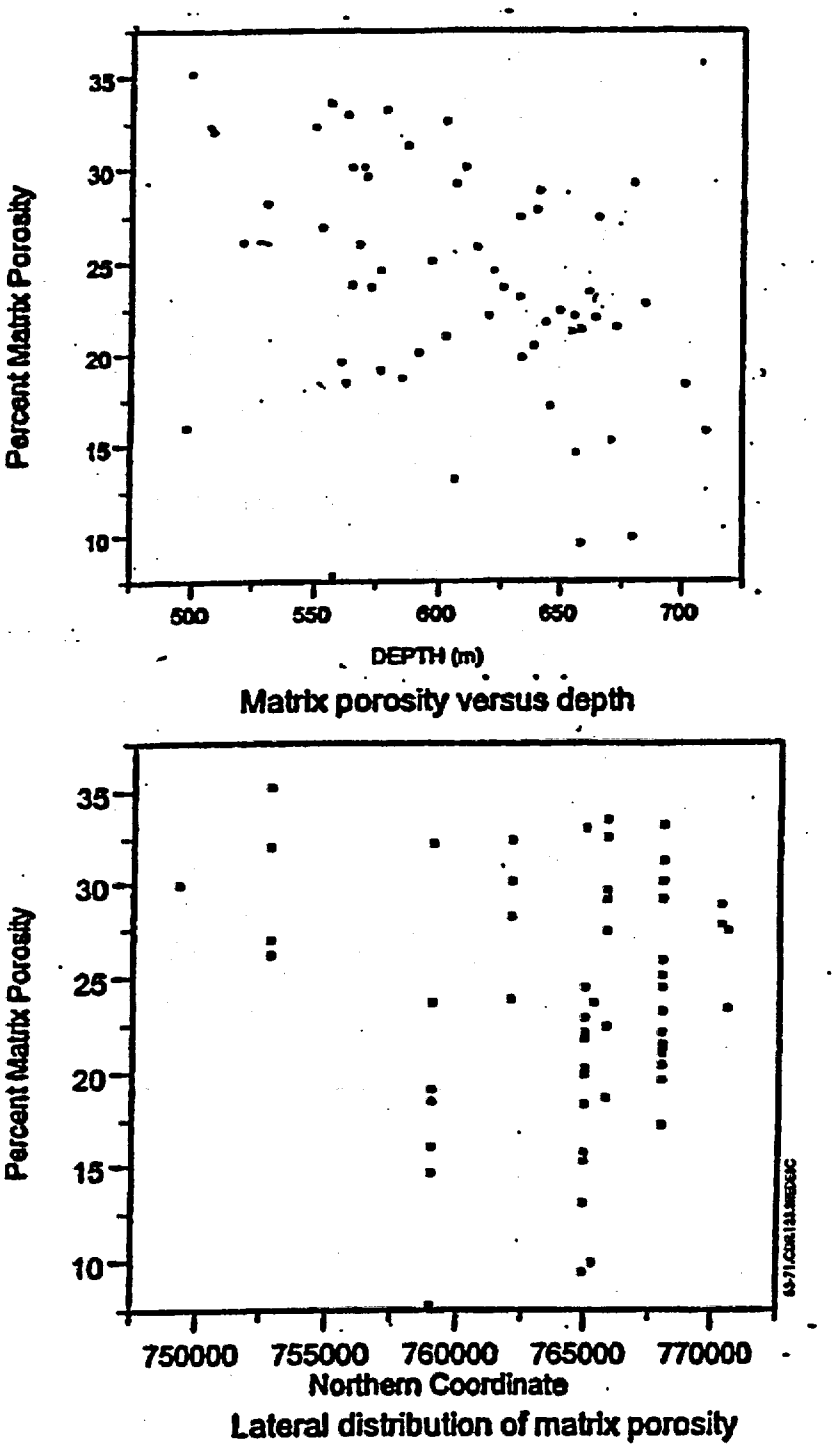

Figure 5.3-71. Vertical and Lateral Distribution of Porosity in the Prow Pass Tuff

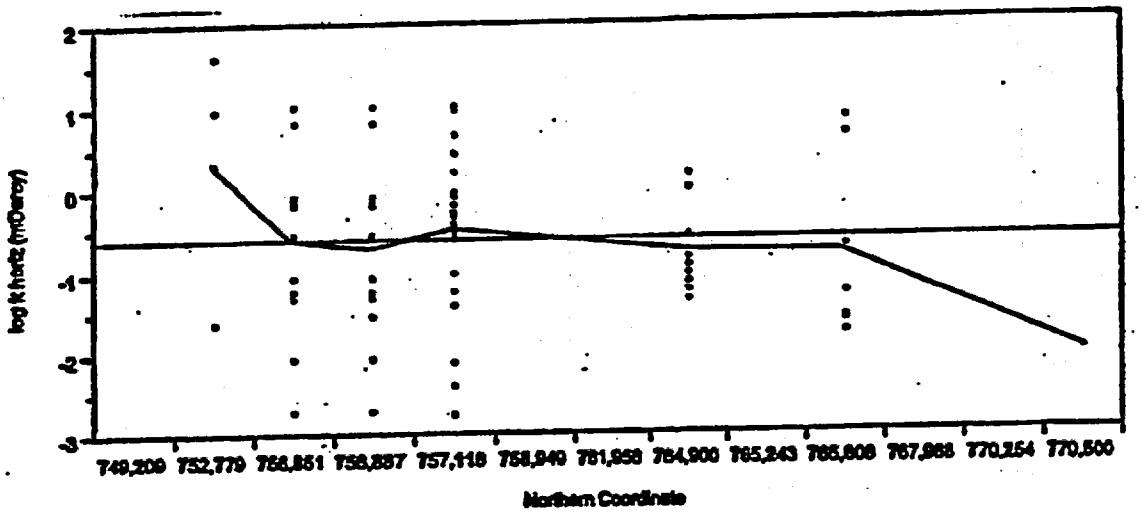

Lateral distribution of horizontal permeability.

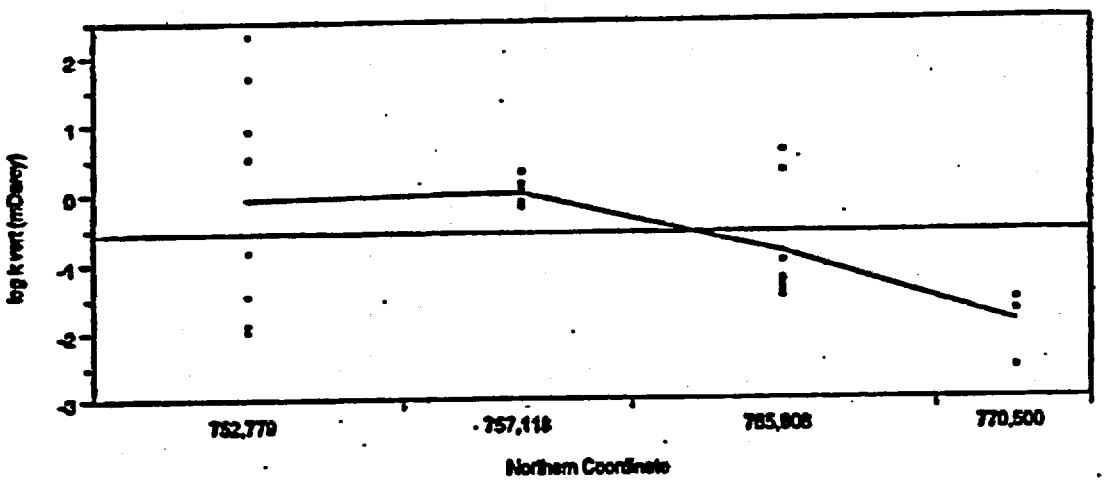

Lateral distribution of vertical permeability

83-72.CDR.133.SITEEXC

Figure 5.3-72. Distribution of Permeability in the Prow Pass Tuff

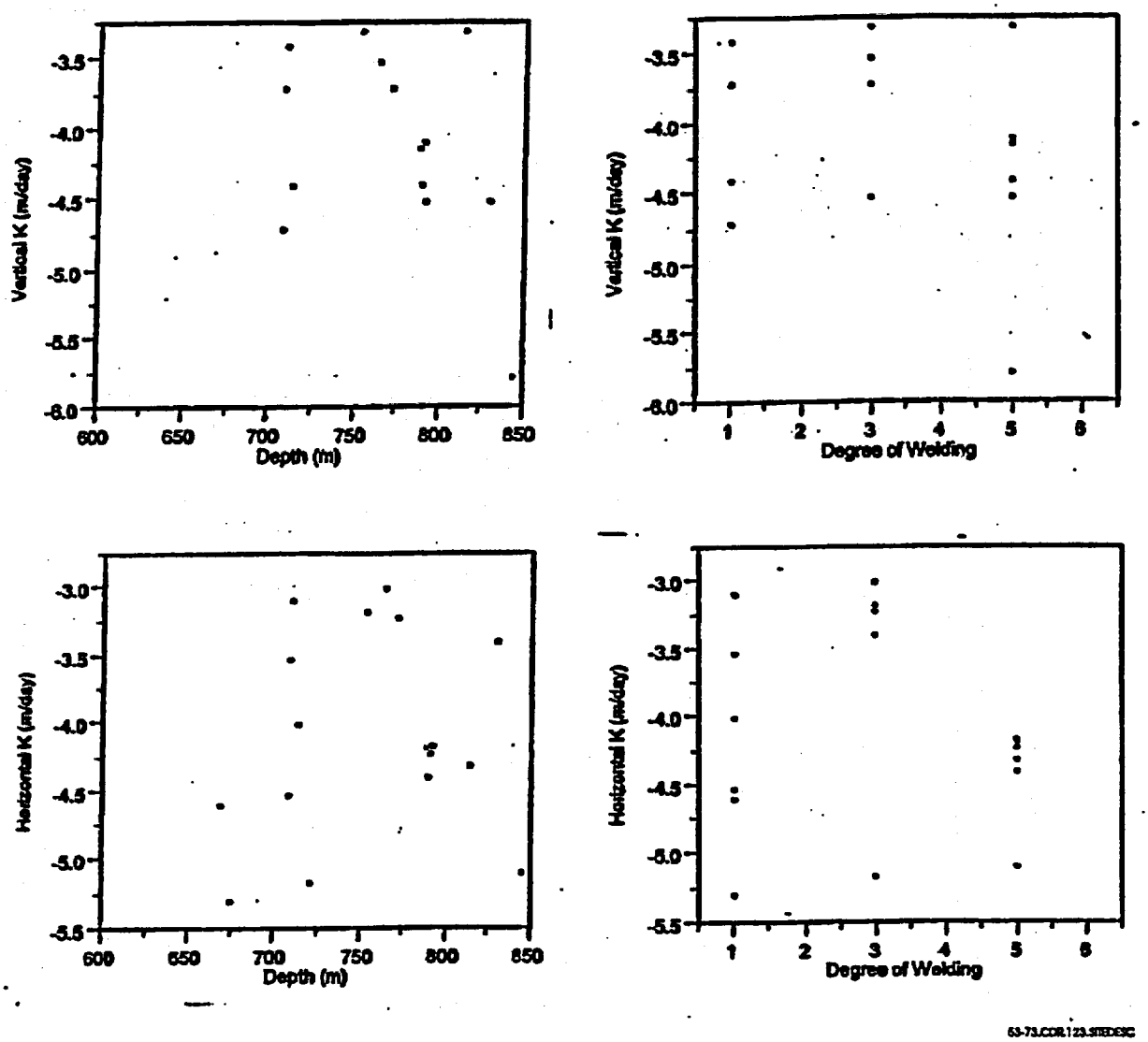

Figure 5.3-73. Relation of Hydraulic Conductivity in the Bullfrog Tuff to Depth and the Degree of Welding

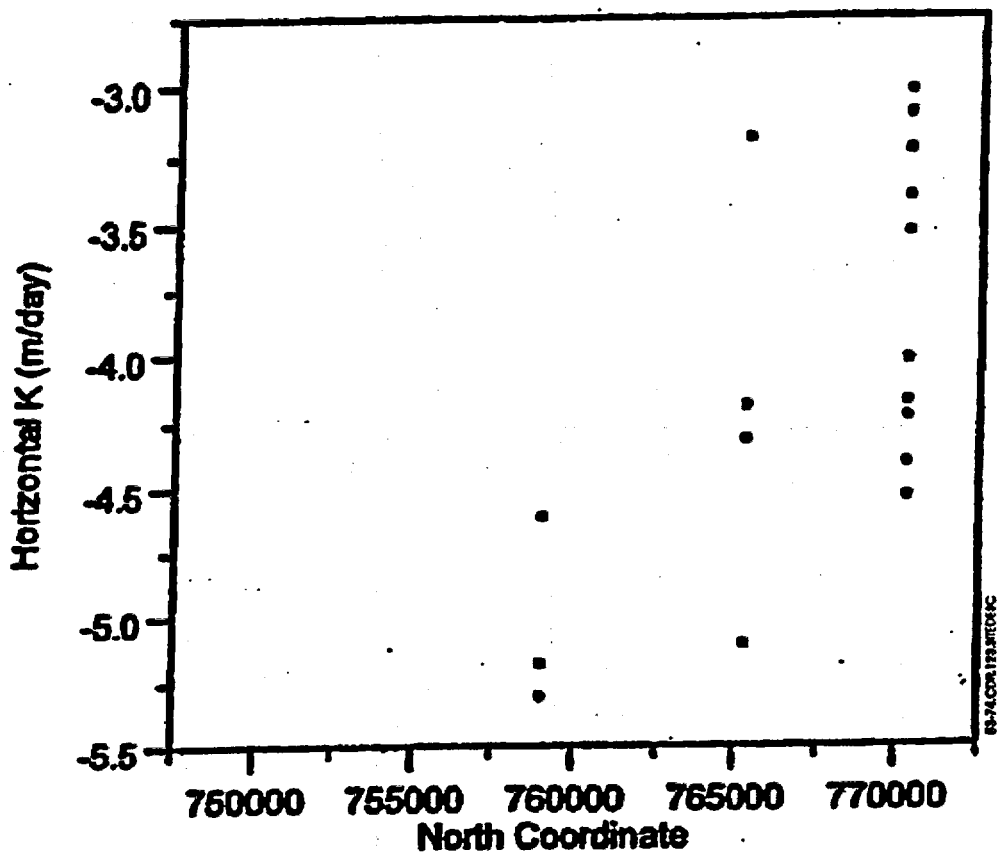

Figure 5.3-74. Lateral Distribution of Hydraulic Conductivity in the Bullfrog Tuff

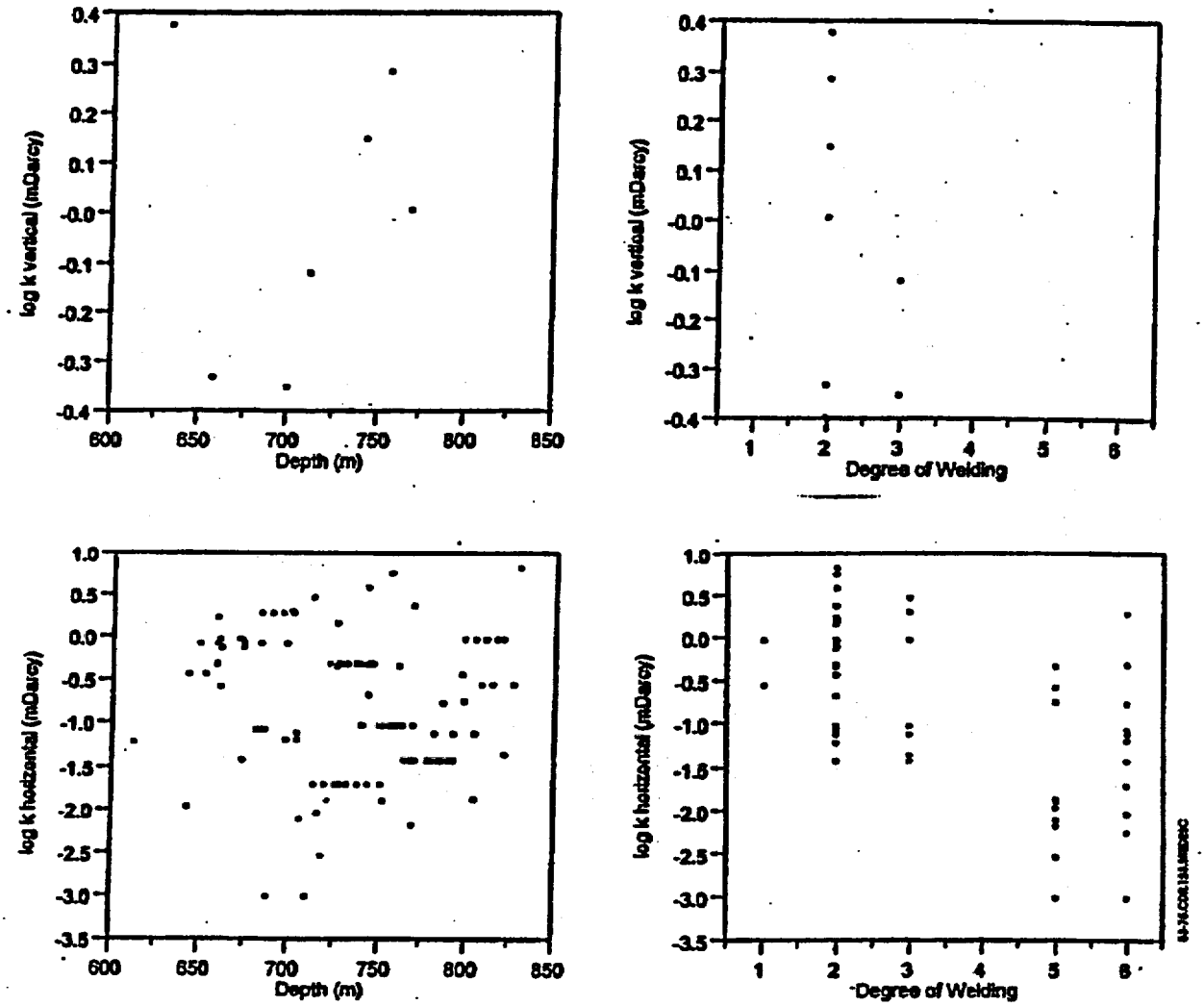

Figure 5.3-75. Permeability and the Relation to Depth and the Degree of Welding in the Bullfrog Tuff

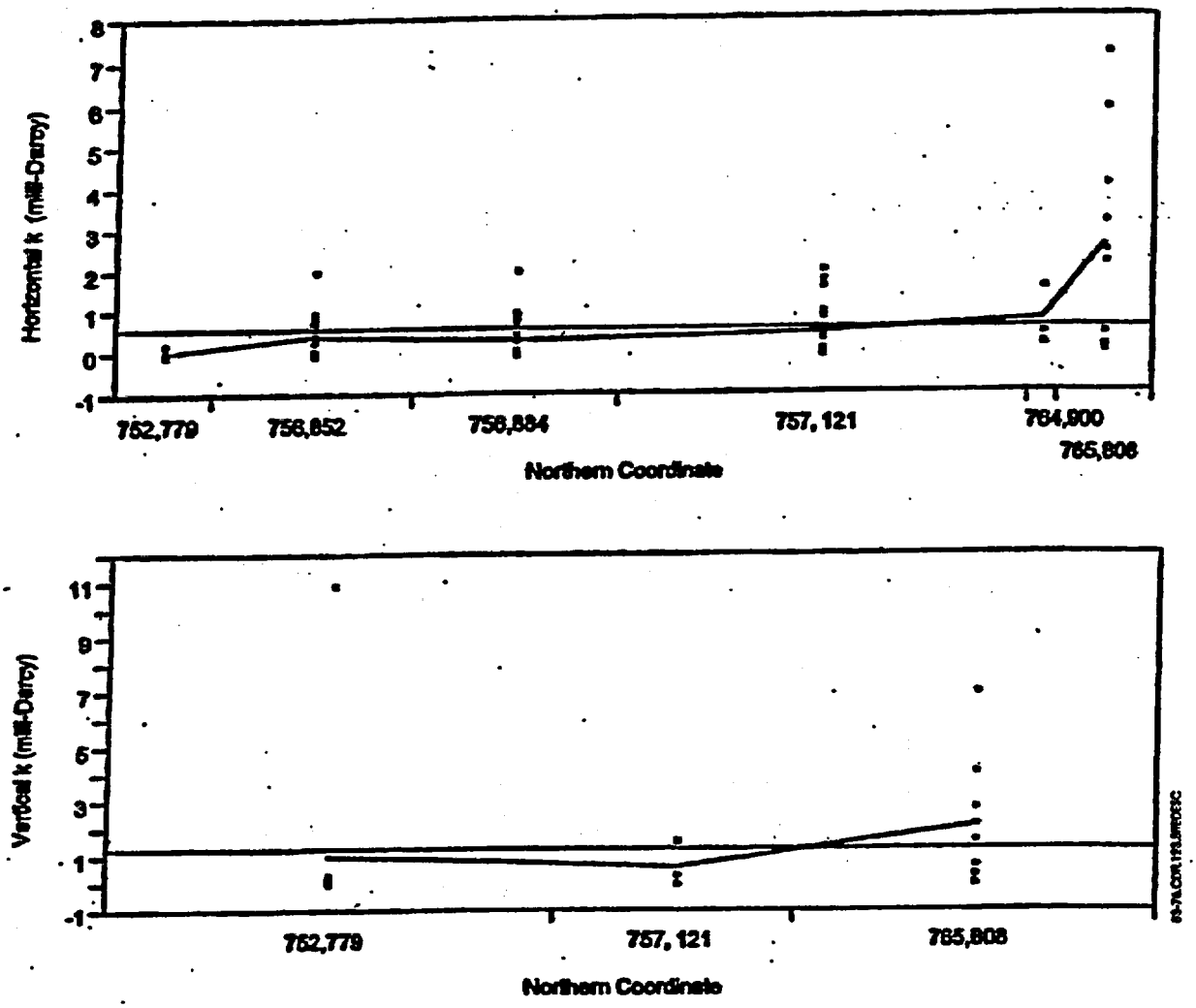

Figure 5.3-76. Distribution of Permeability in the Bullfrog Tuff

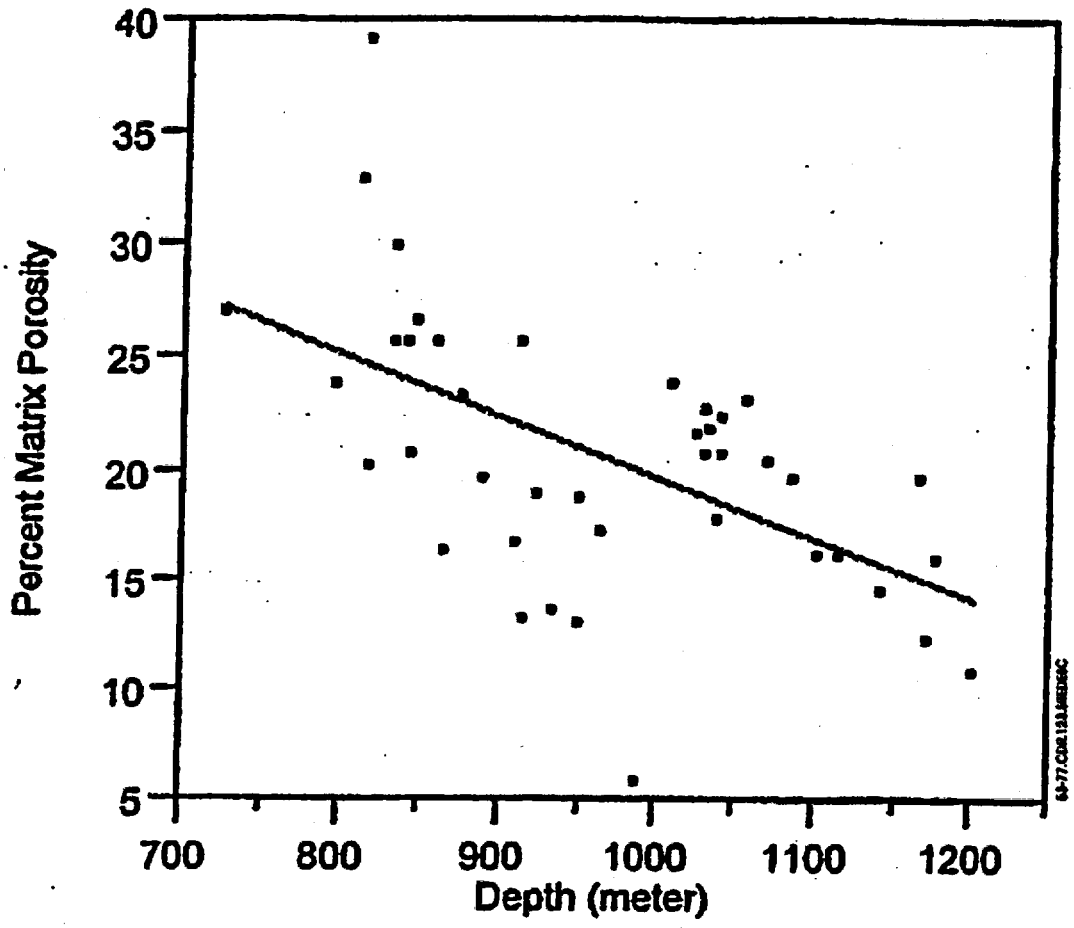

Figure 5.3-77. Relation of Matrix Porosity to Depth in the Tram Tuff

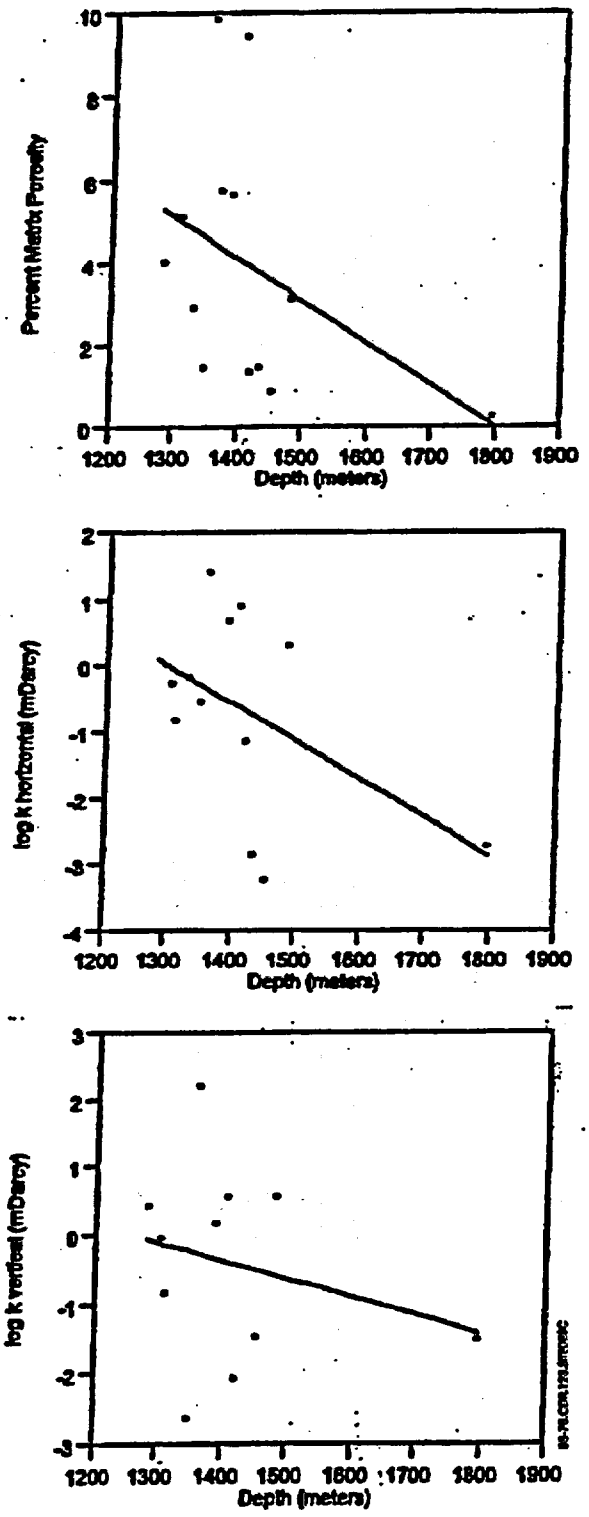

Figure 5.3-78. Changes in Porosity and Permeability with Depth in the Lower Carbonate Aquifer

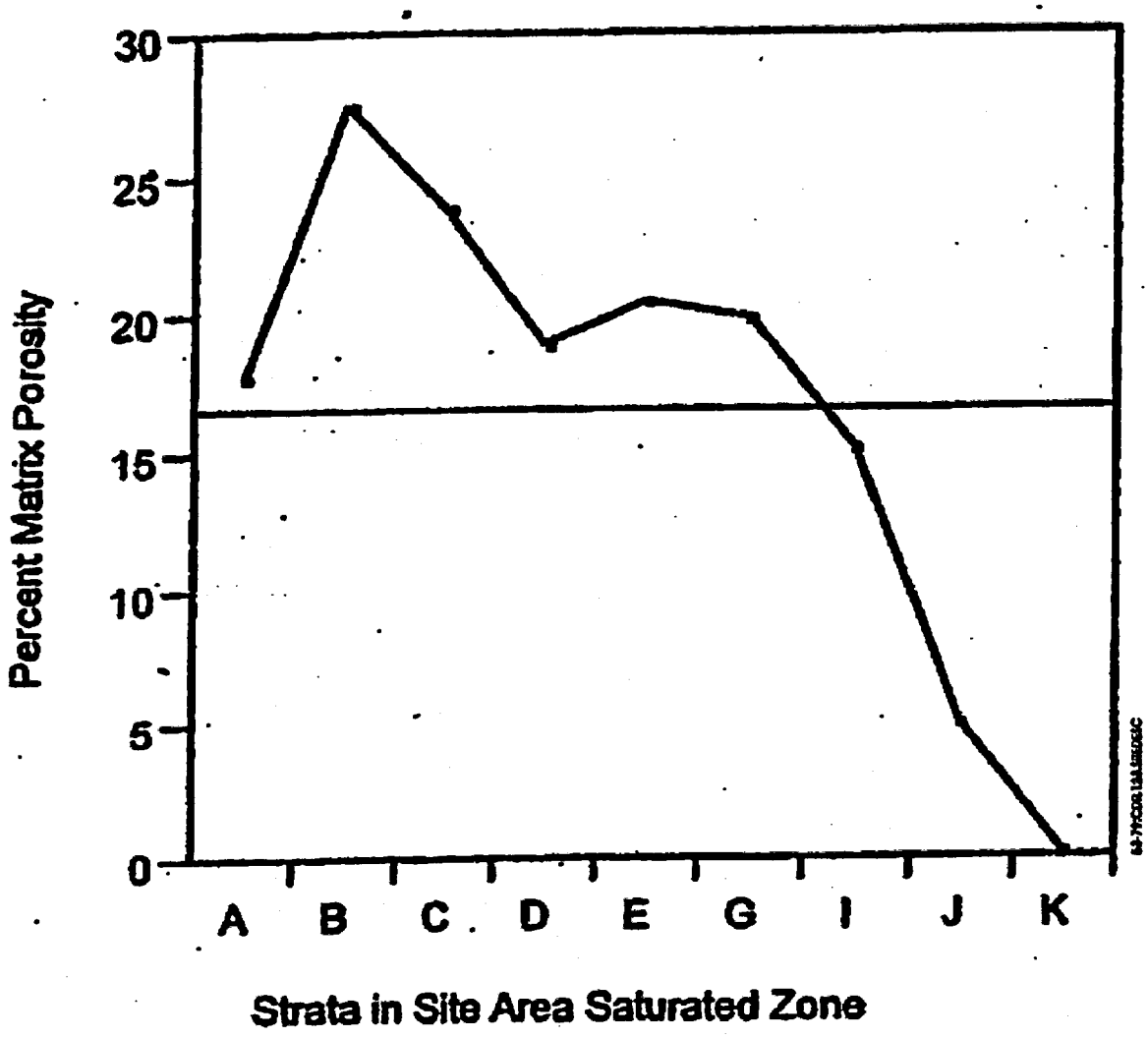

Figure 5.3-79. Mean Porosity for Strata in the Site Area Saturated Zone Groundwater Flow System

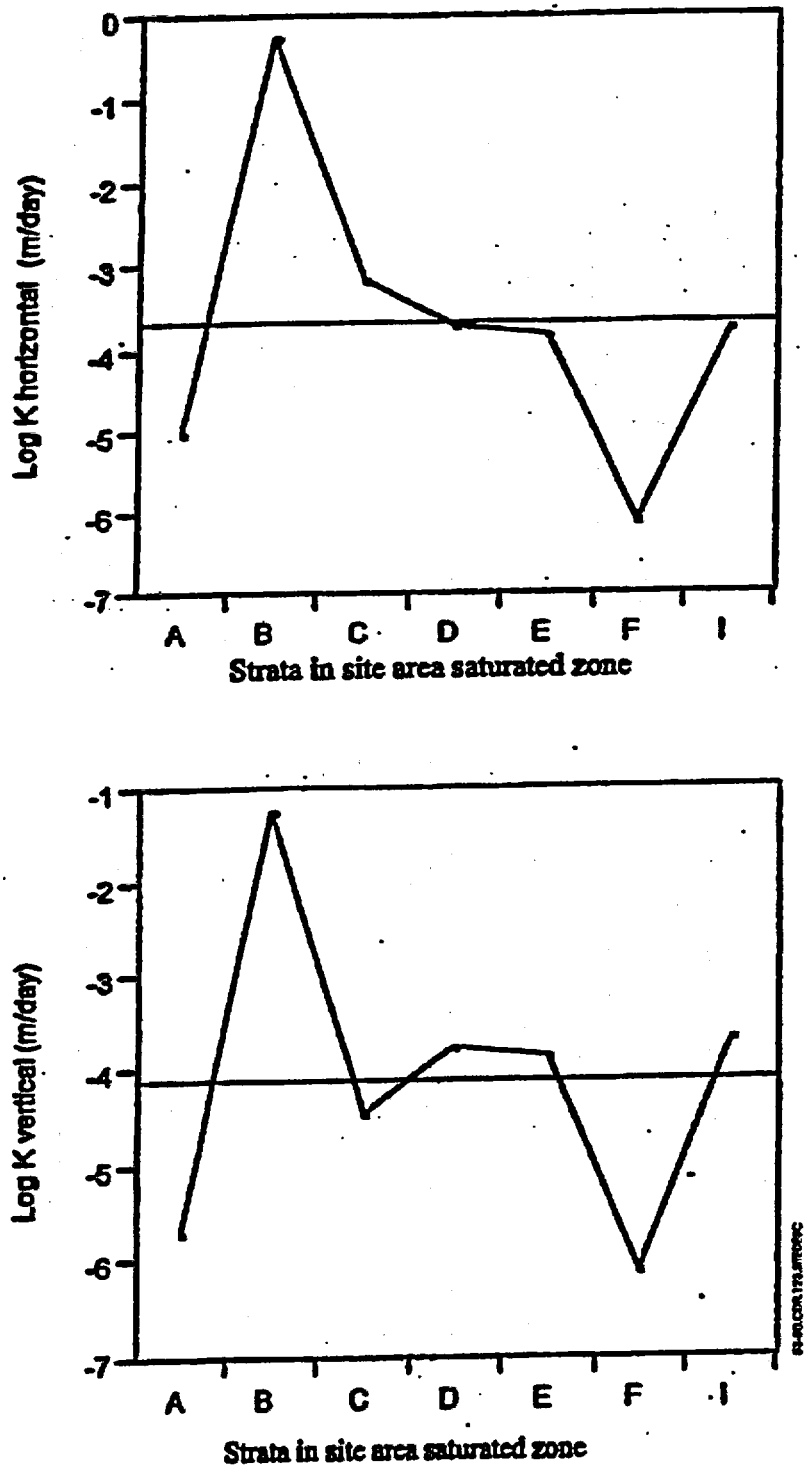

Figure 5.3-80. Hydraulic Conductivity for Strata in the Site Area Saturated Zone

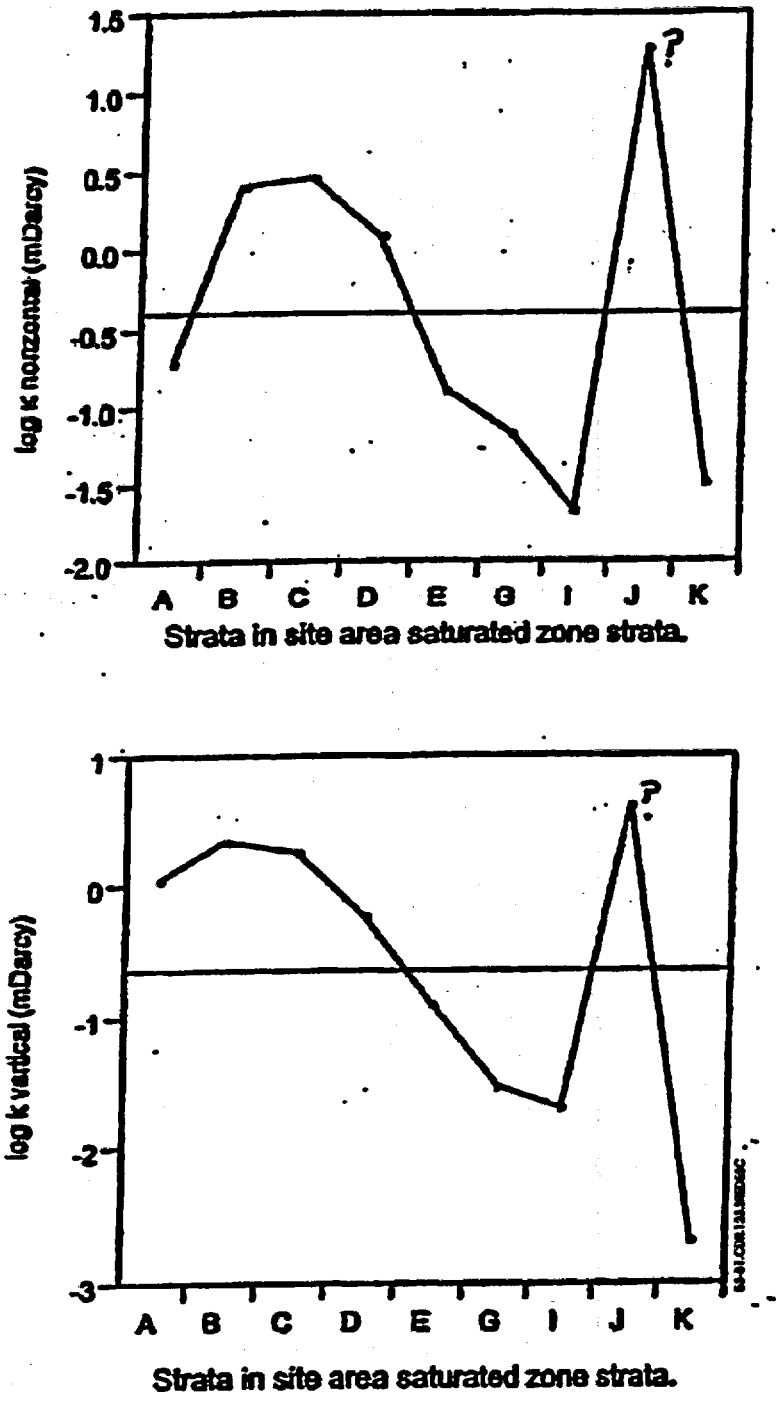

Figure 5.3-81. Permeability for Strata in the Site Area Saturated Zone

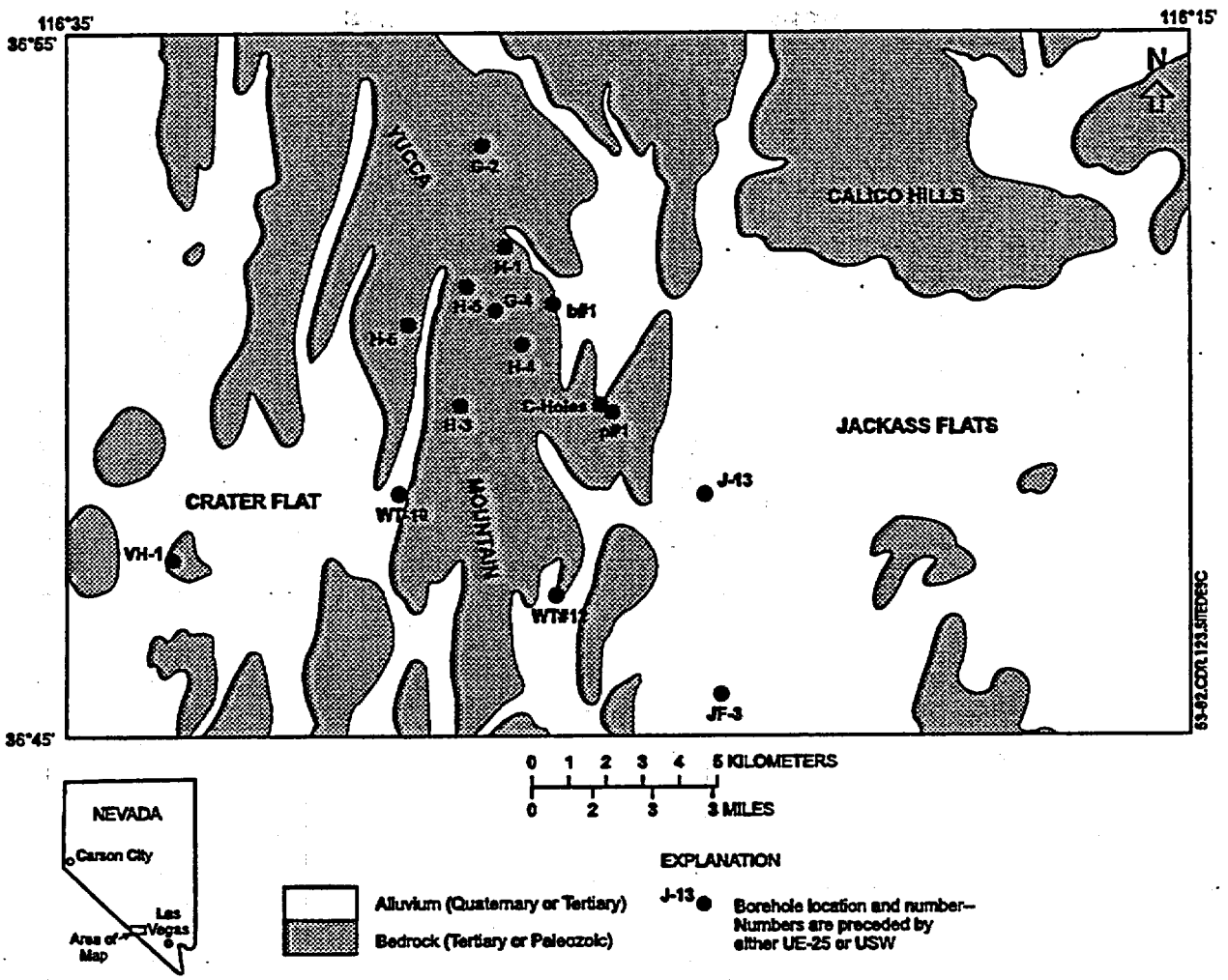

Figure 5.3-82. Locations of Boreholes in Which Hydraulic Tests Have Been Conducted in the Vicinity of Yucca Mountain

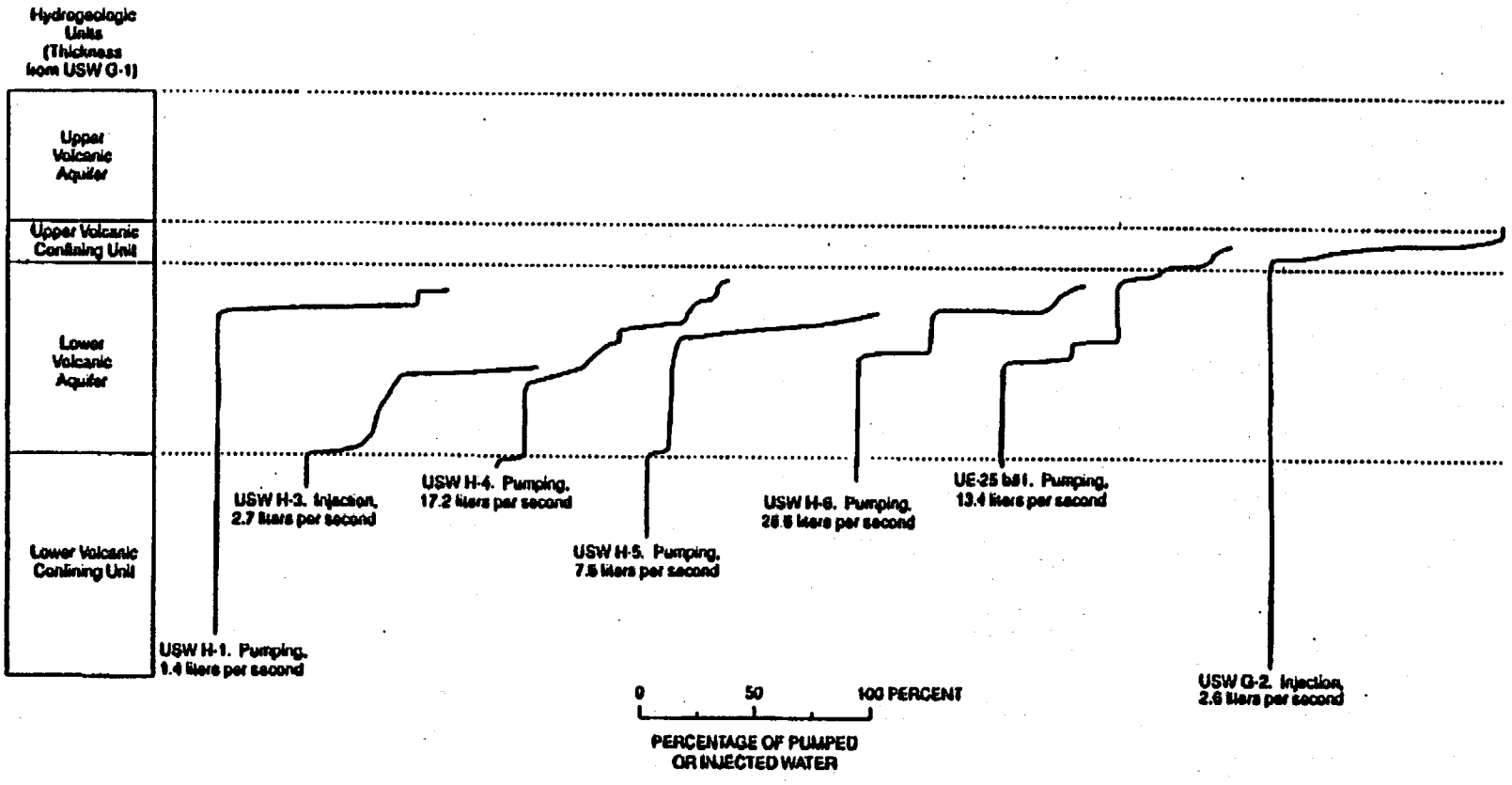

NOTE: Flow surveys adjusted to a "standard thickness" of the lower volcanic aquifer of 524.3 meters and a "standard thickness" of the upper confining unit of 121.3 meters, the thickness of the units in borehole USW G-1. All flow surveys are from 0 to 100 percent of total pumping or injection.

Figure 5.3-83. Flow Surveys for Selected Boreholes in the Yucca Mountain Area

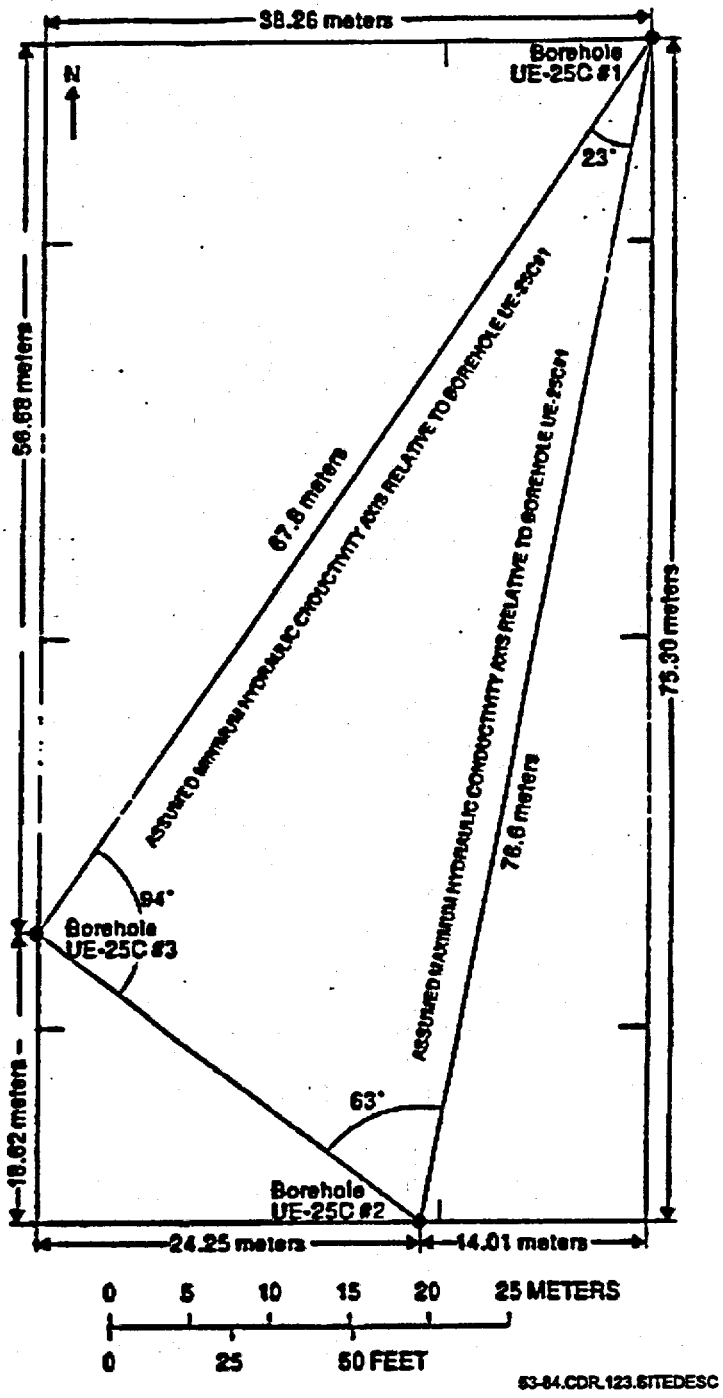

Figure 5.3-84. Locations of Borehole at the C-Hole Complex

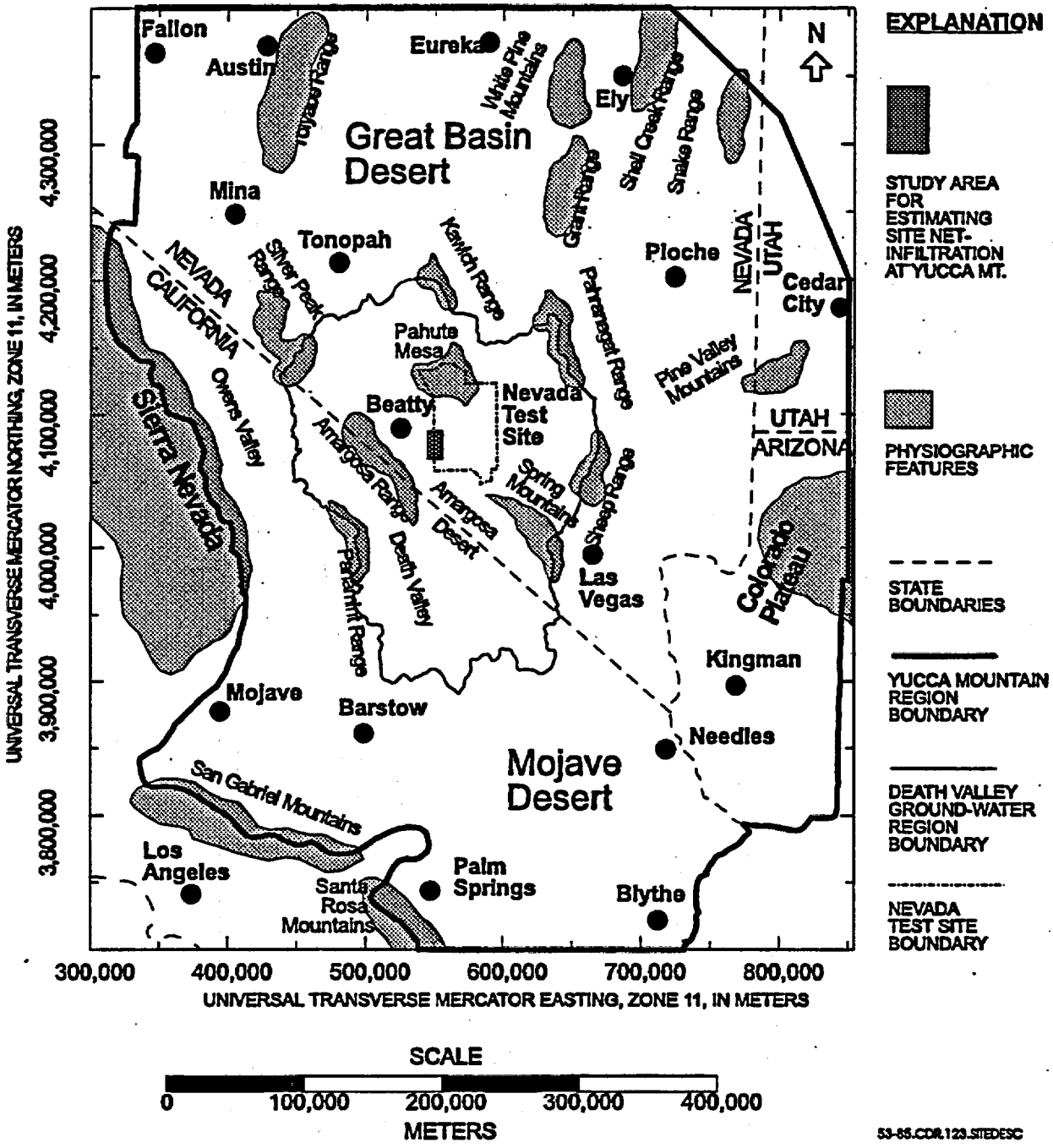

Figure 5.3-85. Regional Study Area for Infiltration and Recharge Studies

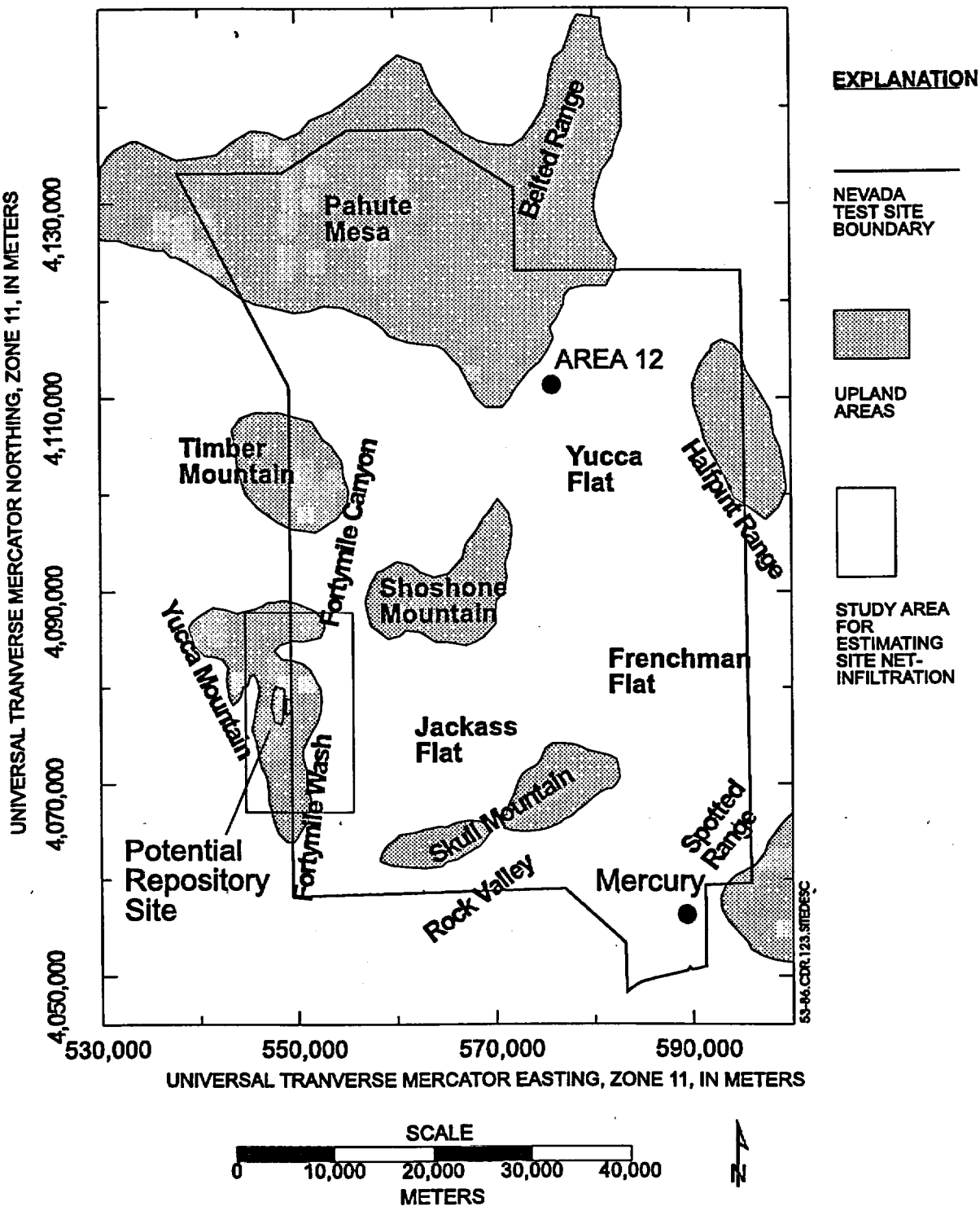

Figure 5.3-86. Location of Study Area for Estimating Site Net Infiltration

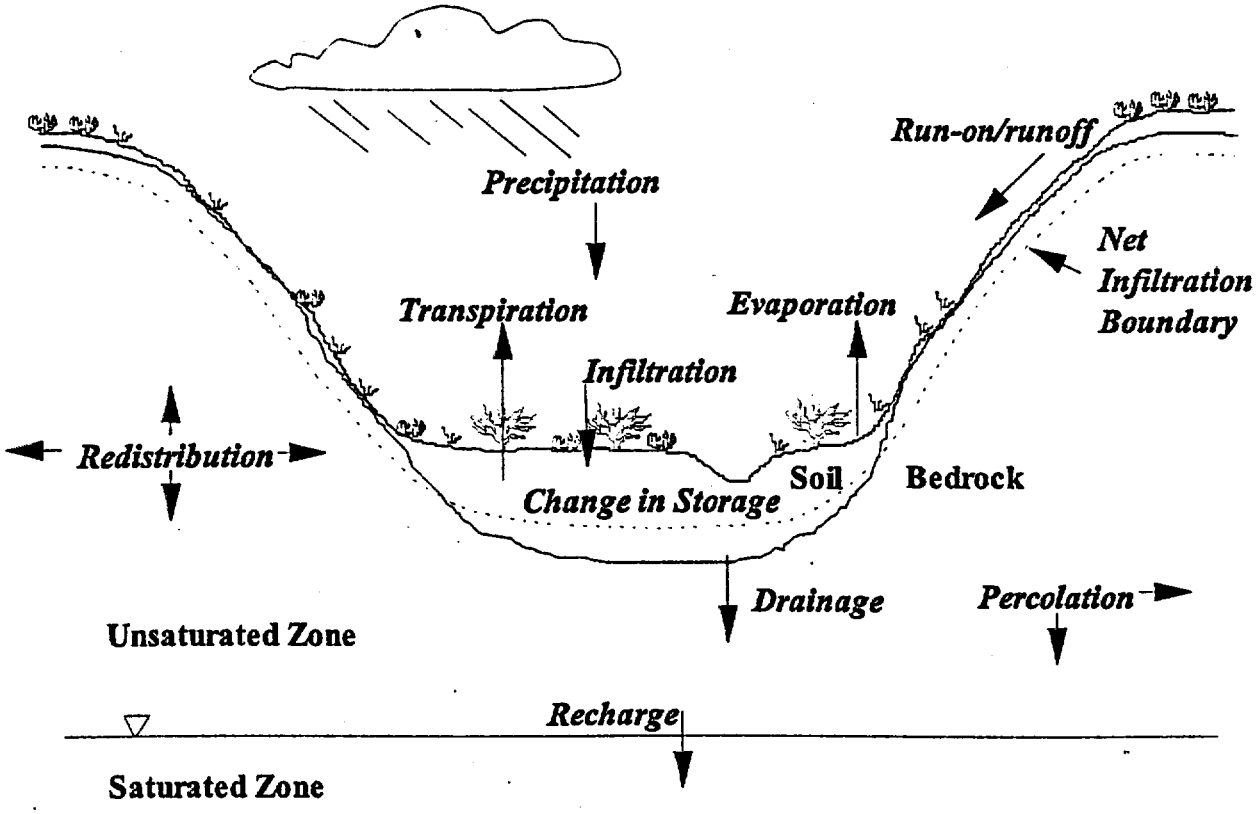

Precipitation + Change in Storage - Drainage - ET - Runoff = 0

53-87.CDR.123.SITEDESC

Figure 5.3-87. Schematic of Hydrologic Cycle Illustrating Surficial and Subsurface Processes Affecting Net Infiltration and Recharge

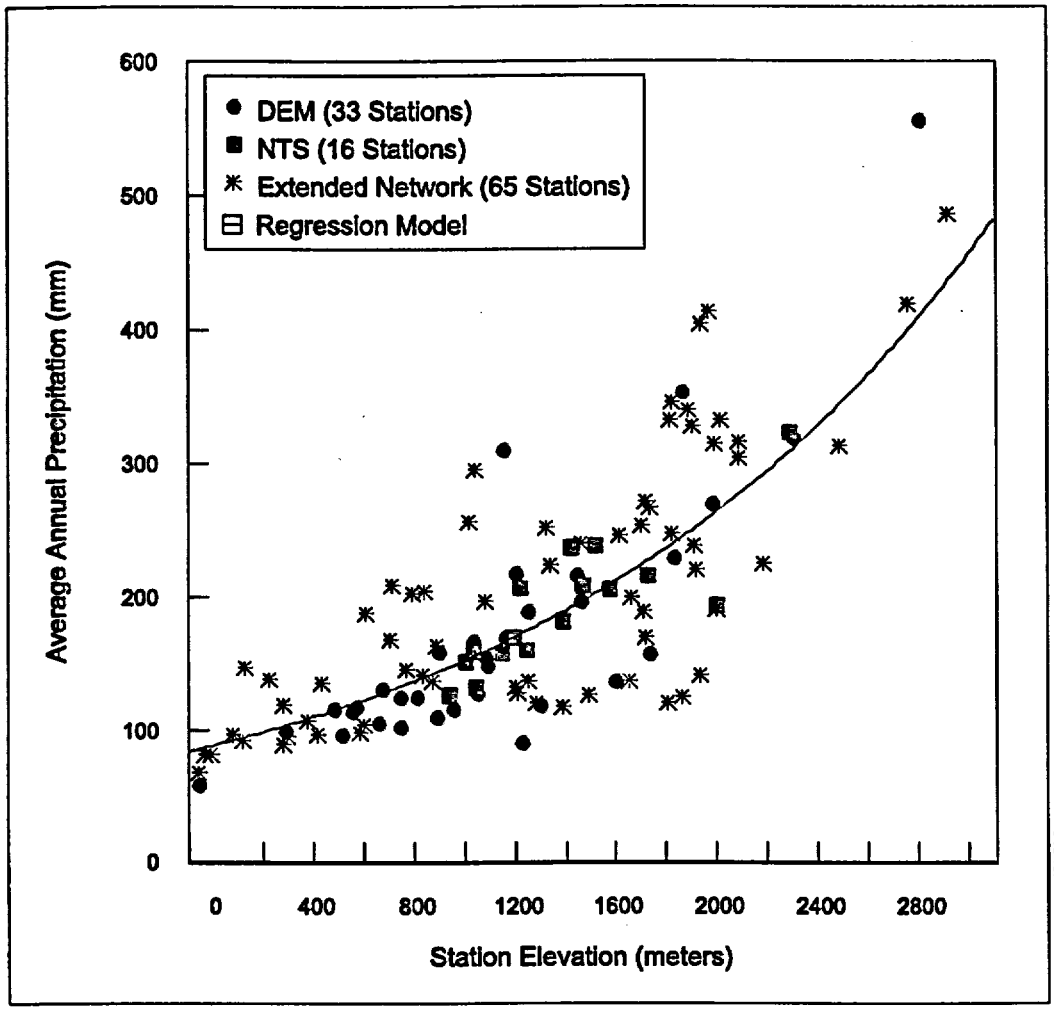

Figure 5.3-88. Average Annual Precipitation Versus Elevation for 114 Precipitation Stations with a Minimum of Eight Complete Years of Record in the Yucca Mountain Region

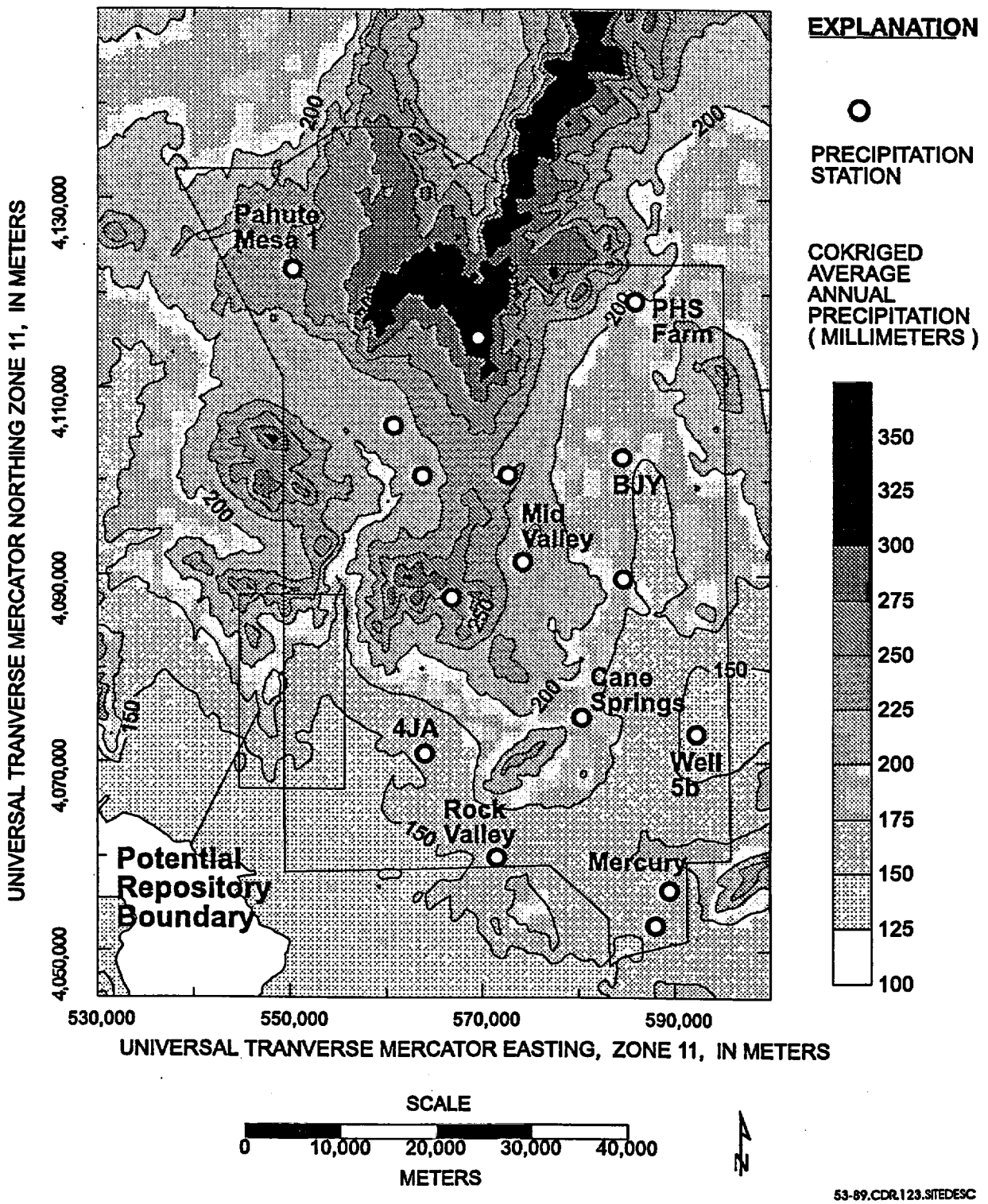

Figure 5.3-89. Estimated Average Annual Precipitation for Yucca Mountain and the Nevada Test Site

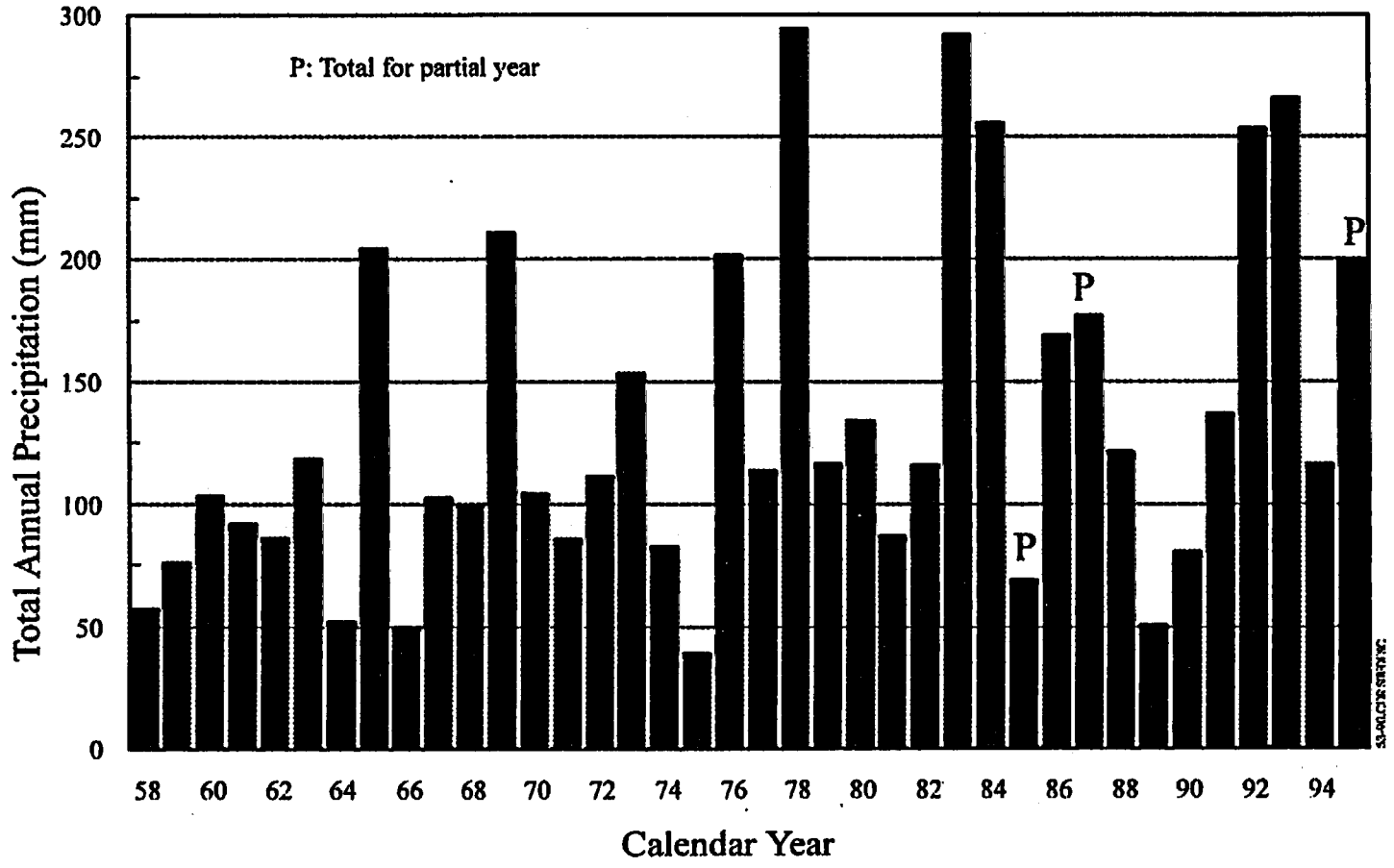

Figure 5.3-90. Total Annual Precipitation for Station 4JA from 1958 through 1995

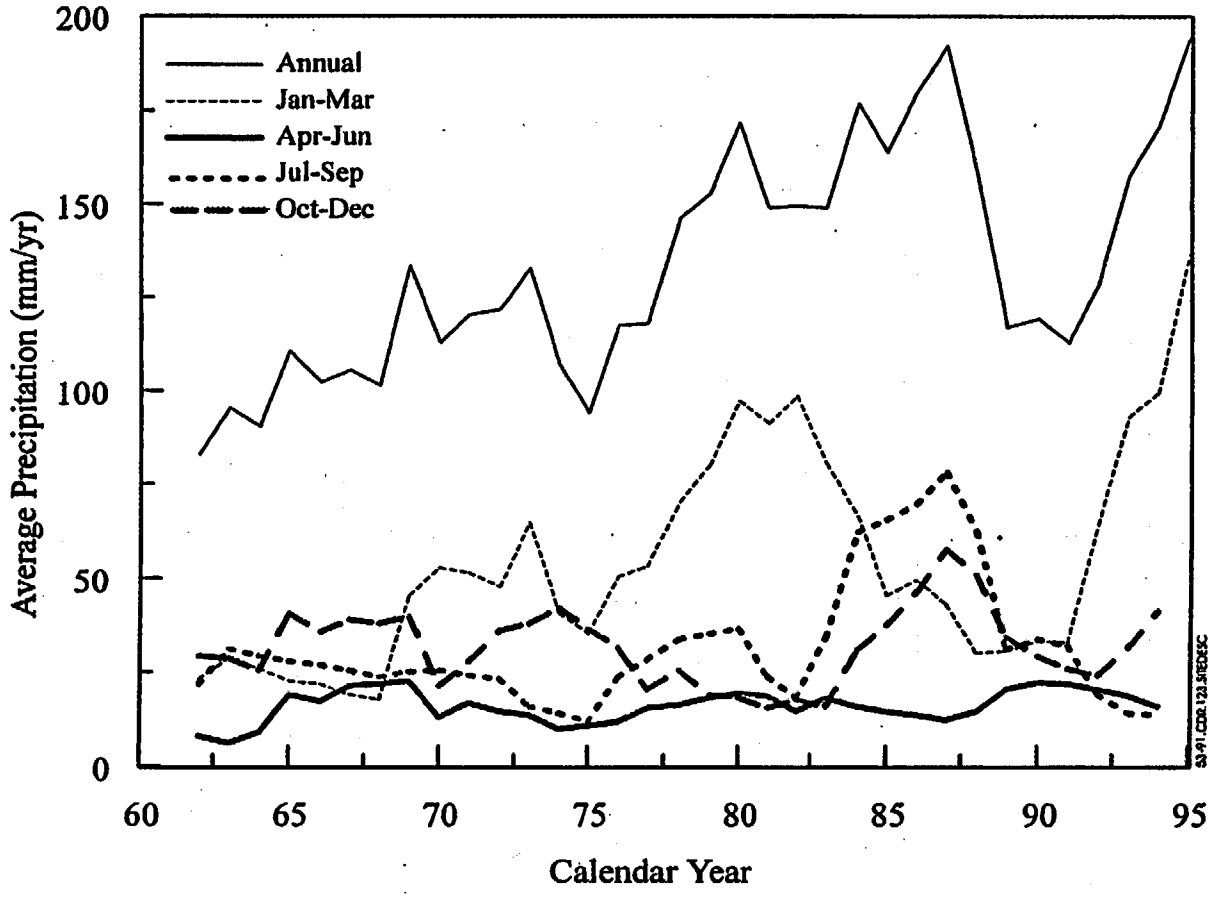

Figure 5.3-91. Five-Year Sliding Mean for Total Annual and Three-Month Total Precipitation at Station 4JA

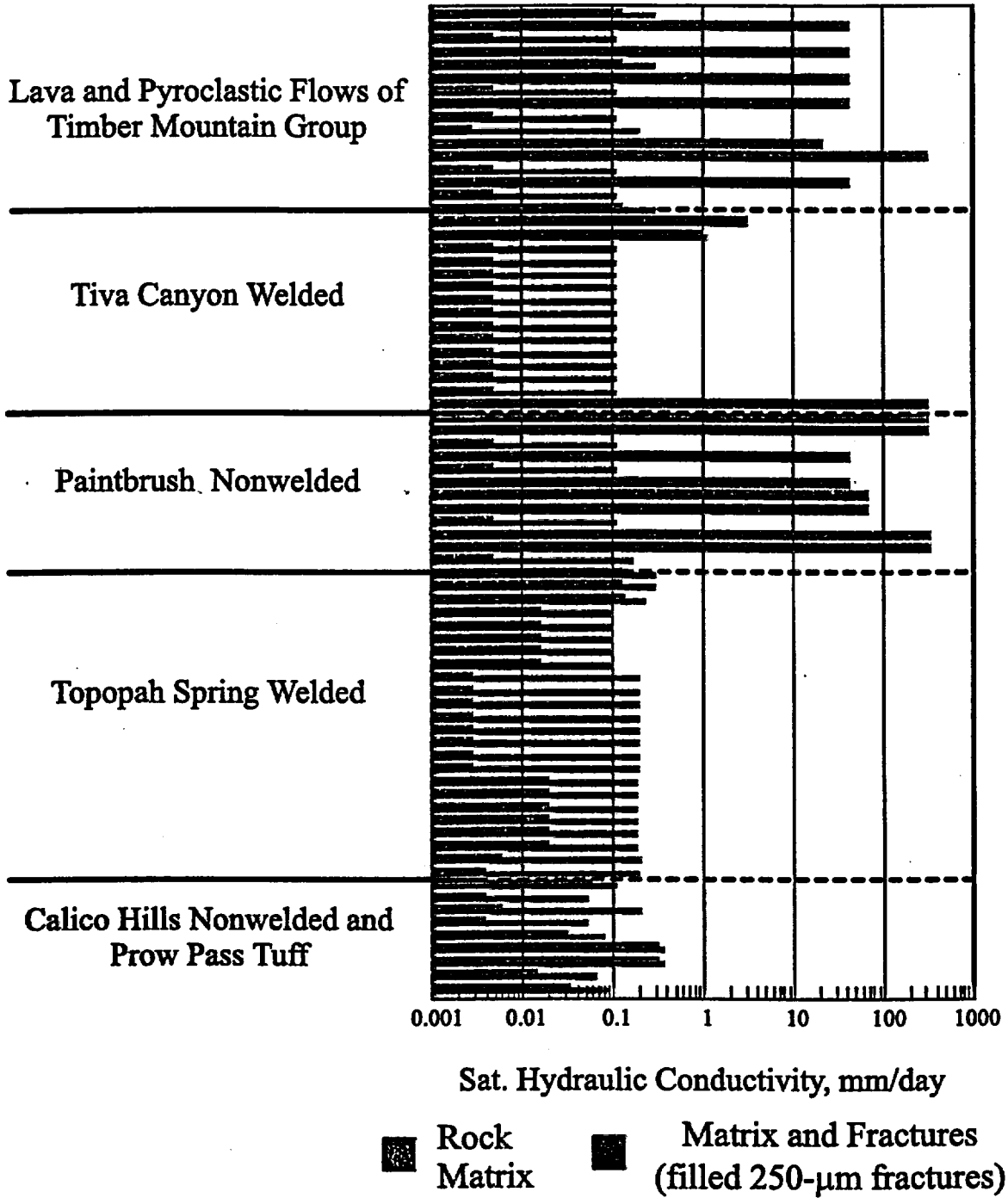

Figure 5.3-92. Saturated Hydraulic Conductivity for Bedrock Matrix and Effective Conductivity for Combined Matrix and Fractures for Filled 250-µm Fractures for Lithostratigraphic Units Within Major Hydrogeologic Units

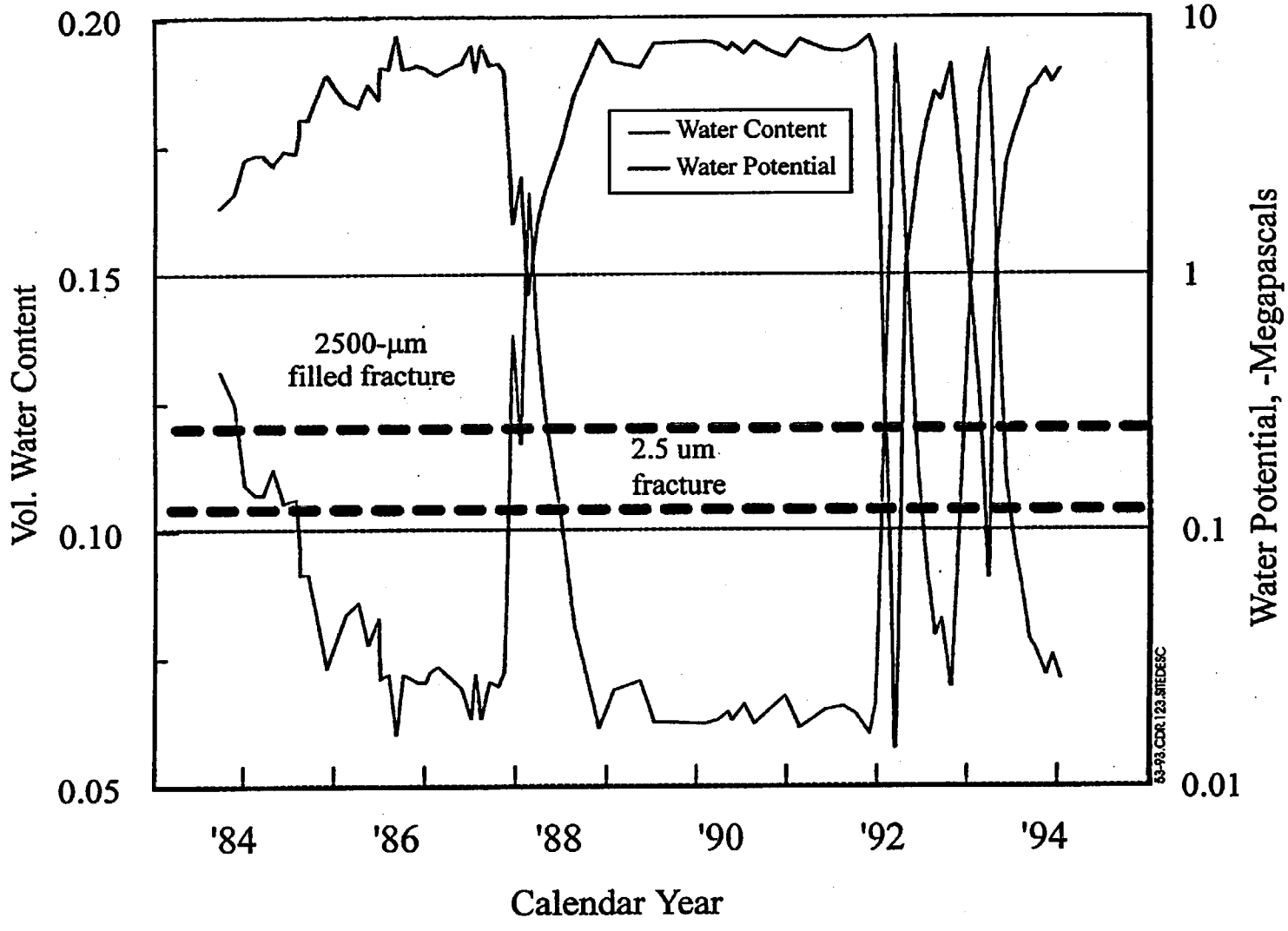

Figure 5.3-93. Water Content and Water Potential at the Soil-Bedrock Interface at a Depth of 2.1 m in Borehole USW UZ-N52

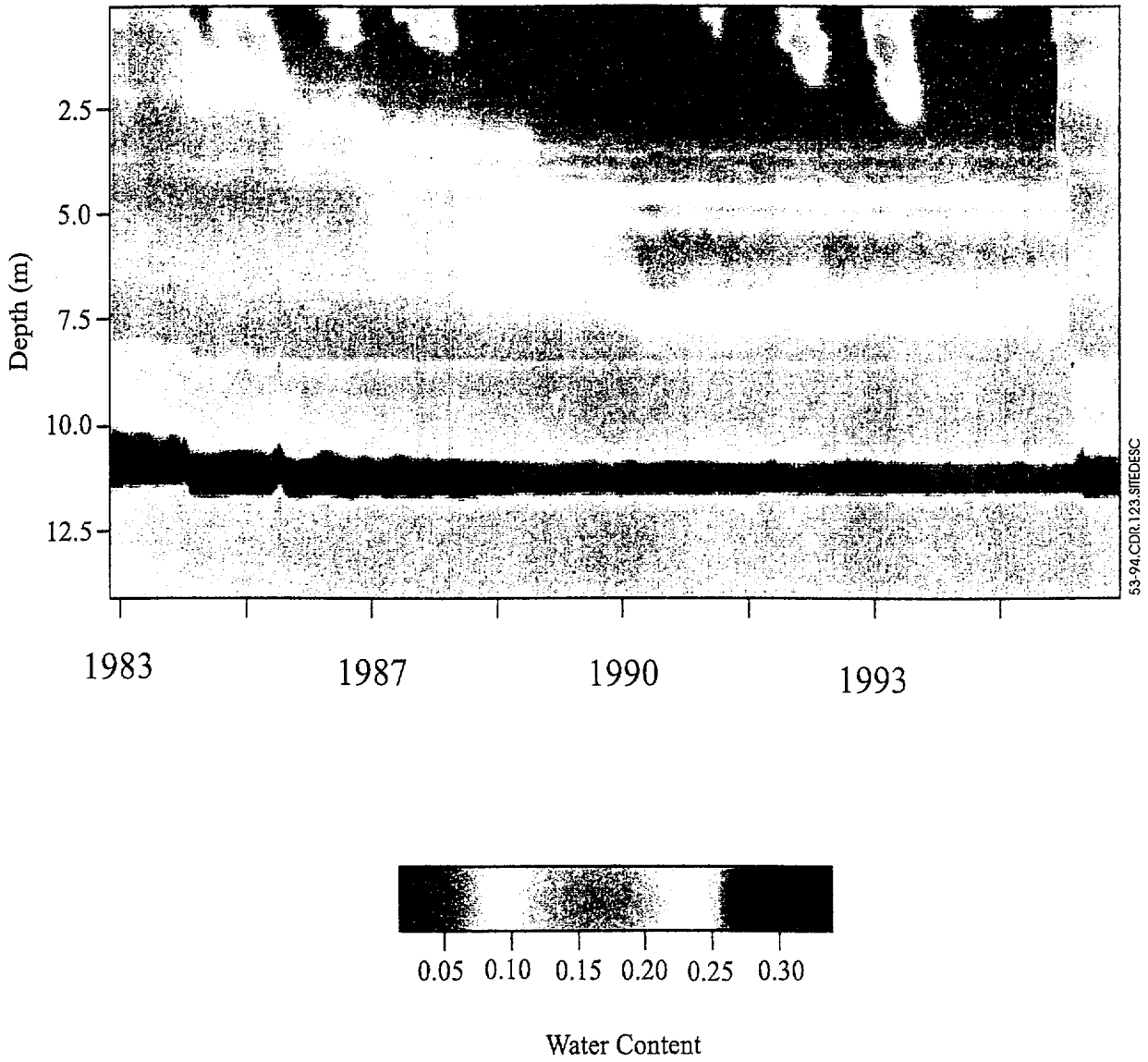

Figure 5.3-94. Depth Versus Time Profile of Measured Water Contents in Borehole N1 for 1984 Through 1995

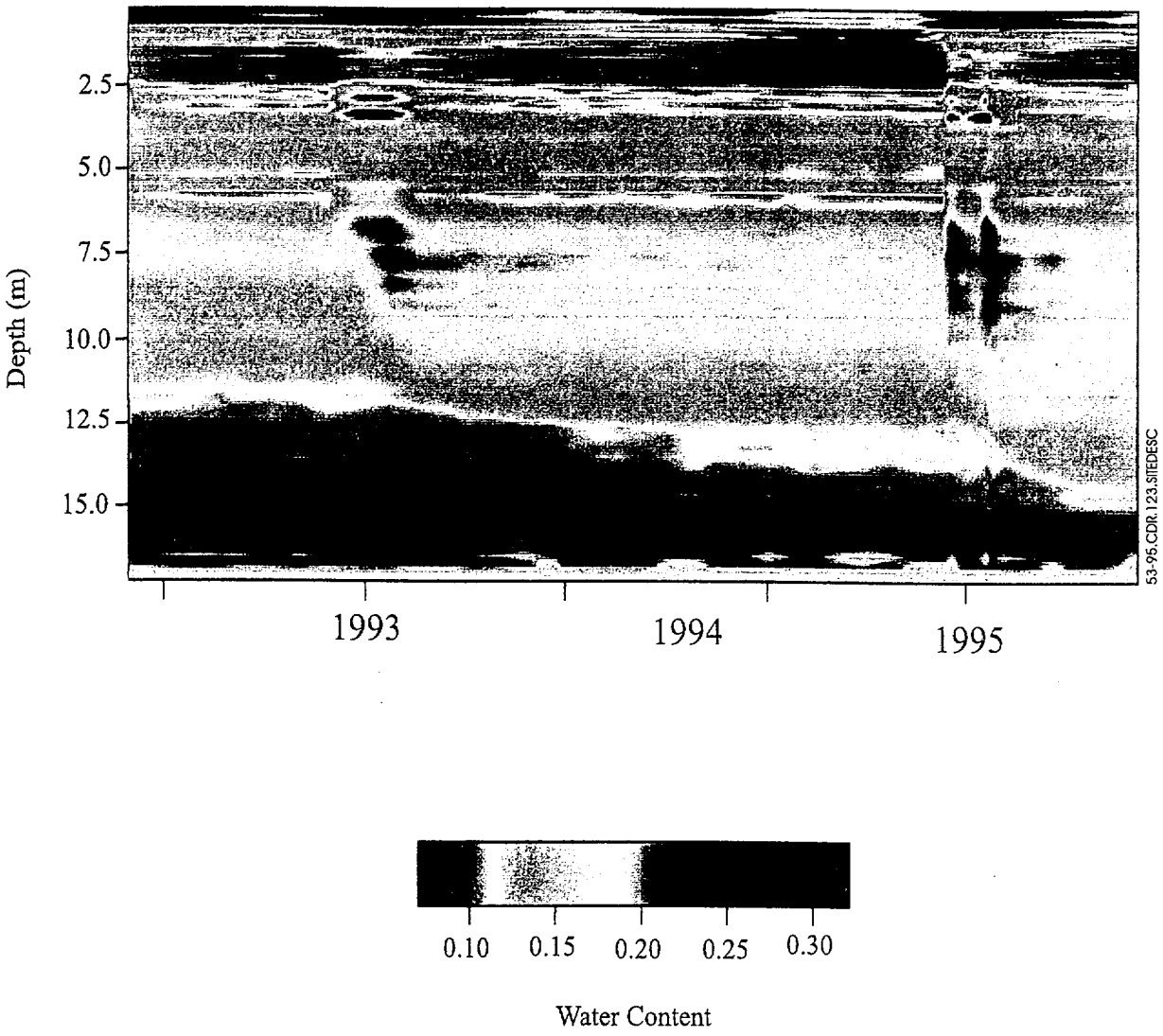

Figure 5.3-95. Depth Versus Time Profile of Measured Water Contents in Borehole N15 for 1993 Through 1995

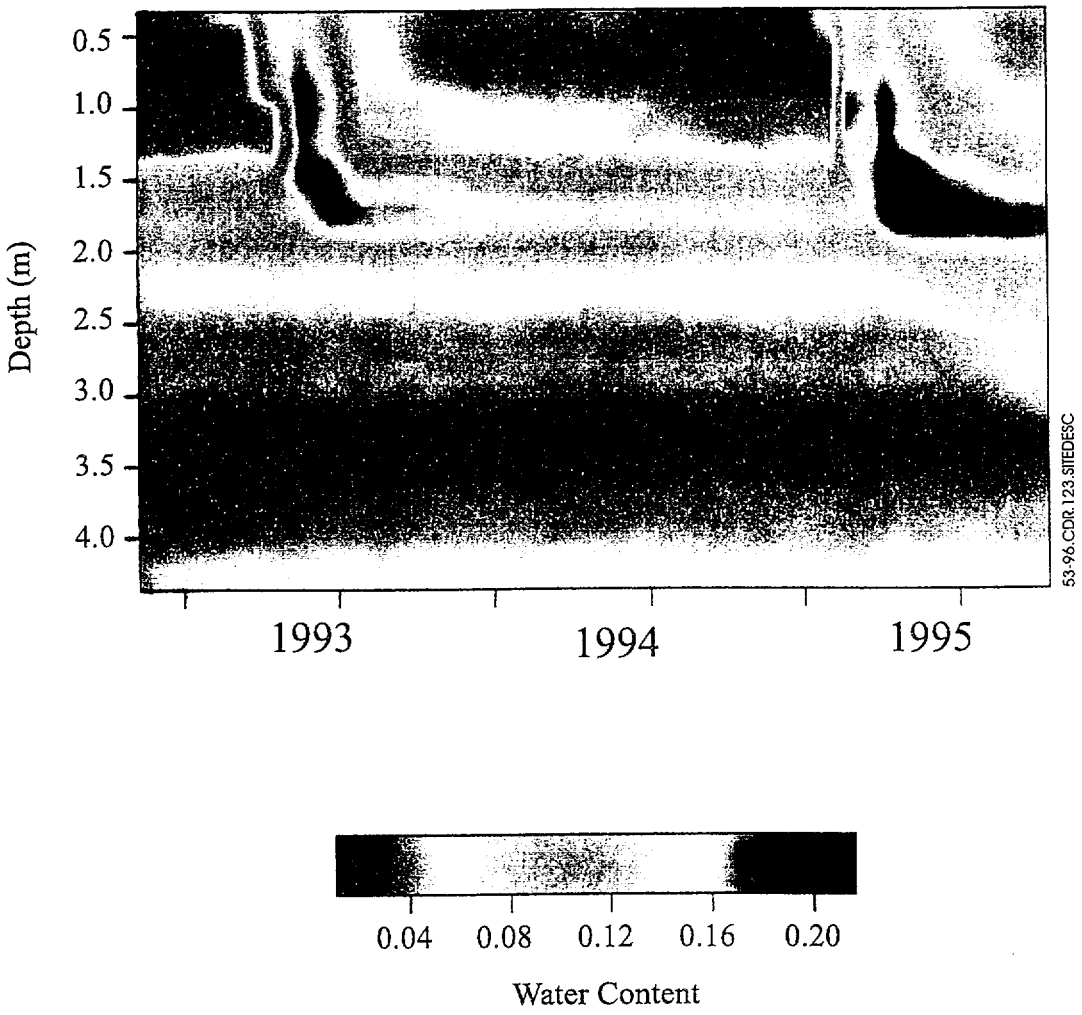

Figure 5.3-96. Depth Versus Time Profile of Measured Water Contents in Borehole N63 for 1993 Through 1995

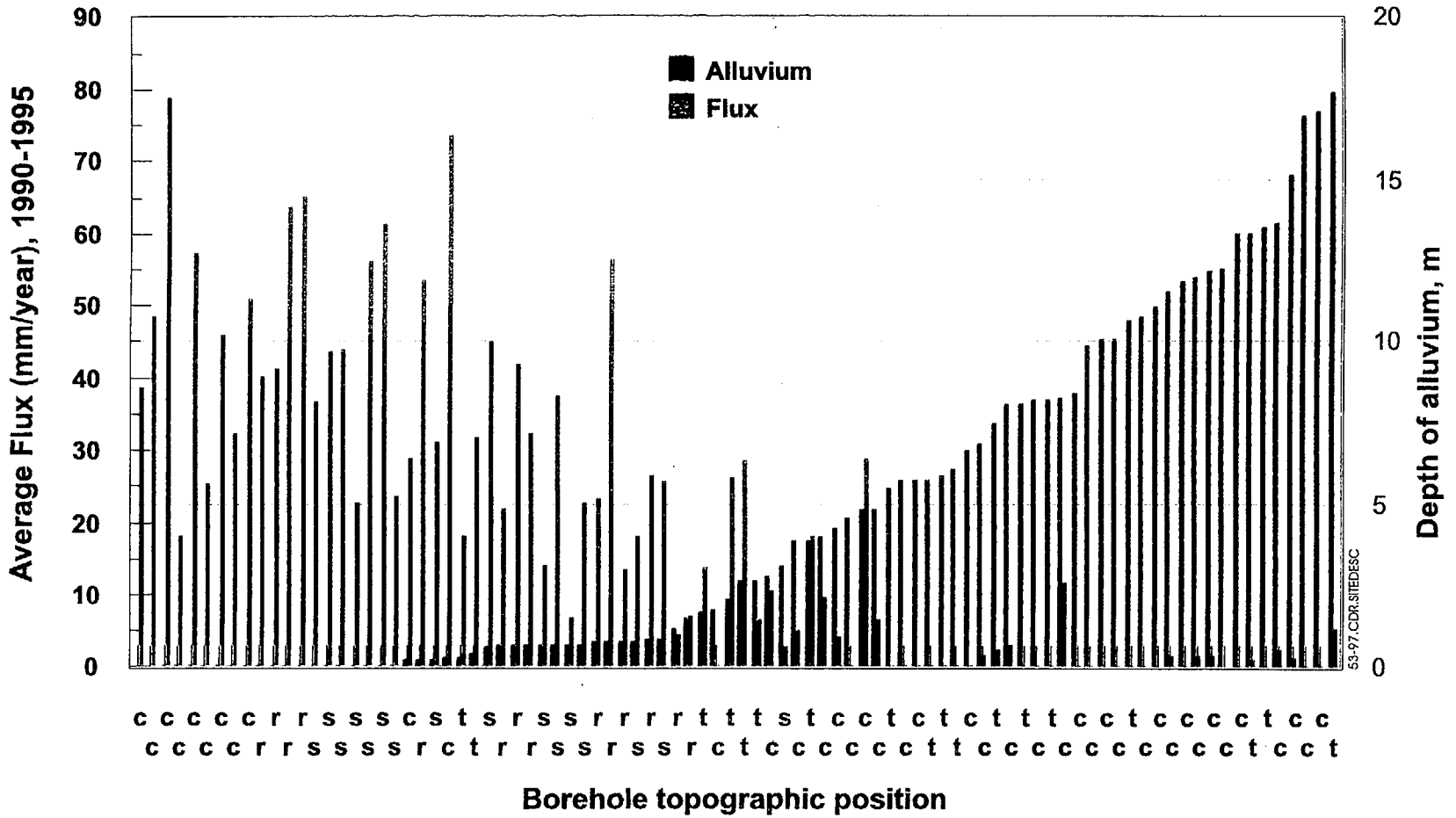

Figure 5.3-97. Average Annual Infiltration Through the Top 1 m of Bedrock at Neutron Boreholes for 1990 through 1995 Compared to Depth of Alluvium

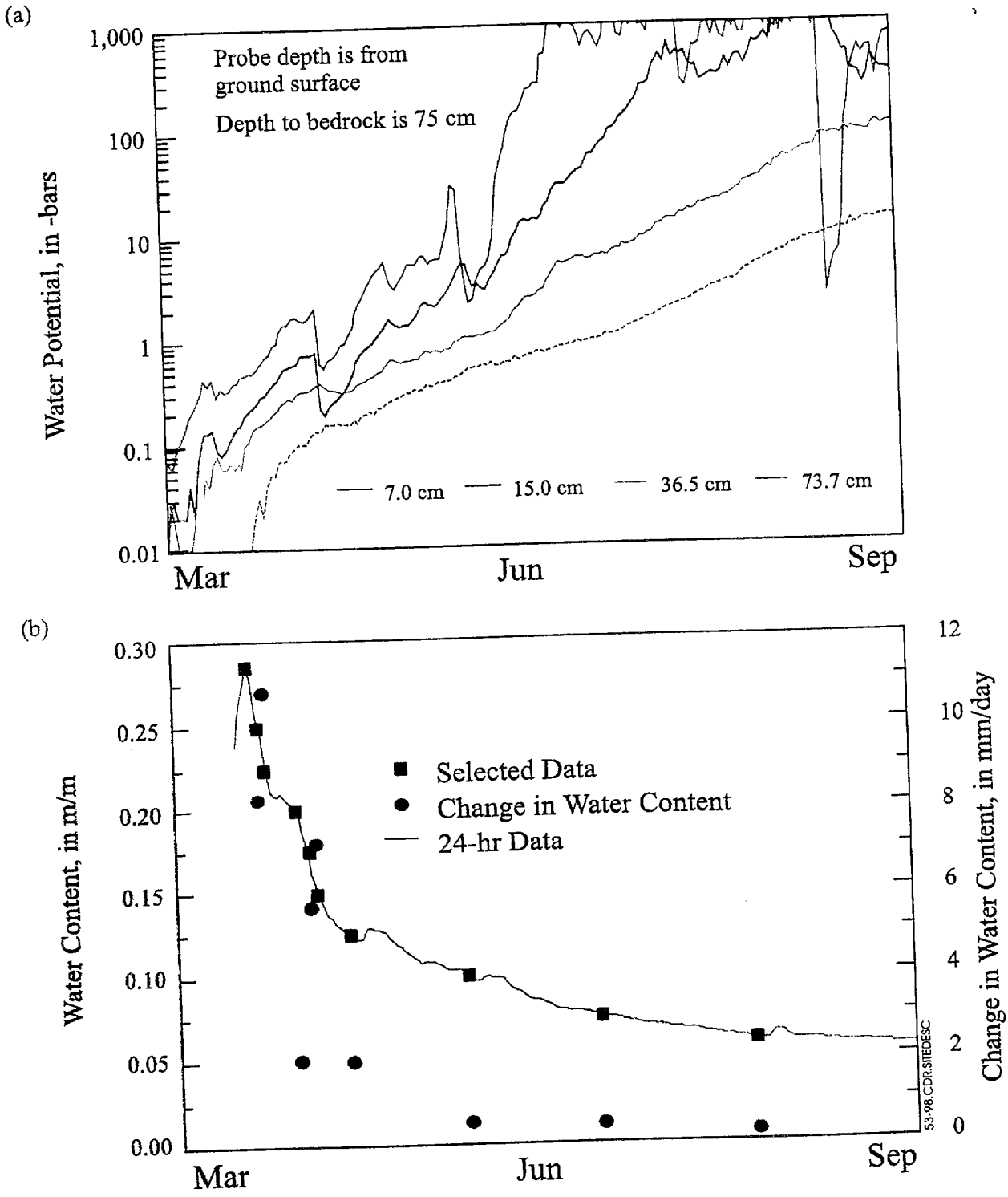

Figure 5.3-98. (a) Water-Potential Measurements at Four Depths near Borehole N15 During March-September 1995 and (b) Calculated Water Content Used to Estimate Infiltration Flux

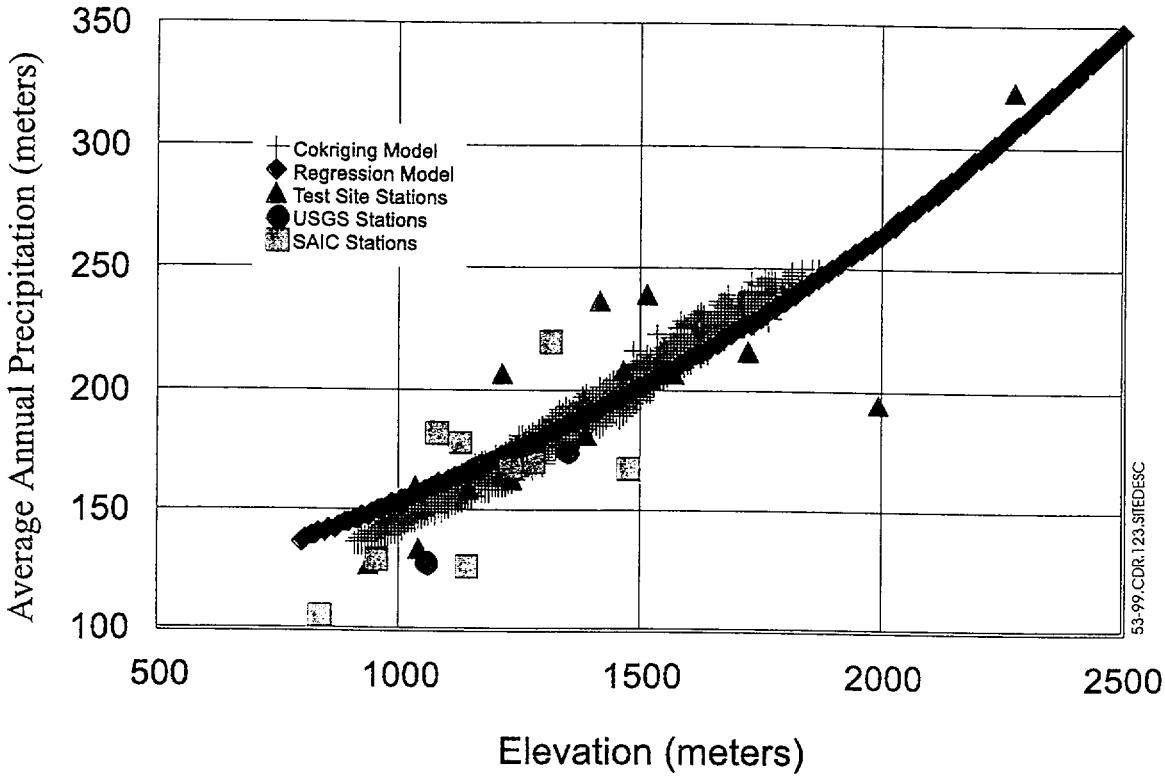

Figure 5.3-99. Comparison of Measured and Modeled Precipitation as a Function of Elevation for Yucca Mountain and the Nevada Test Site

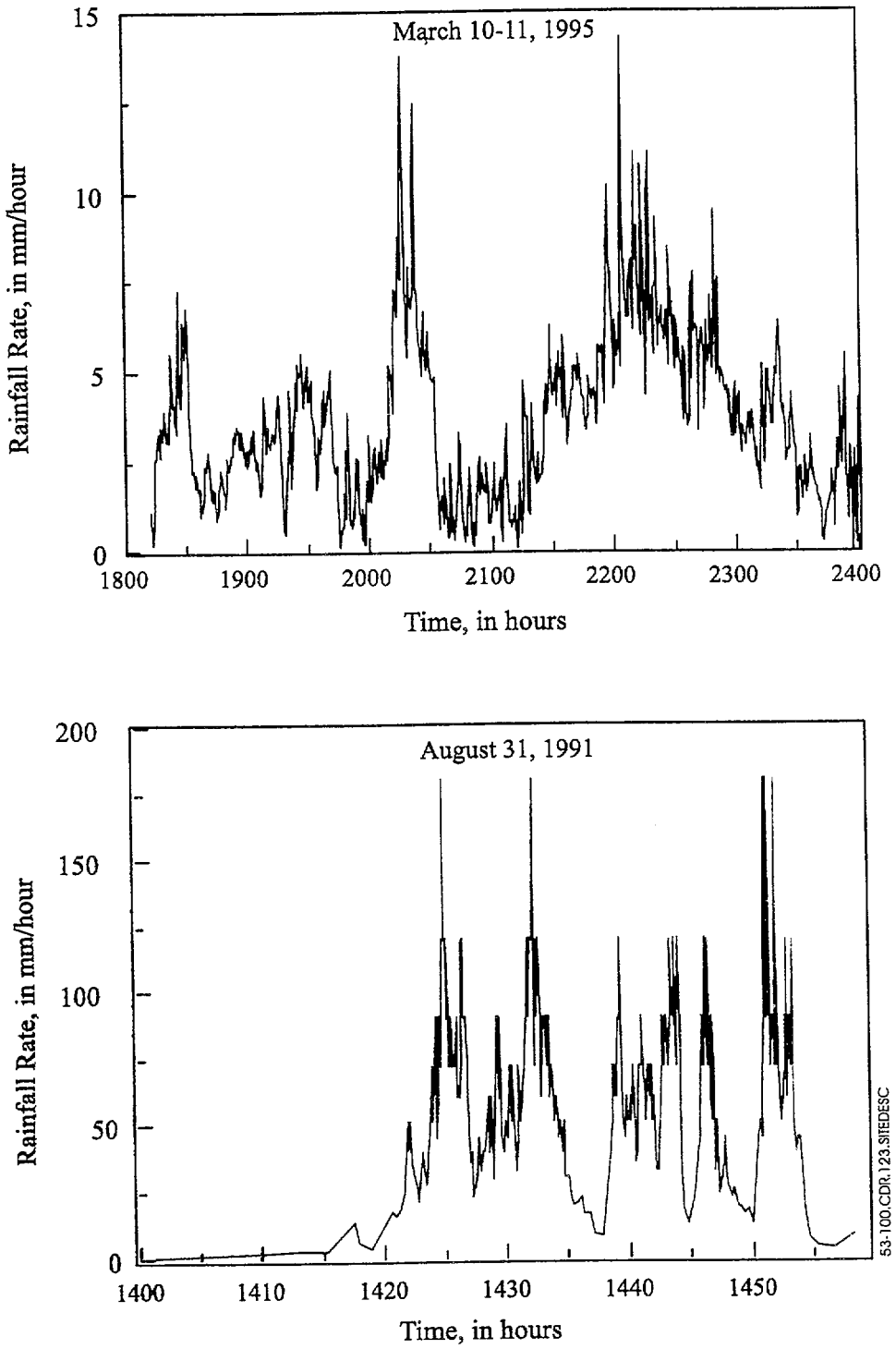

Figure 5.3-100. Measured Precipitation Rates for the Summer Storm of August 31, 1991 and the Winter Storm of March 10 to 11, 1995

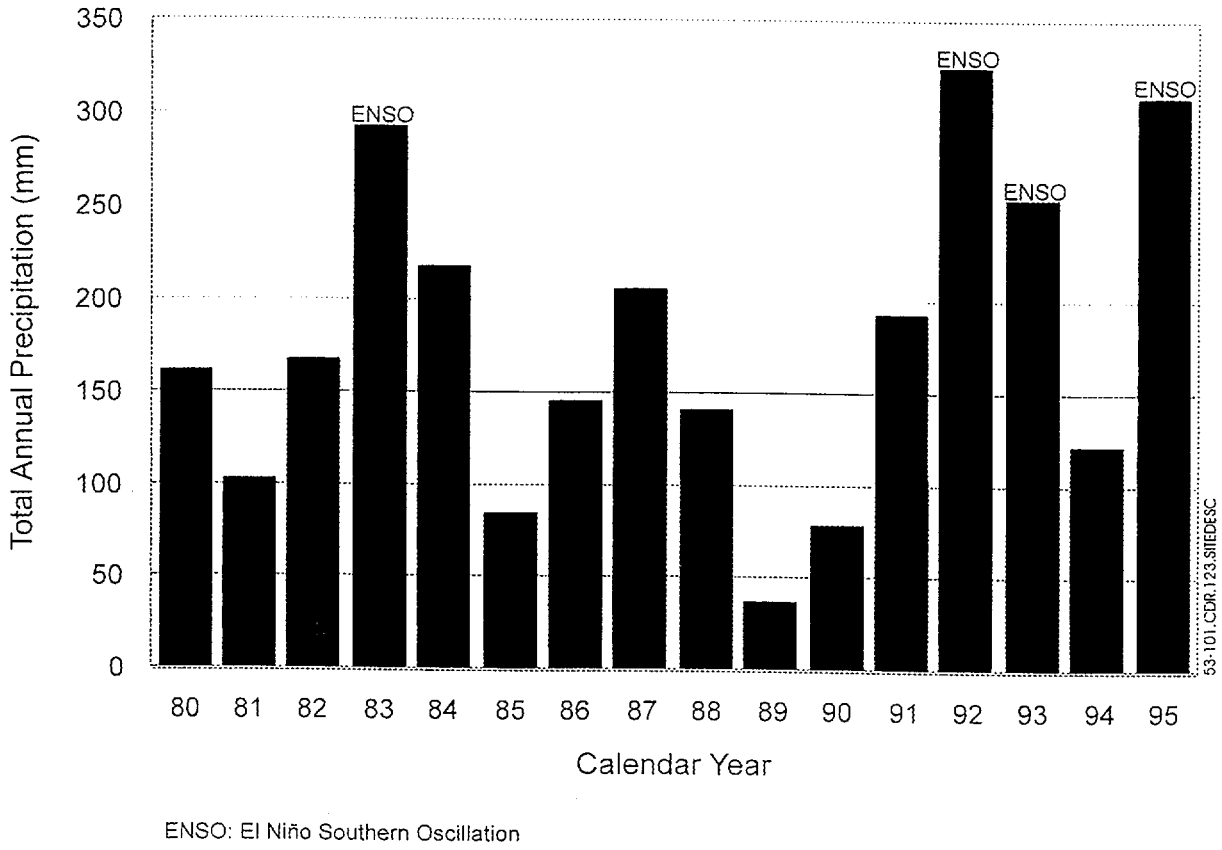

Figure 5.3-101. Developed Annual Precipitation Record for 1980 through 1995 at an Elevation of 1,400 m for the Area of the Potential Repository at Yucca Mountain

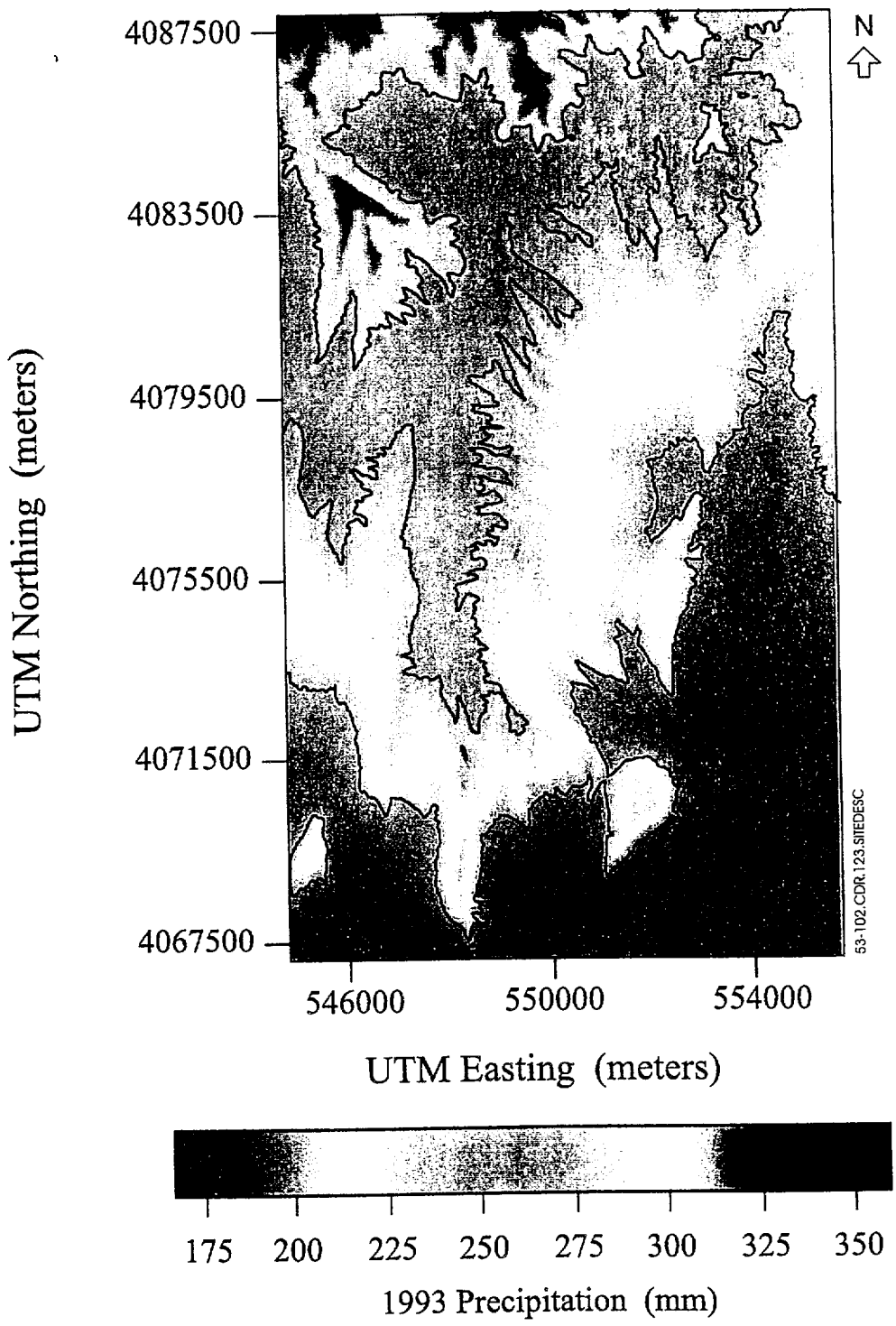

Figure 5.3-102. Spatially Distributed 1993 Total Annual Precipitation for Yucca Mountain

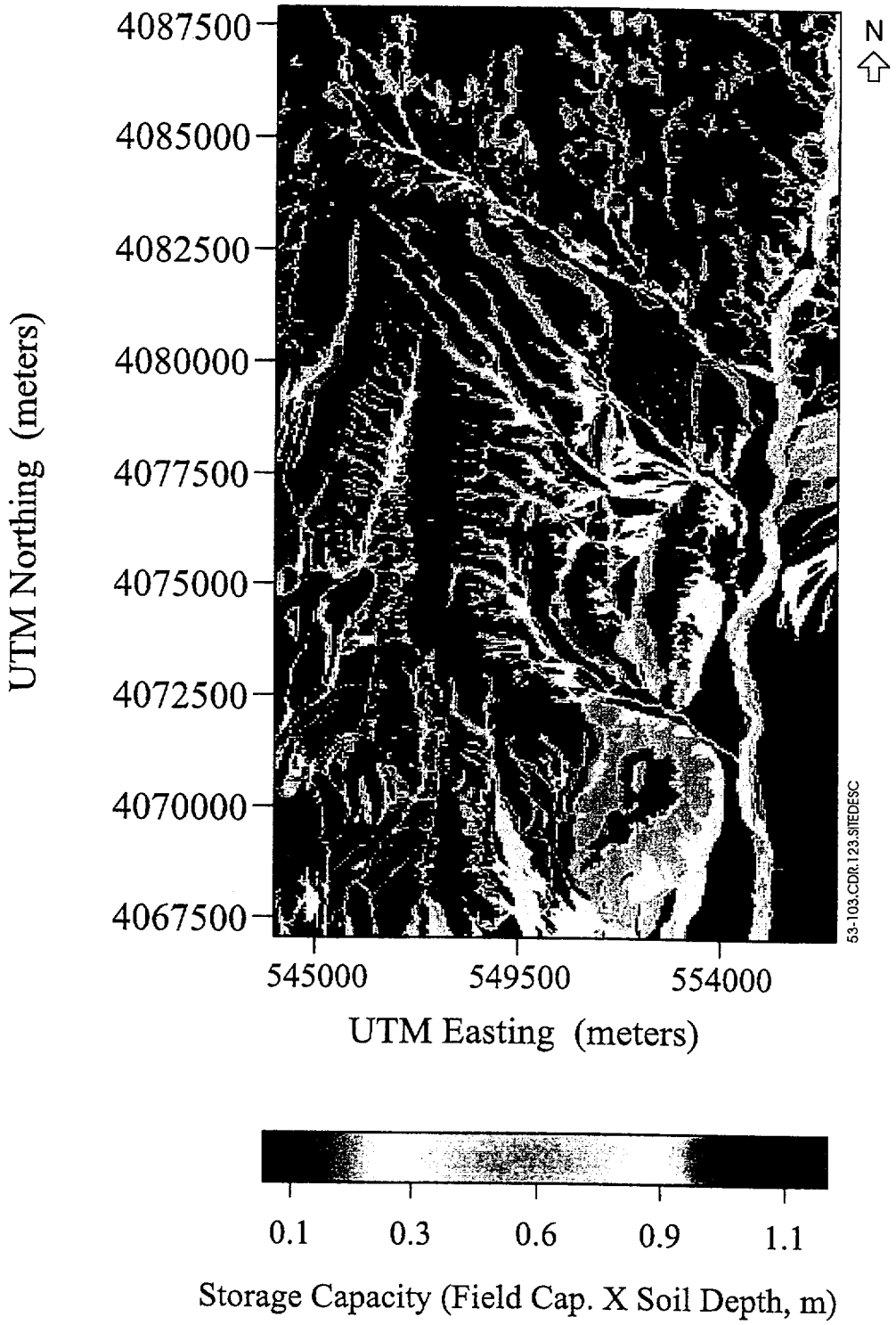

Figure 5.3-103. Calculated Soil Storage Capacity at Yucca Mountain

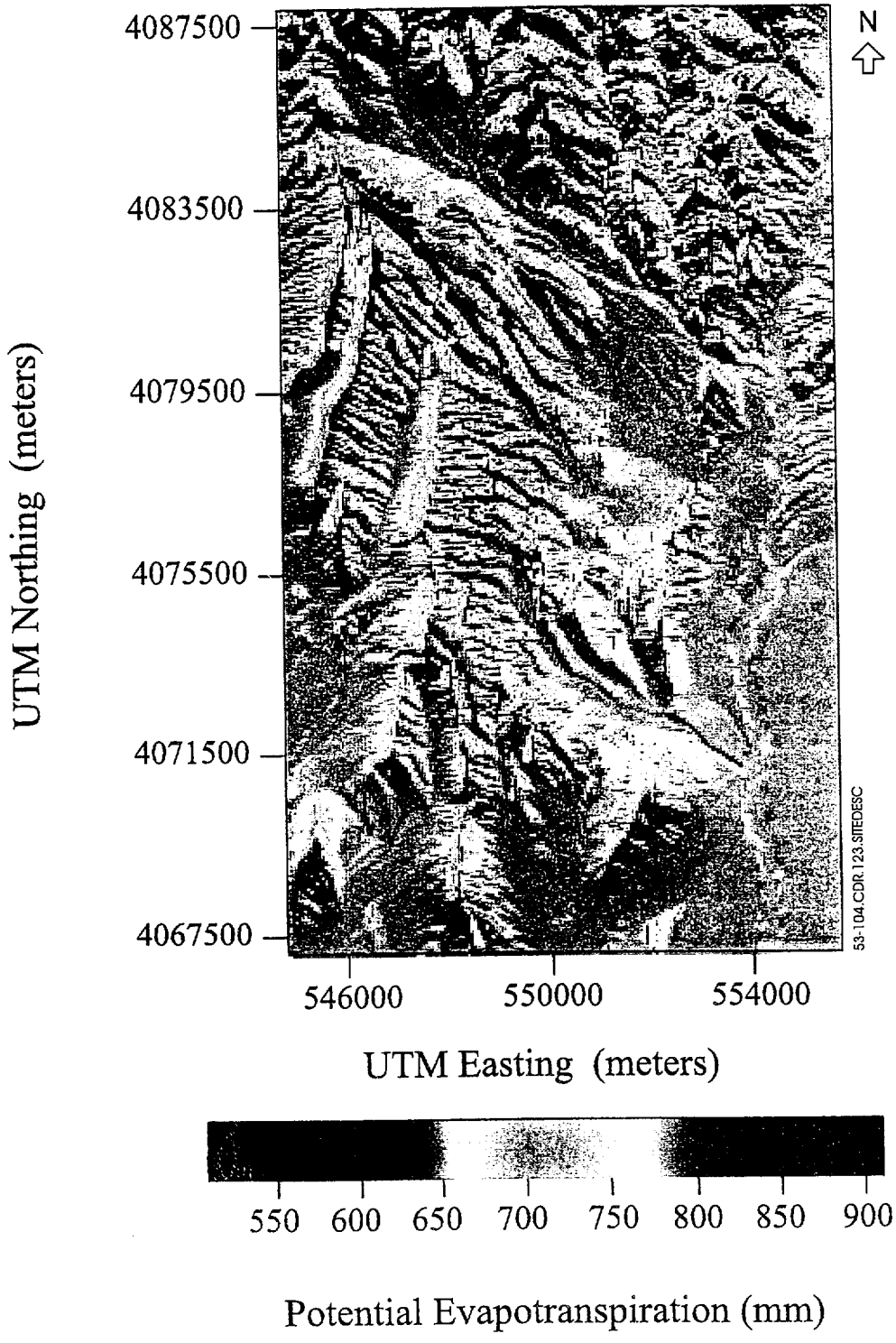

Figure 5.3-104. Modeled Total Annual Potential Evapotranspiration at Yucca Mountain

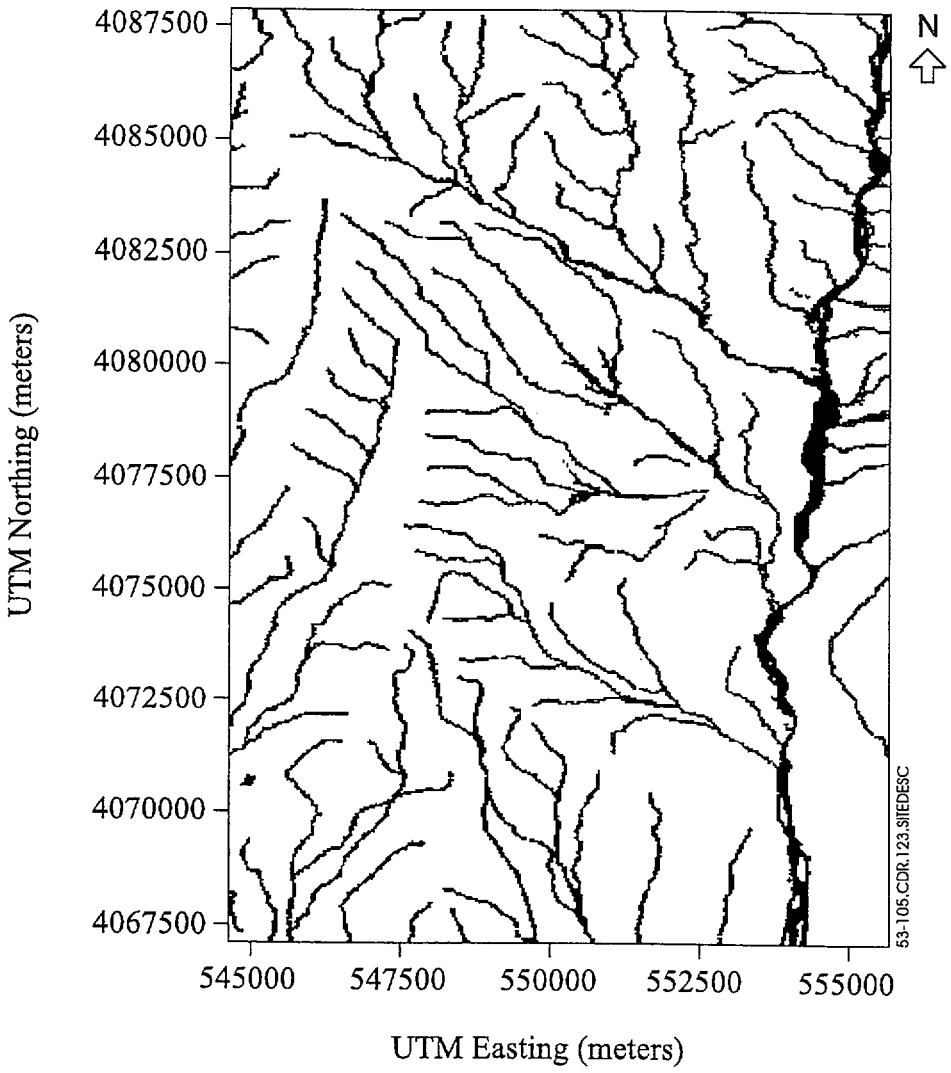

Figure 5.3-105. Surface Runoff Channel Network for Yucca Mountain Defined by 30-Meter Grid Cells Containing One or More Channel Nodes

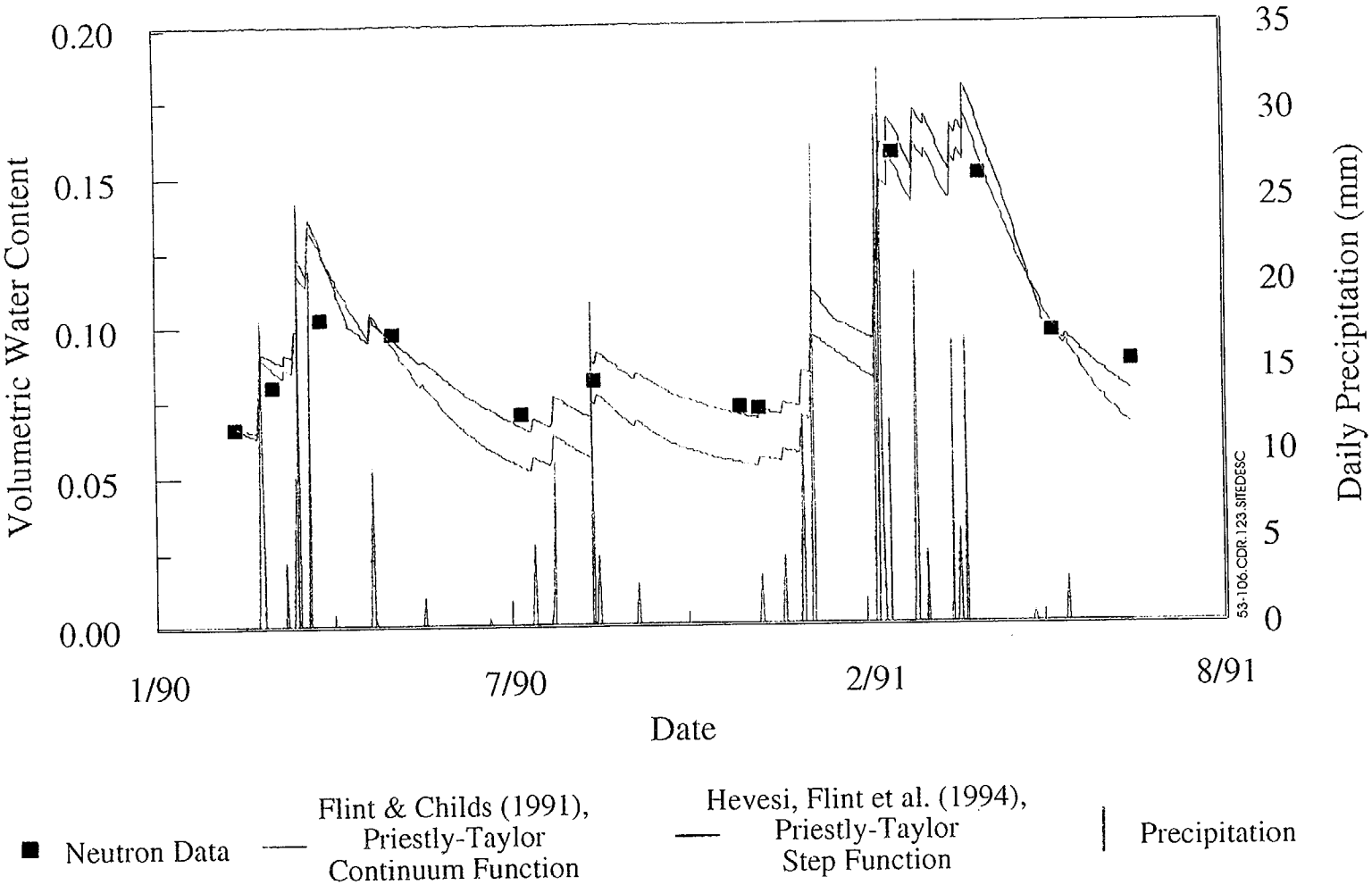

Figure 5.3-106. Comparison of Modeled and Measured Water-Content Changes at Borehole N63 for the Calibrated Net-Infiltration Model

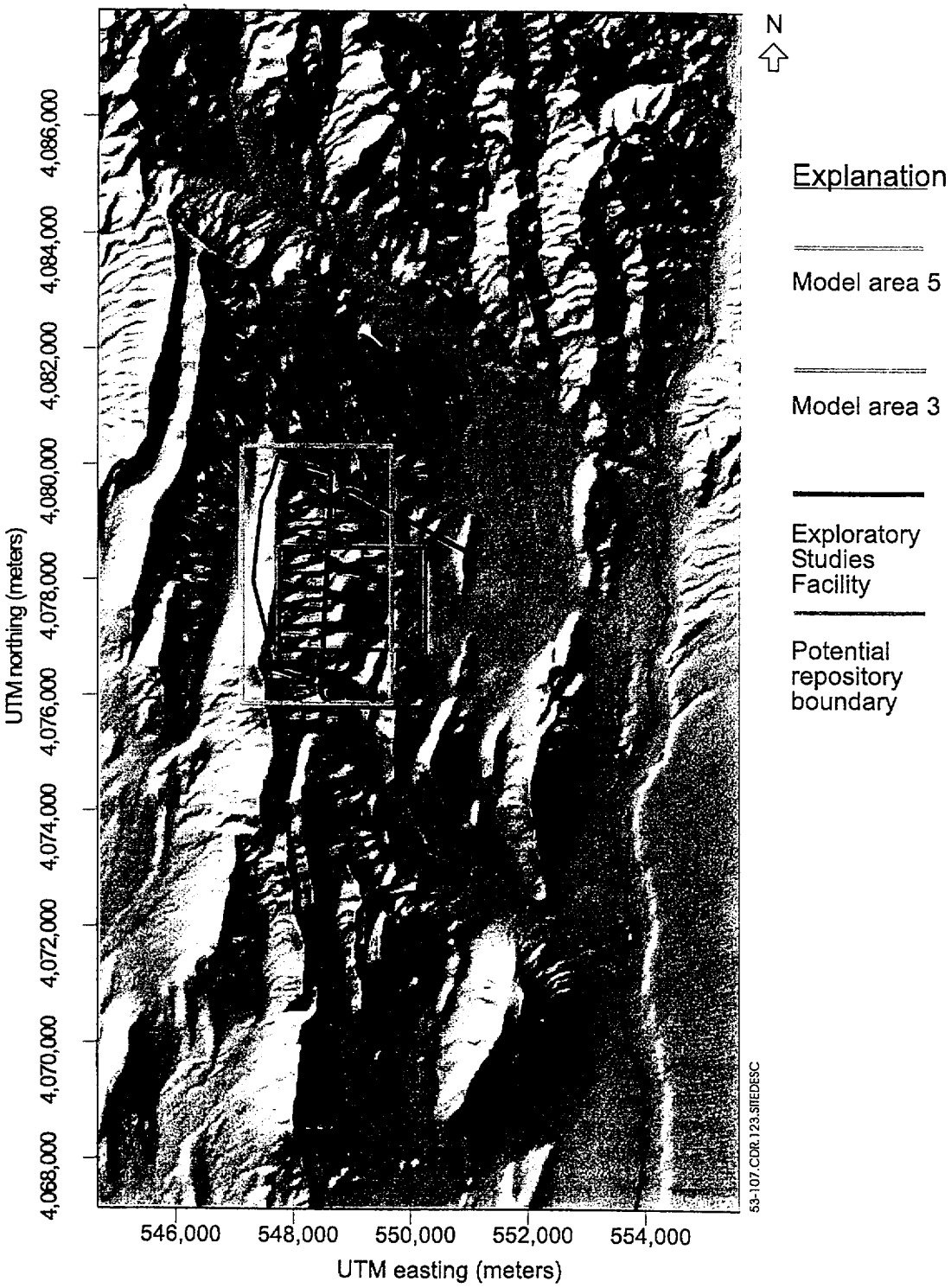

Figure 5.3-107. Domains of the Net-Infiltration Model (Area 1) for the Yucca Mountain Site Area and Submodel Areas in the Vicinity of the Potential Repository Site

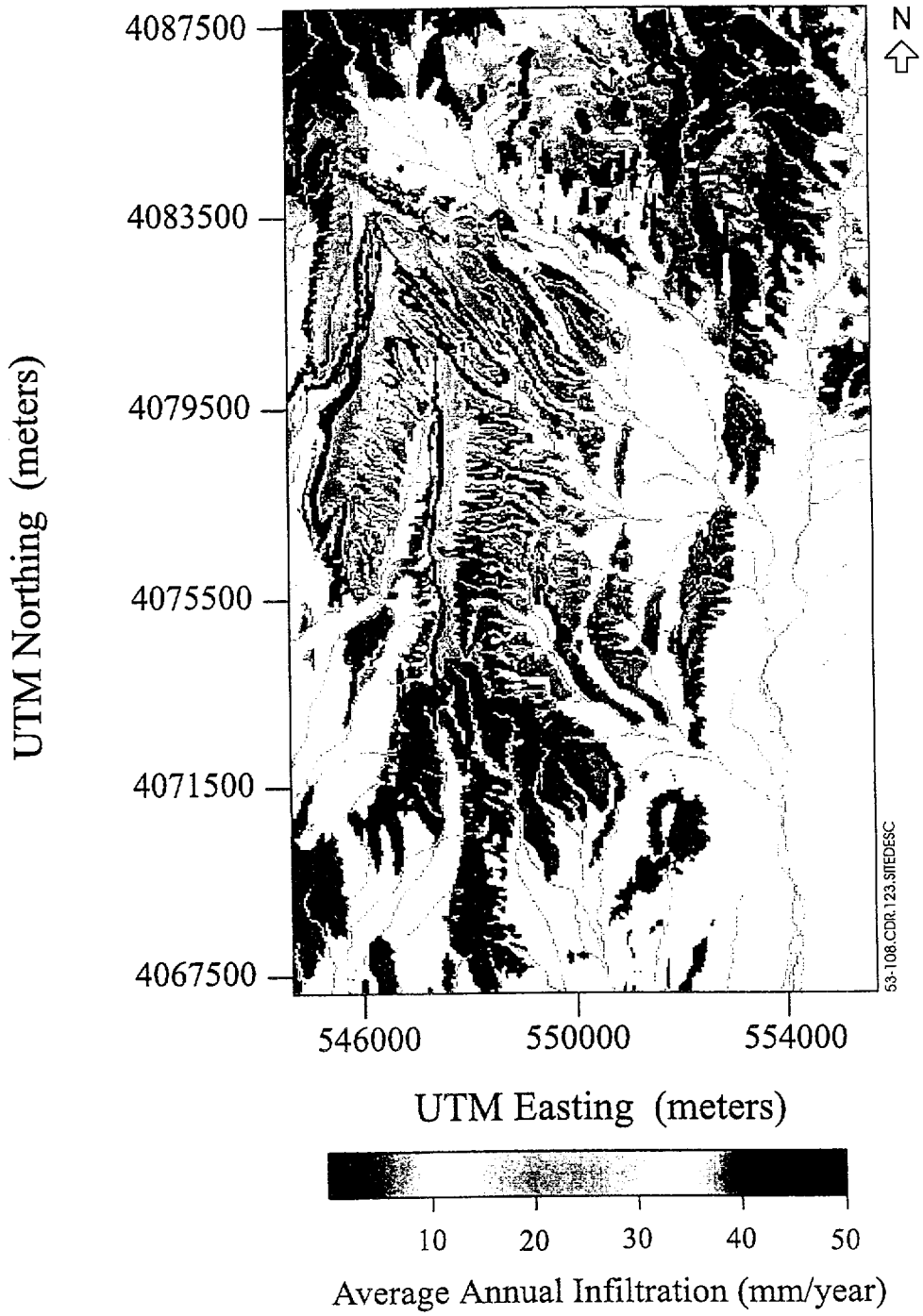

Figure 5.3-108. Simulated Average Annual Net Infiltration for the Yucca Mountain Site Area Using a Scaled 100-Year Stochastic Simulation of Daily Precipitation for Current Climatic Conditions

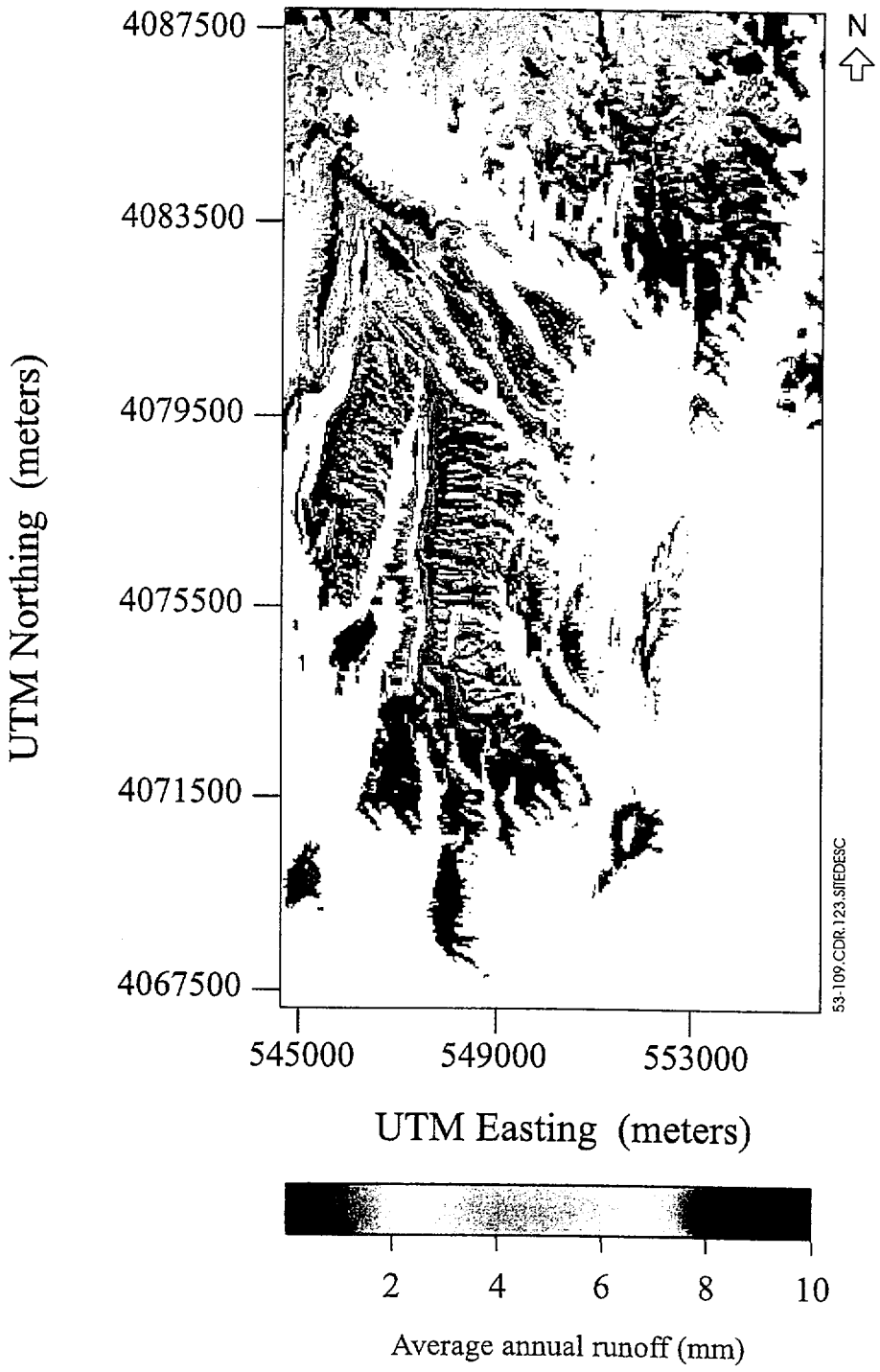

Figure 5.3-109. Simulated Average Annual Runoff for the Yucca Mountain Site Area Using a Scaled 100-Year Stochastic Simulation of Daily Precipitation for Current Climatic Conditions

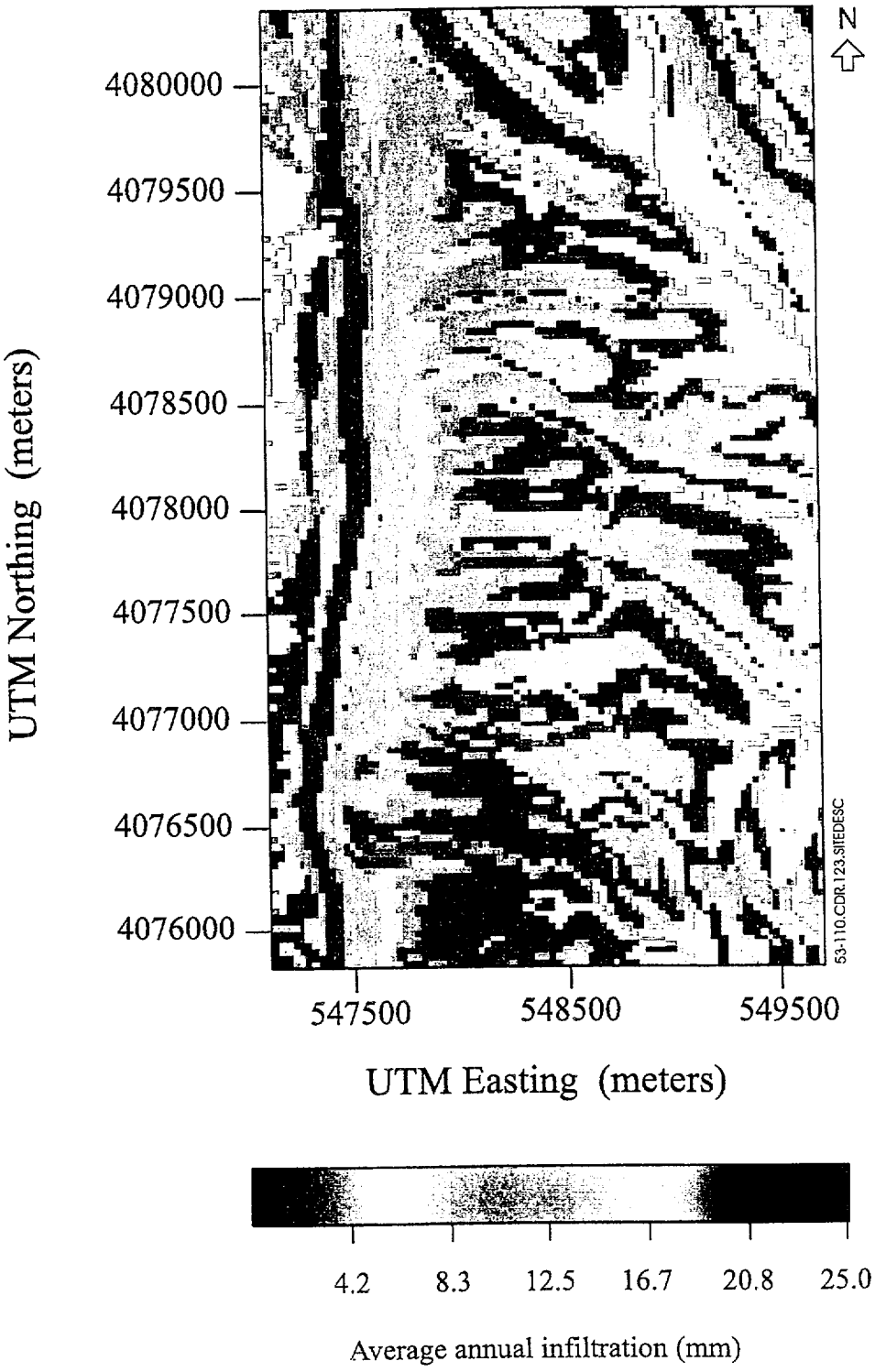

Figure 5.3-110. Simulated Average Annual Net Infiltration for the Area of the Potential Repository (Area 5) Using a Scaled 100-Year Stochastic Simulation of Daily Precipitation for Current Climatic Conditions

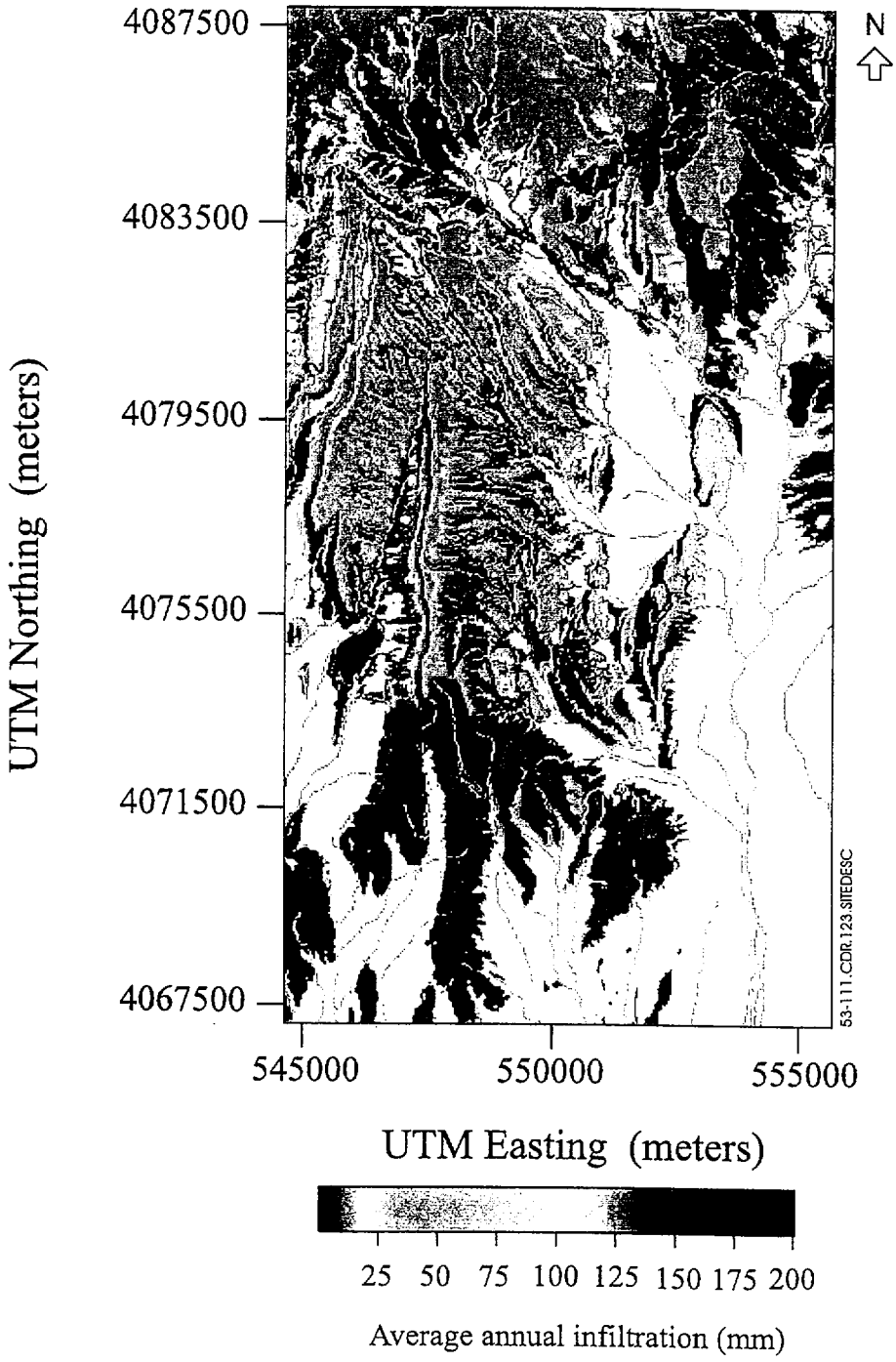

Figure 5.3-111. Simulated Average Annual Net Infiltration for Yucca Mountain Using the 100-Year Stochastic Simulation of Daily Precipitation for the NTS Area 12 Wetter Climate Analog

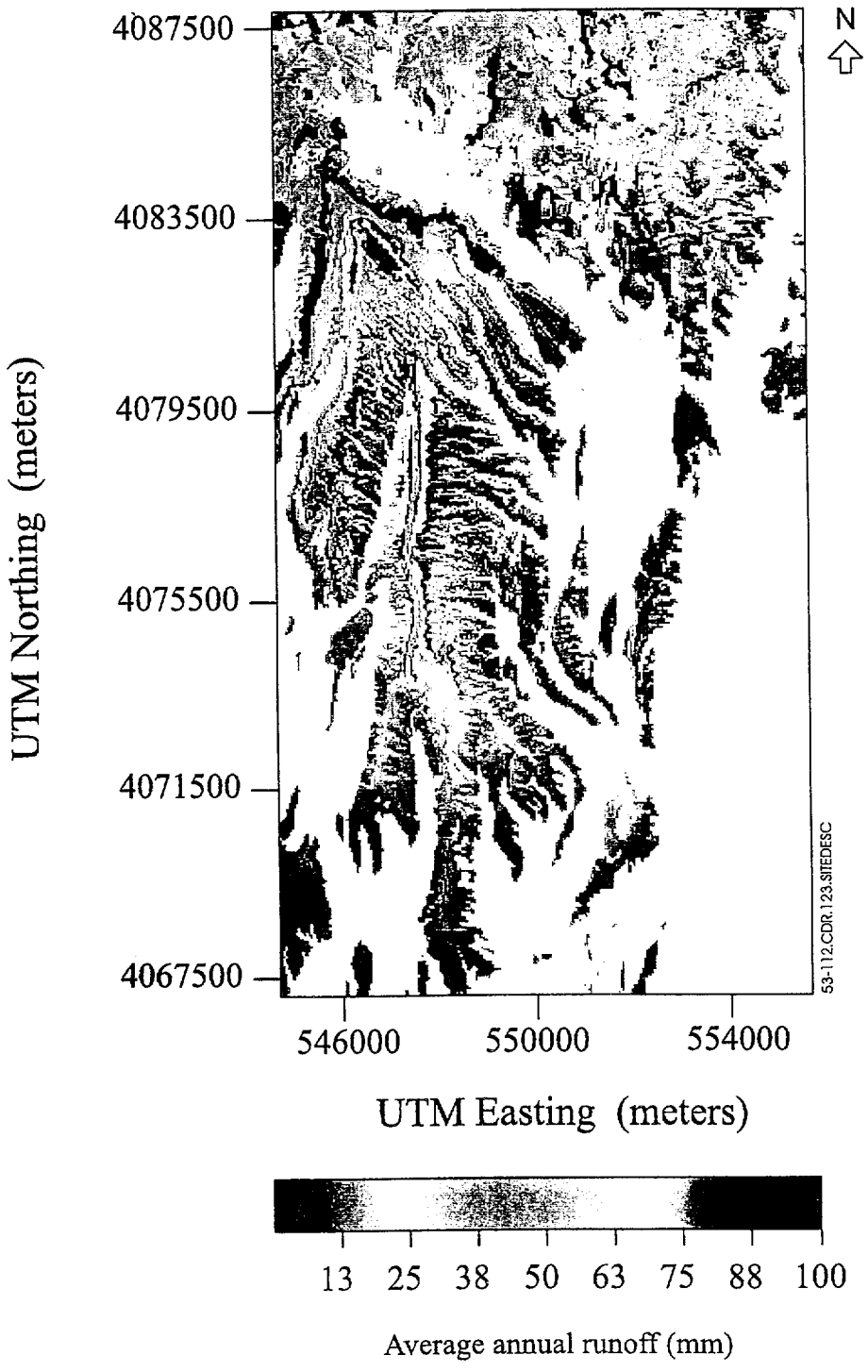

Figure 5.3-112. Simulated Average Annual Runoff for Yucca Mountain Using the 100-Year Stochastic Simulation of Daily Precipitation for the NTS Area 12 Wetter Climate Analog

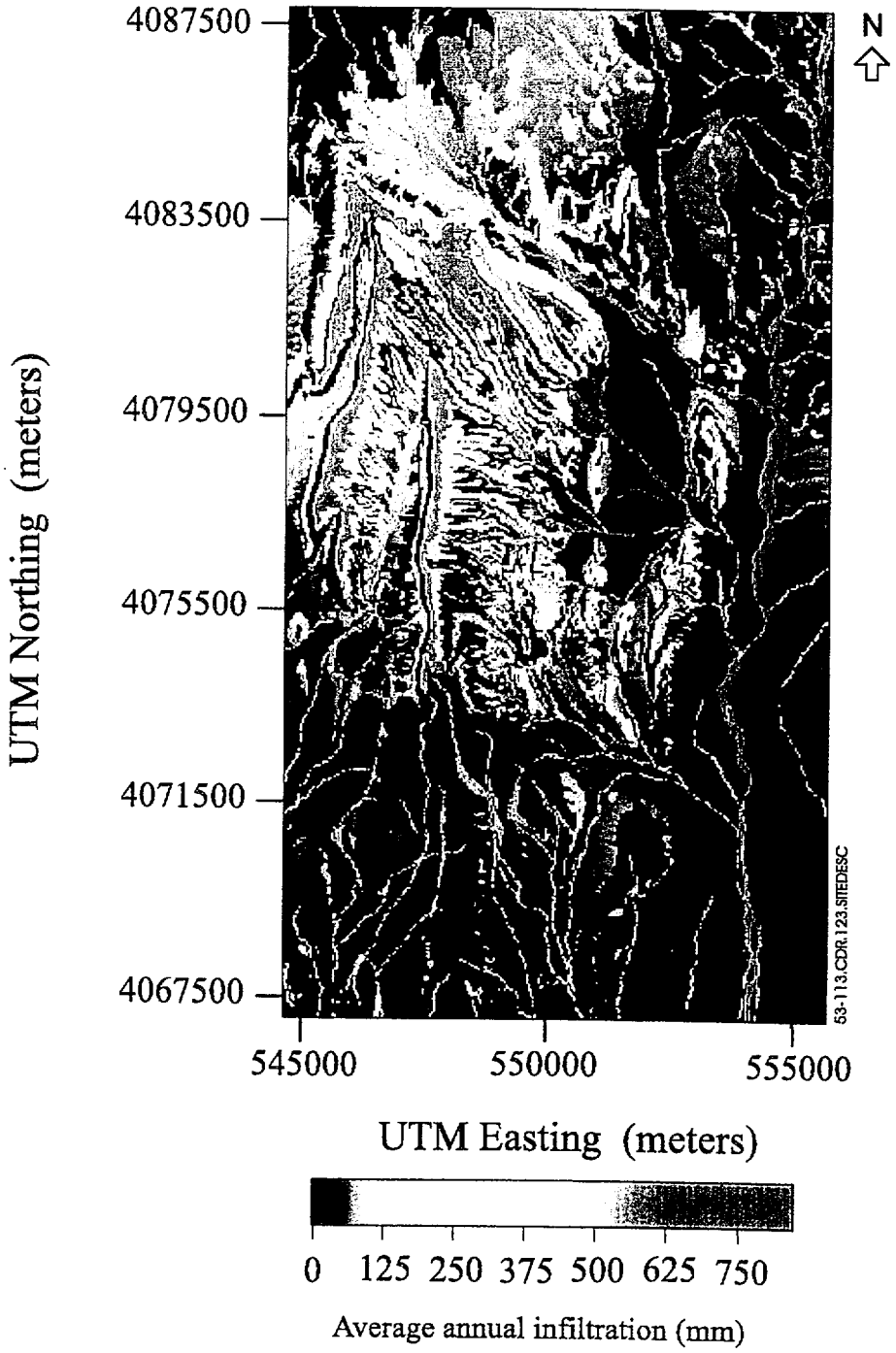

Figure 5.3-113. Simulated Average Annual Net Infiltration for Yucca Mountain Using the 100-Year Stochastic Simulation of Daily Precipitation for the South Lake "Super Pluvial" Analog

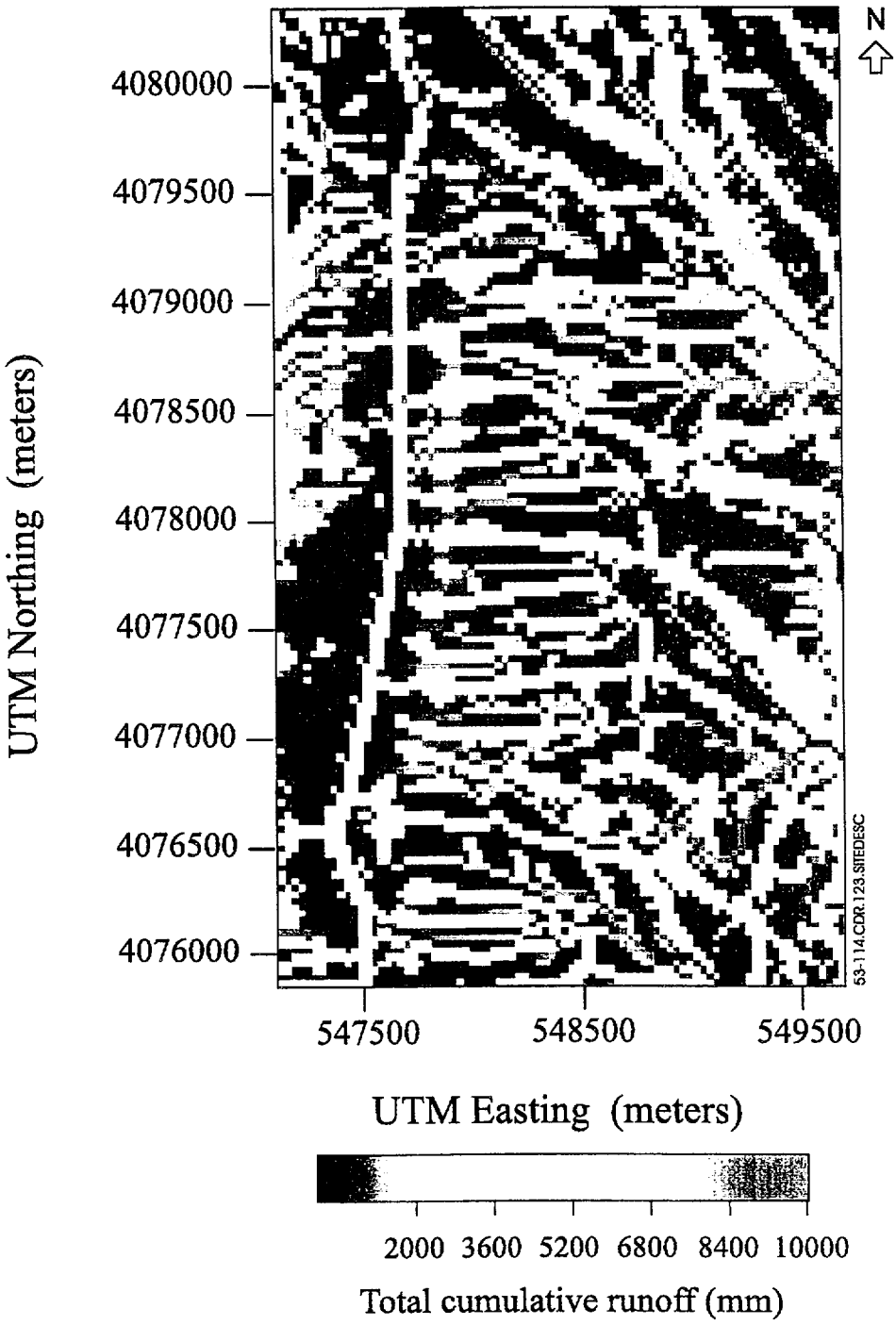

NOTE: White indicates no cumulative runoff; black indicates values greater than 10,000 mm.

Figure 5.3-114. Simulated Cumulative Runoff in the Vicinity of the Potential Repository Site (Area 5) for March 11, 1995, Using a Coupled Infiltration–Runoff-Routing Model and the 1980-1995 Daily Precipitation Record

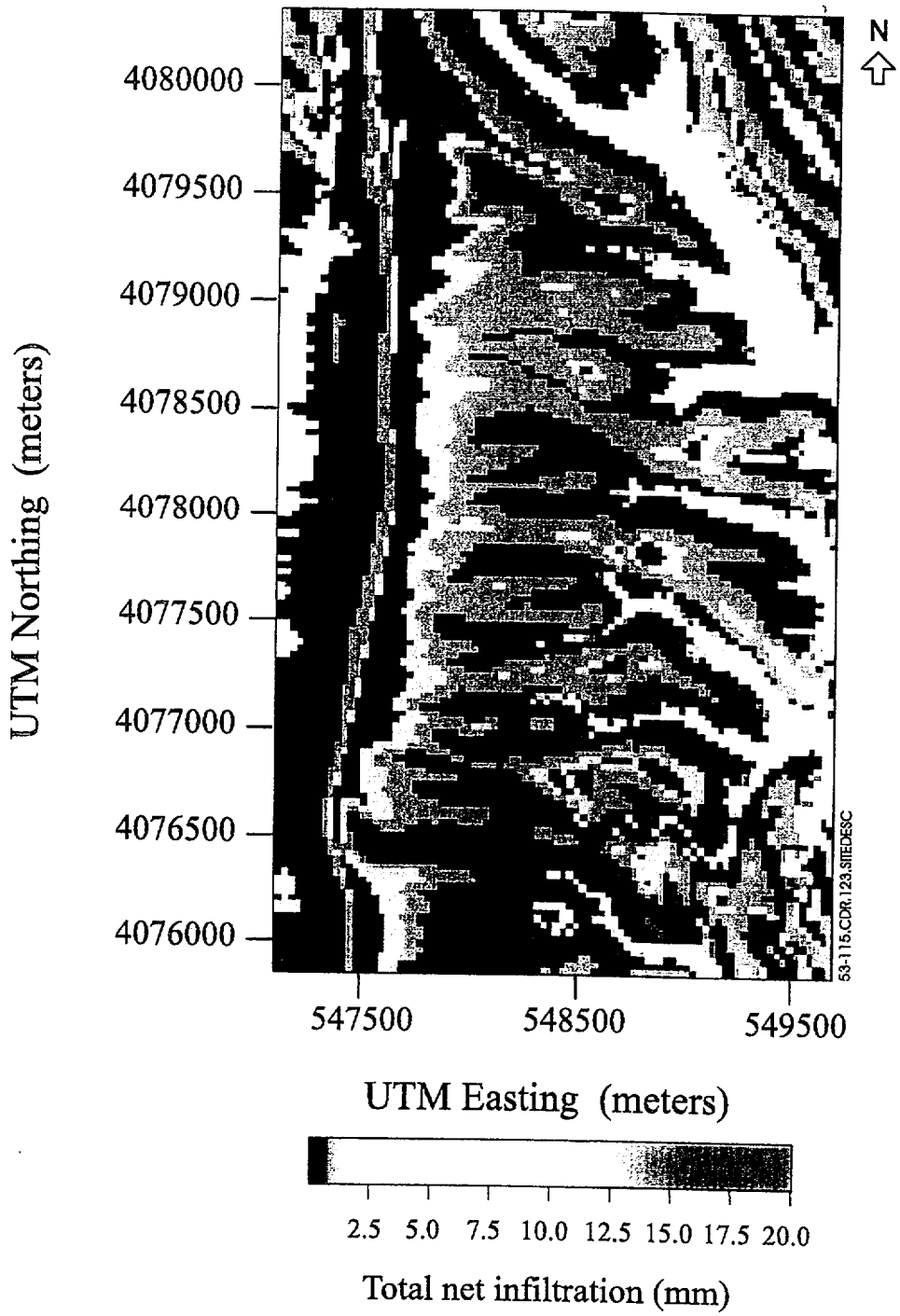

NOTE: White indicates no net infiltration; black indicates values greater than 20 mm.

Figure 5.3-115. Simulated Total 24-Hour Net Infiltration in the Vicinity of the Potential Repository (Area 5) for March 11, 1995, Using a Coupled Infiltration–Runoff Routing Model and the 1980-1995 Daily Precipitation Record

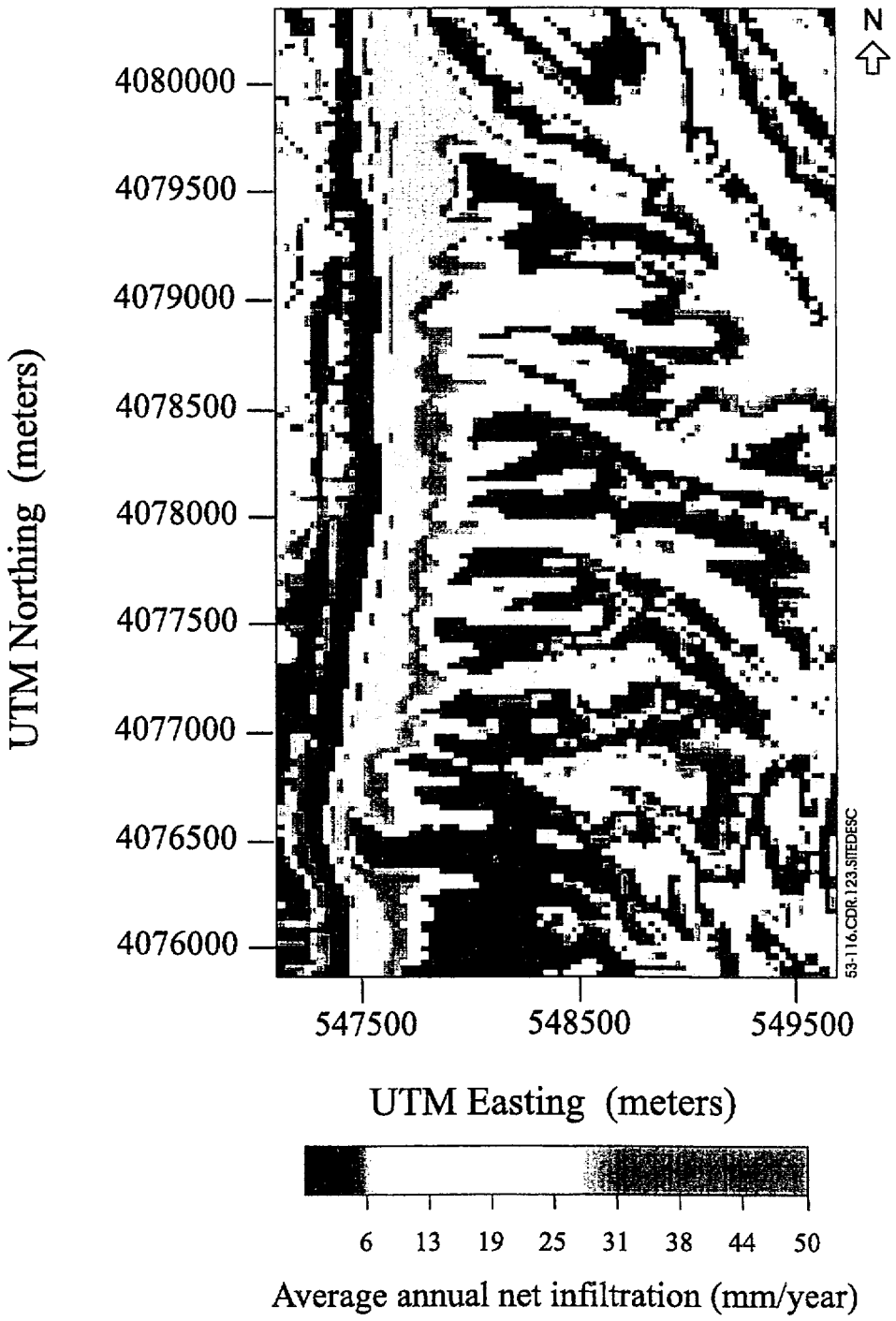

NOTE: White indicates no net infiltration; black indicates values greater than 50 mm.

Figure 5.3-116. Simulated Average Annual Net Infiltration in the Vicinity of the Potential Repository Site (Area 5) Using the Coupled Infiltration–Runoff Routing Model and the 1980-1995 Daily Precipitation Record

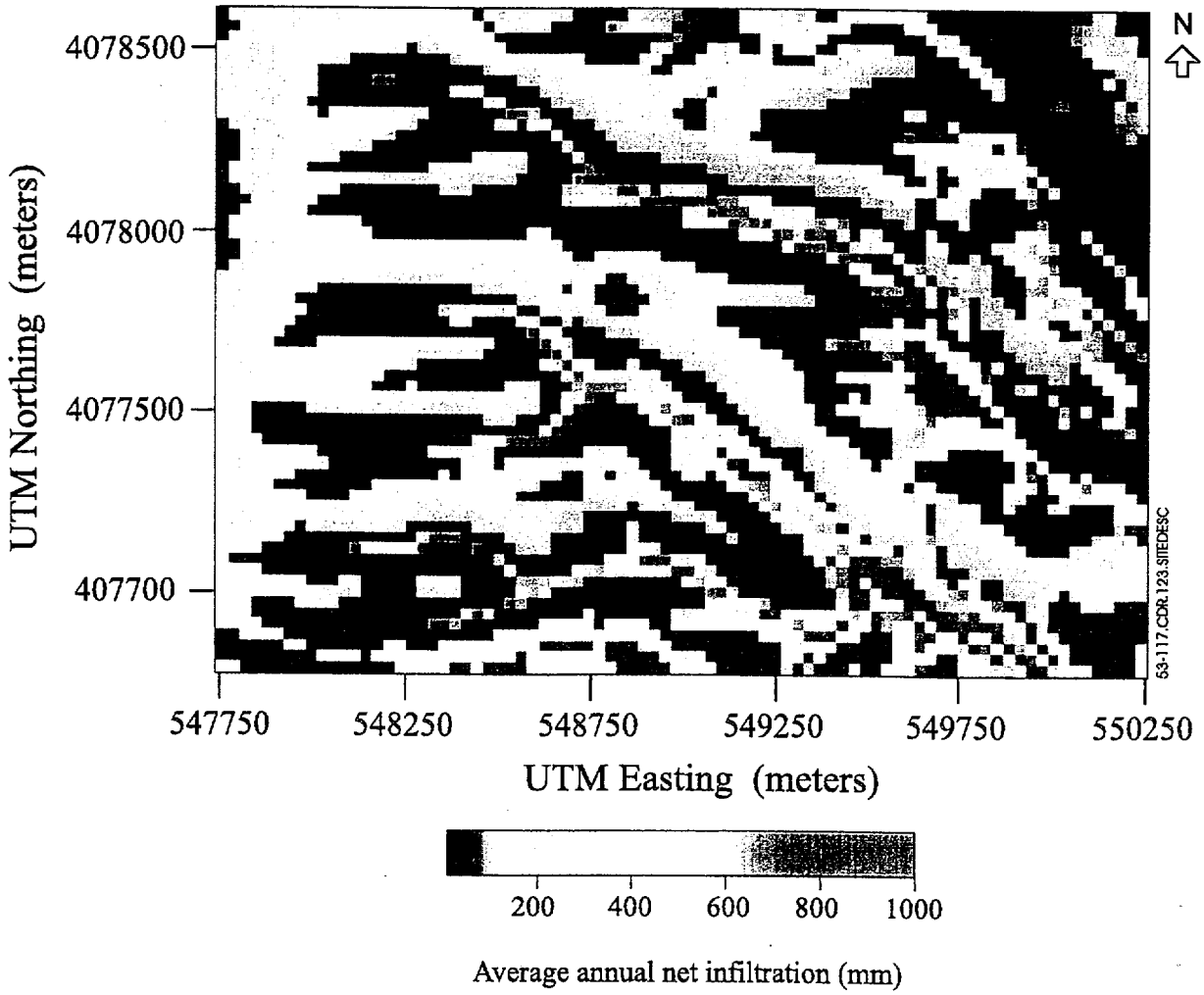

NOTE: Black indicates values greater than 1,000 mm)

Figure 5.3-117. Simulated Average Annual Net Infiltration for the Area of Split and Wt-2 Washes (Area 3) Using the Coupled Infiltration–Runoff Routing Model and the 100-Year Stochastic Simulation for the South Lake "Super Pluvial" Analog

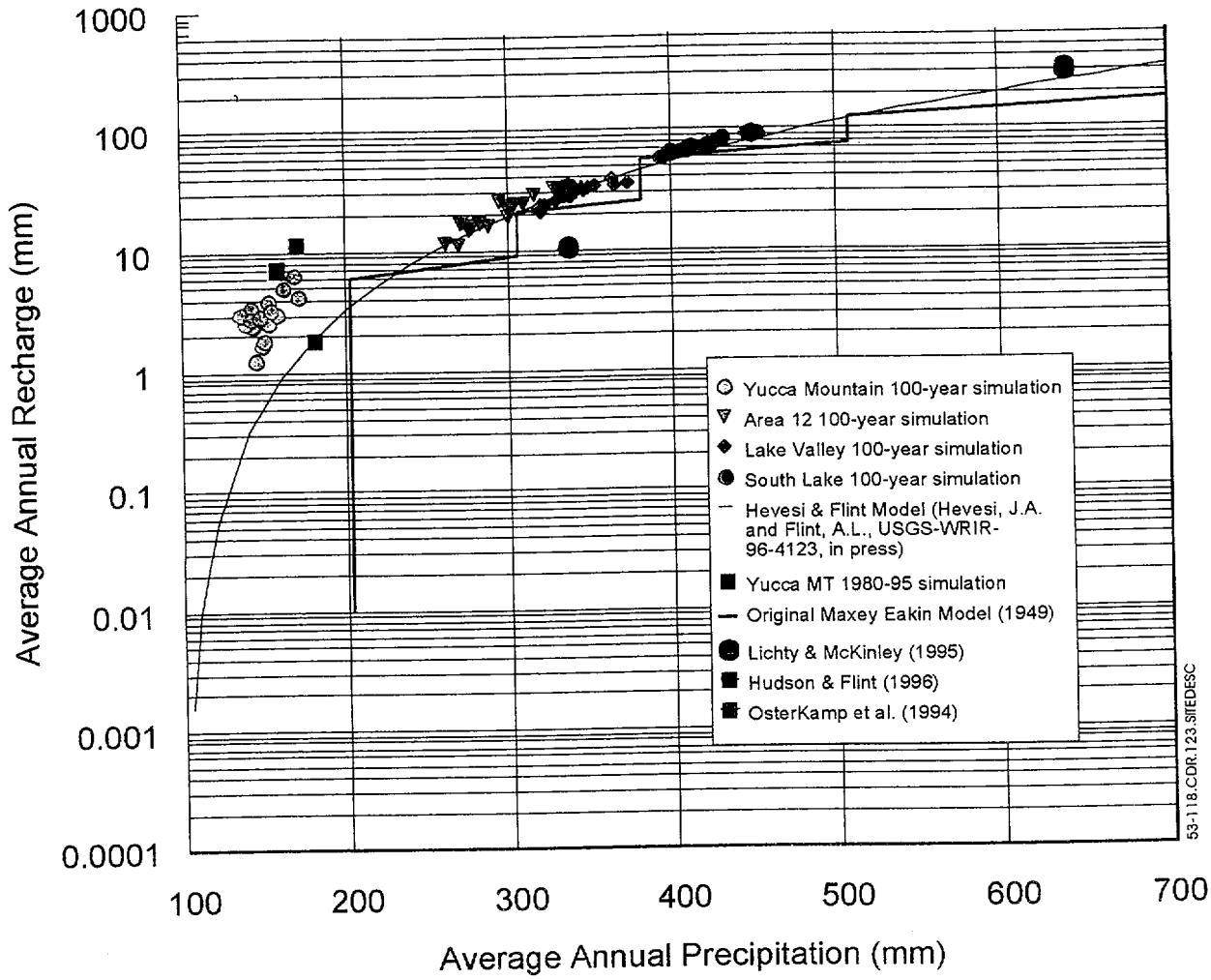

Figure 5.3-118. Relation Between Average Annual Precipitation and Net Infiltration or Recharge for the Methods

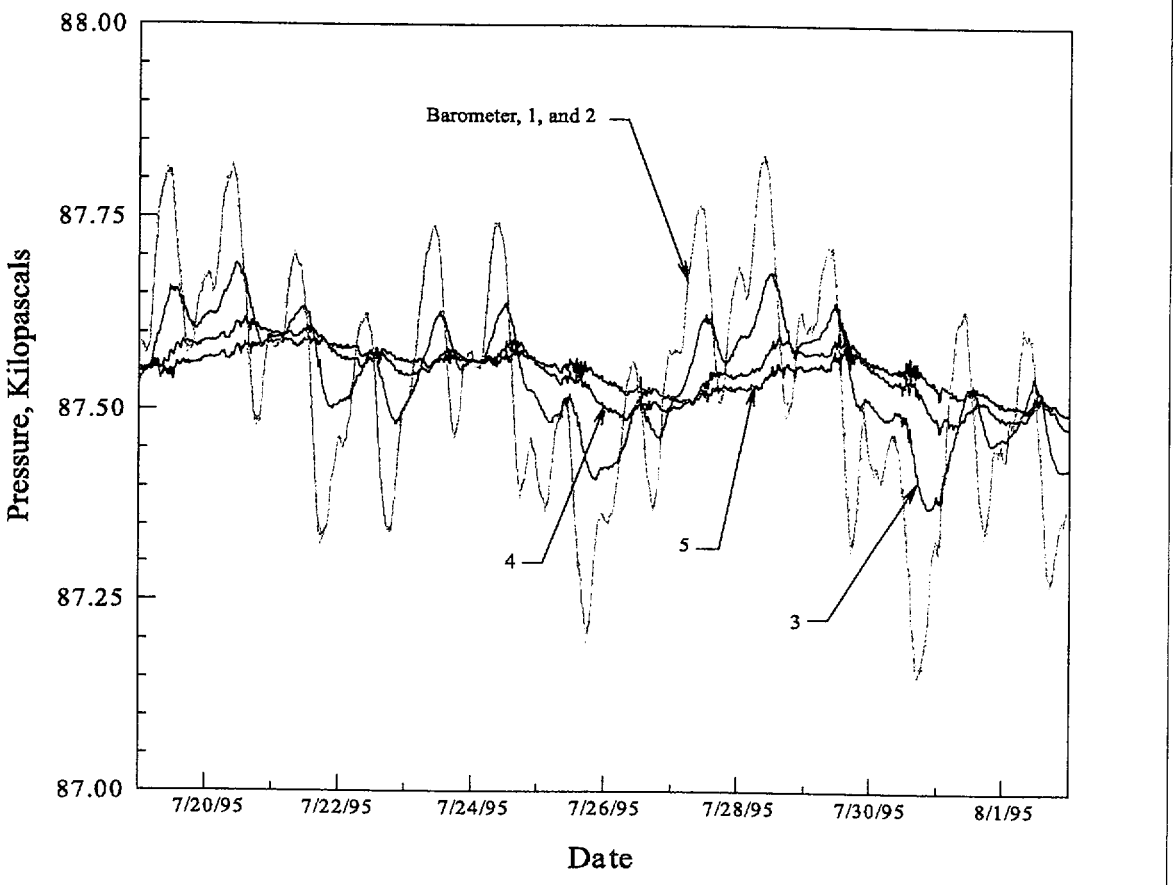

Instrument Station	Depth (meters)	Lithology	Residual Amplitude (percent)	Phase Lag (hours)
1	23.2	Tiva Canyon Upper Lithophysal	99	0.3
2	40.5	Tiva Canyon Columnar	99	0.3
3	57.0	Yucca Mountain Tuff	61	12.2
4	74.1	Pah Canyon Tuff	38	31.6
5	90.8	Pre-Pah Canyon Tuff bedded tuff	31	46.8

53-1119.CDR.123.SITEDESC

Figure 5.3-119. Pneumatic Pressure Record and Results of Cross-Spectral Analysis for Instrument Stations 1 Through 5 in Borehole NRG#5 Prior to the Effects of Exploratory Studies Facility Excavation

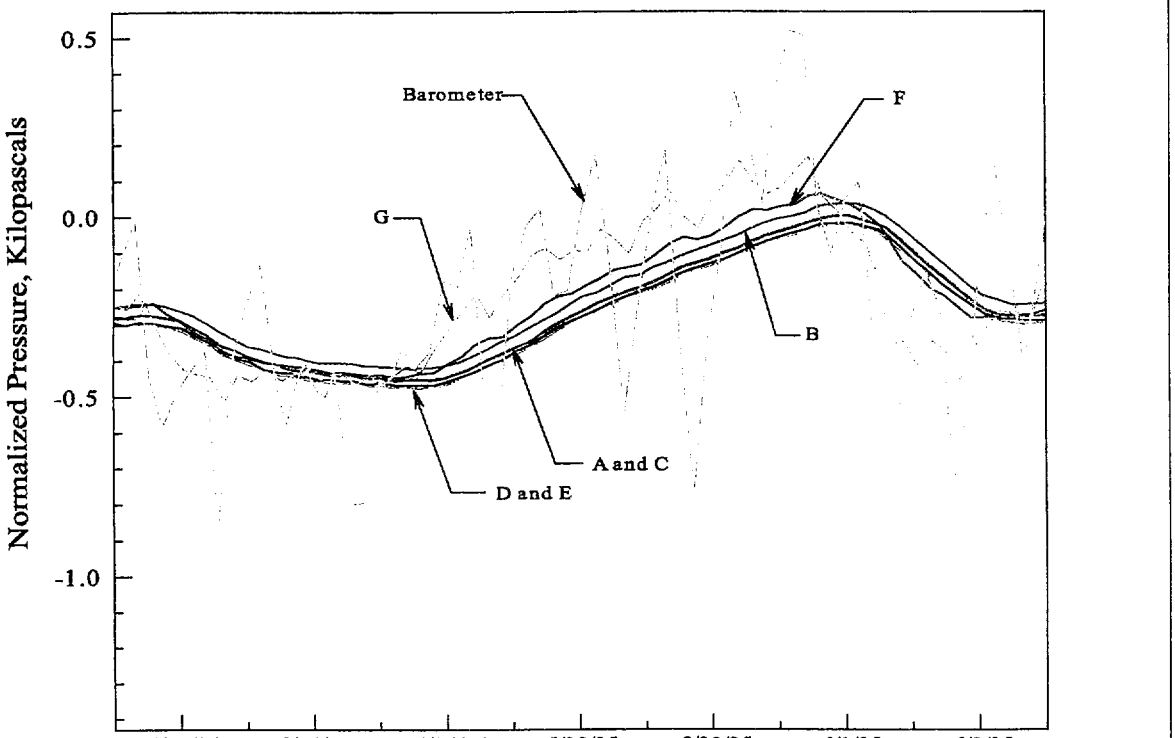

Instrument Station	Depth (meters)	Lithology	Residual Amplitude (percent)	Phase Lag (hours)
G	39.6	Tiva Canyon Columnar	56	1.8
F	54.9	Pah Canyon Tuff	36	31.5
E	85.3	Topopah Spring Crystal-Rich Nonlithophysal	29	42.7
D	106.8	Topopah Spring Crystal-Rich Nonlithophysal	29	42.3
C	138.8	Topopah Spring Upper Lithophysal	30	42.8
B	163.1	Topopah Spring Upper Lithophysal	30	43.1
A	219.4	Topopah Spring Middle Nonlithophysal	30	43.5

53-120.CDR.123.SITEDESC

Figure 5.3-120. Pneumatic Pressure Record and Results of Cross-Spectral Analysis for Borehole NRG-6 Prior to the Effects of Exploratory Studies Facility Excavation

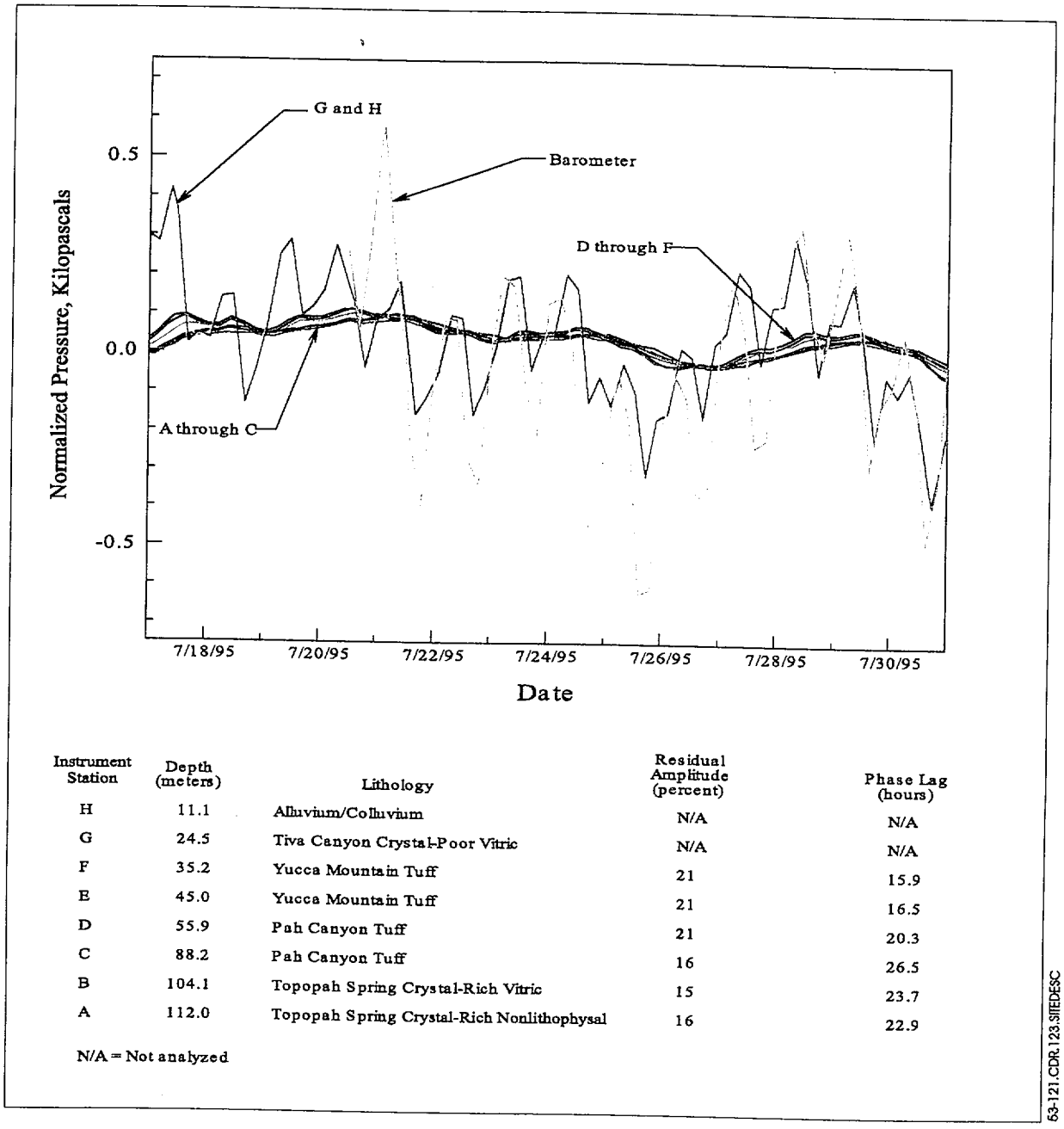

Instrument Station	Depth (meters)	Lithology	Residual Amplitude (percent)	Phase Lag (hours)
H	11.1	Alluvium/Colluvium	N/A	N/A
G	24.5	Tiva Canyon Crystal-Poor Vitric	N/A	N/A
F	35.2	Yucca Mountain Tuff	21	15.9
E	45.0	Yucca Mountain Tuff	21	16.5
D	55.9	Pah Canyon Tuff	21	20.3
C	88.2	Pah Canyon Tuff	16	26.5
B	104.1	Topopah Spring Crystal-Rich Vitric	15	23.7
A	112.0	Topopah Spring Crystal-Rich Nonlithophysal	16	22.9

N/A = Not analyzed

63-121.CDR.123.SIFEDESC

Figure 5.3-121. Pneumatic Pressure Record and the Results of Cross-Spectral Analysis for Borehole UZ#4 Prior to the Effects of Exploratory Studies Facility Excavation

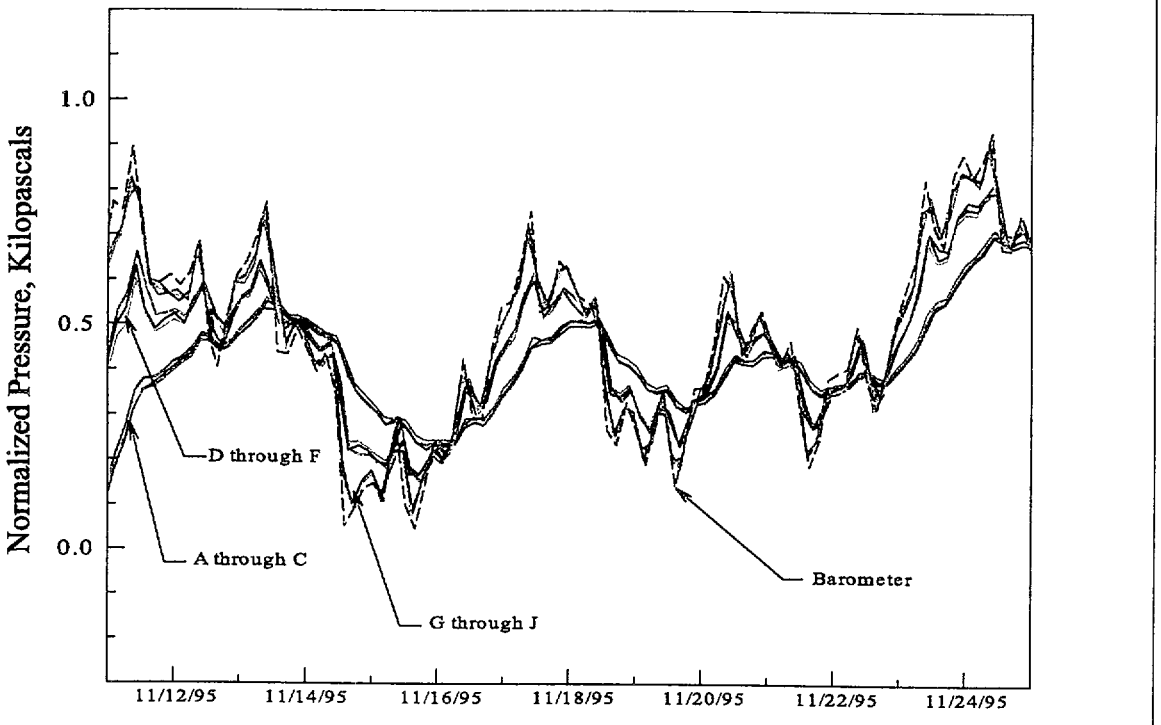

Instrument Station	Depth (meters)	Lithology	Residual Amplitude (percent)	Phase Lag (hours)
J	13.5	Tiva Canyon Lower Lithophysal	100	0.5
I	29.9	Tiva Canyon Columnar	96	0.9
H	45.6	Tiva Canyon Columnar	96	0.9
G	56.3	Tiva Canyon Crystal-Poor Vitric	97	2.5
F	67.1	Pre-Pah Canyon Tuff bedded tuff	79	5.3
E	75.1	Topopah Spring Crystal-Rich Vitric	75	5.2
D	111.0	Topopah Spring Crystal-Rich Nonlithophysal	73	6.0
C	149.8	Topopah Spring Upper Lithophysal	57	14.5
B	178.3	Topopah Spring Middle Nonlithophysal	54	15.1
A	194.0	Topopah Spring Lower Lithophysal	56	16.0

63-122.CDR.123.SITEDESC

Figure 5.3-122. Pneumatic Pressure Record and the Results of Cross-Spectral Analysis for Borehole UZ-7a Prior to the Effects of Exploratory Studies Facility Excavation

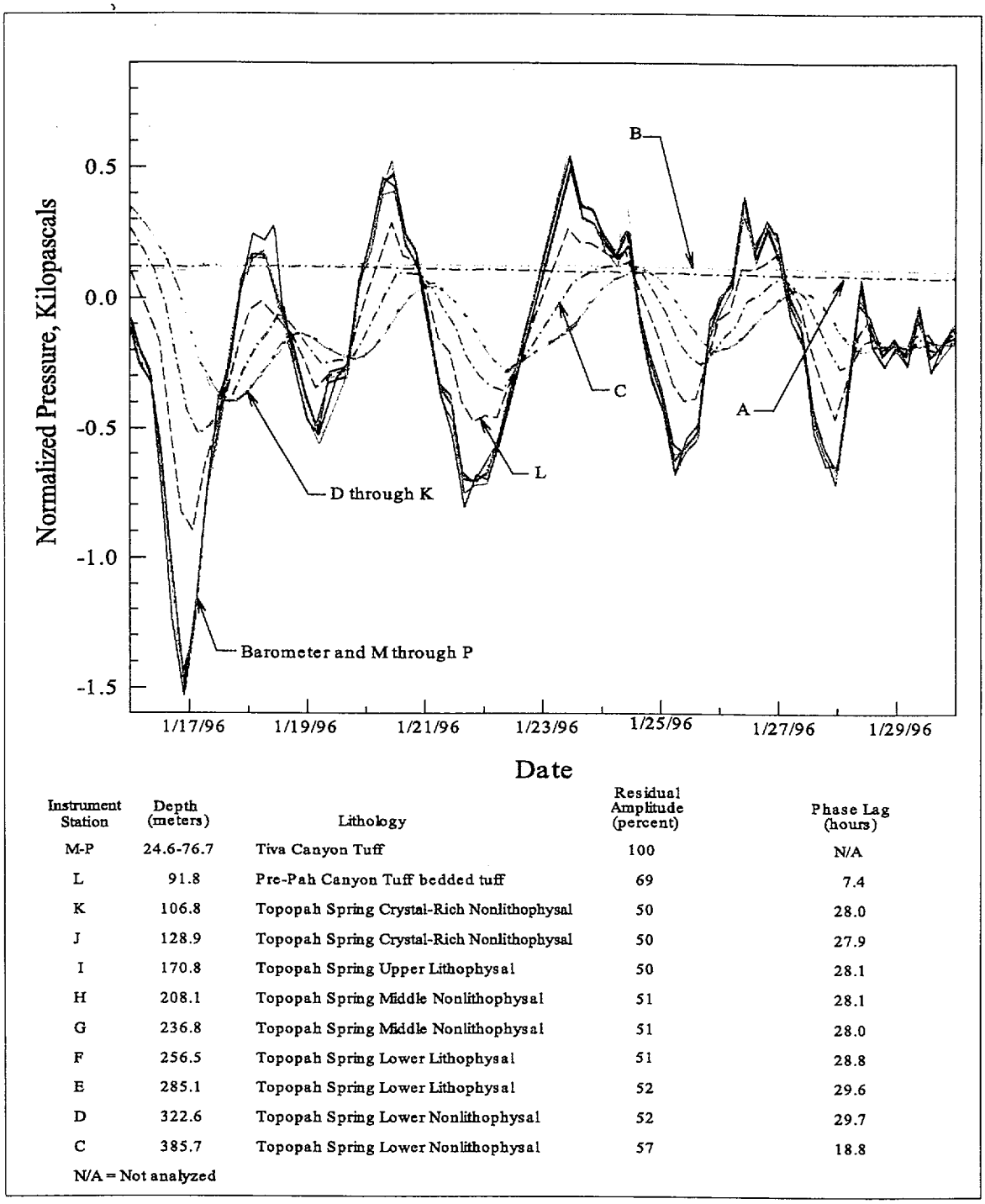

Instrument Station	Depth (meters)	Lithology	Residual Amplitude (percent)	Phase Lag (hours)
M-P	24.6-76.7	Tiva Canyon Tuff	100	N/A
L	91.8	Pre-Pah Canyon Tuff bedded tuff	69	7.4
K	106.8	Topopah Spring Crystal-Rich Nonlithophysal	50	28.0
J	128.9	Topopah Spring Crystal-Rich Nonlithophysal	50	27.9
I	170.8	Topopah Spring Upper Lithophysal	50	28.1
H	208.1	Topopah Spring Middle Nonlithophysal	51	28.1
G	236.8	Topopah Spring Middle Nonlithophysal	51	28.0
F	256.5	Topopah Spring Lower Lithophysal	51	28.8
E	285.1	Topopah Spring Lower Lithophysal	52	29.6
D	322.6	Topopah Spring Lower Nonlithophysal	52	29.7
C	385.7	Topopah Spring Lower Nonlithophysal	57	18.8

N/A = Not analyzed

53-123.CDR.123.SITEDESC

Figure 5.3-123. Pneumatic Pressure Record and the Results of Cross-Spectral Analysis for Borehole SD-12 Prior to the Effects of Exploratory Studies Facility Excavation

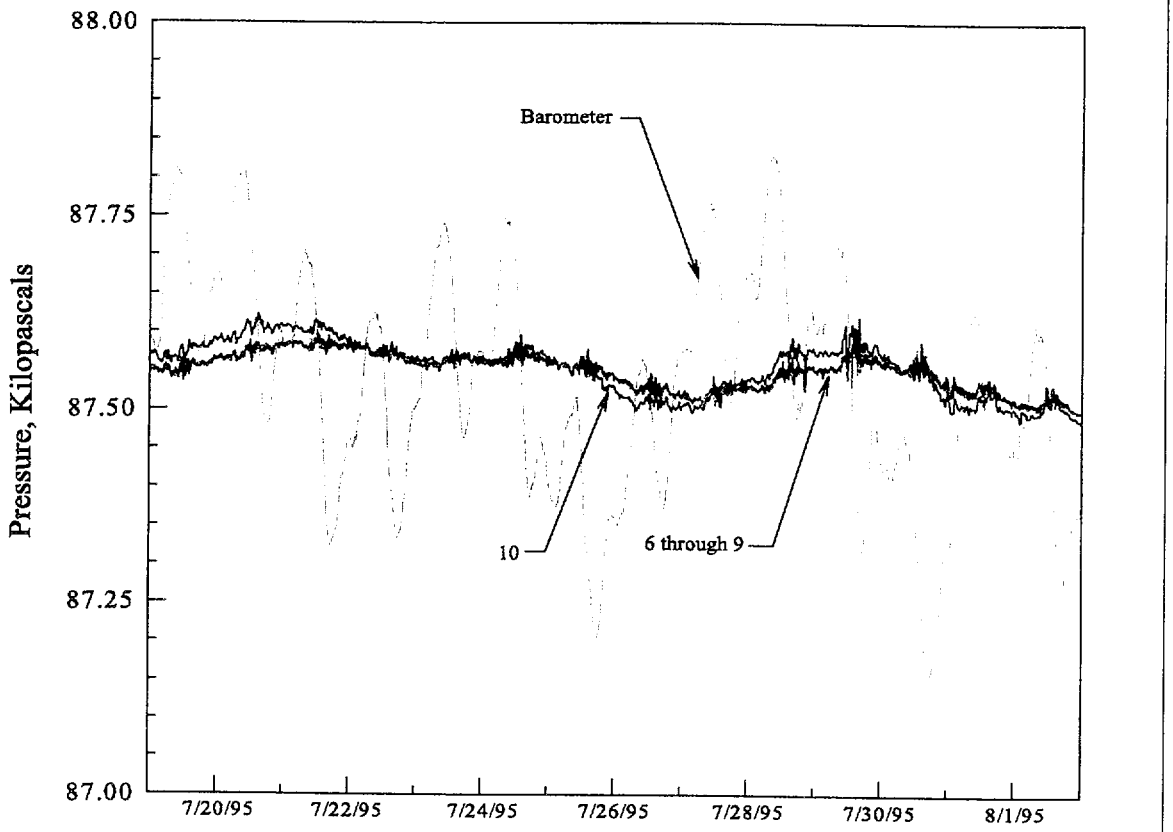

Instrument Station	Depth (meters)	Lithology	Residual Amplitude (percent)	Phase Lag (hours)
6	107.9	Topopah Spring Crystal-Rich Nonlithophysal	30	47.9
7	125.0	Topopah Spring Crystal-Rich Nonlithophysal	29	47.8
8	158.8	Topopah Spring Upper Lithophysal	29	47.9
9	192.9	Topopah Spring Upper Lithophysal	29	48.3
10	226 8	Topopah Spring Upper Lithophysal	39	37 7

63-124.CDR.123.SITEDESC

Figure 5.3-124. Pneumatic Pressure Record and Results of Cross-Spectral Analysis for Instrument Stations 6 Through 10 in Borehole NRG#5 Prior to the Effects of Exploratory Studies Facility Excavation

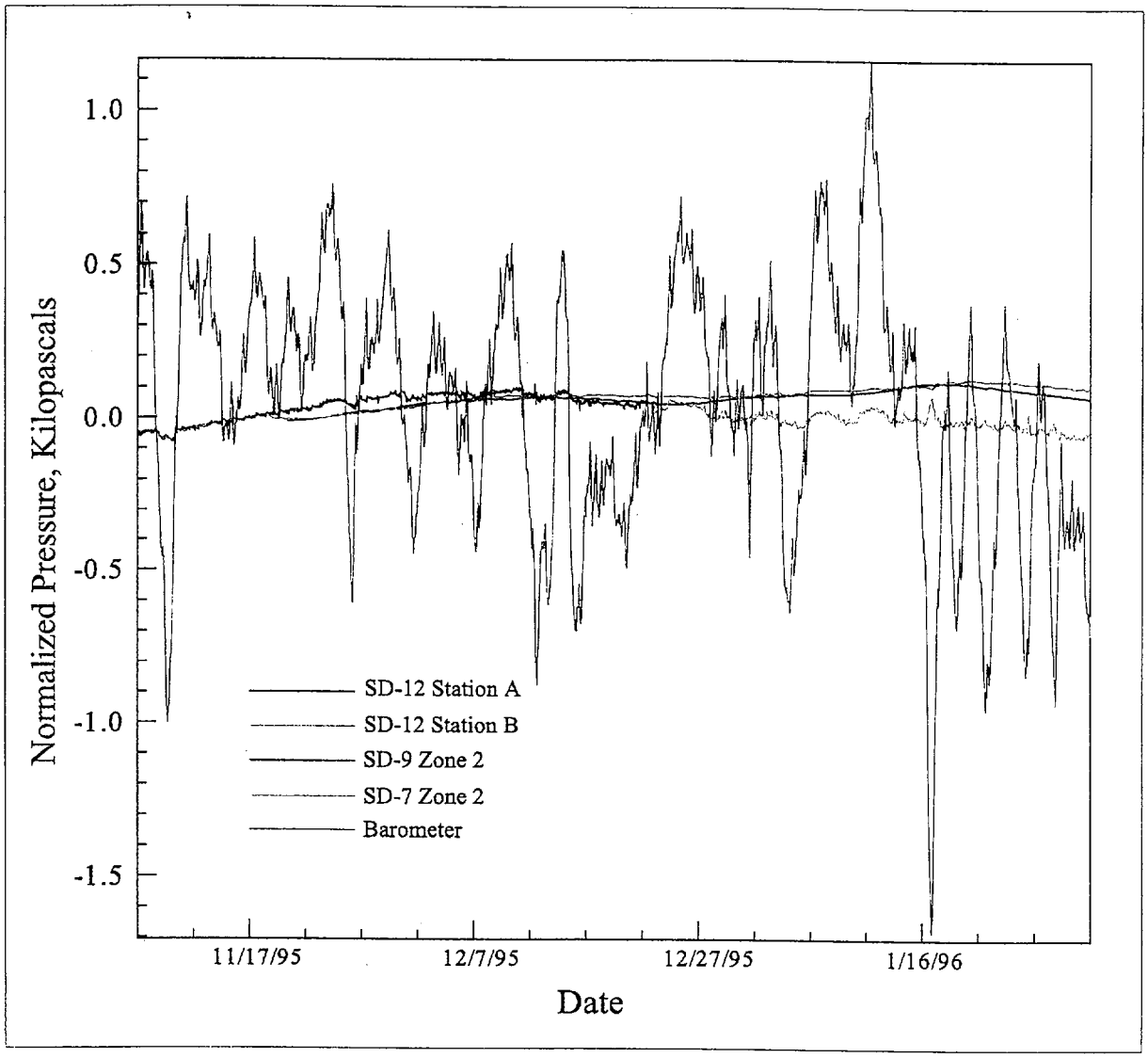

Figure 5.3-125. Pneumatic Pressure Records from Monitoring Locations Below Perched-Water Zones in Boreholes SD-7, SD-9, and SD-12

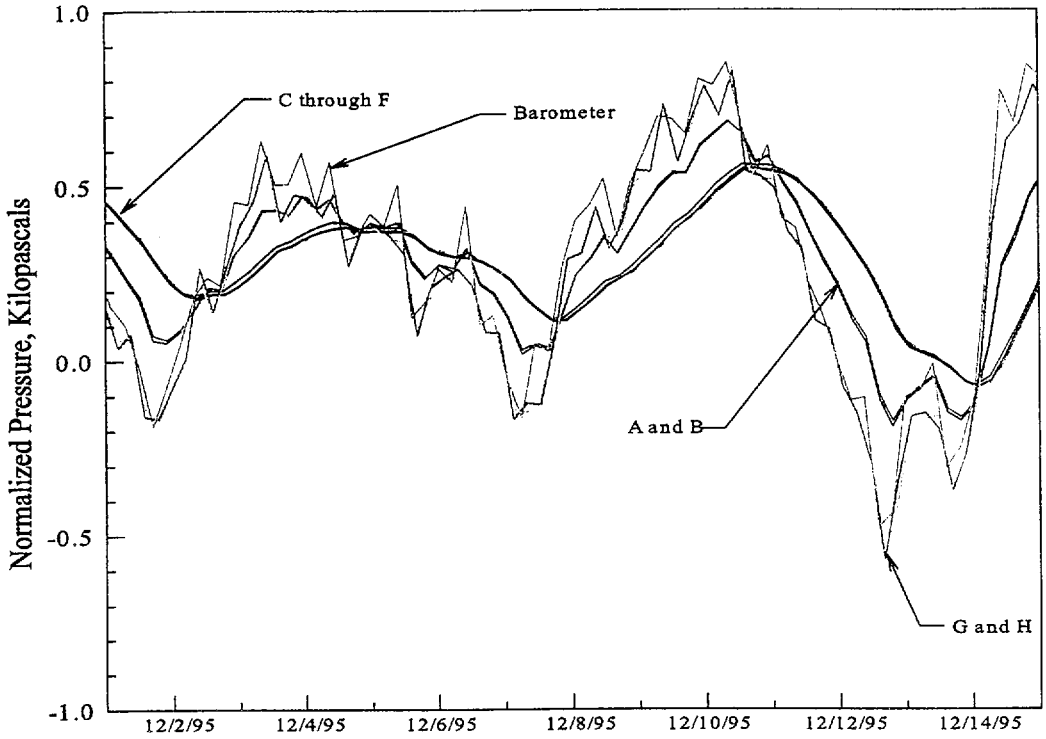

Instrument Station	Depth (meters)	Lithology	Residual Amplitude (percent)	Phase Lag (hours)
H	11.1	Alluvium/Colluvium	100	1.5
G	24.5	Tiva Canyon Crystal-Poor Vitric	100	1.9
F	35.2	Yucca Mountain Tuff	62	26.2
E	45.0	Yucca Mountain Tuff	62	26.7
D	55.9	Pah Canyon Tuff	62	27.0
C	88.2	Pah Canyon Tuff	62	25.6
B	104.1	Topopah Spring Crystal-Rich Vitric	76	10.8
A	112.0	Topopah Spring Crystal-Rich Nonlithophysal	77	10.2

53-126.CDR.123.SITEDESC

Figure 5.3-126. Pneumatic Pressure Record and Results of Cross-Spectral Analysis for Borehole UZ#4 After the Effects of Exploratory Studies Facility Excavation

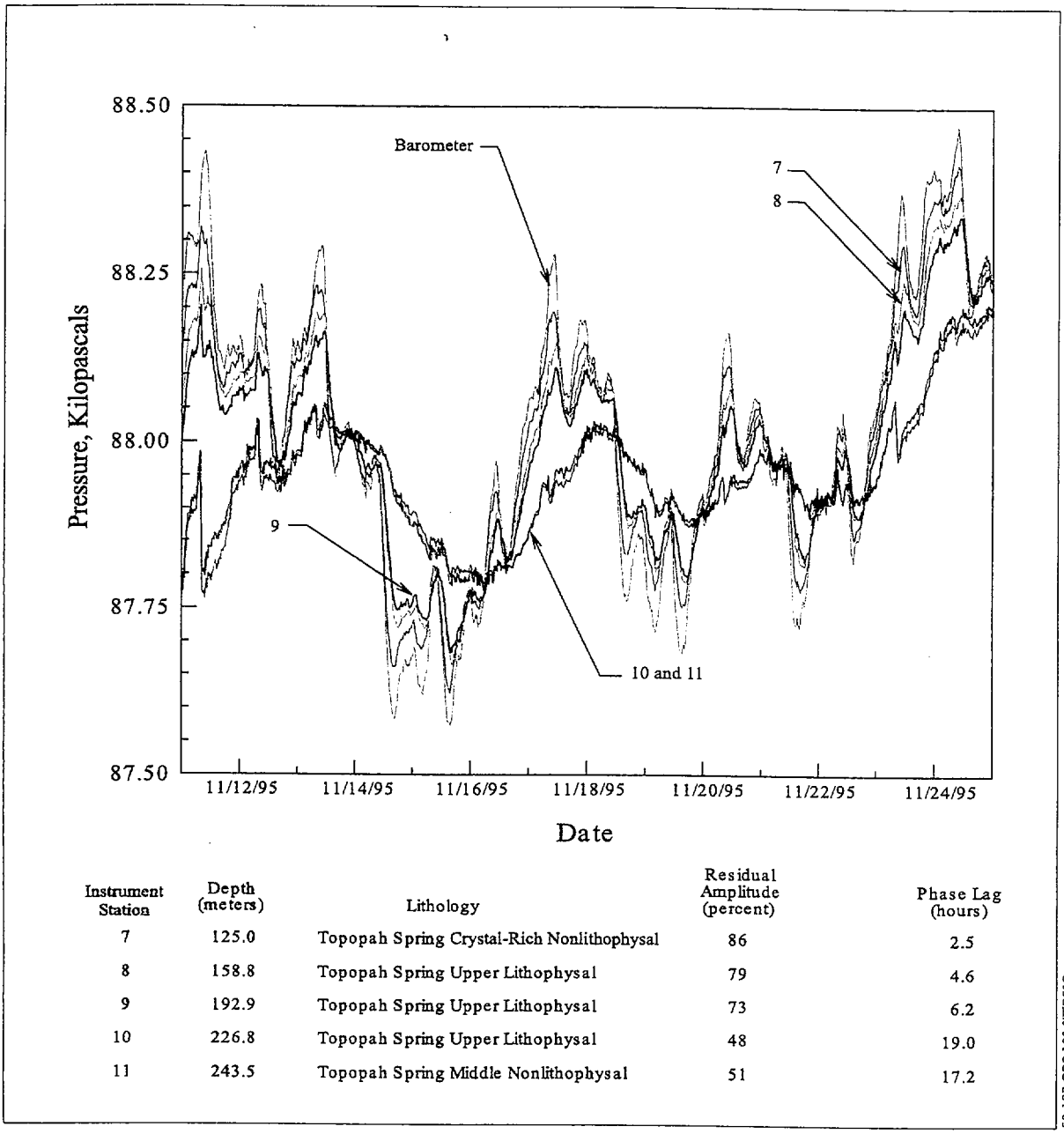

Instrument Station	Depth (meters)	Lithology	Residual Amplitude (percent)	Phase Lag (hours)
7	125.0	Topopah Spring Crystal-Rich Nonlithophysal	86	2.5
8	158.8	Topopah Spring Upper Lithophysal	79	4.6
9	192.9	Topopah Spring Upper Lithophysal	73	6.2
10	226.8	Topopah Spring Upper Lithophysal	48	19.0
11	243.5	Topopah Spring Middle Nonlithophysal	51	17.2

53-127.CDR.123.SIEDESC

Figure 5.3-127. Pneumatic Pressure Record and Results of Cross-Spectral Analysis for Instrument Stations 7 Through 11 in Borehole NRG#5 After the Effects of Exploratory Studies Facility Excavation

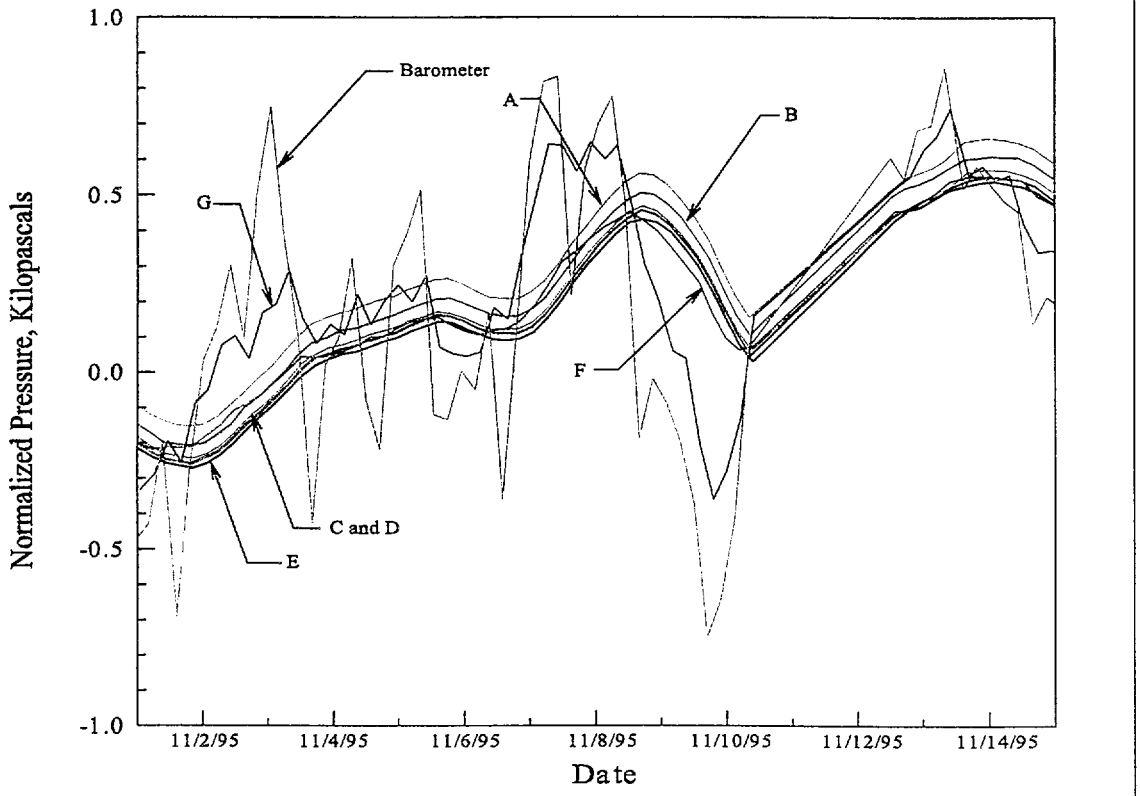

Instrument Station	Depth (meters)	Lithology	Residual Amplitude (percent)	Phase Lag (hours)
G	39.6	Tiva Canyon Columnar	72	5.2
F	54.9	Pah Canyon Tuff	42	29.0
E	85.3	Topopah Spring Crystal-Rich Nonlithophysal	48	33.5
D	106.8	Topopah Spring Crystal-Rich Nonlithophysal	48	33.4
C	138.8	Topopah Spring Upper Lithophysal	48	33.6
B	163.1	Topopah Spring Upper Lithophysal	49	33.7
A	219.4	Topopah Spring Middle Nonlithophysal	49	33.8

53-128.CDR.123.SIIEDESC

Figure 5.3-128. Pneumatic Pressure Record and Results of Cross-Spectral Analysis for Borehole NRG-6 After the Effects of Exploratory Studies Facility Excavation

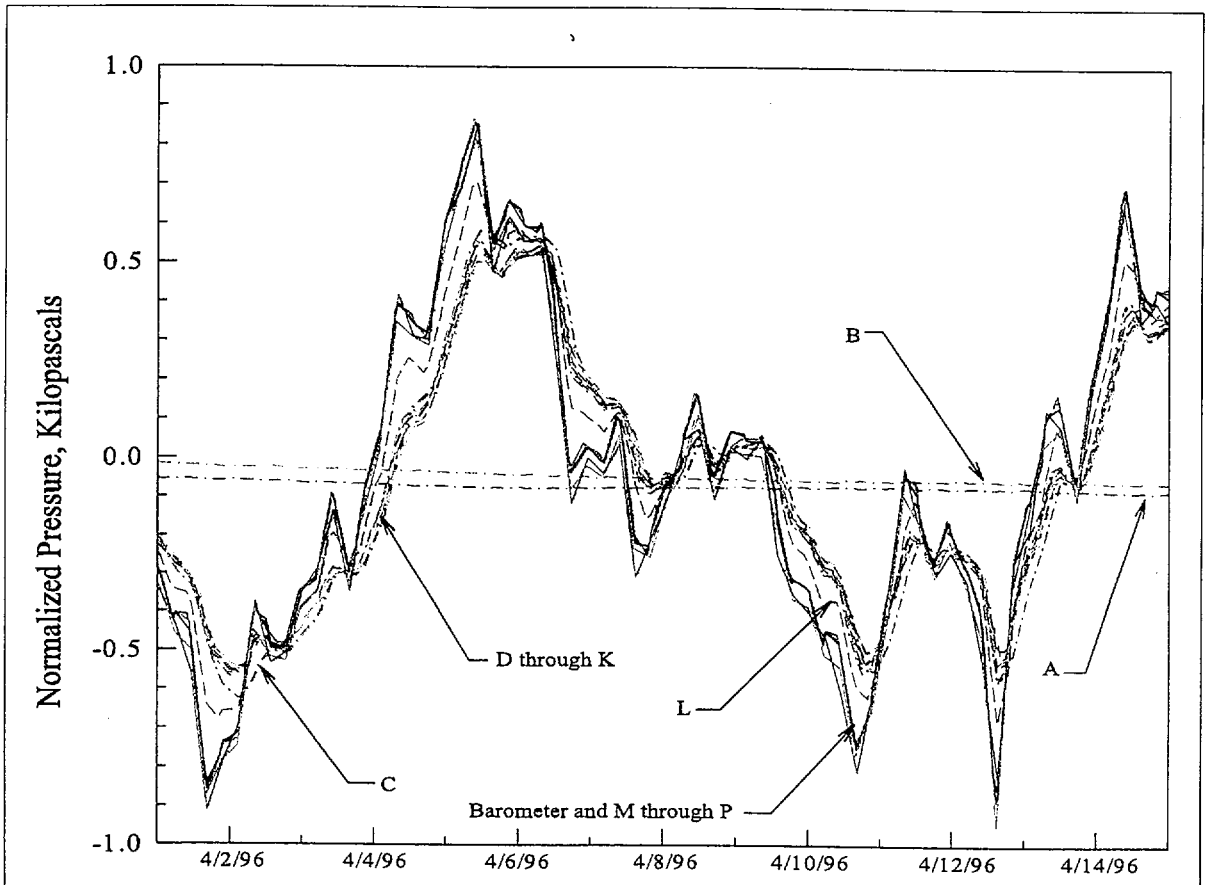

Instrument Station	Depth (meters)	Lithology	Residual Amplitude (percent)	Phase Lag (hours)
N-P	24.6-65.3	Tiva Canyon Tuff	100	0.3
M	76.7	Tiva Canyon Crystal-Poor Vitric	100	0.6
L	91.8	Pre-Pah Canyon Tuff bedded tuff	85	4.4
K	106.8	Topopah Spring Crystal-Rich Nonlithophysal	69	10.3
J	128.9	Topopah Spring Crystal-Rich Nonlithophysal	69	10.4
I	170.8	Topopah Spring Upper Lithophysal	70	10.2
H	208.1	Topopah Spring Middle Nonlithophysal	71	9.3
G	236.8	Topopah Spring Middle Nonlithophysal	72	8.8
F	256.5	Topopah Spring Lower Lithophysal	74	8.2
E	285.1	Topopah Spring Lower Lithophysal	74	8.3
D	322.6	Topopah Spring Lower Nonlithophysal	74	8.6
C	385.7	Topopah Spring Lower Nonlithophysal	80	9.8

53-129.CDR.123.SITEDESC

Figure 5.3-129. Pneumatic Pressure Record and Results of Cross-Spectral Analysis for Borehole SD-12 After the Effects of Exploratory Studies Facility Excavation

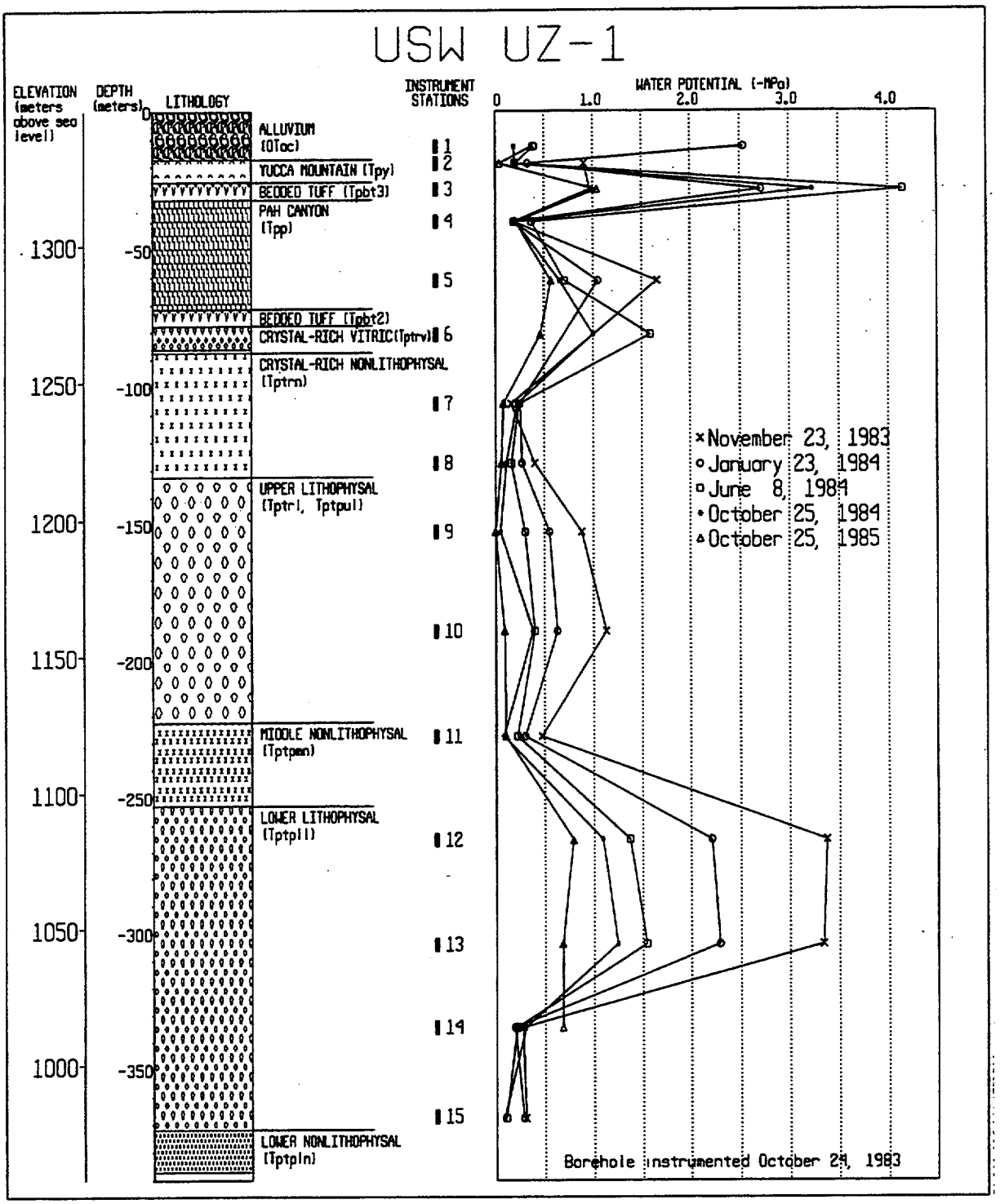

Figure 5.3-130. Time-Series Water-Potential Profiles for November 1983 Through October 1995 for Prototype Borehole UZ-1 in Drill Hole Wash

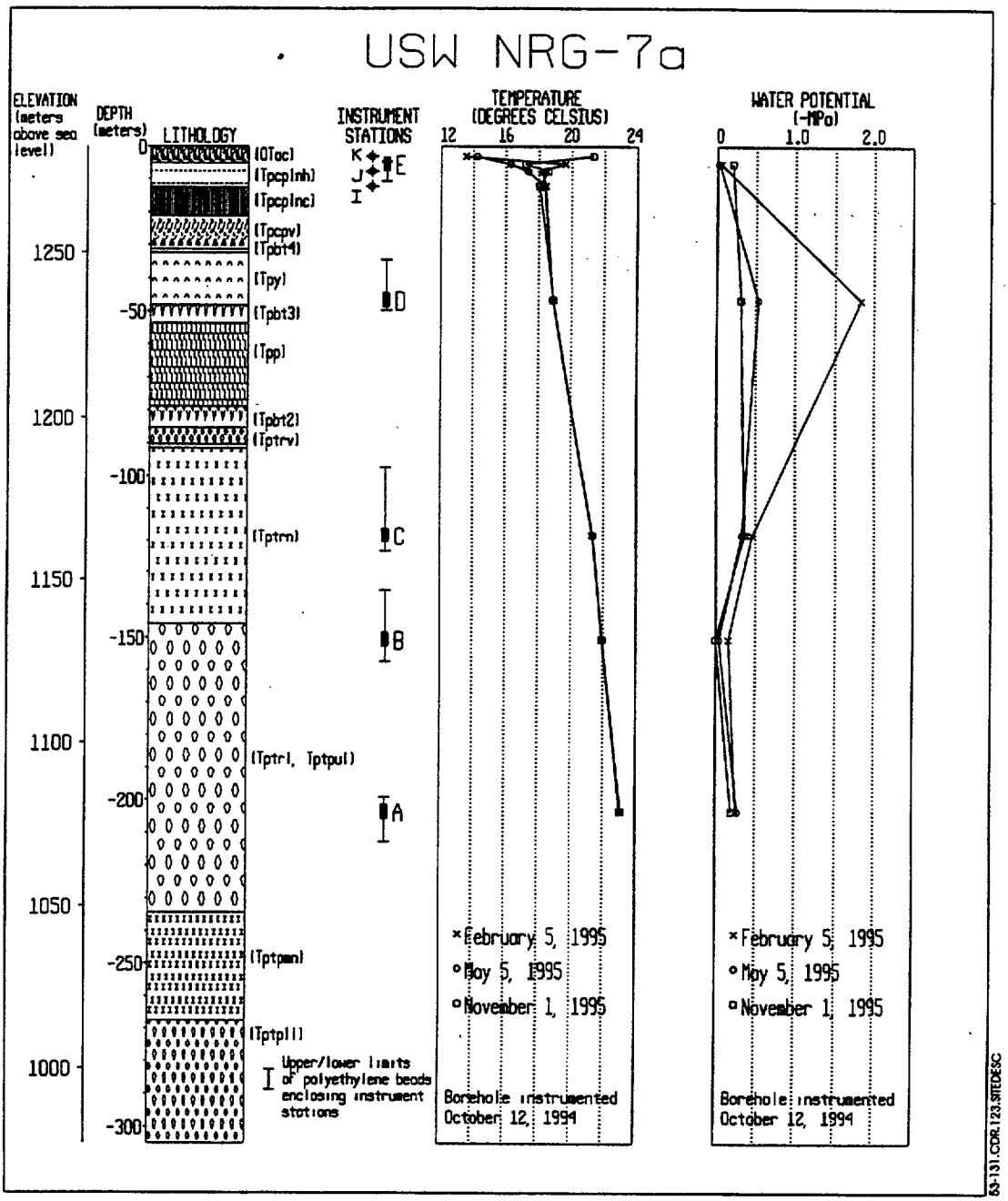

Figure 5.3-131. Selected Temperature and Water-Potential Profiles for Borehole NRG-7a

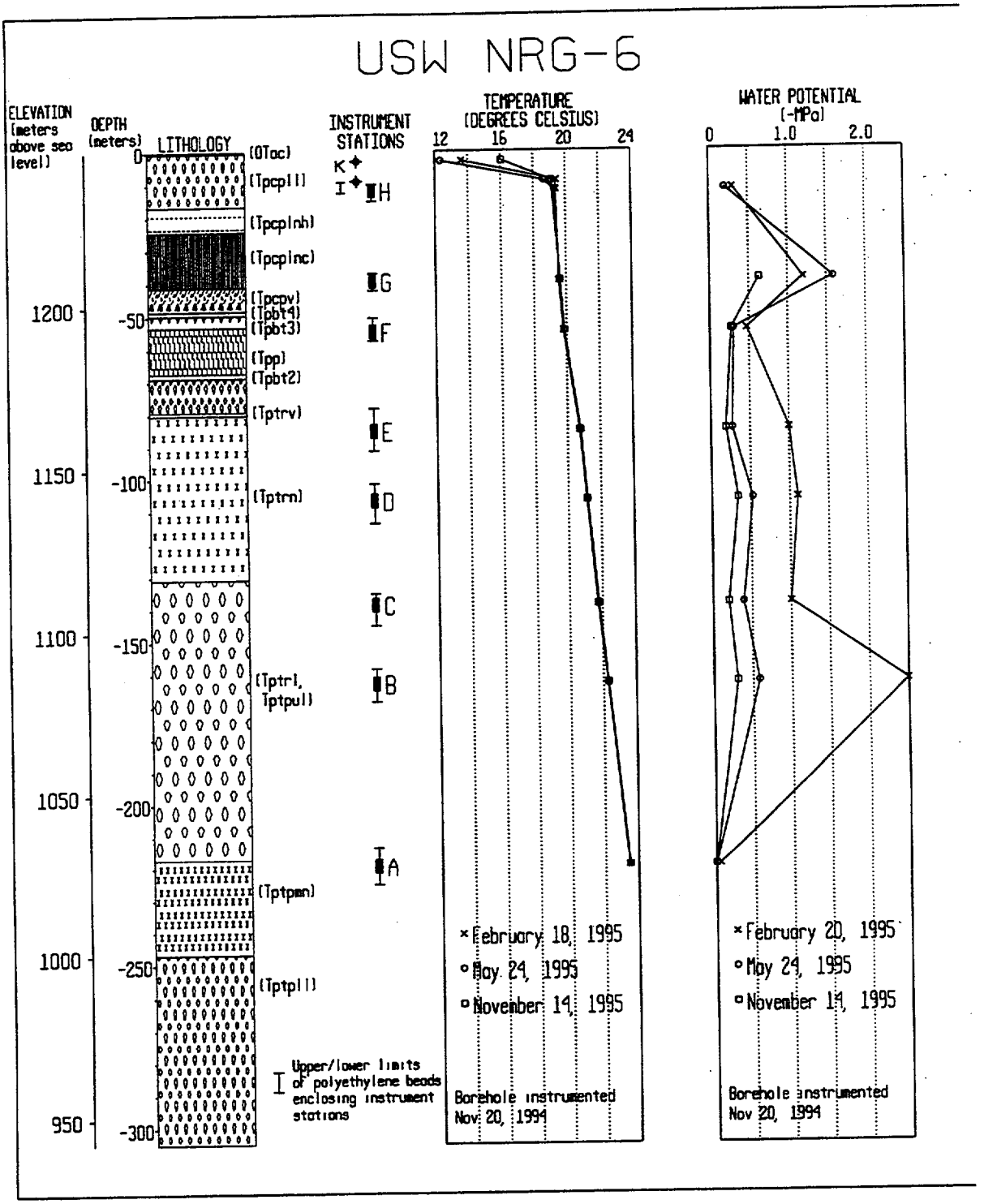

Figure 5.3-132. Selected Temperature and Water-Potential Profiles for Borehole NRG-6

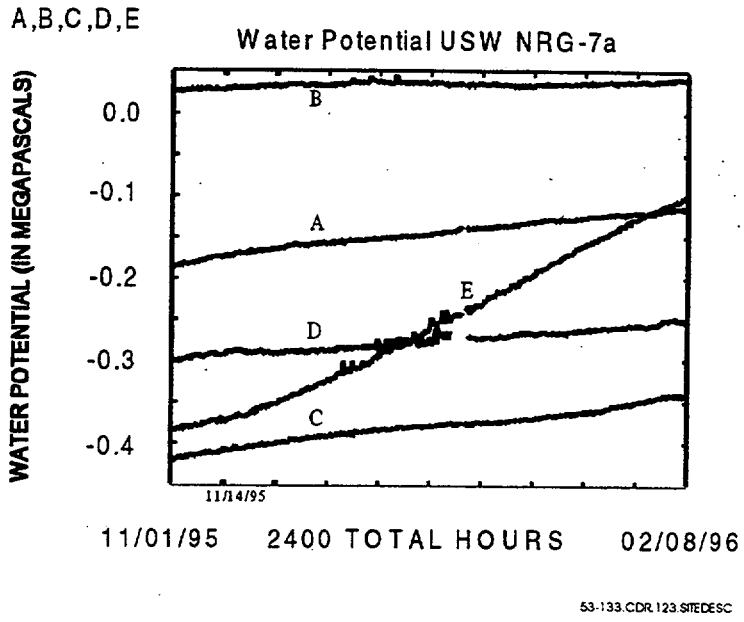

Figure 5.3-133. Time-Series Water-Potential Records for Instrument Stations in Borehole NRG-7a

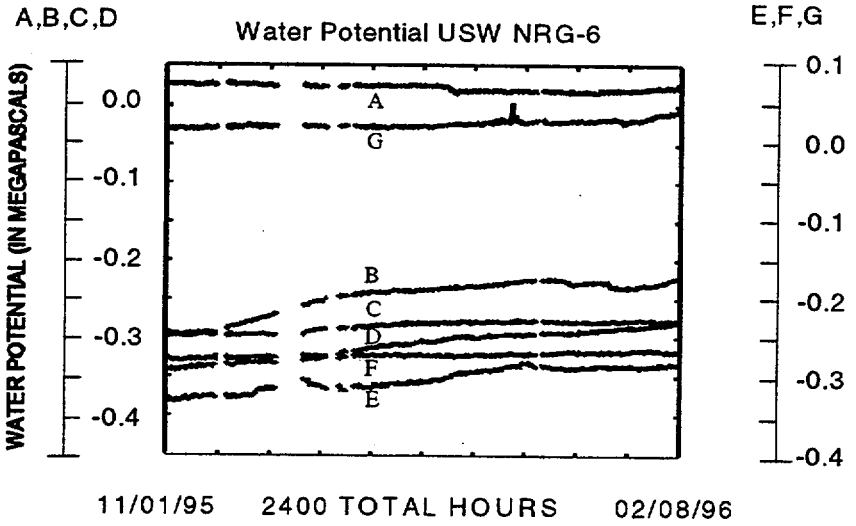

Figure 5.3-134. Time-Series Water-Potential Records for Instrument Stations in Borehole NRG-6

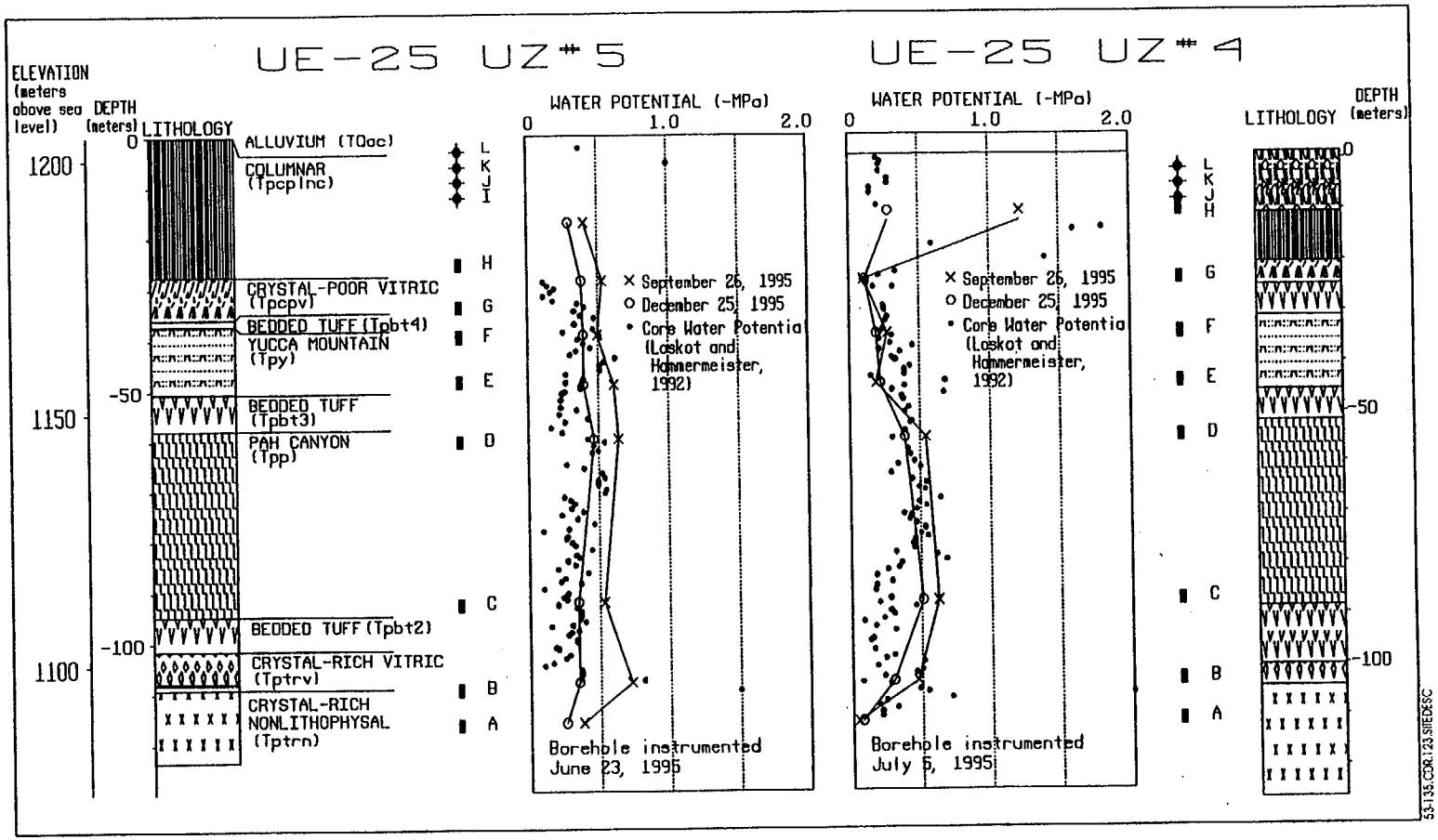

Figure 5.3-135. In Situ and Core Sample Water-Potentials for Boreholes UZ#4 and UZ#5 in Pagany Wash

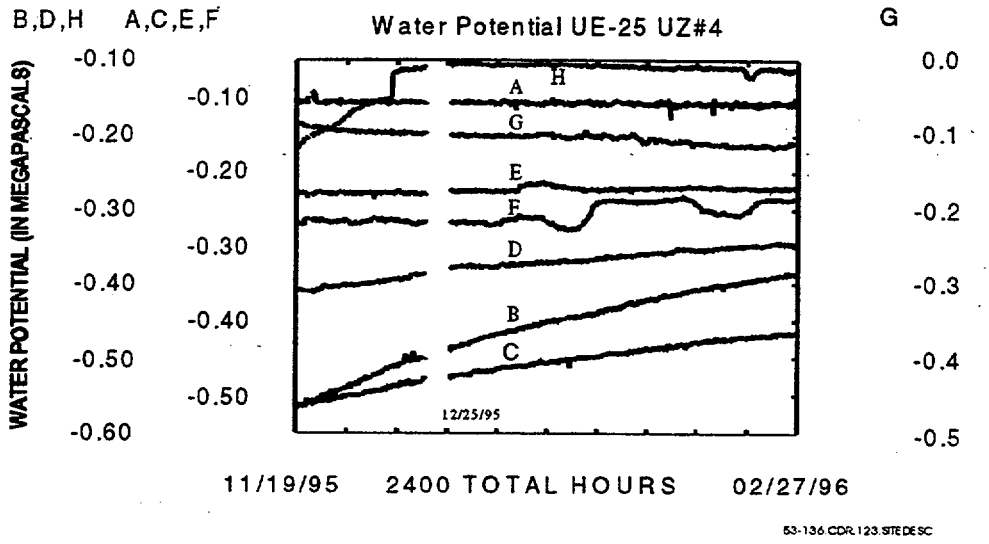

Figure 5.3-136. Time-Series Water-Potential Records for Instrument Stations in Borehole UZ#4

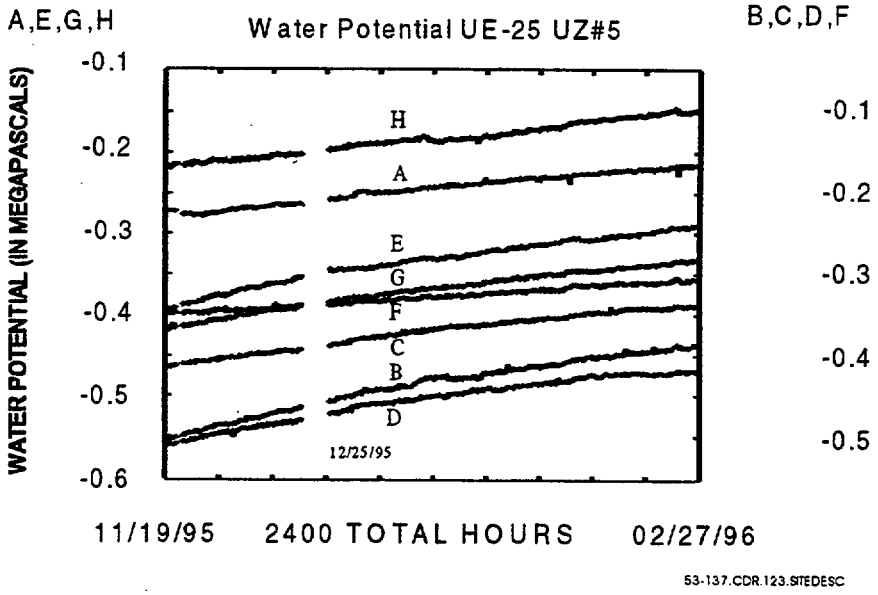

Figure 5.3-137. Time-Series Water-Potential Records for Instrument Stations in Borehole UZ#5

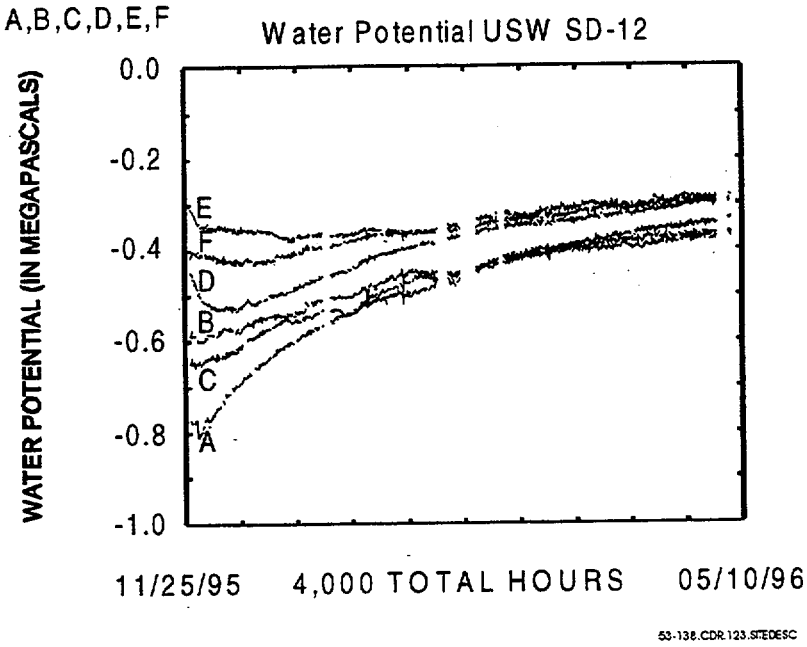

Figure 5.3-138. Time-Series Water-Potential Records for Borehole SD-12 for Instrument Station A in the CHn, Station B in the TSw Basal Vitrophyre, and Stations C, D, E, and F in the TSw Crystal-Poor Lower Nonlithophysal and Lower Lithophysal Units

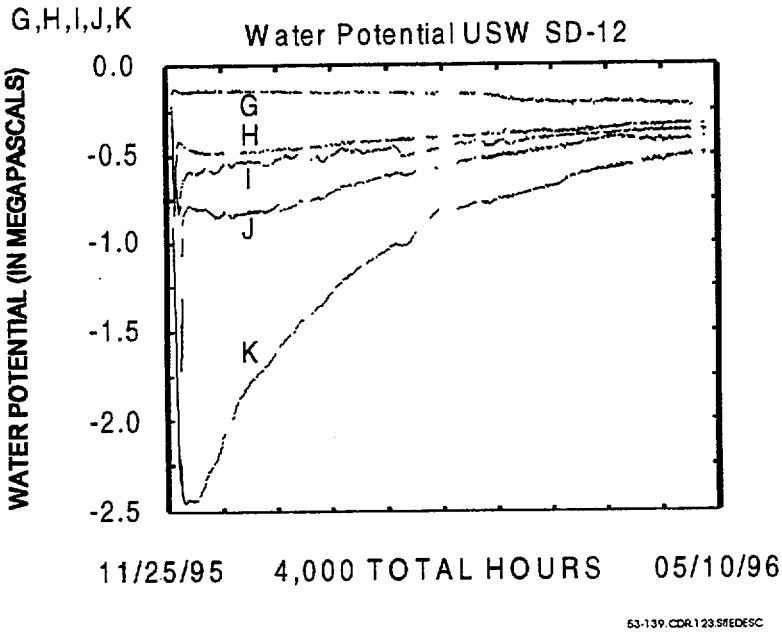

Figure 5.3-139. Time-Series Water-Potential Records for Borehole SD-12 for Instrument Stations G and H in the Tsw Middle Nonlithophysal Unit, Station I in the Tsw Crystal-Poor Upper Lithophysal Unit, and Stations J and K in the TSw Crystal-Rich Nonlithophysal Unit

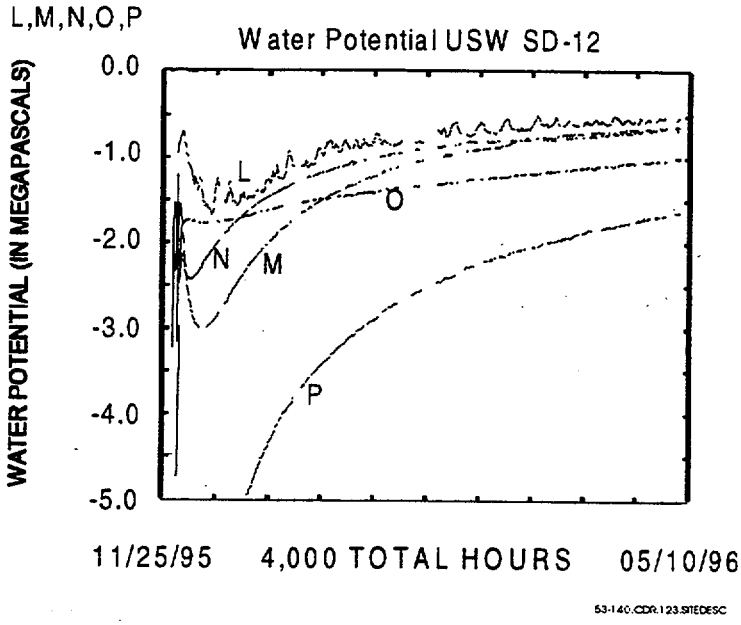

Figure 5.3-140. Time-Series Water-Potential Records for Borehole SD-12 for Instrument Stations L and M in the PTn and Stations N, O, and P in the TCw

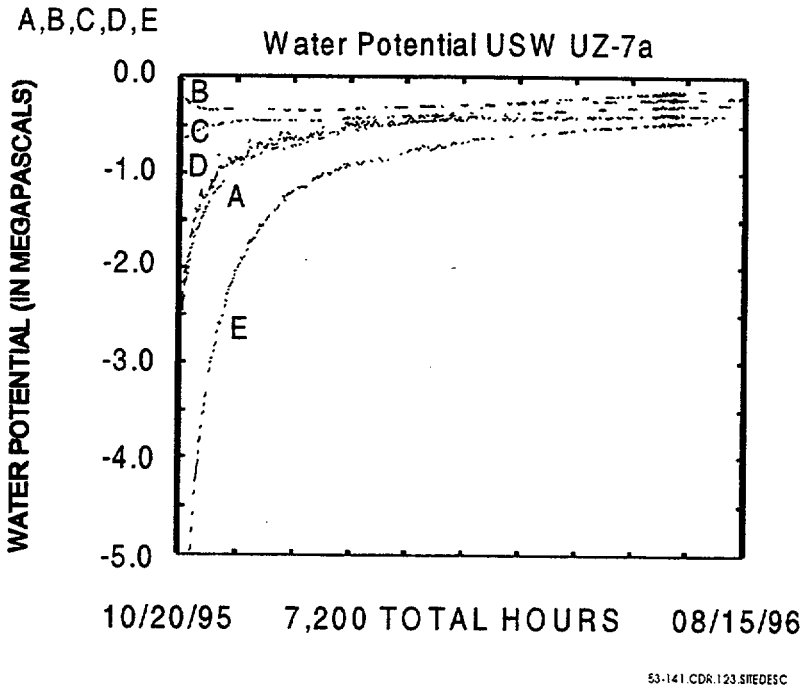

Figure 5.3-141. Time-Series Water-Potential Records for Borehole UZ-7a for Instrument Stations A, B, C, D, and E in the Topopah Spring Welded Hydrogeologic Unit

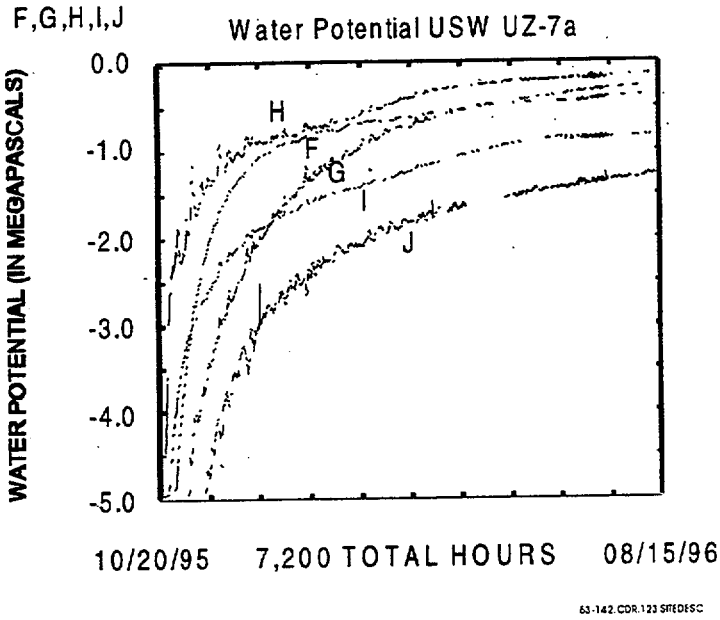

Figure 5.3-142. Time-Series Water-Potential Records for Borehole UZ-7a for Instrument Stations F and G Canyon Welded Hydrogeologic Unit

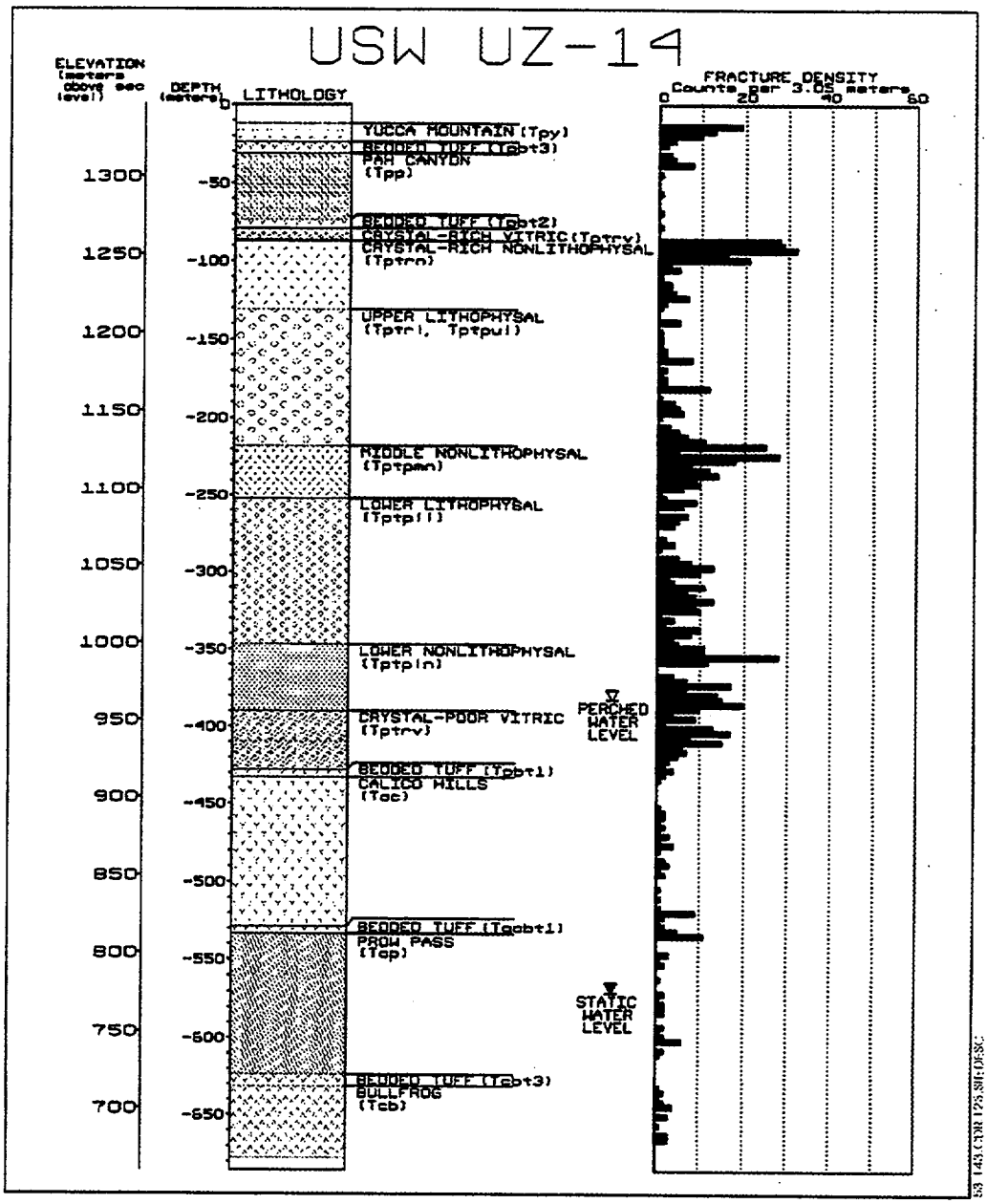

Figure 5.3-143. Lithostratigraphy and Fracture Density for Borehole UZ-14

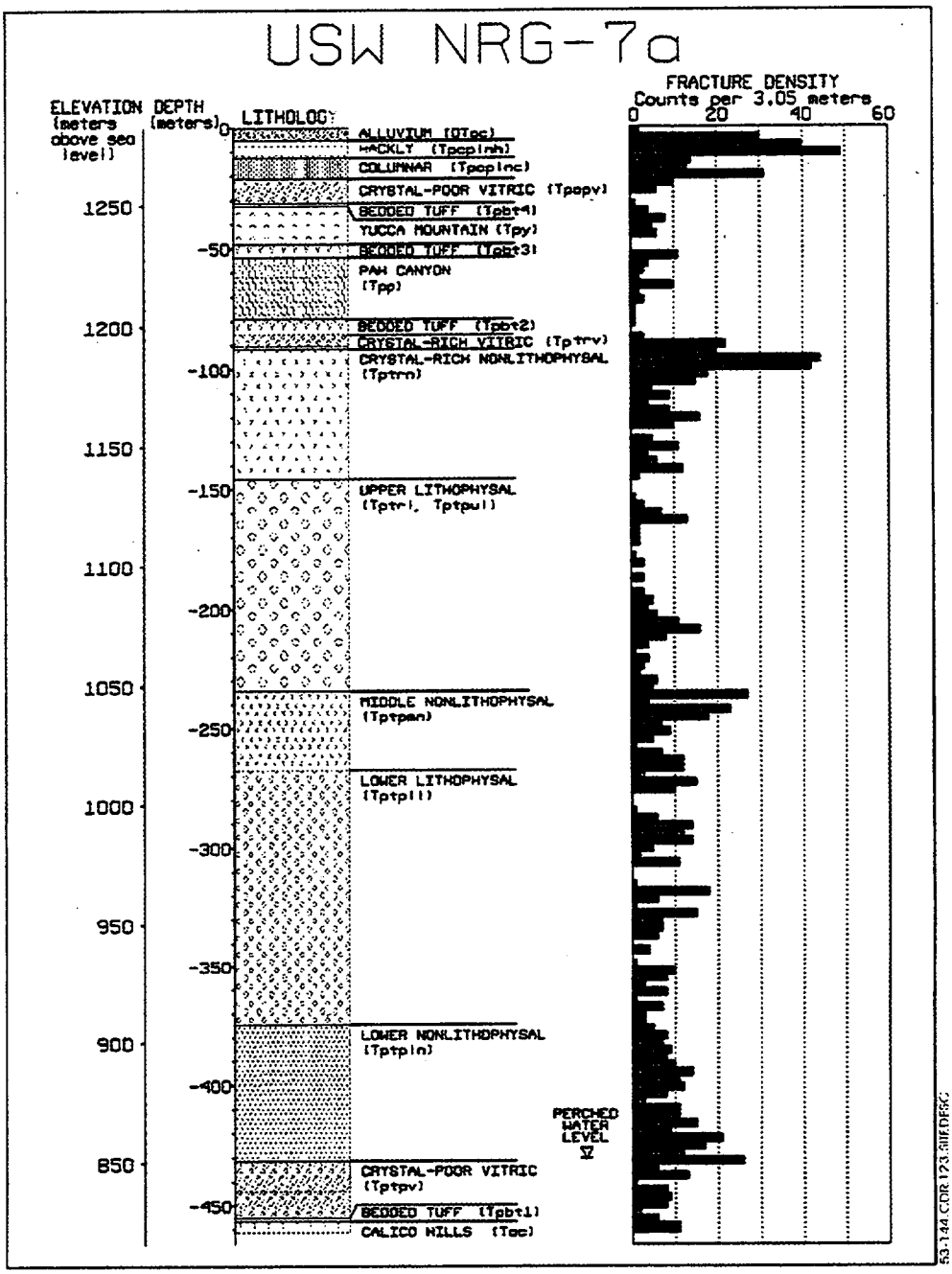

Figure 5.3-144. Lithostratigraphy and Fracture Density for Borehole NRG-7a

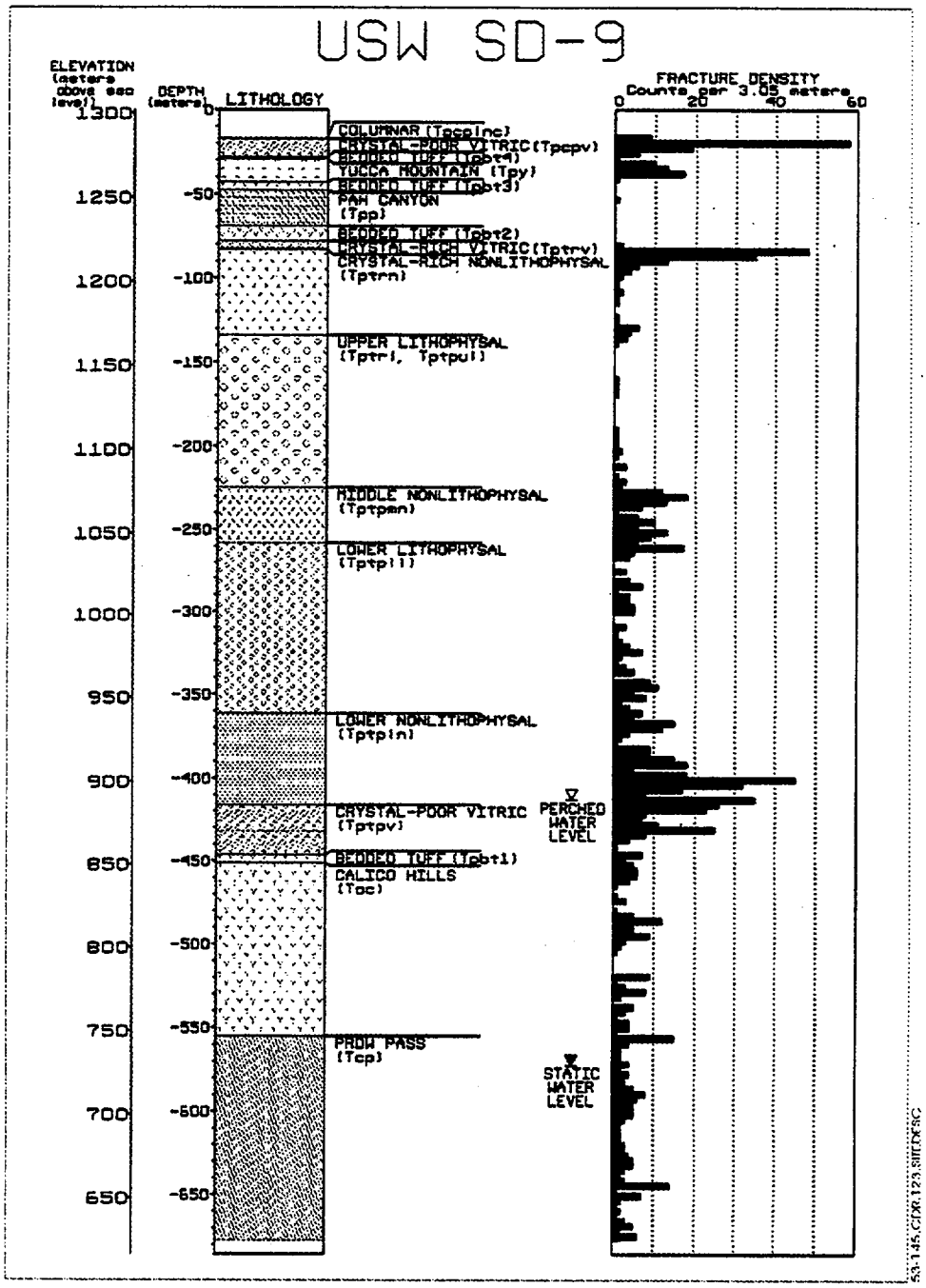

Figure 5.3-145. Lithostratigraphy and Fracture Density for Borehole SD-9

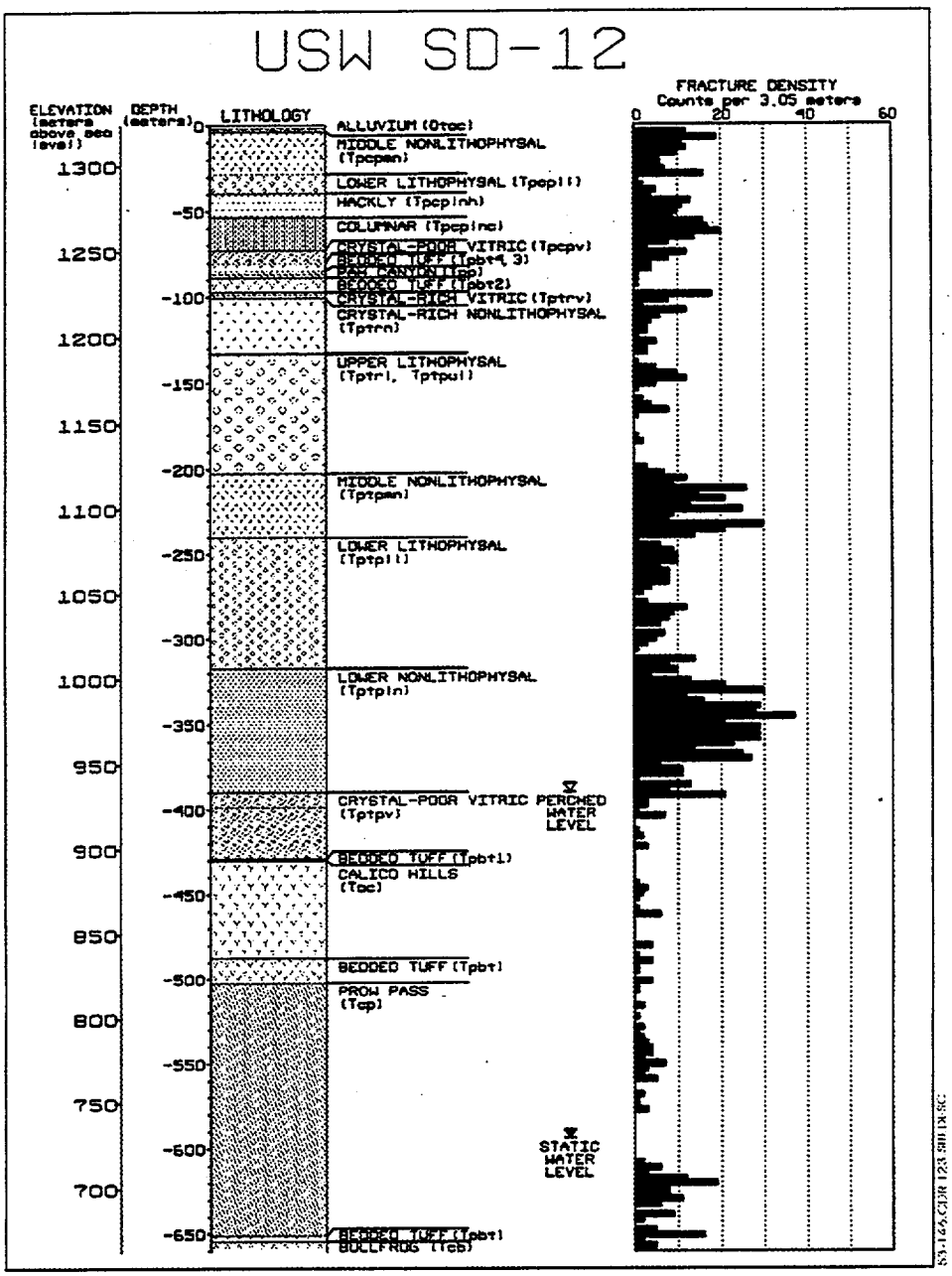

Figure 5.3-146. Lithostratigraphy and Fracture Density for Borehole SD-12

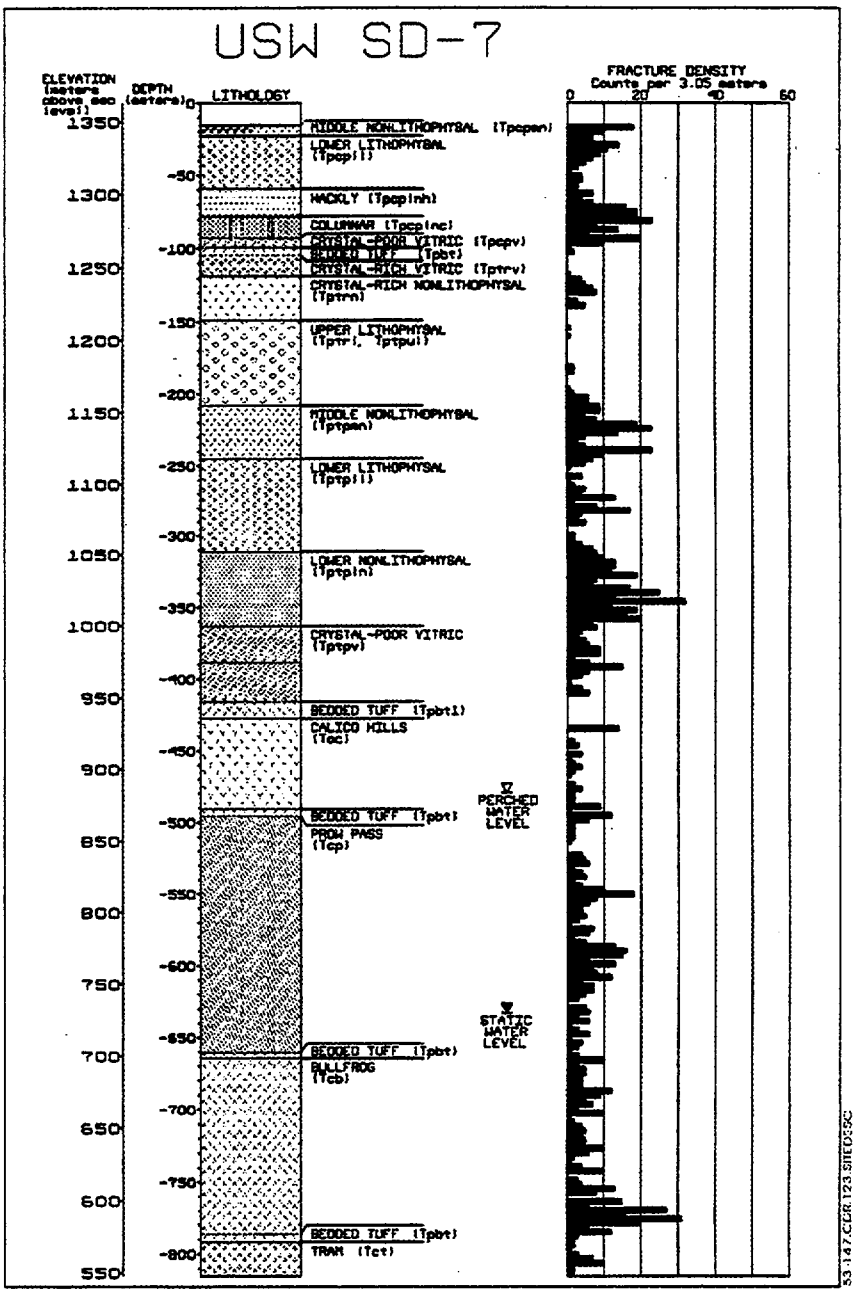

Figure 5.3-147. Lithostratigraphy and Fracture Density for Borehole SD-7

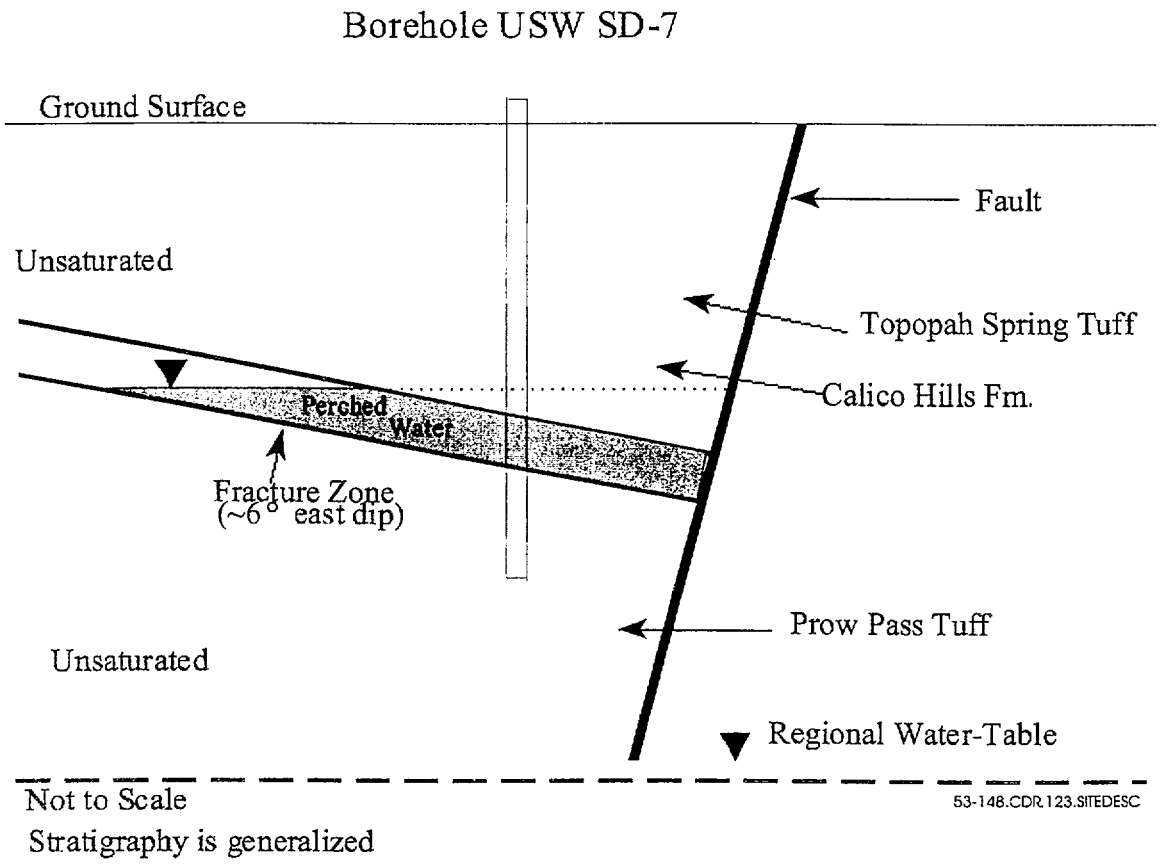

Figure 5.3-148. Idealized Conceptual Model of the Perched-Water Reservoir at Borehole SD-7

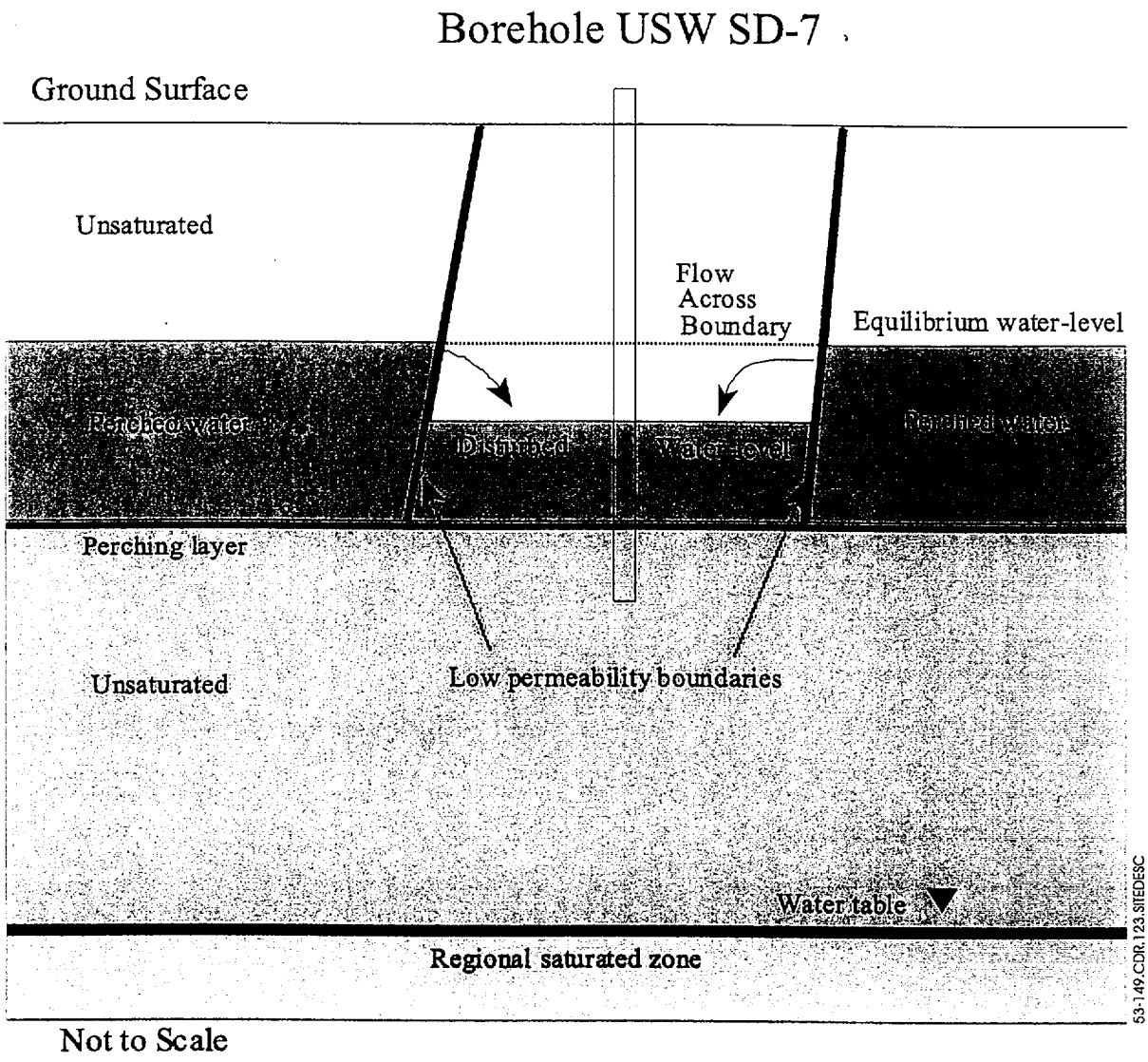

Figure 5.3-149. Conceptual Model of Compartmentalized Flow in the Perched-Water Reservoir at Borehole SD-7

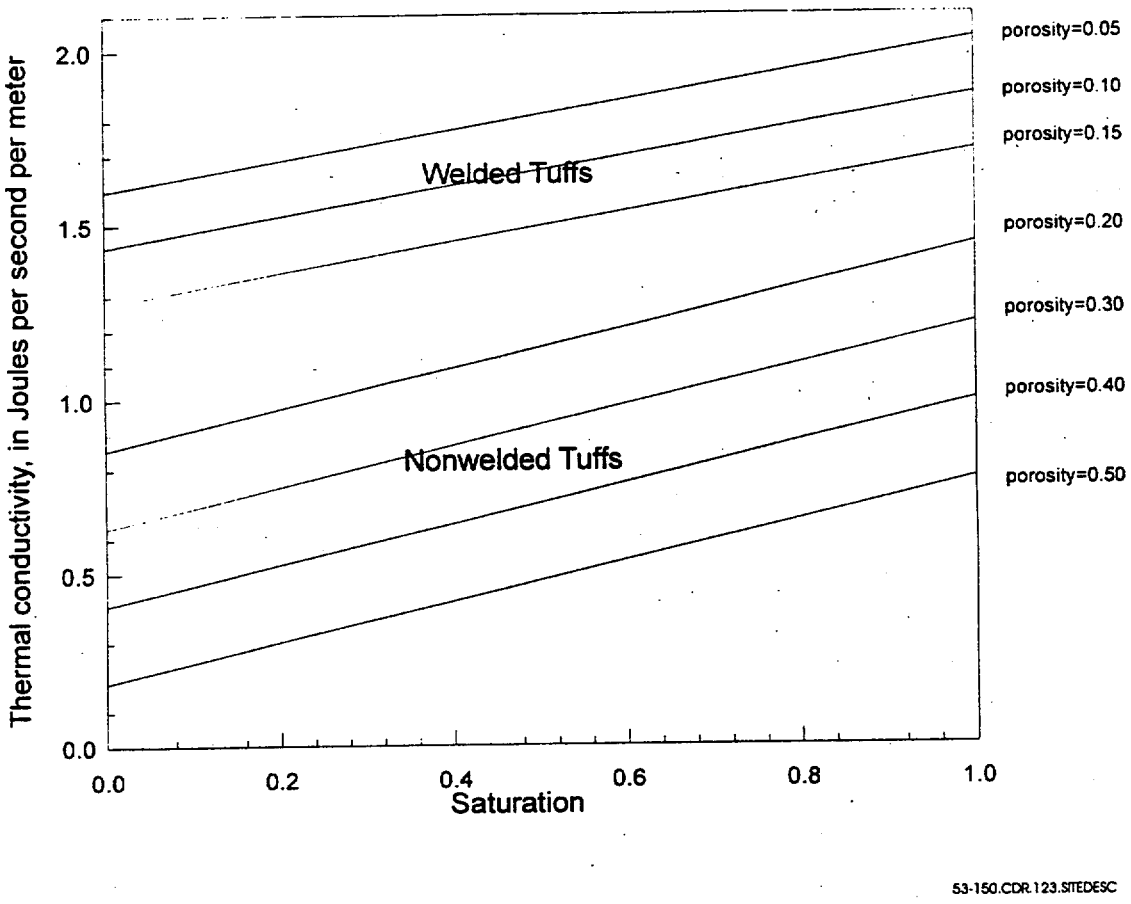

Figure 5.3-150. Relation Between Thermal Conductivity and Saturation and Porosity, Based on Regression Equations Developed by Rautman (1995)

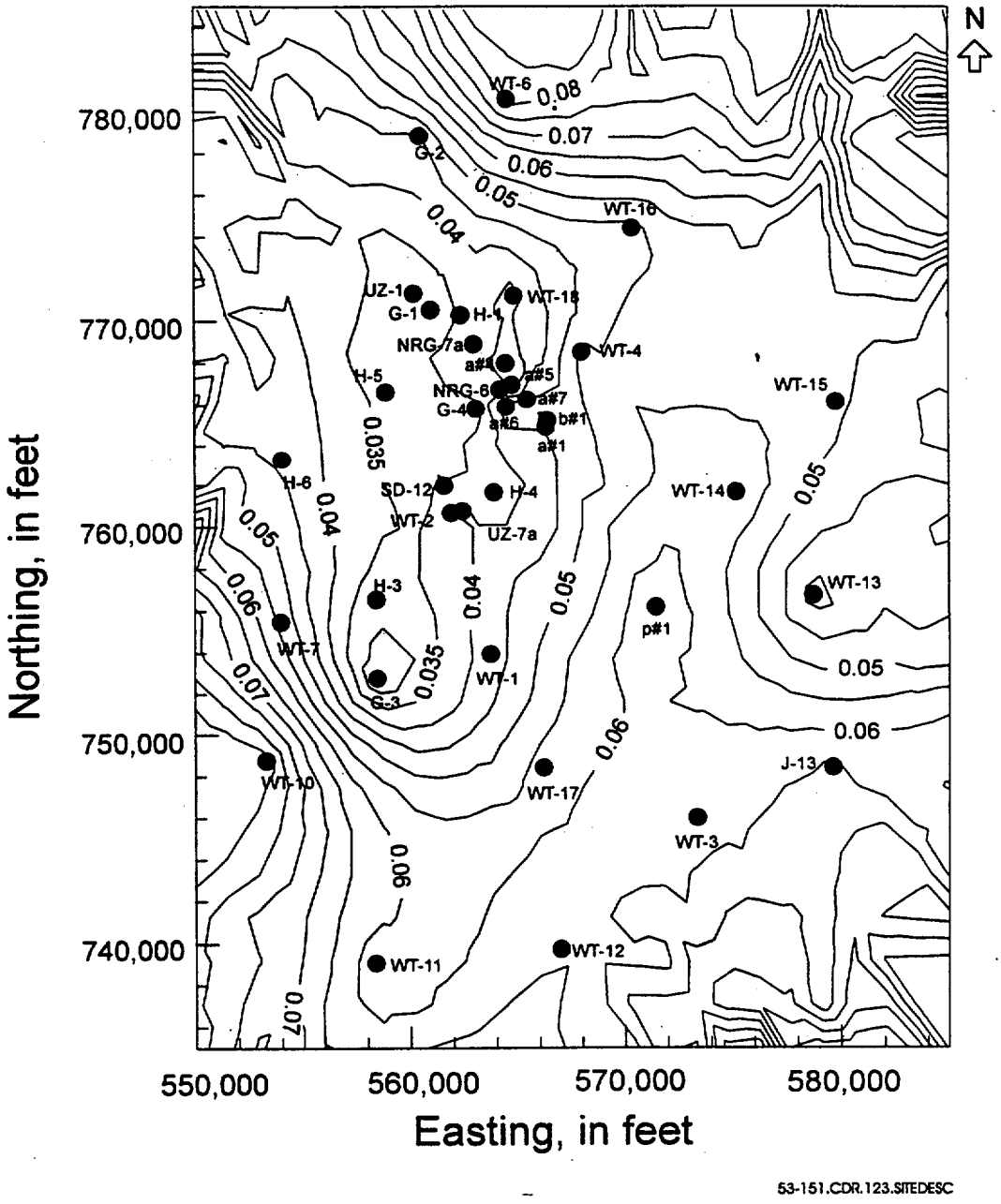

Figure 5.3-151. Calculated Heat Flux in Watts per Meter-Squared in the Topopah Spring Tuff in Boreholes at Yucca Mountain and Vicinity

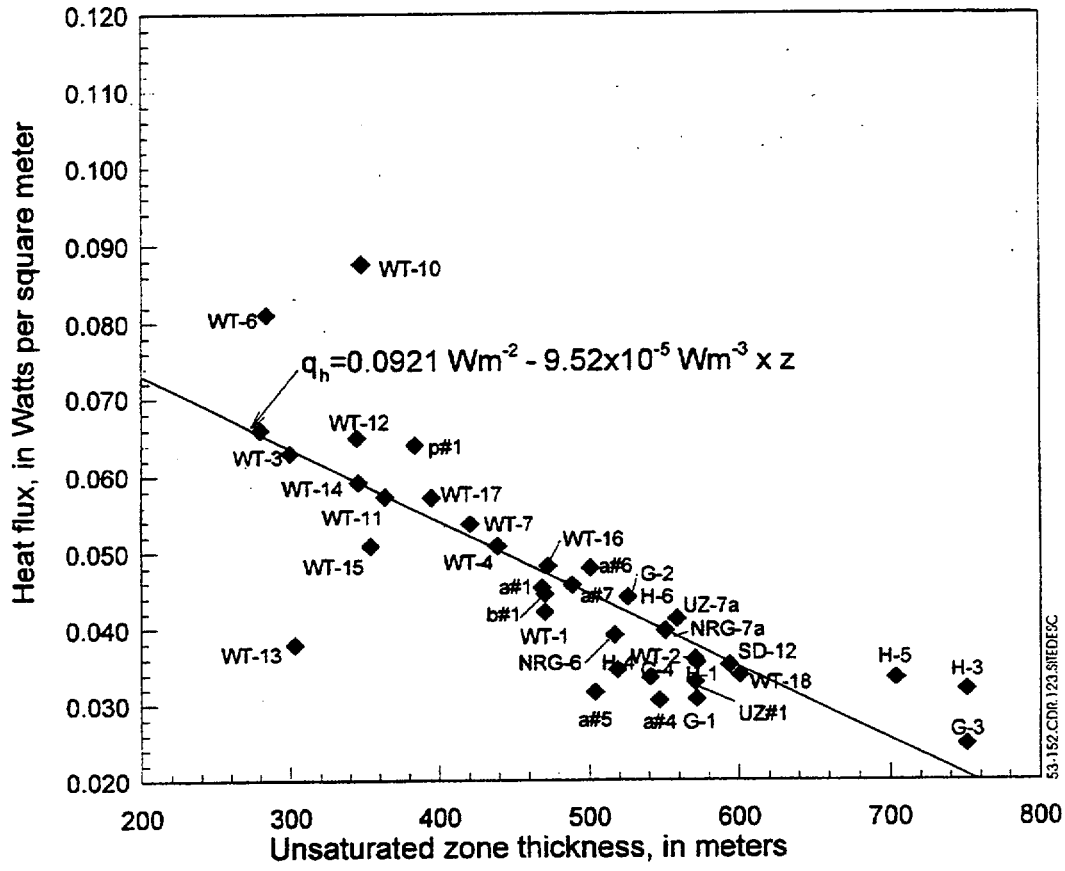

Figure 5.3-152. Heat Flux in the Topopah Spring Tuff as a Function of Unsaturated Zone Thickness

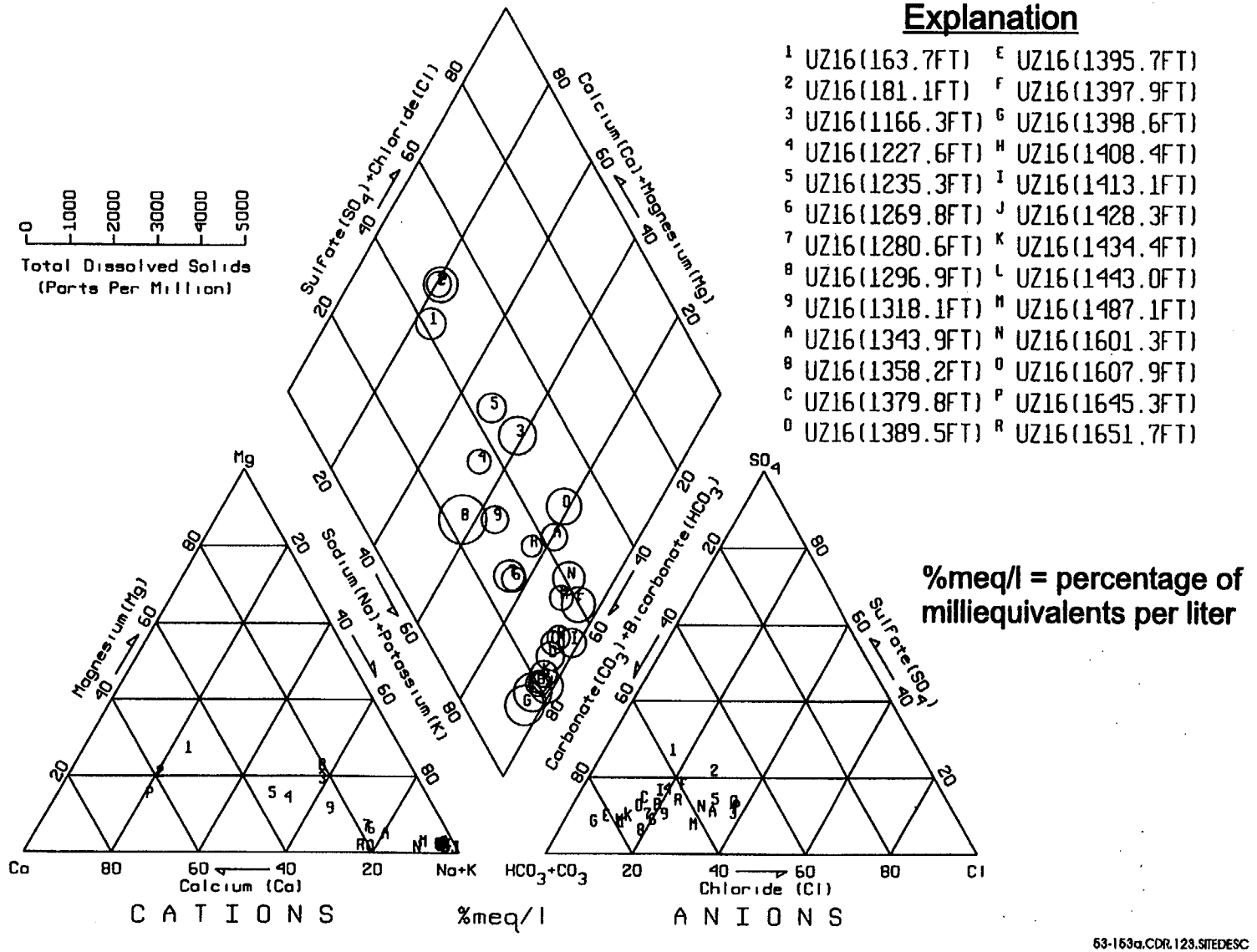

Figure 5.3-153a. Piper Diagrams for Pore Water from the Unsaturated Zone of Boreholes (a) UZ#16, (b) UZ-14, (c) NRG-6 and NRG-7a, and (d) SD-7, SD- 9, and SD-12

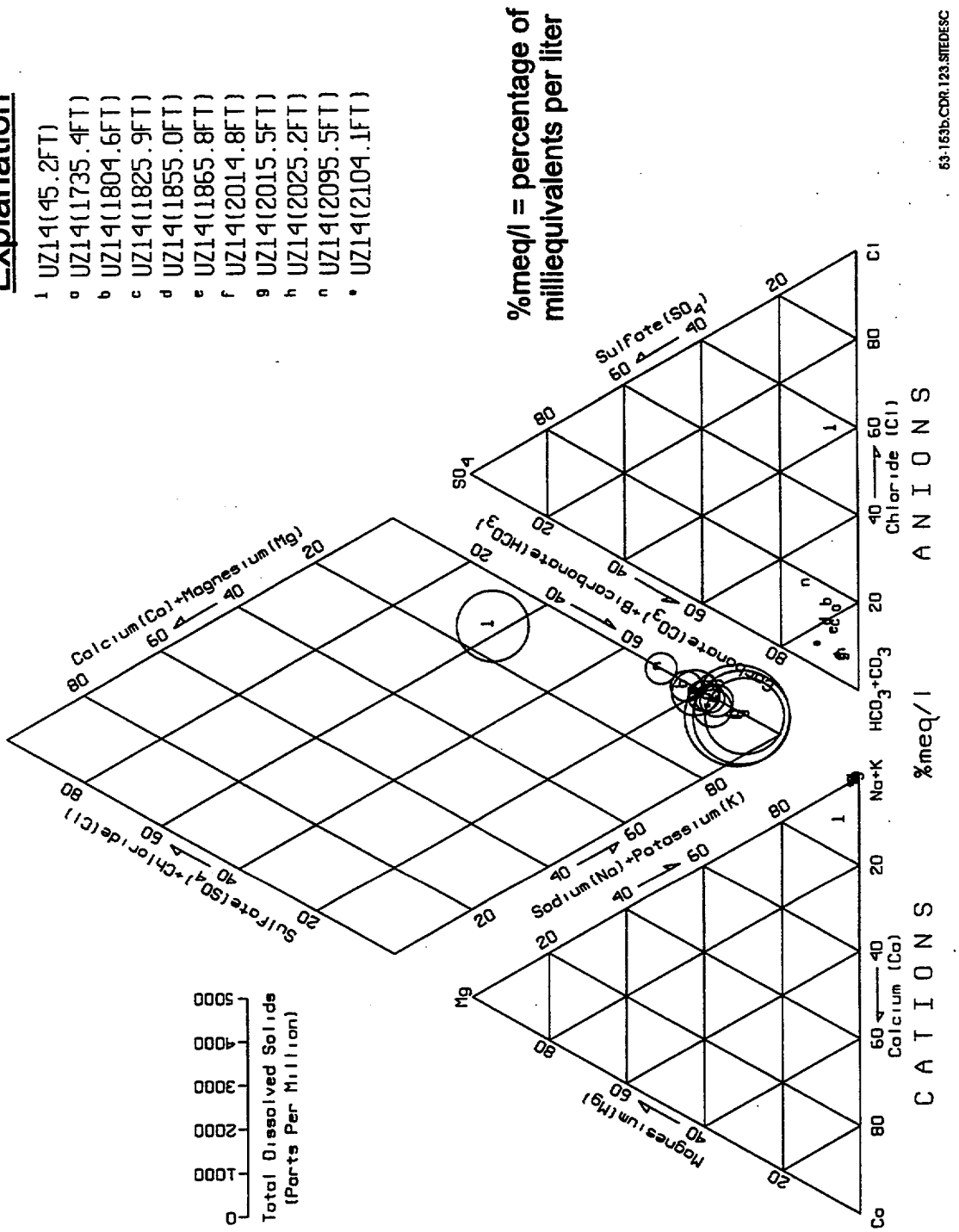

Figure 5.3-153b. Piper Diagrams for Pore Water from the Unsaturated Zone of Boreholes (a) UZ#16, (b) UZ-14, (c) NRG-6 and NRG-7a, and (d) SD-7, SD- 9, and SD-12

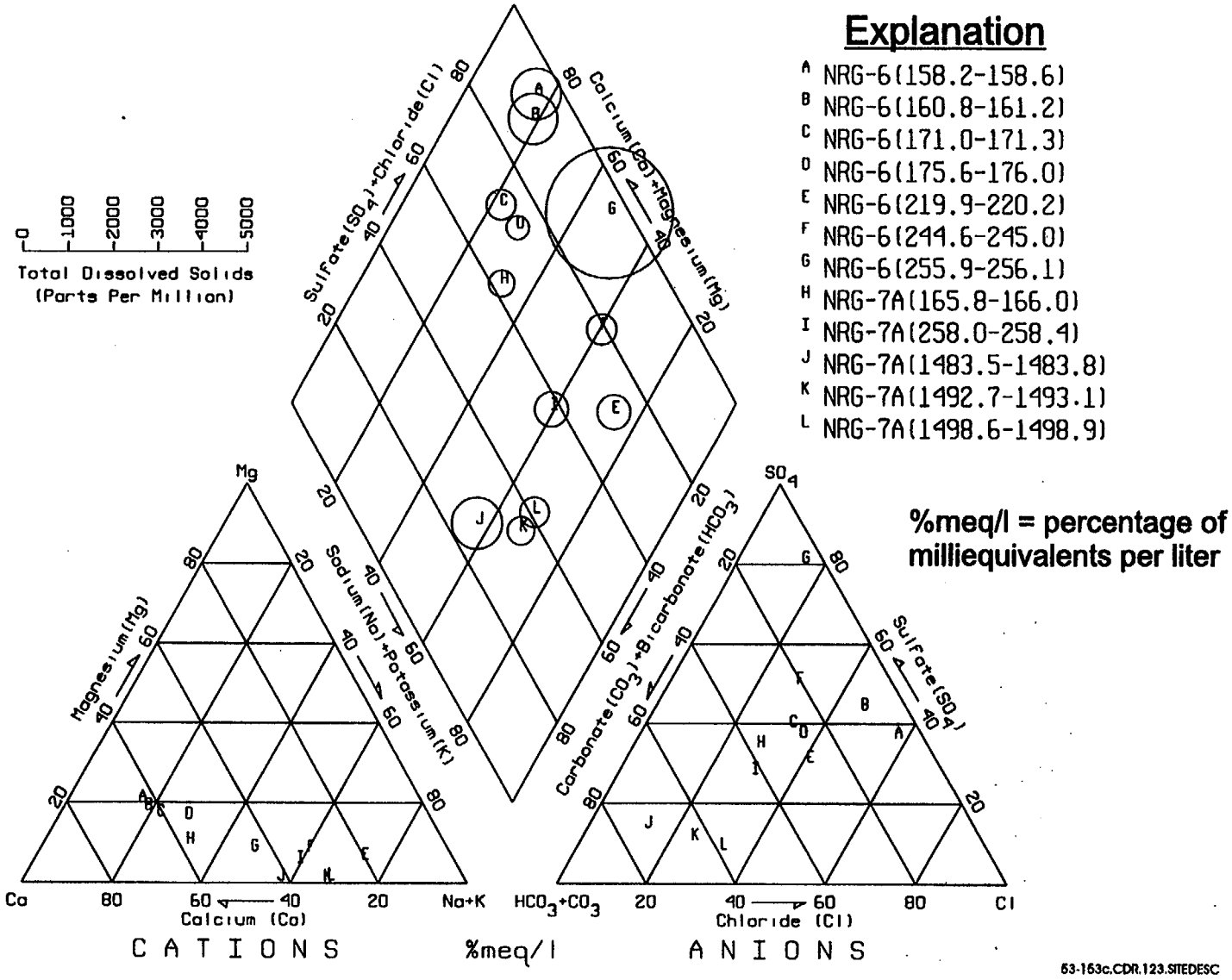

Figure 5.3-153c. Piper Diagrams for Pore Water from the Unsaturated Zone of Boreholes (a) UZ#16, (b) UZ-14, (c) NRG-6 and NRG-7a, and (d) SD-7, SD- 9, and SD-12

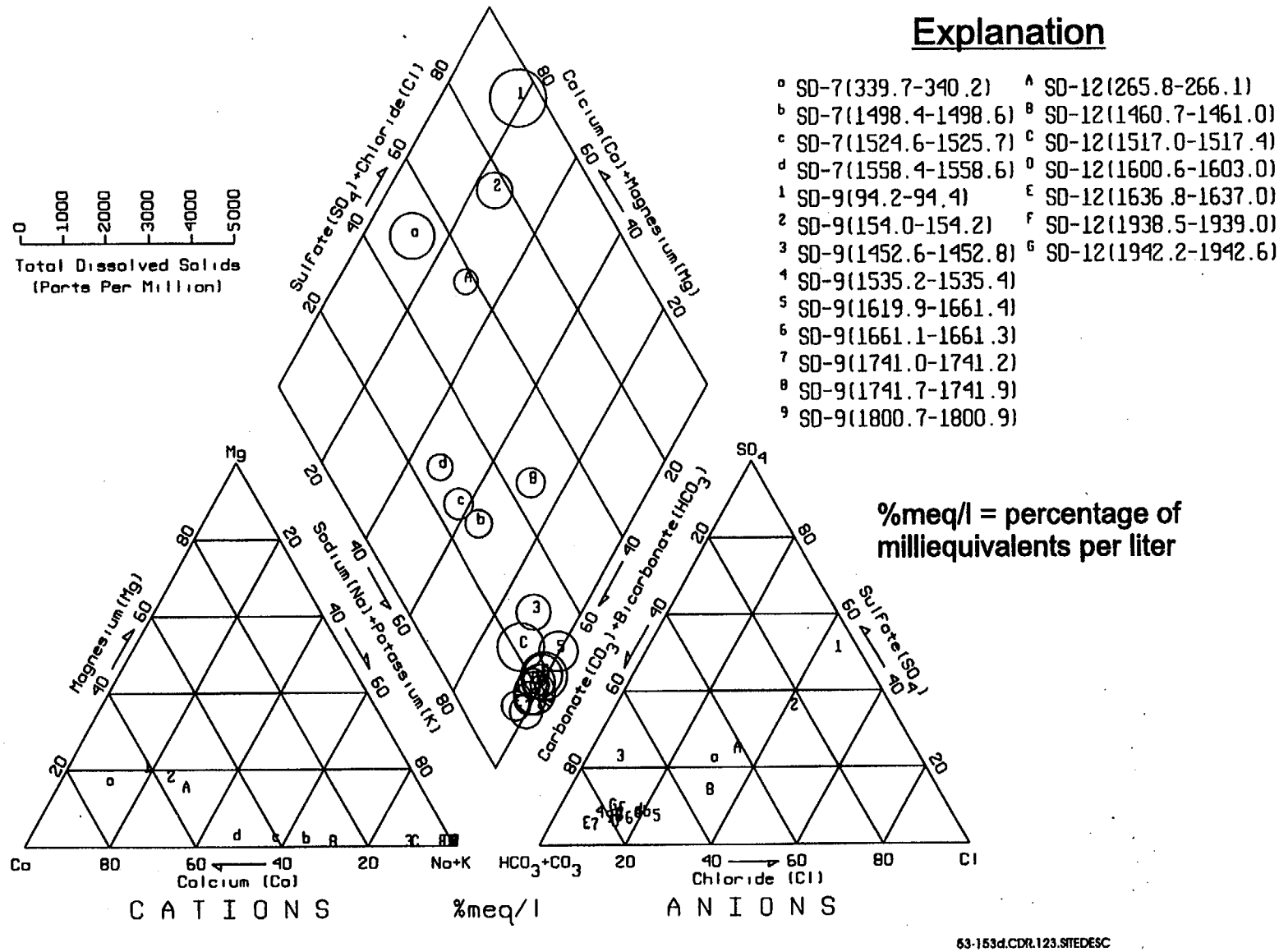

Figure 5.3-153d. Piper Diagrams for Pore Water from the Unsaturated Zone of Boreholes (a) UZ#16, (b) UZ-14, (c) NRG-6 and NRG-7a, and (d) SD-7, SD- 9, and SD-12

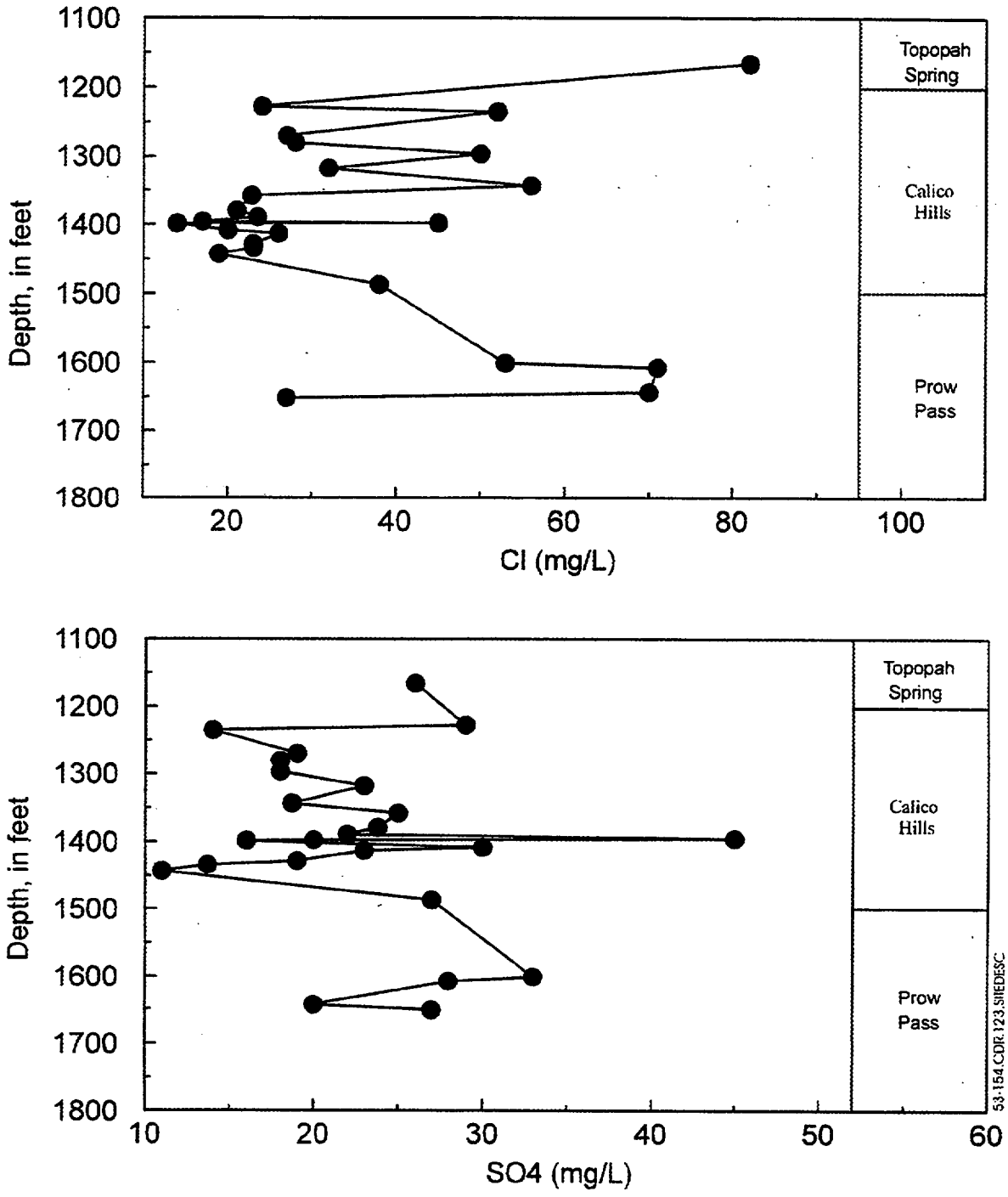

Figure 5.3-154. Chloride and Sulfate Concentrations Versus Depth in Pore Waters from Borehole UZ-16

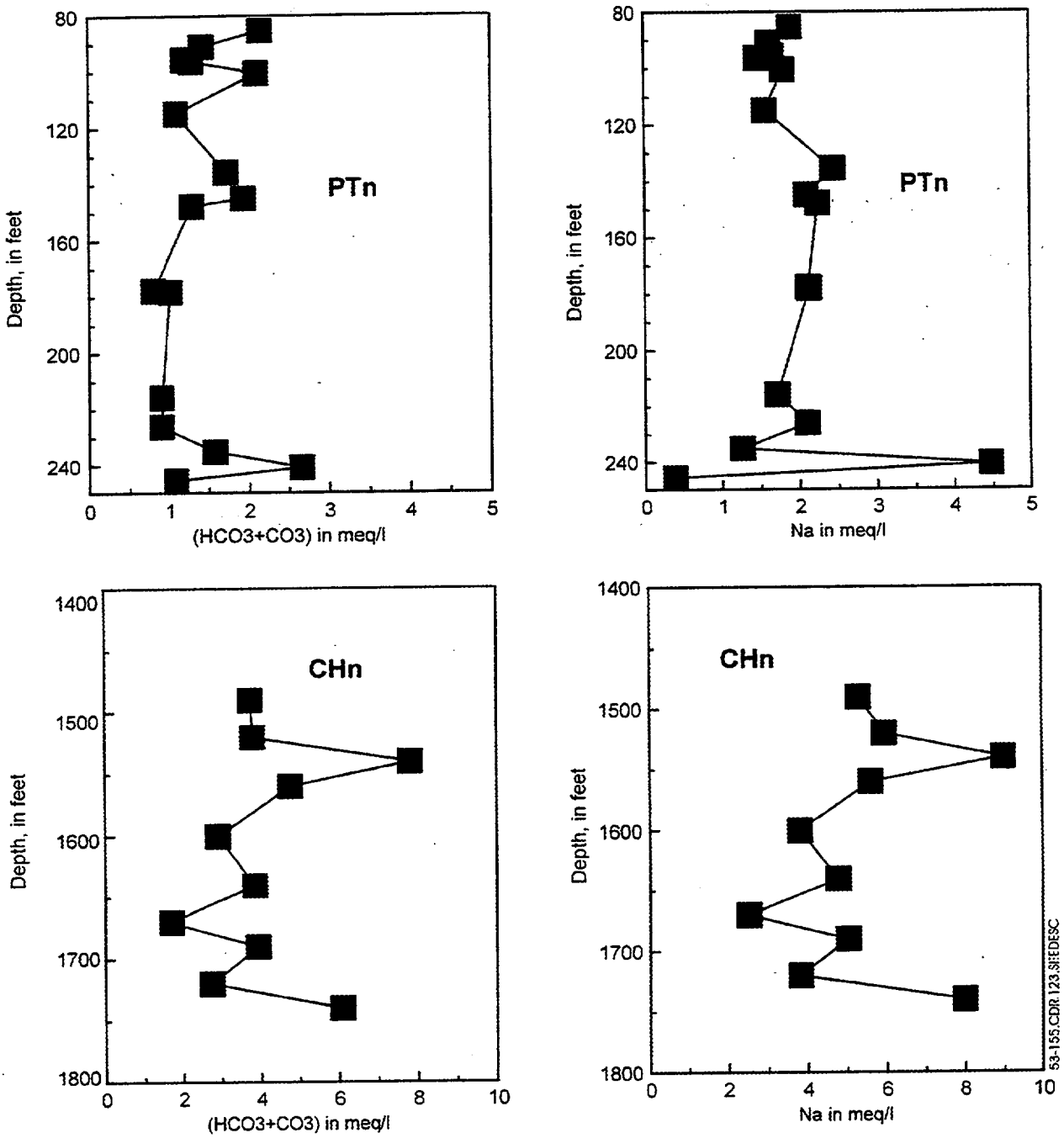

Figure 5.3-155. Sodium and Carbonate Concentrations Versus Depth in Pore Waters from the PTn and Sodium and Carbonate

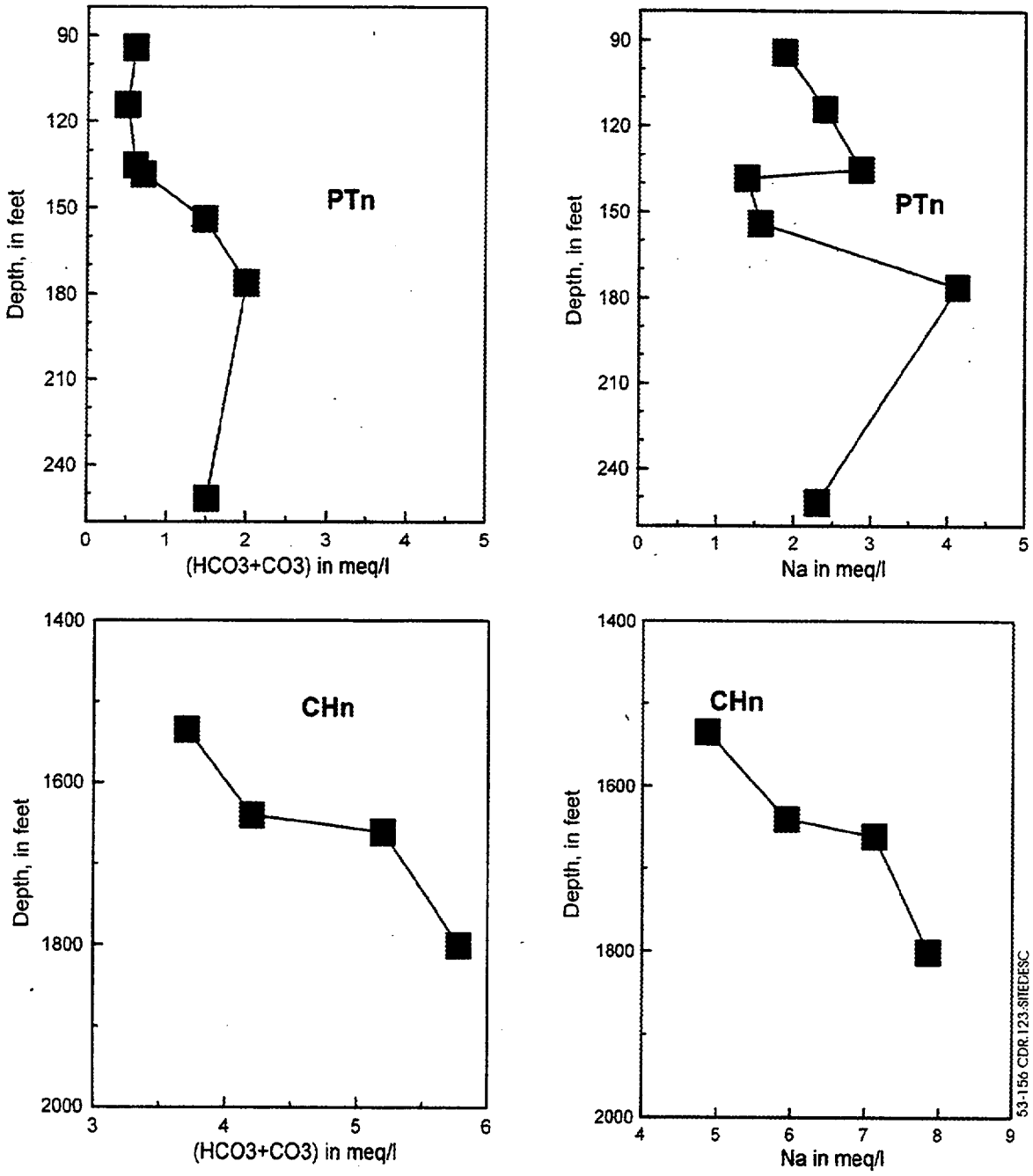

Figure 5.3-156. Sodium and Carbonate Concentrations Versus Depth in Pore Waters from the PTn and CHn in Borehole SD-9

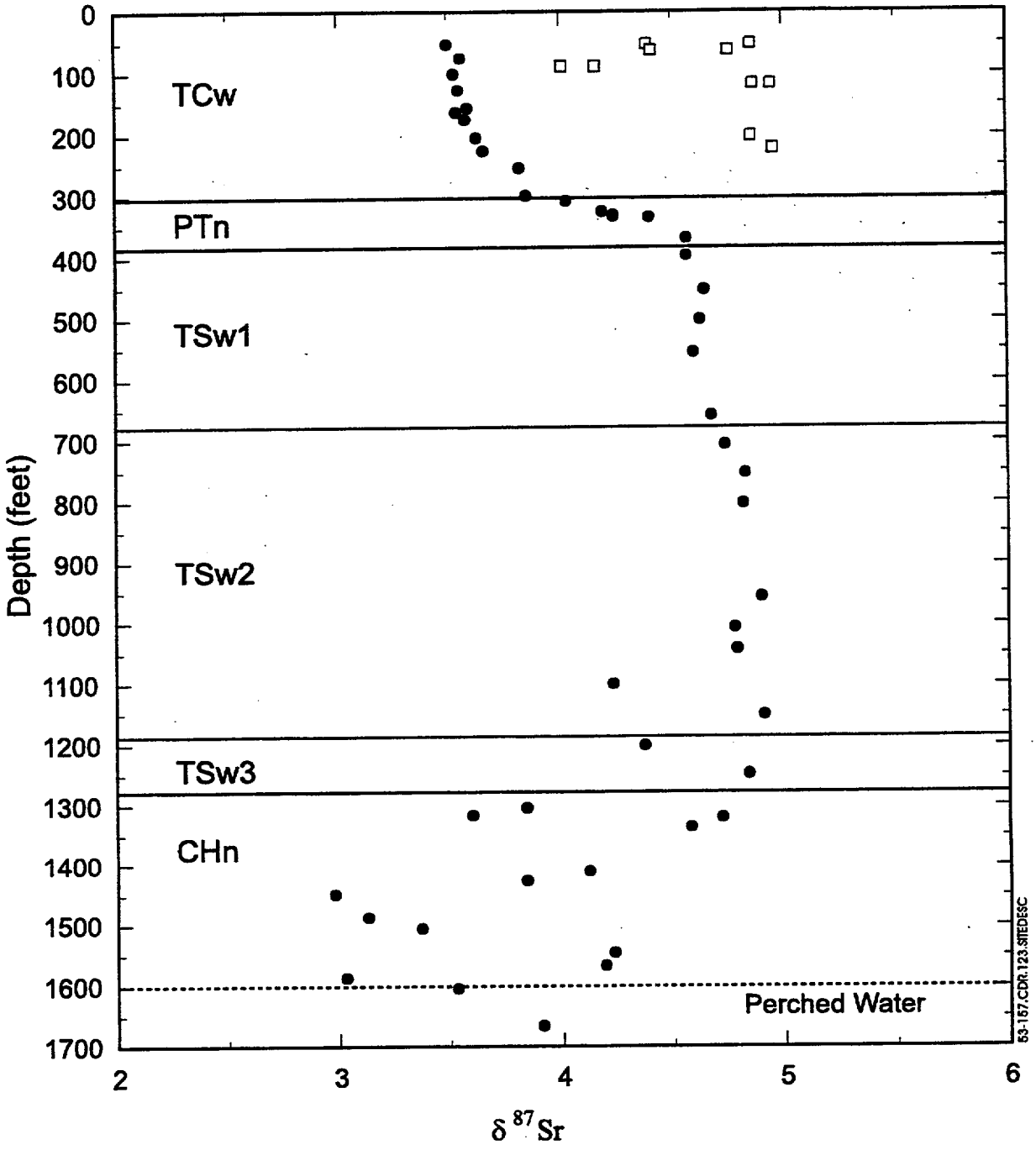

Figure 5.3-157. Strontium Isotope Composition of Pore Water and Calcite Fracture Coatings Versus Depth in Borehole SD-7

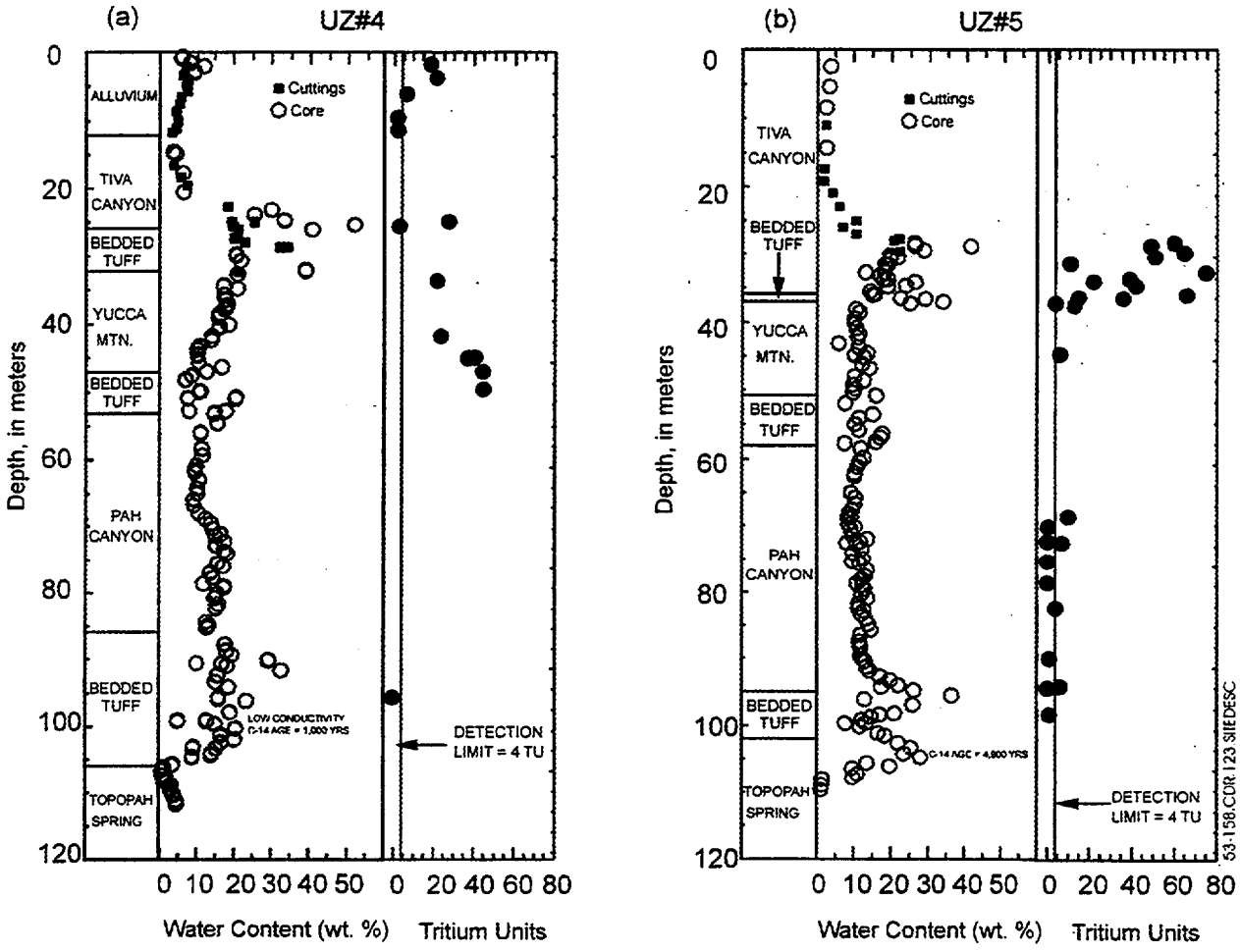

Figure 5.3-158. Lithologic Units, Water Content, and Tritium Concentrations for Boreholes (a) UZ#4 and (b) UZ#5

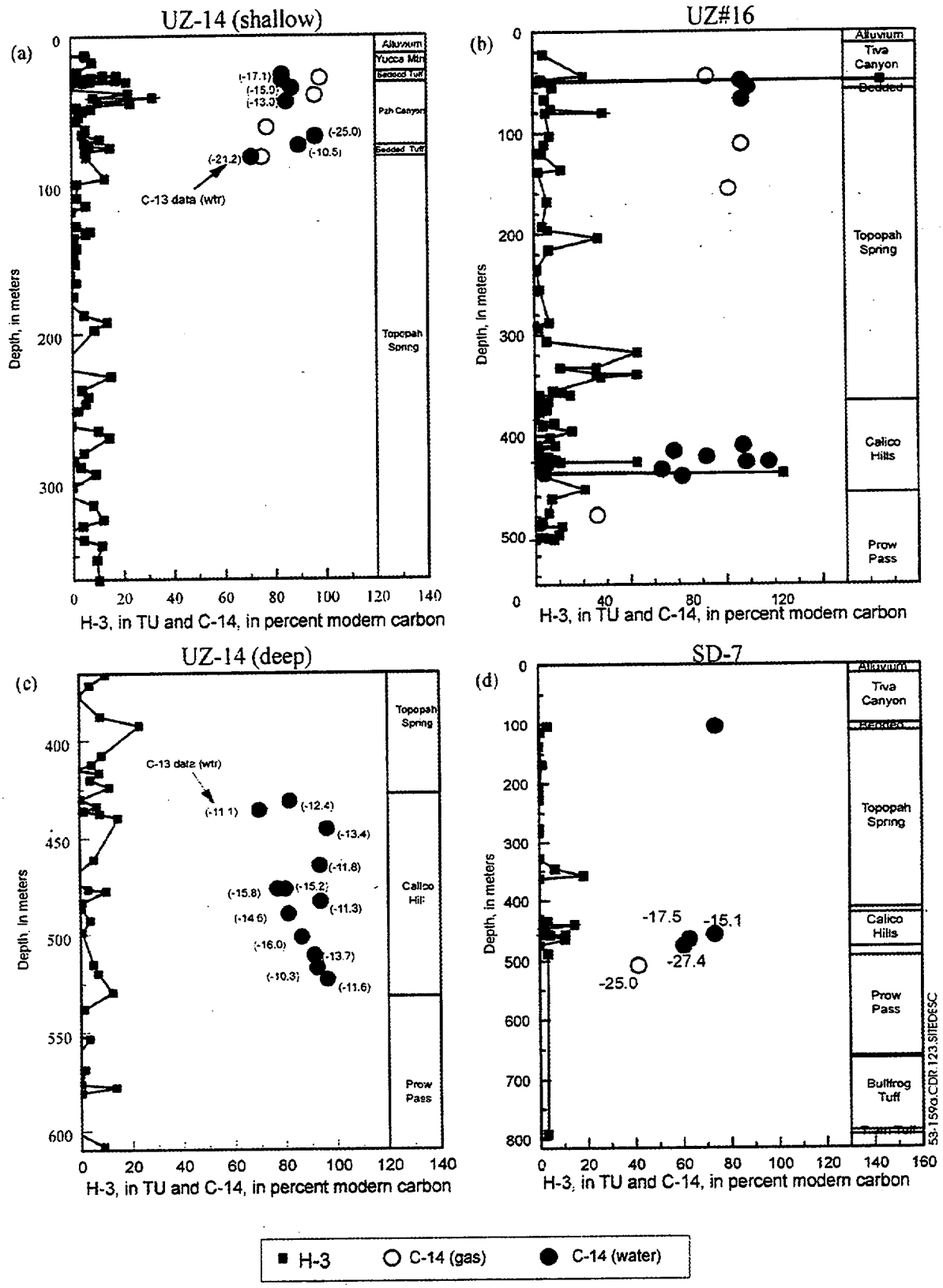

Figure 5.3-159a. Lithologic Units and Tritium and ^{14}C (Water and Gas) Concentrations for Boreholes (a) UZ-14, UZ#16, and SD-7 and (b) SD -9, SD-12, NRG-6, and NRG-7a

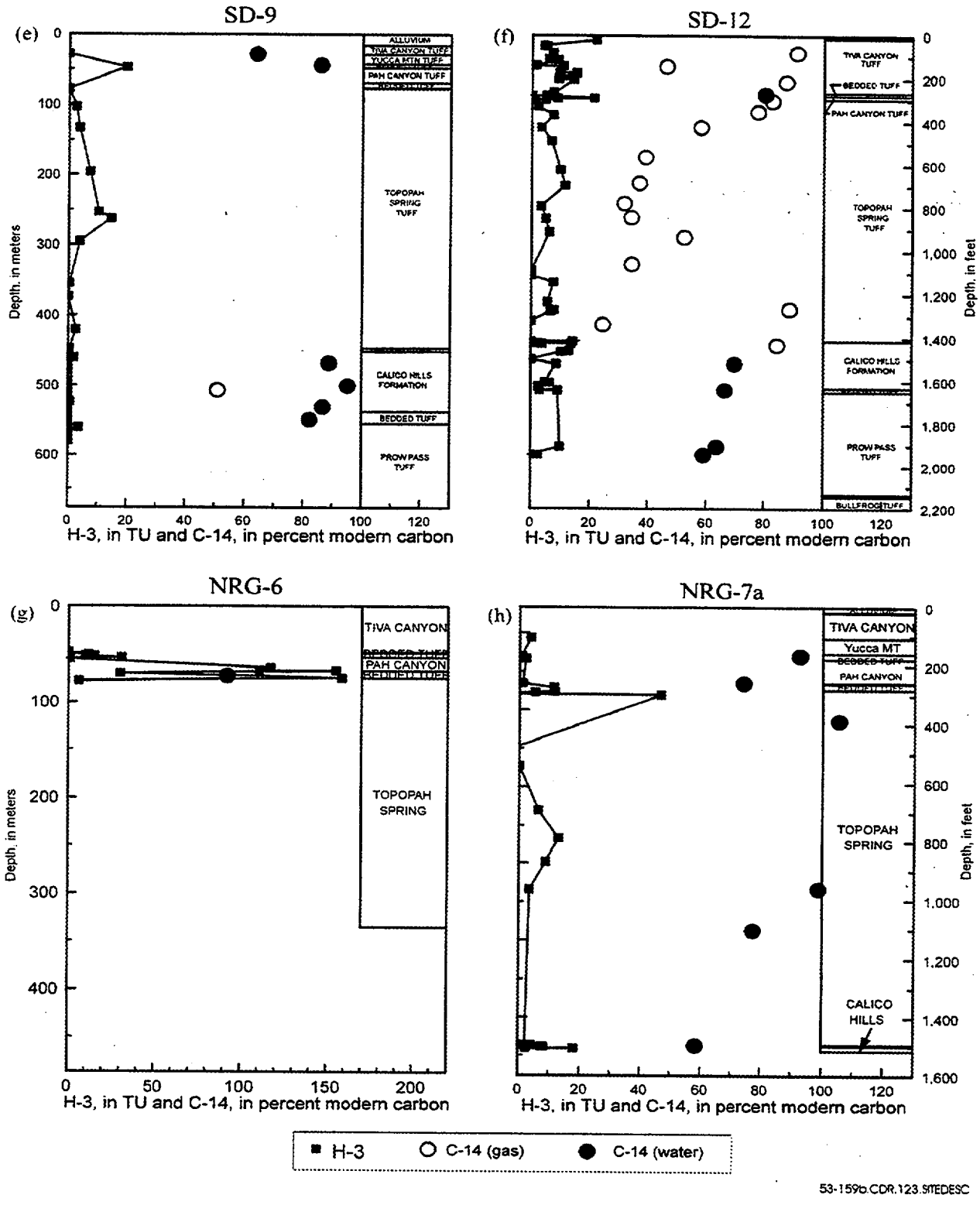

Figure 5.3-159b. Lithologic Units and Tritium and ^{14}C (Water and Gas) Concentrations for Boreholes (a) UZ-14, UZ#16, and SD-7 and (b) SD -9, SD-12, NRG-6, and NRG-7a

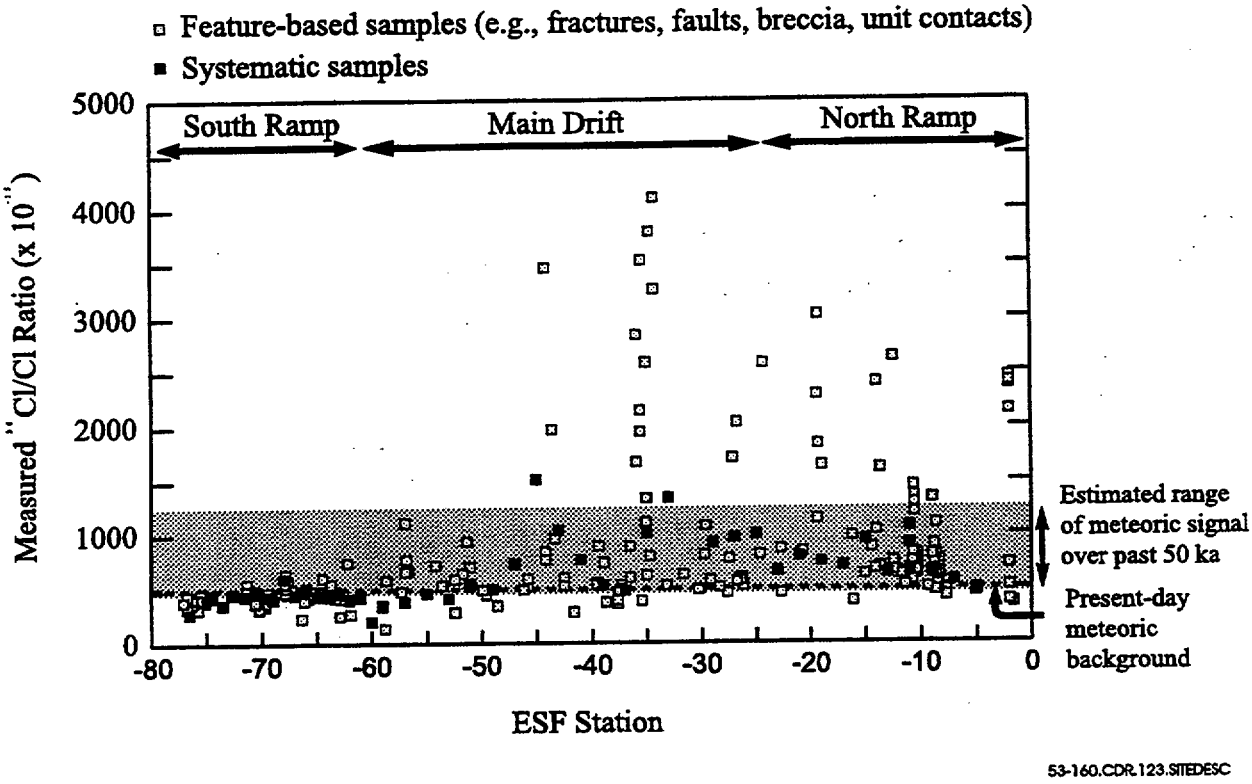

Figure 5.3-160. Distribution of Chlorine-36/Chlorine Measured for Rock Samples, as a Function of Distance along the Exploratory Studies Facility North and South Ramps and Main Drift

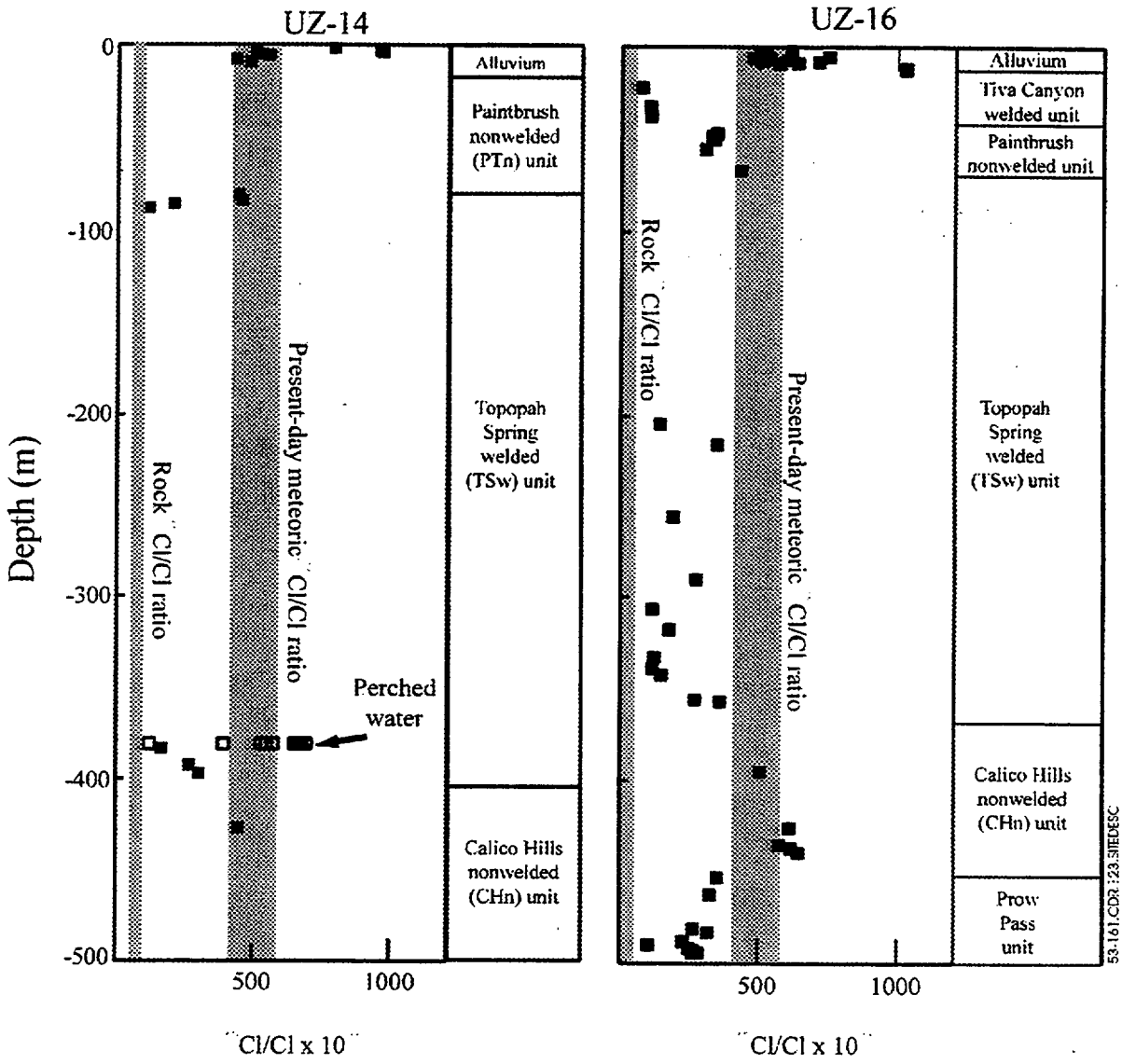

Figure 5.3-161. Measured Chlorine-36/Chlorine Profiles for Boreholes USW UZ-14 and UE-25 UZ#6 (Fabryka-Martin, Turin et al. 1998)

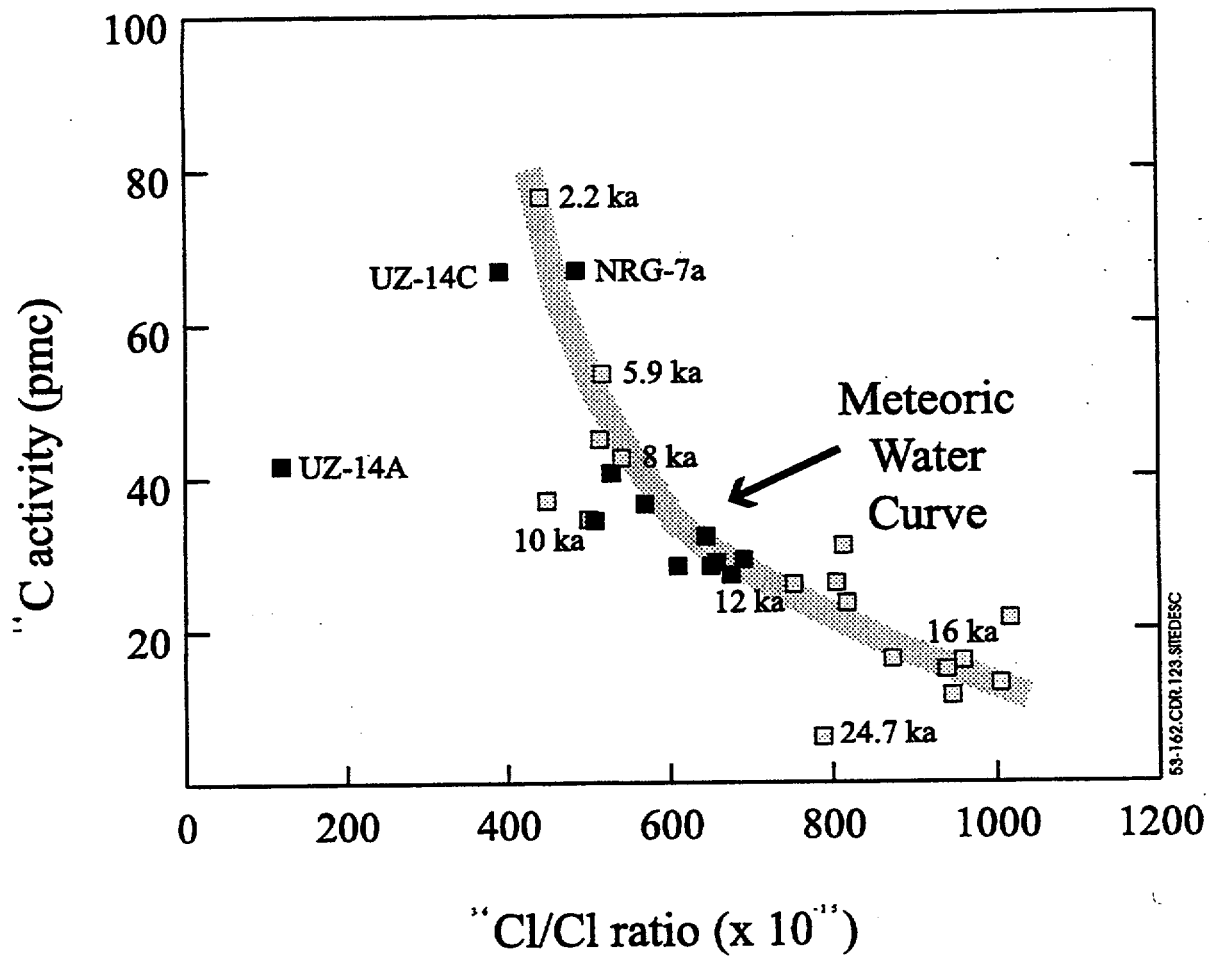

Figure 5.3-162. Reconstructed Carbon-14 and Chlorine-36/Chlorine Activities in the Atmosphere for the Last 20 ka, Compared with Activities Measured in Perched Water from UZ-14, SD-7, and NRG-7a

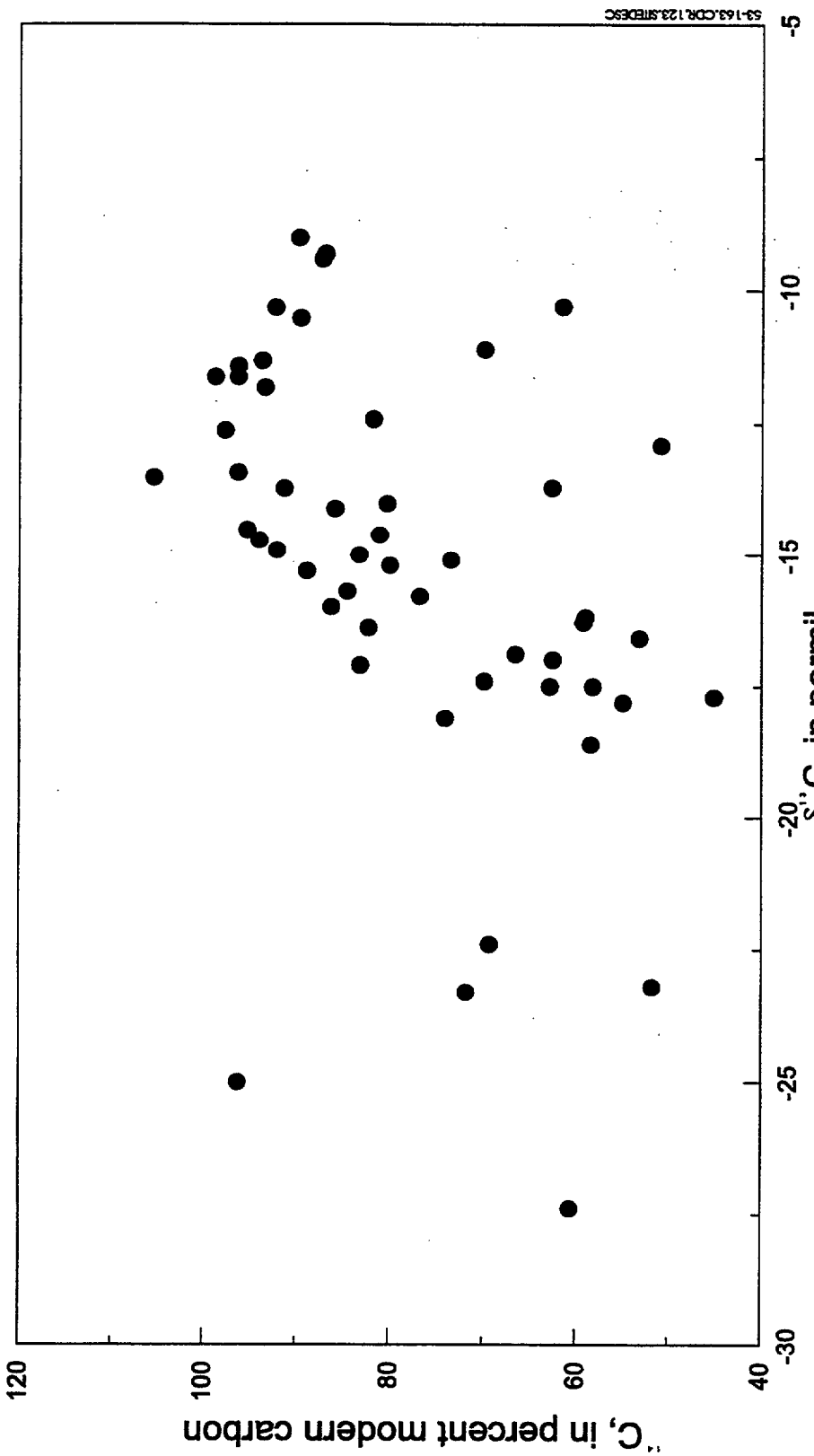

Figure 5.3-163. Plot Showing the Lack of Correlation Between Carbon-14 and Carbon-13

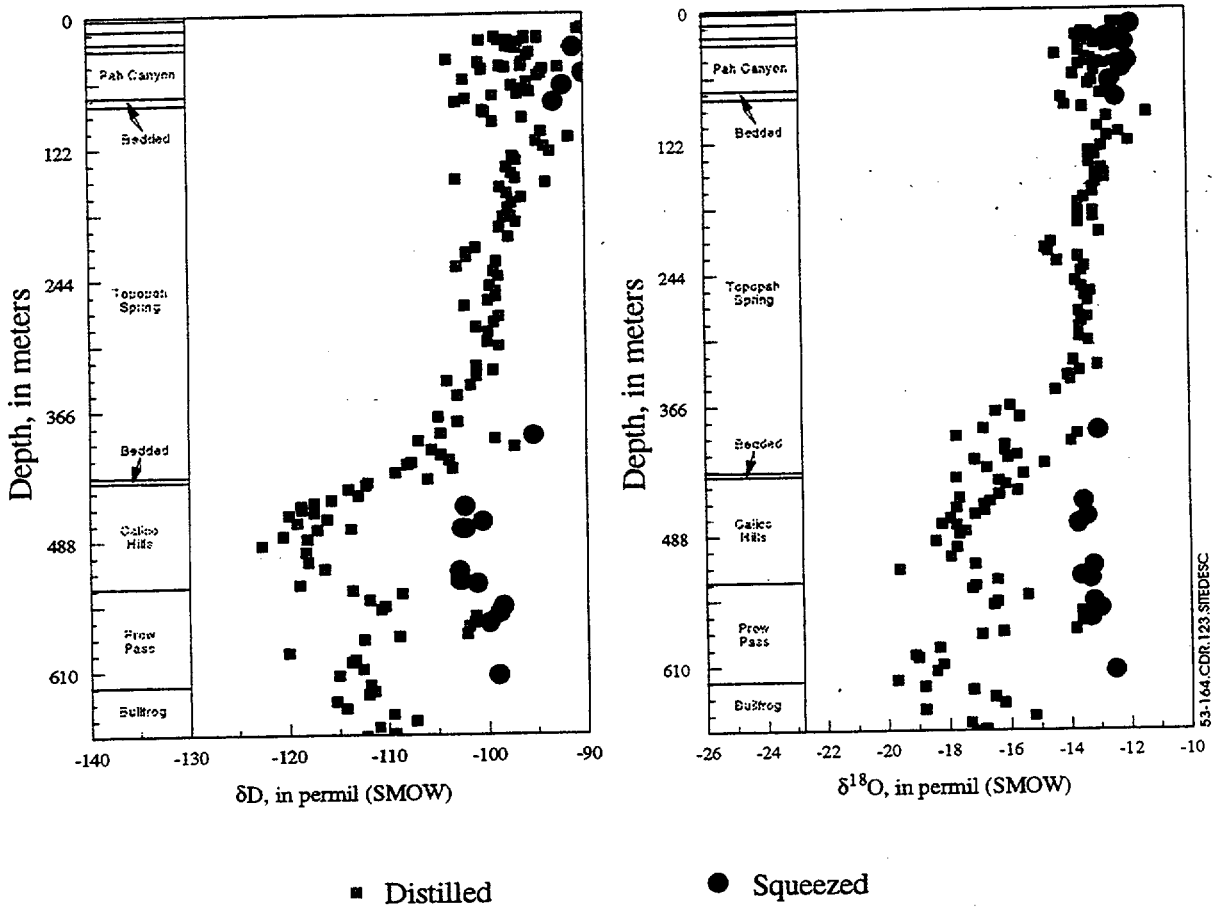

Figure 5.3-164. Delta Deuterium and Delta Oxygen-18 in Pore Water of the Unsaturated Zone as a Function of Depth and Lithology Showing Results of Two Different Methods of Water Extraction

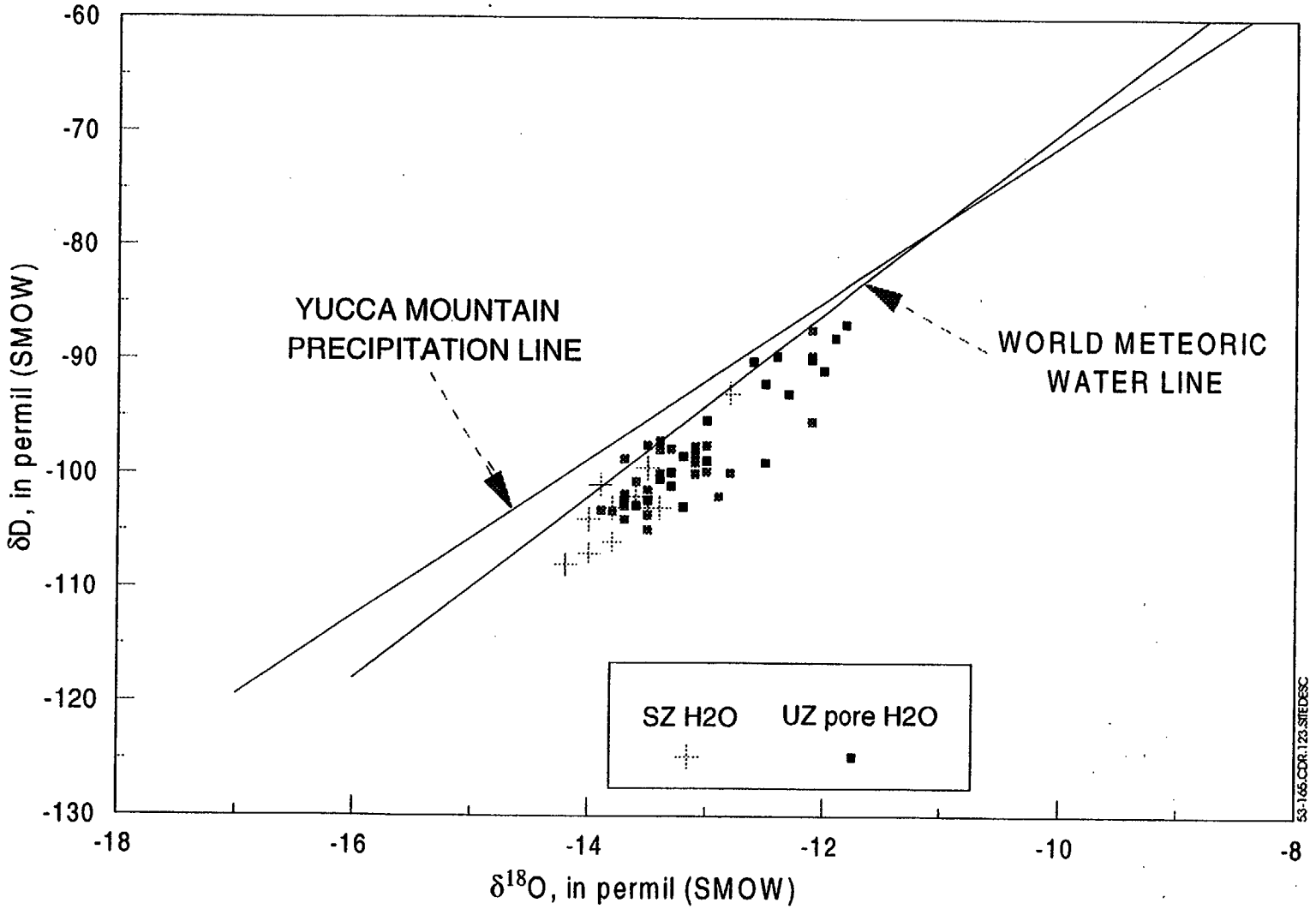

Figure 5.3-165. Delta Deuterium Versus Delta Oxygen-18 Showing Pore Water Compositions from the Unsaturated Zone, the Global Meteoric Water Line (Craig 1961) and Yucca Mountain Precipitation Line (Benson and Klieforth 1989)

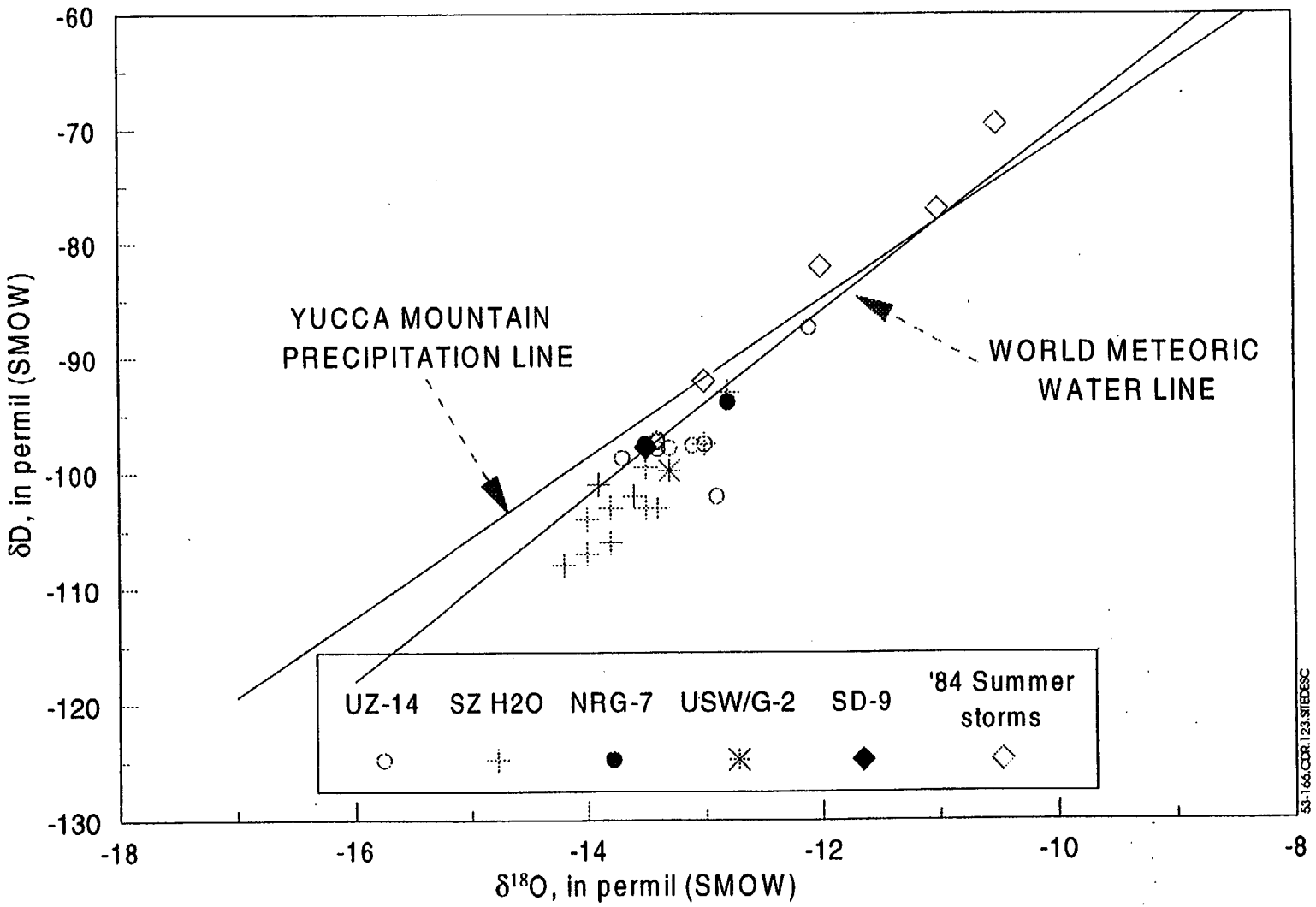

Figure 5.3-166. Delta Deuterium Versus Delta Oxygen-18 Showing Saturated Zone and Perched Water Compositions, and Values for Four Summer Rain Storms. Reference Lines Are: the Global Meteoric Water Line (Craig 1961) and Yucca Mountain Precipitation Line (Benson and Klieforth 1989)

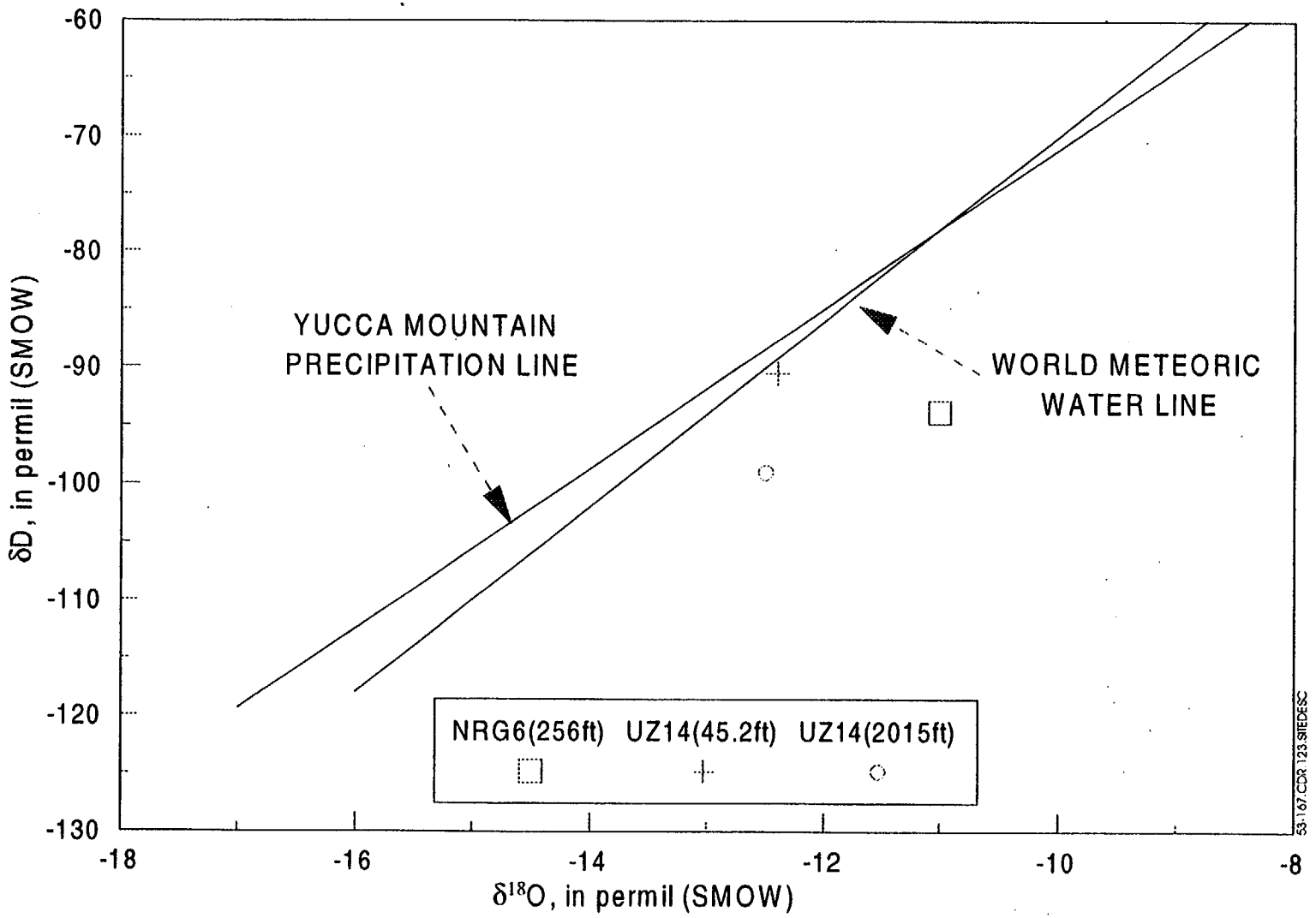

Figure 5.3-167. Delta Deuterium Versus Delta Oxygen-18 Showing Isotopic Compositions of 3 Samples with > 800 ppm Total Dissolved Solids. Reference Lines Are: the Global Meteoric Water Line (Craig 1961) and Yucca Mountain Precipitation Line (Benson and Klieforth 1989)

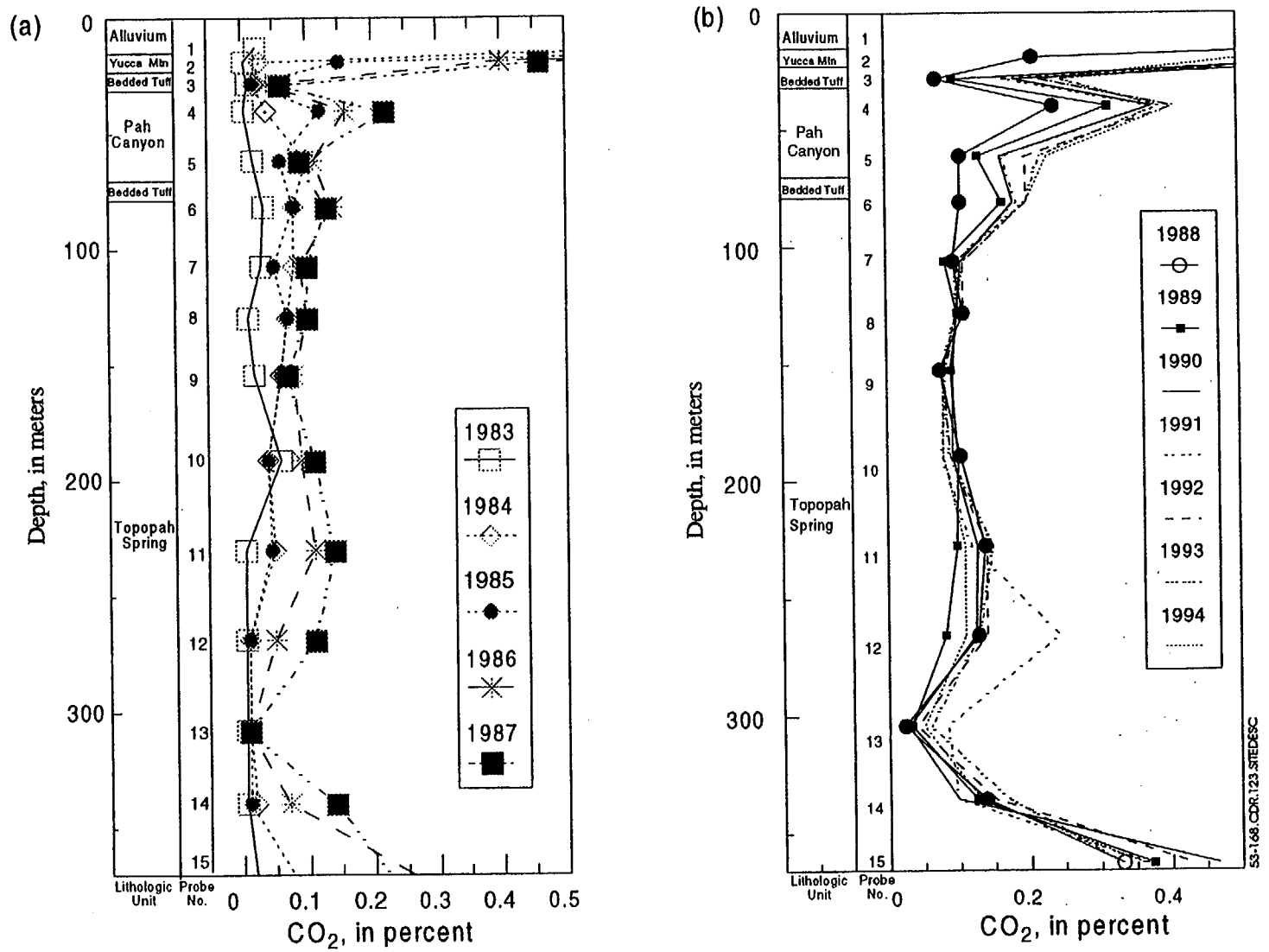

Figure 5.3-168. CO_2 Concentrations in Gas Collected from UZ-1 for the Years 1983 Through 1994

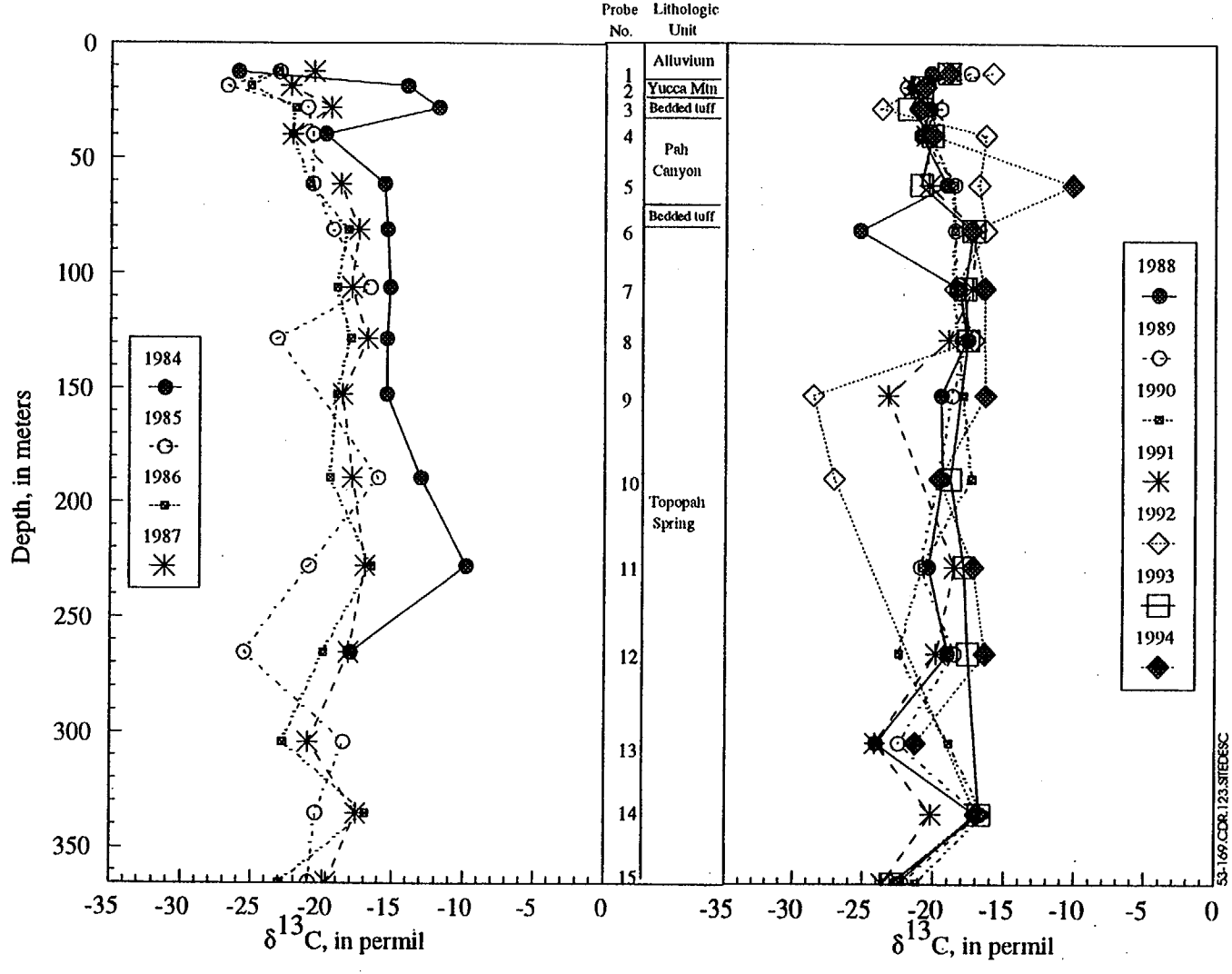

Figure 5.3-169. Delta Carbon-13 in Gas Collected from UZ-1 for the Years 1983 Through 1994

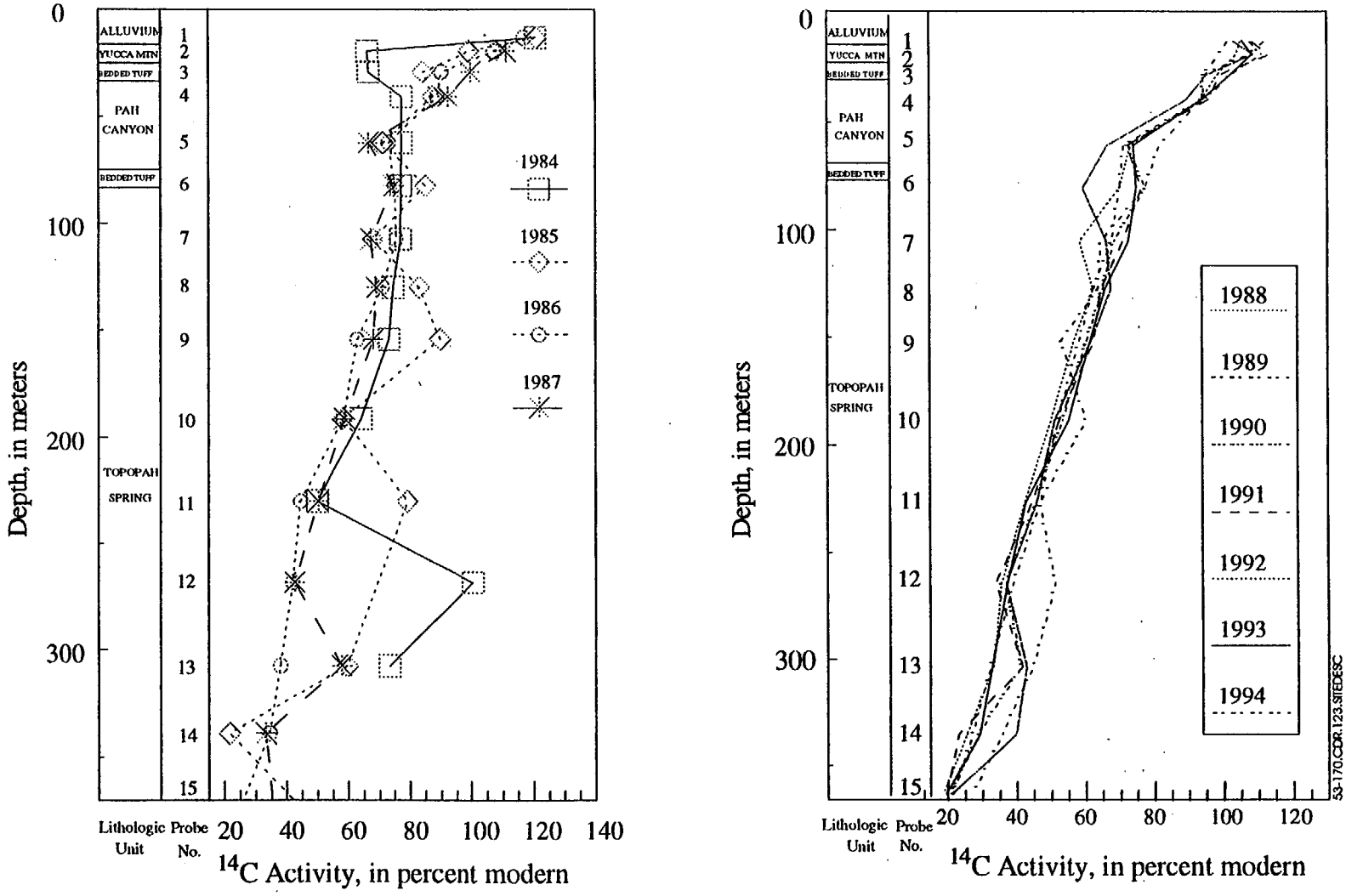

Figure 5.3-170. Carbon-14 in Gas Collected from UZ-1 for the Years 1983 Through 1994

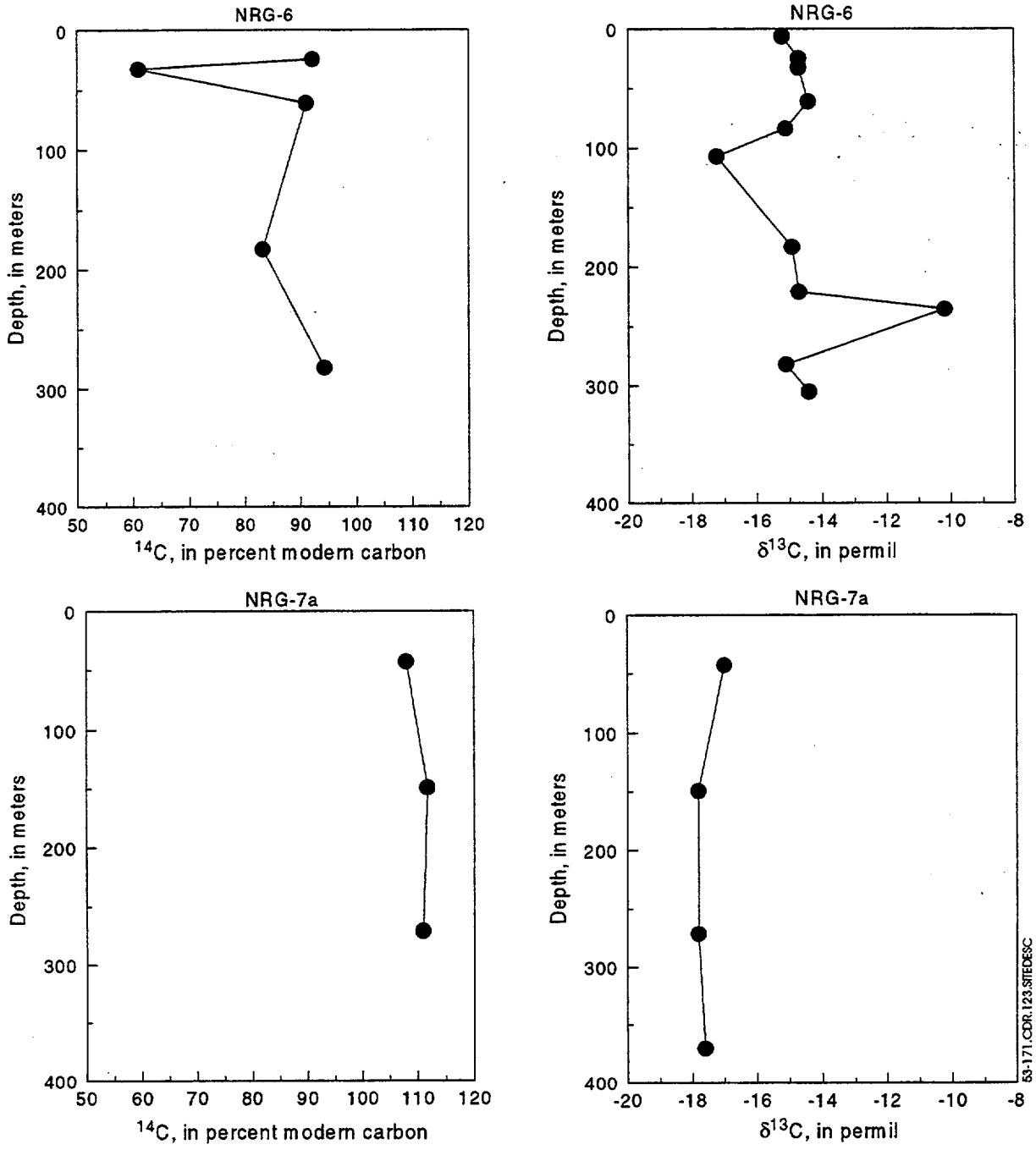

5.3-171. Carbon-14 and Delta Carbon-13 in Gas Collected from Boreholes NRG-6 and NRG-7a

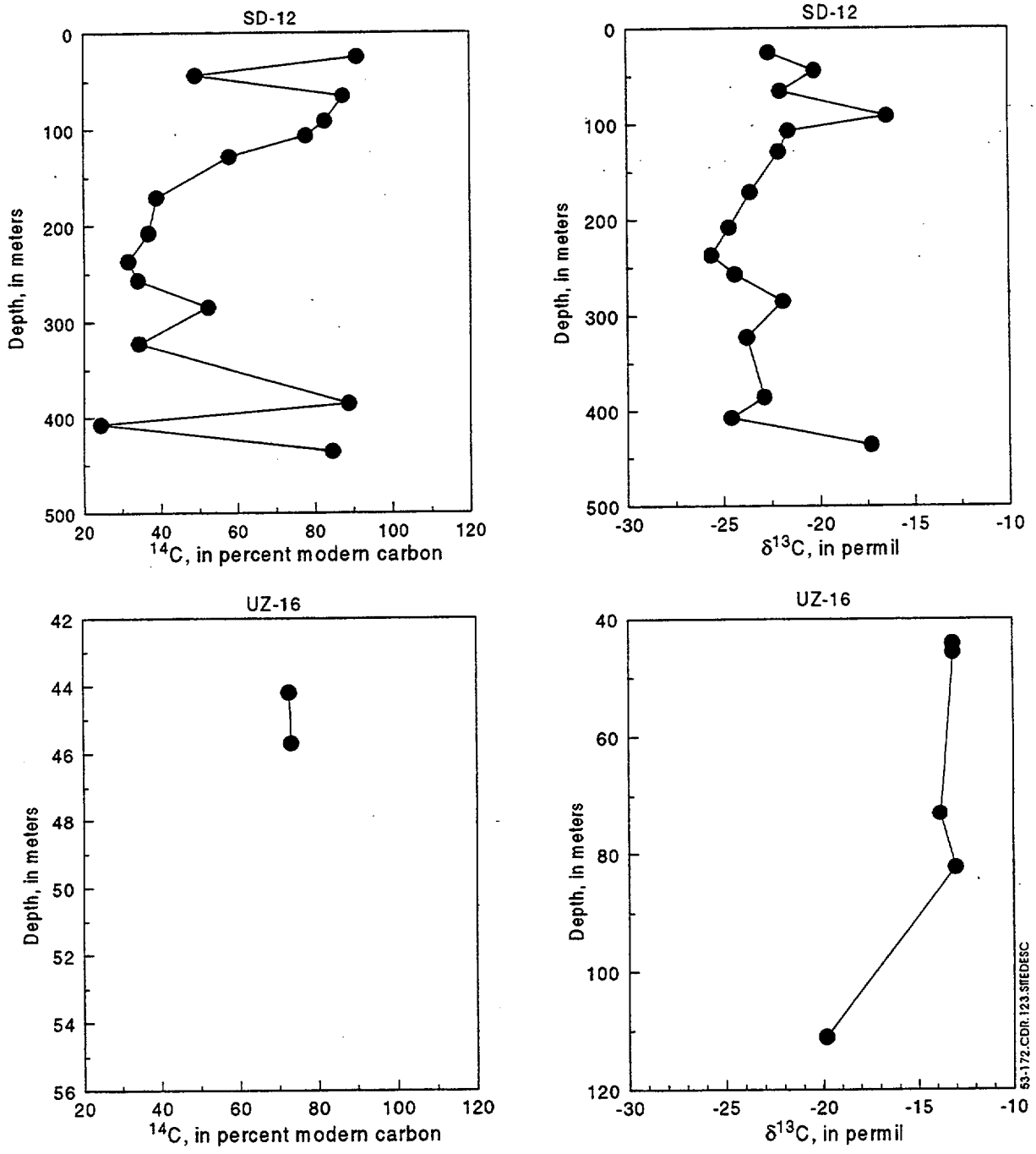

Figure 5.3-172. Carbon-14 and Delta Carbon-13 in Gas Collected from Boreholes SD-12 and UZ#16

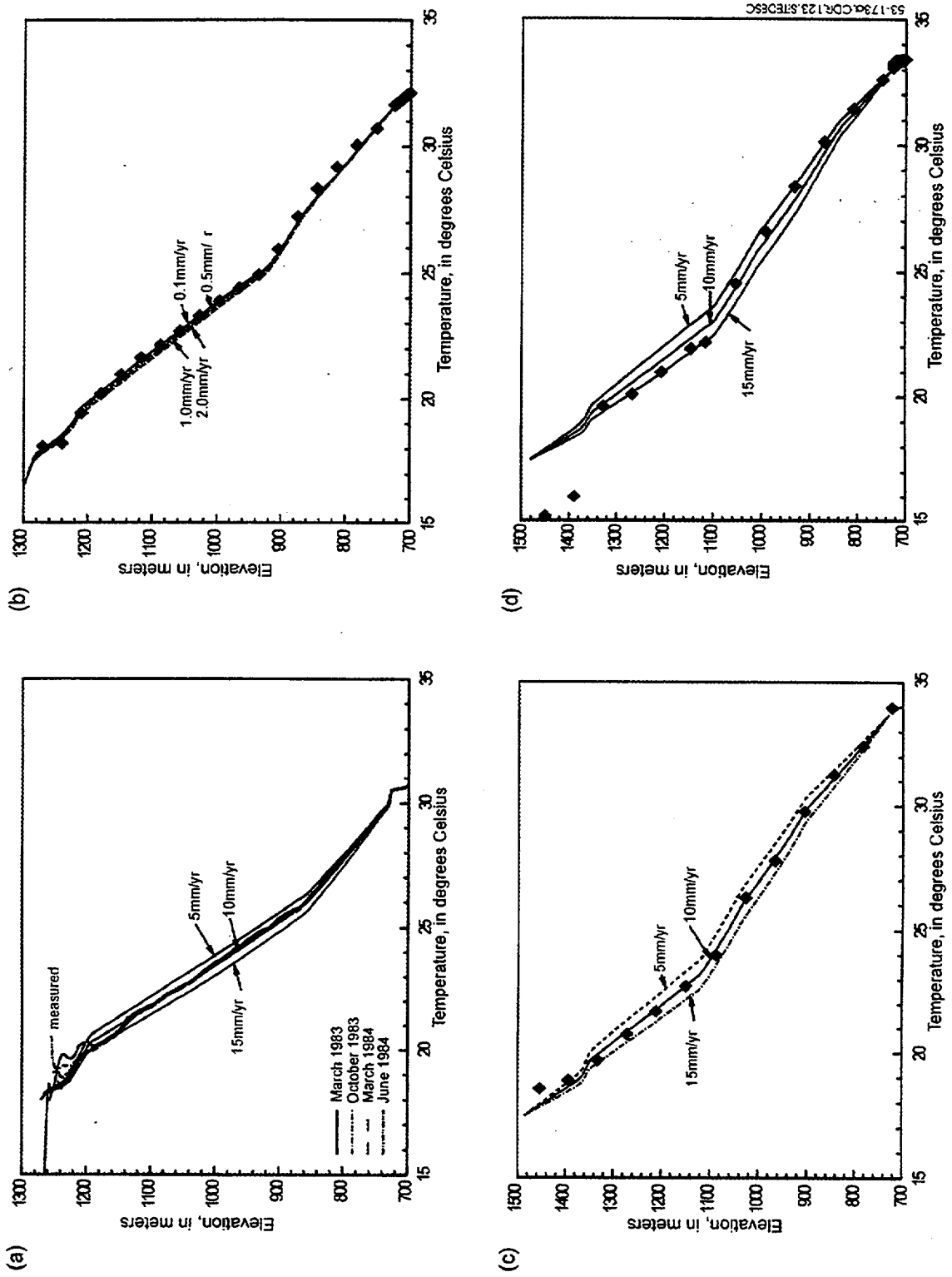

Figure 5.3-173a. Measured and Simulated Temperatures at Boreholes (a) G-4 (b) WT-2 (c) H-3 (d) G-3 (e) H-5 (f) H-1, (g) a#1 (h) WT-12 and (j) UZ-1

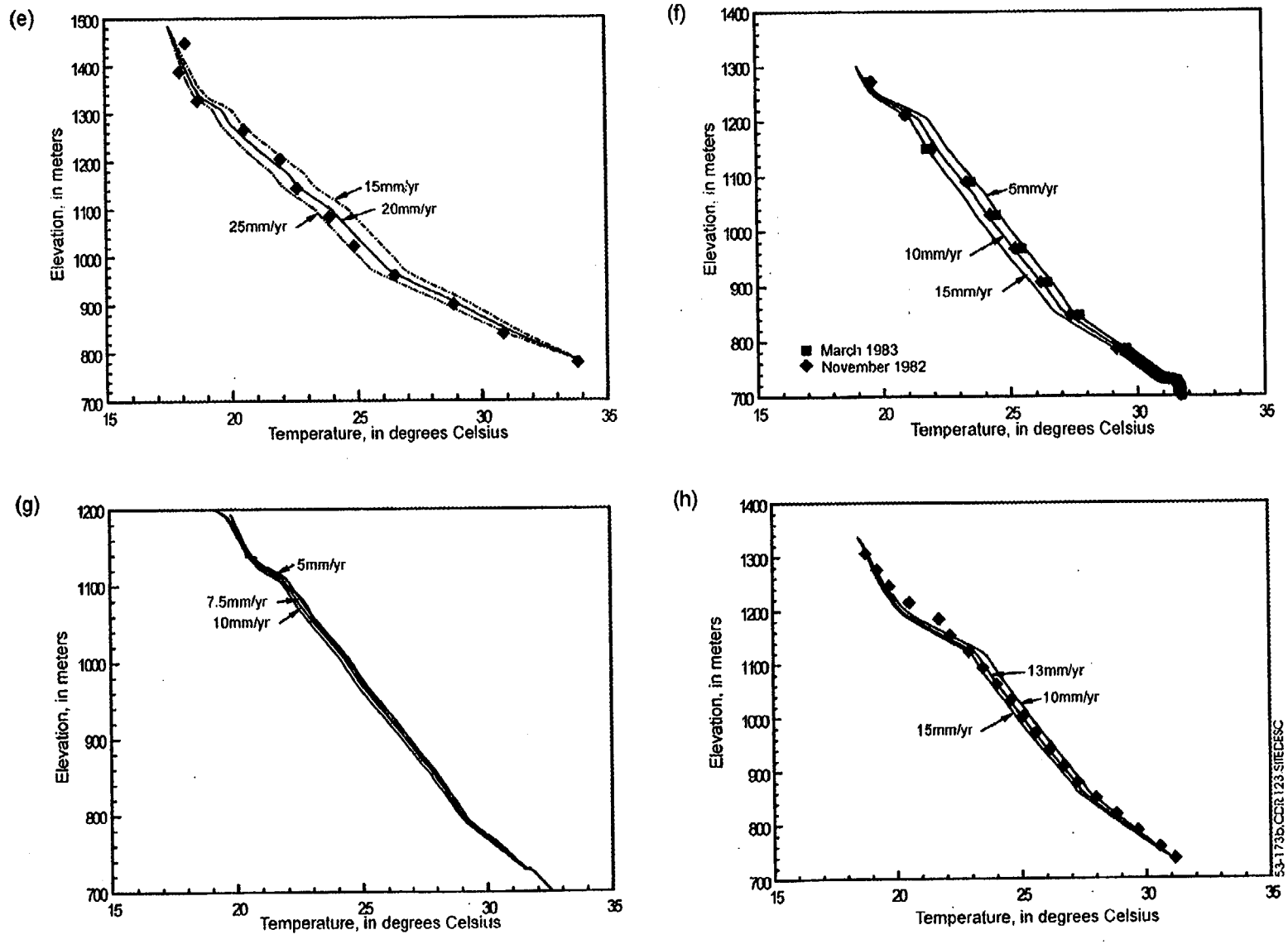

Figure 5.3-173b. Measured and Simulated Temperatures at Boreholes (a) G-4 (b) WT-2 (c) H-3 (d) G-3 (e) H-5 (f) H-1, (g) a#1 (h) WT-18 (i) WT-12 and (j) UZ-1

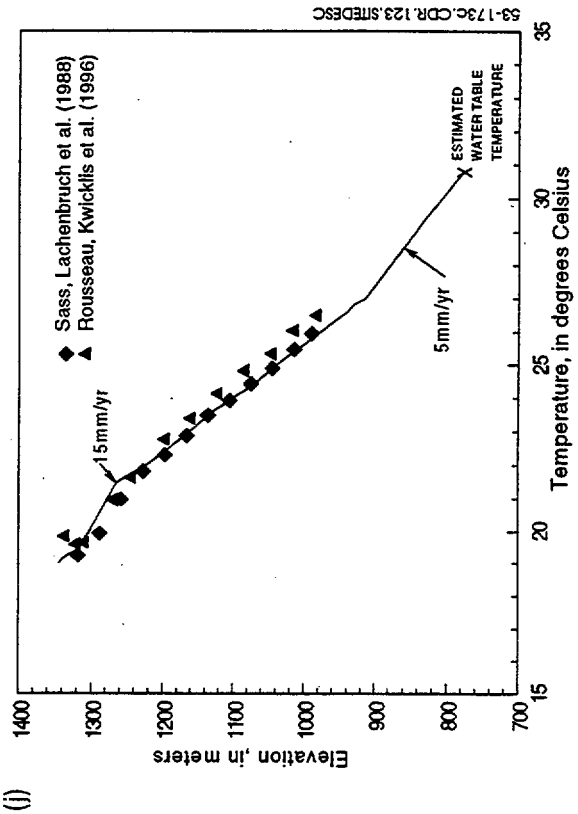

(i)

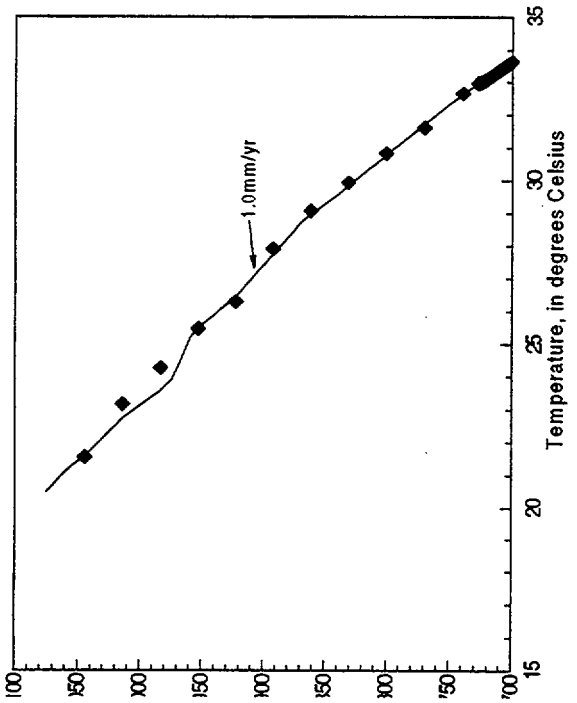

Figure 5.3-173c. Measured and Simulated Temperatures at Boreholes (a) G-4 (b) WT-2 (c) H-3 (d) G-3 (e) H-5 (f) H-1, (g) a#1 (h) WT-18 (i) WT-12 and (j) UZ-1

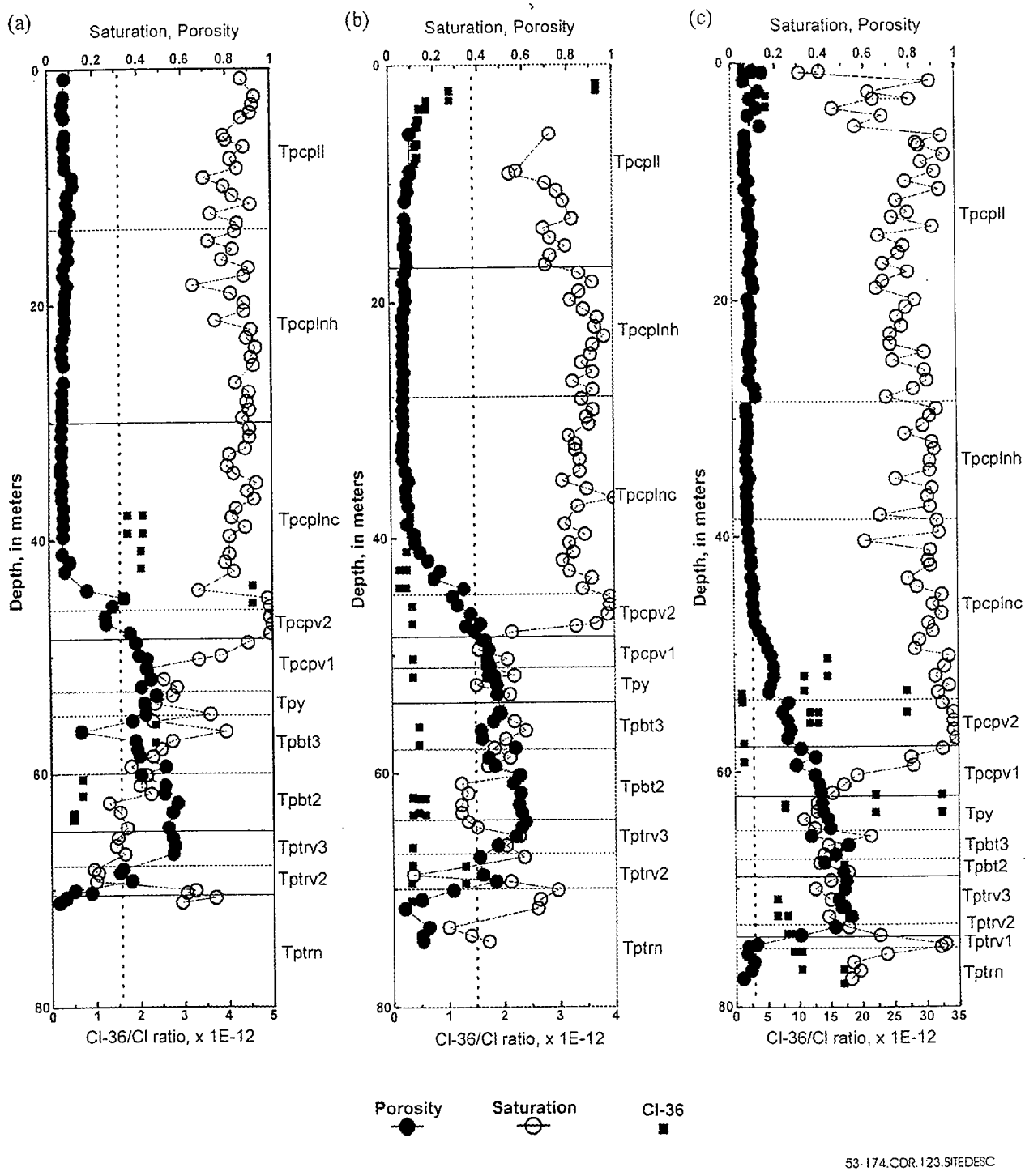

Figure 5.3-174. Chlorine-36/Chlorine Ratios, Saturation and Porosity in Boreholes (a) N-53, (b) N-54 and (c) N-55

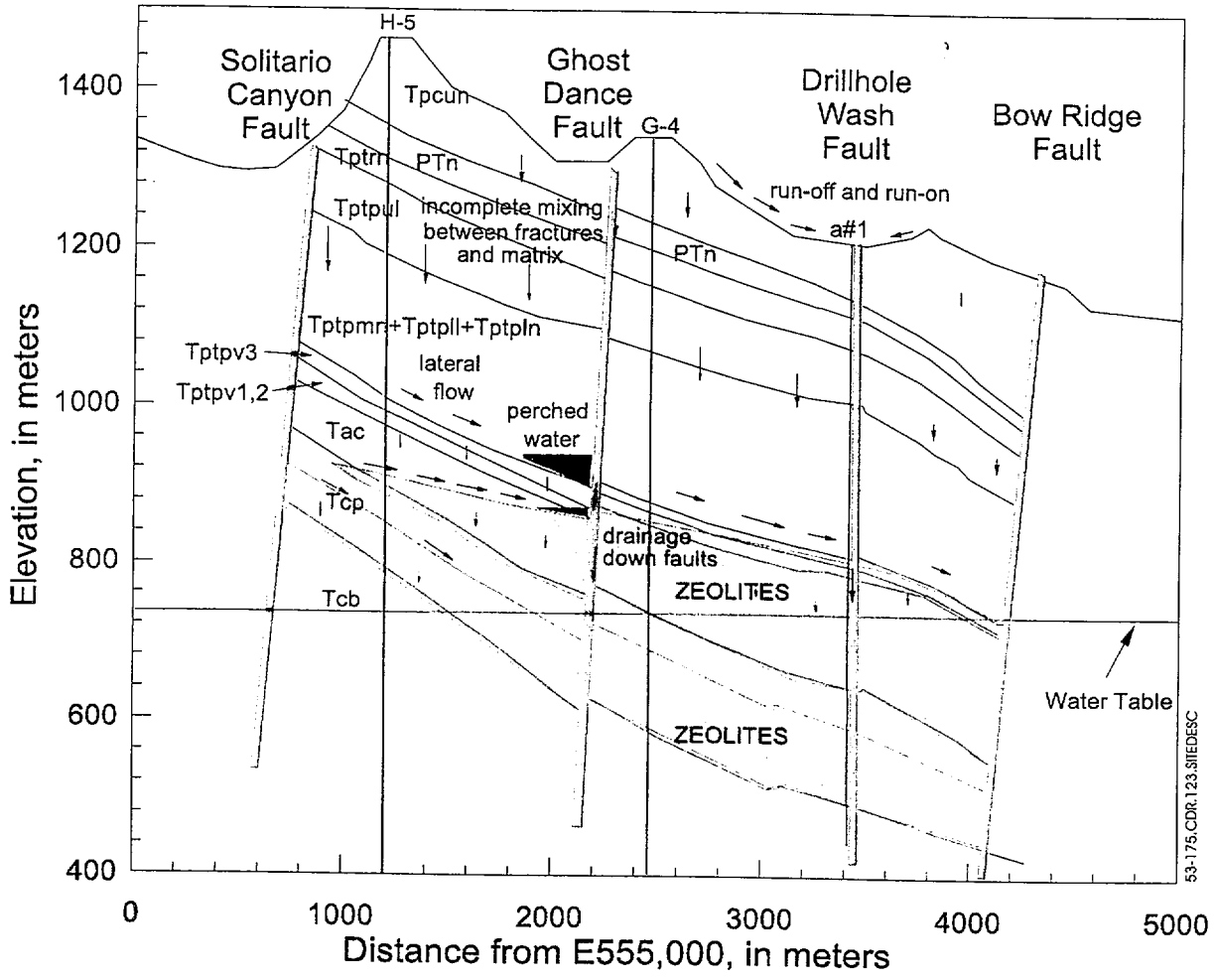

Figure 5.3-175. Aspects of Flow in the Unsaturated Zone at Yucca Mountain that will Cause Departures from the Assumptions of the Chloride Mass-Balance Method

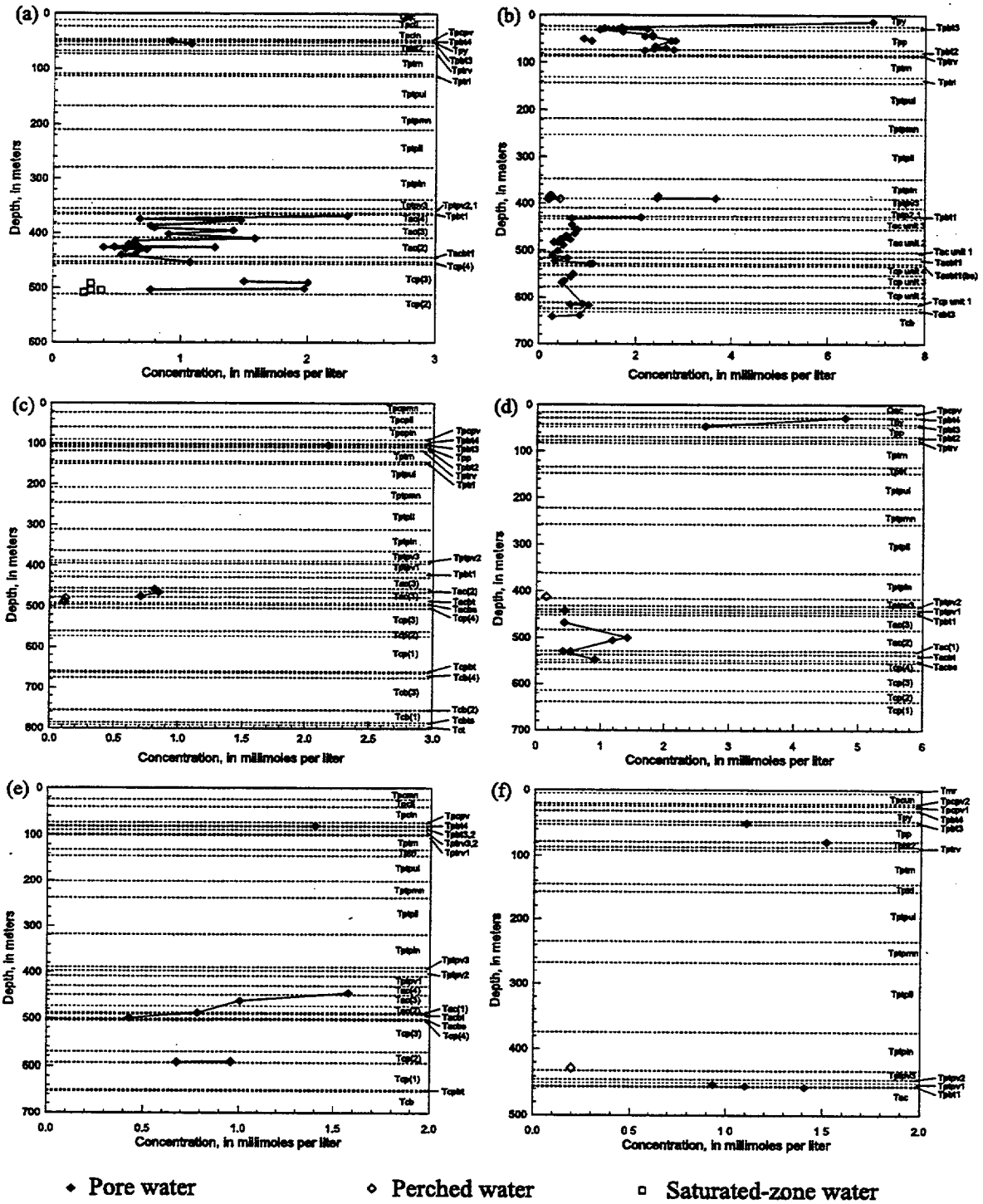

NOTE: Solid diamonds are pore water samples; open diamonds are perched water samples, and open squares are saturated zone W.

Figure 5.3-176. Chloride Concentration as a Function of Depth at Borehole (a) UZ-16 (b) UZ-14 (c) SD-7 (d) SD-9 (e) SD-12 and NRG-7a

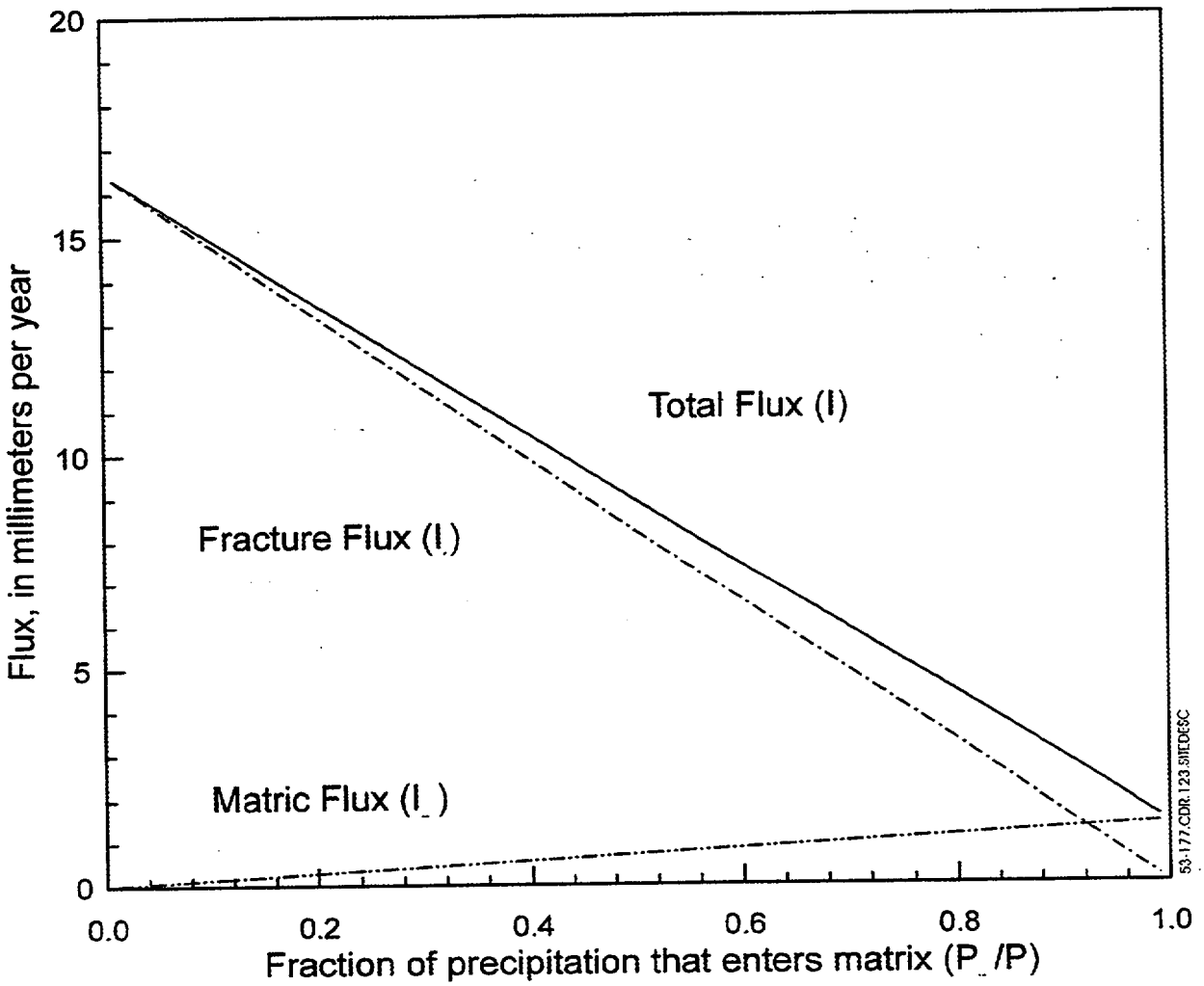

NOTE: Assumed values for C_m and C_f are 74.8 and 6.4 mg/l.

Figure 5.3-177. Effects of Partitioning Precipitation Between Matrix and Fractures on Total Flux (I),Fracture Flux (I_f), and Matrix Flux (I_m) in a Poorly Mixed Fracture-Matrix System

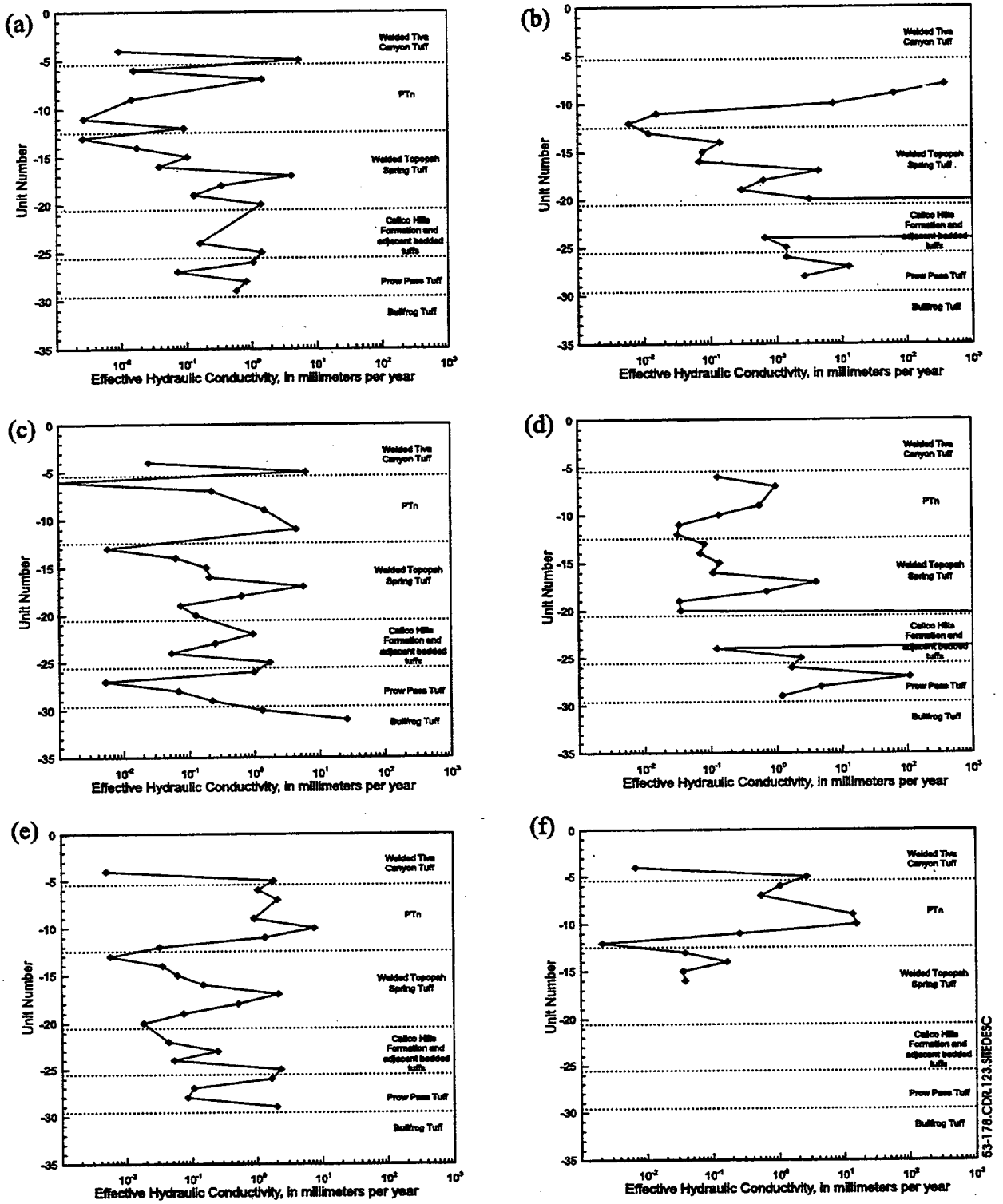

Figure 5.3-178. Effective Hydraulic Conductivities Estimated for the Hydrogeologic Units of L.E. Flint (1998) from Measured Water Saturation Data and Parameters of the van Genuchten Moisture Characteristic Function (a) UZ-16, (b) UZ-14, (c) SD-7, (d) SD-9 and (f) UZ-7a

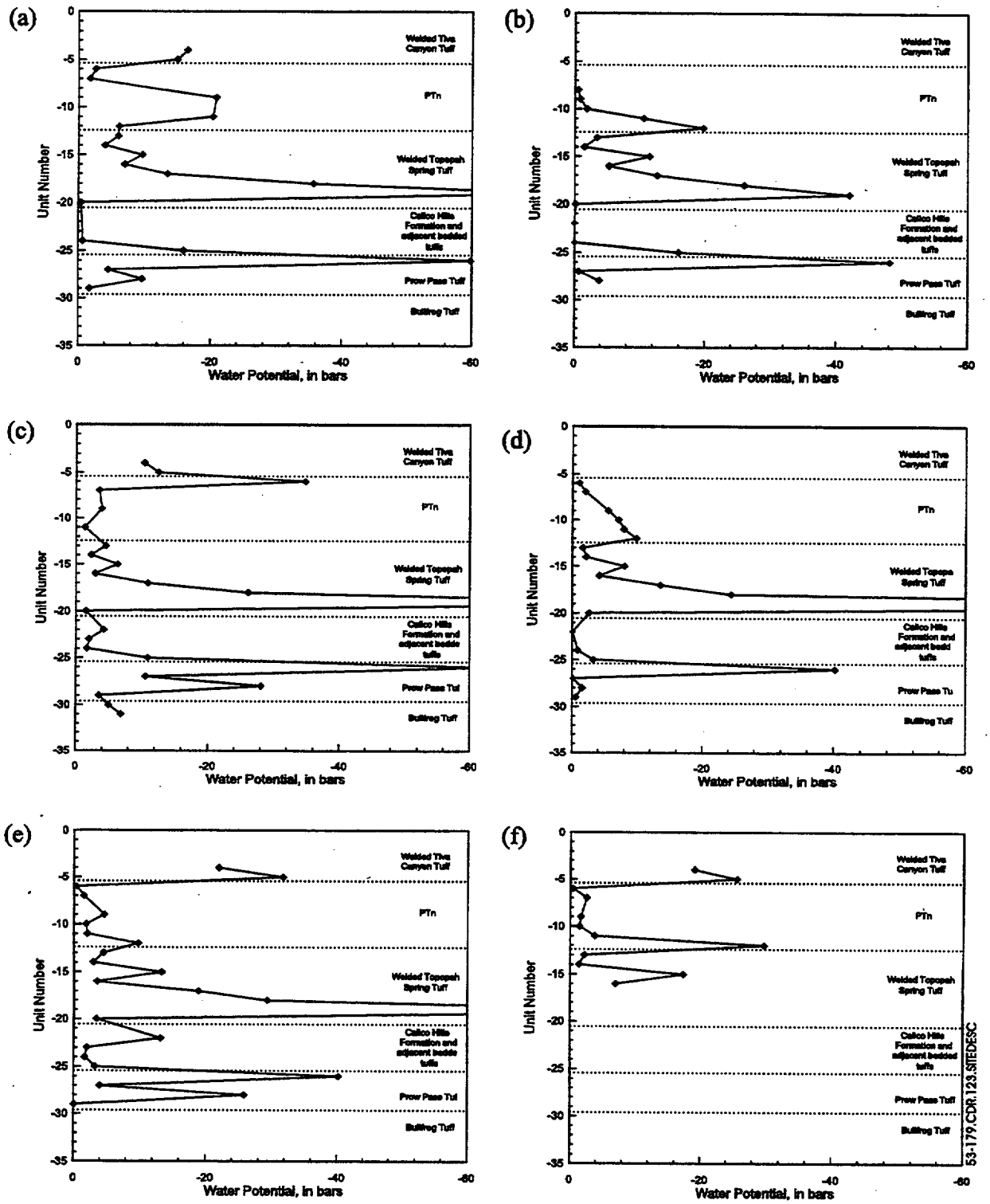

Figure 5.3-179. Water Potentials Estimated for the Hydrogeologic Units of L.E. Flint (1998) from Measured Water Saturation Data and Parameters of the van Genuchten Moisture Characteristic Function (a) UZ-16, (b) UZ-14, (c) SD-7, (d) SD-9, (e) SD-12 and (f) UZ-7a

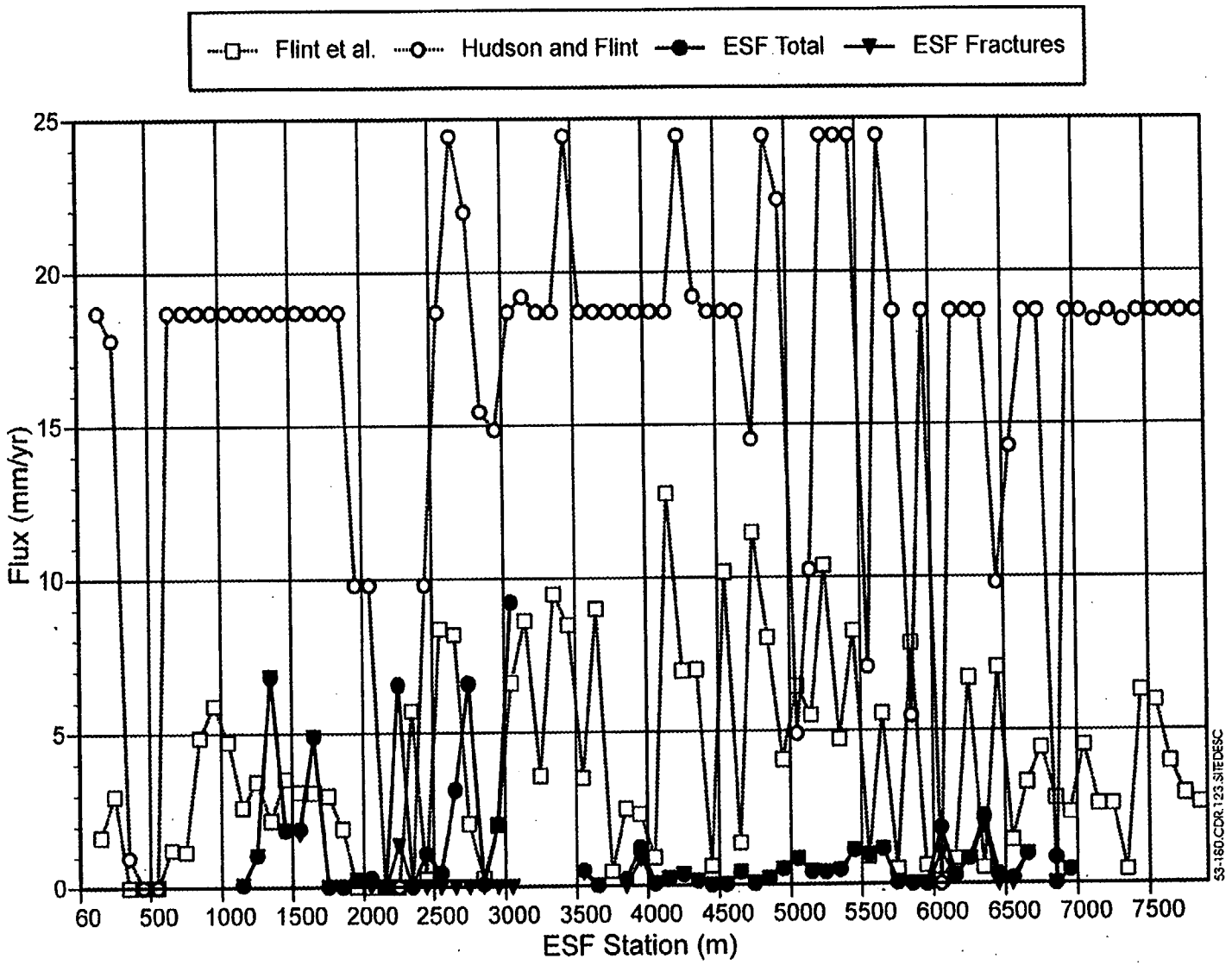

NOTE: From Paces, Marshall et al. (1997)

Figure 5.3-180. Flux Estimates from Secondary Mineral Abundances (Both Total and Those from Fractures Only) as Compared to Two Different Infiltration Flux Estimates

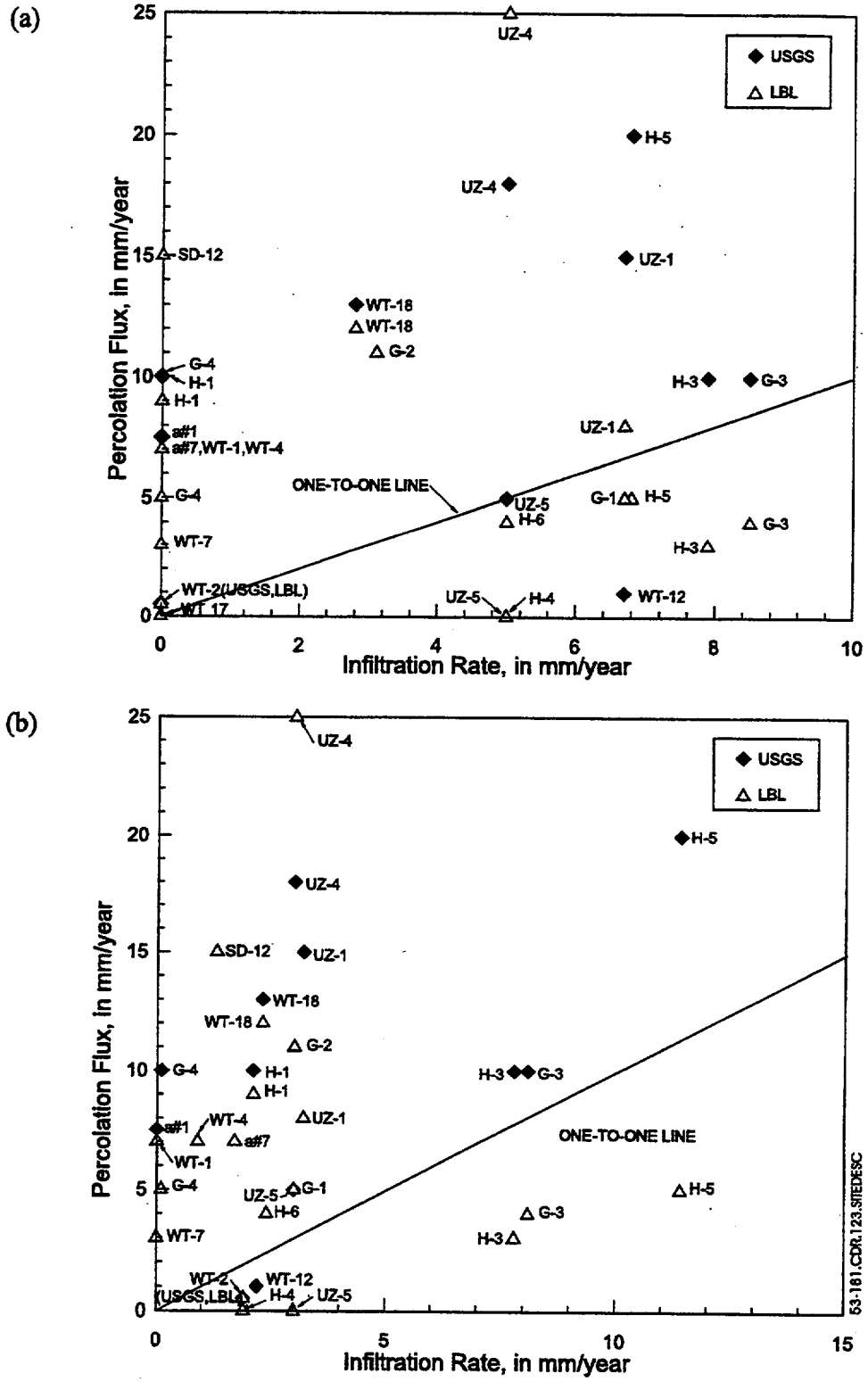

Figure 5.3-181. Comparison of Percolation Flux Rates Estimated Through Analyses of Borehole Temperature Profiles with Infiltration Fluxes Estimated from the Soil Water-Budget Model of Flint, A.L. et al. (1996) for (a) 30 x 30 m Areas Around Borehole Locations

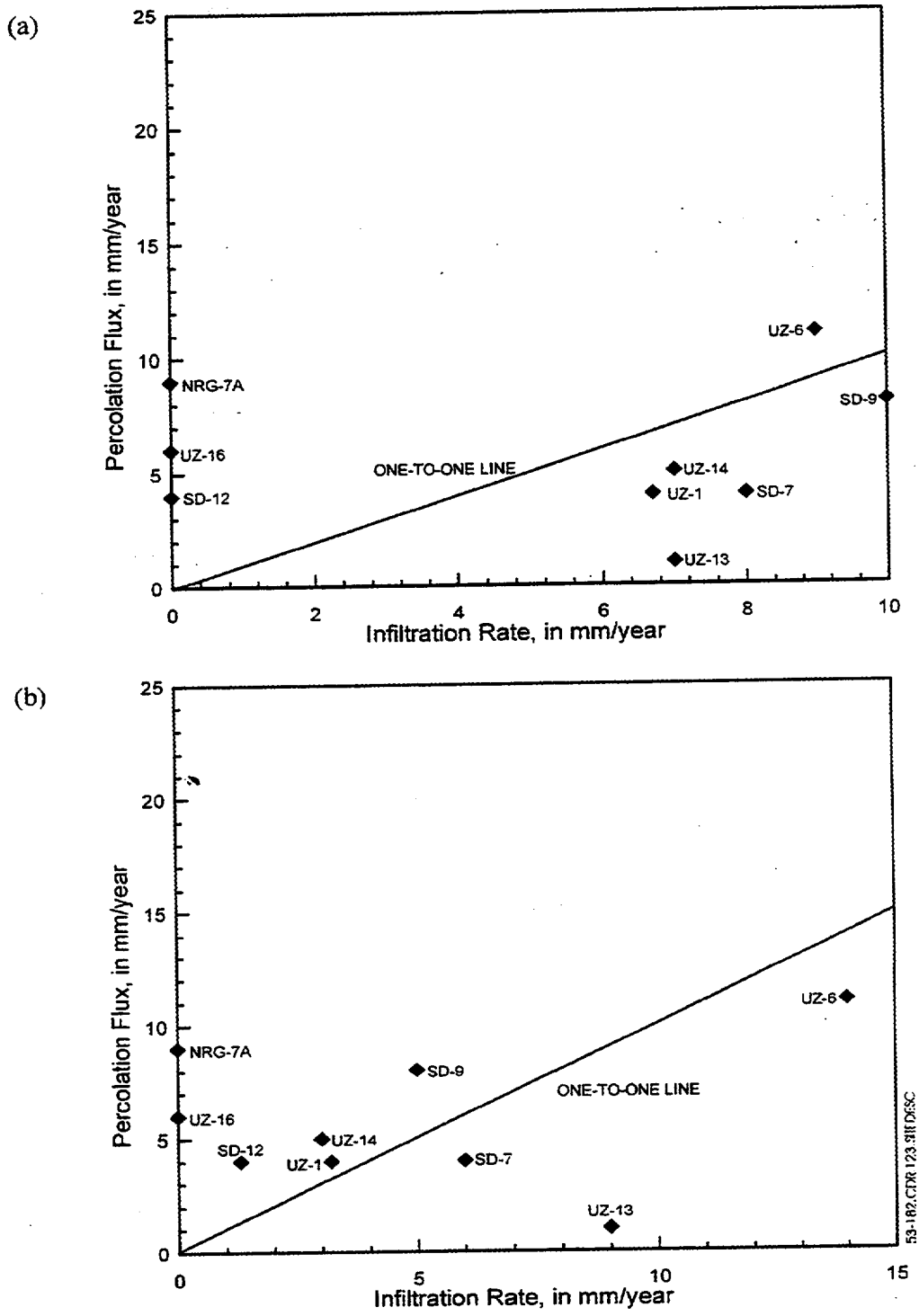

Figure 5.3-182. Comparison of Percolation Flux Rates Estimated Through Analyses of Borehole Carbon-14 Data with Infiltration Fluxes Estimated from the Soil Water-Budget Model of Flint, A.L. et al. (1996) for (a) 30 x 30 m Areas and (b) 90 x 90 m Areas Around Borehole Locations

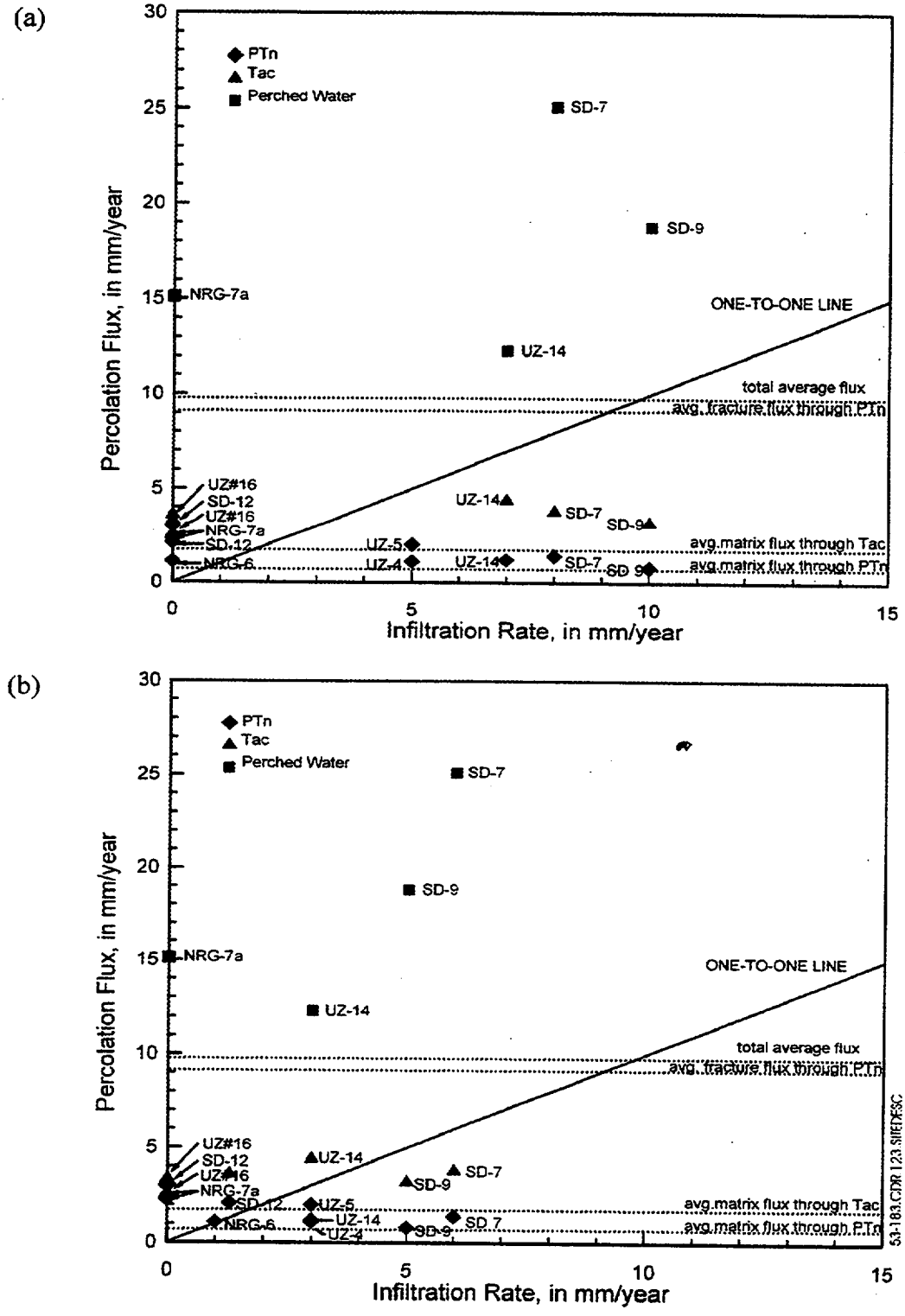

Figure 5.3-183. Comparison of Percolation Flux Rates Estimated Through Analyses of Borehole Chloride Data with Infiltration Fluxes Estimated from the Soil Water-Budget Model of Flint, A.L. et al. (1996) for (a) 30 x 30 m Areas and (b) 90 x 90 m Areas Around Borehole Locations

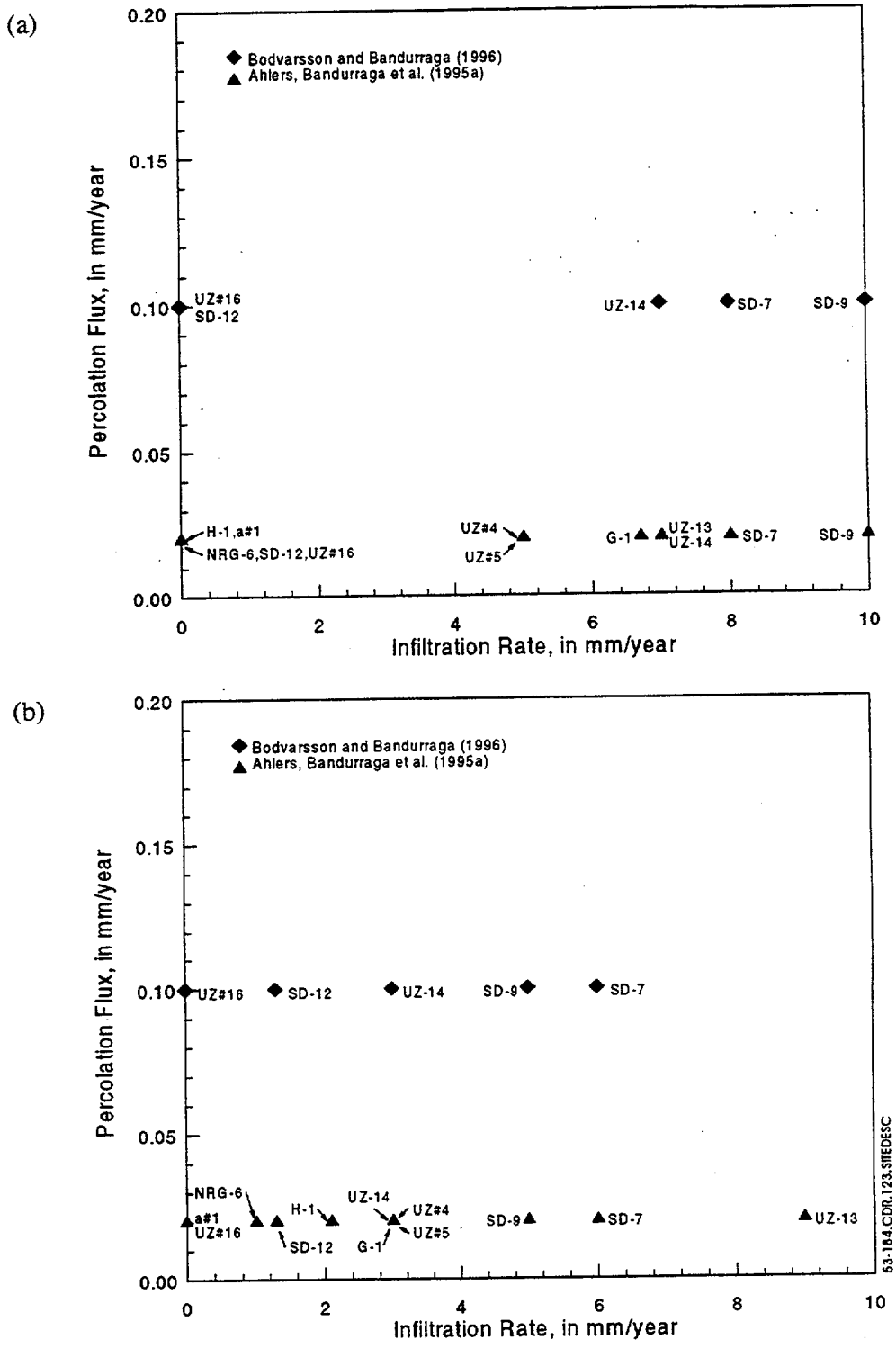

Figure 5.3-184. Comparison of Percolation Flux Rates Estimated by Bodvarsson et al. (1996) and Ahlers, Bandurraga et al. (1995) by Simulations of the Observed Borehole Saturation and Water Potential Data with Infiltration Fluxes Estimated from the Soil Water-Budget Model of Flint, A.L. et al. (1996) for (a) 30 x 30 m Areas and (b) 90 x 90 m Areas Around Borehole Locations

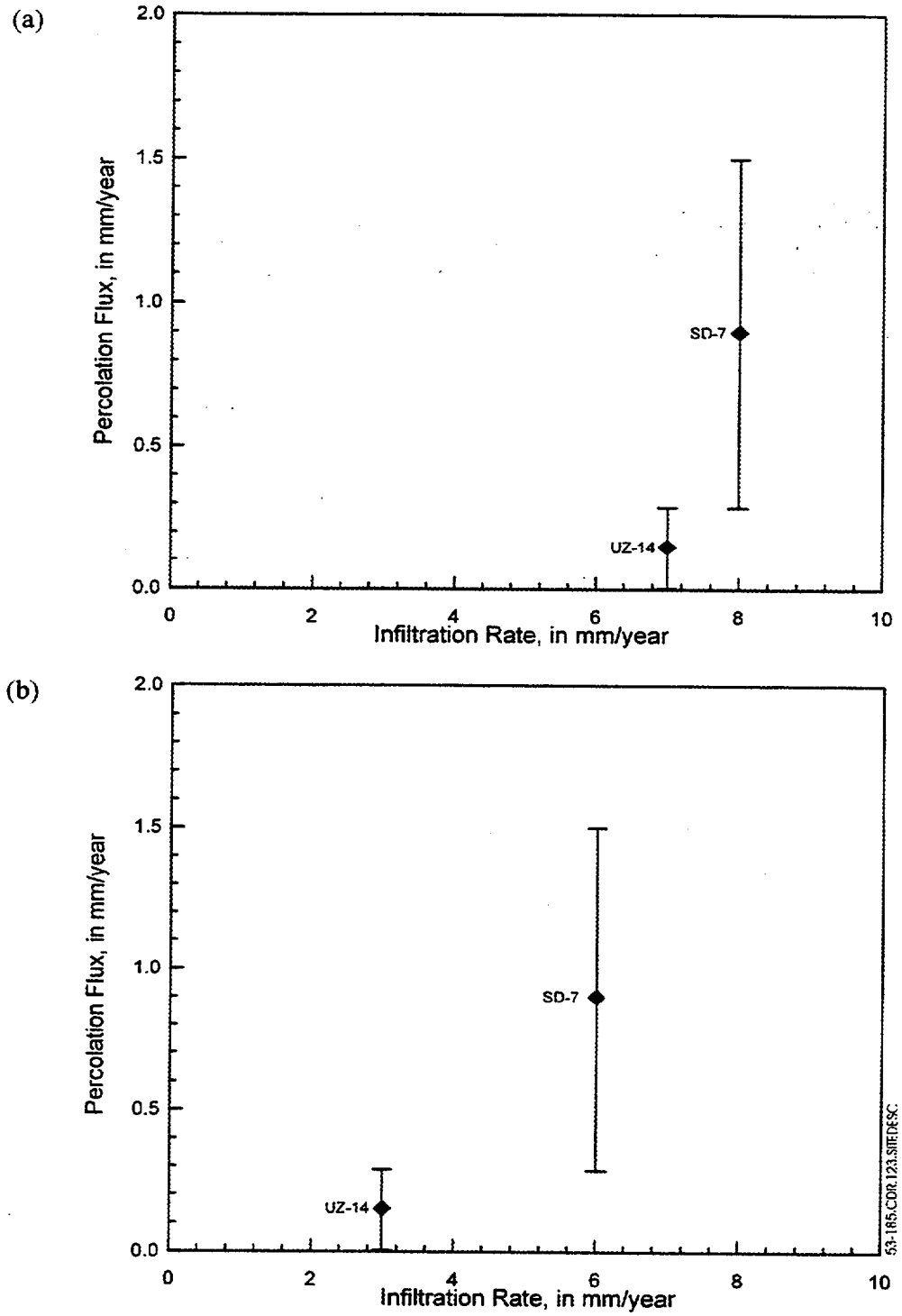

Figure 5.3-185. Comparison of Percolation Flux Rates Estimated from Perched Water Volumes and Residence Times with Infiltration Fluxes Estimated from the Soil Water-Budget Model of Flint, A.L. et al. (1996) for (a) 30 x 30 m Areas and (b) 90 x 90 m Areas Around Borehole Locations

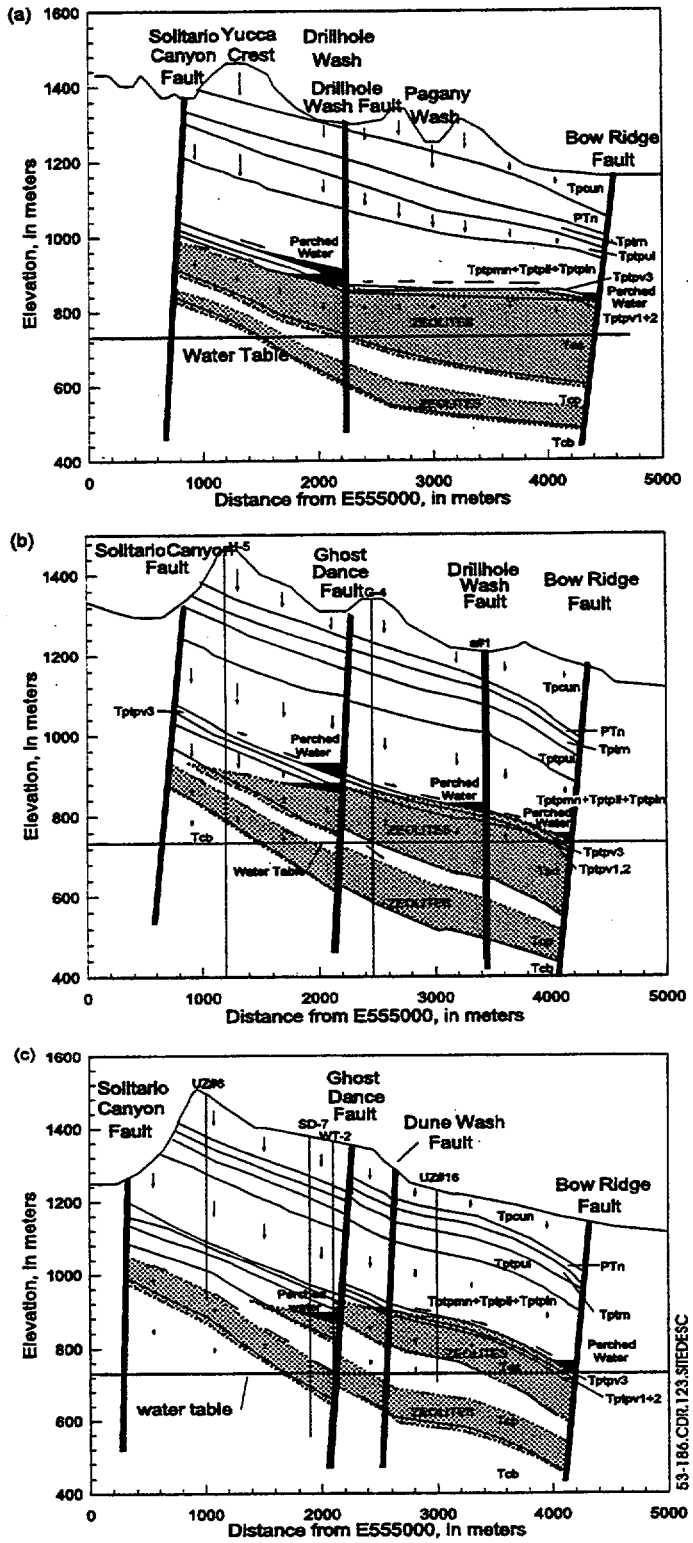

Figure 5.3-186. Geologic Cross-Sections Through Nevada State Coordinates (a) N770,000 Feet (b) N765,000 Feet and (c) N760,000 Feet Showing the Zones of Extensive Zeolite Development and Expected Flow Pathways

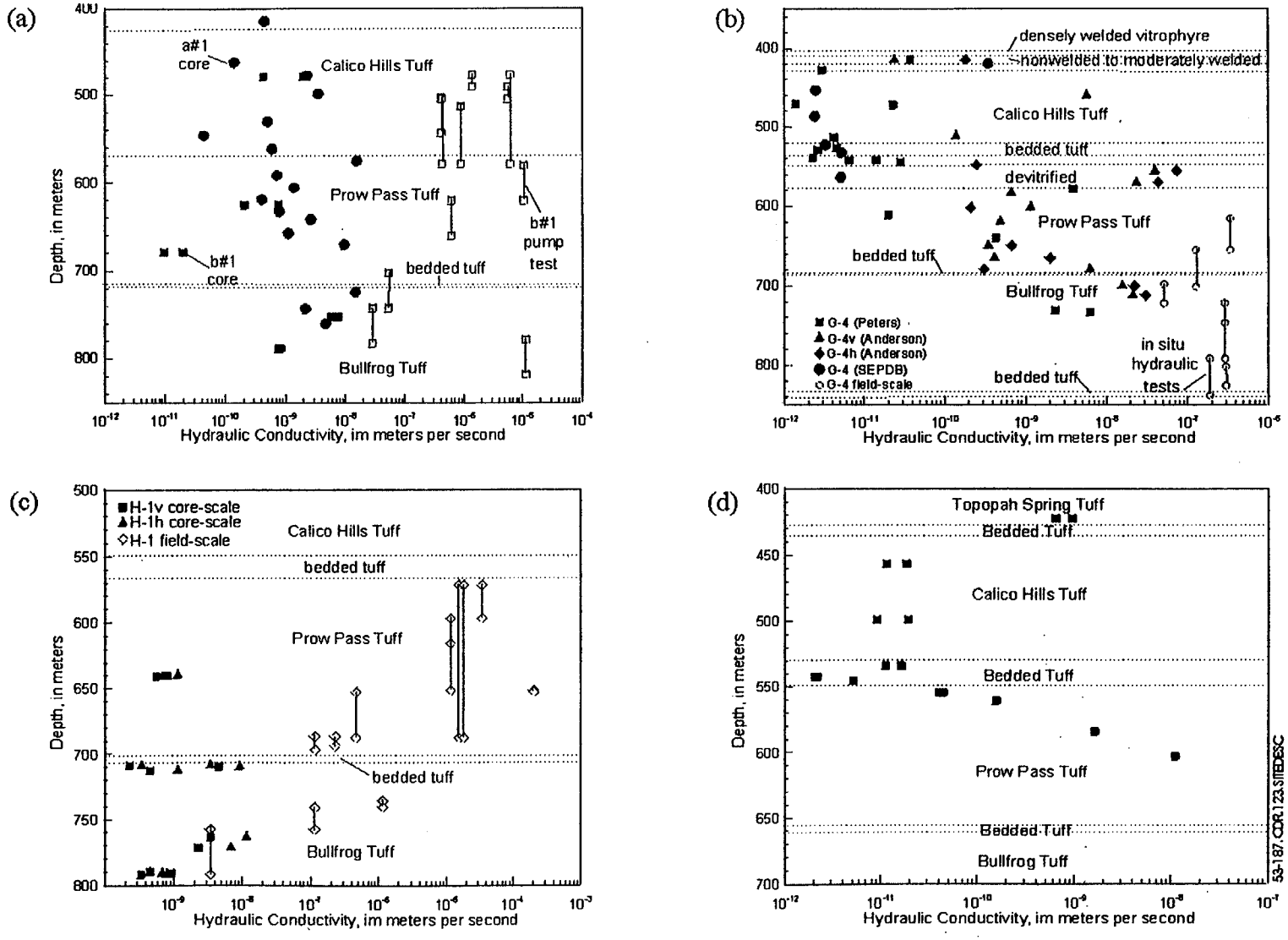

NOTE: From data summarized in Loeven (1993).

Figure 5.3-187. Figure Showing a Comparison Between Hydraulic Conductivities Determined from Core and at the Field Scale for Boreholes (a) a#1/b#1, (b) G-4, (c) H-1 and (d) G-1

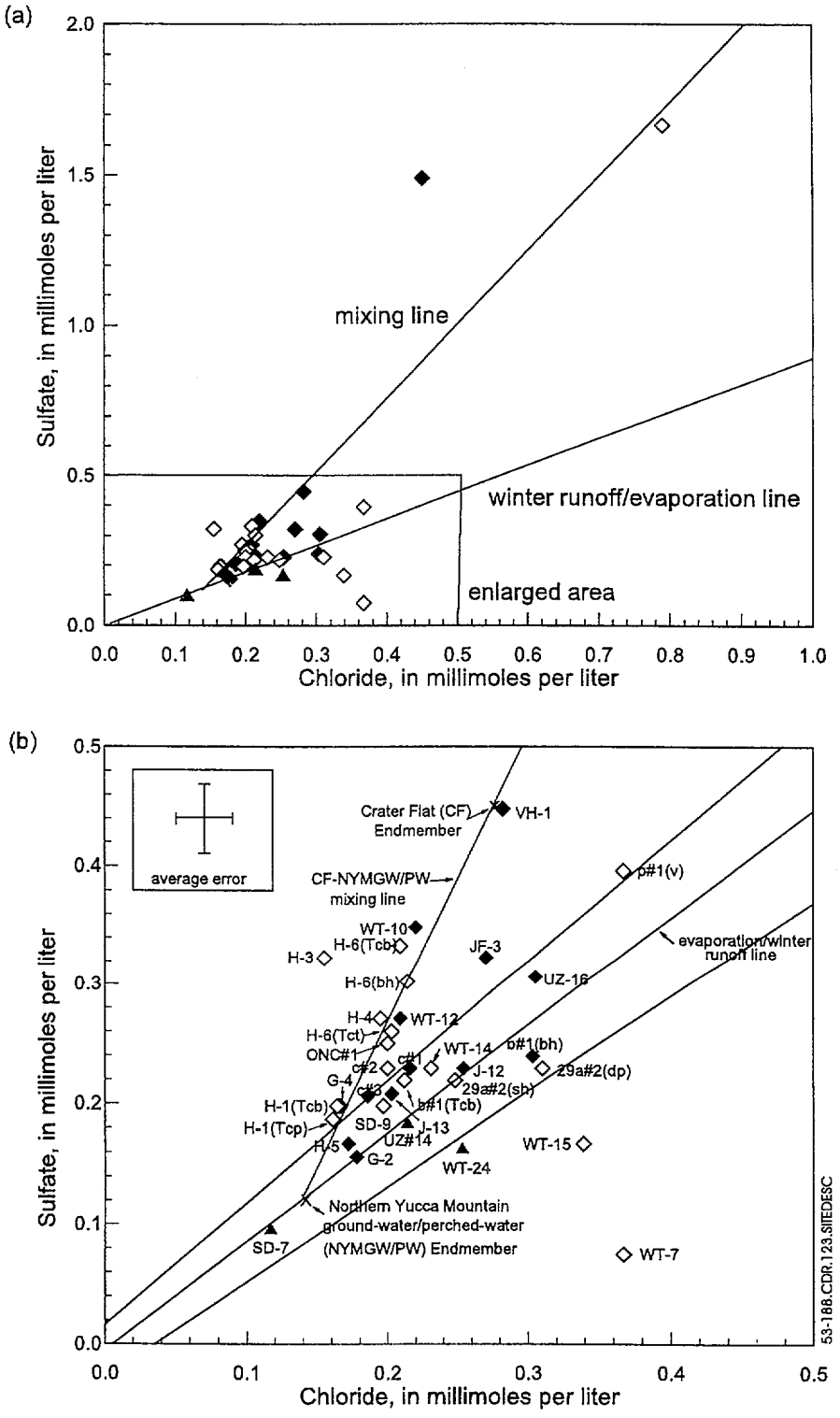

NOTE: From Kwicklis et al., *A Conceptual Model of Unsaturated Zone Flow and Transport, Yucca Mountain, Nevada*, Milestone Report 3GUM612M, U.S. Geological Survey, in preparation).

Figure 5.3-188. Figure Showing the Sulfate (SO_4^{2-}) Versus Chloride (Cl^-) Concentrations of Saturated Zone Groundwater Samples (a) All Samples (b) Samples With Sulfate Concentrations Less Than 0.5 mmol/l

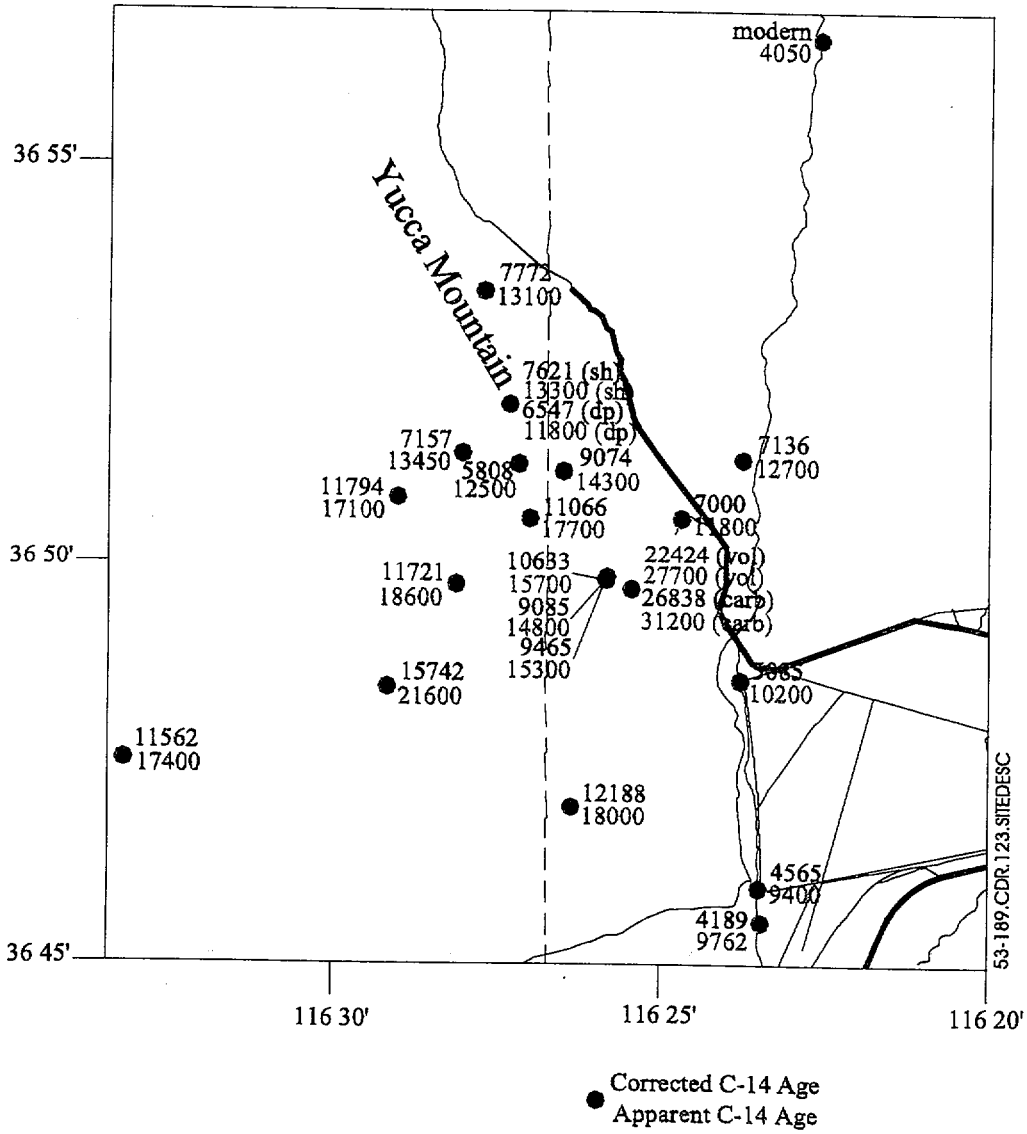

NOTE: From Kwicklis et al. *A Conceptual Model of Unsaturated Zone Flow and Transport, Yucca Mountain, Nevada*, Milestone Report 3GUM612M, U.S. Geological Survey, in preparation.

Figure 5.3-189. Apparent and Corrected Carbon-14 Ages of Saturated-Zone Groundwater Samples from Yucca Mountain and Vicinity

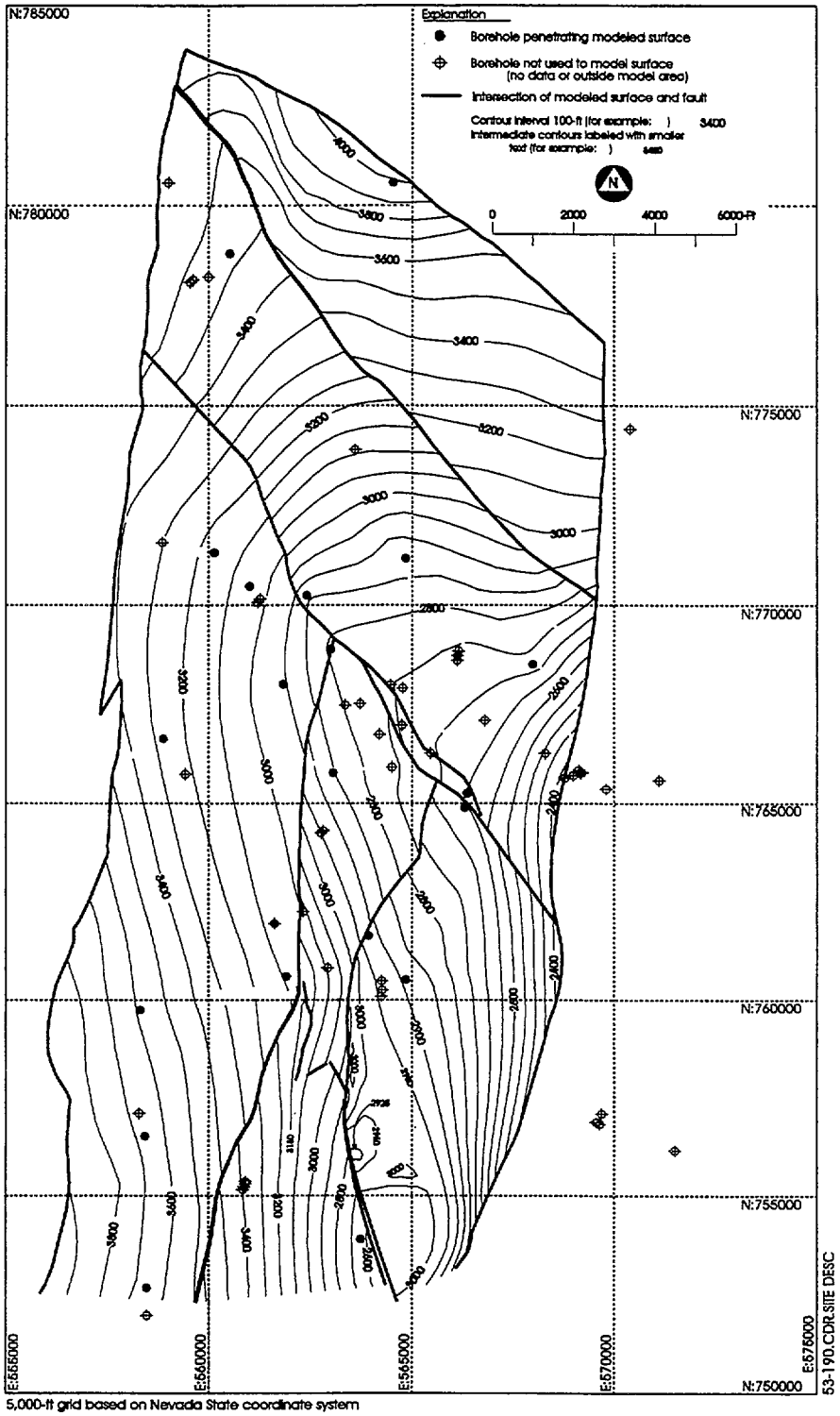

NOTE: From the lithostratigraphic model of Buesch, Nelson et al. (1996)

Figure 5.3-190. Elevation Contours of the Upper Contact of the Densely Welded, Crystal-Poor Vitrophyre of the Topopah Spring Tuff (Tptpv3)

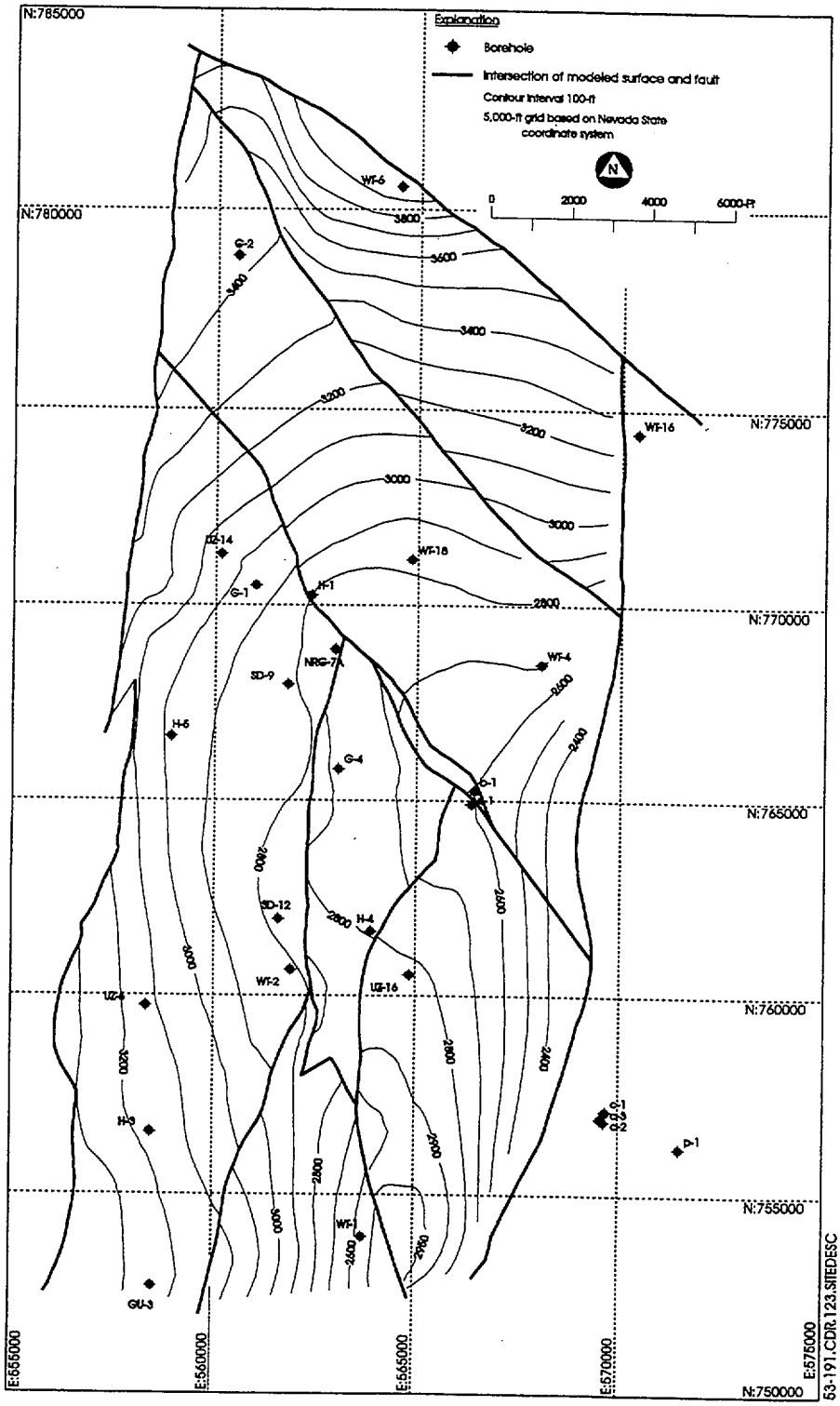

NOTE: From the Lithostratigraphic Model of Buesch, Nelson et al. (1996)

Figure 5.3-191. Elevation Contours of the Uppermost Transition from Vitric to Predominantly Zeolitic Rock

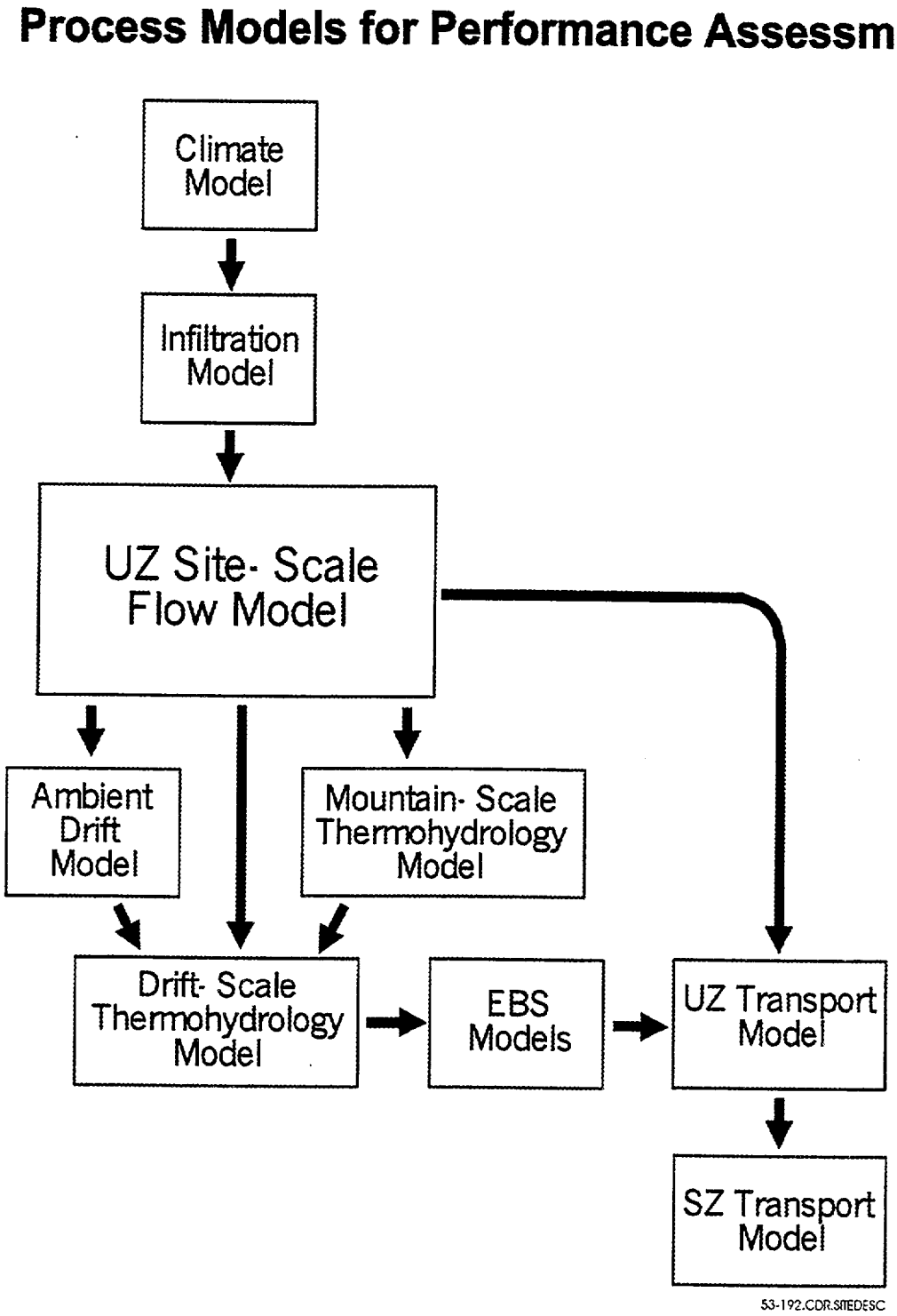

Figure 5.3-192. Relationships Between the Various Process Models Used in the Performance Assessment of Yucca Mountain

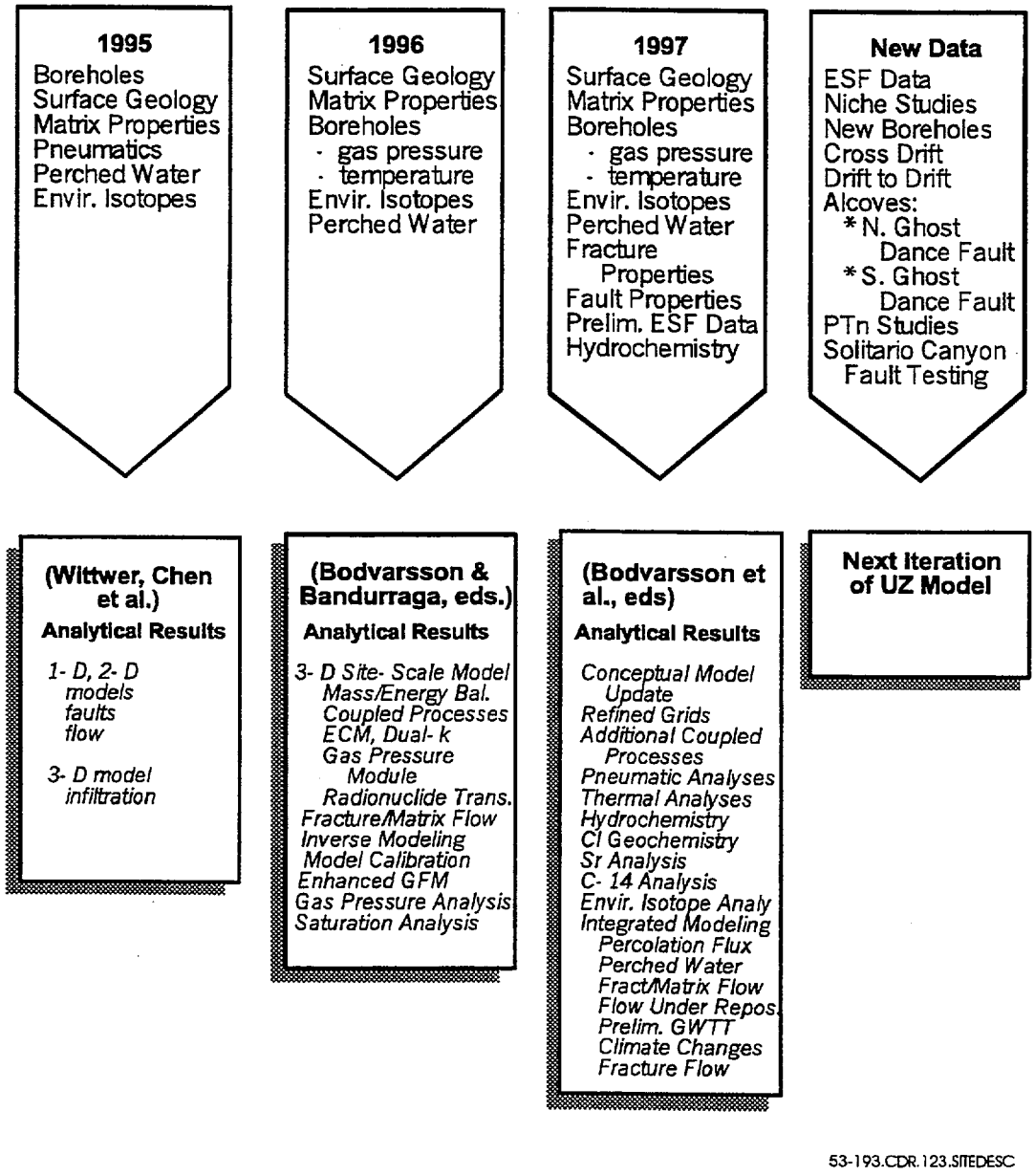

Figure 5.3-193. Evolution of the Development of the Unsaturated Zone Site-Scale Model and Major Field Data Inputs

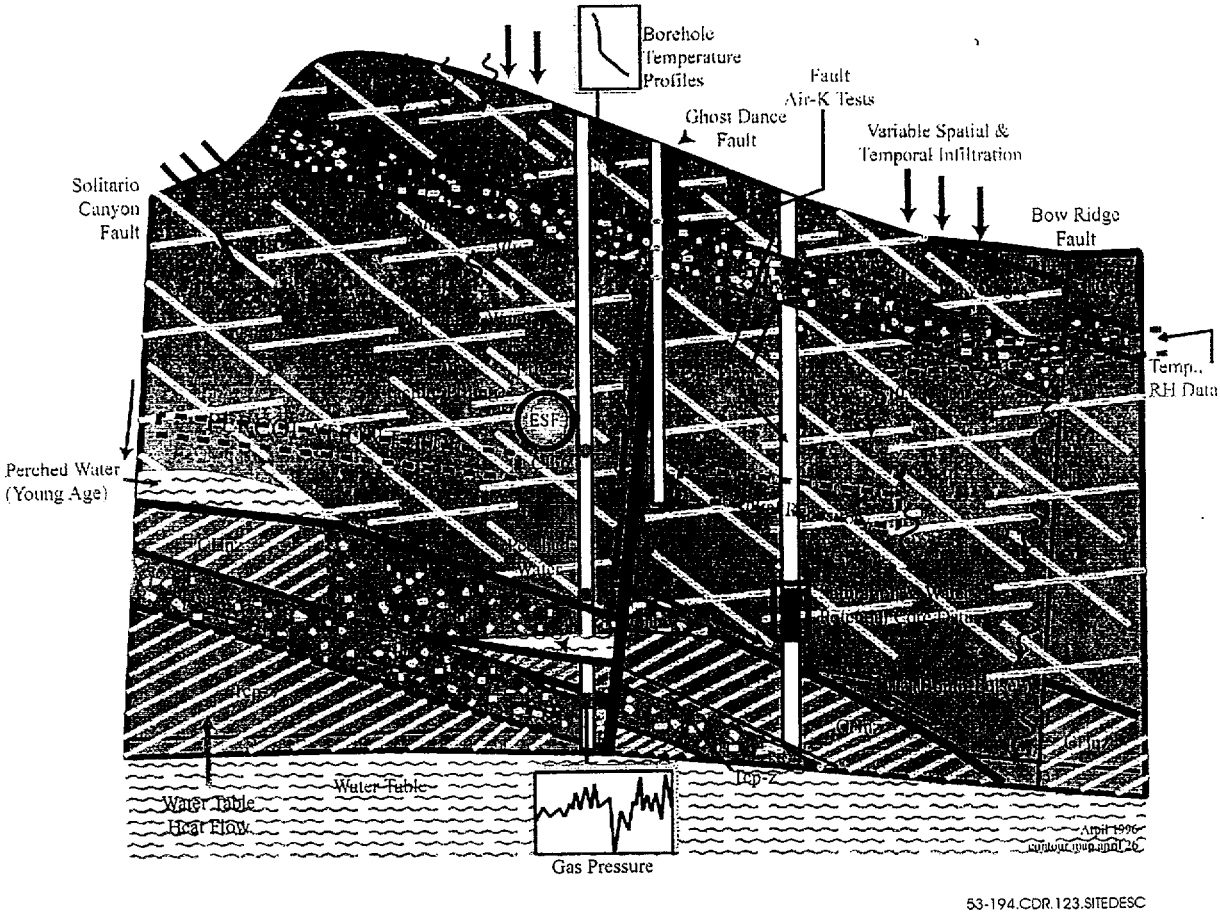

Figure 5.3-194. Schematic Cross-Section Through Yucca Mountain Showing Various Conceptual Model Data and Flow Processes

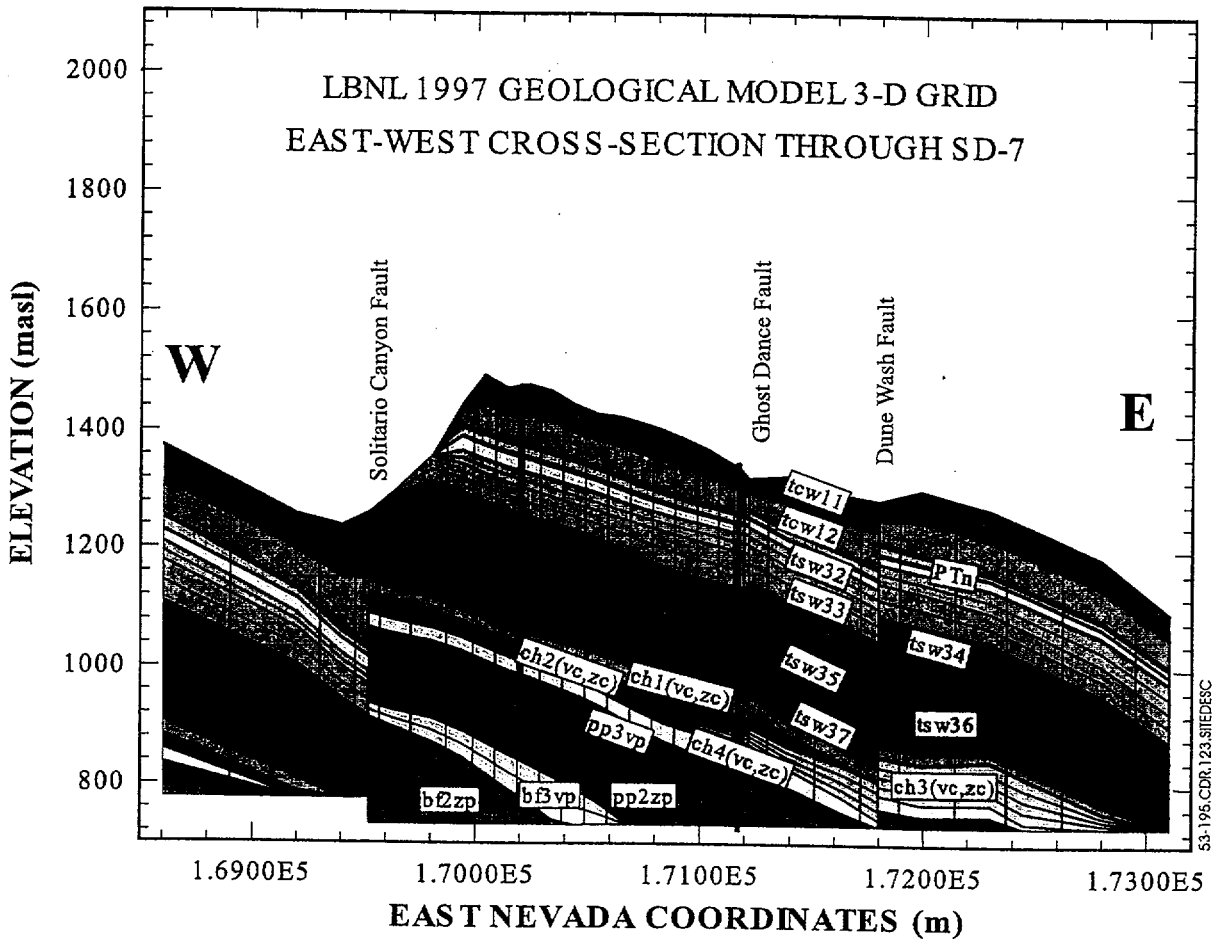

Figure 5.3-195. East-West Vertical Cross-Section Through the 3-D Site-Scale UZ Model Showing Hydrogeological Layering and Offsets along Explicitly Modeled Faults

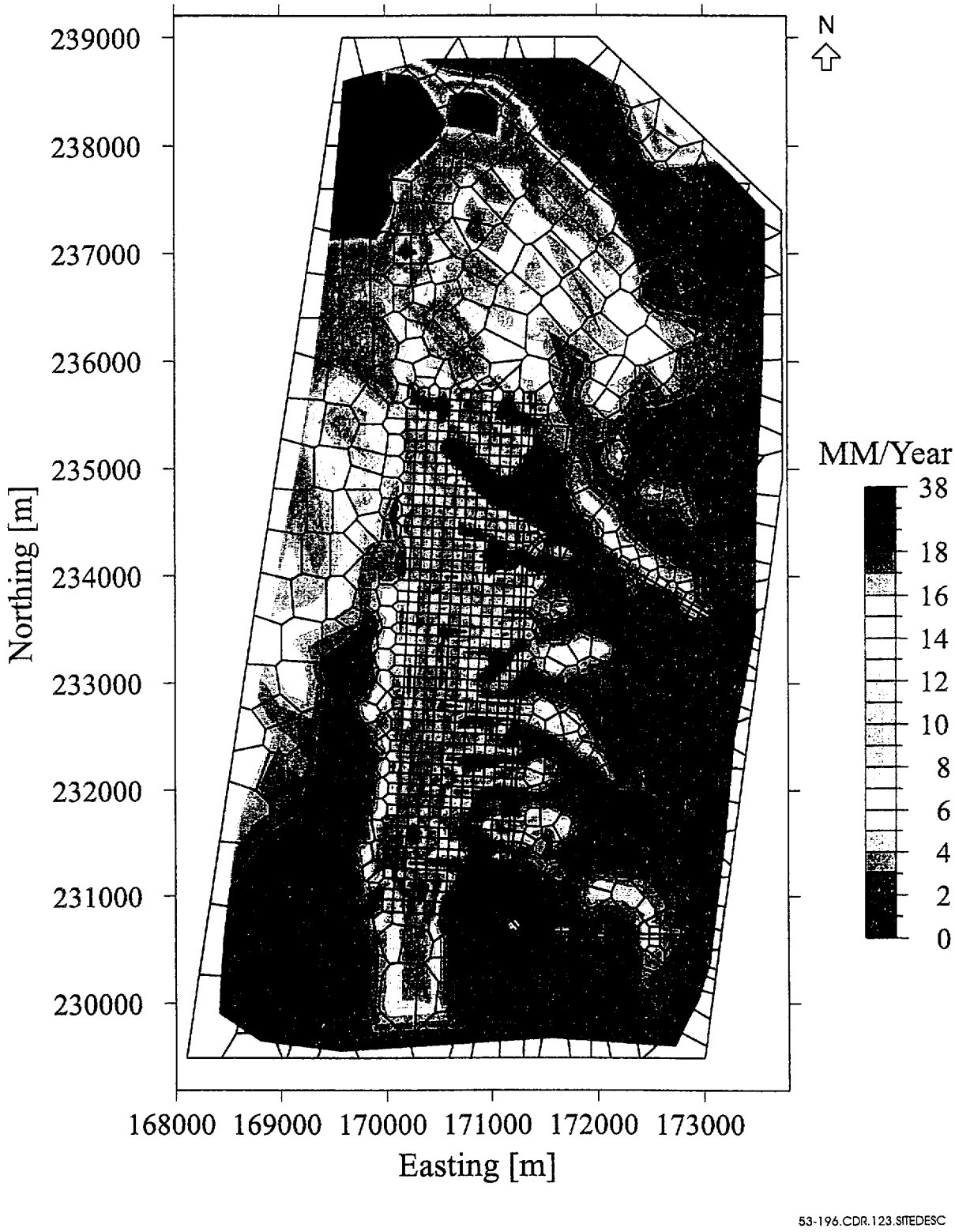

Figure 5.3-196. Net Infiltration Map Showing Average Infiltration Rates and Distributions over Yucca Mountain

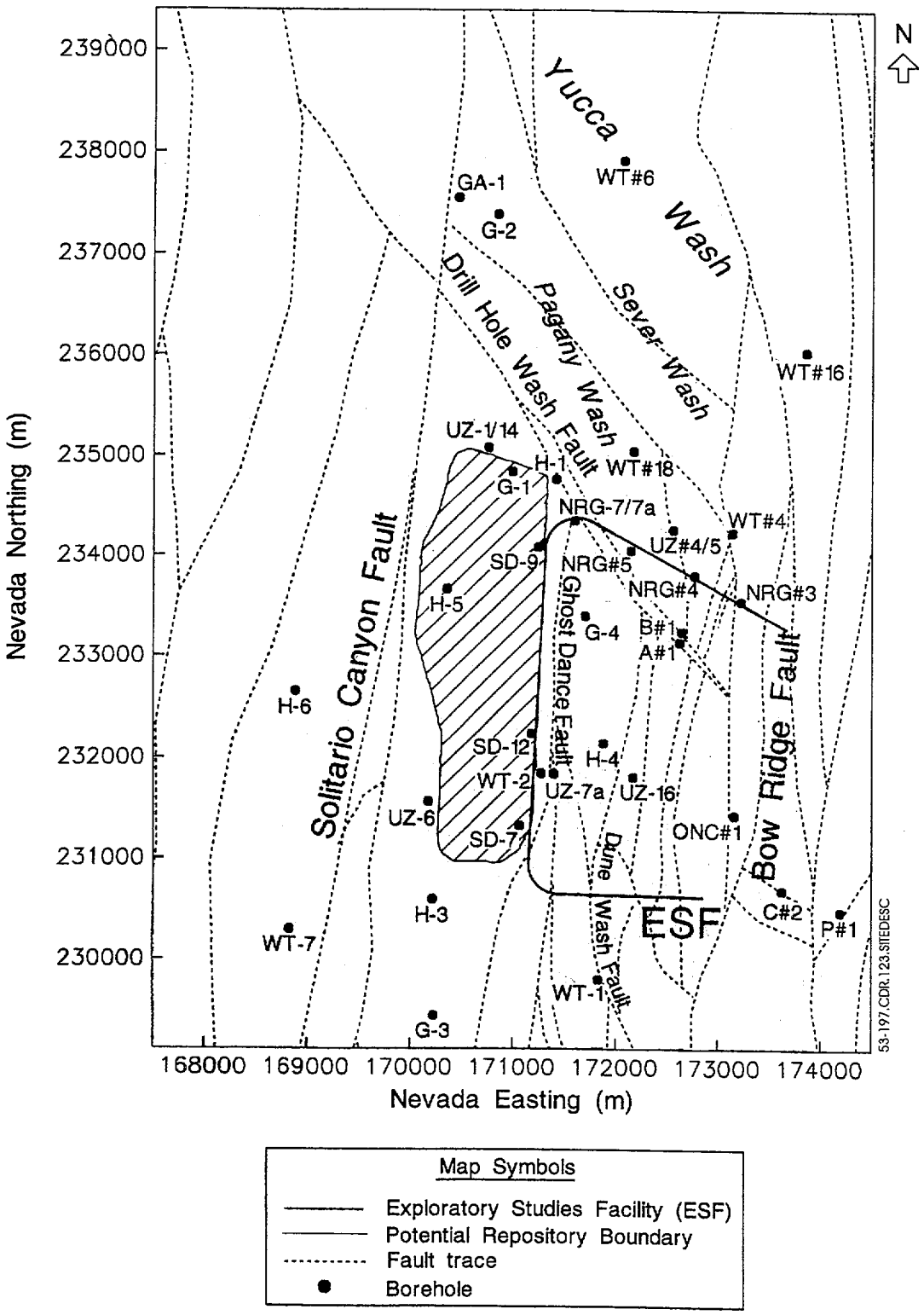

Figure 5.3-197. Location Map with Boreholes, Faults, and Other Important Features at Yucca Mountain

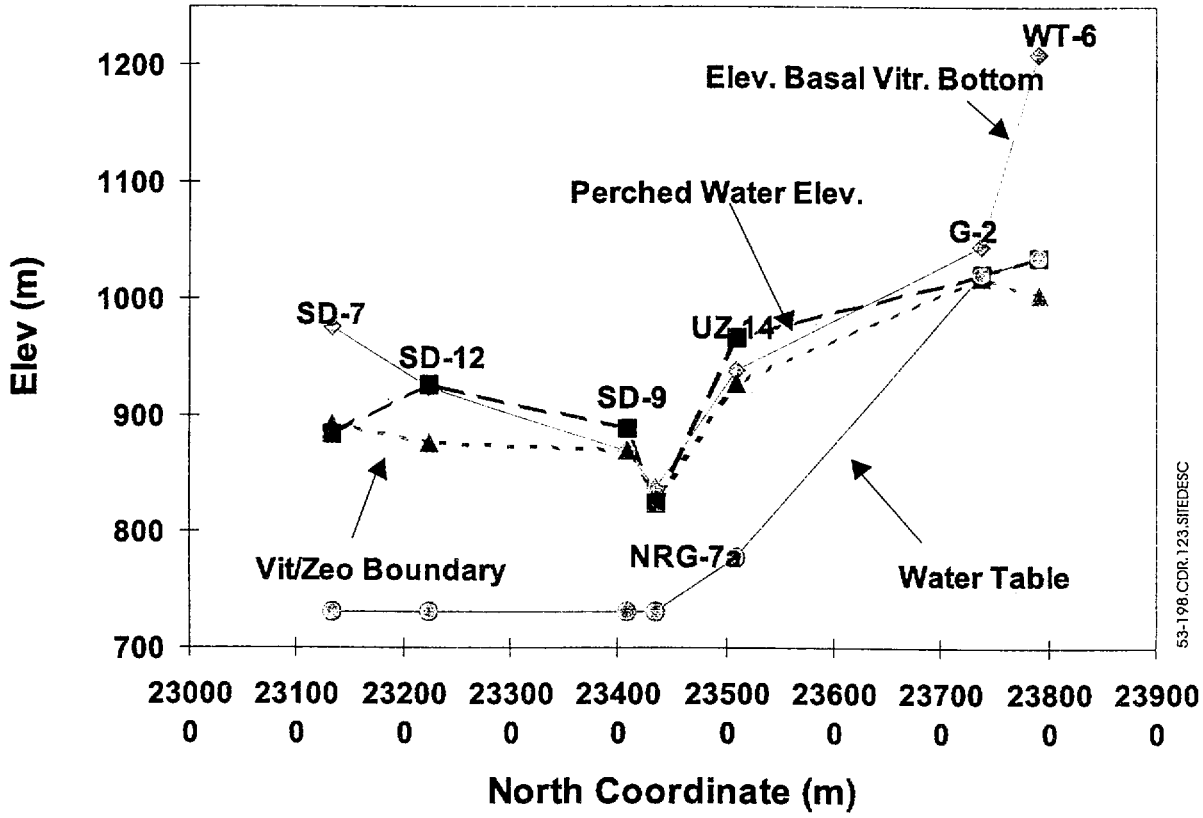

Figure 5.3-198. Perched-Water Locations Projected to a North-South Cross-Section and Their Relationship to Underlying Low-Permeability Unit Boundaries

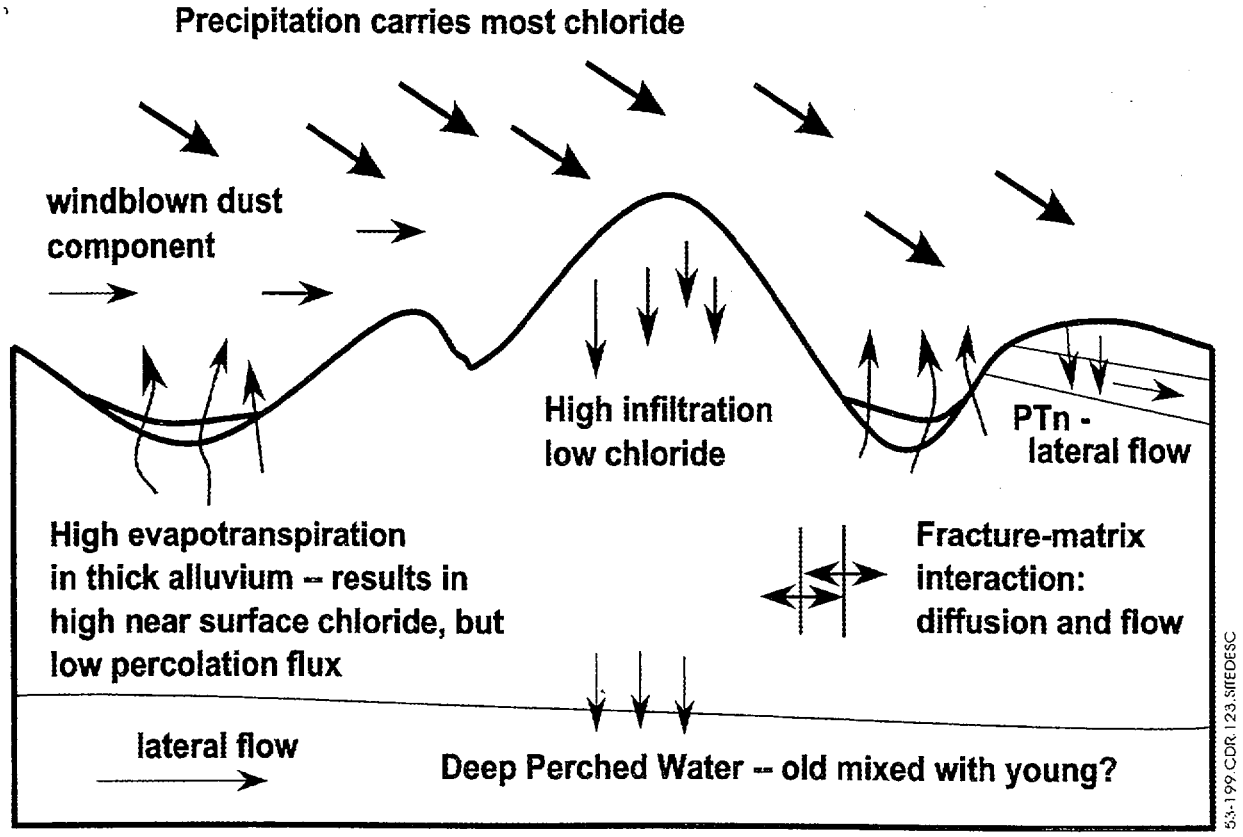

Figure 5.3-199. Schematic Diagram Showing Major Processes Affecting the Chloride Chemistry at Yucca Mountain

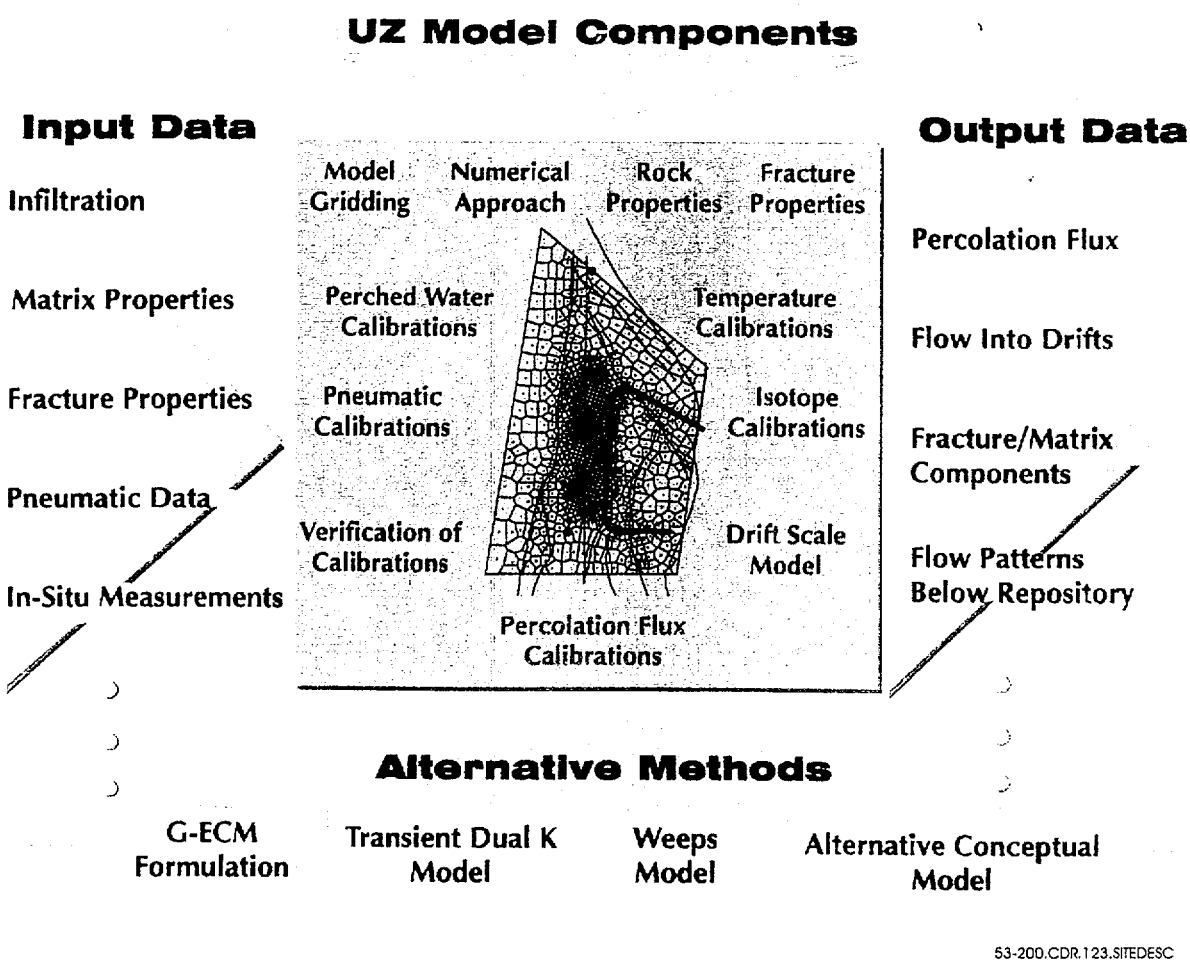

Figure 5.3-200. Major Components of the 3-D Unsaturated Zone Site-Scale Flow Model

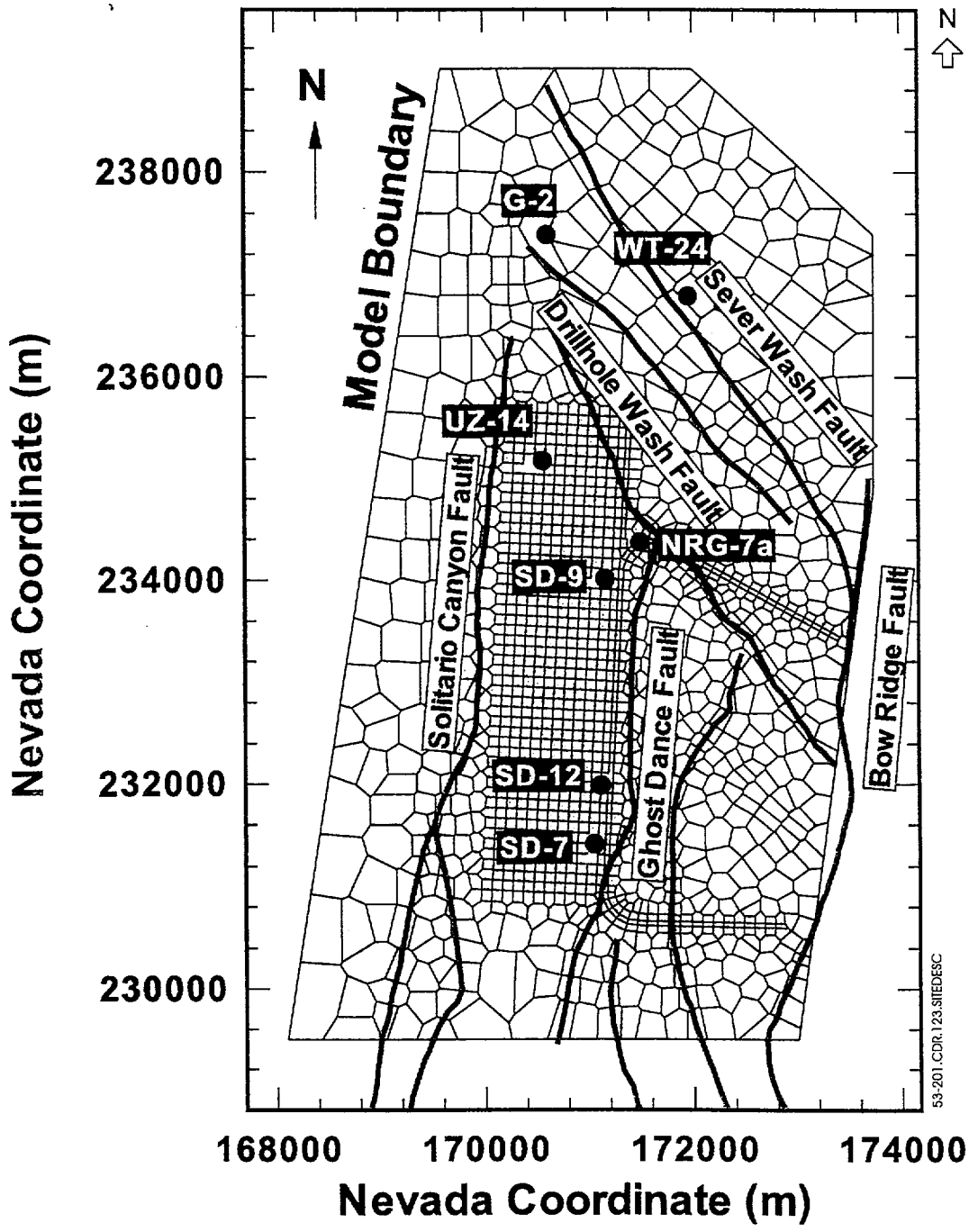

Figure 5.3-201. A Plan View of the Site-Scale UZ Model Domain Showing Model Boundaries, the Location of Several Boreholes, the Numerical Grid with Refinement in the Potential Repository Area, Major Incorporated Faults, and the Exploratory Studies Facility

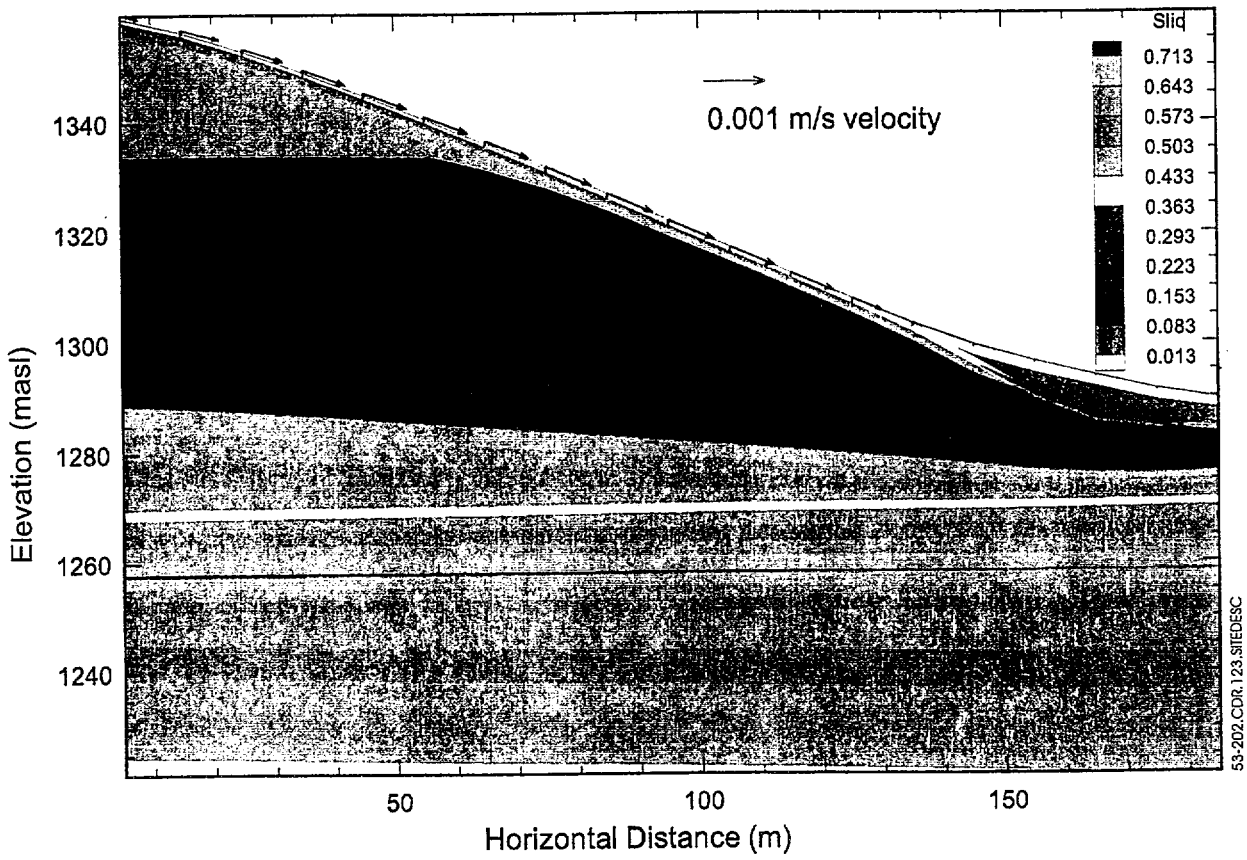

Figure 5.3-202. Liquid Saturation and Liquid-Flow Velocity Vectors for a 2-D North-South Cross-Section Simulation of Precipitation and Evapotranspiration at Wren Wash with 50 cm of Upland Alluvial Thickness. Vectors Show Runoff after Simulated Rainfall of 4 mm/min for 5 Minutes

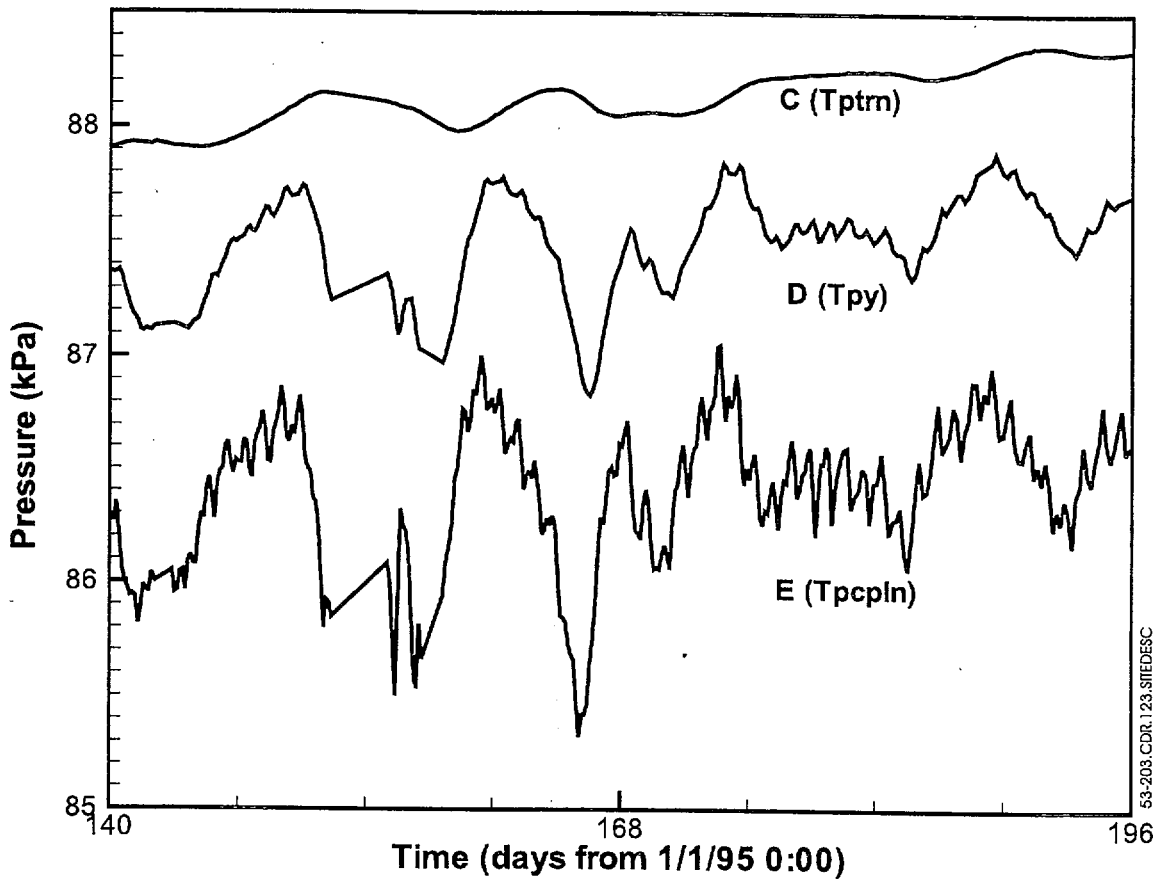

NOTE: The Data Shown Was Collected Prior to Any Influence of the Exploratory Studies Facility.

Figure 5.3-203. Ambient Pneumatic Pressure Data from NRG-7a Instrument Stations C, D, and E

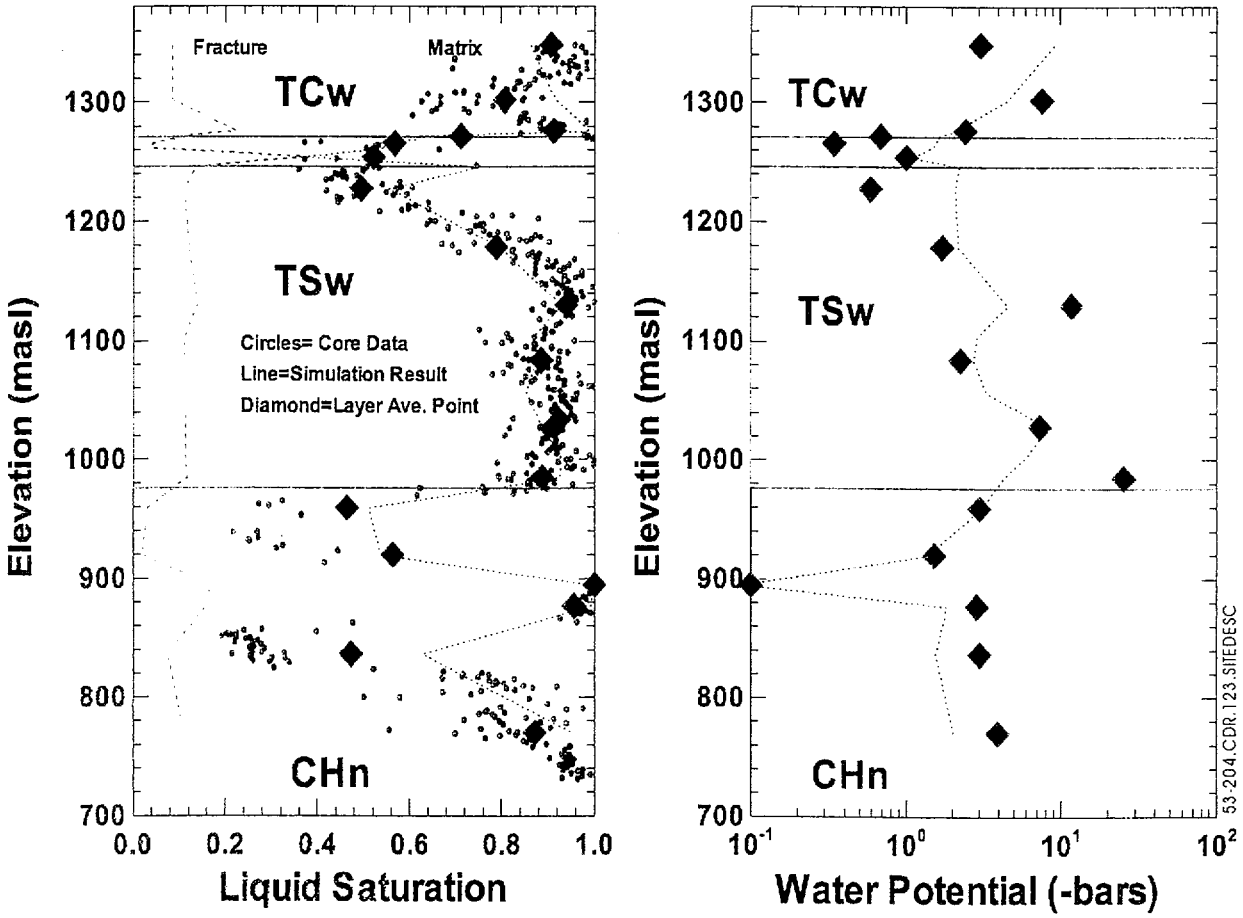

NOTE: Fracture saturation also shown. Measured data source: L.E. Flint (1998).

Figure 5.3-204. Borehole SD-7 Match to Observed Core Sample Saturation and Water Potential Data Using a Calibrated Parameter Set

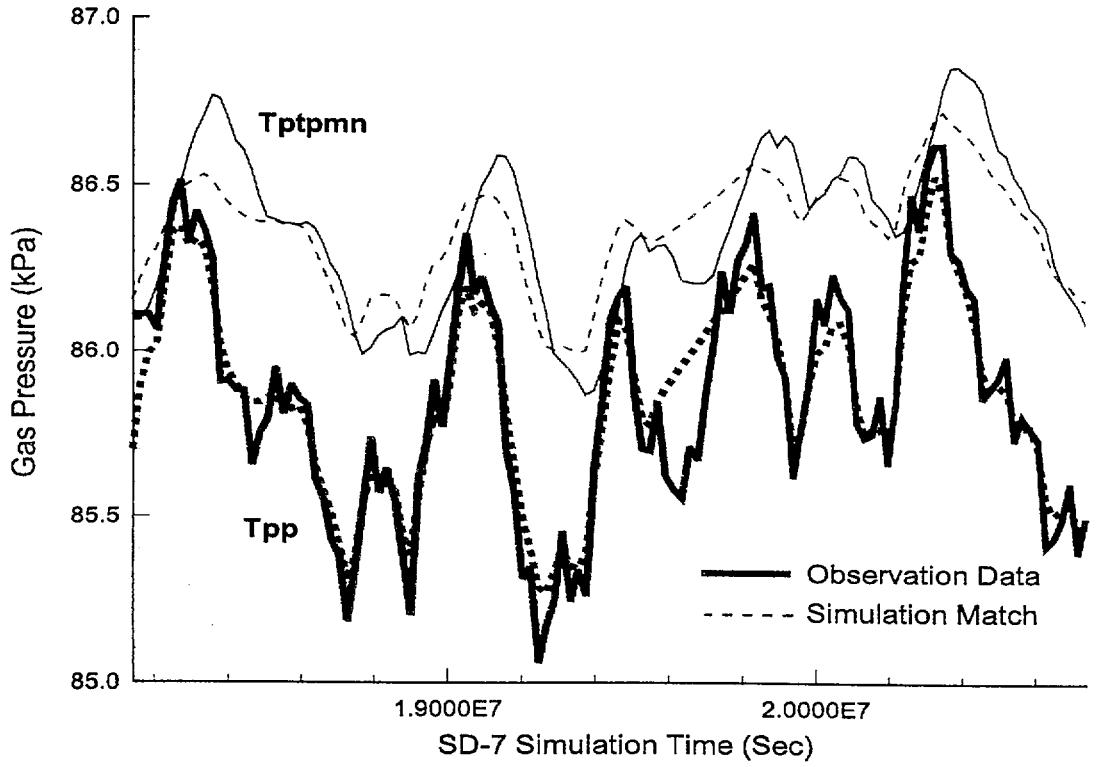

NOTE: Thin solid (observed) and dashed (simulated) lines refer to the Tptpmn, while the heavier solid (observed) and dashed (simulated) lines refer to the Tpp. Data source: Rousseau, Loskot et al. (1997). Base-case parameters with Fm=0.492. Described in detail in Chapter 6 of the FY 97 report (Bodvarsson et al. 1997).

Figure 5.3-205. SD-7 Gas Pressure Calibration Results for the Crystal-Poor, Middle Nonlithophysal Formation (Tptpmn) of the TSw and the Pah Canyon Tuff (Tpp) of the PTn

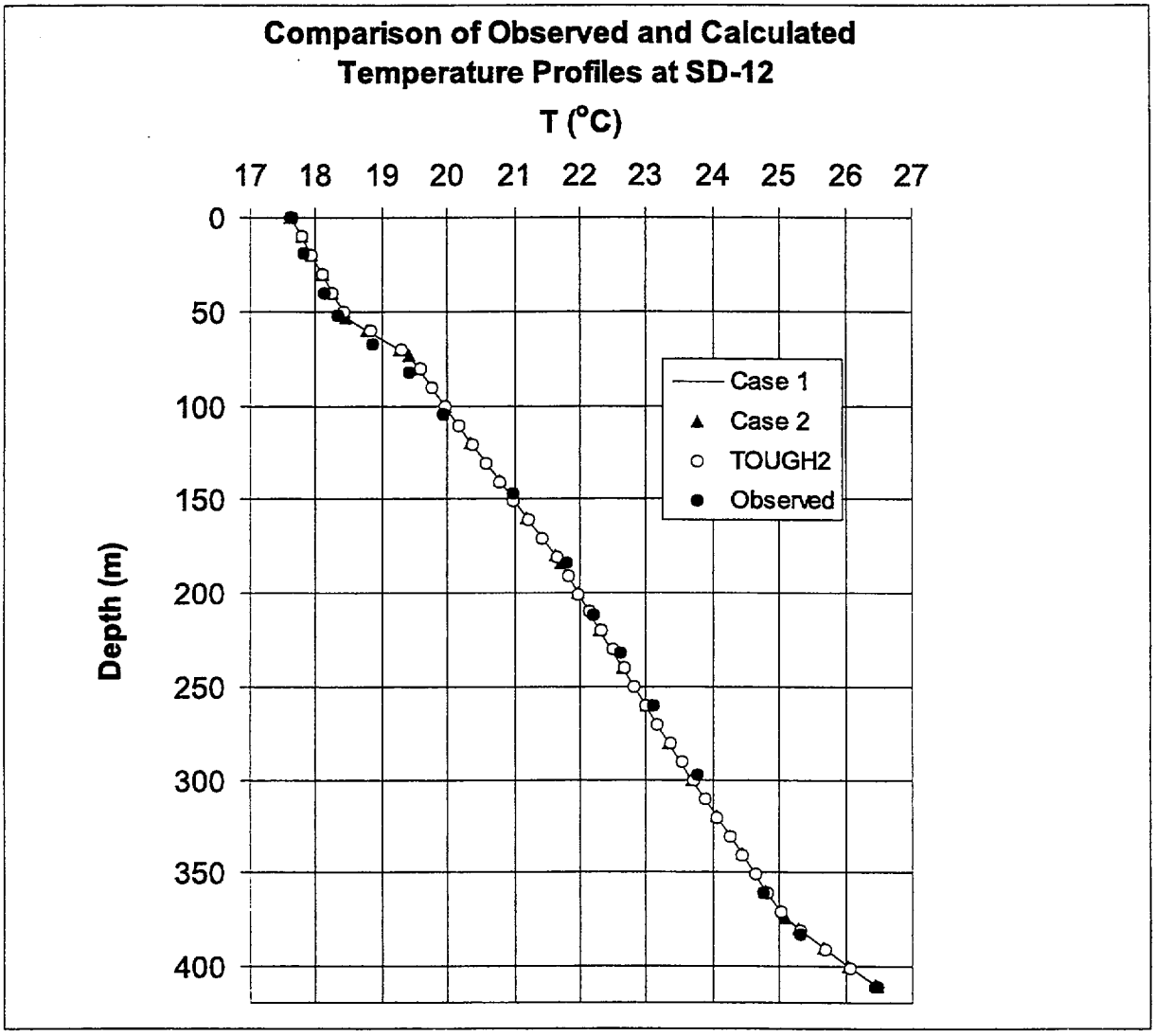

Figure 5.3-206. Comparison of the Observed Temperatures at Borehole SD-12 with Those Obtained by Numerical Simulation Using TOUGH2, and by an Analytical Model Using Either Constant-Flux or Fixed-Temperature Boundary Conditions at the Water Table

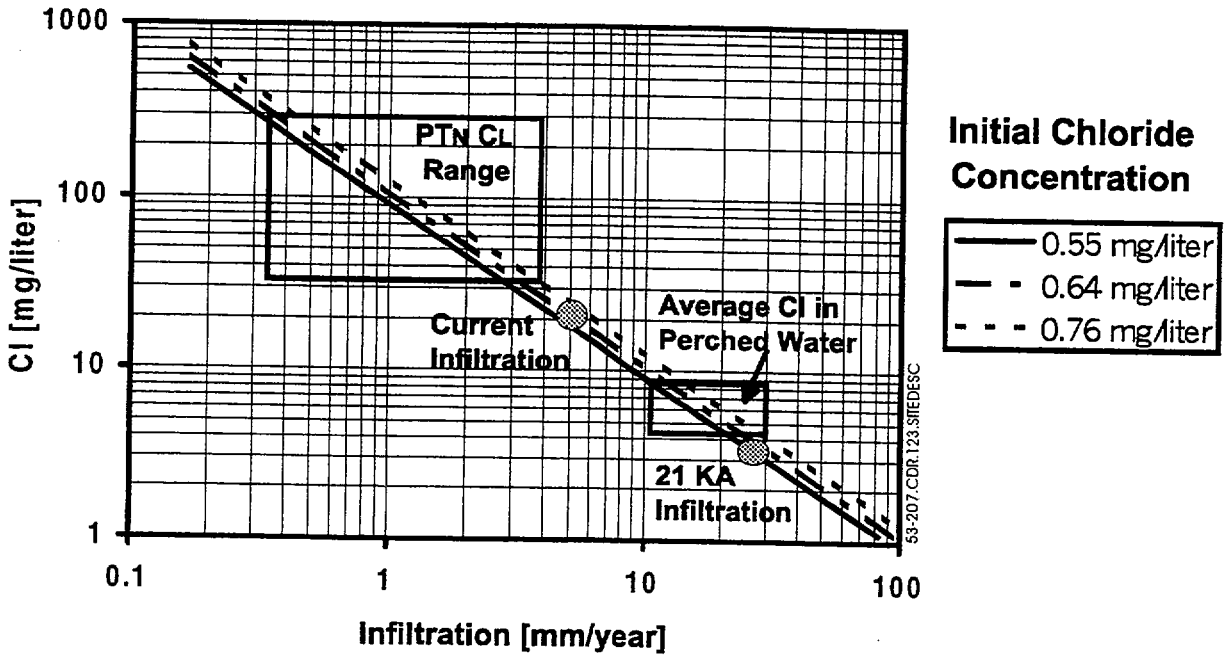

NOTE: The range in concentrations for the PTn and the perched water bodies are shown as boxes. The three lines represent possible differences in estimated concentration of precipitation (rainwater plus windblown dust).

Figure 5.3-207. Calculated Mean Concentrations from the Current Best Estimate of Mean Infiltration and Precipitation for the Current Climate and for the 21 kA Glacial Maximum (Sonnenthal and Bodvarsson 1997)

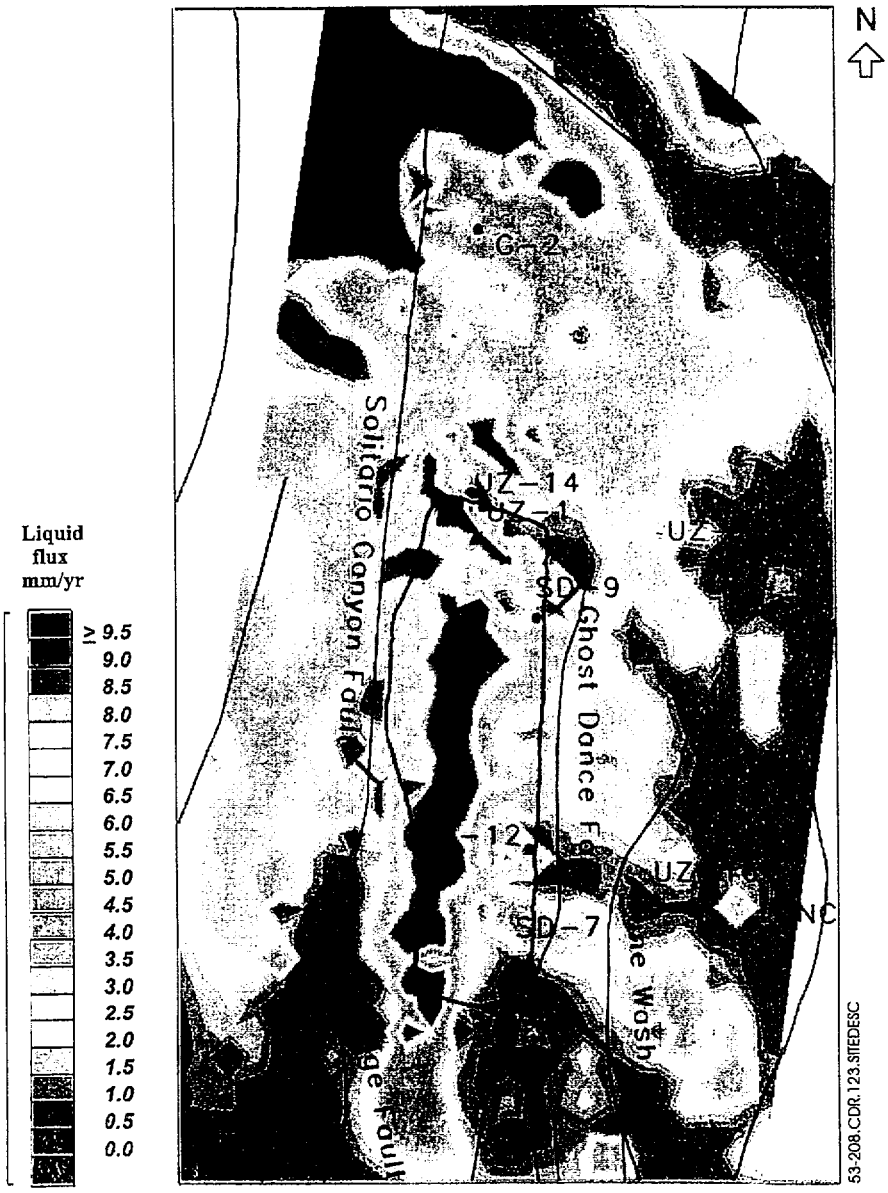

Figure 5.3-208. Fracture Flow Fluxes (Mm/yr) at the Potential Repository Horizon, Simulated Using the Dual-Permeability Model, LBNL Parameter Set #3 (Described in Chapters 6 and 21 of the FY 97 Report (Bodvarsson et al. 1997)), and the Infiltration Map of Flint, A.L. et al. (1996)

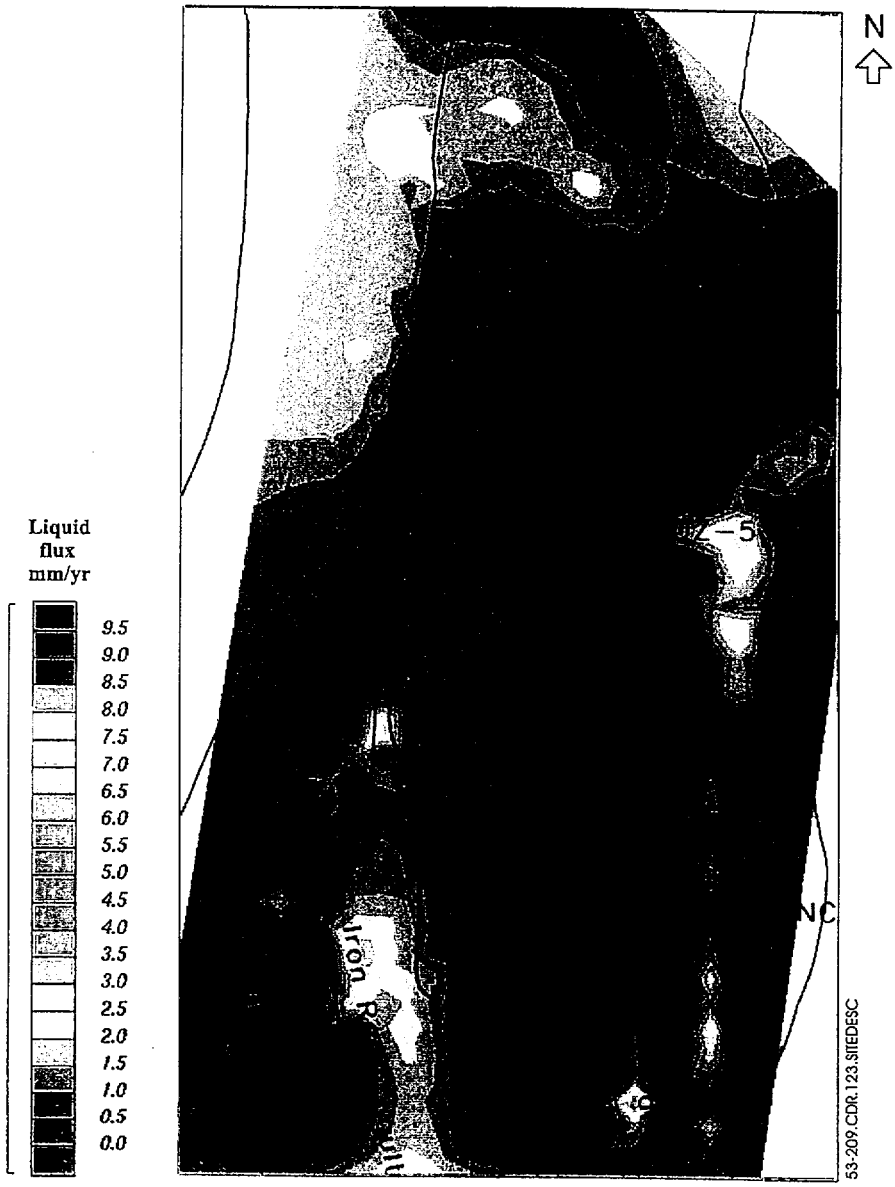

Figure 5.3-209. Matrix Flow in (Mm/yr) at the Potential Repository Horizon, Simulated Using the Dual-Permeability Model, LBNL Parameter Set #3, and the Infiltration Map of Flint, A.L. et al. (1996)

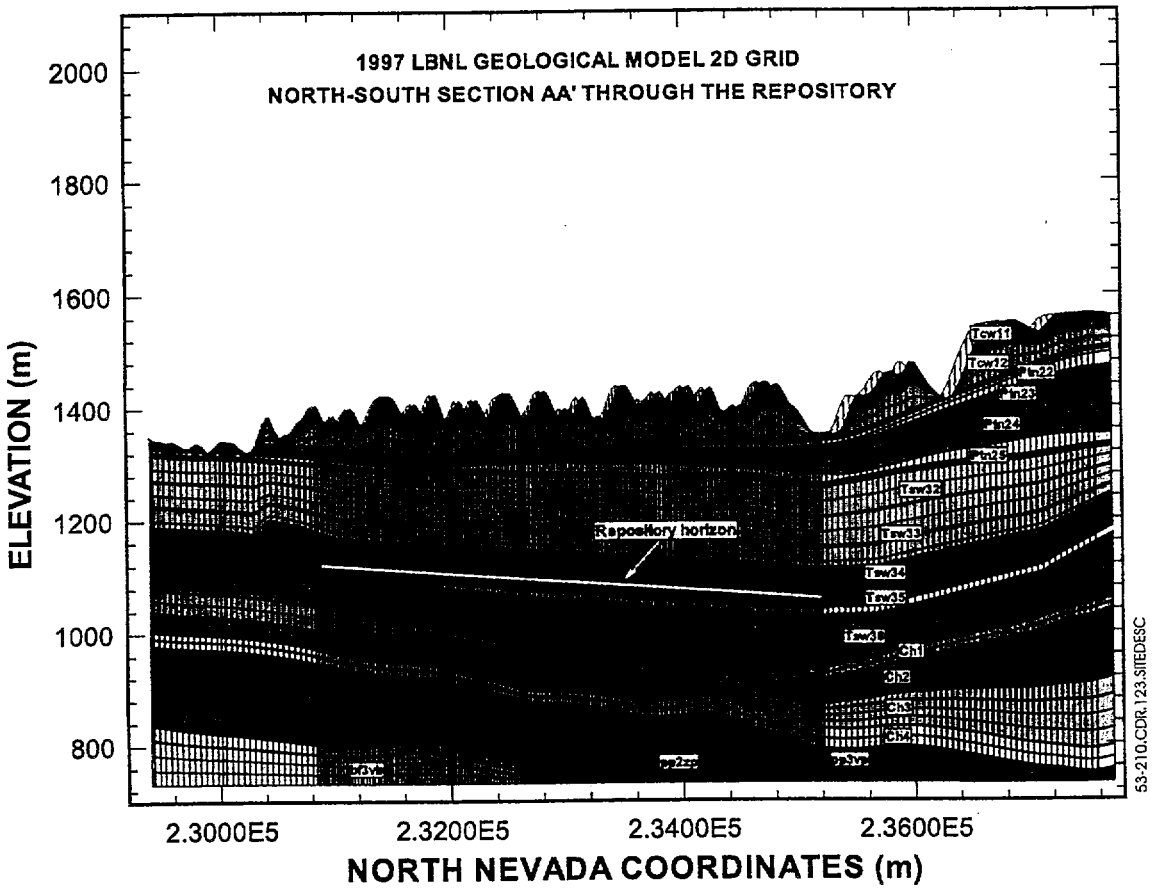

Figure 5.3-210. North-South Vertical Cross-Section Through the Site-Scale UZ Model Showing the Refined 2-D Grid

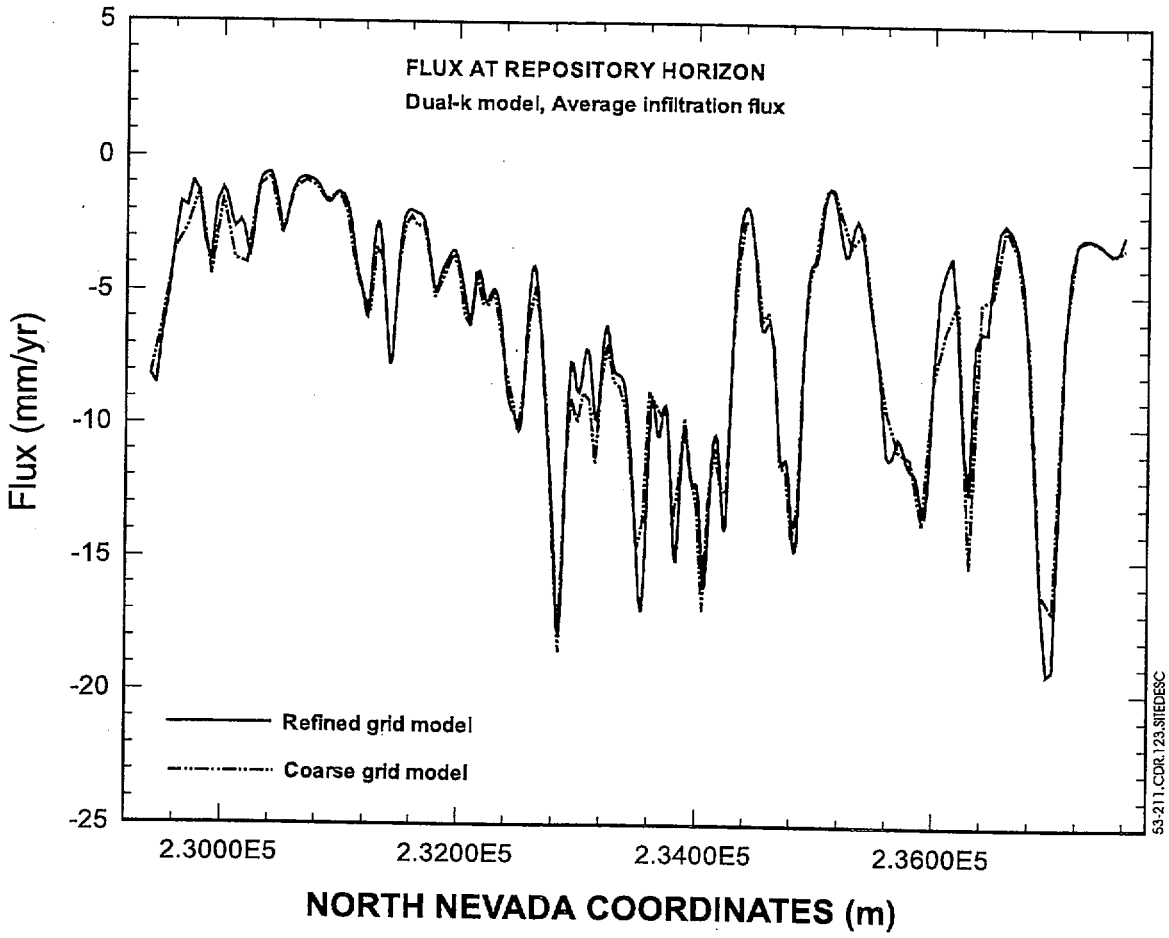

Figure 5.3-211. Modeled Percolation Flux at the Potential Repository Horizon Using the 2-D Refined Grid, Dual-Permeability Method, and the Average Infiltration Map of Flint, A.L. et al. (1996)

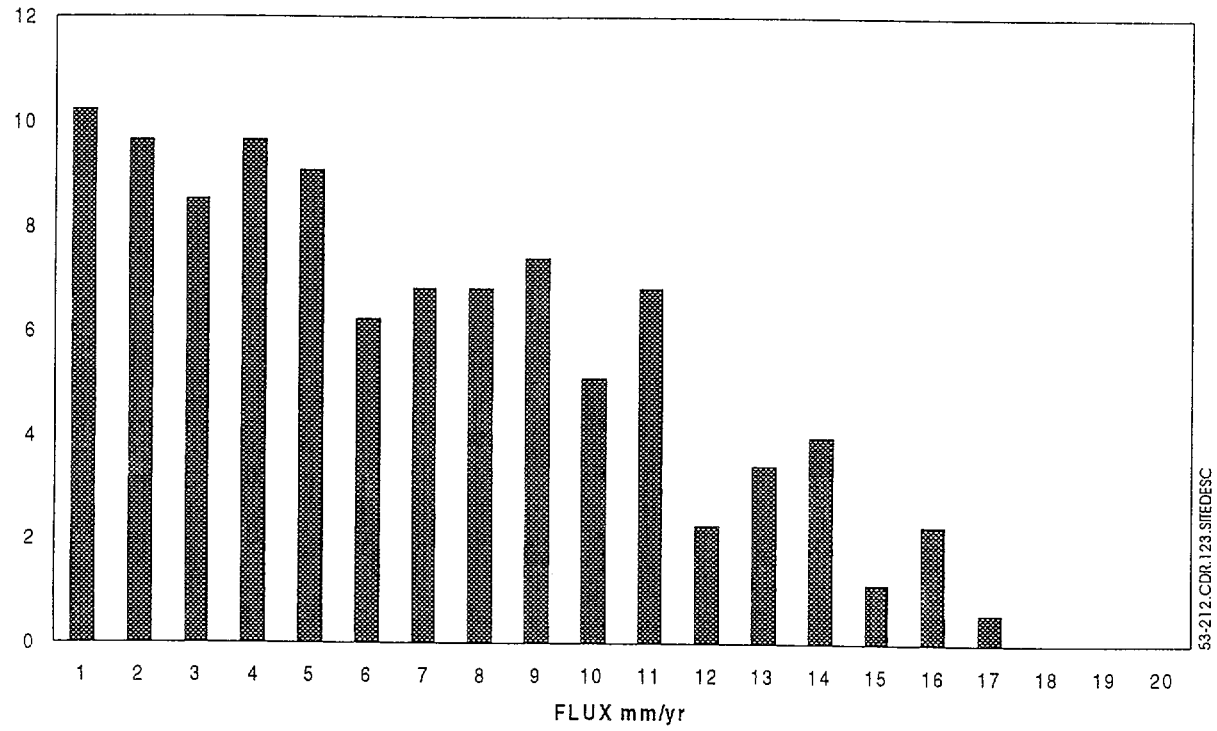

Figure 5.3-212. Distribution of Percolation Flux above the Simulated Drifts Using the Dual-Permeability Model with Average infiltration at the Surface

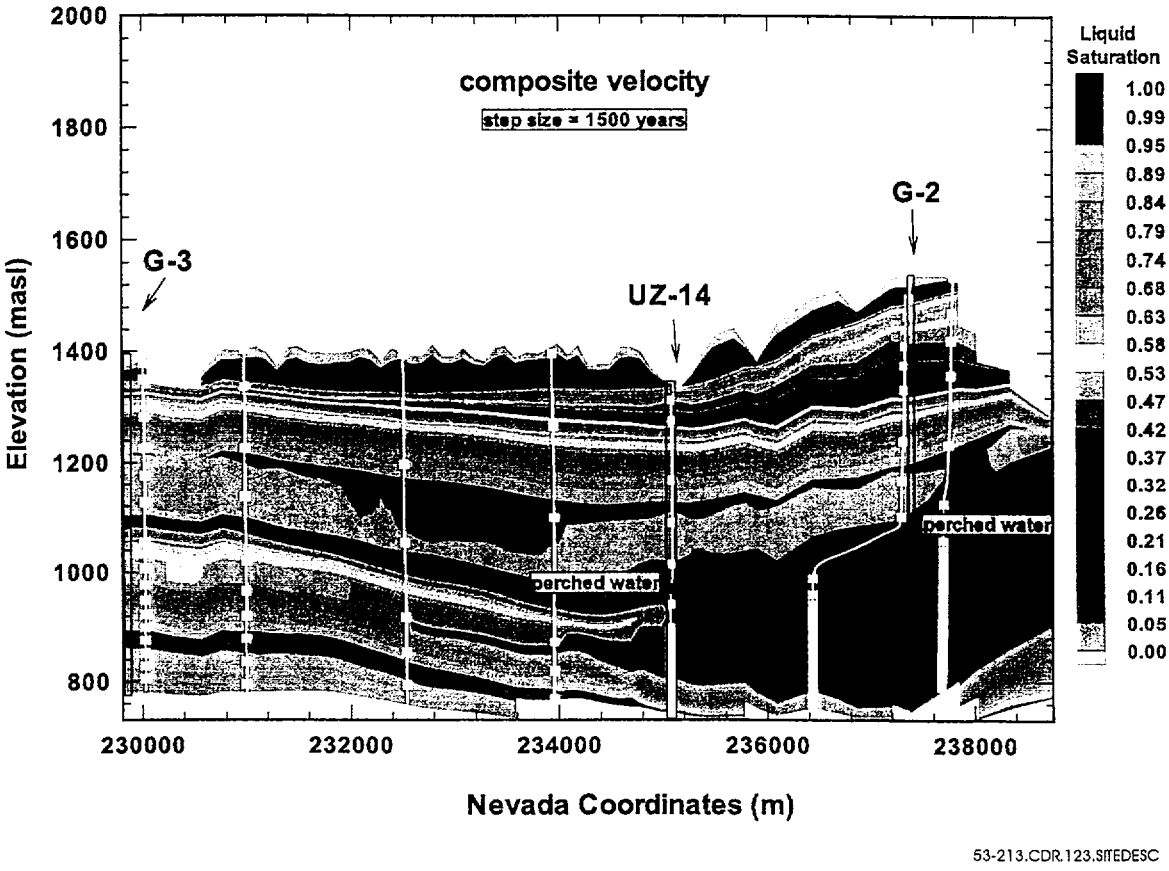

Figure 5.3-213. Velocity Field, Particle Paths, and Liquid Saturations along a South-North Cross-Section Through Boreholes G-2 and UZ-14

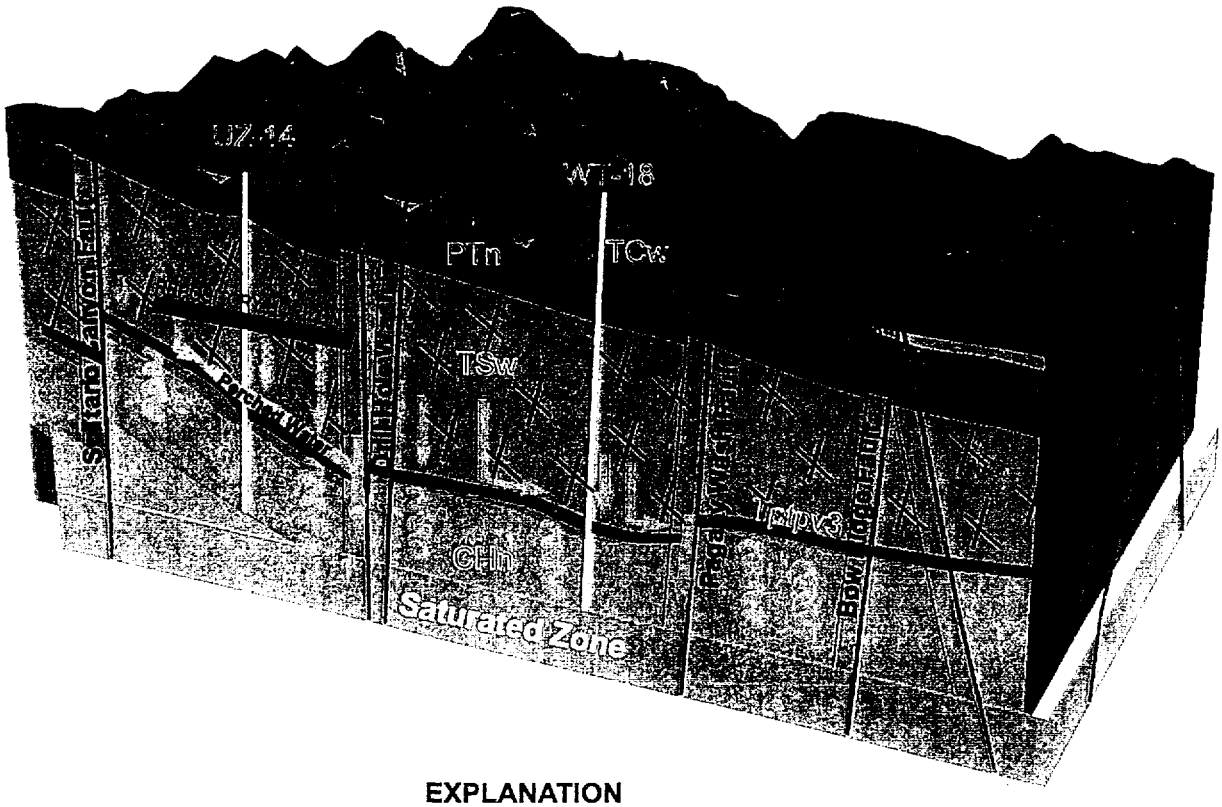

EXPLANATION

TCW	Tiva Canyon welded hydrogeologic unit
PTn	Paintbrush nonwelded hydrogeologic unit
TSw	Topopah Spring welded hydrogeologic unit
Chn	Calico Hills nonwelded hydrogeologic unit (Generally altered)
Tptpv3	Basal vitrophyre of the Tsw unit
	Straight line=fast flowpath
	Curved line=slow flowpath

53-214.CDR.123.SITEDESC

Figure 5.3-214. Schematic Figure Showing Potential Flow Patterns below the Repository Horizon (Approximately East-West Through UZ-14)

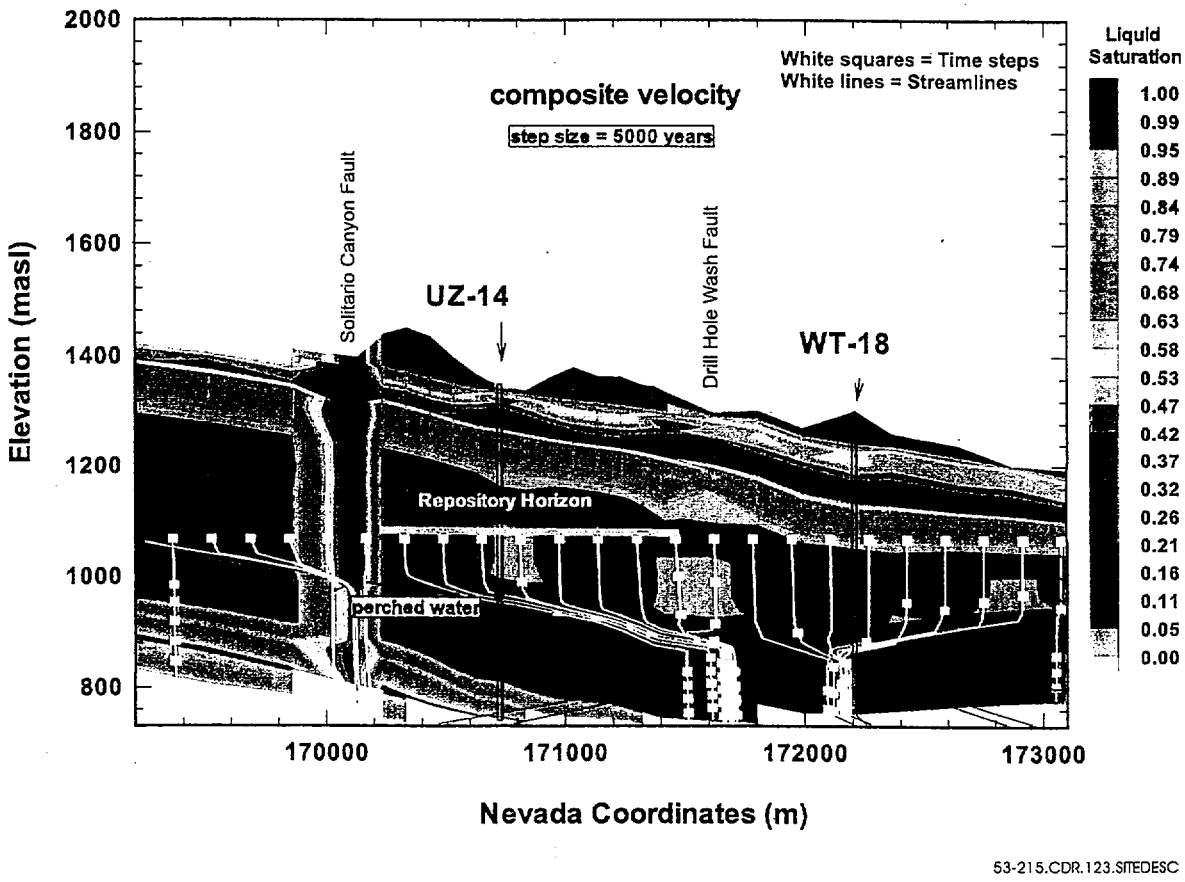

Figure 5.3-215. Simulated Flow Patterns from the Potential Repository Horizon to the Water Table along an East-West Cross-Section Through Borehole UZ-14

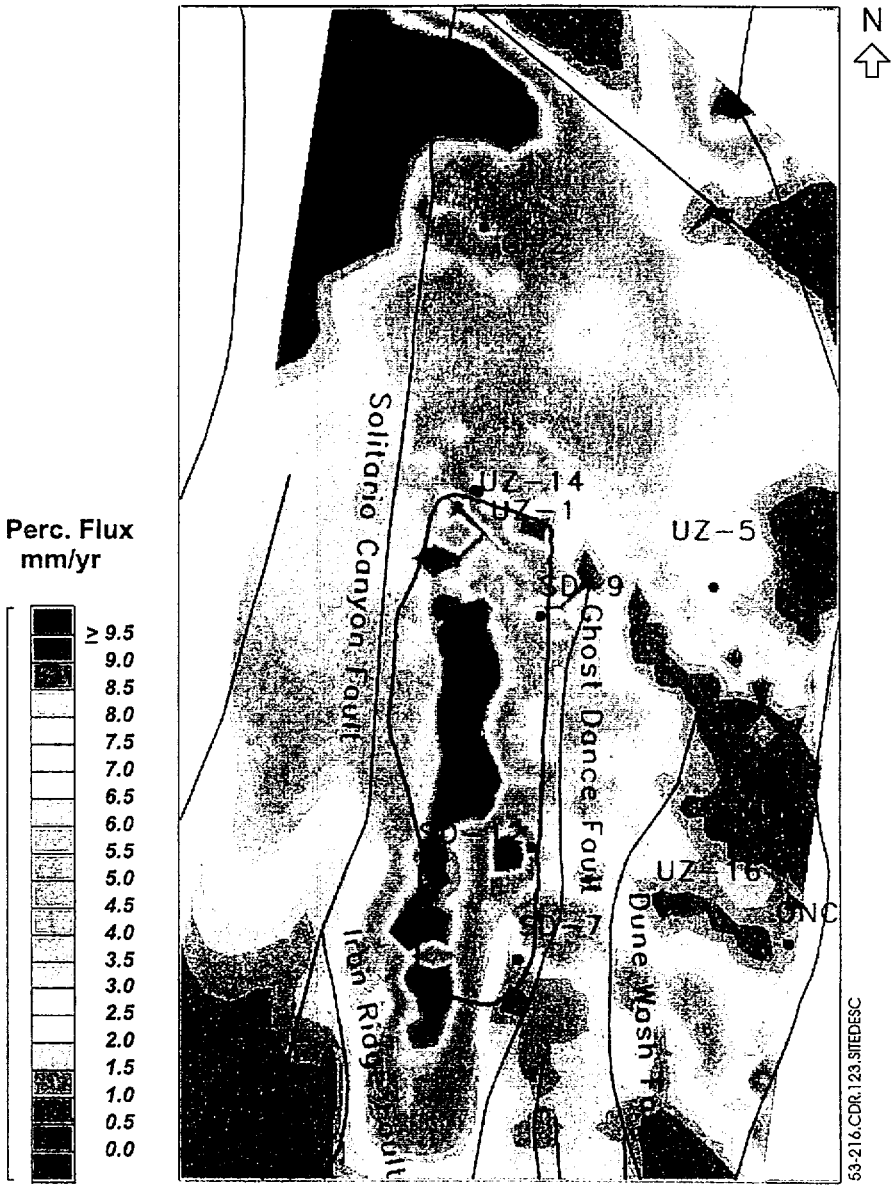

Figure 5.3-216. Map View Showing Percolation Flux Through Fractures and Matrix at the Water Table

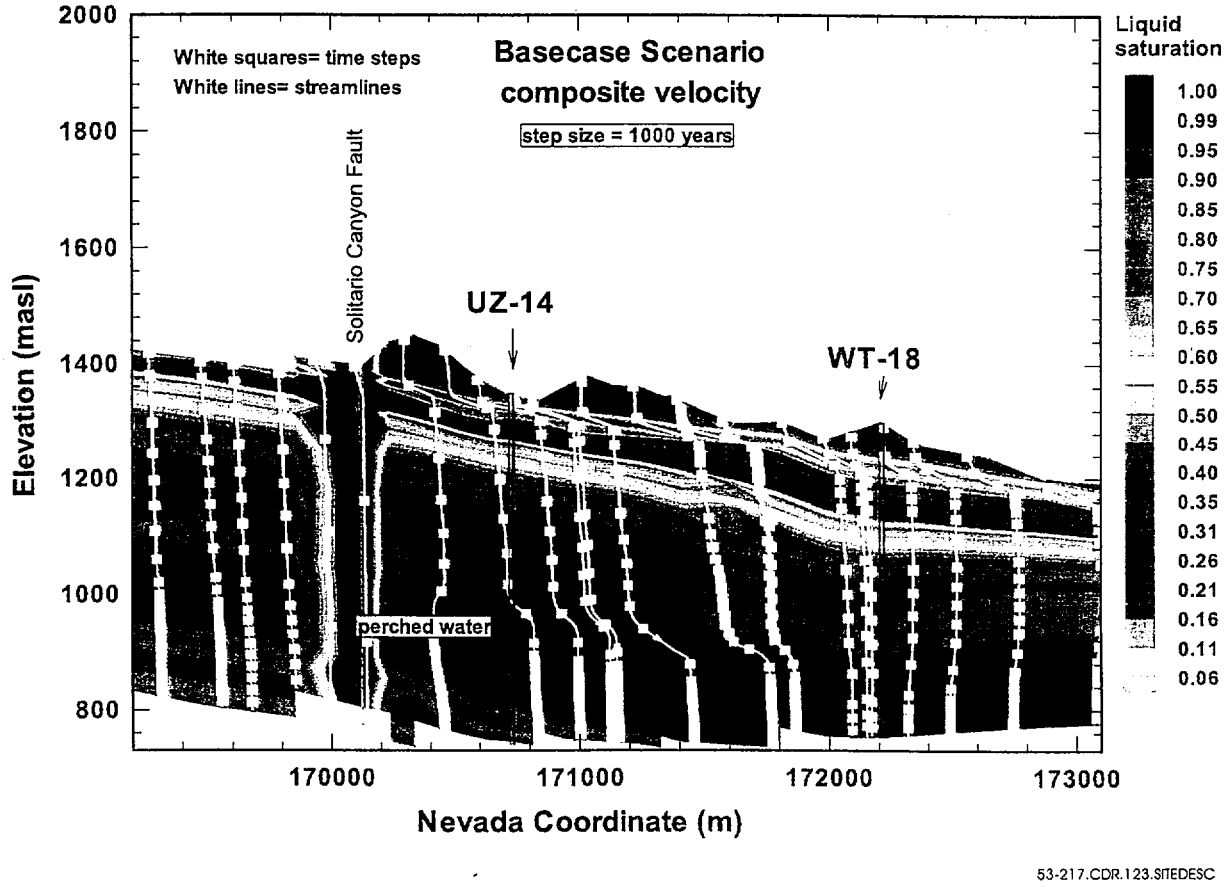

Figure 5.3-217. Saturation Contours and Streamlines along an East-West Cross-Section Through Boreholes UZ-14 and WT-18 for the Present-Day Climate Scenario

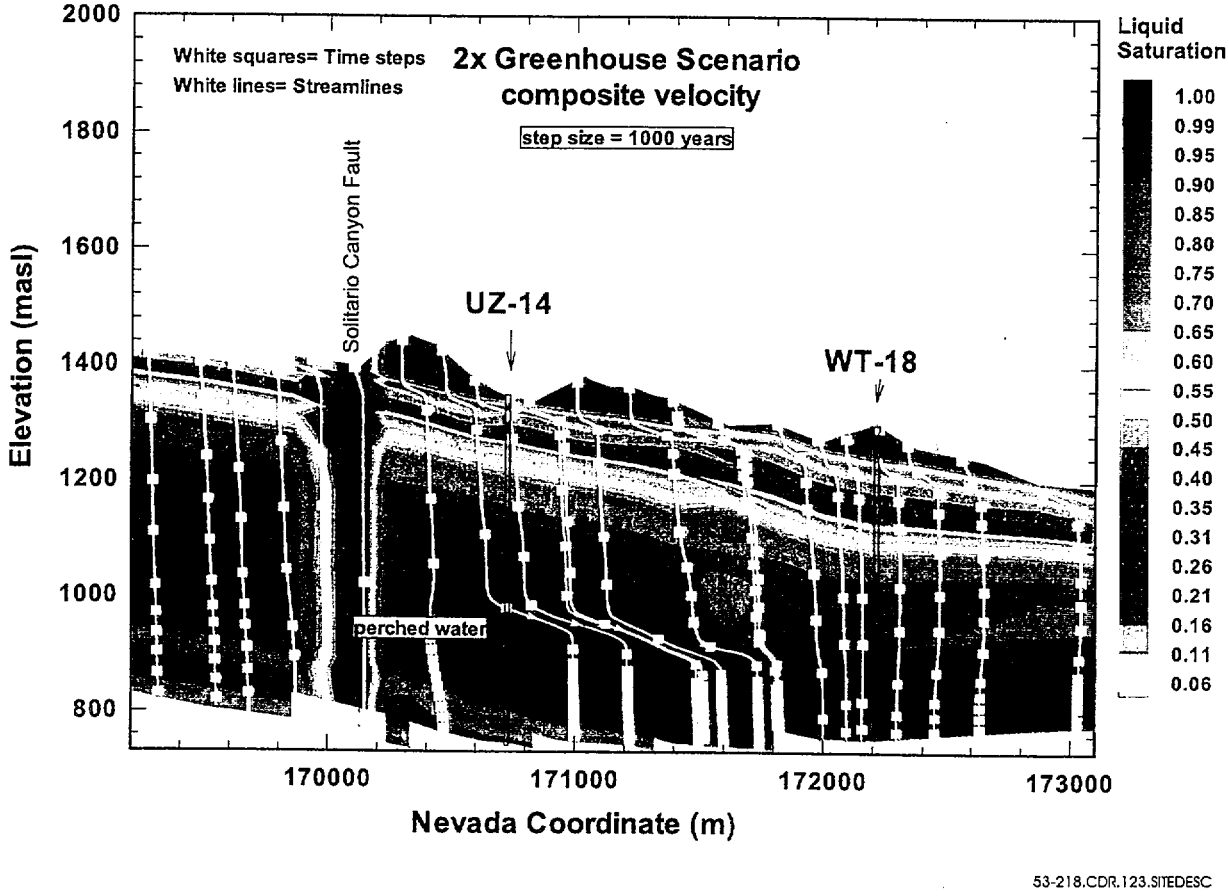

Figure 5.3-218. Saturation Contours and Streamlines along an East-West Cross-Section Through Boreholes UZ-14 and WT-18 for the 2x Climate Scenario

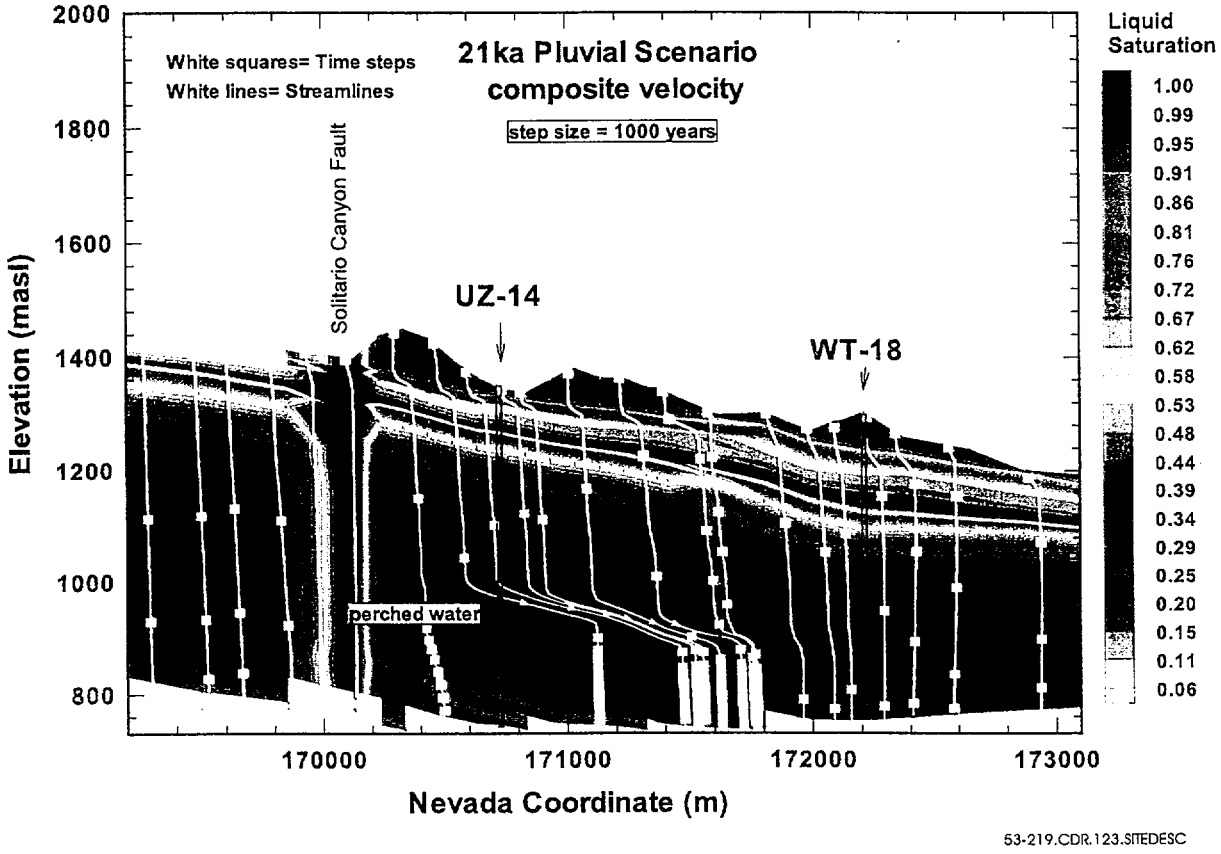

Figure 5.3-219. Saturation Contours and Streamlines along an East-West Cross-Section Through Boreholes UZ-14 and WT-18 for the 21,000-Year Pluvial Scenario

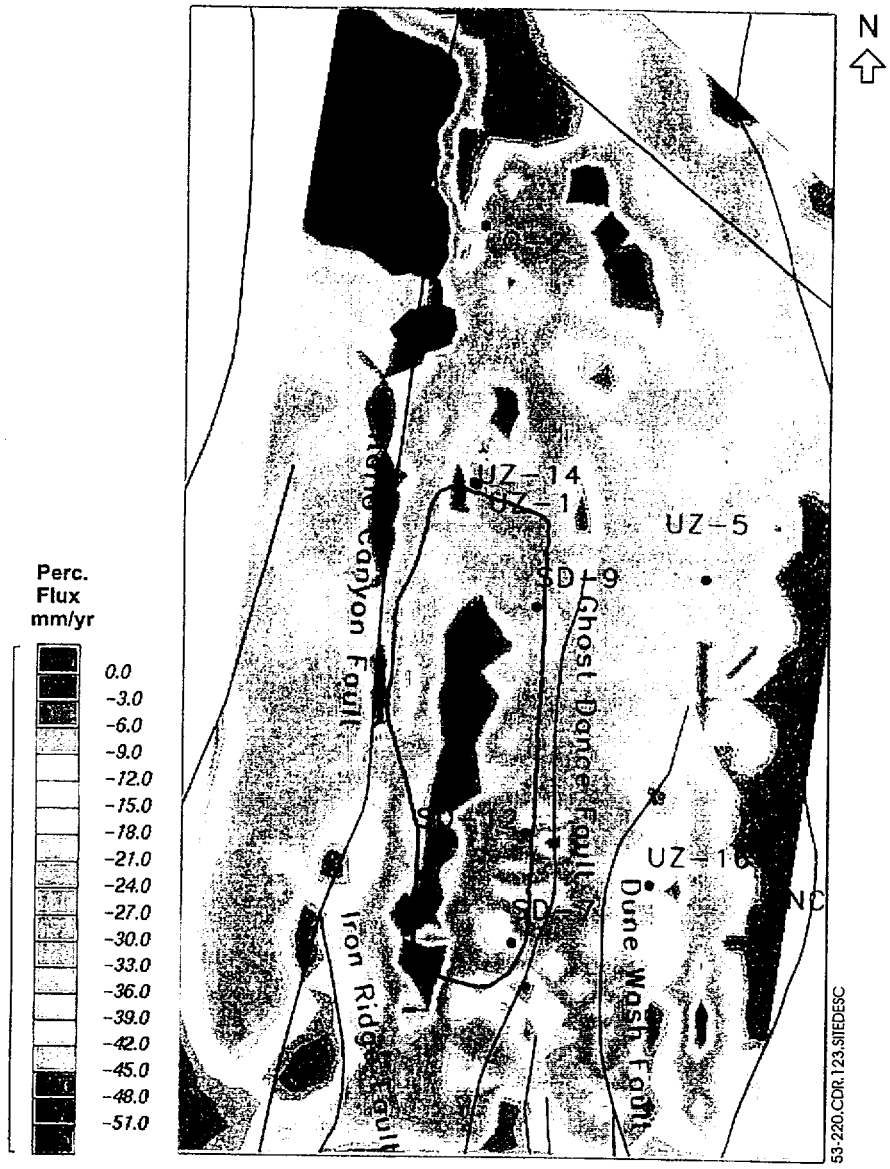

Figure 5.3-220. Map View of Simulated Percolation Flux in the Vertical Direction (Negative Indicating Downward Flow) in mm/yr at the Potential Repository Horizon under 21,000-Year Pluvial Conditions

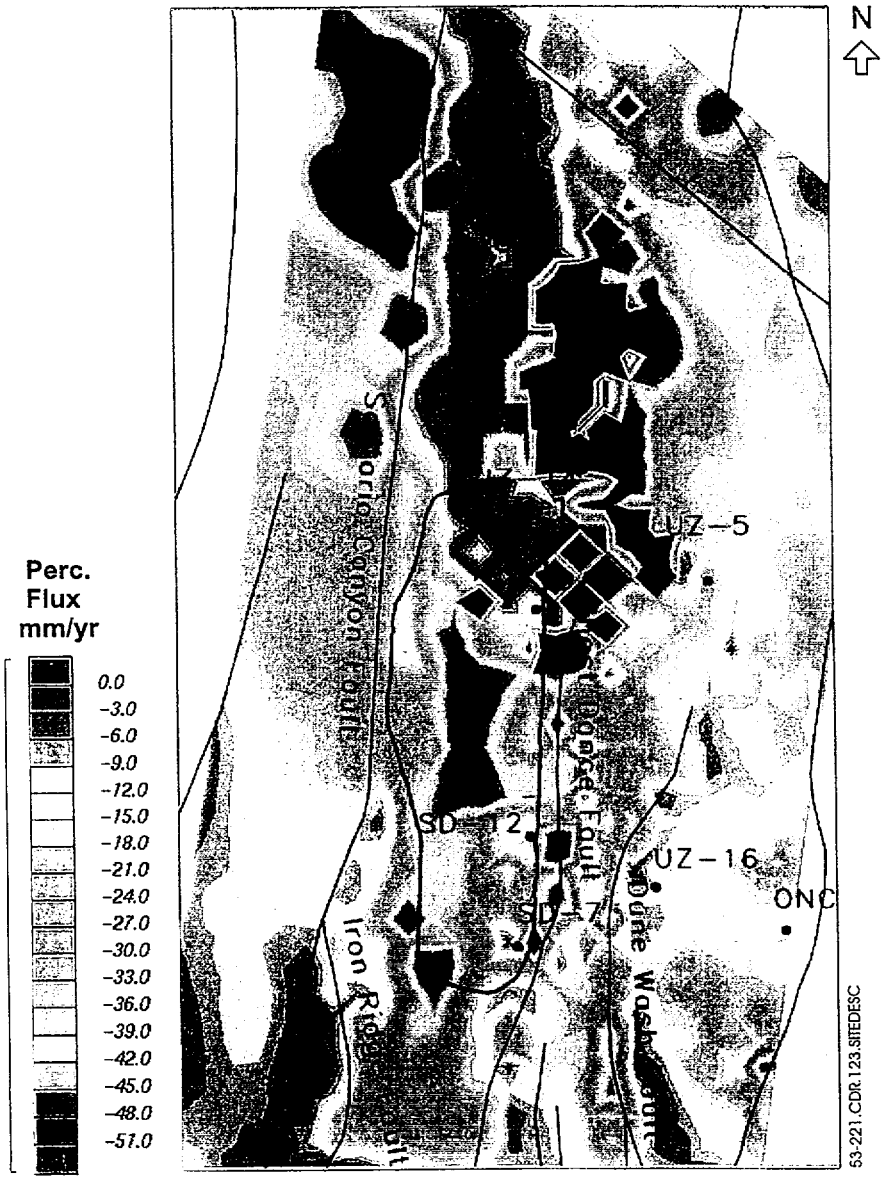

Figure 5.3-221. Map View of Simulated Percolation Flux in the Vertical Direction (Negative Indicating Downward Flow) in mm/yr at the Water Table under 21,000-Year Pluvial Conditions

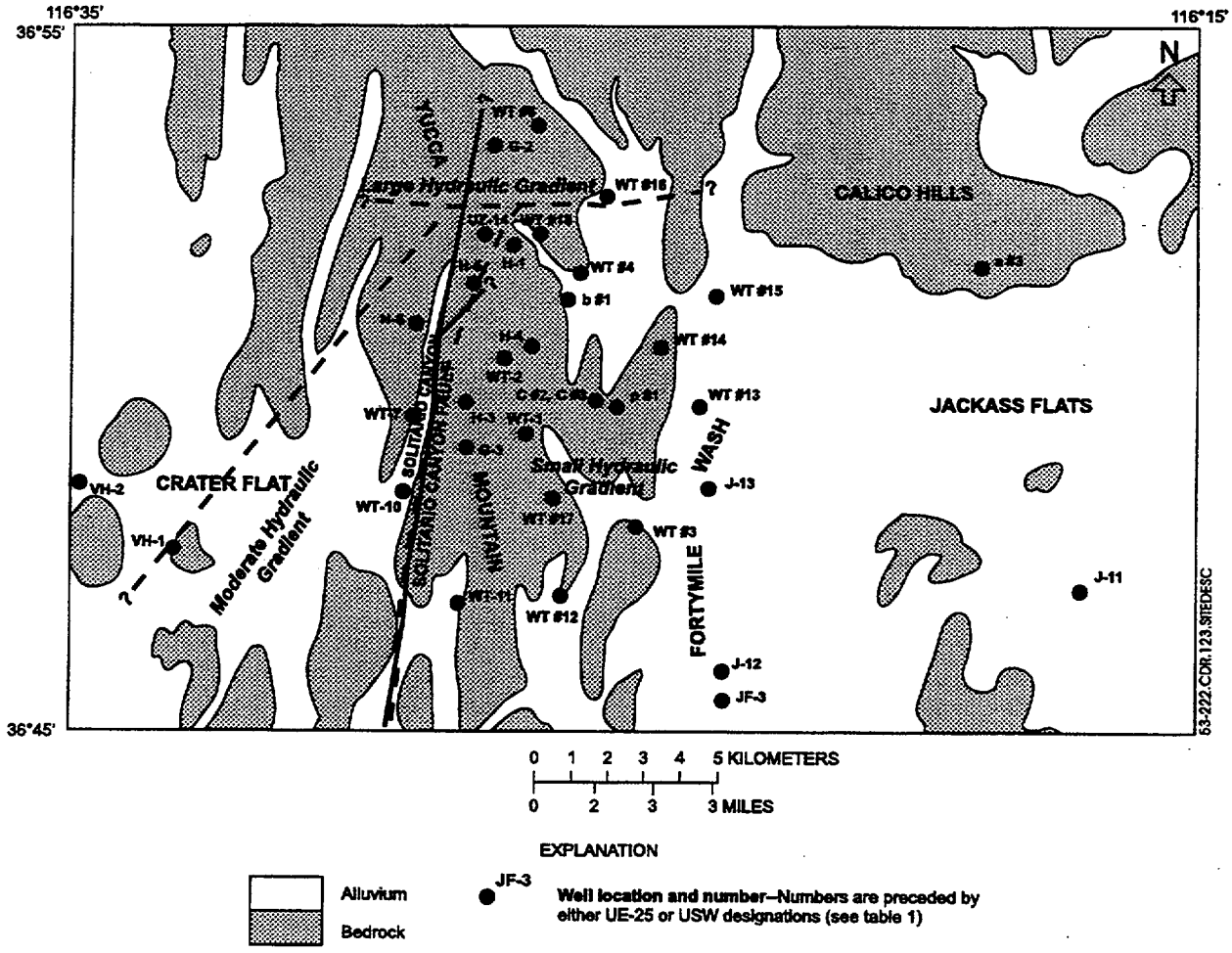

Figure 5.3-222. Location of Large-, Moderate-, and Small-Gradient Areas at Yucca Mountain (from Tucci and Burkhardt 1995, Figure 5)

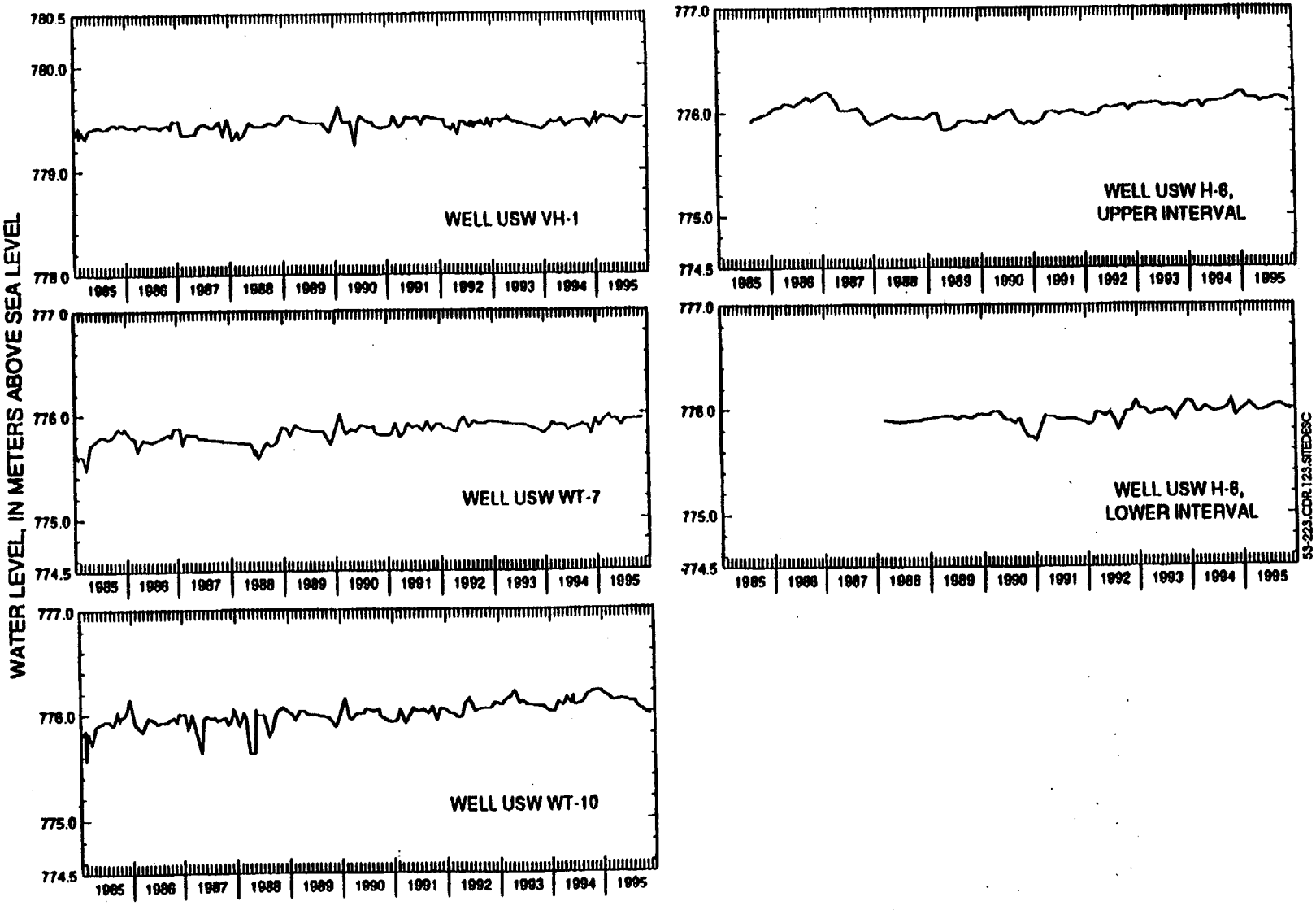

Figure 5.3-223. Water-Level Altitude, 1985 to 1995, for Wells Located in Crater Flat (from Graves et al. 1997, Figure 42)

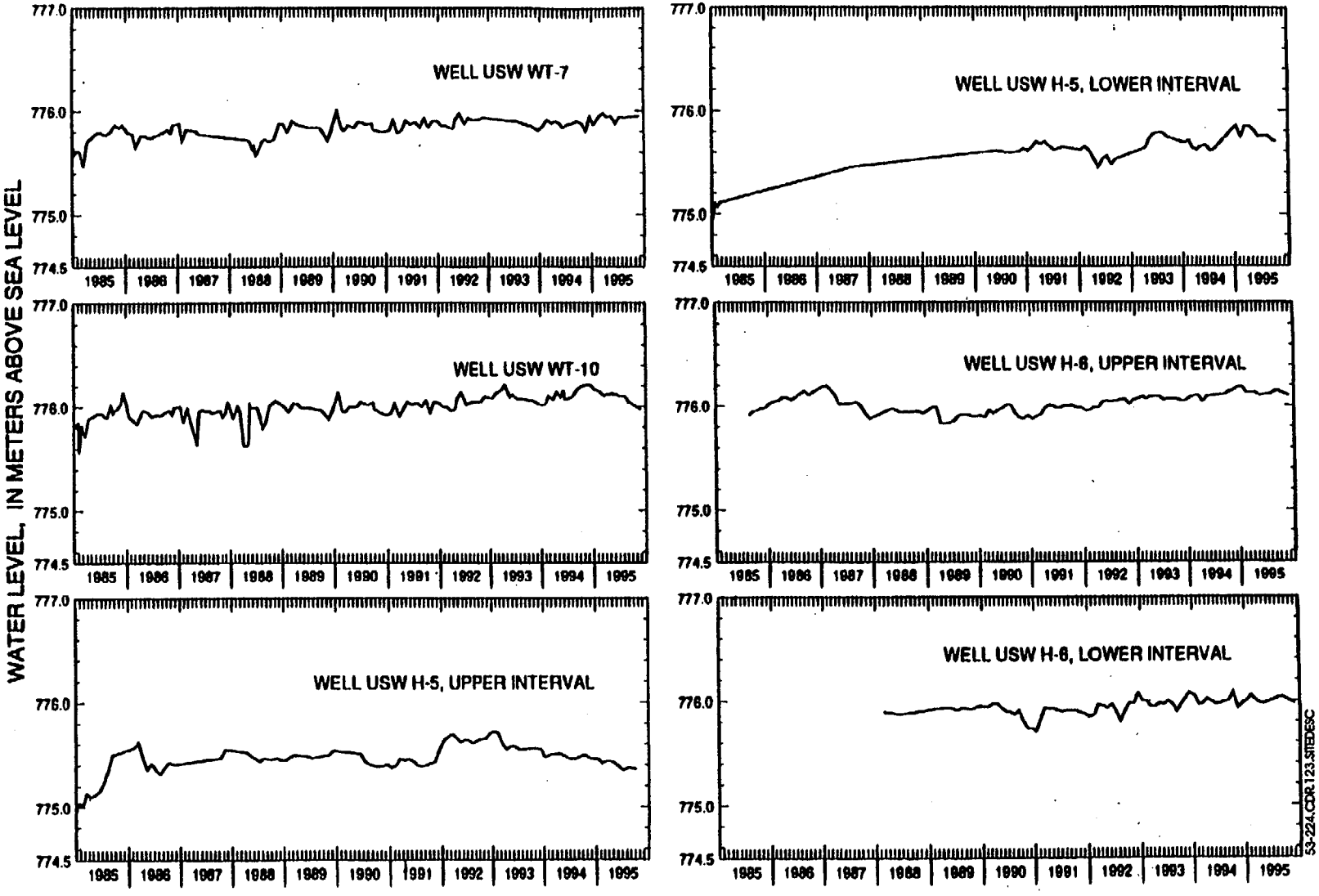

Figure 5.3-224. Water-Level Altitudes, 1985 to 1995, for Wells With an Approximate Water-Level Altitude of 776 Meters (from Graves et al. 1997, Figure 45)

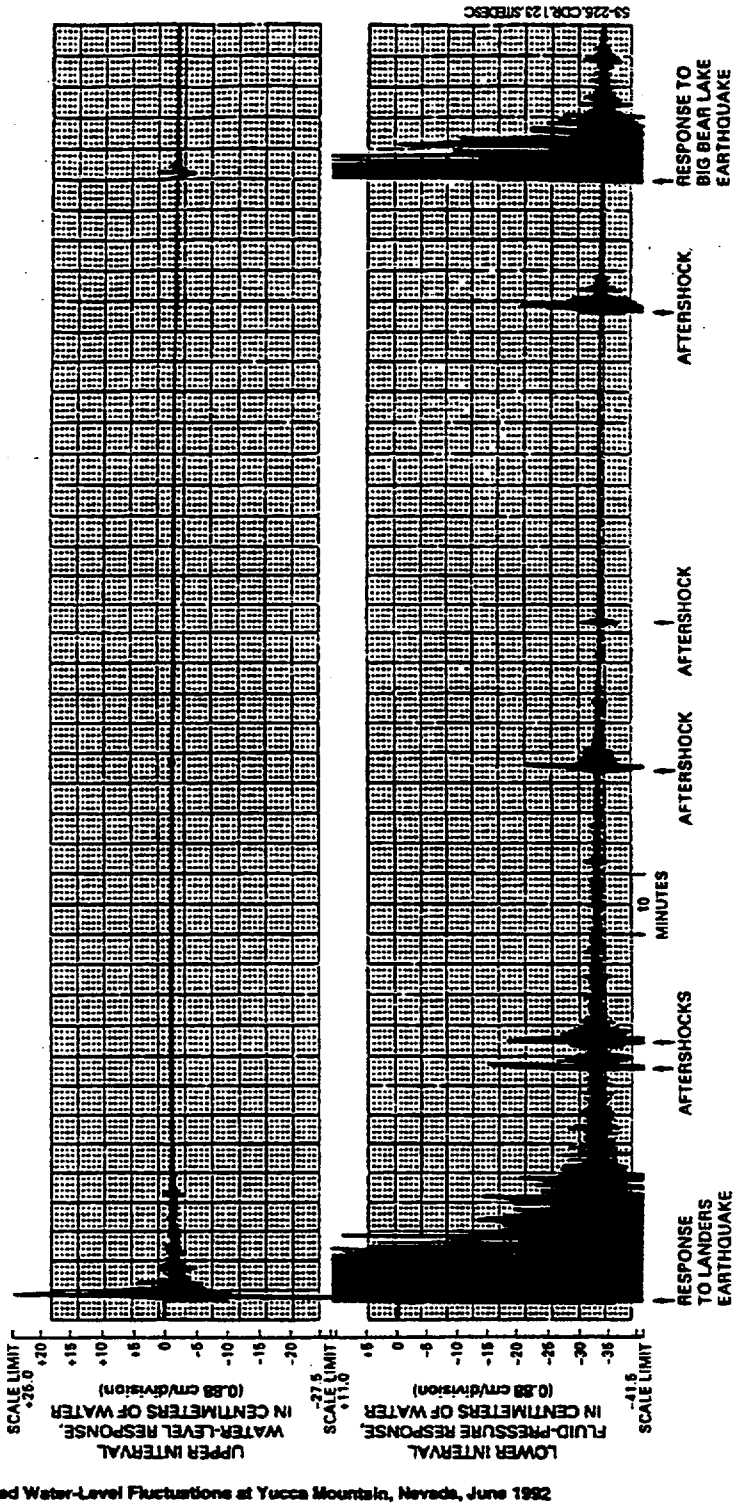

6 Earthquake-Induced Water-Level Fluctuations at Yucca Mountain, Nevada, June 1992

Figure 5.3-225. Well USW H-5 Response to Earthquakes Near Landers (11:57:34 UTC) and Big Bear Lake (15:05:30 UTC), California, on June 28, 1992 (from O'Brien 1993, Figure 2)

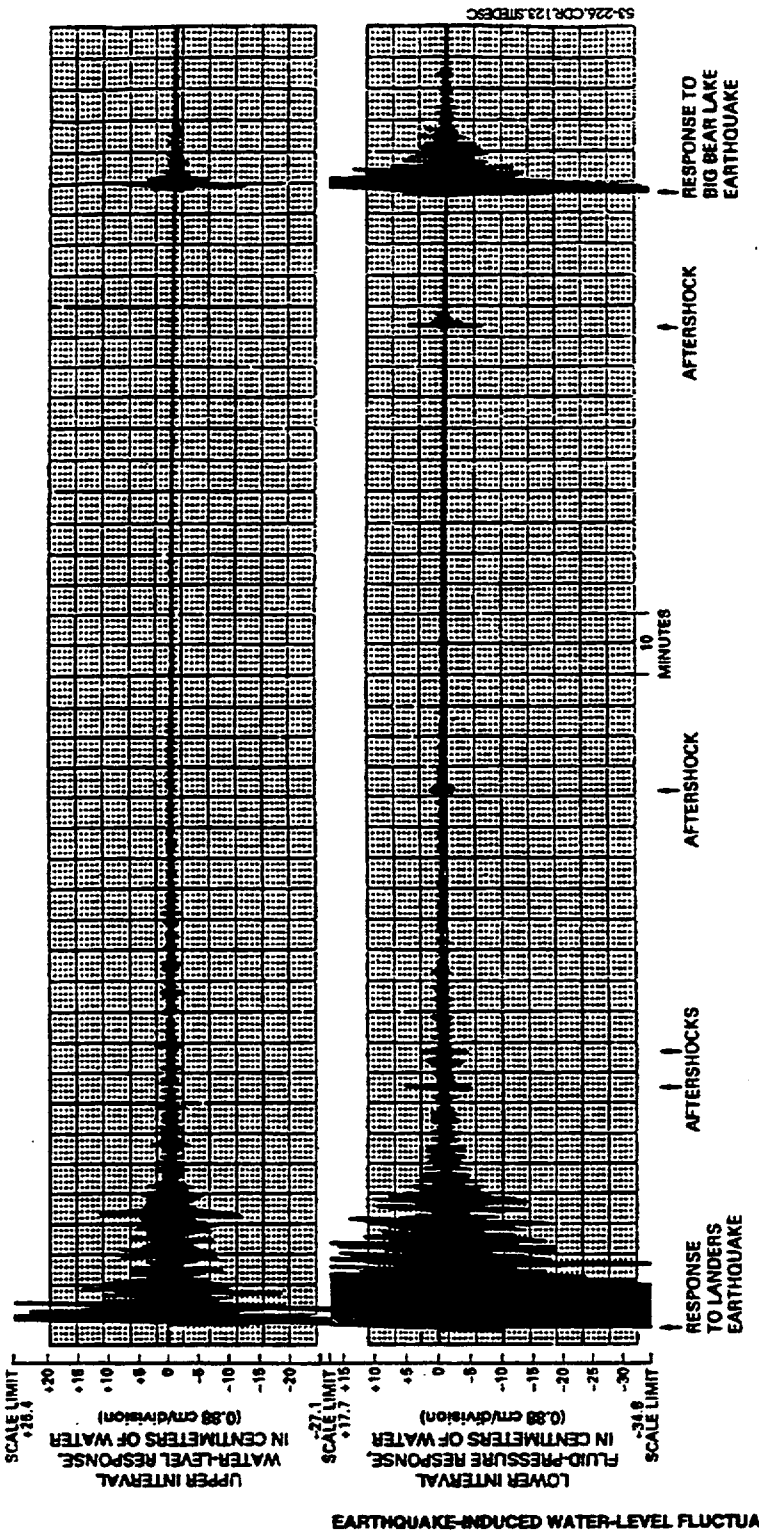

Figure 5.3-226. Well USW H-6 Response to Earthquakes Near Landers (11:57:34 UTC) and Big Bear Lake (15:05:30 UTC), California, on June 28, 1992 (from O'Brien 1993, Figure 3)

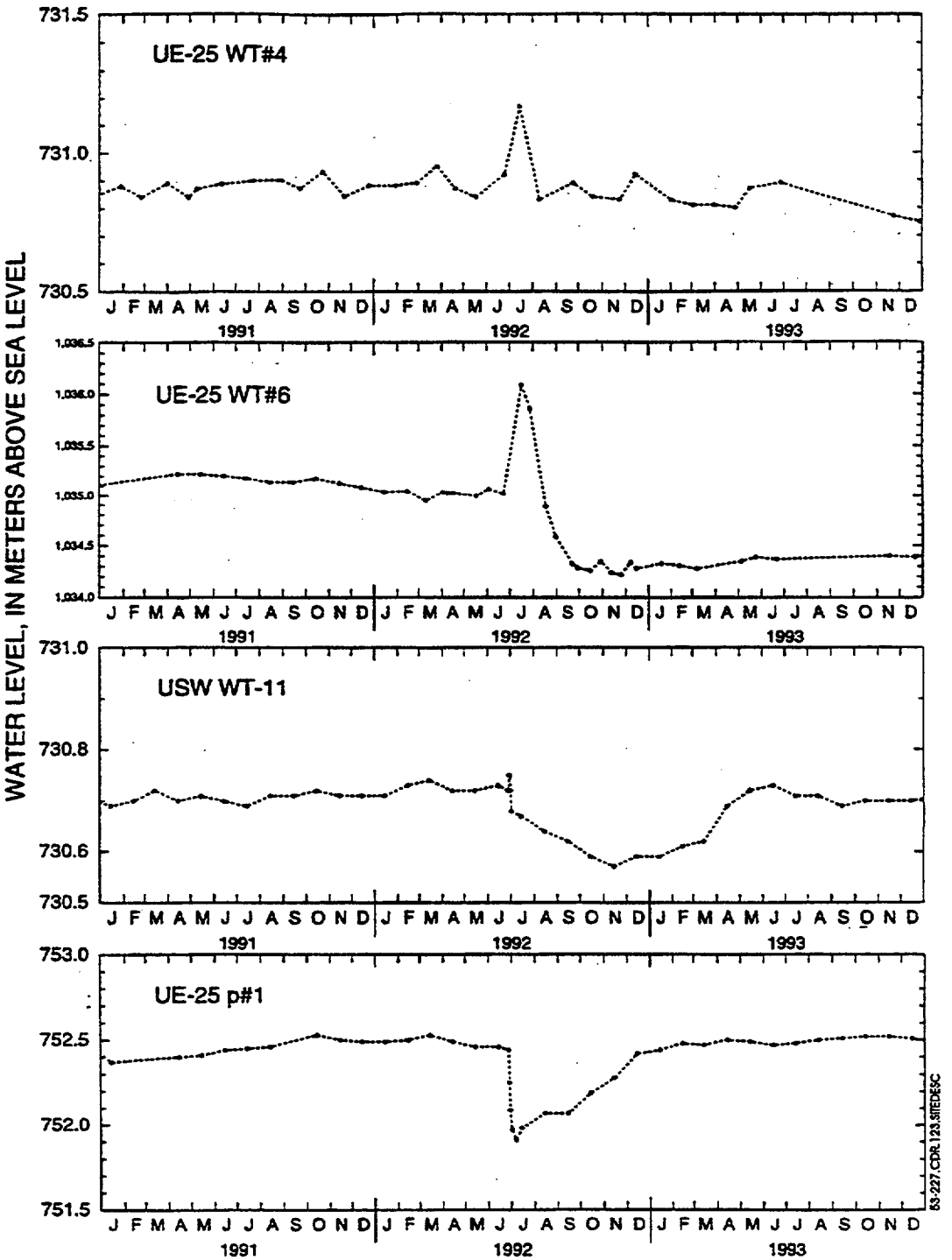

Figure 5.3-227. Water-Level Altitudes in Wells that May Have Been Affected by June 1992 Earthquakes

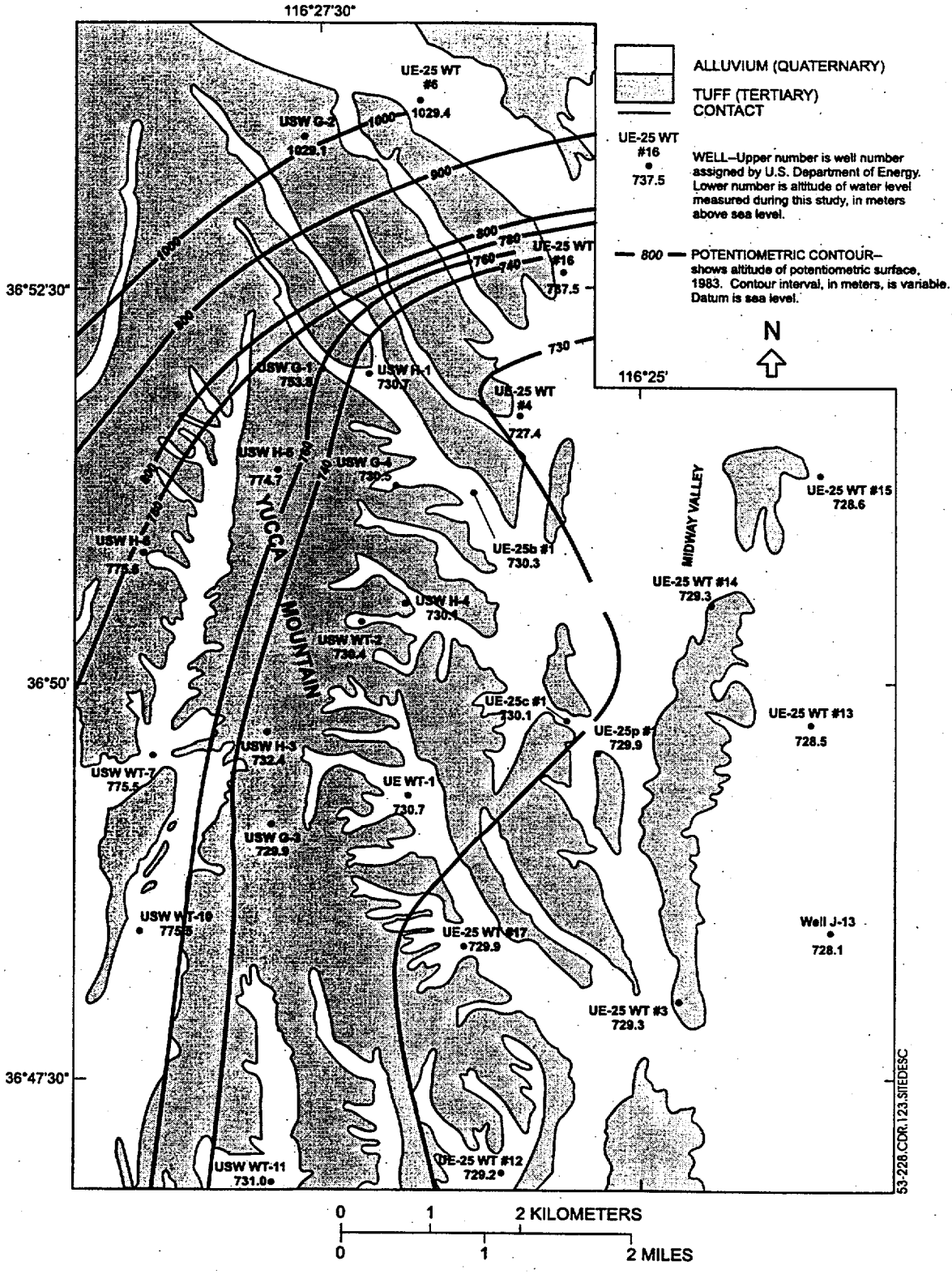

Figure 5.3-228. Potentiometric Surface, Yucca Mountain Area, 1983 (from Robison 1984, Figure 2)

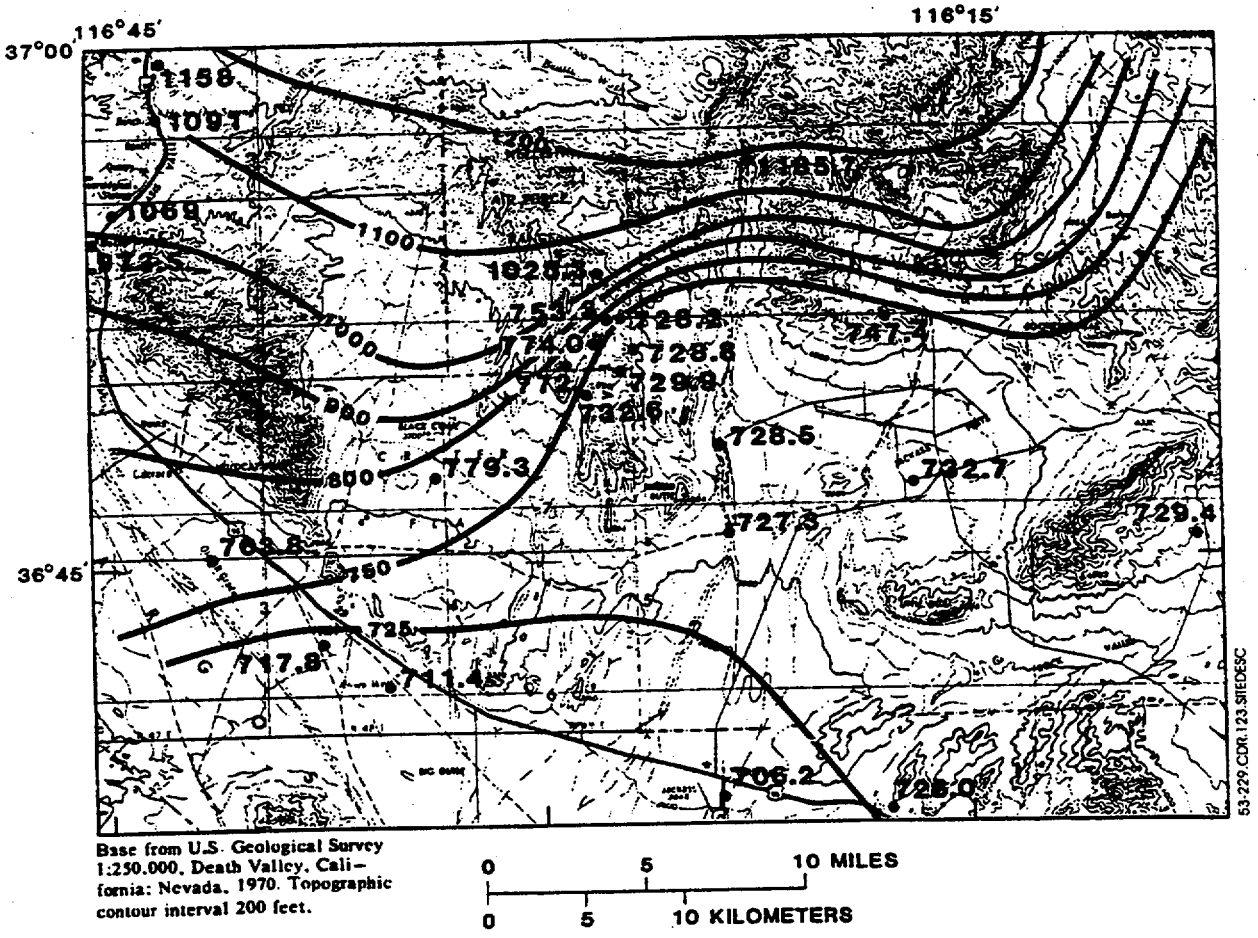

Figure 5.3-229. Potentiometric Surface of Yucca Mountain Site and Vicinity (from Waddell et al. 1984, Figure 8)

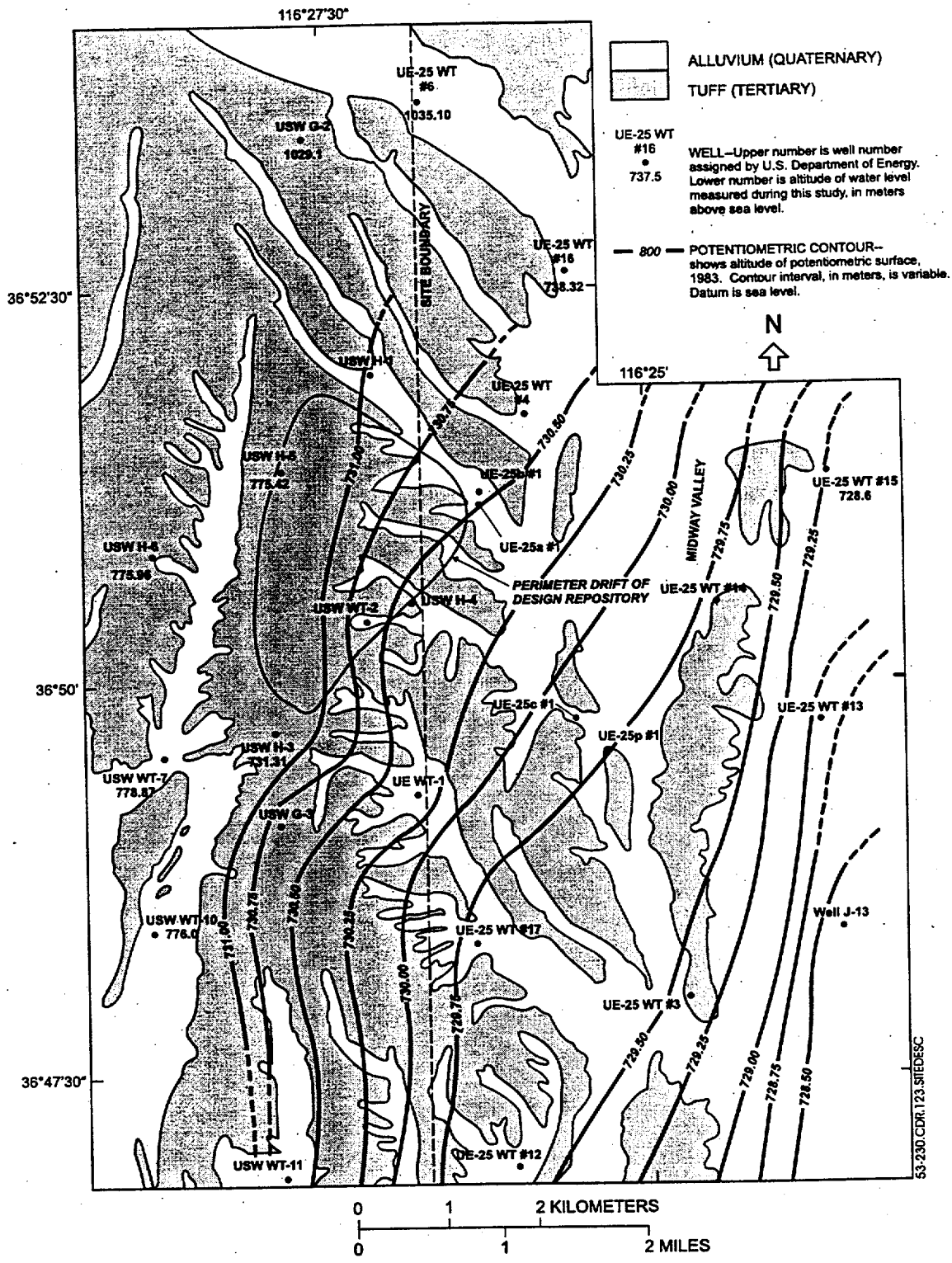

Figure 5.3-230. Potentiometric Surface of an Area of Small Hydraulic Gradient, 1988 Yucca Mountain (from Ervin et al. 1993, Figure 1, after Luckey et al. 1996, Figure 9)

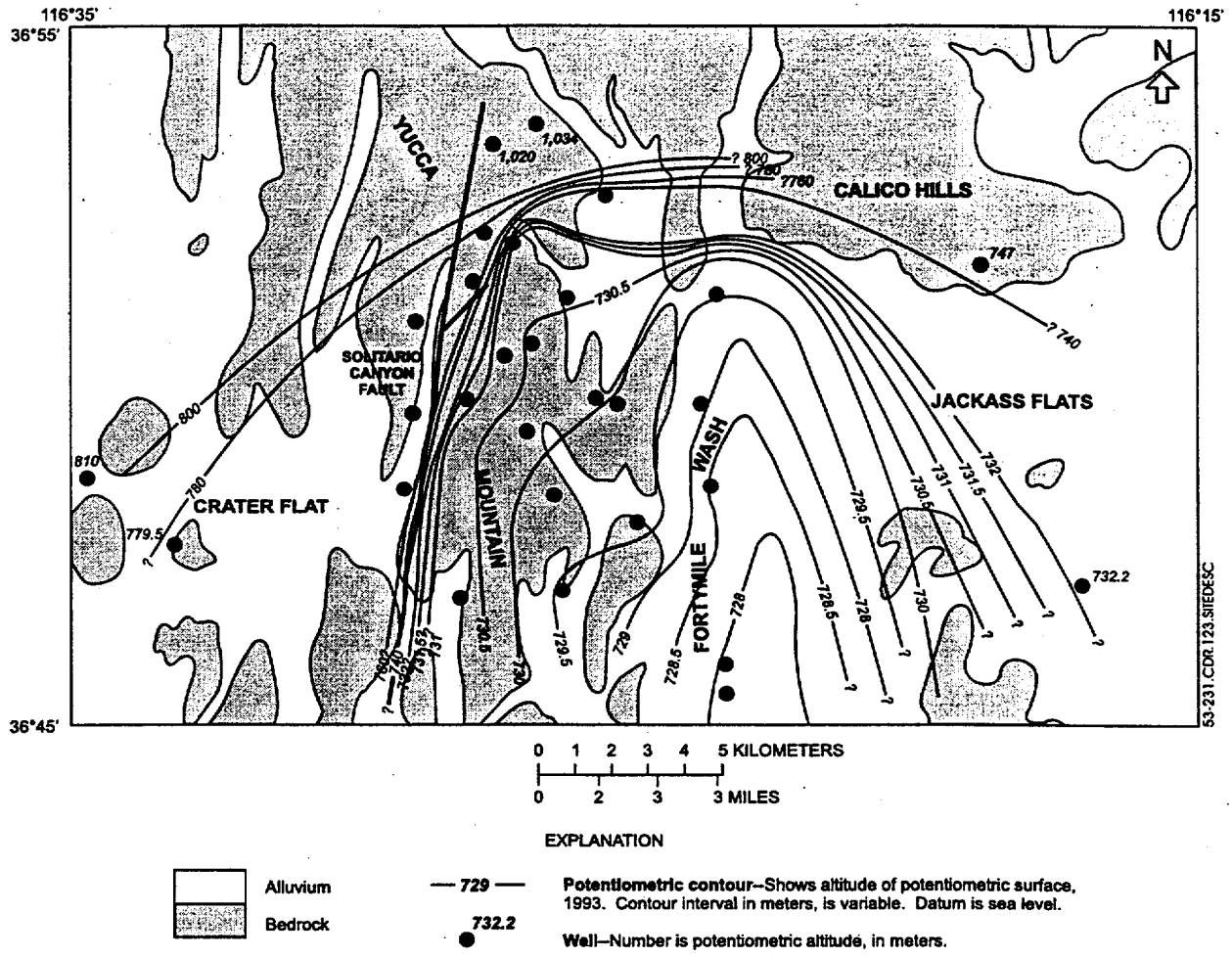

Figure 5.3-231. Potentiometric Surface of the Yucca Mountain Area, 1993 (from Tucci and Burkhardt 1995, Figure 4)

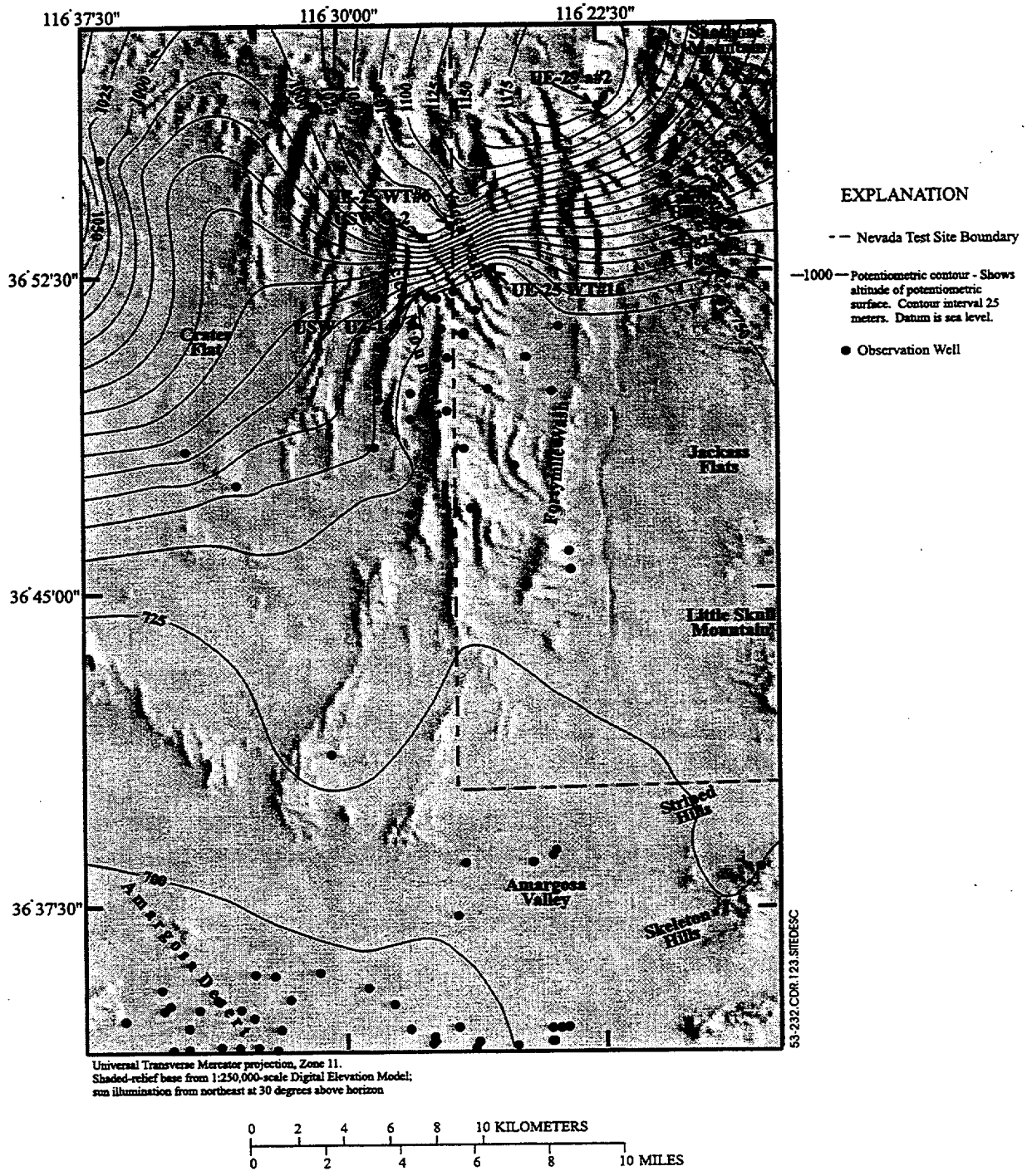

NOTE: Map is computer generated from water levels collected from 1952 - 1996.

Figure 5.3-232. Potentiometric Surface in the Yucca Mountain Site Saturated Zone Flow Model Area (from Czarnecki, Faunt et al. 1997, Figure 5)

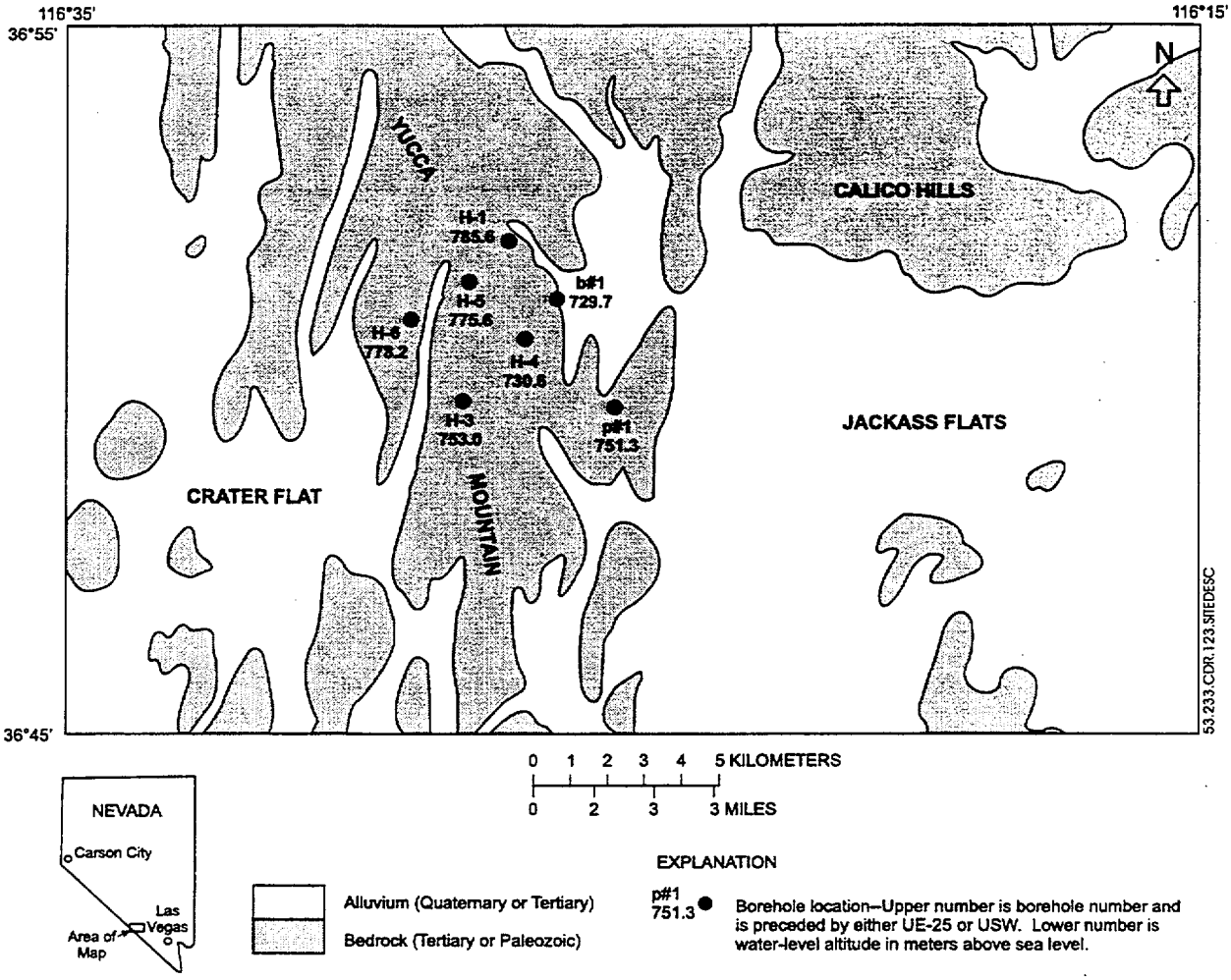

Figure 5.3-233. Potentiometric Levels in the Lower Volcanic Confining Unit and Carbonate Aquifer (from Luckey, Tucci et al. 1996. Figure 10)

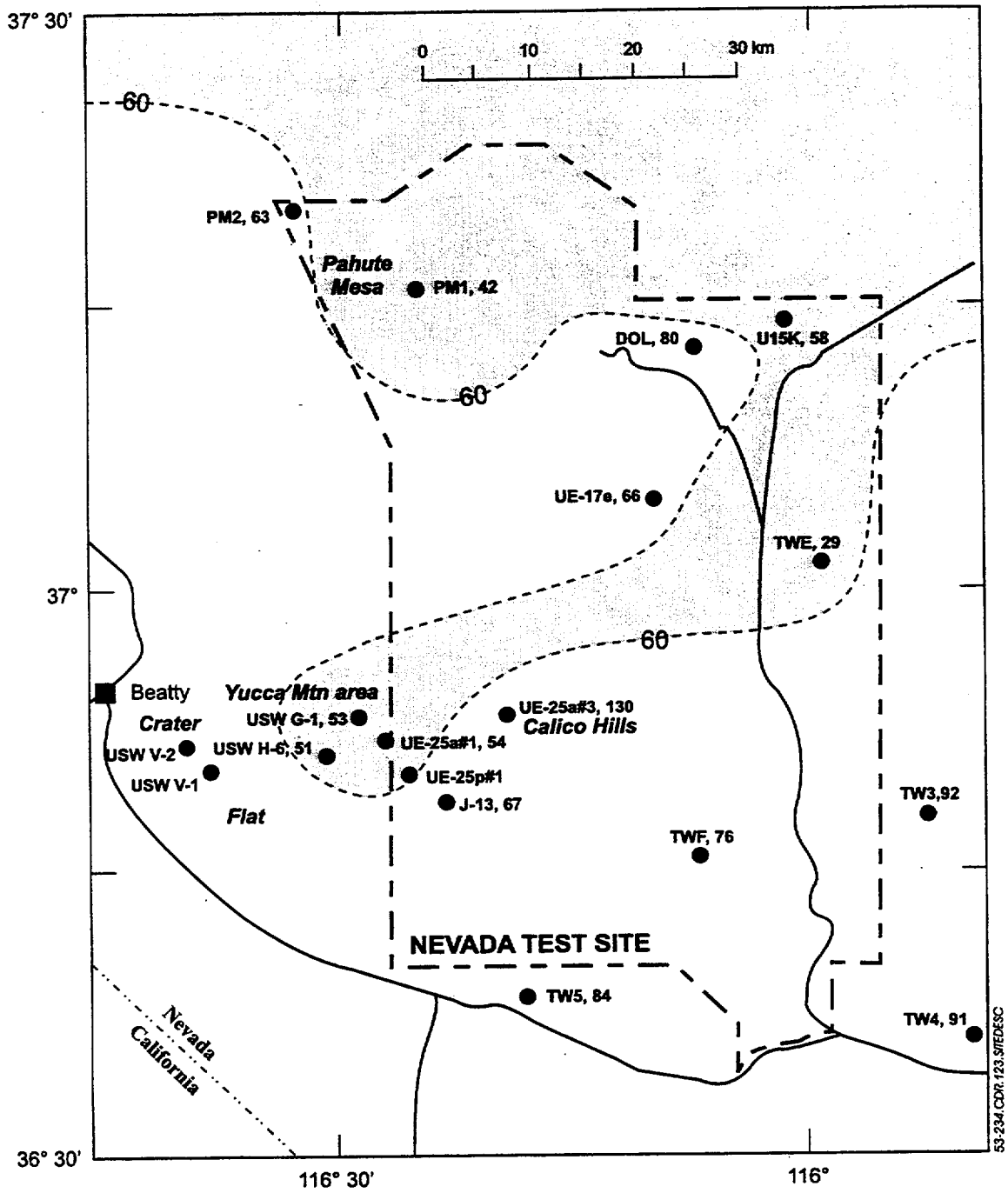

NOTE: The prefix, USW or UE, has been omitted from borehole designations in the vicinity of Yucca Mountain. heat flow is in milliwatts per meter squared (mW m^2). Temperature profiles, but not heat flows, were determined in boreholes USW VH-1 and USW VH-2 (from Sass, Dudley et al. 1995, Figure 8.2).

Figure 5.3-234. Heat Flows Determined for Boreholes at and Near the Nevada Test Site

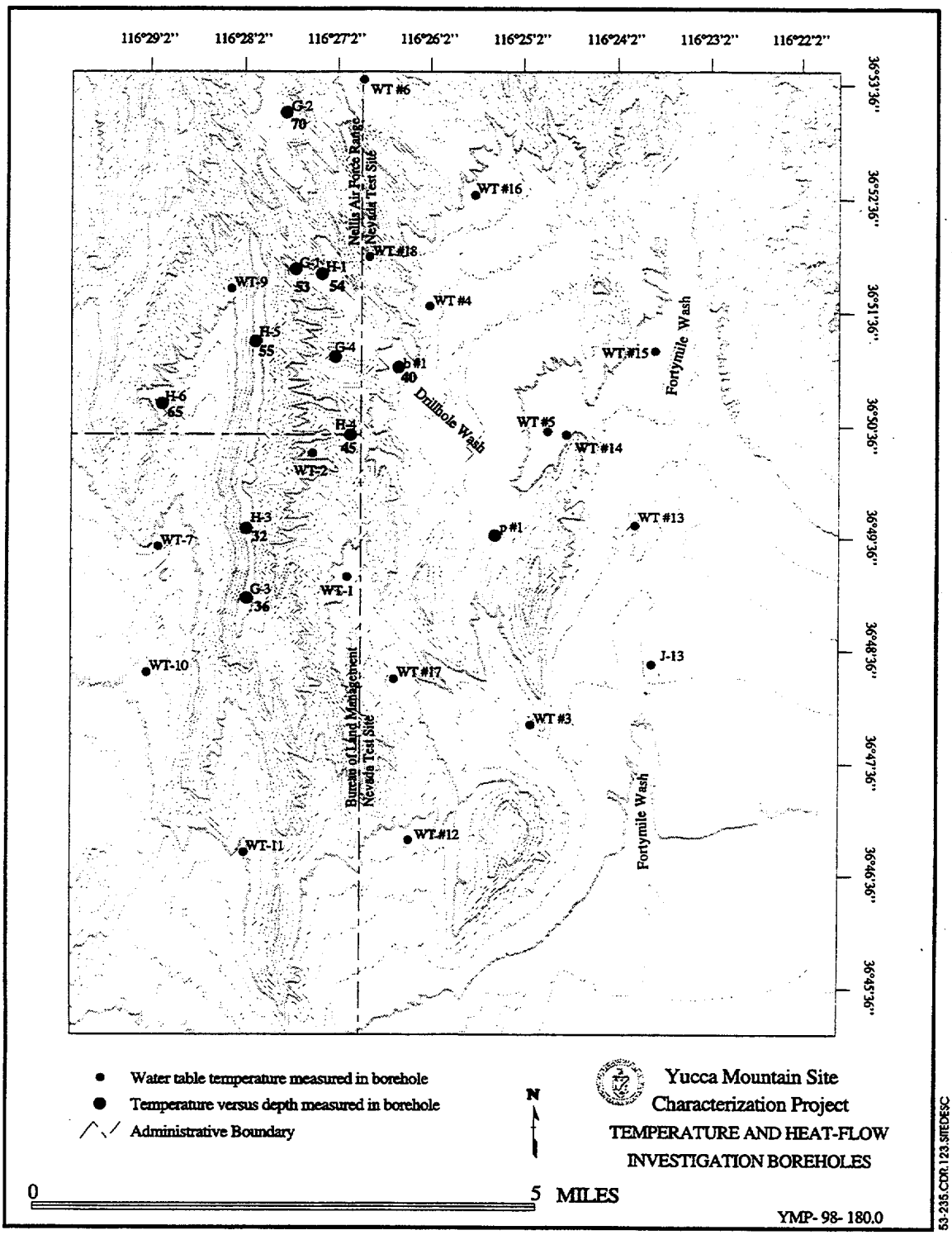

NOTE: Small symbols denote boreholes in which only water-table temperatures were measured. Large symbols denote boreholes in which temperature versus depth also were measured in the saturated zone. Bold-faced numbers are heat flow in the saturated zone, in milliwatts per meter squared (mW m^{-2}).

Figure 5.3-235. Boreholes in the Vicinity of Yucca Mountain Used for Temperature and Heat-Flow Investigations

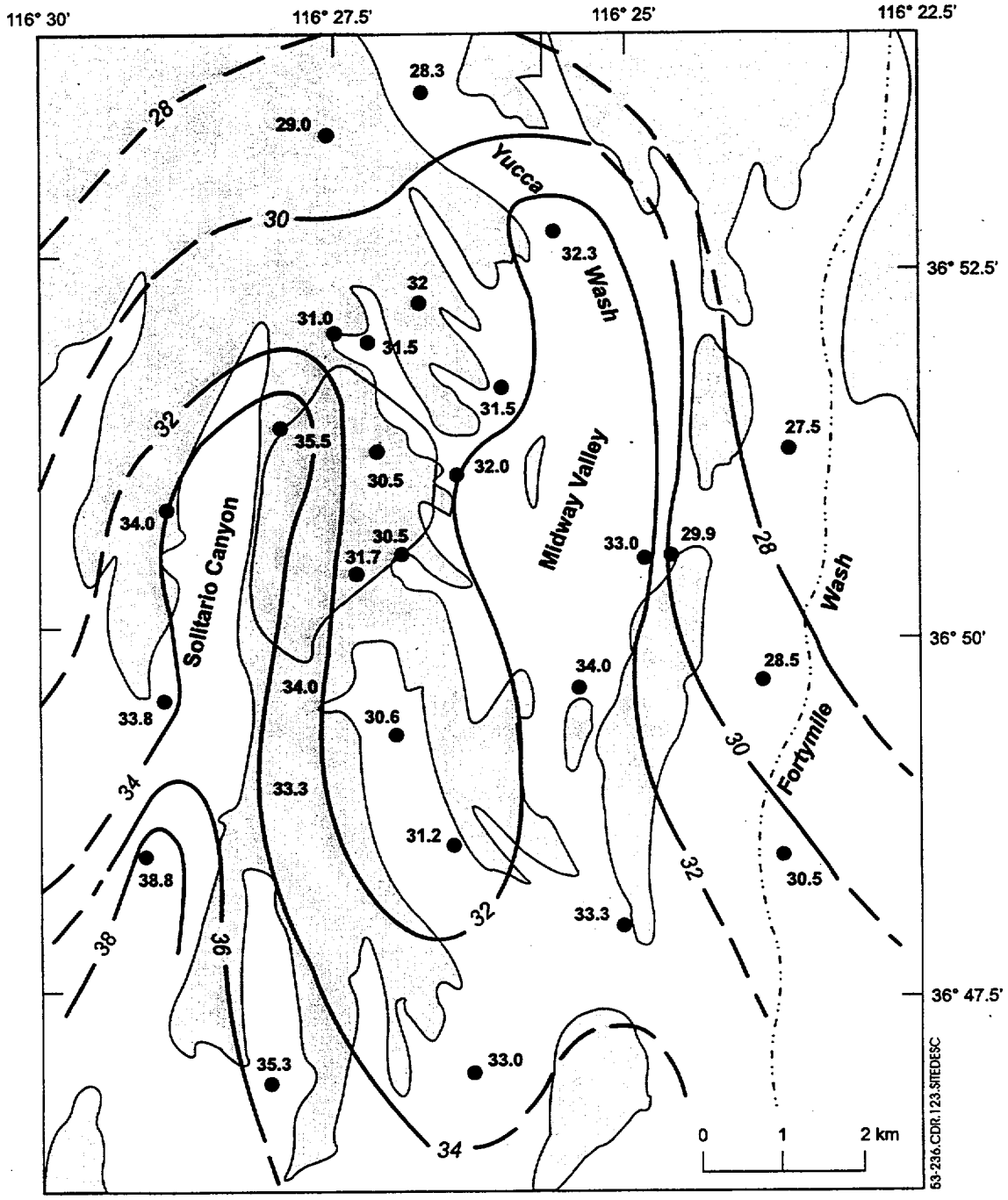

Figure 5.3-236. Temperature at the Water Table in the Vicinity of Yucca Mountain (temperatures are ºC from Sass, Dudley et al. 1995 Figure 8.4)

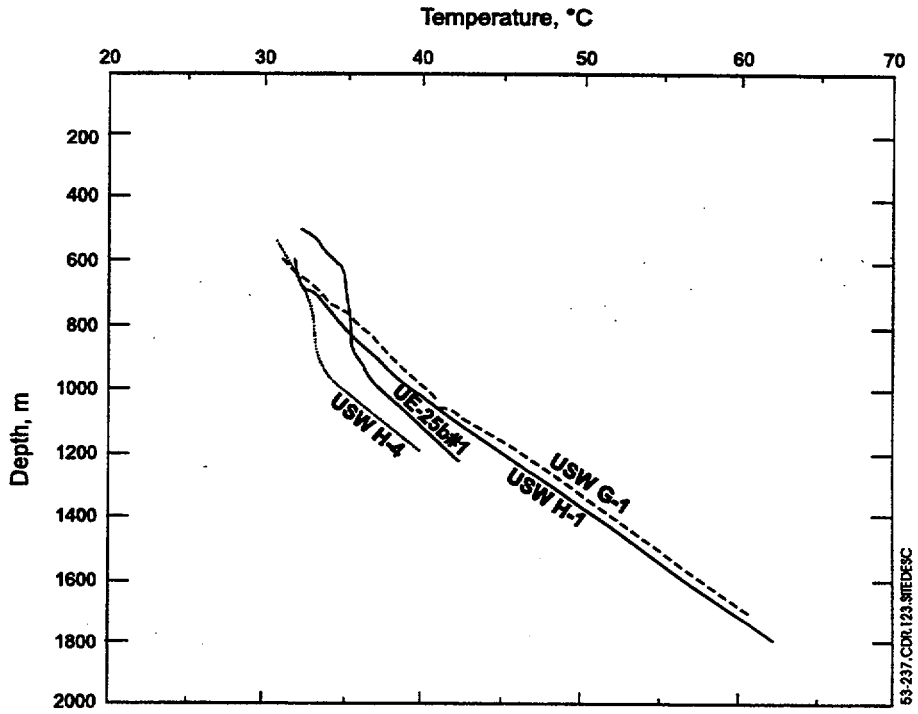

NOTE: from Sass, Lachenbruch et al. 1988

Figure 5.3-237. Temperature Logs for Boreholes in Upper Drillhole Wash and along the Eastern Edge of Yucca Mountain

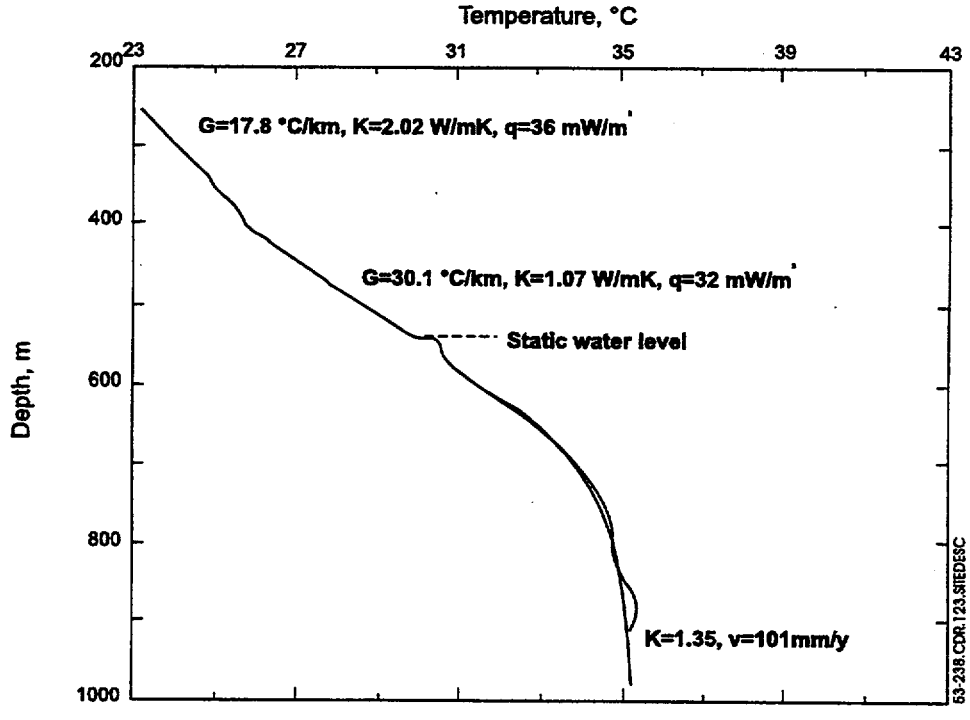

NOTE: after Sass, Lachenbruch et al. 1988, Figure 9

Figure 5.3-238. Temperature Log for USW G-4 and Calculated Curve for One-Dimensional Upward Flow Beneath the Static Water Level in the Borehole

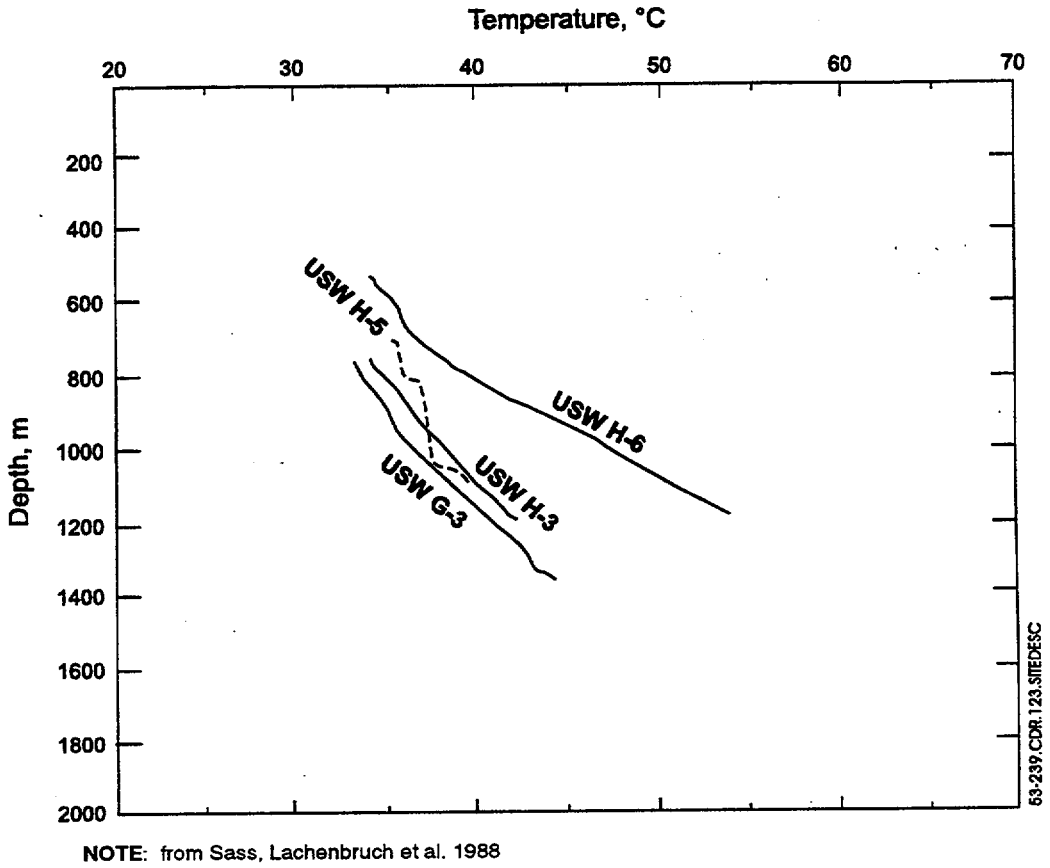

NOTE: from Sass, Lachenbruch et al. 1988

Figure 5.3-239. Temperature Logs for Boreholes in the Vicinity of Solitario Canyon

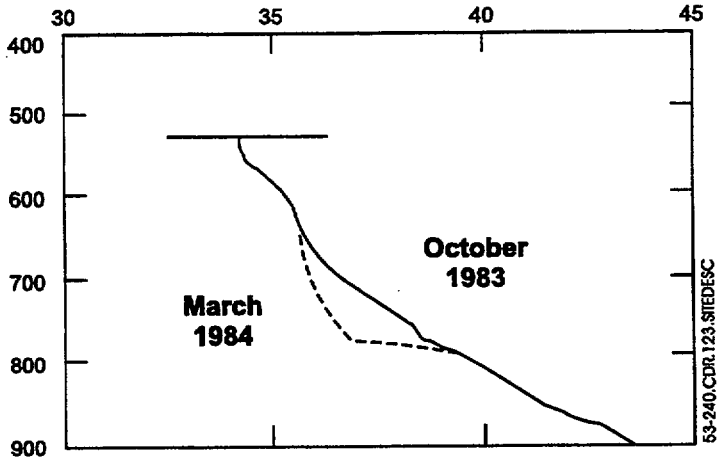

NOTE: from Sass, Lachenbruch et al. 1988

Figure 5.3-240. Temperature Logs for October 1983 and March 1984 in Borehole USW H-6

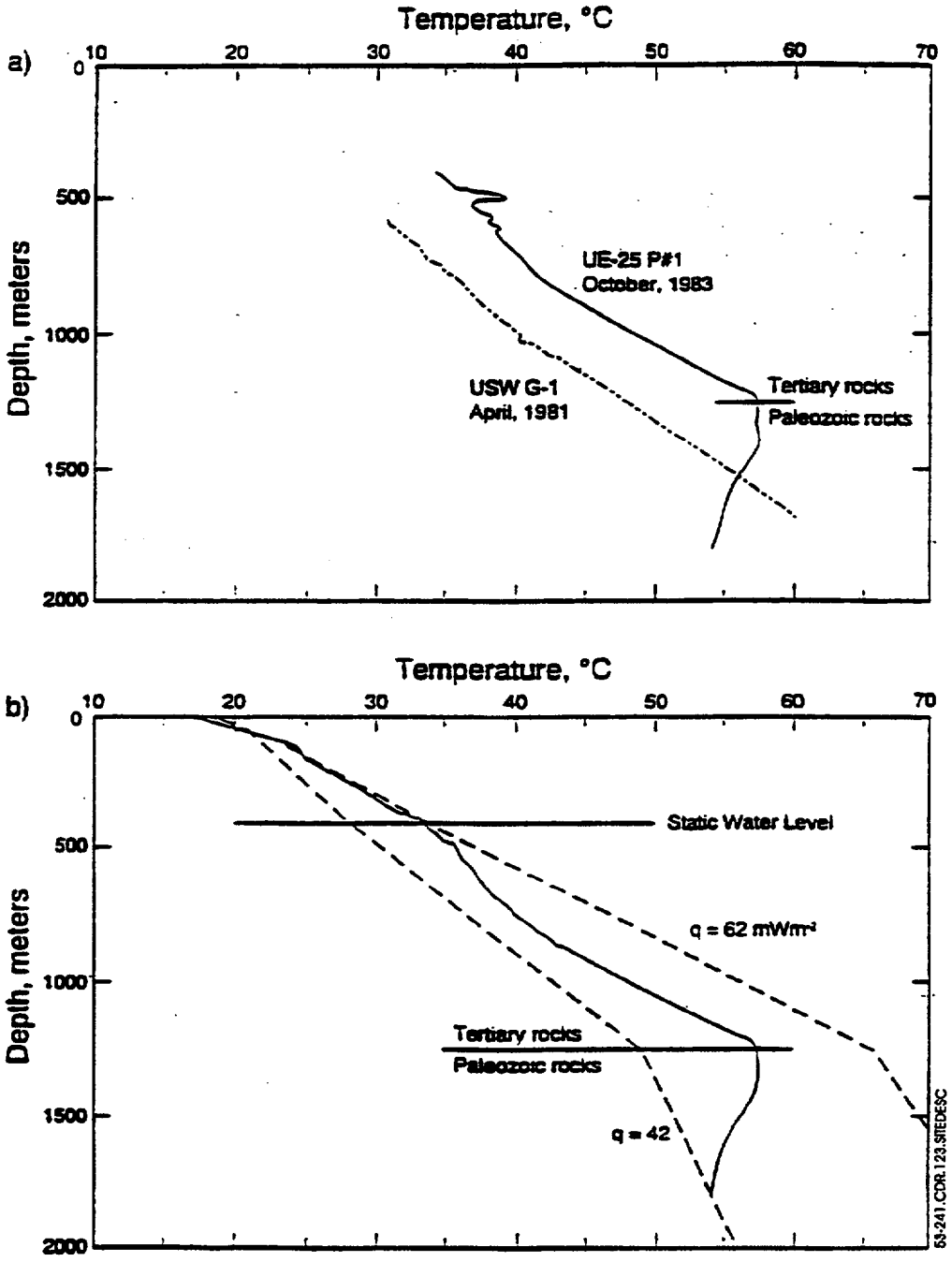

NOTE: The Log of April 1981 for USW G-1 and Calculated Profiles for Conductive Heat Fluxes of 42 and 62 mW m^2 at the UE-25 p#1 Site Are Also Shown for Comparison (from Sass, Dudley et al. 1995, Figure 8.5)

Figure 5.3-241. Temperature Profiles of October 1983 and April 1990 for UE-25

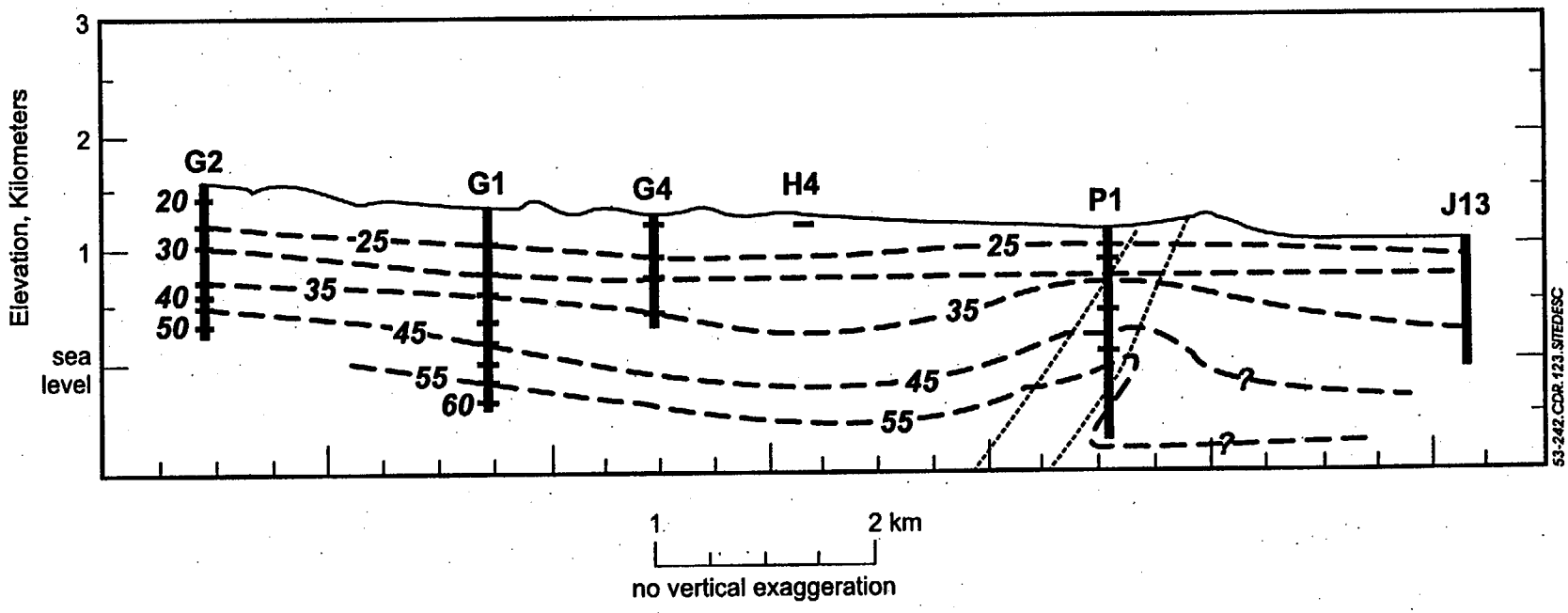

Figure 5.3-242. Interpretive Thermal Cross-Section Between USW G-1 and Well J-13, Showing Upwelling of Isotherms along Faults Intersected in Drillhole UE-25p#1 (adapted from Sass, Lachenbruch et al. 1988)

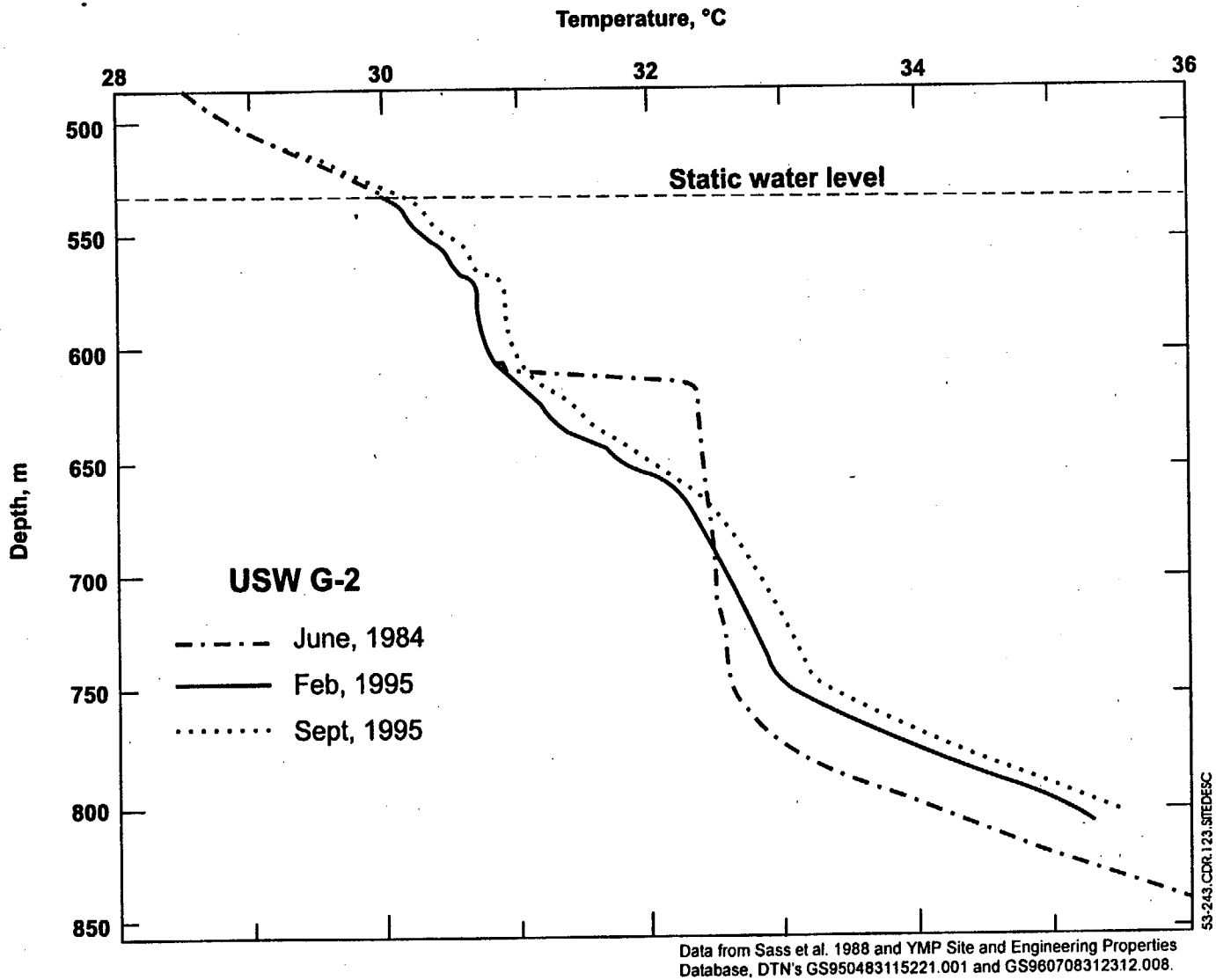

Figure 5.3-243. Sequential Temperature Logs in USW G-2, 1984 and 1995

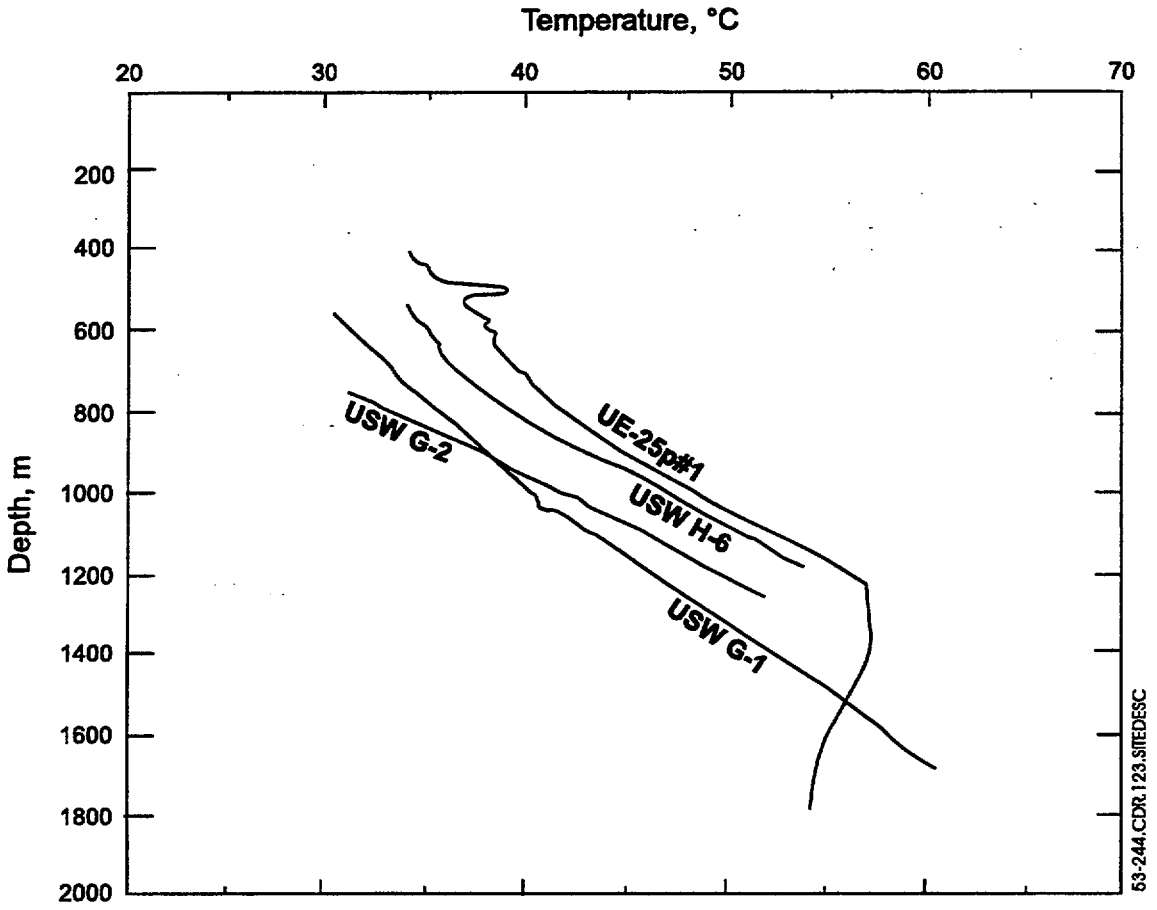

Figure 5.3-244. Saturated-Zone Temperature Logs for USW G-1, USW G-2, USW H-6, and UE-25 p#1 (from Sass, Lachenbruch et al. 1988)

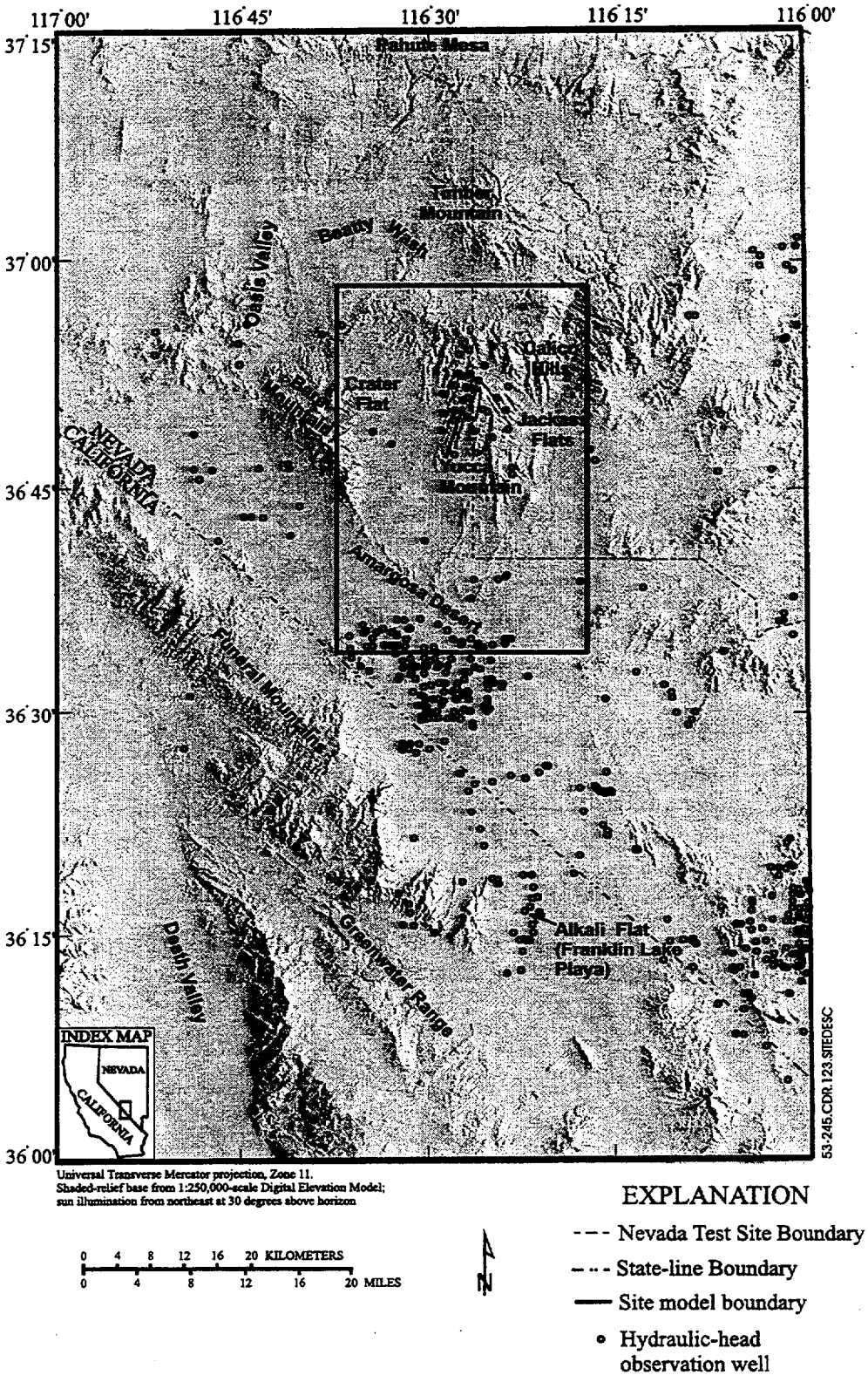

Figure 5.3-245. Location of Model Area, Associated Geographic Features, and Hydraulic-Head Observation Wells

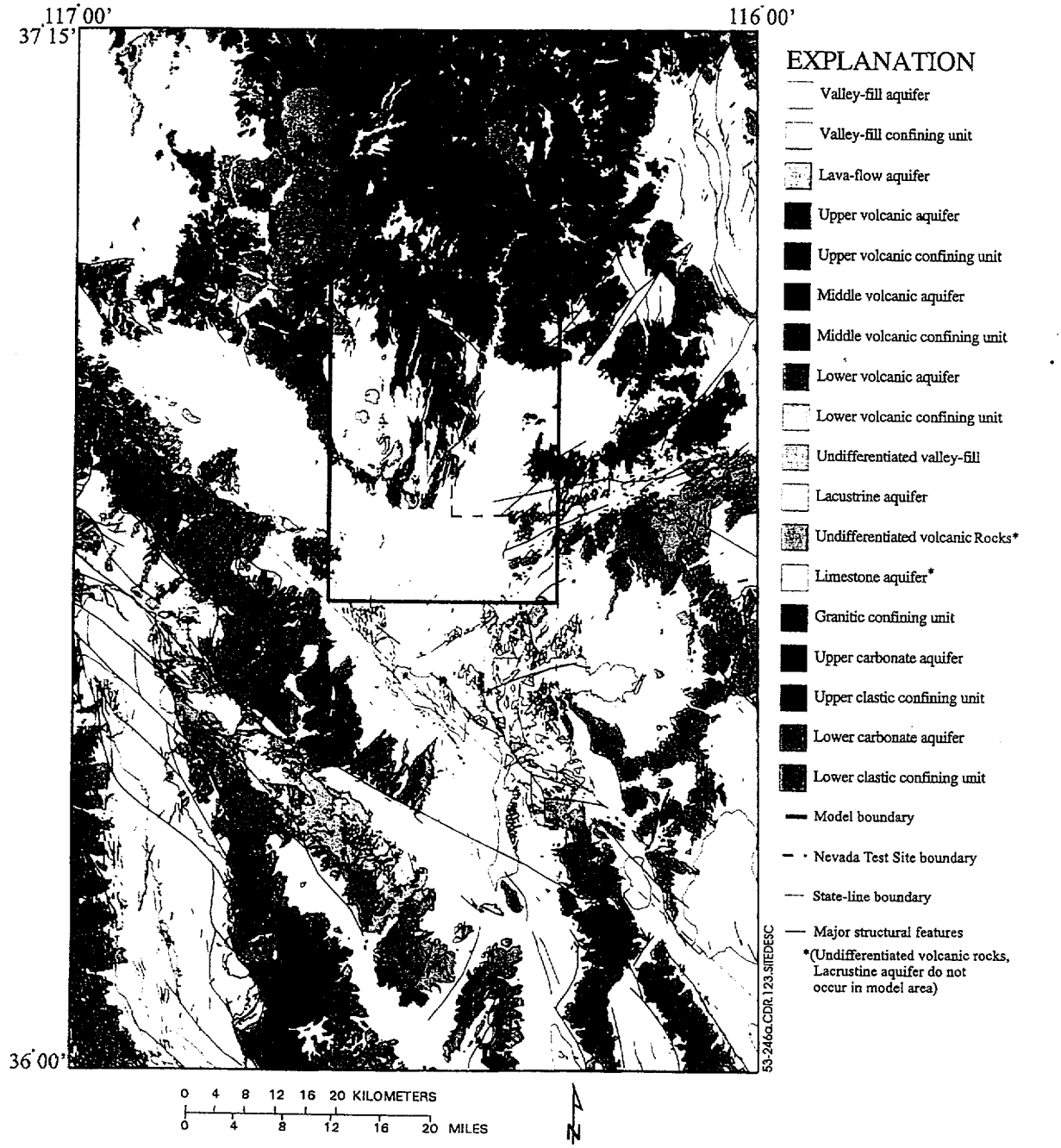

Figure 5.3-246a. Generalized Hydrogeologic Units with Major Structural Features for Region Surrounding the Area of the Site Model

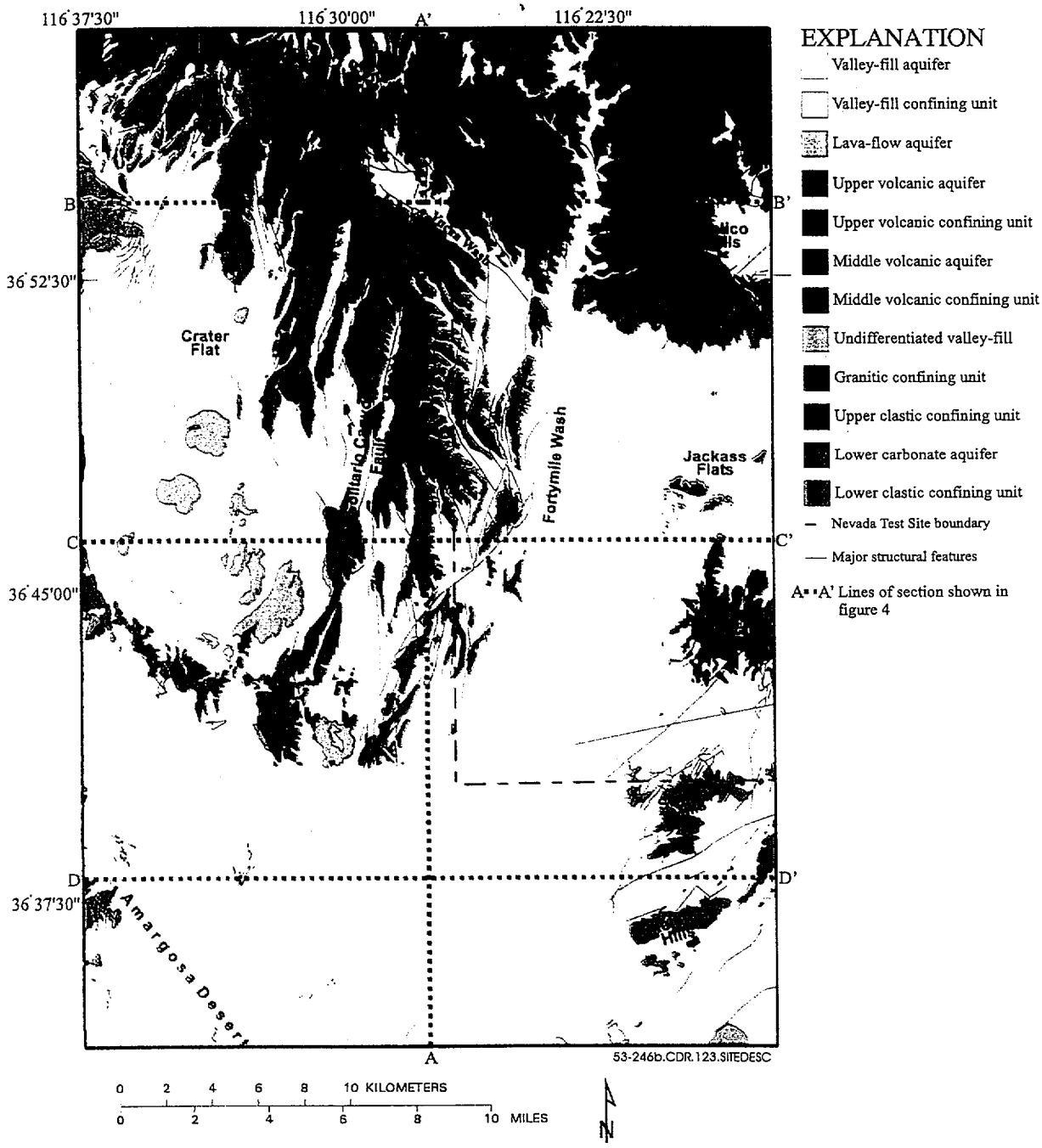

Figure 5.3-246b. Generalized Hydrogeologic Units with Major Structural Features for Lines of Section to the Site Model

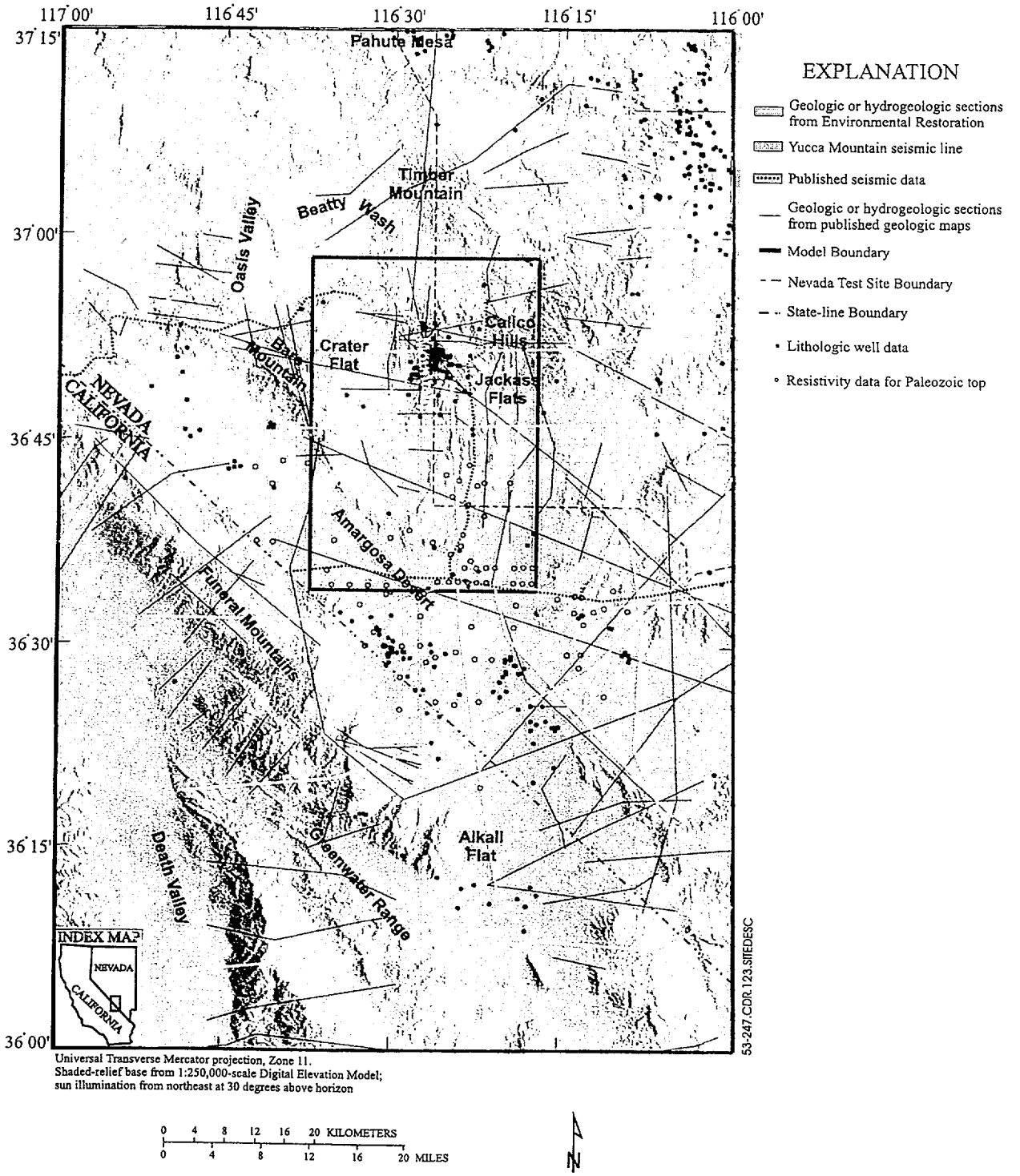

Figure 5.3-247. Geologic, Geophysical, and Well-Data Locations Used in the Construction of the Hydrogeologic Framework Model

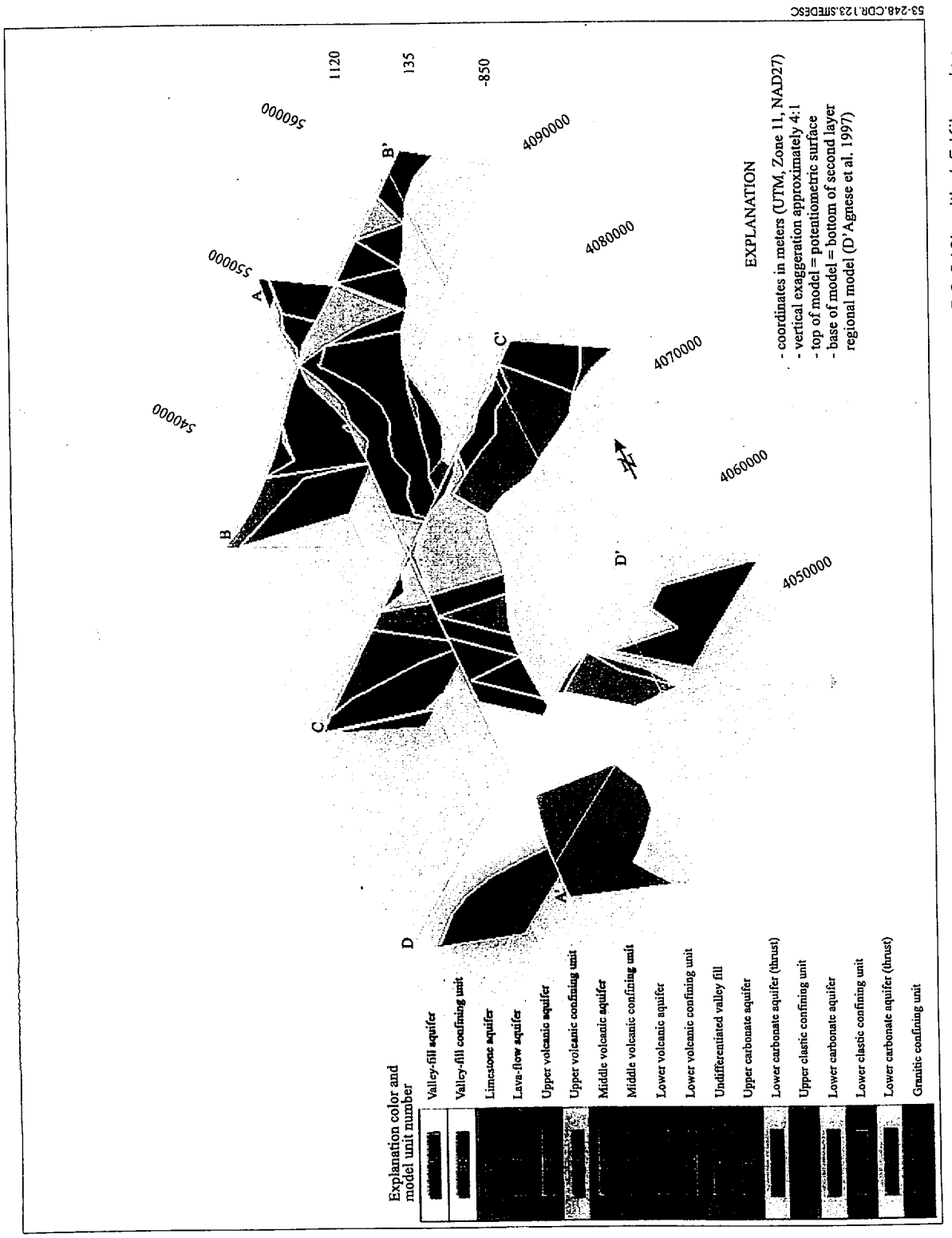

Figure 5.3-248. Fence Diagram Showing Locations Along Lines of Section Shown on Figure 5.3-246b with 1.5 Kilometer Grid Spacing

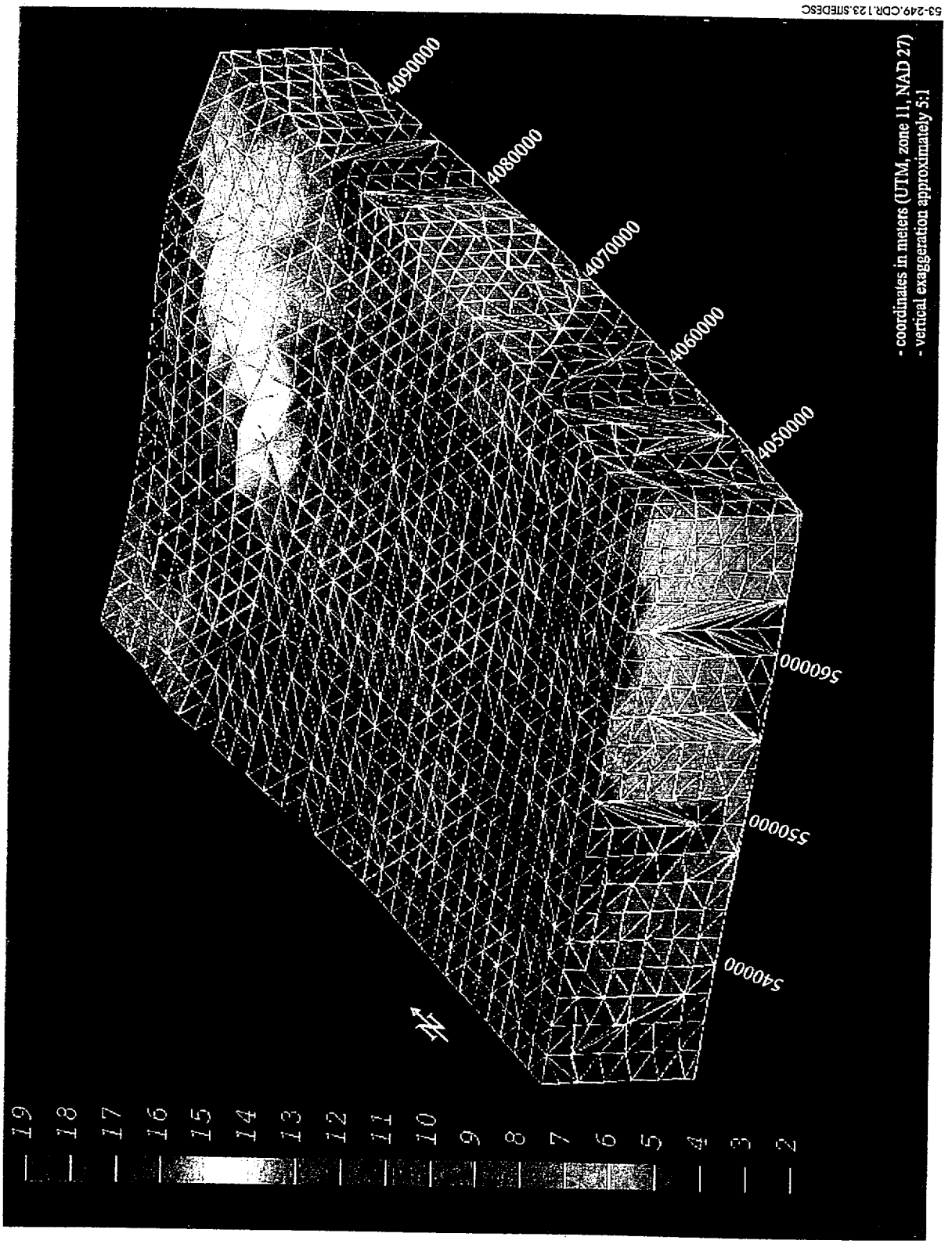

Figure 5.3-249. Three-Dimensional Finite-Element Mesh

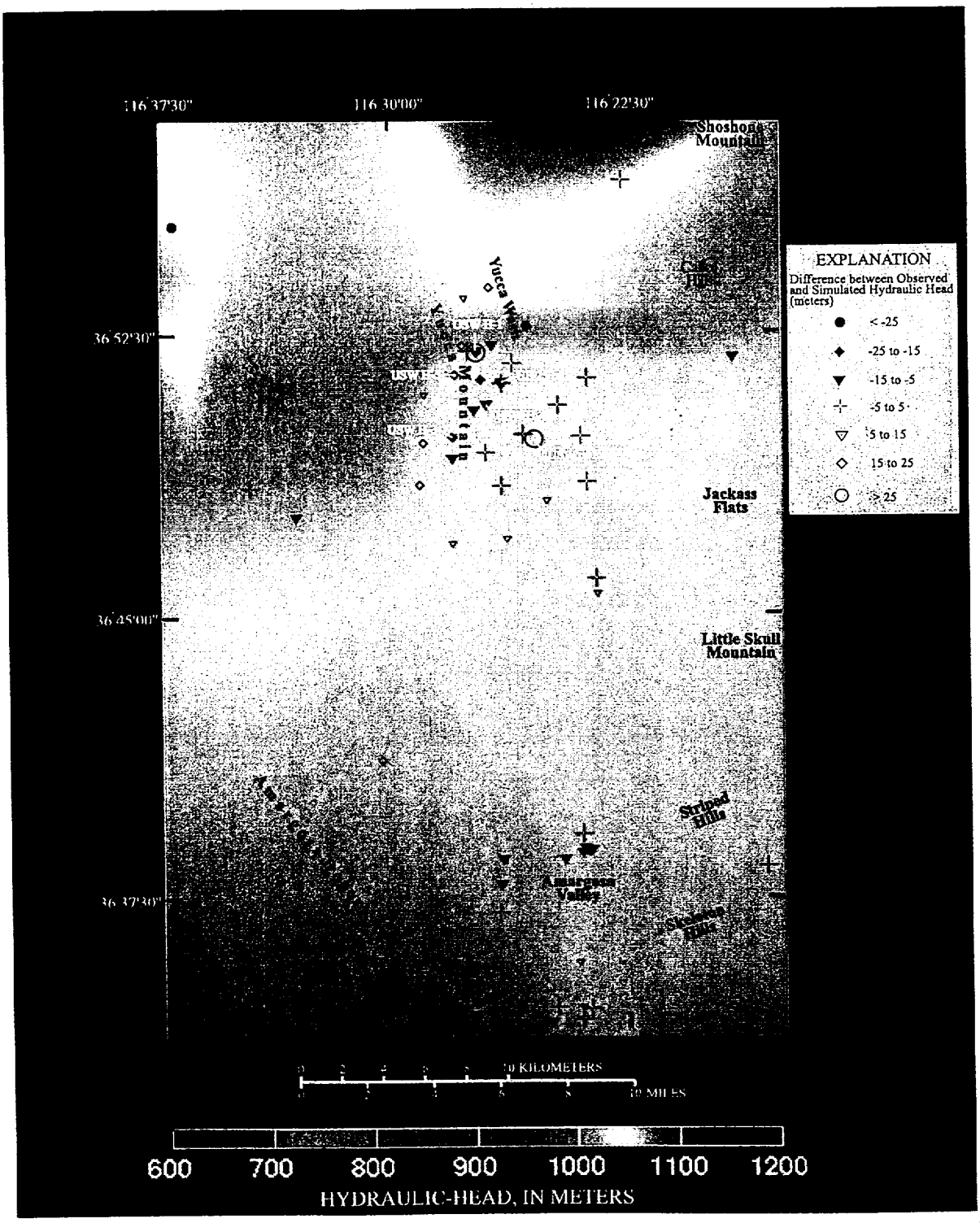

Figure 5.3-250. Simulated Hydraulic Head and Residuals

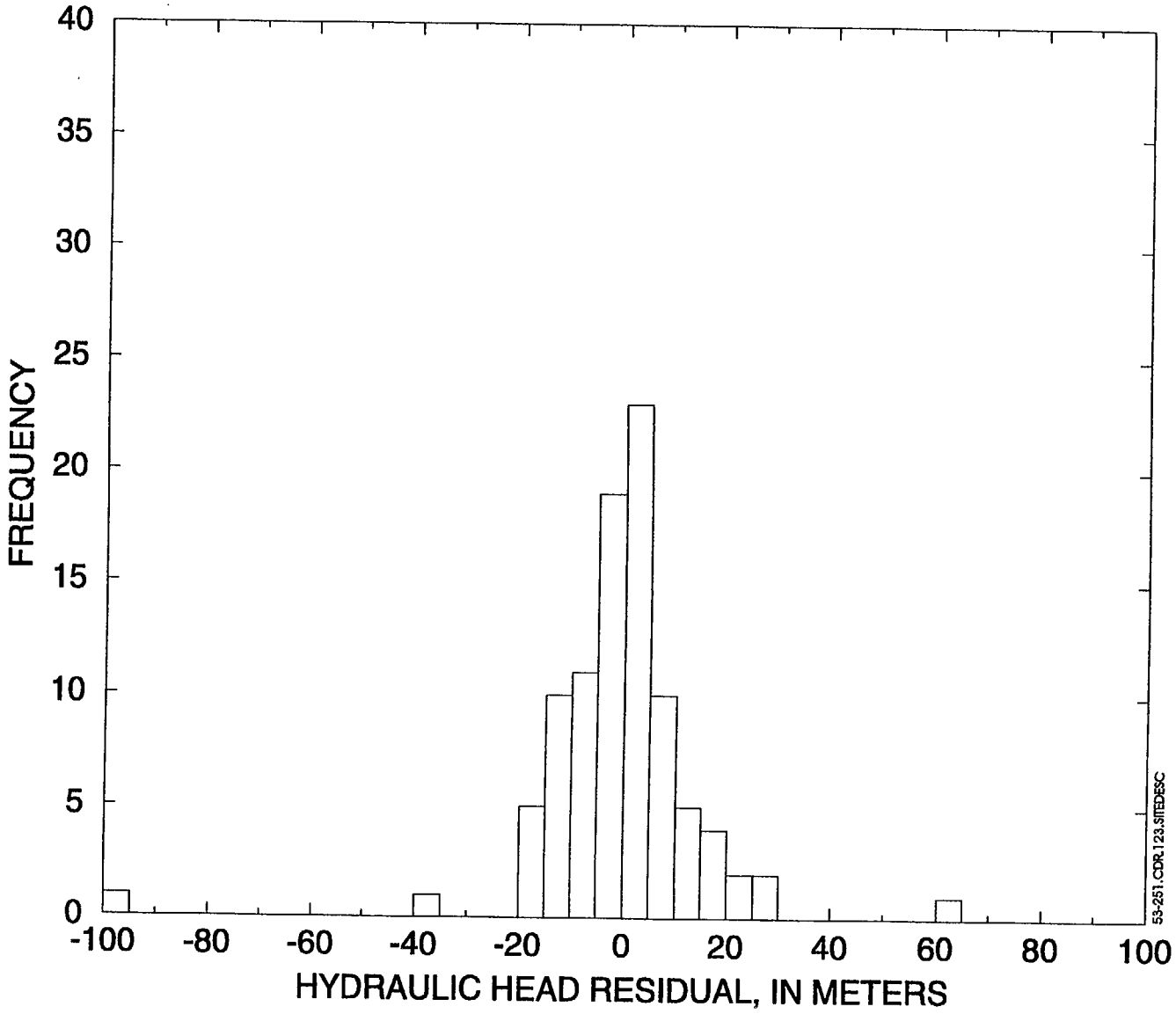

Figure 5.3-251. Histogram of Hydraulic-Head Residuals

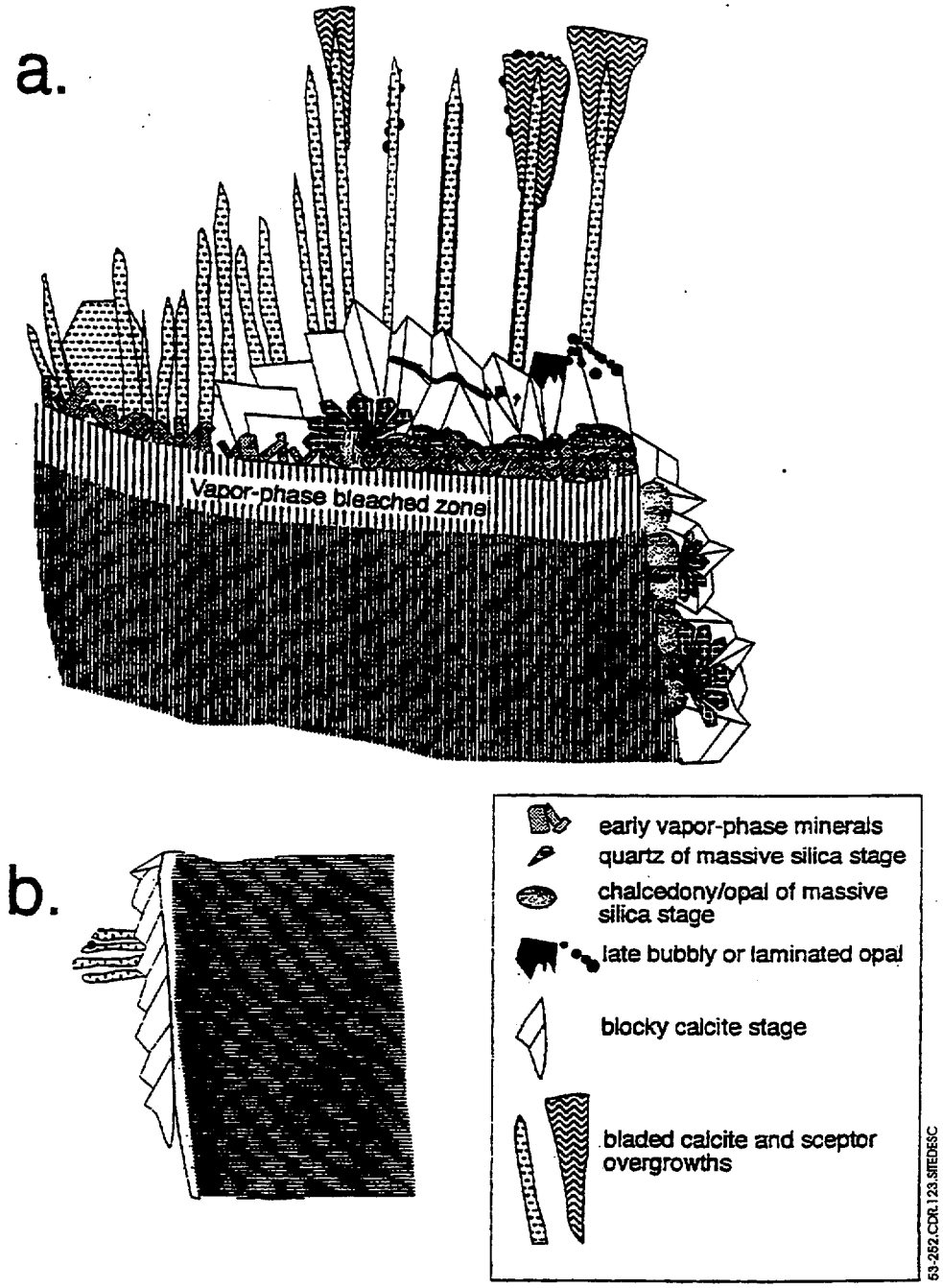

Figure 5.3-252. Schematic Illustrations of the Typical Secondary Mineralization Sequences Found (a) in Lithophysal Cavities and (b) on Fracture Surfaces (from Paces, Neymark et al. 1996)

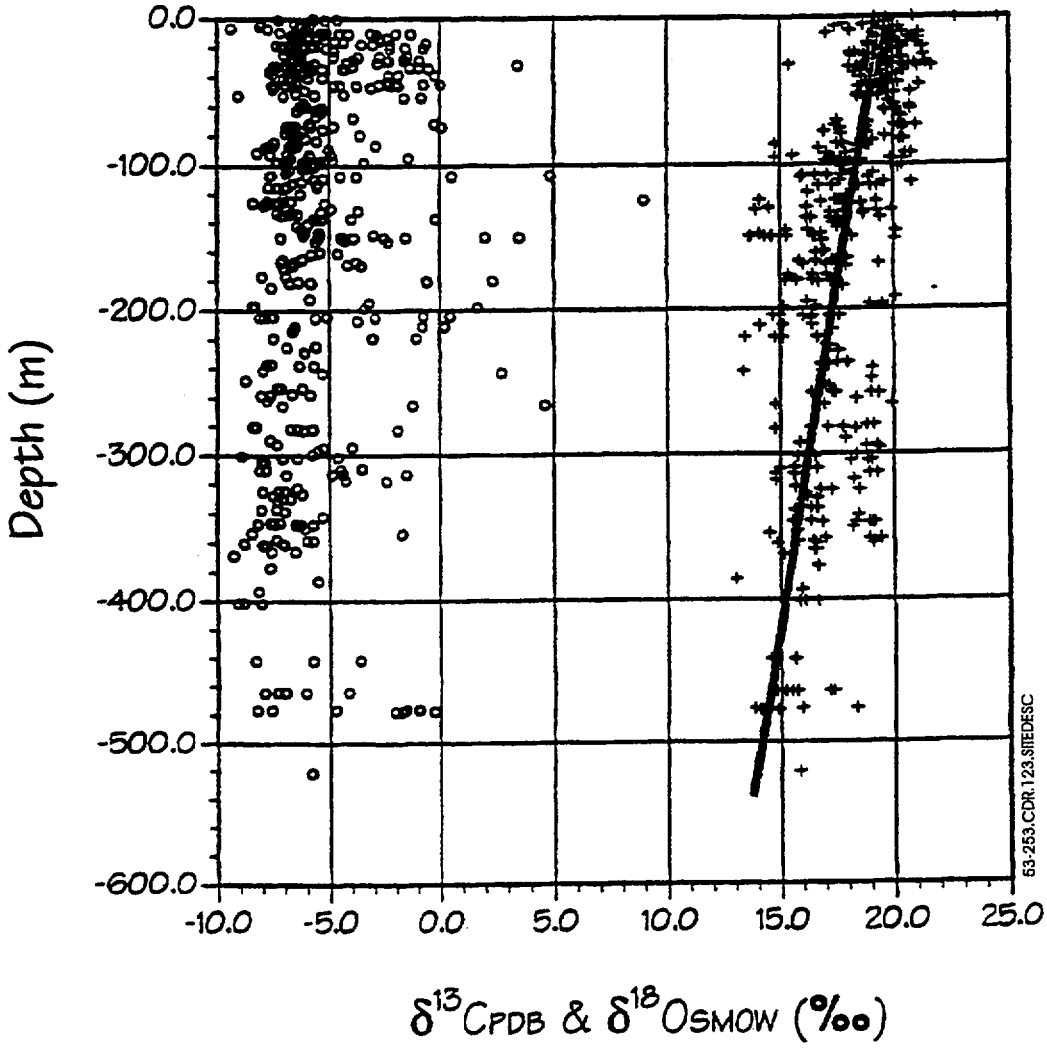

NOTE: The heavy line is the predicted $\delta^{18}O$ of calcite precipitated along a hypothetical geothermal gradient of approximately 34°C/km from water with a $\delta^{18}O$ of -125 ‰.

Figure 5.3-253 Plot of Delta Carbon-13 (circles) and Delta Oxygen-18 (crosses) Values of Calcite Versus Depth (m) Within the Unsaturated Zone

INTENTIONALLY LEFT BLANK